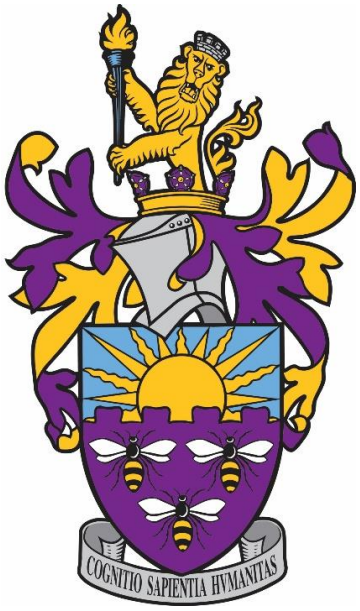

Rare-Earth Cyclobutadienyl and Cyclopentadienyl Complexes: Synthesis, Structure and Magnetism

A thesis submitted to the University of Manchester for the degree of

Doctor of Philosophy

in the Faculty of Science and Engineering

2021

James P Durrant

School of Natural Sciences

Department of Chemistry

Contents

Word count – 62,167

List of Abbreviations

AC	alternating current
BH	bridgehead
C	Raman coefficient
χ_S	adiabatic susceptibility
χ_T	isothermal susceptibility
$\chi''(\nu)$	frequency-dependence of the out-of-phase magnetic susceptibility
$\chi''(T)$	temperature-dependence of the out-of-phase magnetic susceptibility
$\chi_M T(T)$	temperature-dependence of the molar magnetic susceptibility as a function of temperature
Cb	cyclobutadienyl
Cht	cycloheptatrienyl
Cn	cyclononatetraenyl
COT	cyclooctatetraenyl
Cp	cyclopentadienyl
DC	direct current
DFT	density functional theory
DME	dimethoxyethane
FC	field cooled
fc	ferrocene
FTIR	Fourier-transform infrared
FWHM	full width at half maximum
$\boldsymbol{g}$	gyromagnetic tensors
H	magnetic field
H_c	coercive field
Hex	hexane
HMBC	heteronuclear multiple bond correlation
HOMO	highest occupied molecular orbital
^{i}Pr	isopropyl
k_B	Boltzmann constant
KD	Kramers' doublet
Ln	lanthanide

Me	methyl
Mes	mesityl
MVS	metal-vapor synthesis
n	Raman exponent
NMR	nuclear magnetic resonance
Pc	dianion of phthalocyanine
Ph	phenyl
Pn	pentalene
QTM	quantum tunnelling of the magnetization
SMMs	single-molecule magnets
SQUID	superconducting quantum interference device
τ	relaxation time
τ_0	attempt relaxation time
T_H	maximum open hysteresis temperature
TA-QTM	thermally assisted quantum tunnelling of the magnetization
T_B	magnetic blocking temperature
^{t}Bu	tert-butyl
THF	tetrahydrofuran
Tol	toluene
τ_{QTM}^{-1}	rate of quantum tunnelling of the magnetisation
ttt	tri-tert-butyl
U_{eff}	effective energy barrier
ω	angular frequency
ZFC	zero-field cooled

Abstract

Cyclic π-conjugated organic ligands are widely used in rare-earth organometallic chemistry, and our group in particular has shown that cyclopentadienyl ligands are extremely effective in the synthesis of high-performance single-molecule magnets (SMMs). These remarkable magnetic properties are due to the strong axial ligand field that the monoanionic cyclopentadienyl ligands provide, with recent results including the record-breaking SMM $[Dy(\eta^5\text{-}C_5{}^{i}Pr_5)(\eta^5\text{-}C_5Me_5)]^+$.

This thesis focuses on the coordination chemistry of a dianionic cyclobutadienyl ligand in rare-earth chemistry, *i.e.* $[C_4(SiMe_3)_4]^{2-}$. My work on the fundamental coordination chemistry of the cyclobutadienyl ligand towards rare-earth elements and the reactivity of the new complexes is presented herein, in addition to the SMM properties of exemplar systems.

The work presented in this thesis shows that cyclobutadienyl ligands can effectively replace cyclopentadienyl ligands in structurally similar rare-earth complexes, resulting in improved SMM properties. This thesis extends our understanding of magneto-structural correlations currently used in the design of high-performance organometallic rare-earth SMMs, and demonstrates that cyclobutadienyl-ligated SMMs should have the potential to surpass the current records set by bis-cyclopentadienyl dysprosium SMMs.

Declaration

No portion of the work referred to in the thesis has been submitted in support of an application for another degree or qualification of this or any other university or other institute of learning

Copyright Statement

1 The author of this thesis (including any appendices and/or schedules to this thesis) owns certain copyright or related rights in it (the "Copyright") and s/he has given The University of Manchester certain rights to use such Copyright, including for administrative purposes.

1 Copies of this thesis, either in full or in extracts and whether in hard or electronic copy, may be made only in accordance with the Copyright, Designs and Patents Act 1988 (as amended) and regulations issued under it or, where appropriate, in accordance with licensing agreements which the University has from time to time. This page must form part of any such copies made.

1 The ownership of certain Copyright, patents, designs, trademarks and other intellectual property (the "Intellectual Property") and any reproductions of copyright works in the thesis, for example graphs and tables ("Reproductions"), which may be described in this thesis, may not be owned by the author and may be owned by third parties. Such Intellectual Property and Reproductions cannot and must not be made available for use without the prior written permission of the owner(s) of the relevant Intellectual Property and/or Reproductions.

1 Further information on the conditions under which disclosure, publication and commercialisation of this thesis, the Copyright and any Intellectual Property and/or Reproductions described in it may take place is available in the University IP Policy (see http://documents.manchester.ac.uk/DocuInfo.aspx?DocID=2442 0), in any relevant Thesis restriction declarations deposited in the University Library, The University Library's regulations (see http://www.library.manchester.ac.uk/about/regulations/) and in The University's policy on Presentation of Theses.

Acknowledgements

First and foremost, I would like to give my thanks to Richard for giving me an opportunity to carry out a PhD in his research group, and subsequently for all his supervision and support over the course of my studies. I've thoroughly enjoyed the experience, despite the many ups and downs on the rollercoaster that is academic research.

I would also like to extend my thanks to Dr Neil Burton, Professor David Collison and the PGR Chemistry Admin team at Manchester for all of their help during the course of my studies.

Of course, there are many past and present colleagues from the Layfield group to thank for all of their friendship and support during my time in the group, and I'm sorry that I can't name all of you here. However, I'm very grateful to you all for creating such a friendly and sociable work environment. In particular, special thanks go to Dr Benjamin Day for showing me the 'air-sensitive' ropes, for all of your advice during (and after) your time in the group, and of course for sparking up such an amazing project for me to be a part of. I learnt a lot from you in my first few years, and for that I'm very grateful. I would also like to extend my thanks to Dr Nikos Tsoureas, whose knowledge and expertise has been incredibly valuable. Thank you for always being there to help with (literally) anything, and I'm definitely a better chemist for having the pleasure to have worked with you over the past few years. I'd also like to thank Dr Maria Jose Heras Ojea for all of your help during (and after) your time in the group, and for showing me the 'magnetism' ropes! Finally, I'd like to thank Dr Fu-Sheng Guo for all of your help during your time in the group, I'll never forget your amazing advice, should be fine! To the Wednesday Wastemen, thank you for all the fun and games during my time at Sussex and especially during lockdown. Finally, to the squash crew, thanks for all the fun times and beers after work!

To all of my friends and family, thank you so much for all of your support over the course of my PhD, I'm extremely lucky to have such wonderful people in my life. A huge thanks go to Team Chump, for all of your friendship over the years and for pretending to be interested in tiny magnets. To Mike, Bethan, Carys, Ferris and Huey, thank you for such a warm welcome and fantastic place to live during my time in Sussex, I'm extremely grateful to you all for keeping me sane and always having someone to talk to!

Finally, to my sister, mother, and grandparents, I cannot thank you enough for everything that you've done for me. Thank you for pushing me to succeed all those years ago, I'll never forget how much that has influenced my outlook on life. Thank you for always being there for me. Love and hugs to you all.

To my future wife Verity, there are no words to explain how grateful I am for everything you do for me. I'm so glad that we've come through our PhDs together and had this shared experience. I cannot wait to spend the rest of my life with you.

For these reasons I would like to dedicate this thesis to you all, as I wouldn't be here without you.

Chapter 1

Introduction

1.1. Single-Molecule Magnets

1.1.1. Discovery and fundamentals

Single-molecule magnets (SMMs), initially identified in 1993,[1–3] are complexes that possess an effective energy barrier (anisotropy barrier, U_{eff}) to the reversal of their magnetization, often but not always in the absence of an applied magnetic field. This results in magnetic bistability, otherwise known as hysteresis, up to a certain temperature, known as the magnetic blocking temperature (T_B). These properties are entirely molecular in origin and give SMMs potential applications in next generation nanoscale devices, such as high-density information storage and quantum computing.[4–9] This is however, provided that several challenges associated with SMMs can be overcome: firstly, extremely low temperatures are normally required in order to observe any magnetic bistability and, secondly, the U_{eff} of a complex does not correlate with its ability to display magnetic hysteresis with an appreciable coercive field (H_c). This is because more efficient, temperature-independent relaxation mechanisms such as quantum tunnelling of the magnetization (QTM) can result in rapid loss of magnetization at zero-field. Therefore, the targeted synthesis of high-performance SMMs presents a formidable challenge. Nevertheless, almost three decades of research into these systems have significantly advanced our understanding of how to manipulate and improve properties via elegant design strategies.

SMMs are routinely characterised using superconducting quantum interference device (SQUID) magnetometry, where the characteristic behaviour of an SMM is its ability to display slow magnetic relaxation. This is typically observed as a temperature- and frequency-dependence of the out-of-phase magnetic susceptibility, *i.e.* $\chi''(T)$ and $\chi''(\nu)$, respectively. In these AC susceptibility measurements, peaks in χ'' occur due to the magnetization of the sample lagging behind that of the small dynamic magnetic field. Across the temperature range that these maxima occur, relaxation times (τ) can be extracted and used to determine the resulting U_{eff} by fitting the natural log of the relaxation time *vs.* inverse temperature, *i.e.* $\ln\tau(T^{-1})$.[10,11] The shape of the $\ln\tau$ *vs.* T^{-1} plot gives information as to which relaxation processes are dominant at a given temperature. For example, the high-temperature region is typically dominated by thermal relaxation,

whereas the low-temperature regions can be dominated by quantum tunnelling of the magnetization (QTM) (Figure 1).

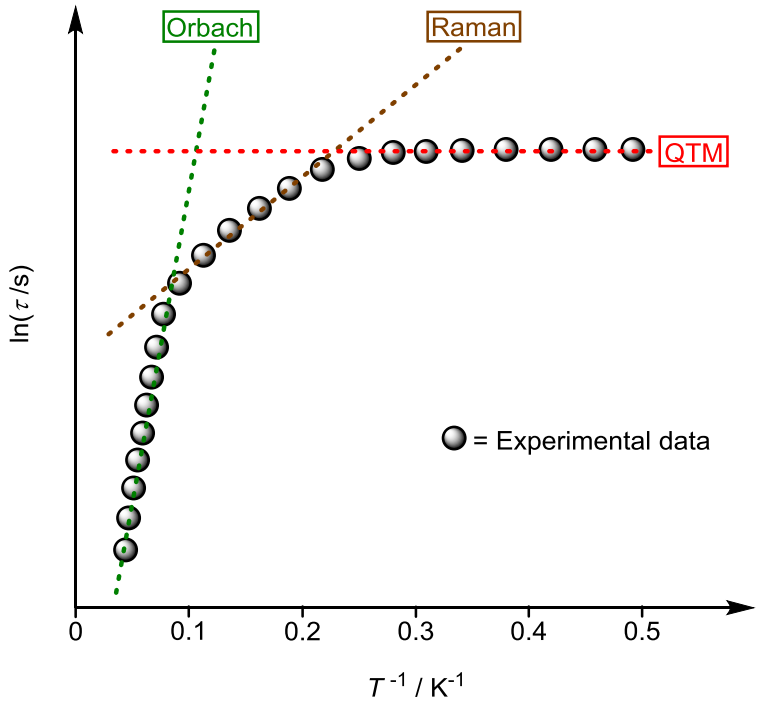

Figure 1. $\ln\tau$ (T^{-1}) graph for a hypothetical lanthanide SMM.

The occurrence of magnetic bistability is a prerequisite for any SMM to be considered in a potential information storage device. Hence, the magnetic blocking temperature (T_B) is an important metric along with U_{eff} for determining the success of an SMM. Unfortunately, there is not a singular way to define T_B, and several methods are routinely used throughout the literature which can additionally be influenced by the sweep rate of the magnetic field. A sweep rate of 5-50 Oe s^{-1} is generally observed for most compounds in the literature, however this can vary up to 700 Oe s^{-1} which is considered to be extremely fast. Therefore, comparisons between any forms of T_B should be made cautiously.[12–14] One of the most common methods is the highest temperature at which open hysteresis (T_H) is observed in the field dependence of the magnetization when sweeping from a positive (+H) to negative (−H) field and vice versa (Figure 2). For simplicity and comparative purposes, this method of T_B will be employed throughout discussion in this thesis. The other two methods of determining T_B are: the temperature at which the field cooled (FC) and zero-field cooled (ZFC) susceptibility diverge, and the temperature at which the relaxation time (τ) is 100 s.[12–15]

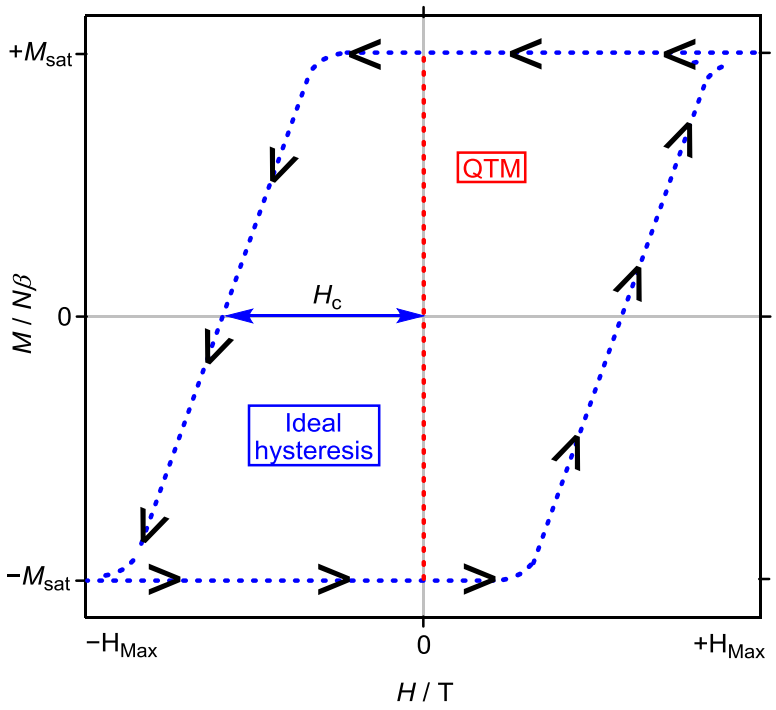

Figure 2. Hysteresis measurement for a hypothetical SMM. Black arrows represent the direction in which the magnetic field is being driven, blue lines represent an ideal loop with appreciable coercivity (H_c) and the red line represents the loss of magnetization at zero-field due to QTM.

1.1.2. Rare-earth SMMs

The chemistry of the rare-earth elements, otherwise known as the lanthanides, is dominated by the (+3) oxidation state, which is largely a consequence of the radially contracted nature of the 4f valence orbitals that are well shielded by the filled 5s and 5p orbitals. Typically, upon the removal of three electrons, the 4f orbitals are stabilized to such a degree that the remaining 4f electrons are chemically inaccessible. This is reflected in the fourth ionization energies, which are greater than the sum of the first three ionization energies in all cases. The most common exception to this is for europium and ytterbium, which have large values for their third ionization energies due to the additional stabilization of their respective half and full 4f orbitals in the (+2) oxidation state.

The shielding of the 4f orbitals results in negligible overlap with ligands, resulting in predominantly electrostatic bonding in lanthanide compounds and only a small crystal field splitting. An important consequence of this scenario for the lanthanides is that the orbital contribution to the magnetic moment is essentially unquenched. This makes lanthanides

attractive targets for SMMs, as those Ln^{3+} ions with strong spin-orbit coupling (SOC) possess an inherently large magnetic anisotropy, *i.e.* a directional preference of their magnetic moments. Therefore, 4f electron-electron repulsion and spin-orbit coupling dominate the electronic structure of Ln^{3+} ions, which are well defined by the Russell-Saunders coupling method to give ground state term symbols described as $^{2S+1}L_J$. This method considers that all of the electrons combine to form a total atomic orbital angular momentum (*L*), which couples with the total spin angular momentum quantum number (*S*) to give the total atomic angular momentum (*J*). The ground states produce 2*J*+1 crystal field states (M_J), which are degenerate in the absence of a crystal field, however when subjected to a crystal field of appropriate symmetry the degeneracy is lifted and creates a barrier which separates opposite orientations of the magnetic ground state. Consequently, the anisotropy barrier in SMMs can be manipulated by controlling the strength and the symmetry of the crystal field of the lanthanide ions.[16]

Since the discovery of the first Ln-based SMM $[Tb(Pc)_2]^-$ (Pc = dianion of phthalocyanine),[17] the most popular lanthanides utilised in SMMs are terbium, dysprosium and erbium, which have very strong SOC and possess the largest magnetic moments. Importantly, these elements have a strong angular dependence of the total 4f charge densities for their respective M_J ground states. For example, in the case of Tb^{3+} and Dy^{3+}, they display an oblate-spheroid shaped magnetic M_J ground state, whilst Er^{3+} has a prolate-spheroid shaped magnetic M_J ground state (Figure 3).[16,18] Thus, by applying an axial crystal field to Tb^{3+} and Dy^{3+} complexes, or an equatorial crystal field to Er^{3+} complexes, the magnetic ground states with the largest M_J values are stabilised whilst simultaneously destabilising the least magnetic ground states.[16]

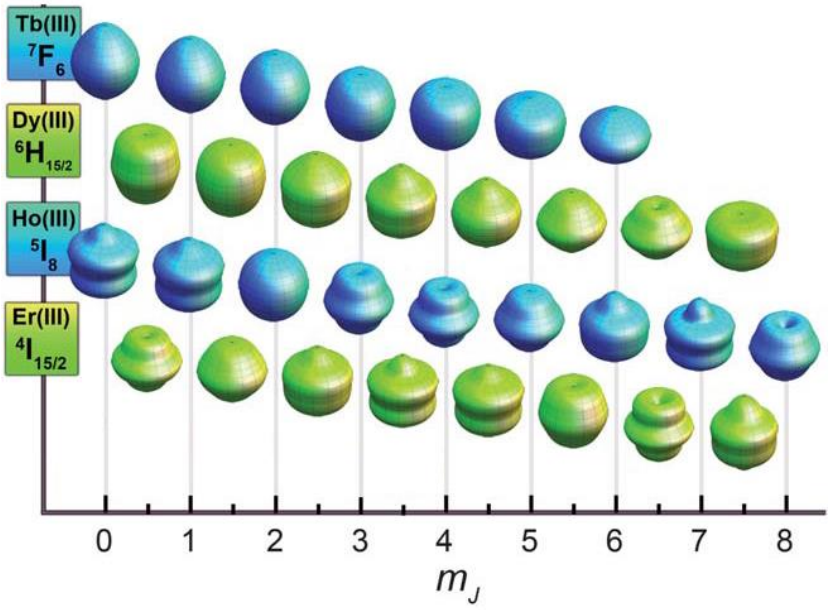

Figure 3. Approximations of the angular dependence of the total 4f charge densities of respective M_J states for Tb^{3+}, Dy^{3+}, Ho^{3+} and Er^{3+}.[16]

The strength of the crystal field is therefore a vital consideration when designing SMMs. For an appropriate molecular geometry, the stronger the crystal field, the larger the anisotropy of the system, which results in larger energy barriers to the reversal of magnetization. It should be noted however that large U_{eff} values do not typically correlate to large blocking temperatures and open hysteresis, which demonstrates the complicated nature of high-performance SMMs. This is because the magnetic relaxation in SMMs can occur via multiple relaxation processes. For example, Dy^{3+} is a Kramers' ion due to its half-integer total spin ($4f^9$) and, therefore, the M_J states occur as a series of eight Kramers' doublets (KD), which are guaranteed to be doubly degenerate.[19] Thus, the ideal magnetic relaxation is via a thermal Orbach process which proceeds via the absorption of acoustic phonons from the lattice, which allows the system to relax from the ground KD (M_J = +15/2) up to the highest KD and then back down the opposite states via the emission of phonons until the opposite ground KD (M_J = −15/2) becomes populated and reaches equilibrium. The energy corresponding to this process gives rise to the U_{eff} of the system. However, in reality, the majority of SMMs feature a complicated mixture of relaxation processes such as Raman, QTM, direct relaxation and thermally assisted QTM (TA-QTM), which reduce the amount of energy of the relaxation process and affect the temperature at which the SMM displays slow magnetic relaxation properties (Figure 4).[14,15]

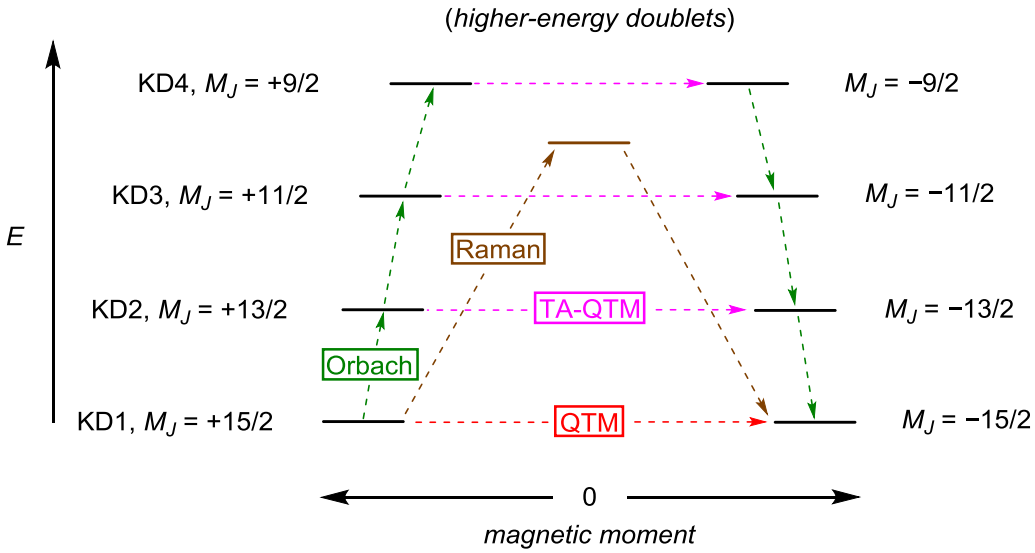

Figure 4. A simplified representation of the four lowest energy KDs (out of a total of eight) and the possible relaxation processes observed in a Dy^{3+} ($^6H_{15/2}$) SMM in an axial crystal field.

Magnetic relaxation via temperature-independent QTM is therefore the most detrimental process and is responsible for the precipitous loss of magnetization at zero-field, which is commonly observed. Therefore, the suppression of QTM in SMMs is of utmost importance to increase the temperatures at which SMMs operate and observe magnetic hysteresis with remanence. Throughout the past three decades of research into SMMs, several methodologies have successfully been employed to this end, such as manipulating the crystal field and increasing the local symmetry of the Ln^{3+} environment.[10,20–27] The introduction of radical bridging ligands between multiple metal centres has also proven to be effective.[28–30] Strategies based on the former have resulted in some of the largest U_{eff} and T_H values to date, whereas the latter are responsible for the most impressive hysteresis properties, including the largest H_c values.

The work carried out in this thesis is based on the strategy of manipulating the crystal field, specifically around Dy^{3+} ions. As Dy^{3+} has an oblate-spheroid shaped electron density, employing a strong axial crystal field increases the anisotropy of the system. Crucially however, if the equatorial component of the crystal field is negligible, relaxation via QTM is suppressed as mixing between the low-lying M_J states is extremely weak. Therefore, modification of the strength of the axial crystal field around Dy^{3+} ions presents an opportunity to improve upon the current state-of-the-art SMMs, provided equatorial ligand coordination can be prevented.

1.2. Organometallic Lanthanide SMMs with Cyclic π-Conjugated Ligands

1.2.1. Background

Cyclic π-conjugated ligands in lanthanide organometallic chemistry are well established, whereby such complexes have advanced our fundamental understanding of lanthanide oxidation states and bonding, in addition to showing applications in areas such as catalysis,[31–33] small-molecule activation,[34,35] and molecular magnetism.[36–39] Complexes incorporating 5-9 membered carbocyclic rings in organometallic lanthanide SMMs are all known, however the smaller 4-membered cyclobutadiene is completely unknown to rare-earth elements, save for our initial studies (Figure 5).

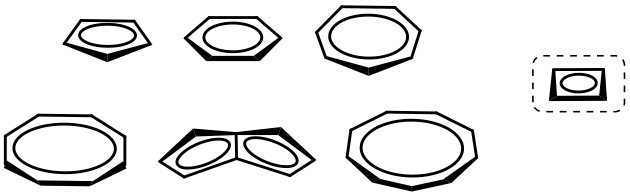

Figure 5. Cyclic π-conjugated ligands discussed in this chapter.

This chapter focuses on cyclic π-conjugated ligands in organometallic lanthanide SMMs, from their relatively recent discovery to current state-of-the-art systems. In addition, earlier seminal discoveries are included where appropriate to illustrate their influence on f-element chemistry. These are ordered via ligand hapticity from η^5-η^9 systems, and finally, the η^4-cyclobutadienyl ligand is introduced, which provides context for the inspiration and work in this thesis.

1.2.2. η^5-Cyclopentadienyl ligands

The venerable 5-membered cyclopentadienyl $[Cp]^-$ ligand is synonymous with organometallic lanthanide chemistry, ever since the inception of the field in 1954 by Birmingham and Wilkinson. The *tris*-cyclopentadienyl complexes $[Ln(\eta^5\text{-}C_5H_5)_3]$ (Ln = Y, La, Ce, Pr, Nd, Sm, Gd, Dy, Er, Yb) were formed in the salt metathesis reactions of $LnCl_3$ with three equivalents of [NaCp] (Scheme 1).[40,41]

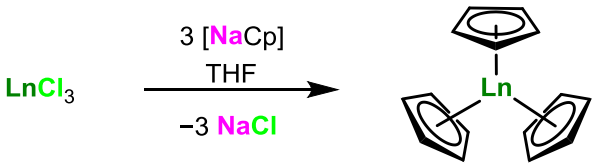

Scheme 1. Synthesis of $[Ln(\eta^5\text{-}C_5H_5)_3]$ (Ln = Y, La, Ce, Pr, Nd, Sm, Gd, Dy, Er, Yb).[40,41]

The monoanionic $[Cp]^-$ ligands are excellent candidates for stabilising the large electropositive lanthanides, with the added ability to fine-tune the substituents and control steric bulk making them very attractive ligands for experimental 'bottom-up' approaches to complex design. Thus, $[Cp^R]^-$ ligands are extremely common in lanthanide chemistry, which gives a large scope for employing these ligands in the synthesis of lanthanide SMMs (Figure 6), whereby subtle manipulation of the crystal field can result in substantial differences in magnetic properties.[14,42]

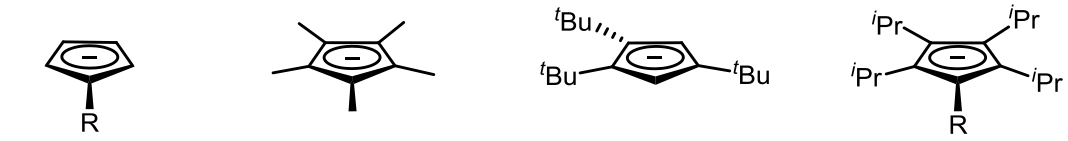

Cp: R = H
Cp^{Me}: R = Me

Cp*

Cp^{ttt}

Cp^{iPr4}: R = H
Cp^{iPr5}: R = ^{i}Pr

Figure 6. Commonly used cyclopentadienyl ligands in organometallic lanthanide SMMs.

With most lanthanides being stable in the trivalent oxidation state, Cp-ligated lanthanide SMMs fall into three general categories: (1) half-sandwich complexes that feature a Cp^R ligand and two additional anionic (X) ligands, *i.e.* $[CpLnX_2]$; (2) sandwich complexes that feature two Cp^R ligands and an X ligand, *i.e.* $[Cp_2LnX]$, and; (3) metallocene complexes, *i.e* cationic sandwich complexes that feature two bulky Cp^R ligands and a non-coordinating

counter anion to balance the charge, *i.e.* $[Cp_2Ln][X]$ (Figure 7). In all of these complexes, the Cp^R ligands typically occupy an axial coordination site, which makes them well-suited to stabilising lanthanides with oblate-spheroid shaped electron density, *i.e.* Dy^{3+} and Tb^{3+}. However, it took six years of experimental research and theoretical calculations to develop the magneto-structural correlations that have resulted in the record-breaking properties observed in state-of-the-art dysprosium metallocene cations.

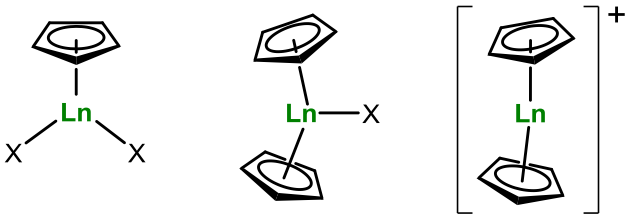

Figure 7. General structures of lanthanide half-sandwich (left), sandwich (middle) and cationic metallocene (right) complexes, where X = an anionic ligand.

Much of the early synthetic work on lanthanide SMMs focussed on either derivatising high-symmetry $[TbPc_2]^-$ systems, or on bimetallic systems, with the aim of strengthening the magnetic exchange interactions between the spin-bearing centres.[13,43,44] The latter was stimulated by the incredible magnetic properties of the radical-bridged N_2^{3-} complex $[K(18\text{-c-6})(THF)_2]^+[(Tb(N(SiMe_3)_2)_2(\mu\text{-}\eta^2\eta^2\text{-}N_2)]^-$ reported by Long and co-workers in 2011, with a modest U_{eff} = 227 cm^{-1} but with hysteresis loops open up to 14 K (Figure 8).[28]

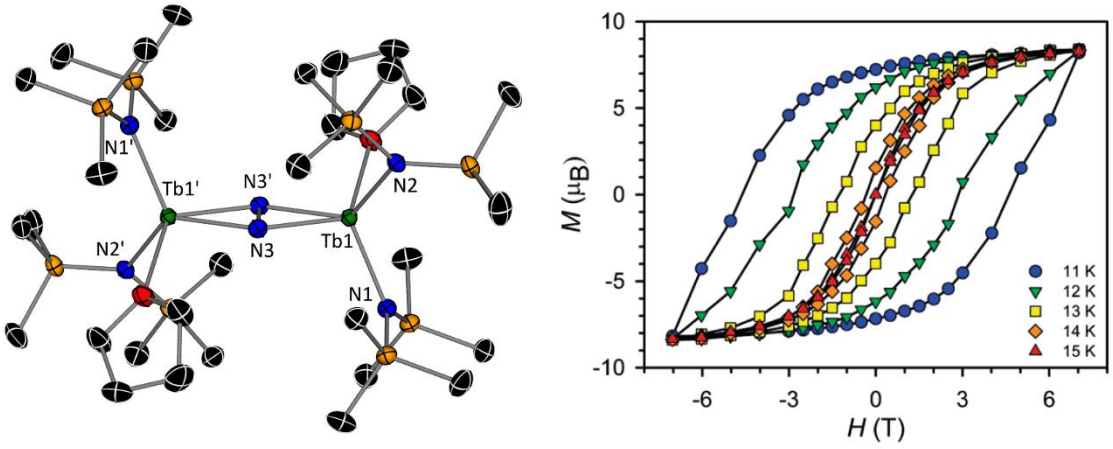

Figure 8. Molecular structure of $[(Tb(N(SiMe_3)_2)_2(\mu\text{-}\eta^2\eta^2\text{-}N_2)]^-$ (left), thermal ellipsoids are set to 30 % probability and the $[K(18\text{-c-6})(THF)_2]^+$ cation and hydrogen atoms have been omitted for clarity. Magnetic hysteresis measurements between 11-15 K with a sweep rate of 9 Oe s^{-1} (right).[28]

However, alternative routes to lanthanide SMMs were also being explored, with the first Cp-ligated organometallic lanthanide SMM reported by Layfield and co-workers in 2010.[45] The bimetallic dysprosium complex $[Dy(\eta^5\text{-}C_5H_5)_2(\mu\text{-bta})]_2$ features two η^5-Cp ligands coordinated to each dysprosium metal centre, which are bridged by two benzotriazolate ligands (Figure 9). Magnetic measurements revealed no exchange interaction between the Dy^{3+} ions, hence the SMM properties were attributed to the single ions, with a U_{eff} = 32(2) cm^{-1} and no open hysteresis loops even at 1.8 K. Notably, the anisotropy barrier is an order of magnitude lower than that of $[TbPc_2]$, *i.e.* U_{eff} = 230 cm^{-1}.[17] Despite the comparatively small energy barrier, this complex set the precedent that it was possible to observe slow magnetic relaxation in organometallic lanthanide complexes, and thus the quest to improve the magnetic properties by manipulating the crystal field around single ions commenced.

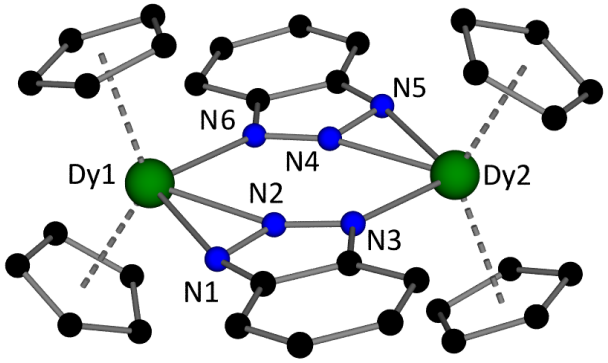

Figure 9. Molecular structure of the first Cp^--ligated lanthanide SMM $[Dy(\eta^5\text{-}C_5H_5)(\mu\text{-bta})]_2$. Hydrogen atoms have been omitted for clarity.[45]

Building upon that initial discovery, between 2012-2017 Layfield and co-workers reported a series of bis-Cp dysprosium metallocene SMMs that featured various equatorial p-block donor atoms (X) bridging between multiple metal centres, of the general formula $[Dy(\eta^5\text{-}Cp^R)_2(\mu\text{-X})]_n$ (*n* = 2 or 3) (Figure 10).[33,46–50] Importantly, these complexes reveal elegant experimental evidence of the magneto-structural correlations for the oblate-spheroid shaped magnetic M_J ground state of Dy^{3+} ions, where a summary of important parameters can be seen in Table 1.

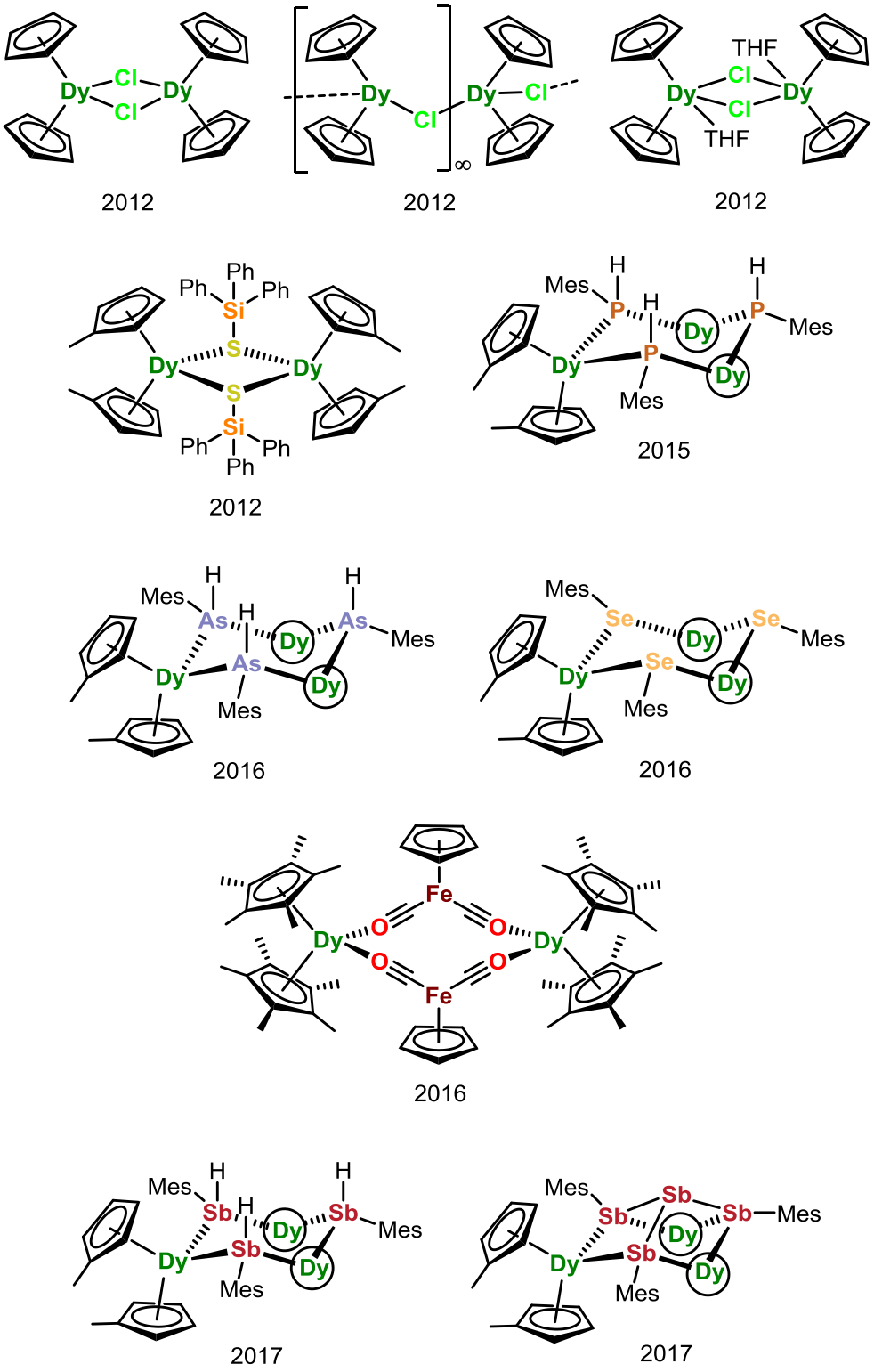

Figure 10. A selection of dysprosium metallocene SMMs that feature various bridging equatorial p-block donor atoms. Circled Dy atoms represent $Dy(Cp^{Me})_2$. Ph = phenyl, Mes = mesityl.

Table 1. Structural parameters and anisotropy barriers of selected bis-cyclopentadienyl dysprosium complexes that feature various bridging equatorial p-block donor atoms.

Compound	Dy-$Cp_c^{\dagger}$ / Å	Cp_c-Dy-$Cp_c^{\dagger}$ / °	Dy-$X^{\dagger}$ / Å	U_{eff} / cm^{-1}	ref
$[Dy(\eta^5\text{-}Cp)_2(\mu\text{-}bta)]_2$	2.358	131.9	2.450	32(2)	[45]
$[Dy(\eta^5\text{-}Cp)_2(\mu\text{-}Cl)]_2$	2.339	131.1	2.685	26(1)	[46]
$[Dy(\eta^5\text{-}Cp)_2(\mu\text{-}Cl)(THF)]_2$	2.396	127.4	2.691	34(1)	[46]
$[Dy(\eta^5\text{-}Cp)_2(\mu\text{-}Cl)]_\infty$	2.338	130.4	2.681	68(1)	[46]
$[Dy(\eta^5\text{-}Cp^{Me})_2\{\mu\text{-}S(SiPh_3)\}]_2$	2.263	128.5	2.750	133(4)	[47]
$[Dy(\eta^5\text{-}Cp^{Me})_2\{\mu\text{-}P(Mes)H\}]_3$	2.357	126.3	2.939	210(5)	[48]
$[Dy(\eta^5\text{-}Cp^{Me})_2\{\mu\text{-}Se(Mes)\}]_3$	2.343	125.7	2.918	252(4)	[49]
$[Dy(\eta^5\text{-}Cp^{Me})_2\{\mu\text{-}As(Mes)H\}]_3$	2.349	127.7	2.997	256(6)	[49]
$[Dy(\eta^5\text{-}Cp^{Me})_3\{\mu\text{-}Sb(Mes)\}_3Sb]$	2.341	130.0	3.130	272	[33]
$[Dy(\eta^5\text{-}Cp^{Me})_2\{\mu\text{-}Sb(Mes)H\}]_3$	2.340	130.2	3.154	345	[33]
$[Dy(\eta^5\text{-}Cp^*)_2(\mu\text{-}Fp)]_2$	2.342	141.5	2.293	662(2)	[50]

† Average values for multiple analogous parameters

The majority of these complexes feature either Cp- or Cp^{Me}-ligands (Cp^{Me} = C_5H_4Me), which typically maintain the same axial crystal field, based on the average Dy-Cp centroid distances and Cp_c-Dy-Cp_c angles remaining roughly the same at *ca.* 2.34 Å and *ca*. 129°, respectively. The major changes in structural and magnetic parameters arise from an increasing equatorial Dy-X distance on descending the p-block series to 'softer' X donors and, therefore, weaker equatorial crystal fields around Dy^{3+}. The periodic change in donor atoms was to correlate with the increasing anisotropy barriers. The isocarbonyl-bridged dimer $[Dy(\eta^5\text{-}Cp^*)_2(\mu\text{-}Fp)]_2$ (Cp* = C_5Me_5, Fp = $FeCp(CO)_2$) presents itself as an anomaly to this correlation, with much shorter average Dy-O distances of 2.293 Å and an exceptionally

high U_{eff} = 662(3) cm^{-1}. These properties can be explained by the larger Cp^R_c-Dy-Cp^R_c angle of 141.5°, which along with the higher electron donating properties of the Cp*-ligands serve to increase the strength of the axial crystal field around Dy^{3+} ions. The isocarbonyl bridges generate a weak equatorial crystal field and are not detrimental to the anisotropy barrier. However, their perturbation into the oblate-spheroid shaped electron density of the Dy^{3+} M_J ground state is most likely responsible for QTM at low temperatures, as evidenced by waist-restricted hysteresis loops between 1.8-6.2 K.

These examples demonstrate how subtle changes to the crystal field around Dy^{3+} ions can have significant effects on the SMM properties, with increasing the strength of the axial crystal field and decreasing equatorial ligand contributions resulting in increased anisotropy barriers. This agreed with parallel research into design criteria established from electrostatic models,[16,51] theoretical *ab initio* calculations,[52–54] and experimental research into organometallic lanthanide complexes without π-bonded ligands,[55,56] which in 2016 displayed impressive anisotropy barriers up to a then-record of 1261(1) cm^{-1}.[21] It should be noted that despite the high anisotropy barrier, the presence of weak equatorial ligands were detrimental to the magnetic hysteresis, with prominent QTM resulting in waist-restricted loops at low temperatures.[21] Therefore, a cationic dysprosium metallocene of the type $[Dy(\eta^5\text{-}Cp^R)_2]^+$ was predicted to be an attractive target for a high-performance SMM, with removal of equatorial ligands maximising the axial crystal ligand around Dy^{3+} and hence the anisotropy of the system.[50] From a synthetic perspective however, this was predicted to be a considerable challenge due to the highly electrophilic nature of Dy^{3+} along with its large radius. This was exemplified by the abundance of $[Dy\{\eta^5\text{-}Cp^R\}_2(\mu\text{-}X)]$ systems, with a notable example being $[Dy(\eta^5\text{-}Cp^*\}_2(\mu\text{-}Ph)_2BPh_2]$ (Figure 11), in which the Cp* ligands are not bulky enough to hinder interactions with the $[BPh_4]^-$ anion.[57,58]

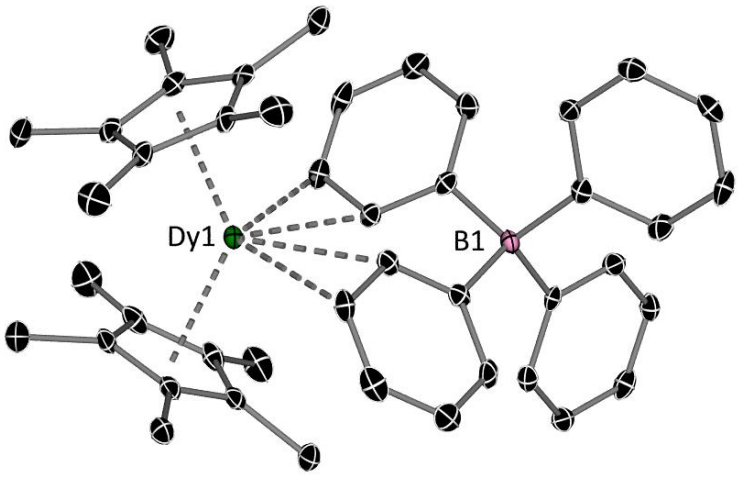

Figure 11. Molecular structure of $[Dy(\eta^5\text{-}Cp^*\}_2(\mu\text{-}Ph)_2BPh_2]$. Thermal ellipsoids are set to 50 % probability and hydrogen atoms have been omitted for clarity.[57,58]

With the careful manipulation of steric bulk on the $[Cp]^-$ ligands, research by Layfield,[22,27] Mills and Chilton,[23] and Long,[25] provided access to a series of dysprosium metallocene cations $[Dy(\eta^5\text{-}Cp^R)_2]^+$, which all form as salts of the non-coordinating $[B(C_6F_5)_4]^-$ anion. These compounds were synthesised by the abstraction of X ligands from the precursor complexes $[Dy(\eta^5\text{-}Cp^R)_2X]$ (X = Cl, I, BH_4) using the super-electrophile $[(Et_3Si)_2(\mu\text{-}H)]^+[B(C_6F_5)_4]^-$ (Scheme 2). A summary of important structural and magnetic parameters can be seen in Table 2. The SMM properties of these complexes are exceptional, with extremely high anisotropy barriers, and most importantly, appreciable coercive fields and magnetic hysteresis at high temperatures.

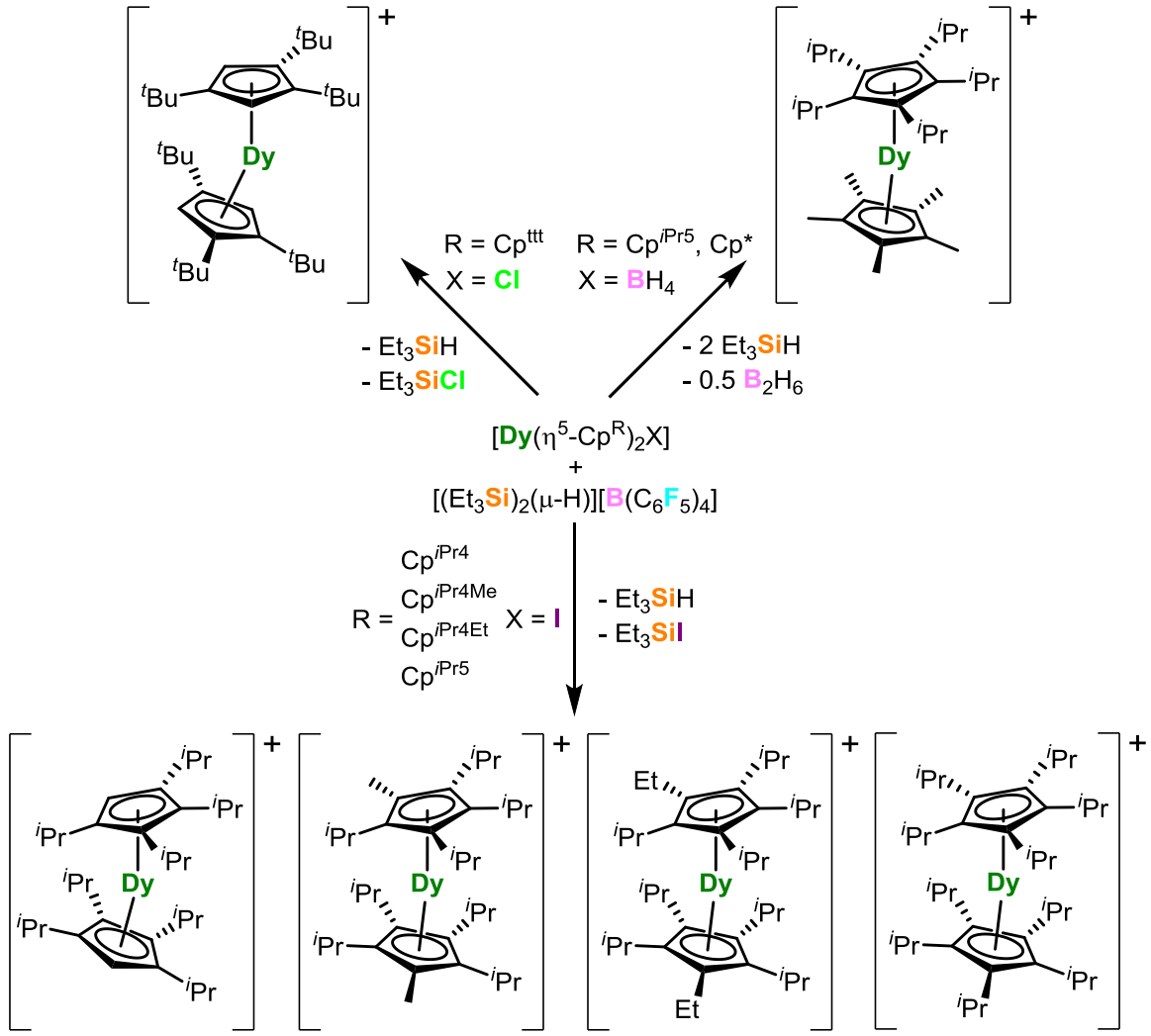

Scheme 2. Synthesis of dysprosium metallocene cations $[Dy(\eta^5\text{-}Cp^R)_2]^+$.[22,23,25,27]

Table 2. Structural parameters and SMM properties of reported dysprosium metallocene cations.

Compound	Dy-$Cp_c^{\dagger}$ / Å	Cp_c-Dy-$Cp_c^{\ddagger}$ / °	U_{eff} / cm^{-1}	T_H / K	ref
$[Dy(\eta^5\text{-}C_5{}^iPr_5)(\eta^5\text{-}Cp^*)]^+$	2.284(1), 2.296(1)	162.507(1)	1541	80	[27]
$[Dy(\eta^5\text{-}C_5{}^iPr_4Me)_2]^+$	2.298(5)	156.6(3)	1468	72	[25]
$[Dy(\eta^5\text{-}C_5{}^iPr_4Et)_2]^+$	2.302(6)	161.1(2)	1380	66	[25]
$[Dy(\eta^5\text{-}C_5{}^iPr_5)_2]^+$	2.340(7)	162.1(7)	1334	66	[25]
$[Dy(\eta^5\text{-}C_5{}^iPr_4H)_2]^+$	2.29(1)	147.2(8)	1285	32	[25]
$[Dy(\eta^5\text{-}Cp^{ttt})_2]^+$	2.316(3)	152.70(7)	1277, 1233	60	[22,23]

† Average value for highest occupancy component in the crystal structure. ‡ Average value across all disordered components or analogous parameters in the crystal structure.

Notably, the only heteroleptic sandwich complex $[Dy(\eta^5\text{-}C_5{}^iPr_5)(\eta^5\text{-}Cp^*)]^+$ is the best performing SMM, and shows well-defined maxima in the $\chi''(\nu)$ plots up to 130 K, resulting in a record U_{eff} = 1541(11) cm^{-1}, and with open hysteresis loops up to 80 K (Figure 12). Accordingly, it is the first SMM to show hysteresis above the boiling point of liquid nitrogen, an impressive feat that renews optimism into utilising SMMs in device applications at practical temperatures. The magnetic properties of the precursor complex $[Dy(\eta^5\text{-}C_5{}^iPr_5)(\eta^5\text{-}Cp^*)(\kappa^2\text{-}BH_4)]$ are much worse, with a U_{eff} = 7(1) cm^{-1} and waist-restricted hysteresis loops at 1.8 K. This is due to the presence of the equatorial borohydride ligand, which affords a competing crystal field and promotes magnetic relaxation via QTM.[27]

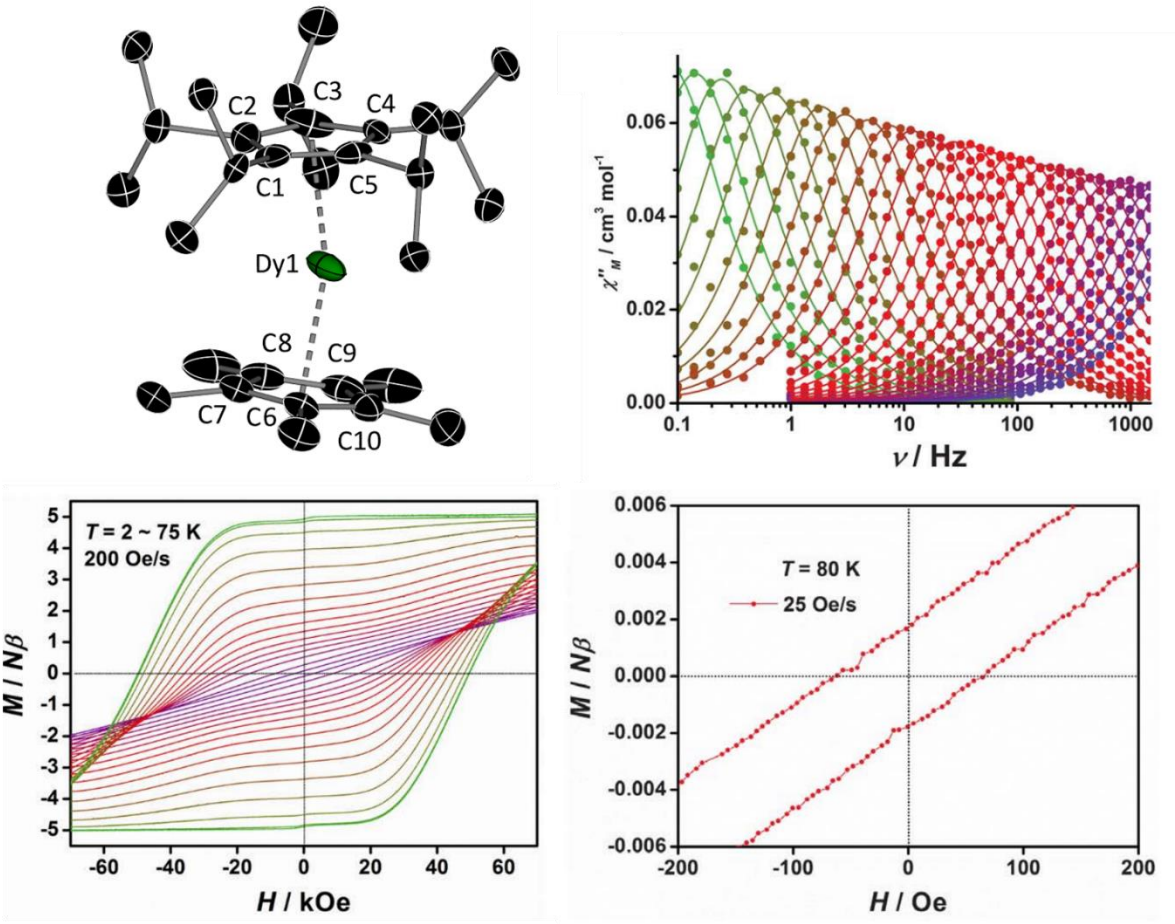

Figure 12. Molecular structure of $[Dy(\eta^5\text{-}C_5{}^iPr_5)(\eta^5\text{-}Cp^*)]^+$ (top left), thermal ellipsoids are set to 50 % probability and the $[B(C_6F_5)_4]^-$ anion and hydrogen atoms have been omitted for clarity. Frequency-dependence of the out-of-phase susceptibility, $\chi''(\nu)$, in zero DC field between 82 K (green points) and 138 K (purple points) (top right), magnetic hysteresis measurements between 2-75 K with a sweep rate of 200 Oe s^{-1} (bottom left), and hysteresis loops at 80 K with a sweep rate of 25 Oe s^{-1} (bottom right).[27]

The magnetic properties of this series of dysprosium metallocenes can be explained as a consequence of the synergistic effects of two important structural parameters: (1) the Dy-C bond distances, and hence, the Cp_c distance, which determines the strength of the crystal field, *i.e.* shorter distances mean stronger crystal fields, and (2) the Cp_c-Dy-Cp_c angle, which determines the axiality of the system, *i.e.* wider angles equate to greater axiality. The combination of ligands in $[Dy(\eta^5\text{-}C_5{}^iPr_5)(\eta^5\text{-}Cp^*)]^+$ features the shortest average Dy-Cp_c distance and the largest Cp_c-Dy-Cp_c angle, therefore resulting in the strongest crystal field around Dy^{3+} with the highest axiality. In contrast, despite a similarly large Cp_c-Dy-Cp_c angle in $[Dy(\eta^5\text{-}C_5{}^iPr_5)_2]^+$, the average Dy-$Cp_c$ distance is longer (*ca.* 0.05 Å) due to the bulky substituents preventing a closer approach of the ligands to the metal centre, resulting in an overall weaker crystal field. Conversely, the less bulky $[Cp^R]^-$ ligands in $[Dy(\eta^5\text{-}C_5{}^iPr_4H)_2]^+$ and $[Dy(\eta^5\text{-}Cp^{ttt})_2]^+$ (Cp^{ttt} = $C_5{}^tBu_3H_2$) feature short Dy-Cp_c distances and, hence, a strong crystal field. However, the smaller Cp_c-Dy-Cp_c angles result in a reduced axiality, which is detrimental to the magnetic properties. Moreover, *ab initio* spin dynamic calculations into $[Dy(\eta^5\text{-}Cp^{ttt})_2]^+$ have shown how the presence of C-H vibrational modes on the Cp^{ttt} ligand facilitate the initial ($|\pm15/2> \rightarrow |\pm13/2>$) relaxation step, hence the removal of these hydrogen atoms for alkyl groups have indeed resulted in improved magnetic properties.[23]

The highly axial nature of the $[Dy(\eta^5\text{-}Cp^R)_2]^+$ series present an opportunity to study the influence on non-Kramers' ions, such as Tb^{3+}, which require a highly axial crystal field in order to induce a doubly degenerate ground state. To this end, Long and co-workers extended the same synthetic methodology to form the cationic bis-Cp^{iPr5} terbium separated ion pair complex $[Tb(\eta^5\text{-}C_5{}^iPr_5)_2]^+[B(C_6F_5)_4]^-$. In addition, the synthetic route to the perfectly linear divalent bis-Cp^{iPr5} sandwich complexes $[Ln(\eta^5\text{-}C_5{}^iPr_5)_2]$ (Ln = Tb^{2+}, Dy^{2+}) was also described, which were formed by reacting the precursor complex with two equivalents of KC_8 instead of the super-electrophile $[(Et_3Si)_2(\mu\text{-}H)]^+[B(C_6F_5)_4]^-$ (Scheme 3).[59]

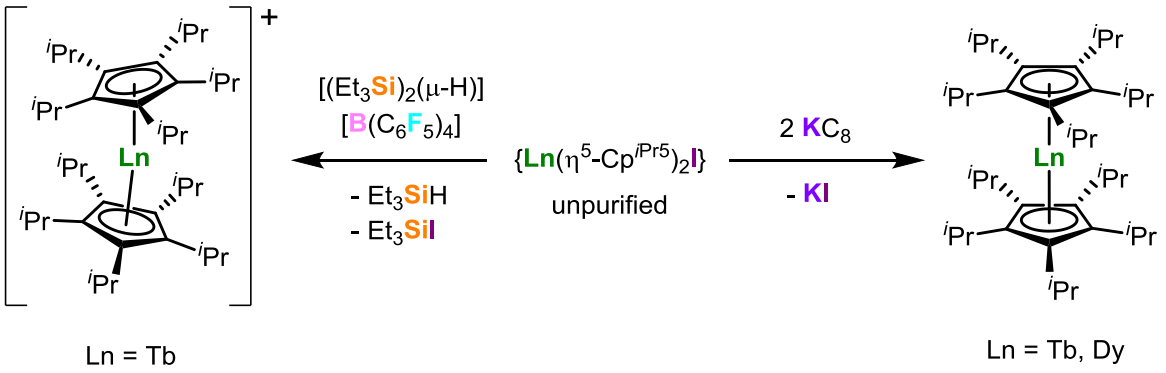

Scheme 3. Synthesis of $[Tb(\eta^5\text{-}C_5{}^iPr_5)_2]^+[B(C_6F_5)_4]^-$ and $[Ln(\eta^5\text{-}C_5{}^iPr_5\}_2]$ (Ln = Tb, Dy).[59]

The molecular structure of $[Tb(\eta^5\text{-}C_5{}^iPr_5)_2]^+[B(C_6F_5)_4]^-$ reveals that, despite almost co-planar Cp^{iPr5} rings, the Tb^{3+} ion lies off-centre resulting in a Cp_c-Tb-Cp_c angle of 159.8(4)°. However, upon reduction to the divalent complexes this angle increases to a perfectly linear 180° (Figure 13). The average Tb-Cp_c distance in the cationic trivalent complex is 2.356(6) Å, which increases to 2.416(1) Å upon reduction. The analogous distance in the divalent dysprosium analogue is 2.385(1) Å, which represents a similar increase when compared to the average Dy-Cp_c distance in the previously reported cationic complex $[Dy(\eta^5\text{-}C_5{}^iPr_5)_2]^+[B(C_6F_5)_4]^-$ (2.340(7) Å). The elongation of Ln-Cp_c distances in the divalent complexes are a consequence of the resulting f^n d^1 (Tb n = 8, Dy n = 9) configurations upon reduction.[60]

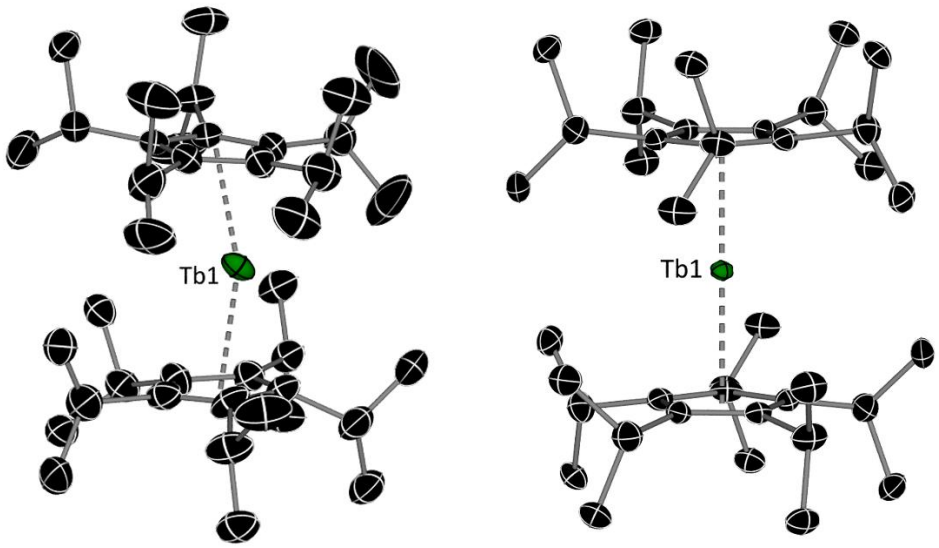

Figure 13. Molecular structure of $[Tb(\eta^5\text{-}C_5{}^iPr_5)_2]^+$ (left), thermal ellipsoids are set to 30 % probability and the $[B(C_6F_5)_4]^-$ anion and hydrogen atoms have been omitted for clarity, and $[Tb(\eta^5\text{-}C_5{}^iPr_5)_2]$ (right), thermal ellipsoids are set to 50 % probability and hydrogen atoms have been omitted for clarity.[59]

Dynamic magnetic susceptibility measurements reveal that the trivalent cationic terbium complex displays prominent magnetic relaxation via Raman and QTM, precluding the extraction of an anisotropy barrier. This suggests that the system is not axial enough to induce a well-defined doubly degenerate ground state for the non-Kramers' Tb^{3+} ion. Conversely, upon reduction to Tb^{2+} and, hence to a Kramers' ion, a U_{eff} of 1205 cm^{-1} was determined and open hysteresis loops up to 55 K were observed, a record for a non-Dy^{3+} SMM. Despite the perfectly linear geometry around Dy^{2+}, the non-Kramers' ion nature results in significant QTM, where the application of a DC field (500 Oe) results in a barrier of 37 cm^{-1}. Even though there is an almost negligible anisotropy barrier, the Dy^{2+} complex exhibits butterfly-shaped magnetic hysteresis from 2-75 K. These results highlight the importance of the Kramers' ion nature of Tb^{2+}/Dy^{3+} when constructing high-performance SMMs, and indeed how strict axial symmetry is a necessity with the non-Kramers' Tb^{3+} ion.

Organometallic lanthanide sandwich complexes featuring Cp ligands therefore represent the current state of the art in single-molecule magnetism. However, the deviation in magnetic properties across the $[Dy(\eta^5\text{-}Cp^R)_2]^+$ series is quite remarkable considering the relatively small differences in bond lengths and angles. Once again this shows how subtle changes to the crystal field around Dy^{3+} ions can have significant effects on the SMM properties. Thus, further experimental and theoretical research into $[Dy(\eta^5\text{-}Cp^R)_2]^+$ derivatives will prove extremely valuable to current magneto-structural correlations. From an experimental perspective this presents itself as an opportunity, as there remains scope for improvement by further enhancing the crystal field strength and / or axiality, which is a direct aim of the research in this thesis.

1.2.3. η^6-Arene ligands

The prototypical metal-arene complex is bis(benzene)chromium, [Cr(η^6-C_6H_6)$_2$], first synthesized by Fischer and Hafner in 1955 by reacting $CrCl_3$ with $AlCl_3$, aluminium metal and benzene.[61] This method was subsequently applied to the f-elements in the attempt to synthesise analogous sandwich complexes, which instead resulted in the half-sandwich arene-ligated complexes [U(η^6-C_6H_6)(κ^2-$AlCl_4$)$_3$] and [Sm(η^6-C_6Me_6)(κ^2-$AlCl_4$)$_3$].[62,63] These f-element complexes feature the metals in a trivalent oxidation state, with the undesired reactivity being a consequence of the strong resistance of the f-elements to form the zero-valent state in a molecular compound. In the case of the lanthanides, the electropositive elements have reduction potentials in excess of −2 V from the +3 to 0 oxidation state *vs.* a standard hydrogen electrode,[64] thus the chemical or electrochemical reduction as a route to lanthanide(0) species is extremely difficult to achieve. An alternative successful approach was employed by Cloke and co-workers, in which bis(arene) lanthanide sandwich complexes were formed in metal-vapor synthesis (MVS) reactions by the co-condensation of metal vapour with excess [1,3,5-tri-*tert*-butylbenzne] under high vacuum conditions. The use of lanthanide metal atoms in their already zero-valent form managed to avoid the issue of reducing the highly electropositive metals.[65–68]

Several arene-ligated SMMs are known, with the first example reported by Gao and co-workers in 2014,[69] with two derivatives later reported in 2017.[70] The half-sandwich complexes [Dy(η^6-C_6Me_6)(κ^2-$AlCl_4$)$_3$], [Dy(η^6-C_6H_5Me)(κ^2-$AlCl_4$)$_3$] and [Dy(η^6-C_6H_5Me)(κ^2-$AlBr_4$)$_3$] were formed by the same method used by Cotton and Schwotzer to synthesize the first arene-ligated lanthanide complex, *i.e.* [Sm(η^6-C_6Me_6)(κ^2-$AlCl_4$)$_3$]. The complexes feature an η^6-arene ligand and tetrahaloaluminate ligands in a κ^2-coordination mode (Figure 14). This results in a distorted pentagonal bipyramidal geometry. The arene$_{cent}$-Dy distance in [Dy(η^6-C_6Me_6)(κ^2-$AlCl_4$)$_3$] is 2.471 Å, which is significantly longer than the analogous distances typically observed in Cp-ligated SMMs (*ca*. 2.3-2.4 Å), indicative that the arene ligands create a much weaker crystal field. This is further highlighted in the toluene derivatives [Dy(η^6-C_6H_5Me)(κ^2-$AlCl_4$)$_3$] and [Dy(η^6-C_6H_5Me)(κ^2-$AlBr_4$)$_3$], which display similar arene$_{cent}$-Dy distances of 2.476 and 2.503 Å, respectively.

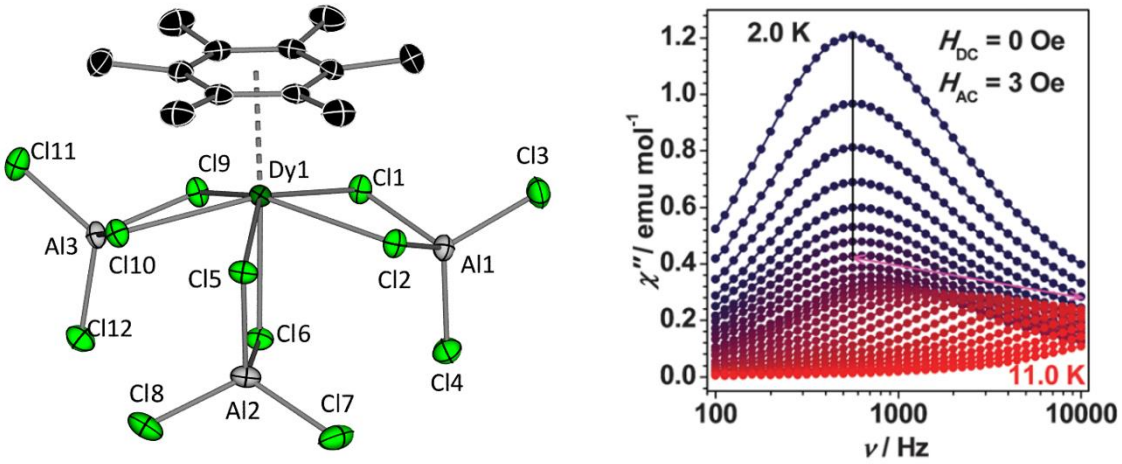

Figure 14. Molecular structure of $[Dy(\eta^6\text{-}C_6Me_6)(\kappa^2\text{-}AlCl_4)_3]$ (left), thermal ellipsoids are set to 50 % probability and hydrogen atoms have been omitted for clarity. Frequency-dependence of the out-of-phase susceptibility, $\chi''(\nu)$, in zero DC field between 2-11 K (right).[69]

Dynamic magnetic susceptibility measurements on $[Dy(\eta^6\text{-}C_6Me_6)(\kappa^2\text{-}AlCl_4)_3]$ revealed SMM properties, with $\chi''(\nu)$ displaying maxima in the temperature range of 2-11 K, with QTM dominating the relaxation at lower temperatures (Figure 14). Thus, a U_{eff} = 70 cm^{-1} was determined, with suppression of QTM via the application of an applied DC field (2 kOe) resulting in an increase to 89 cm^{-1}. *Ab initio* calculations showed that the direction of the easy axis of magnetization coincides with the Cl6-Dy-$arene_{cent}$ axis, which explains the poor SMM properties due to the weak crystal field provided by the neutral η^6-arene ligand. Upon replacing the hexamethylbenzene ligand with the smaller toluene ligand in $[Dy(\eta^6\text{-}C_6H_5Me)(\kappa^2\text{-}AlCl_4)_3]$ and $[Dy(\eta^6\text{-}C_6H_5Me)(\kappa^2\text{-}AlBr_4)_3]$, slight improvements upon the magnetic properties were observed, with effective energy barriers of 77 and 76 cm^{-1}, respectively. The exchange of halide from Cl to Br had very little effect, with the improvements thought to arise due to less distortion from ideal D_{5h} symmetry when compared to the hexamethylbenzene derivative.[70]

The weak crystal field generated by η^6-arene ligands results in poor SMM properties for Dy^{3+} complexes when it occupies the axial ligand field. However, this poor crystal field can be exploited when utilised under the correct conditions, *i.e.* in an equatorial ligand field for Dy^{3+}, as was reported by Gao and co-workers in 2018.[71] The reactions of $[Ln(CH_2SiMe_3)_3(THF)_2]$ (Ln = Tb, Dy, Ho, Er, Tm) with two equivalents of the bulky phenol

ArOH (Ar = bis-2,6-(2,6-diisopropylphenyl)phenyl) resulted in the formation of [(ArO)Ln(OAr')] (Scheme 4).

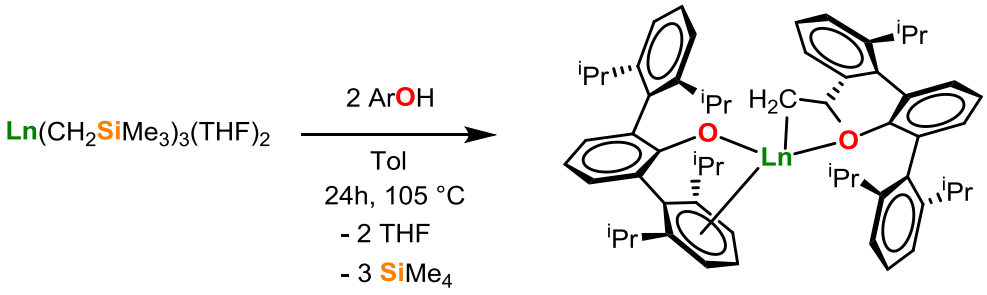

Scheme 4. Synthesis of [(ArO)Ln(OAr')] (Ln = Tb, Dy, Ho, Er, Tm).[71]

The molecular structures reveal a pseudo-4-coordinate geometry around the metal, where one ArO ligand is coordinated to the metal centre through the oxygen atom and features an η^6-arene interaction via one diisopropylphenyl ring. The other phenoxide ligand coordinates through the oxygen atom and undergoes an additional deprotonation of an ^{i}Pr substituent to form a 'tuck-in' CH_2 ligand to the metal centre (OAr') (Figure 15). For the dysprosium analogue, the two bulky phenoxide ligands result in Dy-O distances of 2.126(4) (Dy1-O1) and 2.191(4) Å (Dy1-O2), with an O1-Dy-O2 angle of 144.7°. The $arene_{cent}$-Dy distance is 2.649(3) Å, with the relatively long centroid distance indicative of the weak crystal field provided by the η^6-arene.

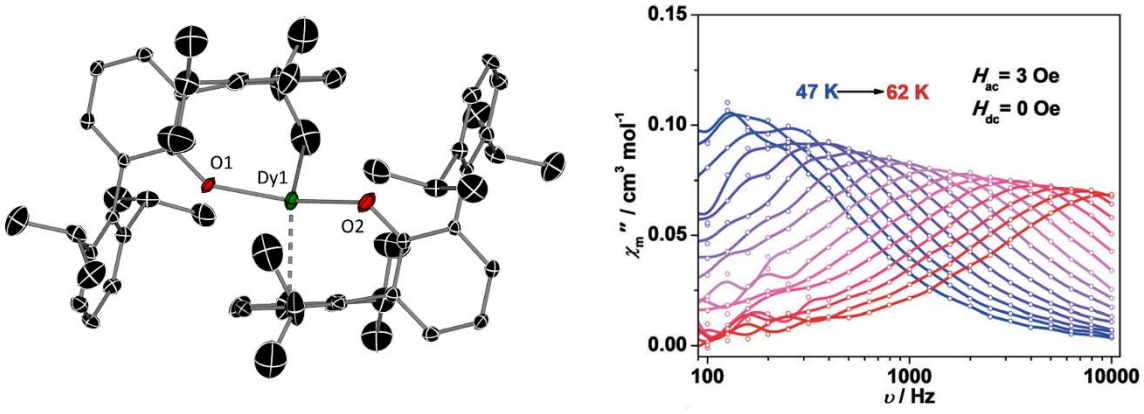

Figure 15. Molecular structure of [(ArO)Dy(OAr')] (left), thermal ellipsoids are set to 30 % probability and hydrogen atoms have been omitted for clarity. Frequency-dependence of the out-of-phase susceptibility, $\chi''(\nu)$, in zero DC field between 47-62 K (right).[71]

Dynamic magnetic susceptibility measurements on all lanthanide complexes in zero-applied DC field revealed that only the dysprosium analogue displayed SMM properties, with a strong temperature and frequency-dependence of the magnetic susceptibility between a wide temperature range of 2-70 K (Figure 15). An effective energy barrier of 688 cm^{-1} was determined, with magnetic hysteresis measurements revealing waist-restricted loops up to 6 K, indicative that magnetic relaxation via QTM dominates the low-temperature regime. In the case of the erbium analogue, the application of an applied DC field (1 kOe) resulted in the suppression of QTM and the observation of peaks in the $\chi''(\nu)$ plots between 2-12K, resulting in a field-induced U_{eff} of 60 cm^{-1}. *Ab initio* calculations determined that the orientations of the easy axes of the magnetic ground states are in different planes for the dysprosium and erbium analogues, *i.e.* along the O-Dy-O axis and perpendicular to the O-Er-O axis, respectively. Thus, the SMM properties of the dysprosium analogue can be qualitatively described by a strong axial crystal field arising from the phenoxide ligands resulting in a large U_{eff}, with weak equatorial contributions arising from the η^6-arene ligand and the 'tuck-in' CH_2 ligand promoting QTM at low temperatures. Moreover, despite the relatively poor SMM properties of the erbium analogue, these arene-ligated complexes are an example of the same ligand system being able to stabilise both oblate- and prolate-spheroid shaped magnetic $|M_J|$ = 15/2 ground states for dysprosium and erbium, respectively.

Early work by Lappert and co-workers had shown how benzene ligands were capable of being reduced to various degrees.[72–74] An alternative route into incorporating reduced arene ligands into lanthanide-based SMMs has been reported by Diaconescu and co-workers, in which a quadruply reduced biphenyl ligand can form inverse sandwich complexes.[75] A reaction between two equivalents of $[Ln(NN^{TBS})I(THF)_2]$ (Ln = Gd, Dy, Er) (NN^{TBS} = 1,1'-fc(NSi^tBuMe_2)$_2$) and biphenyl in the presence of four equivalents of KC_8 resulted in the formation of the inverse sandwich complexes $[(NN^{TBS})Ln\{\mu\text{-}\eta^6\eta^6\text{-}C_{12}H_{10}\}Ln(NN^{TBS})(K(C_7H_8)_2]$ (Figure 16). These complexes feature a bridging η^6:η^6-C_6 ring coordinating to two lanthanides and the other connected to a C_6 ring bridging between two potassium ions, which are capped by toluene molecules. The potassium ions can be encapsulated by two equivalents of 18-crown-6 to form the separated ion pairs $[(K(18\text{-}c\text{-}6)(THF)_{1.5})_2]^{2+}[(NN^{TBS})Ln(\mu\text{-}\eta^6\eta^6\text{-}C_{12}H_{10})Ln(NN^{TBS})]^{2-}$ (Ln = Gd, Dy, Er) (Figure 16). Previous experimental and computational studies by the same group indicated that the quadruply

reduced biphenyl ring has the charge located on the phenyl ring coordinated to the two rare-earth metal centres, resulting in a formal 10π-electron configuration for the coordinated C_6 ring.[76,77]

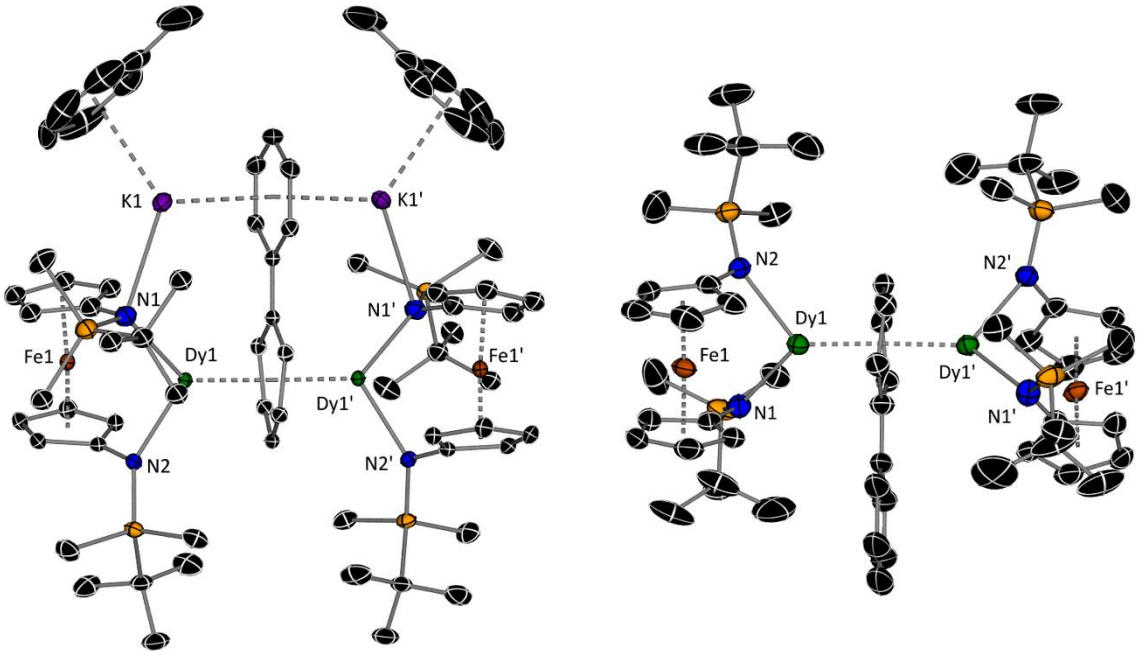

Figure 16. Molecular structures of $[(NN^{TBS})Dy\{\mu\text{-}\eta^6\eta^6\text{-}C_{12}H_{10}\}Dy(NN^{TBS})(K(C_7H_8)_2]$ (left) and $[(NN^{TBS})Dy\{\mu\text{-}\eta^6\eta^6\text{-}C_{12}H_{10}\}Dy(NN^{TBS})]^{2-}$ (right) (NN^{TBS} = 1,1'-fc(NSi^tBuMe_2)$_2$). Thermal ellipsoids are set to 50 % probability and hydrogen atoms have been omitted for clarity.[75]

The SMM properties of the inverse sandwich complexes were investigated in the hopes that the quadruply reduced biphenyl ring could promote magnetic exchange interactions between the two lanthanide metal centres. Unfortunately, this was not the case, as the measurements revealed that the dysprosium complex with the contact potassium ions was the only derivative to show any slow magnetic relaxation properties in zero-field, which were plagued with significant QTM at low temperatures. An effective energy barrier of 24 cm^{-1} was extracted, with an applied DC field (900 Oe) suppressing the QTM and the barrier increasing to 37 cm^{-1}. Surprisingly, the ion-separated dysprosium complex showed no clear slow magnetic relaxation, even with an applied DC field, which was attributed to dominant ferromagnetic interactions between the two dysprosium ions at low temperatures that promote significant QTM. This ferromagnetic interaction was confirmed by the static magnetic susceptibility measurements, in which the temperature dependence of $\chi_M T$, where χ_M is the molar magnetic susceptibility, shows an increase at low temperatures.

Ab initio calculations predicted that the ground state easy axes for both dysprosium complexes are orientated in the direction of the shortest Dy-N bond (Dy1-N2, Figure 16). Thus, the poor SMM properties in the biphenyl-bridged complexes can be attributed to the weakly axial crystal field around the Dy^{3+} ions, with the quadruply reduced bridging biphenyl ring and the second nitrogen atom producing a competing equatorial ligand field.

1.2.4. η^7-Cycloheptatrienyl ligands

The coordination chemistry of the 7-membered cycloheptatrienyl ligand is intriguing, with the ligand being capable of satisfying Hückel's aromaticity rule in two ways. The first is the monocationic 6π-electron ligand $[\eta^7\text{-}C_7H_7]^+$ that is isoelectronic to Cp^- or benzene, and the second is the trianionic 10π-electron ligand $[\eta^7\text{-}C_7H_7]^{3-}$ (Cht^{3-}), which is isoelectronic to $[COT]^{2-}$.

The first f-element Cht^{3-} complex was reported by Ephritikhine and co-workers in 1994, an inverse cycloheptatrienyl uranium sandwich separated ion pair complex $[U(BH_4)_2(THF)_5]^+[(BH_4)_3U\{\mu\text{-}\eta^7\text{:}\eta^7\text{-}C_7H_7\}U(BH_4)_3]^-$.[78] A year later, the same group reported the only example of a bis-(η^7-Cht) complex. The uranium sandwich complex forms as the separated ion pairs $[K(18\text{-c-}6)]^+[U(\eta^7\text{-}C_7H_7)_2]^-$ from the reaction of UCl_4 with potassium metal and an excess of cycloheptatriene, followed by recrystallisation in THF in the presence of 18-crown-6 (Figure 17).[79]

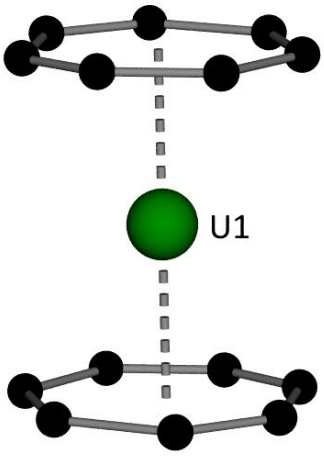

Figure 17. Molecular structure of the $[U(\eta^7\text{-}C_7H_7)_2]^-$ anion. The $[K(18\text{-c-}6)]^+$ cation and hydrogen atoms have been have been omitted for clarity.[79]

With respect to the lanthanides, complexes of Cht^{3-} ligands are rare, with only five examples existing to date. The lack of synthetic routes to cycloheptatriene pro-ligands hampers potential reactivity with rare-earth elements. Reports by Miller and Dekock in 1981 stated that, in the presence of lanthanide and actinide chlorides, three equivalents of the cycloheptadienyl anion $[LiC_7H_9]^-$ could be readily converted to the cycloheptatrienyl trianion $[C_7H_7]^{3-}$ and two equivalents of cycloheptadiene $[C_7H_{10}]$ in a disproportionation reaction.[80] This reactivity is thought to involve the f-element because solutions of $[LiC_7H_9]^-$ do not disproportionate. However, complexes formed in these reactions could not be structurally characterised.

It was not until 1997 that the first lanthanide Cht^{3-} complex was reported and structurally identified by Ephritikhine and co-workers. The reaction of $[Nd(BH_4)_3(THF)_2]$ with 1.5 equivalents of $[KC_7H_9]^-$ produced the inverse sandwich complex $[(THF)(BH_4)_2Nd\{\mu\text{-}\eta^7\eta^7\text{-}C_7H_7\}Nd(BH_4)(THF)_3]$ (Figure 18).[81] Two equivalents of cycloheptadiene $[C_7H_{10}]$ were detected as a by-product, indicating that the reaction may have proceeded via the previously proposed mechanism by Miller and Dekock.

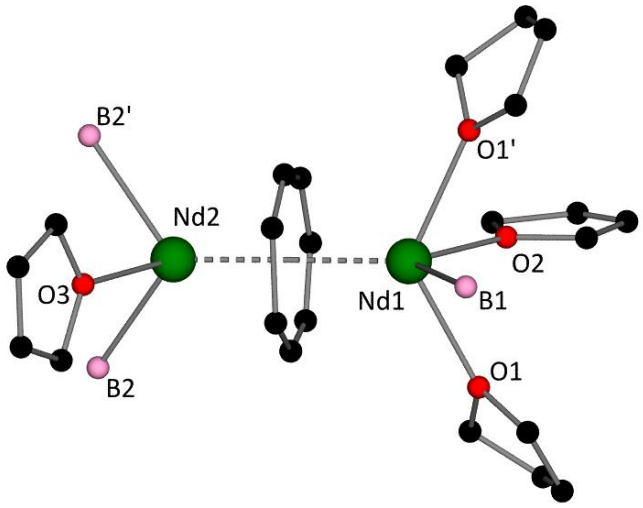

Figure 18. Molecular structure of $[(THF)(BH_4)_2Nd\{\mu\text{-}\eta^7\eta^7\text{-}C_7H_7\}Nd(BH_4)(THF)_3]$. Hydrogen atoms have been omitted for clarity.[81]

The other four lanthanide complexes were reported by Murugesu and co-workers in 2017, with three of those currently being the only examples of Cht-ligated SMMs.[82] The inverse cycloheptatrienyl sandwich complexes $[K(N(SiMe_3)_2)Ln\{\mu\text{-}\eta^7\eta^7\text{-}C_7H_7\}Ln(N(SiMe_3)_2)_2]$ (Ln = Gd, Dy, Er) were formed by the reaction of two equivalents of $[Ln(N(SiMe_3)_2)_3]$ (Ln = Gd, Dy,

Er) with [KC_7H_9] (Scheme 5). Additionally, the THF-solvated erbium derivative [$(THF)_2K(N(SiMe_3)_2)Er\{\mu\text{-}\eta^7\text{:}\eta^7\text{-}C_7H_7\}Er\{N(SiMe_3)_2\}_2$] was isolated following extraction into THF. In a similar fashion to previous reactivity, the cycloheptadienyl anion $[C_7H_9]^-$ is doubly deprotonated to form the 10π-electron Cht^{3-} ligand. However, in this case the generation of two equivalents of [$HN(SiMe_3)_2$] as a by-product indicates that the proton abstractions occur via the amido ligands, not another two equivalents of [KC_7H_9], as observed in previous examples which generate two equivalents of cycloheptadiene [C_7H_{10}].

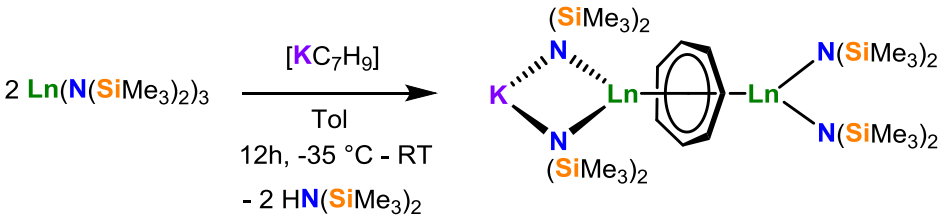

Scheme 5. Synthesis of [$K(N(SiMe_3)_2)Ln\{\mu\text{-}\eta^7\text{:}\eta^7\text{-}C_7H_7\}Ln(N(SiMe_3)_2)_2$] (Ln = Gd, Dy, Er).[82]

The inverse sandwich complexes feature two Ln^{3+} ions bridged by an η^7-Cht^{3-} ligand, with each metal being capped by two amido nitrogen atoms (Figure 19). On one side, a potassium ion interacts with two amido nitrogen atoms, which exhibits long contacts to a neighbouring molecule resulting in a linear coordination polymer. The unsolvated Er^{3+} complex features Cht_{cent}-Er distances of 1.948(3) and 2.010(3) Å, with an Er···Er distance of 3.9580(7) Å. The additional solvated Er^{3+} complex features two molecules of THF coordinated to the potassium ion, with similar centroid and Er···Er distances.

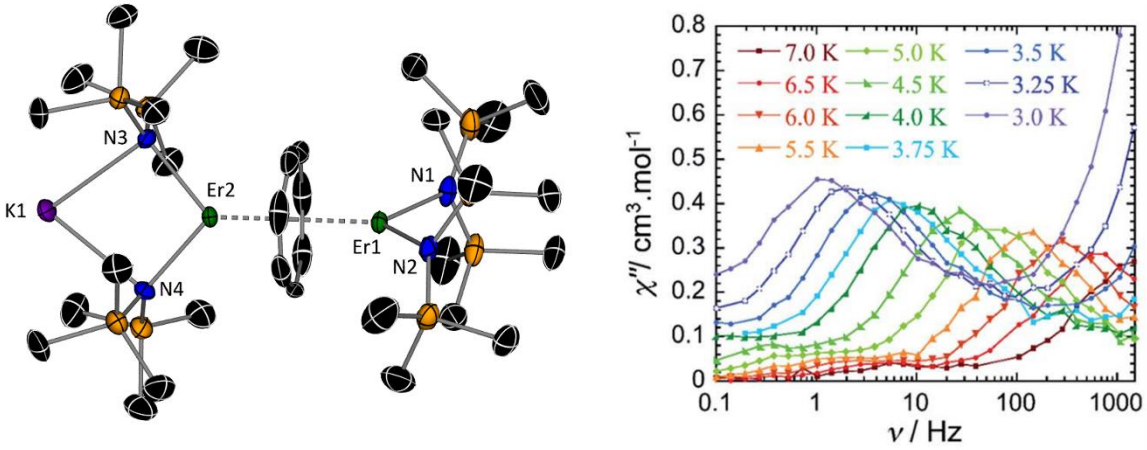

Figure 19. Molecular structure of [$K(N(SiMe_3)_2)Er\{\mu\text{-}\eta^7\text{:}\eta^7\text{-}C_7H_7\}Er(N(SiMe_3)_2)_2$] (left), thermal ellipsoids are set to 50 % probability and hydrogen atoms have been omitted for clarity. Frequency-dependence of the out-of-phase susceptibility, $\chi''(\nu)$, in an applied DC field of 800 Oe between 3-7 K (right).[82]

Due to the relatively short Ln···Ln distances, it is thought that the Cht^{3-} ligand could find use in promoting magnetic exchange coupling between lanthanide centres, which is a method employed to increase magnetic blocking of SMMs.[28–30,43,83,84] Therefore, static magnetic measurements on the isotropic gadolinium analogue revealed a weak, yet non-negligible exchange coupling constant of $J = -0.134$ cm^{-1} ($-2J$ formalism). Comparisons of the coupling constant with 6- and 8-membered rings reveal that the value of the 7-membered ring is slightly smaller, therefore a trend between ring size and charge density could not be inferred.

Dynamic magnetic susceptibility measurements on the dysprosium and both erbium analogues revealed significant QTM and no out-of-phase signals. However, SMM properties were observed after the application of an optimised DC field (Dy = 2000 Oe, Er = 800 Oe and $Er(THF)_2$ = 2000 Oe). The dysprosium analogue showed peaks in the AC susceptibility below 4 K, however the positions of the peaks are essentially temperature and frequency independent, which indicates that magnetic relaxation is still dominated by QTM at these temperatures. Thus, an effective energy barrier could not be extracted. In contrast, the unsolvated erbium complex revealed temperature and frequency dependant maxima in the AC susceptibility between 3-7 K (Figure 19), allowing a U_{eff} of 40 cm^{-1} to be determined. For the solvated erbium derivative, two independent relaxation processes are observed below 4 K, however, despite attempts to probe each of these processes with various DC fields, no energy barriers could be determined. *Ab initio* calculations show that the direction of the principal magnetic axis in the ground KD lies parallel with the DyN_2 plane, and perpendicular to the ErN_2 planes.

Thus, with the Dy^{3+} analogue showing poor SMM properties and the unsolvated Er^{3+} complex showing a field-induced U_{eff} = 40 cm^{-1}, it is indicative that the Cht^{3-} ligand is perhaps better suited to stabilisation of a prolate-spheroid shaped magnetic M_J ground states. However, as the slow magnetic relaxation properties of the Er^{3+} complex are field-induced, it suggests that the particular combination of Cht^{3-} with the two amido ligands does not provide a strong equatorial crystal field.

1.2.5. η^8-Cyclooctatetraenyl ligands

The dianionic 8-membered cyclooctatetraenyl ligand, or $[COT]^{2-}$, is well suited to coordination with the large electropositive f-elements. Perhaps the most famous examples are uranocene $[U\{\eta^8\text{-}C_8H_8\}_2]$ and cerocene $[Ce\{\eta^8\text{-}C_8H_8\}_2]$, which have been known since 1968 and 1976, respectively.[85,86] Despite cerium being the only lanthanide to show extensive chemistry in the (+4) oxidation state, the electronic structure of cerocene has proved to be more ambiguous than originally expected, with a multiconfigurational $Ce^{3+/4+}$ state thought to be the most appropriate description.[87–90]

The large ring size and dianionic charge allow close approach of COT ligands to lanthanide centres, which results in a strong equatorial crystal field. This was demonstrated by Gao and co-workers in 2011, with the characterisation of the first COT-ligated SMM $[Er(\eta^8\text{-}C_8H_8)(\eta^5\text{-}Cp^*)]$, which was formed in the reaction of $[Er(\eta^8\text{-}C_8H_8)Cl(THF)]$ with NaCp* using a previously published procedure.[91,92] The molecular structure features an Er^{3+} cation sandwiched between the two carbocyclic rings, with COT_{cent}-Er and Cp_{cent}-Er distances of 1.622 and 2.271 Å, respectively, and a COT_{cent}-Er-Cp_{cent} angle of *ca.* 172° (Figure 20). The shorter COT^{2-} centroid distance highlights the strong electrostatic interaction between the lanthanide metal centre and the large dianionic ring when compared to the smaller Cp ligand. Dynamic magnetic susceptibility measurements revealed two well-defined slow magnetic relaxation processes between 10-20 K (Figure 20), with U_{eff} = 137 and 224 cm^{-1}, respectively.

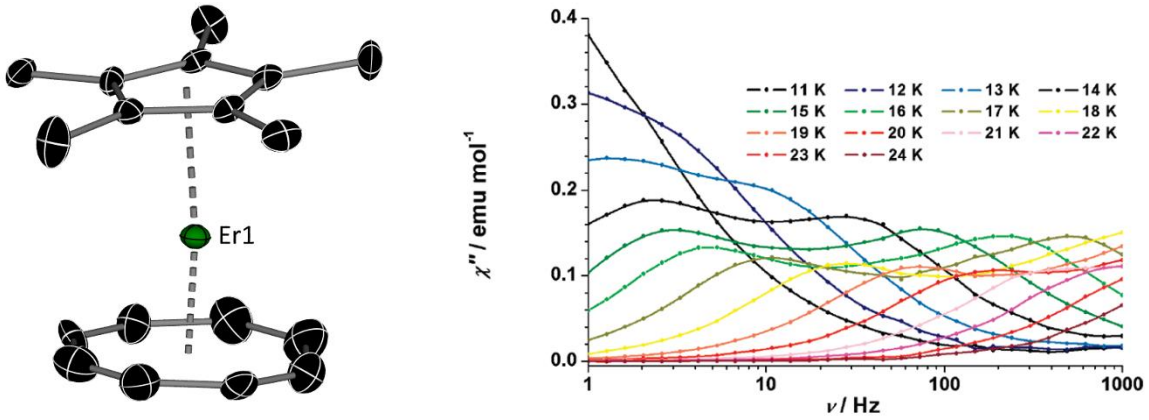

Figure 20. Molecular structure of $[Er(\eta^8\text{-}C_8H_8)(\eta^5\text{-}Cp^*)]$ (left), thermal ellipsoids are set to 50 % probability and hydrogen atoms have been omitted for clarity. Frequency-dependence of the out-of-phase susceptibility, $\chi''(\nu)$, in zero DC field between 11-24 K (right).[91]

The occurrence of the observed dual relaxation processes were attributed to different structural confirmations of the COT ligand, which displays static disorder at temperatures of 10, 20 and 120 K. Despite the very slight differences between the two structural confirmations, the resulting effective energy barriers are significantly affected, indicative of how sensitive the SMM properties are to the coordination environment. Magnetic hysteresis measurements revealed waist-restricted loops open up to 5 K, indicating that magnetic relaxation via QTM is dominant across the low temperature regime. A series of derivatives [Ln(η^8-C_8H_8)(η^5-Cp*}] (Ln = Tb, Dy, Ho, Tm) were reported the following year, which have similar structures.[93] The dysprosium and holmium derivatives were the only complexes to show slow magnetic relaxation in the absence of an applied magnetic field, however in both cases the QTM is prominent, resulting in a U_{eff} of 18 and 5 cm^{-1}, respectively.

Based on current understanding, the SMM properties can be qualitatively described by the large 8-membered COT ligand providing a dominant equatorial crystal field, due to its closer proximity to the Ln^{3+} metal centres and the π-electron density extending into the equatorial plane. The observation of modest energy barriers for [(Cp*)Er(COT)] and open hysteresis loops up to 5 K reflect stabilisation of the prolate-spheroid shaped magnetic $|M_J|$ = 15/2 ground state. However, the Cp ligand provides a competing axial crystal field, which in the case of Er^{3+} simultaneously destabilises the $|M_J|$ = 15/2 state and promotes magnetic relaxation via QTM at low temperatures. In contrast, due to the oblate-spheroid shaped magnetic M_J ground states of Dy^{3+} and Ho^{3+}, the dominant equatorial crystal field of COT destabilises the M_J = ±15/2 and ±8 ground states, respectively, and facilitates QTM, resulting in small U_{eff} values of 18 and 5 cm^{-1}, respectively.

This hypothesis was further illustrated by Long, Chibotaru and Murugesu in their studies on the homoleptic sandwich complex [Er(η^8-COT)$_2$]$^-$.[94,95] The contact-ion pair complexes [Er(η^8-C_8H_8)$_2$K(18-c-6)] feature two η^8-COT ligands coordinated to the Er^{3+} metal centre, with a potassium ion η^8-coordinated to one COT ligand and capped by 18-crown-6. The separated ion pair [K(18-c-6)(THF)$_2$]$^+$[Er(η^8-C_8H_8)$_2$]$^-$ can be formed via modification of the crystallisation conditions (Figure 21).

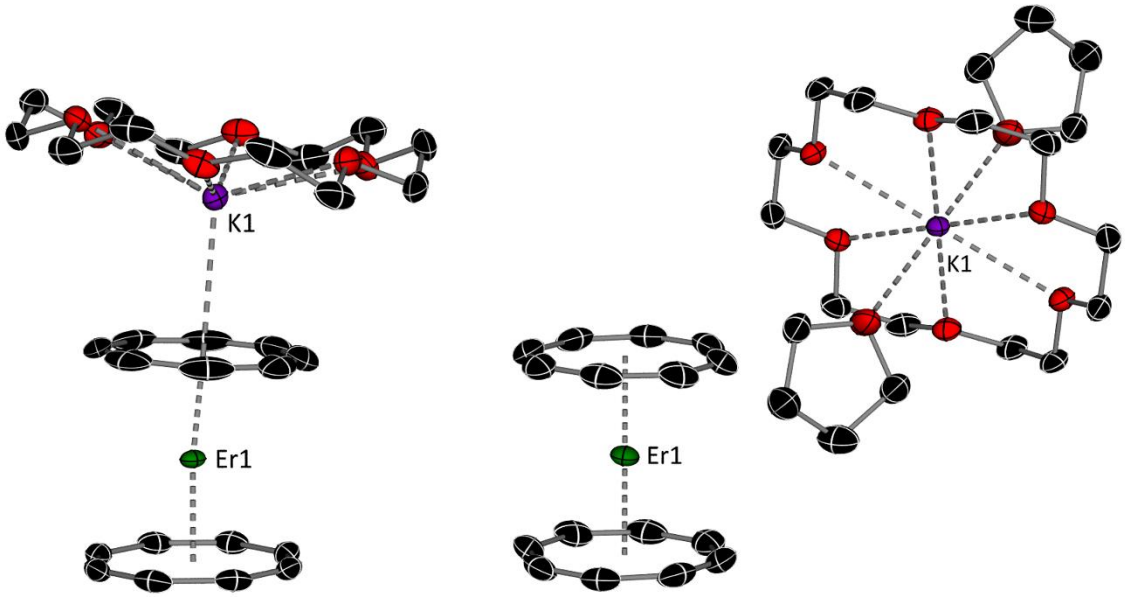

Figure 21. Molecular structures of $[Er(\eta^8\text{-}C_8H_8)_2K(18\text{-}c\text{-}6)]$ (left) and $[K(18\text{-}c\text{-}6)(THF)_2]^+[Er(\eta^8\text{-}C_8H_8)_2]^-$ (right). Thermal ellipsoids are set to 30 % probability and hydrogen atoms have been omitted for clarity.[94,95]

In the contact-ion complexes, the two COT ligands are almost co-planar, with COT_{cent}-Er-COT_{cent} angles of *ca.* 175.19(12)°,[94] and 173.85(6)°,[95] with average COT_{cent}-Er distances of *ca.* 1.87 Å. Dynamic magnetic susceptibility measurements in zero-field applied revealed slow magnetic relaxation in the temperature range 15-27 K, and 12-31 K, resulting in U_{eff} = 147(1) cm^{-1},[94] and U_{eff} = 199(1) cm^{-1},[95] respectively. Despite the relatively low energy barriers, the strong equatorial crystal field provided by the bis-COT ligands is reflected in the hysteresis measurements, which show waist-restricted loops open up to 10 K, with appreciable coercivity of 0.7 T at 1.8 K (Figure 22). The separated ion-pair complex $[K(18\text{-}c\text{-}6)(THF)_2]^+[Er(\eta^8\text{-}C_8H_8)_2]^-$ displays almost identical structural parameters, and hence magnetic properties, with U_{eff} = 147(1) cm^{-1} and comparable hysteresis loops.[94] The dysprosium derivative $[Dy(\eta^8\text{-}C_8H_8)_2K(18\text{-}c\text{-}6)]$ once again showed poor SMM properties due to the dominant equatorial crystal field, with U_{eff} = 9(1) cm^{-1},[94] and U_{eff} = 8(1) cm^{-1}.[95]

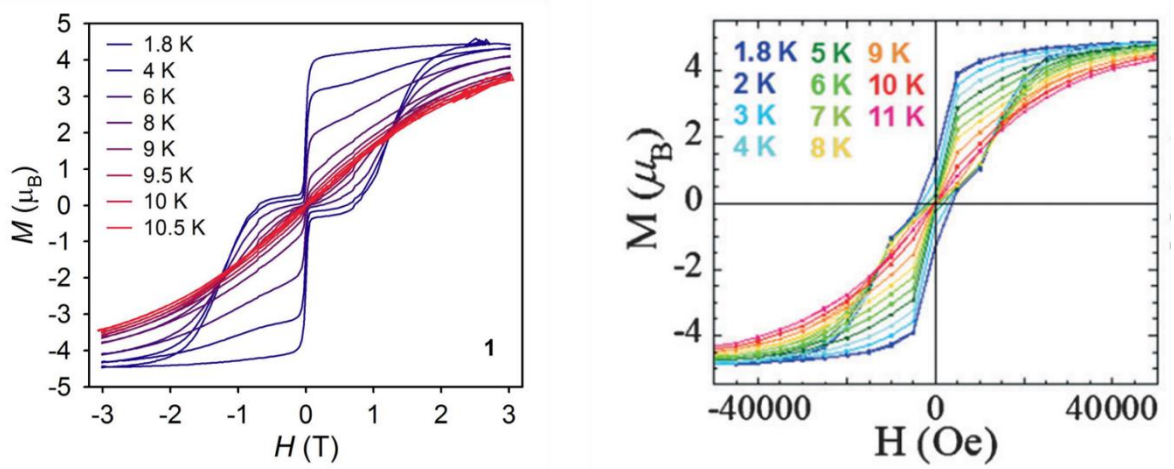

Figure 22. Magnetic hysteresis measurements for [Er(η^8-C_8H_8)$_2$K(18-c-6)] between 1.8-10.5 K with a sweep rate of 7.8 Oe s^{-1} (left),[94] and between 1.8-11 K with a sweep rate of 35 Oe s^{-1} (right).[95]

The negative effects of using equatorial COT ligands in Dy^{3+}-based SMMs were further highlighted by Murugesu and co-workers, with the characterisation of a bis-COT complex [Dy{η^8-$C_8(SiMe_3)_2H_6$}$_2$Li(THF)(DME)] and a multi-decker complex [(Dy{η^8-$C_8(SiMe_3)_2H_6$})$_2${μ-$\eta^8\eta^8$-$C_8(SiMe_3)_2H_6$}].[96,97] Investigations into the SMM properties revealed an energy barrier of 13 cm^{-1} for the double-decker complexes and 6 cm^{-1} for the triple-decker complex, with both complexes plagued by significant QTM. However, by switching the 'oblate' Dy^{3+} for 'prolate' Er^{3+}, the sandwich complex [Li(DME)$_3$]$^+$[Er{η^8-$C_8(SiMe_3)_2H_6$}$_2$]$^-$ and triple-decker [(Er{η^8-$C_8(SiMe_3)_2H_6$})$_2${μ-$\eta^8\eta^8$-$C_8(SiMe_3)_2H_6$}] showed improved SMM properties, with U_{eff} = 130(1) and 224(7) cm^{-1} and waist-restricted hysteresis loops open up to 8 and 12 K, respectively (Figure 23).[84,98] DC magnetic susceptibility measurements on the isotropic gadolinium analogue revealed a magnetic coupling constant of J = −0.448 cm^{-1} (–2J formalism), therefore the improved magnetic properties of the triple-decker complex are thought to be a consequence of the magnetic exchange coupling between the Er^{3+} metal centres, which feature an Er···Er distance of 4.1109(5) Å.

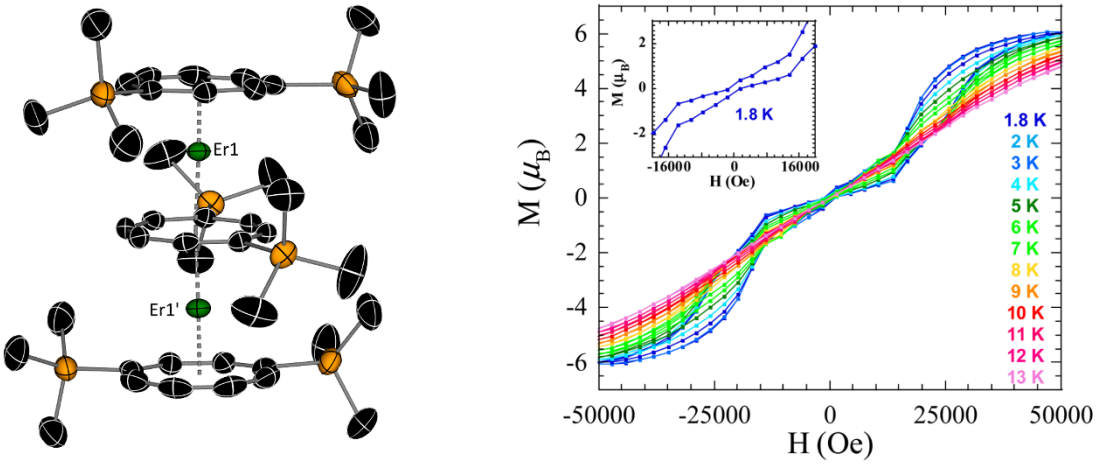

Figure 23. Molecular structure of [(Er{η^8-$C_8(SiMe_3)_2H_6$})$_2${μ-$\eta^8\eta^8$-$C_8(SiMe_3)_2H_6$}] (left), thermal ellipsoids are set to 50 % probability and hydrogen atoms have been omitted for clarity. Magnetic hysteresis measurements between 1.8-13 K with a sweep rate of 22 Oe s^{-1} (right).[84]

Recent investigations by Gao and co-workers into improving the properties of COT-ligated Er-SMMs have been explored by manipulating the crystal field with the introduction of electron deficient heteroatomic rings.[99] The heteroleptic sandwich complex [Er(η^8-C_8H_8)(η^6-C_5BH_5Me)] has a U_{eff} of 293 cm^{-1}, which is a record for an Er^{3+}-based system. However, the hysteresis is only open up to 6 K (Figure 24).

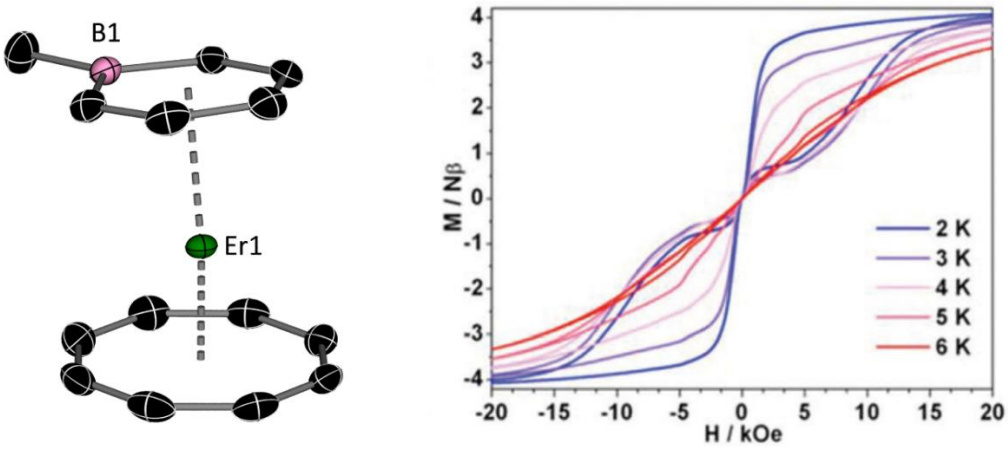

Figure 24. Molecular structure of [Er(η^8-C_8H_8)(η^6-C_5BH_5Me)] (left), thermal ellipsoids are set to 50 % probability and hydrogen atoms have been omitted for clarity. Magnetic hysteresis measurements between 2-6 K with a sweep rate of 19 Oe s^{-1} (right).[99]

1.2.6. η^8-Pentalene ligands

The first and, currently, only published example of a dianionic η^8-pentalene (Pn) ligated SMM was reported by Layfield, Cloke and co-workers in 2018.[100] The heteroleptic sandwich complexes $[Ln\{\eta^8\text{-}C_8(Si^iPr_3)_2H_4\}(\eta^5\text{-}Cp^*)]$ (Ln = Y, Dy) were formed by the reactions of one equivalent of $[K_2\{C_8(Si^iPr_3)_2H_4\}]^{2-}(K_2Pn^{TIPS})$ with $LnCl_3$ (Ln = Y, Dy) in THF, followed by the addition of NaCp* (Scheme 6).

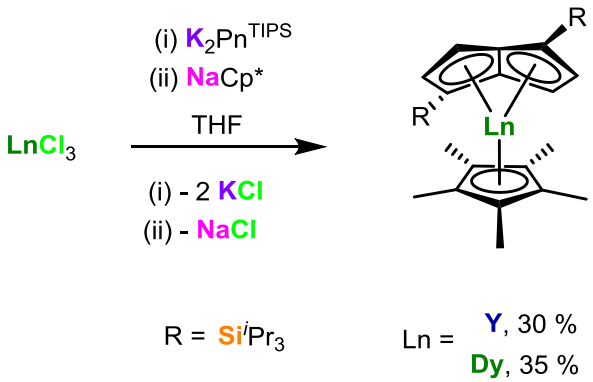

Scheme 6. Synthesis of $[Ln\{\eta^8\text{-}C_8(Si^iPr_3)_2H_4\}\{\eta^5\text{-}C_5(Me)_5\}]$ (Ln = Y, Dy).[100]

The two compounds are isostructural with an η^8-coordination mode of the Pn^{2-} ligand and η^5-coordination of Cp* (Figure 25). The Dy-Cp_{cent} distance is 2.344(5) Å, with the Dy-Pn_{cent} distances being significantly shorter at 2.235(3) Å. The mixed-sandwich complex features a Cp_{cent}-Dy-Pn_{BHcent} (BH = bridgehead) angle of 169.30(13)°, with two Cp_{cent}-Dy-Pn_{cent} angles of 152.47(11) and 153.05(11)°.

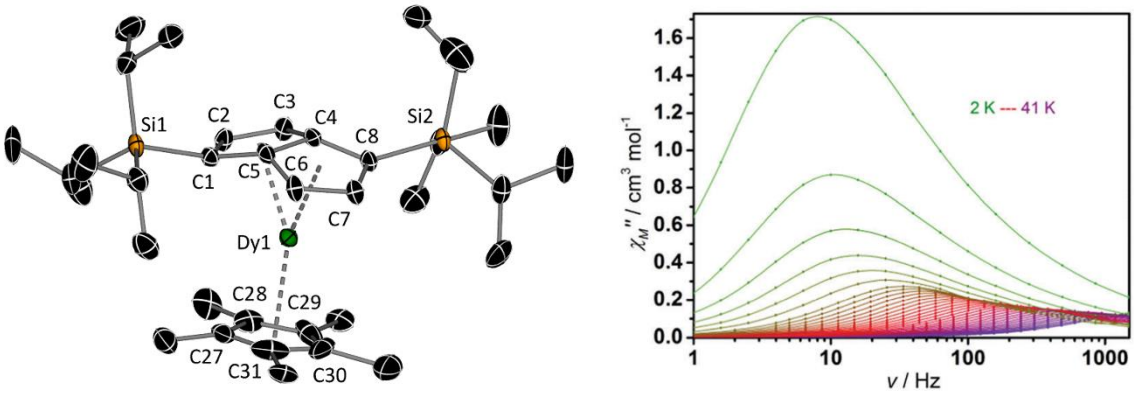

Figure 25. Molecular structure of $[Dy\{\eta^8\text{-}C_8(Si(^iPr)_3)_2)\}\{\eta^5\text{-}C_5(Me)_5)]$ (left), thermal ellipsoids are set to 30 % probability and hydrogen atoms have been omitted for clarity. Frequency-dependence of the out-of-phase susceptibility, $\chi''(\nu)$, in zero DC field between 2-41 K (right).[100]

Dynamic magnetic susceptibility measurements revealed slow magnetic relaxation in the absence of an applied magnetic field in the temperature range 2-41 K (Figure 29), with U_{eff} = 188(11) cm^{-1}, which can be increased to U_{eff} = 245(28) cm^{-1} via magnetic dilution (5 % Dy, 95% Y). Despite the axiality of the system, there is a strong influence of QTM at lower temperatures. This is thought to arise as a consequence of the competing equatorial ligand field provided by the folded η^8-Pn ligand, specifically the wing-tip carbon atoms (Figure 29, C2 & C7).

Thus, with η^8-pentalene ligands displaying a strong influence on the equatorial ligand field, this is counter intuitive to a high-performance Dy^{3+} SMM. However, applying these unique ligands into lanthanide organometallic complexes with prolate-spheroid shaped magnetic M_J ground states, that would benefit from such an equatorial crystal field, *i.e.* $[Er\{\eta^8\text{-}C_8(R)_2H_4\}_2]^-$ or $[Er\{\eta^8\text{-}C_8(R)_2H_4\}\{\eta^8\text{-}C_8H_8\}]^-$ (R = $SiMe_3$, Si^iPr_3), could indeed prove fruitful (Figure 26). Nevertheless, as this is based on one example, further studies on unique η^8-pentalene ligated SMMs are required in order to confirm this magneto-structural correlation.

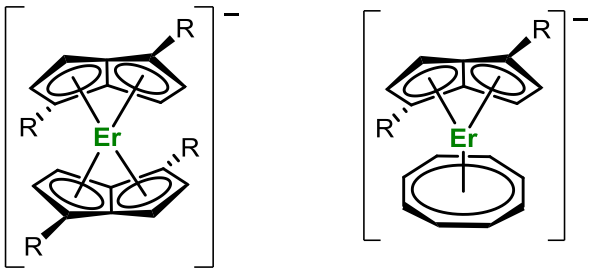

Figure 26. Hypothetical anionic Er^{3+} complexes $[Er\{\eta^8\text{-}C_8(R)_2H_4\}_2]^-$ (left) and $[Er\{\eta^8\text{-}C_8(R)_2H_4\}\{\eta^8\text{-}C_8H_8\}]^-$ (right) (R = $SiMe_3$ or Si^iPr_3) containing Pn^{2-} ligands, which could display SMM properties.

1.2.7. η^9-Cyclononatetraenyl ligands

The 9-membered monoanionic cyclononatetraenyl (Cn) ligand is a 10 π-electron aromatic system, which is isoelectronic to the dianionic COT^{2-} ligand and should therefore be a promising candidate for organometallic sandwich complexes. However, as with the smaller 6- and 7-membered carbocycles, complexes of the larger C_9 ring are rare. It was not until 2017 that the first f-element cyclononatetraenyl complexes were reported by Nakajima

and co-workers.[101] The homoleptic Eu^{2+} sandwich complex [Eu(η^9-C_9H_9)$_2$] was formed via the salt metathesis reaction between EuI_2 and two equivalents of [KC_9H_9], with the complex featuring Cn_{cent}-Eu distances of 1.984 Å and a Cn_{cent}-Eu-Cn_{cent} angle of 180°. However, it should be noted that this complex was only isolated in a 4 % yield. Nevertheless, the photoluminescence of the divalent europium complex was investigated, revealing a blue-green emission at 516 nm, which is significantly shifted when compared to a bis-COT Eu^{2+} sandwich complex [Eu{(η^8-C_8H_8)Li(DME)}$_2$] (λ_{em} = 630 nm). The photophysical properties of the Cn-ligated complexes therefore contrast to those of other Eu^{2+} organometallics, such as those containing Cp and COT ligands, which typically show red photoluminescence. This blue-shift is thought to be due to the weakened electrostatic crystal field provided by the larger 9-membered carbocyclic ring.

In 2018, Nocton and co-workers reported the divalent lanthanide bis(cyclononatetraenyl) complexes [Ln(η^9-C_9H_9)$_2$] (Ln = Sm, Eu, Tm, Yb) (Figure 27),[102] with the europium analogue being isostructural to that previously reported by Nakajima and co-workers. The sandwich complexes feature Cn_{cent}-Ln-Cn_{cent} angles of 180° and were designated as 'lanthanidocenes' in reference to their linear structures being reminiscent of ferrocene and uranocene. The structure of [K(C_9H_9)(Et_2O)] displayed disorder around one carbon atom on the C_9 ring, indicating that two isomers were present, the *cis*-isomer, where all carbon atoms form a regular nonagon, and the *trans*-isomer, where one C–H bond is oriented toward the centre of the ring. Reactions of [KC_9H_9] as the mixture of isomers with YbI_2 were initially hampered due to the poor solubility of [KC_9H_9], resulting in low yields. By utilising different solvent conditions, the target sandwich complex [Yb(η^9-C_9H_9)$_2$] was formed in 43 % yields, however the ^{1}H NMR spectrum revealed that three isomers were present in solution, [Yb(*cis*-C_9H_9)$_2$], [Yb(*trans*-C_9H_9)$_2$] and [Yb(*cis*-C_9H_9)(*trans*-C_9H_9)]. Dissolving the mixture of isomers in THF or MeCN resulted in formation of the separated ion-pairs [Yb(*cis*/*trans*-C_9H_9)$(THF)_4]^+$[*cis*-$C_9H_9]^-$ and $[Yb(MeCN)_7]^{2+}$[*cis*-$C_9H_9]^-_2$, respectively. Importantly, the exposure of either of these solvated complexes to 10^{-3} mbar vacuum for 8 hours results in the formation of [Yb(*cis*-C_9H_9)$_2$]. The same method was then applied to the other divalent lanthanides to obtain [Ln(*cis*-C_9H_9)$_2$] with Ln = Sm, Eu and Tm.

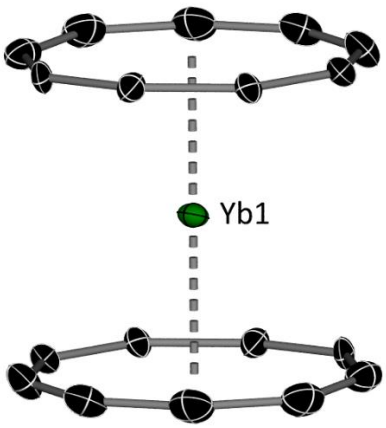

Figure 27. Molecular structure of [Yb(η^9-C_9H_9)$_2$]. Thermal ellipsoids are set to 50 % probability and hydrogen atoms have been omitted for clarity.[102]

The only investigations into the magnetic properties of a Cn-ligated complex were reported by Roesky and co-workers in 2019.[103] The heteroleptic sandwich complexes [Ln(η^8-C_8H_8)(η^9-C_9H_9)] (Ln = Nd, Sm, Dy, Er), which were initially targeted by Streitweiser and co-workers in 1971,[104] were formed by the salt metathesis reactions of [$KC_9H_9(DME)_2$] with [Ln(η^8-C_8H_8)I(THF)$_n$] (Ln = Nd, *n* = 3, Sm, Dy, Er, *n* = 2). In this case the potassium salt of cyclononatetraenyl was recrystallised from DME as the all-*cis* isomer in the solid-state. The Er^{3+} sandwich complex [Er(η^8-C_8H_8)(η^9-C_9H_9)] displays complicated crystallographic disorder, with split positions of the Er^{3+} ion and disordered C_8 / C_9 rings (Figure 28). This structure displays an Er1-COT_{cent} distance of 1.6725(4) Å, with a slightly longer Er1'-Cn_{cent} distance of 1.7248(4) Å. DFT geometry optimization found the energetic minimum of [Er(η^8-C_8H_8)(η^9-C_9H_9)] to be a perfect sandwich-type molecule, with a COT_{cent}-Er-Cn_{cent} angle of 177.516(2)°.

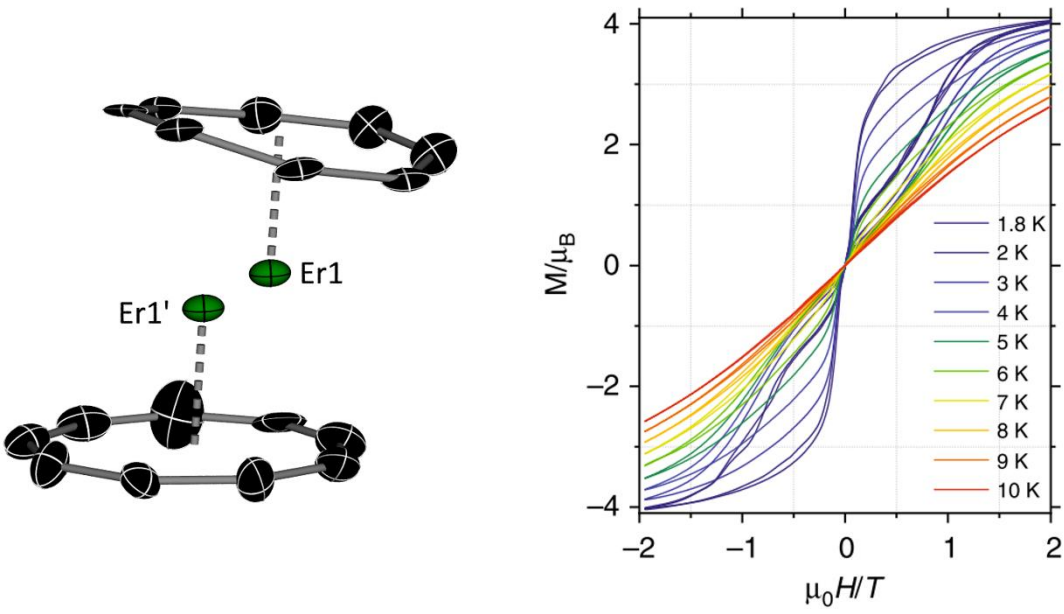

Figure 28. Molecular structure of [Er(η^8-C_8H_8)(η^9-C_9H_9)] (left), thermal ellipsoids are set to 30 % probability and disordered rings and hydrogen atoms have been omitted for clarity. Magnetic hysteresis measurements between 1.8-10 K with a sweep rate of 700 Oe s^{-1} (right).[103]

The $\chi''(\nu)$ data for [(COT)Er(Cn)] reveals the presence of a single peak at each temperature and fitting the magnetic relaxation data reveals a U_{eff} = 251(1) cm^{-1}, which is a slight improvement upon the effective energy barriers derived for [Er(η^8-COT)$_2$]$^-$ in two separate studies (147(1) and 199(1) cm^{-1})[94,95] and the two relaxation barriers determined for [(COT)Er(Cp*)] (137 and 224 cm^{-1}).[91] Magnetic hysteresis measurements reveal waist-restricted loops between 2-10 K, with no appreciable coercivity due to QTM. A possible explanation for the magnetic relaxation observed in [(COT)Er(Cn)] was reasoned by the presence of antisymmetric vibrations of the C_8 / C_9 rings detected in the Raman spectrum at 240 cm^{-1}, which is remarkably similar to the theoretical and experimental effective energy barriers of 268 and 251(1) cm^{-1}, respectively, and may facilitate spin-phonon coupling.

1.2.8. η^4-Cyclobutadienyl ligands

Following the theoretical prediction in 1956 that the smaller 4-membered cyclobutadiene (Cb) ring could potentially be stabilised via transition-metal complexation,[105] the synthesis of the first substituted Cb complexes [Ni(η^4-C_4Me_4)Cl_2]$_2$ and [Fe(η^4-C_4Ph_4)CO_3] were

reported in 1959 and structurally authenticated in 1962 and 1960, respectively.[106–109] Subsequently, the parent cyclobutadiene was stabilized as the iron tricarbonyl complex [Fe(η^4-C_4H_4)CO_3].[110]

Prior to initial research in our group,[111,112] cyclobutadienyl ligands were completely unknown in rare-earth chemistry. This can perhaps primarily be explained by the differences in bonding between 3d- and 4f-elements, whereby the electrostatic bonding in the latter has precluded the synthesis of cyclobutadienyl complexes through the cyclodimerization of alkynes, which is used to great effect in transition-metal chemistry.[113–118] Only one actinide cyclobutadienyl complex was previously known, *i.e.* the diuranium-cyclobutadienyl inverse sandwich complex [U{HC(SiMe$_2$NAr)$_3$}$_2$(μ-η^5:η^5-C_4Ph_4)] (Ar = 3,5-$Me_2C_6H_3$), which was formed in a reductive [2+2]-cycloaddition reaction between four equivalents of diphenylacetylene and a diuranium(V) precursor.[119] The bridging $[C_4Ph_4]^{2-}$ ligand engages in η^4-Cb interactions with the uranium metal centres, with each uranium ion additionally interacting with the π-system of a phenyl substituent.

The first examples of rare-earth η^4-cyclobutadienyl complexes were reported by Layfield and co-workers in 2018.[111] The rare-earth bis(cyclobutadienyl) sandwich complexes [K_2Ln{η^4-C_4(SiMe$_3$)$_4$}{η^4-C_4(SiMe$_3$)$_3$-κ-CH_2(SiMe$_2$)}C_7H_8] (Ln = Y, Dy) with a protonated [K{η^3-C_4(SiMe$_3$)$_4$H}C_7H_8] by-product were formed by salt metathesis reactions of $LnCl_3(THF)_{3.5}$ with two or three equivalents of [K_2{η^4-C_4(SiMe$_3$)$_4$}] (Scheme 7). This work builds on the pioneering work of Sekiguchi and co-workers, who first reported the stable cyclobutadiene pro-ligand [C_4{SiMe$_3$}$_4$] and its dilithium complex.[120–122]

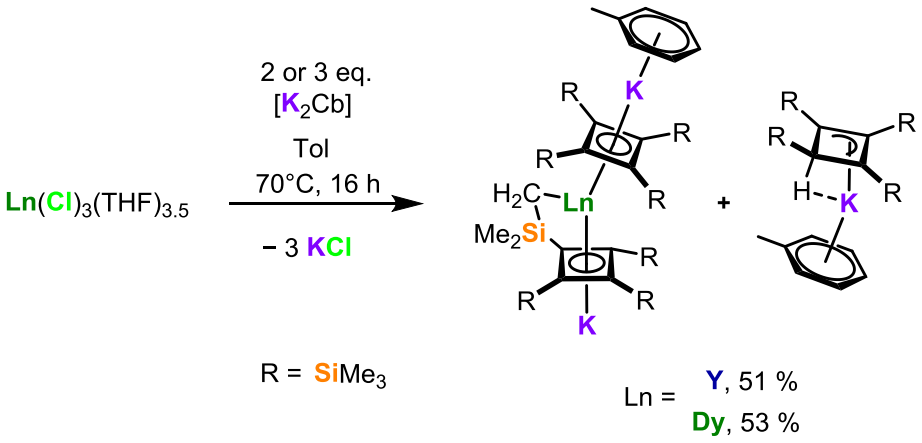

Scheme 7. Synthesis of [K_2Ln{η^4-C_4(SiMe$_3$)$_4$}{η^4-C_4(SiMe$_3$)$_3$-κ-(CH_2(SiMe$_2$)}C_7H_8] (Ln = Y, Dy).[111]

The dysprosium and yttrium complexes are isostructural and feature η^4-coordination modes of both C_4 rings to the rare-earth metal and a bridging interaction to potassium. The potassium ion of one C_4 unit is capped by a toluene molecule, and the other C_4 unit features a deprotonated 'tuck-in' silylmethyl ligand (Figure 29). Each Cb ring is planar and has C-C distances comparable to those of $[K_2\{\eta^4\text{-}C_4(SiMe_3)_4\}]$, indicating that both have retained their dianionic aromatic character. Despite the dianionic nature of each Cb ligand, the Dy-Cb_{cent} distances of 2.354(3) and 2.376(3) Å are longer than the analogous Dy-Cp_{cent} distances in $[Dy(\eta^5\text{-}C_5{}^iPr_5)(\eta^5\text{-}Cp^*)]^+$, which are 2.284(1) and 2.296(1) Å, respectively.[27] This feature may be a consequence of the steric bulk of the trimethylsilyl groups, as well as the 'tuck-in' activation mode. A Cb_{cent}-Dy-Cb_{cent} angle of 156.42(9)° indicates that the 'tuck-in' equatorial ligand pushes the two η^4-Cb ligands away from an ideal axial geometry.

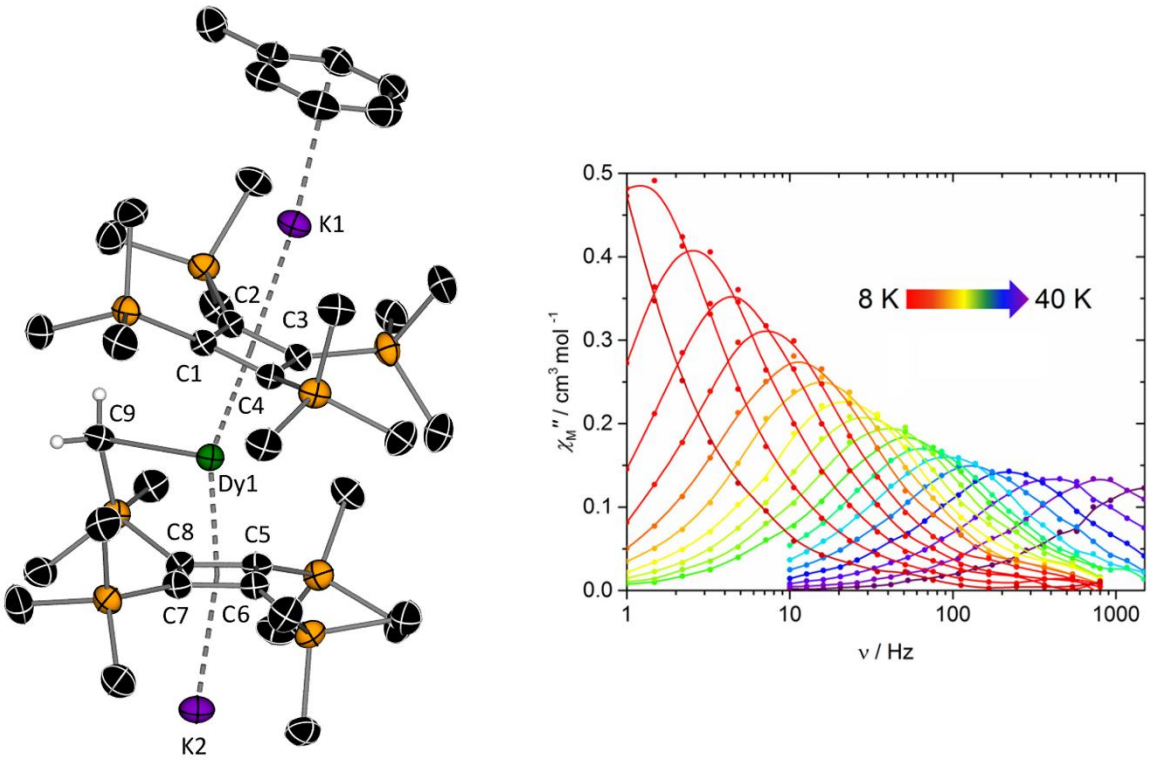

Figure 29. Molecular structure of $[K_2Dy\{\eta^4\text{-}C_4(SiMe_3)_4\}\{\eta^4\text{-}C_4(SiMe_3)_3\text{-}\kappa\text{-}CH_2(SiMe_2)\}C_7H_8]$ (left), thermal ellipsoids are set to 30 % probability and for clarity, only the hydrogen atoms bound to the 'tuck-in' CH_2 (C9) are shown. Frequency-dependence of the out-of-phase susceptibility, $\chi''(\nu)$, in an applied DC field of 1000 Oe between 8-40 K (right).[111]

The detrimental effect of the equatorial 'tuck-in' ligand is reflected in the magnetic measurements on the dysprosium version, whereby QTM dominates in zero-field at low temperatures, despite the strong axial ligand field provided by the Cb^{2-} ligands. However,

the application of a DC field of 1000 Oe suppressed the QTM, allowing maxima in the temperature range of 8-40 K to be observed (Figure 29), and a U_{eff} = 323(22) cm^{-1} to be extracted. *Ab initio* calculations confirmed that the Cb^{2-} ligands can provide a strong axial crystal field orientated toward the centres of the cyclobutadienyl ligands. However, the transverse components of the g-tensors in the magnetic ground state (g_x = 0.0076, g_y = 0.0130 and g_z = 19.734) are sufficient to induce QTM in the absence of an applied magnetic field despite being relatively small values. These results suggested that an 'unactivated' bis(cyclobutadienyl) complex of the type $[Dy\{\eta^4\text{-}C_4(SiMe_3)_4\}_2]^-$ should have excellent properties, however more control over the transfer of the Cb^{2-} ligands to rare-earth metals is needed to avoid activation of the trimethylsilyl substituents.

A new class of rare-earth cyclobutadienyl complexes were reported by Layfield and co-workers in 2020, whereby the use of a sodium Cb^{2-} pro-ligand results in a double ligand activation of the trimethylsilyl subsituents.[112] The rare-earth cyclobutadienyl sandwich complexes $[NaLn\{\eta^4\text{-}C_4(SiMe_3)_3\text{-}\kappa\text{-}CH_2(SiMe_2)\}\{\eta^3\text{-}C_4(SiMe_3)_4H\}]$ (Ln = Y, Dy, Lu) were formed in the salt metathesis reactions of $LnCl_3(THF)_n$ (where Ln = Y, Dy, n = 3.5, and Ln = Lu, n = 3) with two equivalents of $[Na_2\{\eta^4\text{:}\eta^4\text{-}C_4(SiMe_3)_4\}(THF)]_2$ (Scheme 8).

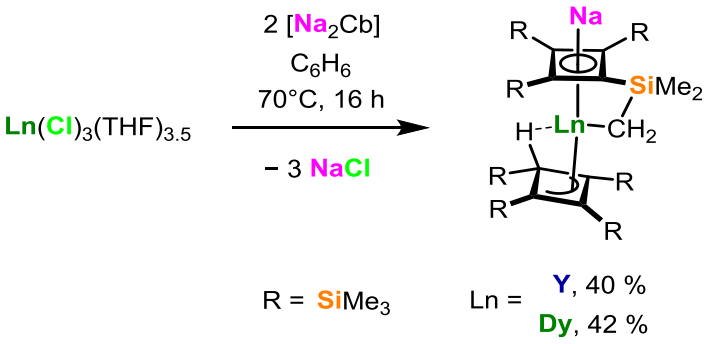

Scheme 8. Synthesis of $[NaLn\{\eta^4\text{-}C_4(SiMe_3)_3\text{-}\kappa\text{-}CH_2(SiMe_2)\}\{\eta^3\text{-}C_4(SiMe_3)_4H\}]$ (Ln = Y, Dy, Lu).[112]

The molecular structures are isostructural coordination polymers, and feature an η^4-coordination mode of one C_4 ring to the rare-earth metal, which displays a deprotonated 'tuck-in' interaction analogous to that described in the preceding section, and is capped by a sodium counter ion with a slipped η^4-interaction. The second Cb ring displays an η^3-allyl coordination mode of a protonated C_4 in addition to an agostic-type interaction with the Cb C–H bond (Figure 30). The η^4-Cb ring is square and planar, indicative of its aromatic character, whereas the protonated carbon of the η^3-Cb ring lies out of the plane of the η^3-

carbons by 0.26(2) Å. The $SiMe_3$ group attached to the protonated carbon is displaced by an angle of 119.2(7)°. The Dy-Cb_{cent} distances for the η^4-Cb and η^3-Cb are 2.308(5) and 2.460(5) Å, respectively, with an η^4-Cb_{cent}-Dy-η^3-Cb_{cent} angle of 159.157(5)°. The η^4-Cb centroid distance is 0.046 Å shorter than the shortest analogous distance in [$K_2Dy\{\eta^4$-$C_4(SiMe_3)_4\}\{\eta^4$-$C_4(SiMe_3)_3$-κ-$(CH_2(SiMe_2)\}C_7H_8$], with a slight increase in the Cb_c-Ln-Cb_c sandwich angle of 2.737°.

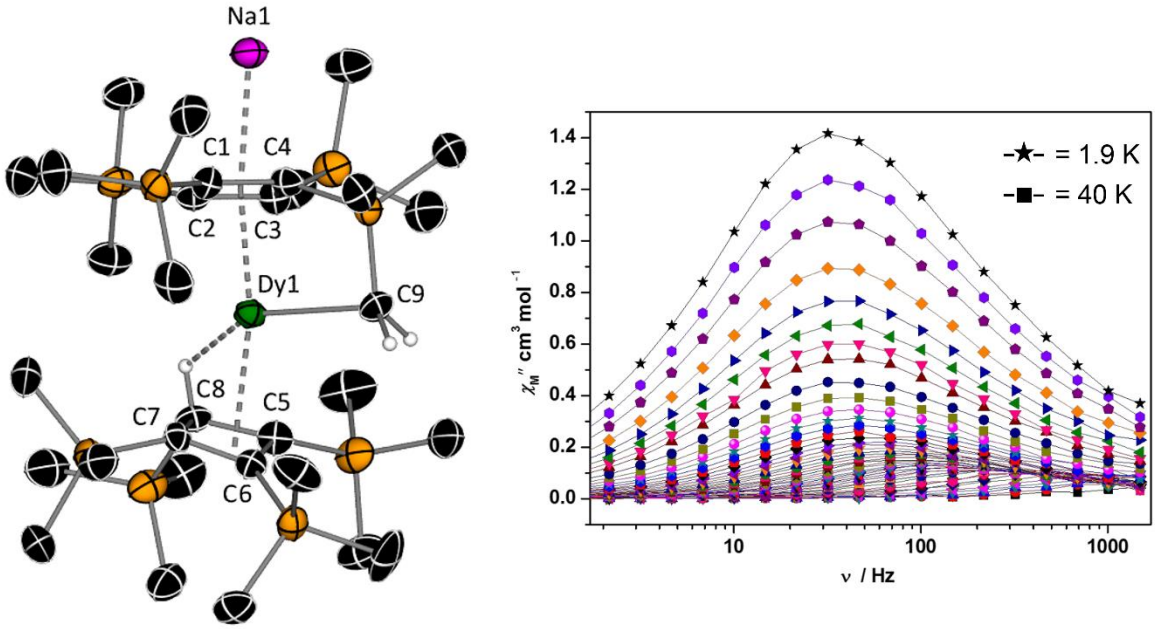

Figure 30. Molecular structure of [$NaDy\{\eta^4$-$C_4(SiMe_3)_3$-κ-$(CH_2(SiMe_2)\}\{\eta^3$-$C_4(SiMe_3)_4H\}$] (left), thermal ellipsoids are set to 50 % probability and for clarity, only the hydrogen atoms bound to the 'tuck-in' CH_2 (C9) and the protonated Cb ring are shown. Frequency-dependence of the out-of-phase susceptibility, $\chi''(\nu)$, in zero DC field between 1.9-40 K (right).[112]

Dynamic magnetic susceptibility measurements of the doubly activated dysprosium cyclobutadienyl complex revealed slow magnetic relaxation in the absence of an applied magnetic field in the temperature range 1.9-40 K, with strong QTM at lower temperatures (Figure 30). Fitting the relaxation data with Orbach, Raman and QTM components results in a barrier of U_{eff} = 309(20) cm^{-1}. This value is similar to that of the singly activated cyclobutadienyl system, however as the effective energy barrier was determined under zero applied magnetic field, this indicates that the double ligand activation results in a less-influential equatorial crystal field than that in [$K_2Dy\{\eta^4$-$C_4(SiMe_3)_4\}\{\eta^4$-$C_4(SiMe_3)_3$-κ-$CH_2(SiMe_2)\}C_7H_8$]. Moreover, this improvement in magnetic properties could be a

consequence of the shorter η^4-Cb centroid distance and the larger bis-Cb bending angle, providing a stronger axial crystal field for the Dy^{3+} ion.

These results highlight the complexity of rare-earth cyclobutadienyl chemistry, in which several activation modes of the trimethylsilyl substituents can occur simultaneously. These activation modes have a detrimental effect on the SMM properties of dysprosium cyclobutadienyl complexes, therefore further research into preventing them could unlock the potential of cyclobutadienyl ligands as platforms for the design of SMMs.

1.3. Thesis Aims

There are two main aims of this thesis:

1. To explore the fundamental chemistry of the smaller 4-membered cyclobutadienyl ligand with rare-earth elements and build upon our limited understanding of these systems.
2. To employ the cyclobutadienyl ligand in Dy^{3+} SMMs and contribute to the current magneto-structural correlations that exist in the field of lanthanide-based SMMs, *i.e.* an understanding of the relationship between structure and magnetic properties. Specifically, the aim is to increase the strength of the axial crystal field by using cyclobutadienyl ligands and, therefore, improve upon the current benchmark systems. The general structure of the key target complex is depicted in Figure 31.

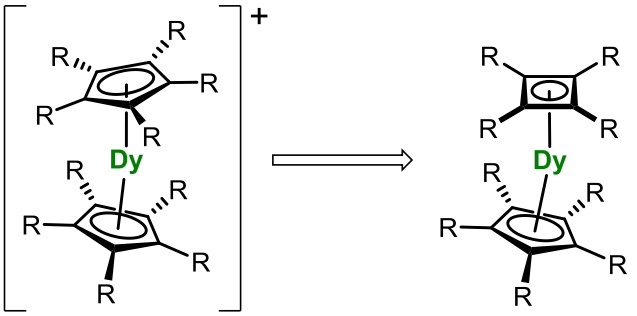

Figure 31. A representation of the current benchmark SMM systems (left) and a hypothetical Dy^{3+} complex containing a cyclobutadienyl ligand (right) that could show improved SMM properties.

Chapter 2

Organometallic Rare-Earth Half-Sandwich Complexes: Synthesis, Structure and Magnetic Studies

2.1. Cyclopentadienyl Rare-Earth Half-Sandwich Complexes

2.1.1. Background

In recent years, cationic bis-cyclopentadienyl rare-earth sandwich complexes have established themselves at the forefront of the high-performance SMM field.[22,23,25,27,42] However, the magnetic properties of their precursor complexes remain comparatively understudied, with measurements on only one dysprosium half-sandwich complex being reported, *i.e.* [Dy(η^5-$C_5{}^{i}Pr_5$)(κ^3-BH_4)$_2$(THF)].[27] There are a few other examples of dysprosium half-sandwich complexes with Cp ligands, however these are not precursors to metallocene complexes.[123,124] Thus, further investigations into the synthesis and characterization of metallocene precursor half-sandwich complexes are needed in order to strengthen the magneto-structural correlations that are currently used to predict and rationalize the properties of organometallic lanthanide SMMs.[14,22,23,25,27,52,125] Such studies should help to establish how subtle changes to the ligand steric bulk modify the crystal field around the Dy^{3+} ions and, hence, how they affect the magnetic properties. Ultimately, these studies should enable the design of SMMs with improved properties.

This section describes the synthesis, characterization, and magnetic properties of two cyclopentadienyl-dysprosium half-sandwich complexes with bulky substituents. The first example uses the relatively bulky tri-*tert*-butyl cyclopentadienyl ligand (Cp^{ttt}), which was chosen due to the breakthrough SMM properties of its cationic metallocene derivative [Dy(η^5-Cp^{ttt})$_2$]$^+$.[22,23] The second uses the less bulky tetramethyl-*tert*-butyl cyclopentadienyl ligand (Cp^{Me4tBu}), which has not been used to date in organometallic lanthanide SMMs.

*2.1.2. Synthesis and characterization of [Ln(η^5-Cp^{ttt})(κ^3-BH_4)$_2$(THF)] (Ln = Y (**1**), Dy (**2**))*

The synthesis of the cyclopentadienyl half-sandwich complexes [Ln(η^5-Cp^{ttt})(κ^3-BH_4)$_2$(THF)] (Ln = Y (**1**), Dy (**2**)) was achieved by the salt metathesis reaction between KCp^{ttt} and $Ln(BH_4)_3(THF)_3$ (Ln = Y, Dy) in toluene at 60 °C overnight (Scheme 9). After subsequent work up, storing a saturated hexane solution at –40 °C overnight produced white or pale yellow crystals of **1** and **2**, in isolated yields of 74 and 72 %, respectively.

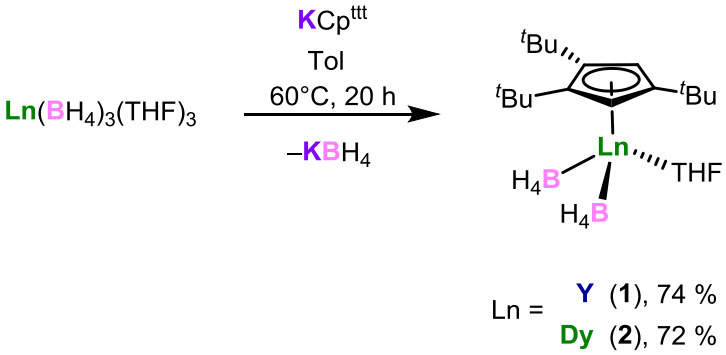

Scheme 9. Synthesis of **1** and **2**.

Compounds **1** and **2** are isostructural, with both featuring η^5-coordination of the Cp^{ttt} ligand, one THF ligand and two κ^3-borohydride ligands (Figure 32). In both **1** and **2**, the complexes display a disordered Cp ring split across two positions with approximately 50 % occupancy for each position (53:47 for **1**, 51:49 for **2**). For the disordered part 1 of complex **2**, the Dy-C bond distances range from 2.607(12)-2.727(12) Å, with a Dy1-Cp_{cent} distance of 2.37232(6) Å. For the disordered part 2 of complex **2**, the Dy-C bond distances are statistically different and range from 2.571(12)-2.692(14) Å, with a Dy1-Cp_{cent} distance of 2.35030(6) Å. The average Dy-Cp_{cent} distance in **2** therefore lies 0.0157 Å closer than the analogous distance in the related complex $[Dy(\eta^5\text{-}C_5{}^iPr_5)(\kappa^3\text{-}BH_4)_2(THF)]$ (2.377(1) Å).[27]

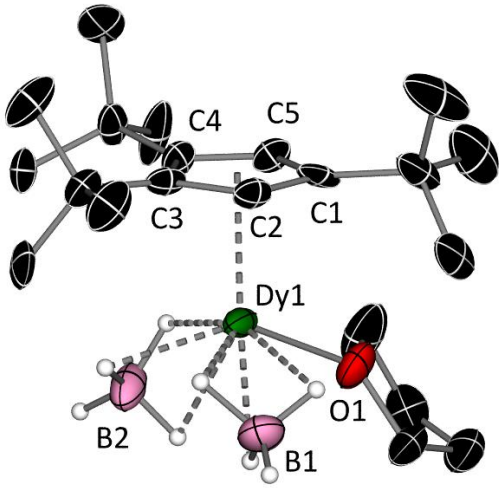

Figure 32 Molecular structure of $[Dy(\eta^5\text{-}Cp^{ttt})(\kappa^3\text{-}BH_4)_2(THF)]$ (**2**). Thermal ellipsoids are set to 50 % probability and for clarity, only the hydrogen atoms bound to boron are shown. Selected bond distances (Å) for **2**: C1-C2 1.416(17), C2-C3 1.440(12), C3-C4 1.452(15), C4-C5 1.424(14), C1-C5 1.401(12), Dy1-Cp_{cent} 2.37232(6), Dy1-B1 2.508(8), Dy1-B2 2.505(7), Dy1-O1 2.335(4).

The ^{1}H NMR spectrum of **1** in D_6-benzene shows signals at 1.26 (s, 9H) and 1.55 ppm (s, 18H), corresponding to the methyl protons of the *tert*-butyl groups. A small downfield signal at 6.40 ppm (s, 2H) corresponds to the two protons on the C_5 ring. Two additional multiplets can be seen at 1.00 (m, 4H) and 3.53 ppm (m, 4H), indicating that the THF ligand remains coordinated in solution. Broad signals can be seen between 0.70-1.50 ppm, corresponding to the two BH_4 ligands, however, these signals cannot be accurately integrated due to overlap with the THF and ^{t}Bu signals (Figure S1). The ^{1}H{^{11}B} NMR spectrum shows an additional signal for the expected borohydride groups at 1.06 ppm, which is still overlapped with the THF signal, however it roughly integrates to the expected 8H with a full width at half maximum (FWHM) = 21 Hz (Figure S2). The ^{13}C{^{1}H} NMR spectrum of **1** shows the expected nine peaks, with signals for the *tert*-butyl methyl protons and the quaternary carbon attached to C1 at 31.94 and 32.77 ppm and for C3/4 at 34.09 and 34.33 ppm, respectively. Three signals corresponding to the C_5 ring, which all appear as 1:1 doublets through coupling to ^{89}Y (I = ½) are centred at 111.37 ($^{1}J_{CY}$ = 1 Hz), 137.81 ($^{1}J_{CY}$ = 2 Hz) and 137.84 ppm ($^{1}J_{CY}$ = 1 Hz). The final two signals for the THF ligand occur at 73.70 and 24.83 ppm (Figure S3). The ^{11}B{^{1}H} spectrum displays a sharp signal at −22.69 ppm (FWHM = 48 Hz), and the ^{11}B spectrum displays a 1:4:6:4:1 quintet centred on −22.69 ppm ($^{1}J_{BH}$ = 86 Hz) (Figures S4, S5). The sharp peaks in the boron NMR spectra with well resolved coupling suggest that both borohydride ligands are in a high-symmetry environment, as expected based on the solid-state molecular structure of **1**.

The FTIR spectra of compounds **1** and **2** are essentially identical, with absorptions at very similar frequencies in the range $\tilde{\nu} =$ 4000-450 cm^{-1} (Figure 33). Characteristic C-H absorptions can be seen just above 3000 cm^{-1} for the Cp^{ttt} ring protons, and unsaturated stretches in the range 3000-2850 cm^{-1} corresponding to the saturated methyl groups and THF ligand. Two sets of B-H absorptions can be seen at 2450 and 2300-2100 cm^{-1}, reflecting the terminal and bridging nature of the B–H bonds.[126] Elemental analysis (C, H) of **1** and **2** were both consistent with their respective solid-state molecular structures, with % found (calculated) for **1** $C_{21}H_{45}YB_2O$: C 59.29 (59.47); H 10.60 (10.70), and **2** $C_{21}H_{45}DyB_2O$: C 50.54 (50.68); H 9.06 (9.11).

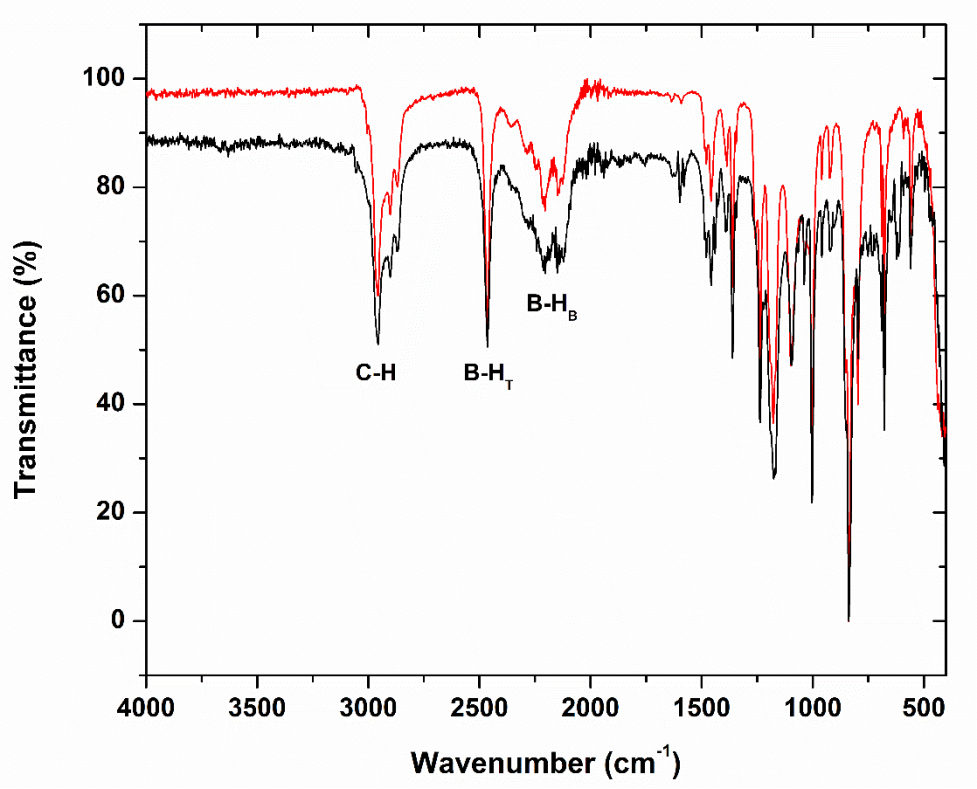

Figure 33. FTIR spectra of **1** (red line) and **2** (black line). Selected absorptions (cm^{-1}): 3000-2850 (C-H), 2450 ($B\text{-}H_T$), 2300-2100 ($B\text{-}H_B$).

*2.1.3. Magnetic property measurements on [Dy(η^5-Cp^{ttt})(κ^3-BH_4)$_2$(THF)] (**2**)*

The magnetic susceptibility of compound **2** was investigated using a SQUID magnetometer in both static (DC) and dynamic (AC) modes. In a static field of 1000 Oe, the temperature dependence of the molar magnetic susceptibility as a function of temperature, $\chi_M T(T)$, for **2** in the range 2-300 K is typical of a monometallic Dy^{3+} complex in which the lanthanide has a $^6H_{15/2}$ ground multiplet (Figure 34). At high temperatures, $\chi_M T$ approaches the free-ion value of 14.17 cm^3 K mol^{-1},[127] with a value of 14.01 cm^3 K mol^{-1} at 300 K. Upon lowering the temperature, a decrease in $\chi_M T$ occurs due to the thermal depopulation of excited crystal field levels, which drops sharply at very low temperature to a value of 12.09 cm^3 K mol^{-1} at 2 K. This sharp drop may indicate magnetic blocking, whereby the individual magnetic moments become unresponsive to an external magnetic field due to significant anisotropy in the system.[25,30]

Field dependence of the magnetisation measurements, $M(H)$, for **2** display typical curves for a strongly anisotropic Dy^{3+} complex (Figure 34). At a temperature of 1.9 K, as the field increases, M rises sharply at low fields before almost becoming saturated at 5.37 $N\beta$ at 7 T. As the temperature increases, the sharp increase in M becomes more gradual and requires a higher field to approach saturation. The experimental values observed are roughly half that of the theoretical value expected for a Dy^{3+} free-ion (10 Nβ), showing that the magnetization cannot saturate even at the lowest temperatures and highest fields permitted by the instrument. This behaviour is typical for strongly anisotropic Dy^{3+} complexes.[10,25,27,42]

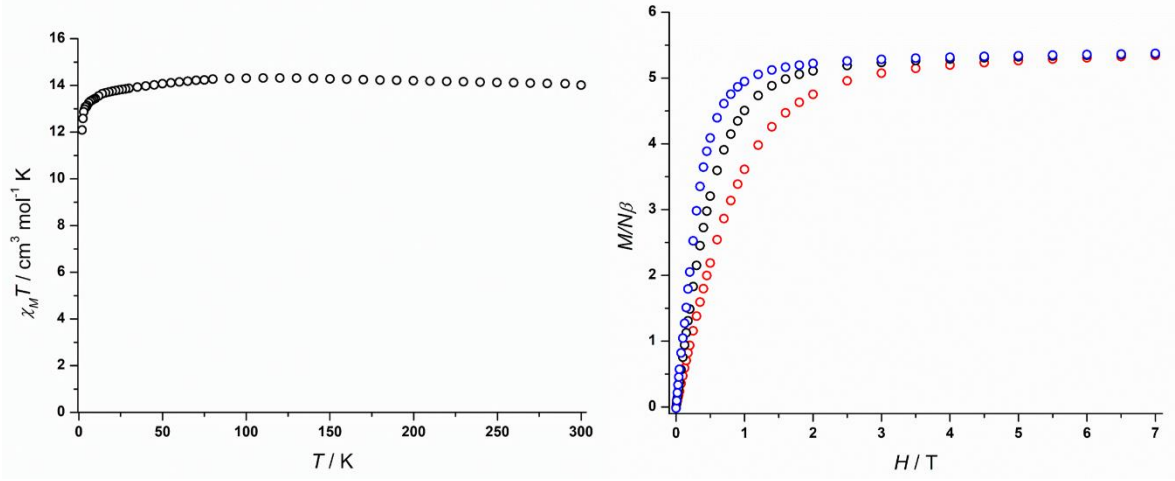

Figure 34. Plot of $\chi_M T(T)$ for **2** (left) in an applied field of 1000 Oe. $\chi_M T$ (300 K) = 14.01 cm^3 K mol^{-1}, $\chi_M T$ (2 K) = 12.09 cm^3 K mol^{-1}. Field (H) dependence of the magnetisation (M) for **2** (right) at 1.9 K (blue circles), 3.0 K (black circles) and 5.0 K (red circles). M = 5.37 Nβ at 1.9 K and 7 T.

The occurrence of magnetic remanence and coercivity is a prerequisite for any SMM to show genuine magnet-like behaviour, therefore, the hysteresis properties of SMMs are of particular interest.[10,14,42,128,129] The dynamic field-dependence of the magnetization for **2** was investigated at T = 1.9 K by applying a varying sweep rate across different fields (Figure 35). These measurements revealed waist-restricted hysteresis loops with a precipitous loss of magnetisation at zero-field and negligible coercivity. This is indicative of strong QTM dominating the magnetic relaxation in the cyclopentadienyl half-sandwich complex at low temperatures.[12] Due to the presence of such strong QTM at 1.9 K, further hysteresis measurements at higher temperatures were not performed.

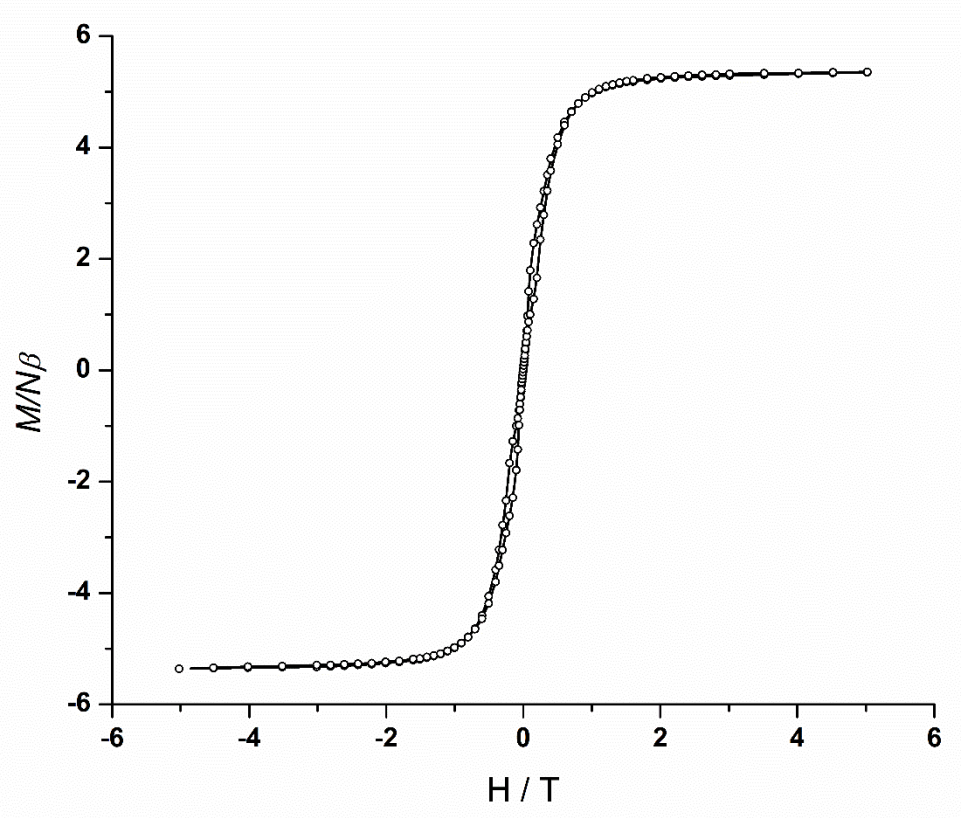

Figure 35. Magnetic hysteresis loops for **2**. The data were continuously collected at 1.9 K under a varying field sweep rate (1.1 mT s^{-1} |0-1| T, 3.0 mT s^{-1} |1-2| T, 4.5 mT s^{-1} |2-3| T and 8.5 mT s^{-1} |3-5| T). Solid lines are a guide to the eye.

The SMM properties of compound **2** were further probed by measuring the frequency-dependence of the real, $\chi'(\nu)$, and imaginary, $\chi''(\nu)$, components of the AC susceptibility across a temperature range of 1.9-27 K and AC frequencies in the range ν = 1-1488 Hz.

For compound **2**, the $\chi''(\nu)$ plots display maxima in the temperature range 1.9-20 K (Figure 36). Between 1.9-5 K, the frequency at which the maxima occur are essentially temperature independent, indicating a non-thermal relaxation process is dominating across this low temperature regime, *i.e.* QTM. At higher temperatures, the frequency maxima become temperature dependent before reaching the upper frequency limit of 1488 Hz, indicating that thermally activated relaxation processes are now dominant.[11,130]

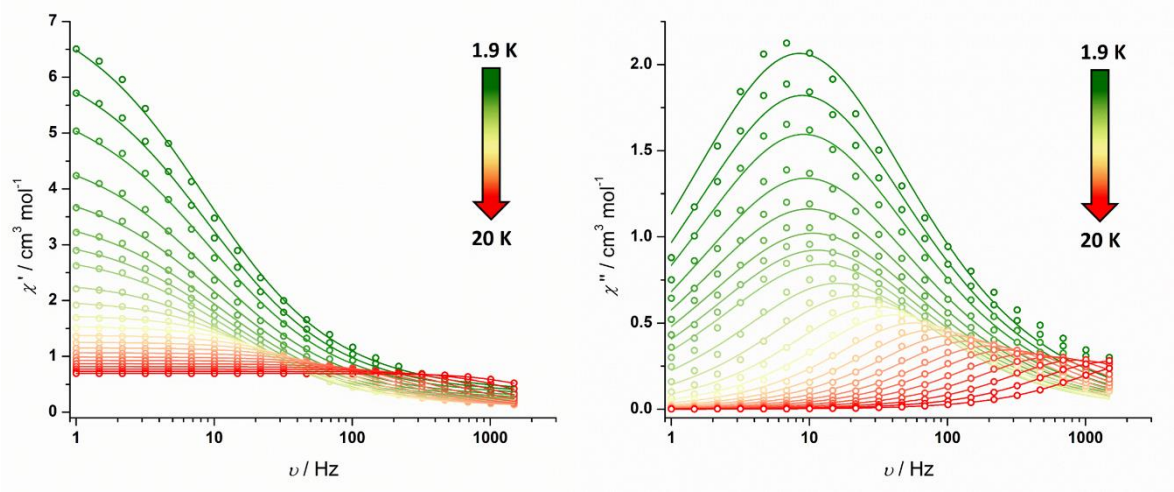

Figure 36. Frequency-dependence of the in-phase (χ') (left) and out-of-phase (χ'') (right) susceptibility for **2** in zero DC field at ν = 1-1488 Hz and temperatures of 1.9 to 20 K. Solid lines represent fits to the data using Equation 1.

In order to probe the relaxation dynamics of **2**, the maxima from the in-phase and out-of-phase susceptibility measurements from 1.9-20 K were plotted against each other to give semi-circular Cole-Cole plots, which were then fitted to the generalised Debye model shown in Equation (1) (Figures 37, 38):[11,130]

$$\chi_{\mathrm{AC}}{}^{(\omega)} = \chi_{\mathrm{S}} + \frac{\chi_{\mathrm{T}} - \chi_{\mathrm{S}}}{1 + (i\omega\tau)^{(1-\alpha)}} \qquad (1)$$

In this equation, χ_T and χ_S represent the isothermal and adiabatic susceptibility, respectively, ω is the angular frequency ($\omega = 2\pi\nu$), τ is the magnetic relaxation time and α is a fit parameter indicating the range of relaxation times in the systems ($0 < \alpha < 1$). The relaxation time τ is determined by the point at which the angular frequency reaches its maximum ($\tau = \omega^{-1}$). An α-parameter of 0 corresponds to a relaxation process with one time constant and larger α values represent a flattening of the distribution time constants around τ.[11,130]

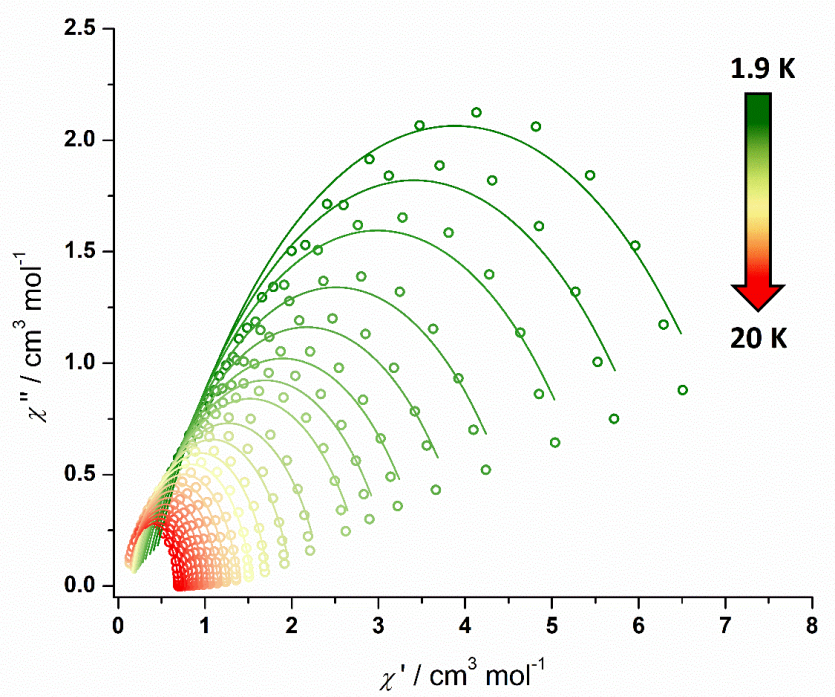

Figure 37. Cole-Cole plots for the AC susceptibilities in zero DC field for **2** from 1.9-20 K. Solid lines represent fits to the data using Equation 1.

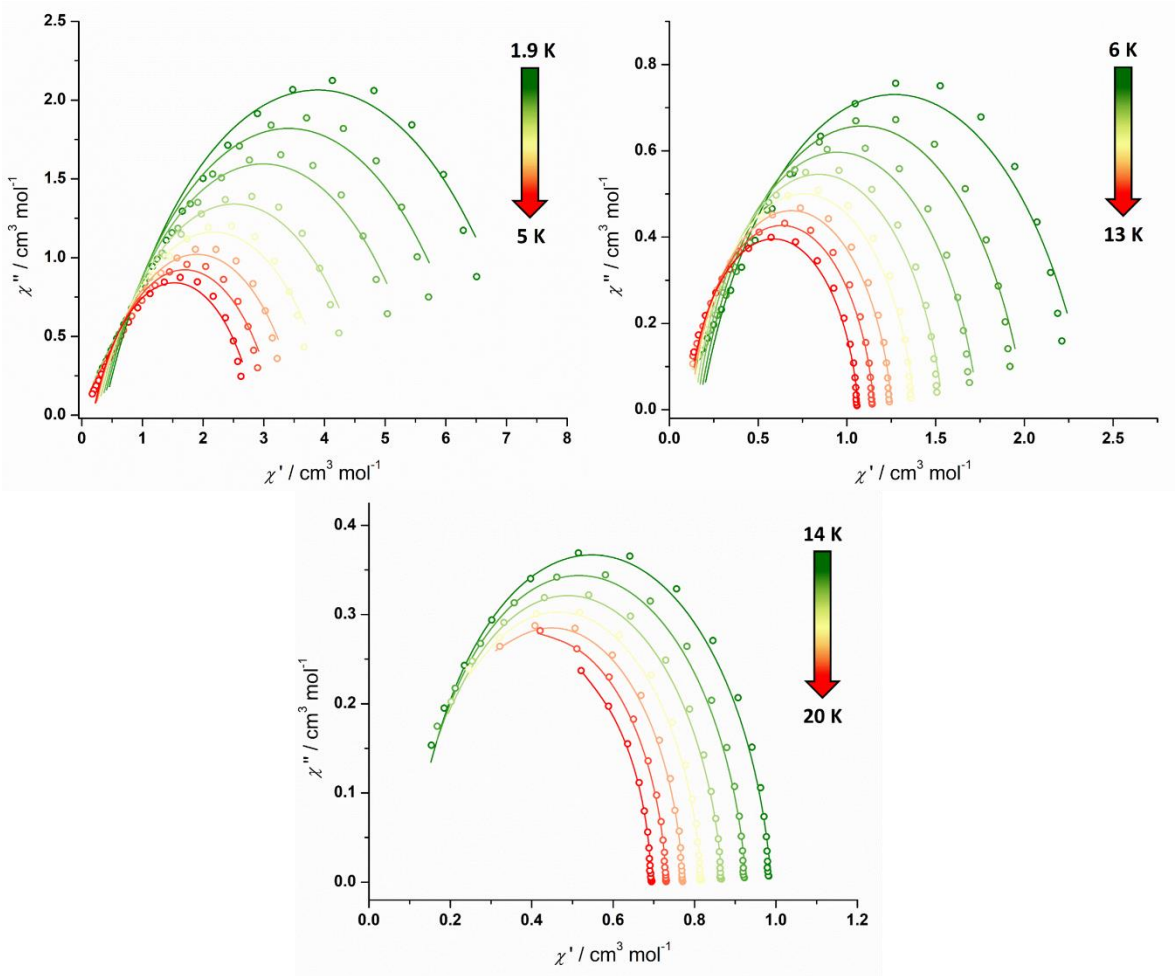

Figure 38. Cole-Cole plots for the AC susceptibilities in zero DC field for **2** from 1.9-5 K (top left), 6-13 K (top right) and 14-20 K (bottom). Solid lines represent fits to the data using Equation 1.

The results of parameters obtained from fitting the experimental data of compound **2** to the described model in Equation 1 are represented in Figures 36-38, with the tabulated results shown in the Supplementary Table S10. The fit shows a good agreement with the experimental data, with α-parameters ranging from 0.04-0.32, and τ values ranging from 0-0.019 s. The values for the α-parameters are largest at the lowest temperatures and indicate a broad distribution of relaxation times, further suggesting multiple relaxation pathways across the measured temperature range.[11,130] The origins of the large α-parameter range could be a consequence of the crystallographic disorder found in **2**, which has recently been shown to correlate with larger α-parameters in disordered dysprosium metallocenes.[131]

In order to gain more insight into the relaxation processes for compound **2**, as well as to extract the effective energy barrier to the reversal of magnetisation, the temperature dependence of the relaxation times were analysed in the form of the natural log of the relaxation time *vs.* inverse temperature, $\ln \tau$ (T^{-1}) (Figure 39). An excellent fit to the data (R^2 = 0.99991) was obtained using Equation (2):

$$\tau^{-1} = {\tau_0}^{-1} e^{-U_{\mathrm{eff}}/k_{\mathrm{B}}T} + CT^n + \tau_{QTM}^{-1} \qquad (2)$$

This equation is a sum of multiple relaxation processes, in which the first term represents the Orbach parameters (τ_0 is a pre-exponential factor also known as the attempt time, k_B is the Boltzmann constant), the second term represents the Raman parameters (C is the Raman coefficient, n is the Raman exponent), and the third term corresponds to the rate of quantum tunnelling of the magnetisation (τ_{QTM}^{-1}).[11]

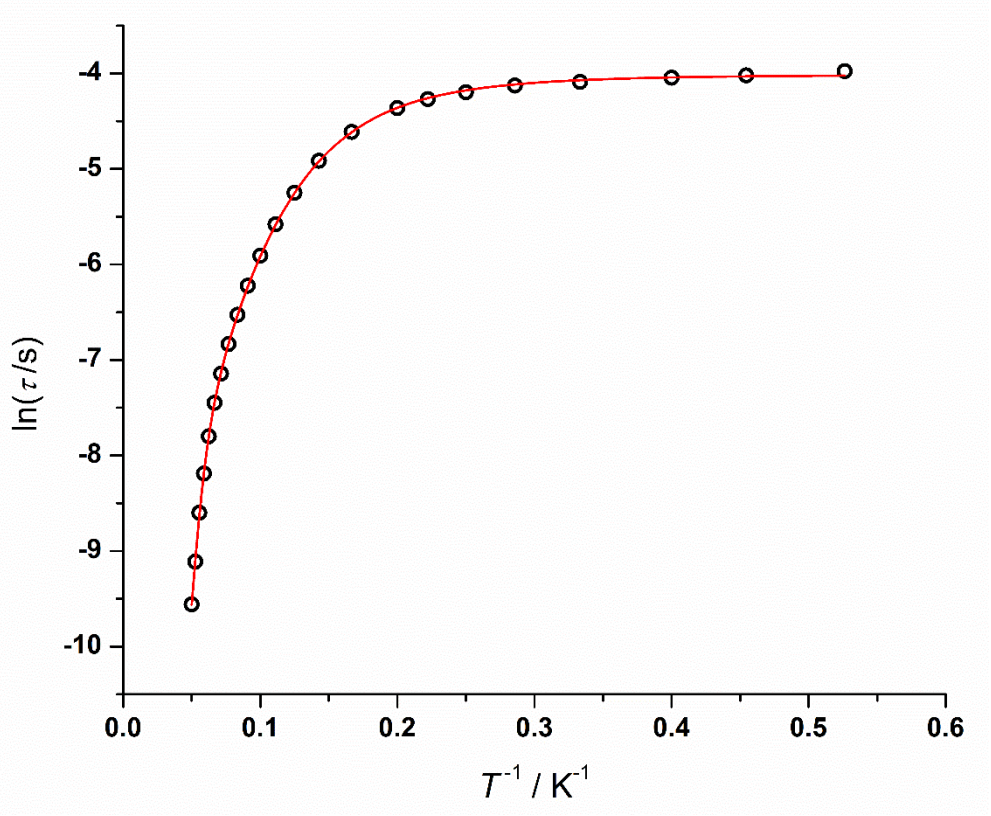

Figure 39. Plot of natural log of the relaxation time (τ) *vs.* inverse temperature for **2**. The black points are from the AC susceptibility measurements. The solid red line is the best fit (adjusted R^2 = 0.99991) to $\tau^{-1} = \tau_0^{-1}e^{-U_{\text{eff}}/k_{\text{B}}T} + CT^n + \tau_{QTM}^{-1}$, giving: U_{eff} = 165(5) cm^{-1}, τ_0 = 7.0(2) × 10^{-7} s, C = 5.2(4) × 10^{-2} s^{-1} K^{-n}, n = 3.78(3) and τ_{QTM} = 1.810(1) × 10^{-2} s.

At the highest measurement temperatures, the data is roughly linear and strongly temperature-dependent, indicative of relaxation via a thermally activated or Orbach process. At lower temperatures, the data begins to deviate from linearity, indicative of Raman relaxation processes, before becoming almost temperature independent, indicating that relaxation via QTM dominates the low temperature regime. For compound **2**, a fit of the data was achieved with the following parameters: U_{eff} = 165(5) cm^{-1}, τ_0 = 7.0(2) × 10^{-7} s, C = 5.2(4) × 10^{-2} s^{-1} K^{-n}, n = 3.78(3) and τ_{QTM} = 1.810(1) × 10^{-2} s. The Raman exponent (n), and the attempt relaxation time (τ_0) are typical of monometallic Dy^{3+} metallocene SMMs, which generally range from n = 2-5 and τ_0 = 10^{-7}-10^{-12} s, respectively.[14,15,132]

Based on the solid-state structure of **2**, its SMM properties can be qualitatively described by the Dy^{3+} metal centre experiencing a strong axial crystal field from the Cp^{ttt} ligand, resulting in an energy barrier to the reversal of magnetisation of 165(5) cm^{-1}. However, a competing equatorial field that arises from the THF and borohydride ligands destabilises

the magnetic ground state (or stabilizes the excited states) and promotes magnetic relaxation via QTM.

A comparison of the SMM properties of **2** can be drawn with [Dy(η^5-$C_5{}^{i}Pr_5$)(κ^3-BH_4)$_2$(THF)], which is a zero-field SMM with a U_{eff} = 241(7) cm^{-1}, τ_0 = 6.4(3) × 10^{-11} s, C = 2.24(1) s^{-1} K^{-n}, n = 3.6(1) and τ_{QTM} = 5.0(1) × 10^{-3} s.[27] The effective energy barrier of **2** is *ca.* 76 cm^{-1} smaller than the Cp^{iPr5} derivative, which is significant. This is surprising given the structural similarity, with average Dy-C bond distances across all disordered components of *ca.* 2.655 and 2.661 Å for **2** and the Cp^{iPr5} derivative, respectively. The average Dy···B distances are almost identical, with values of *ca.* 2.51 and 2.50 Å for **2** and the Cp^{iPr5} derivative, respectively, however the Dy-O distance in **2** is slightly shorter by *ca.* 0.055 Å. The significant decrease in U_{eff} can potentially be explained by the presence of C-H oscillators on the Cp^{ttt} ligand in **2**, which have previously been suggested to facilitate the initial |±15/2> → |±13/2> relaxation step in [Dy(η^5-Cp^{ttt})$_2$]$^+$.[23] The attempt relaxation time (τ_0) is four-orders of magnitude larger in **2** when compared to the Cp^{iPr5} derivative, which could be a consequence of the lower anisotropy barrier.

*2.1.4. Synthesis and characterization of [Ln(η^5-$C_5Me_4{}^{t}Bu$)(κ^3-BH_4)$_2$(THF)] (Ln = Y (**3**), Dy (**4**))*

The synthesis of the cyclopentadienyl half-sandwich complexes [Ln(η^5-$C_5Me_4{}^{t}Bu$)(κ^3-BH_4)$_2$(THF)] (Ln = Y (**3**), Dy (**4**)) was achieved in a similar fashion to compounds **1** and **2**, using equimolar amounts of NaCp^{Me4tBu} and Ln(BH$_4$)$_3$(THF)$_3$ (Ln = Y, Dy) in toluene at 60 °C overnight (Scheme 10). After subsequent work up, storing saturated hexane solutions at –40 °C overnight resulted in the formation of white or pale yellow crystals of **3** and **4**, in isolated yields of 60 and 62 %, respectively.

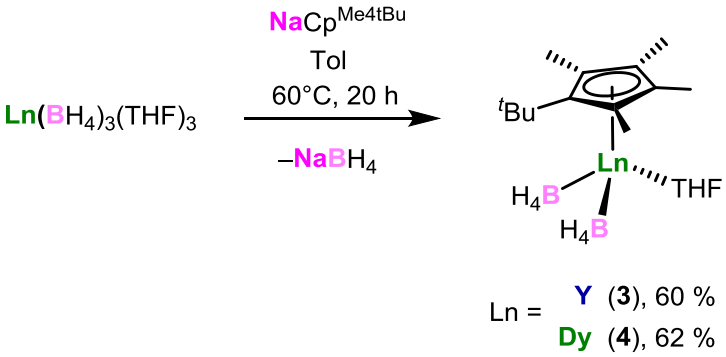

Scheme 10. Synthesis of **3** and **4**.

Molecules of **3** and **4** are isostructural, whereby there is an η^5-coordination of the Cp ring to the metal, which is also coordinated by one THF ligand and two κ^3-borohydride ligands, similar to the Cp^{ttt} and Cp^{iPr5} derivatives discussed in the previous section (Figure 40). The Dy-C bond distances in **4** lie in a narrow range of 2.592(5)-2.641(5) Å, with a Dy1-Cp_{cent} distance of 2.3166(2) Å. The centroid distance is shorter than the analogous distance in both the Cp^{ttt} and Cp^{iPr5} derivatives by *ca.* 0.045 and 0.060 Å, respectively, which is presumably a consequence of the reduced steric bulk of the Cp^{Me4tBu} ligand.

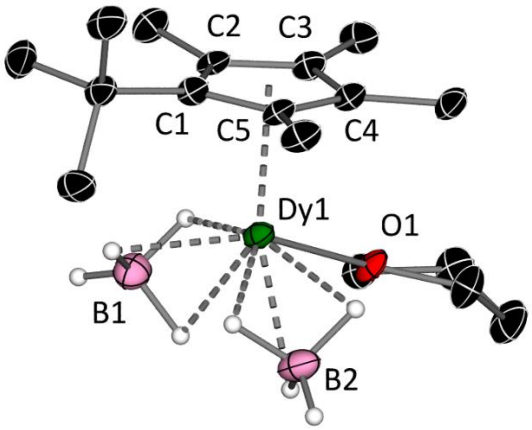

Figure 40. Molecular structure of [Dy(η^5-$C_5Me_4{}^tBu$)(κ^3-BH_4)$_2$(THF)] (**4**). Thermal ellipsoids are set to 50 % probability and for clarity, only the hydrogen atoms bound to boron are shown. Selected bond distances (Å) for **4**: C1-C2 1.437(7), C2-C3 1.410(7), C3-C4 1.413(7), C4-C5 1.412(7), C1-C5 1.424(7), Dy1-Cp_{cent} 2.3166(2), Dy1-B1 2.488(7), Dy1-B2 2.521(7), Dy1-O1 2.333(3).

The ^{1}H NMR spectrum of the yttrium compound **3** in D_6-benzene shows signals at 2.39 (s, 6H) and 1.92 ppm (s, 6H), corresponding to the two methyl group protons on the C_5 ring, and a signal at 1.52 ppm (s, 9H) corresponding to the *tert*-butyl methyl groups. Two additional multiplets can be seen at 0.99 (m, 4H) and 3.43 ppm (m, 4H), indicating that the

THF ligand remains coordinated in solution. Four broad signals could be seen as a 1:1:1:1 quartet in the range of 0.61-1.24 ppm, which integrate to a total of eight protons and correspond to the two BH_4 ligands (Figure S6). The $^{13}C\{^1H\}$ NMR spectrum displays the expected nine signals; two at 11.71 and 15.80 ppm ($C_5\underline{Me}_4{}^tBu$), two at 32.84 and 35.51 ppm corresponding to the ^{t}Bu methyl groups and the quaternary carbon, respectively, two at 24.90 and 73.50 ppm (THF), and finally three signals at 121.71, 133.27 and 151.94 ppm, which correspond to the C_5 ring. The signal centered on 121.71 ppm is a doublet, which arises through coupling to ^{89}Y ($^1J_{CY}$ = 12.4 Hz), with the other two C_5 ring signals showing unresolved $^1J_{CY}$ coupling (Figure S7). The $^{11}B\{^1H\}$ spectrum displays a singlet at −23.23 ppm (FWHM = 26 Hz), and the ^{11}B spectrum displays a well-defined 1:4:6:4:1 quintet centred on −22.24 ppm ($^1J_{BH}$ = 86 Hz), indicating the same coordination environment for the two borohydride ligands (Figures S8, S9).

The FTIR spectra of compounds **3** and **4** are essentially identical and are comparable to the FTIR spectra of the Cp^{iPr5} derivative,[27] with key absorptions summarized in the caption to Figure 41.[126] Elemental analyses of **3** and **4** were both consistent with their respective solid-state molecular structures, with % found (calculated) for **3** $C_{17}H_{37}YB_2O$: C 54.76 (55.48); H 10.38 (10.13), and **4** $C_{17}H_{37}DyB_2O$: C 46.15 (46.24); H 8.54 (8.45).

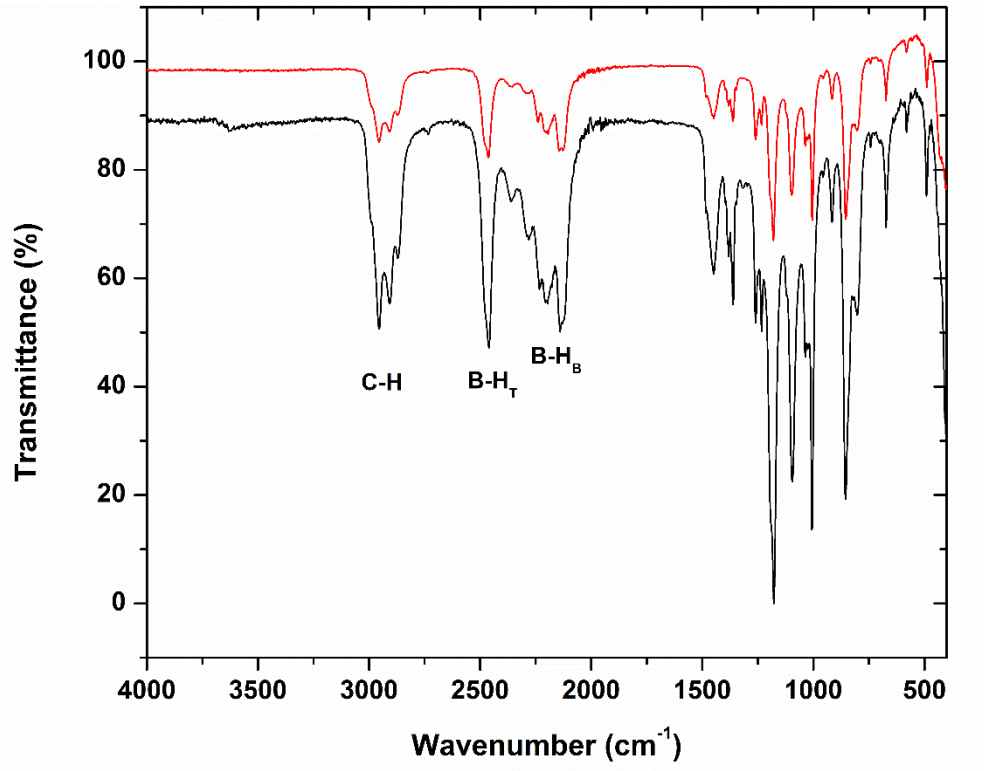

Figure 41. FTIR spectra of **3** (red line) and **4** (black line). Selected absorptions (cm^{-1}): 3000-2850 (C-H), 2450 (B-H$_T$), 2300-2100 (B-H$_B$).

2.1.5. *Magnetic property measurements on [Dy(η^5-$C_5Me_4{}^tBu$)(κ^3-BH_4)$_2$(THF)] (**4**)*

The magnetic susceptibility of compound **4** was investigated by a SQUID magnetometer in both DC and AC fields, in a similar fashion to compound **2**. In a DC field of 1000 Oe, the magnetic susceptibility of **4** was found to be typical of a monometallic Dy^{3+} complex with a $^6H_{15/2}$ ground multiplet, with $\chi_M T$ values of 13.25 and 10.39 cm^3 K mol^{-1} at 300 and 2 K, respectively. The value of 13.25 cm^3 K mol^{-1} at 300 K is *ca.* 6.5 % lower than the expected value of 14.17 cm^3 K mol^{-1} for a Dy^{3+} free ion,[127] which could be due to several reasons such as a slight diamagnetic impurity, *i.e.* $NaBH_4$, or a splitting of the $^6H_{15/2}$ ground state.[20,57,133] In the field dependence of the magnetization plots, a magnetization value of 4.91 Nβ was observed at 1.9 K and 7 T (Figure 42).

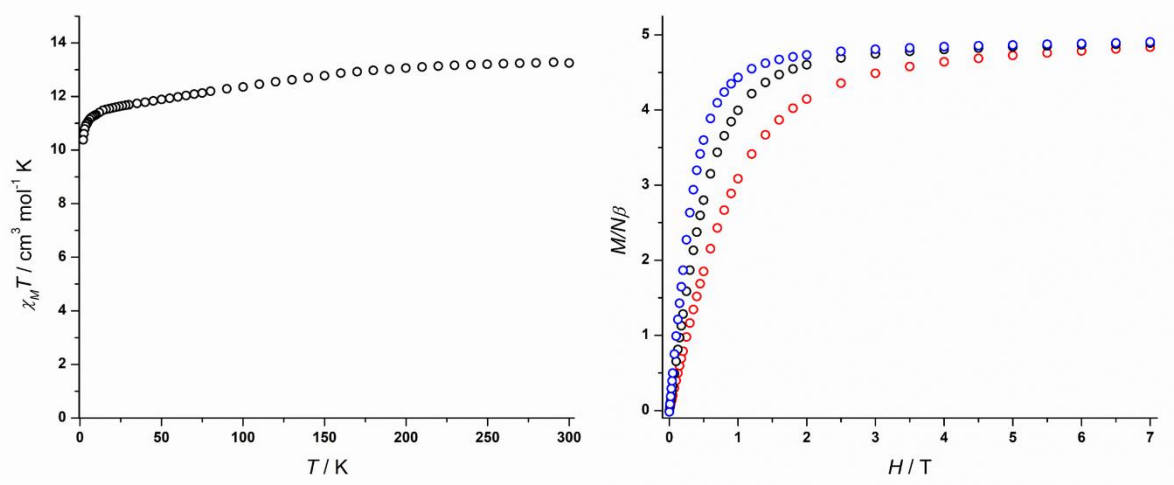

Figure 42. Plot of $\chi_M T(T)$ for **4** (left) in an applied field of 1000 Oe. $\chi_M T$ (300 K) = 13.25 cm^3 K mol^{-1}, $\chi_M T$ (2 K) = 10.39 cm^3 K mol^{-1}. Field (H) dependence of the magnetisation (M) for **4** (right) at 1.9 K (blue circles), 3.0 K (black circles) and 5.0 K (red circles). M = 4.91 $N\beta$ at 1.9 K and 7 T.

The magnetic hysteresis behaviour of **4** was investigated at 1.9 K by applying a varying sweep rate across different fields (Figure 43). The results are similar to those obtained for **2**, in which waist-restricted hysteresis loops with a precipitous loss of magnetisation at zero-field with negligible coercivity were observed. This is indicative that magnetic relaxation via QTM dominates the low-temperature regime in **4**, as in compound **2**.

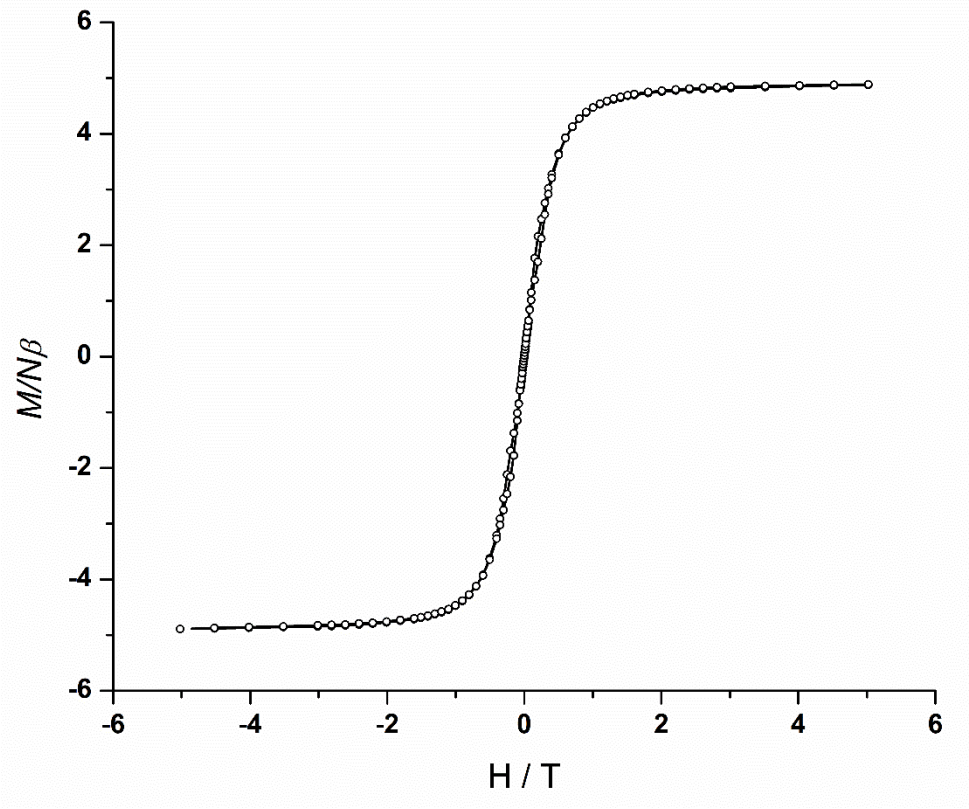

Figure 43. Magnetic hysteresis loops for **4**. The data were continuously collected at 1.9 K under a varying field sweep rate (1.1 mT s^{-1} |0-1| T, 3.0 mT s^{-1} |1-2| T, 4.5 mT s^{-1} |2-3| T and 8.5 mT s^{-1} |3-5| T). Solid lines are a guide to the eye.

The $\chi''(\nu)$ plots for **4** display maxima in the temperature range 1.9-22 K (Figure 44), which are shifted by *ca.* +100 Hz compared to the Cp^{ttt} half-sandwich derivative **2**. As with **2**, between 1.9-5 K, the frequency at which the maxima occur for **4** are essentially temperature independent, indicating dominant relaxation via QTM. At higher temperatures, the frequency maxima become temperature dependent before reaching the upper frequency limit of 1488 Hz, indicating that thermally activated relaxation is now dominant. This is consistent with the measurements observed in **2** and the analogous Cp^{iPr5} half-sandwich derivative.[27]

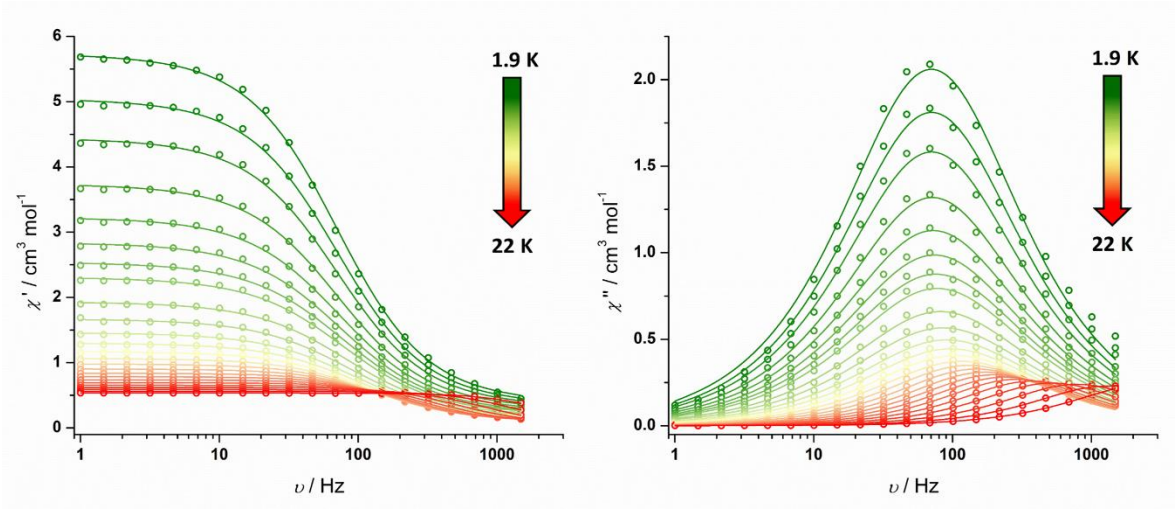

Figure 44. Frequency-dependence of the in-phase (χ') (left) and out-of-phase (χ'') (right) susceptibility for **4** in zero DC field at ν = 1-1488 Hz and temperatures of 1.9 to 22 K. Solid lines represent fits to the data using Equation 1.

Cole-Cole plots for the AC susceptibility data in the range 1.9-22 K reveal asymmetric semi-circles and were fitted to the generalised Debye model according to Equation 1 (Figures 45, 46).

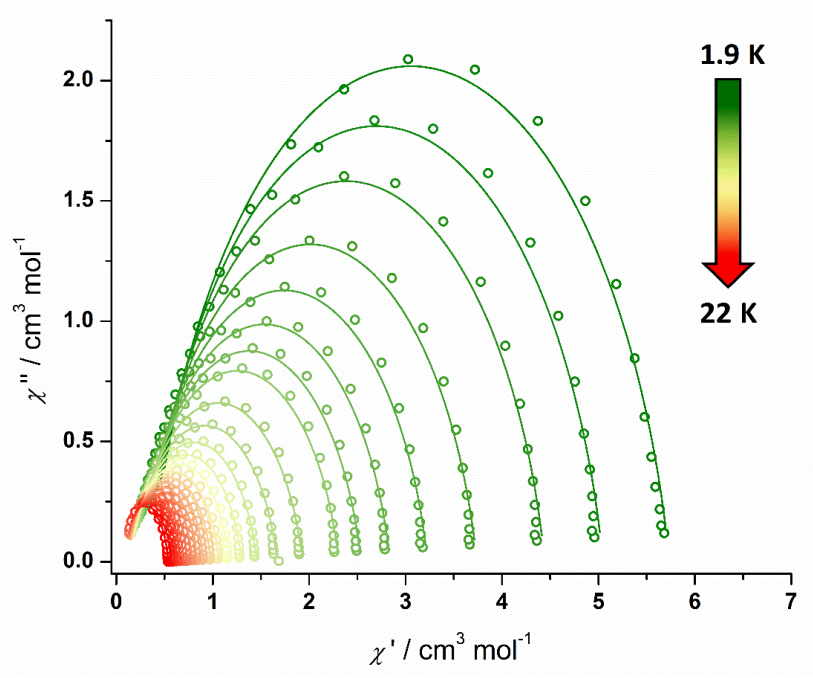

Figure 45. Cole-Cole plots for the AC susceptibilities in zero DC field for **4** from 1.9-22 K. Solid lines represent fits to the data using Equation 1.

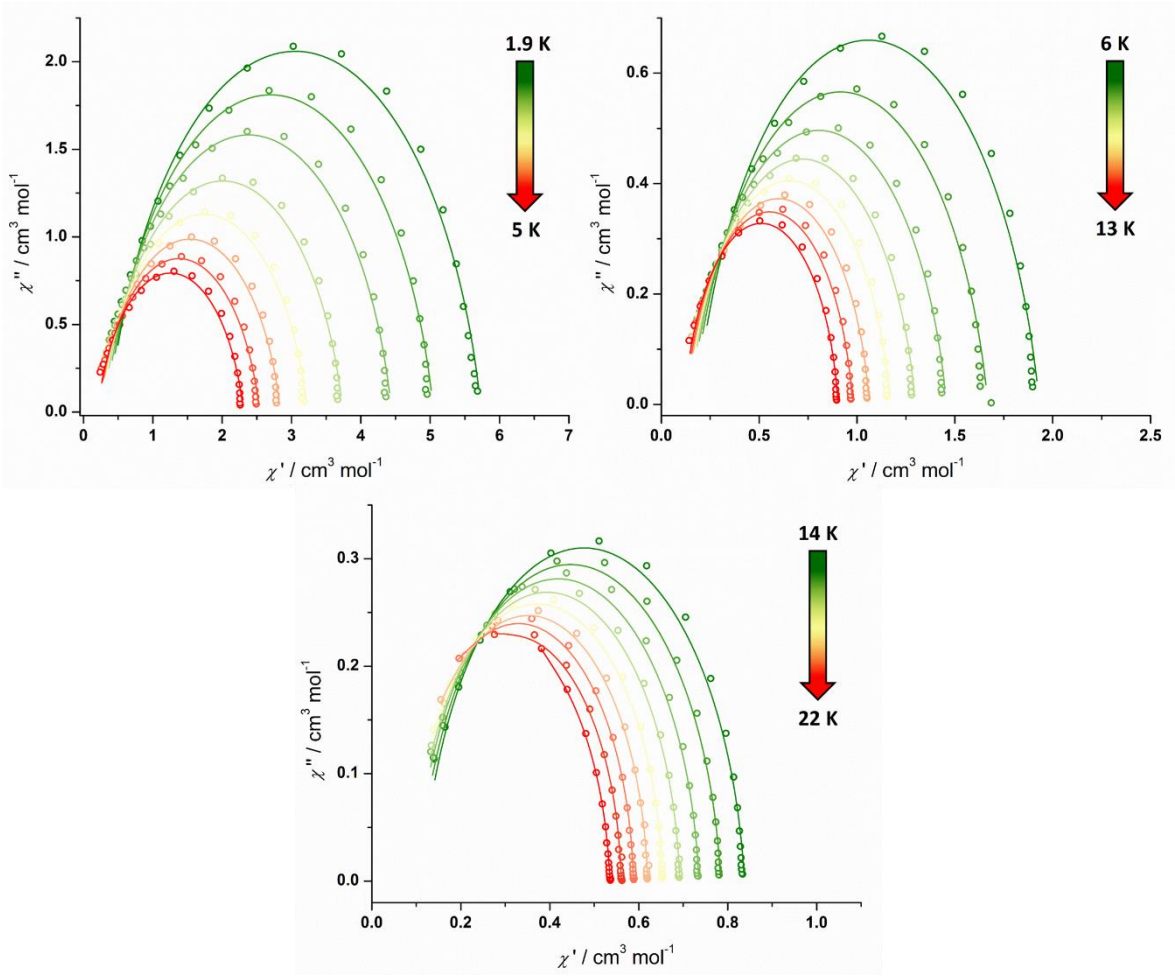

Figure 46. Cole-Cole plots for the AC susceptibilities in zero DC field for **4** from 1.9-5 K (top left),6-13 K (top right) and 14-22 K (bottom). Solid lines represent fits to the data using Equation 1.

The tabulated results from this fit are shown in the Supplementary Table S11. The fit shows a good agreement with the experimental data, with α-parameters ranging from 0.06-0.16, and τ values ranging from 0-0.002 s. These values are very similar to those observed in the analogous Cp$^{i\text{Pr}5}$ half-sandwich derivative (α = 0.05-0.18, τ = 0-0.005 s).[27] The values for the α-parameters are largest at the lowest temperatures and imply a broad distribution of relaxation times, indicative of multiple relaxation pathways across the measured temperature range, as with **2**. The α-parameter range in **4** is half of that observed in compound **2**, which may be a consequence of the solid-state structure of **4** displaying no crystallographic disorder around the C_5 ring.[131]

Analysing the $\ln\tau(T^{-1})$ plots for compound **4**, the data shows a strong temperature dependence of τ, and an excellent fit to the data set (R^2 = 0.99917) was obtained by using Equation 2, which incorporates Orbach, Raman and QTM relaxation parameters (Figure 47).

The plot shows a similar profile to that of compound **2** and the Cp^{iPr5} derivative, which is unsurprising given the nature of their structural similarity, however the curvature in the high-temperature region is less-pronounced with **4**. For compound **4**, fits to the data give U_{eff} = 241(12) cm^{-1}, τ_0 = 1.2(10) × 10^{-11} s, C = 0.10(3) s^{-1} K^{-n}, n = 3.3(1) and τ_{QTM} = 2.20(3) × 10^{-3} s.

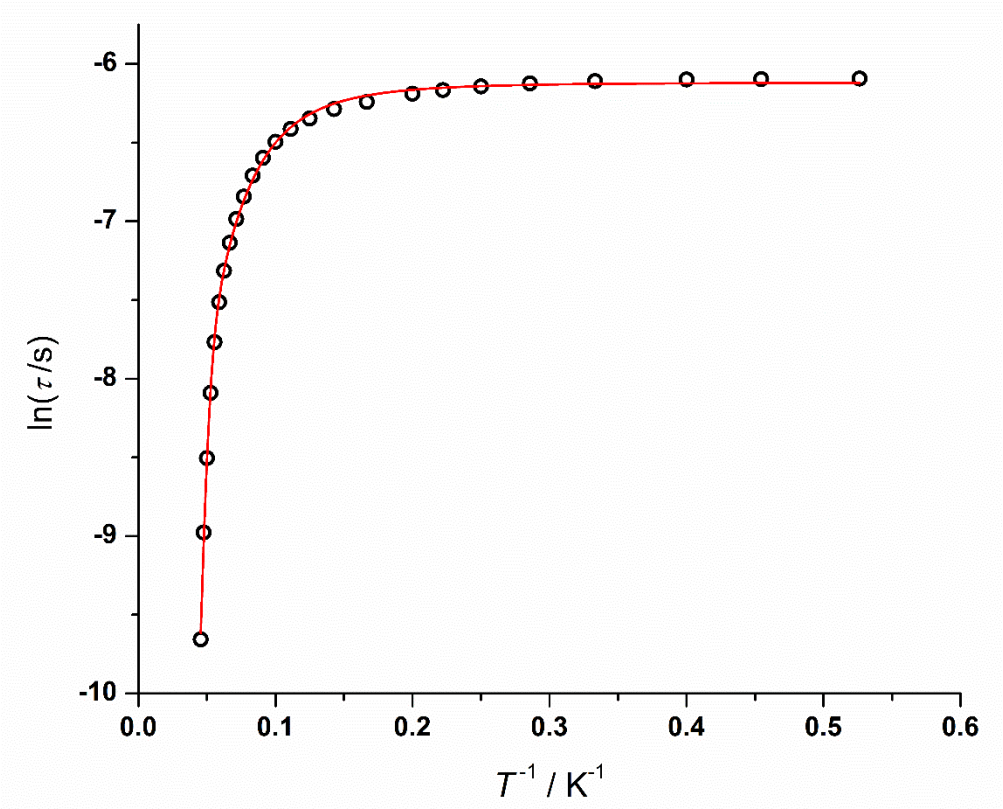

Figure 47. Plot of natural log of the relaxation time (τ) *vs.* inverse temperature for **4**. The black points are from the AC susceptibility measurements. The solid red line is the best fit (adjusted R^2 = 0.99917) to $\tau^{-1} = \tau_0^{-1} e^{-U_{eff}/k_B T} + CT^n + \tau_{QTM}^{-1}$, giving: U_{eff} = 241(12) cm^{-1}, τ_0 = 1.2(10) × 10^{-11} s, C = 0.10(3) s^{-1} K^{-n}, n = 3.3(1) and τ_{QTM} = 2.20(3) × 10^{-3} s.

Based on the solid-state structure of **4**, its SMM properties can be qualitatively described by the Dy^{3+} metal centre experiencing a strong axial crystal field from the Cp^{Me4tBu} ligand, resulting in an energy barrier to the reversal of magnetisation of 241(12) cm^{-1}. However, as with compound **2**, the competing equatorial field from the THF and borohydride ligands destabilises the ground state and promotes magnetic relaxation via QTM at low temperatures.

Upon comparing the SMM properties of **4** with the Cp^{ttt} derivative **2** and the Cp^{iPr5} derivative [Dy(η^5-$C_5{}^iPr_5$)(κ^3-BH_4)$_2$(THF)],[27] the effective energy barrier of **4** is *ca.* 76 cm^{-1}

larger than the value determined for **2,** but is the same as that determined for the Cp^{iPr5} derivative, *i.e.* 241(8) cm^{-1}. The increase in U_{eff} when compared to **2** can be explained by the shorter Dy-Cp_{cent} distance and the substitution of the C-H groups on the Cp^R ligand. The Dy-Cp_{cent} distance in **4** is slightly shorter than the analogous distance in the Cp^{iPr5} derivative and should therefore provide a marginally stronger crystal field around the Dy^{3+} ion, however this is most likely offset by the slightly reduced Dy-O distance in **4** of *ca.* 0.058 Å, resulting in the two complexes having markedly similar magnetic properties.

2.1.6. Conclusions on cyclopentadienyl half-sandwich SMMs

In this section, the synthesis of the cyclopentadienyl half-sandwich complexes [Ln(η^5-Cp^{ttt})(κ^3-BH_4)$_2$(THF)] (Ln = Y (**1**), Dy (**2**)) and [Ln(η^5-$C_5Me_4{}^tBu$)(κ^3-BH_4)$_2$(THF)] (Ln = Y (**3**), Dy (**4**)) was described. The Cp^R ligands contain substituents with varying steric bulk in order to complement what is known through published systems, and to strengthen the magneto-structural correlations used to design high-performance dysprosium metallocene SMMs.

The static magnetic susceptibility properties of **2** and **4** were investigated by SQUID magnetometry, with the complexes being typical of monometallic complexes of Dy^{3+}. Dynamic magnetic susceptibility measurements in zero DC field revealed slow magnetic relaxation properties, with Orbach processes dominating the relaxation at higher temperatures (22-10 K) and strong QTM at lower temperatures (>5 K). Fitting the magnetic relaxation times with Orbach, Raman and QTM parameters results in a U_{eff} = 165(5) cm^{-1} for **2**, and 241(12) cm^{-1} for **4**. Magnetic hysteresis measurements on both complexes reveal waist-restricted loops with negligable coercivity at 1.9 K, indicative of strong QTM. Comparisons of **2** and **4** with the known Cp^{iPr5} half-sandwich derivative [Dy(η^5-$C_5{}^iPr_5$)(κ^3-BH_4)$_2$(THF)], which has U_{eff} = 241(8) cm^{-1}, revealed a lower effective energy barrier for **2**, which can probably be attributed to the C-H oscillators on the Cp ring initiating thermally activated relaxation. The magnetic properties of **4** are almost identical to those of [Dy(η^5-$C_5{}^iPr_5$)(κ^3-BH_4)$_2$(THF)], which is unsurprising based on the structural similarities and fully substituted nature of the Cp rings.

Therefore, the main finding in this section is that substitution of the C-H groups on a Cp^R ligand appears to affect the magnetic relaxation dynamics of cyclopentadienyl half-sandwich complexes, and result in modified effective energy barriers.

2.2. Improved Synthesis of Tetrakis(Trimethylsilyl)Cyclobutadiene

2.2.1. Background

For dysprosium SMMs, the key feature of the electronic structure for inducing a large U_{eff} and T_B is to have a strong and highly axial crystal field.[22,23,25,27] As the current record SMM $[Dy(\eta^5\text{-}C_5{}^iPr_5)(\eta^5\text{-}Cp^*)]^+ [B(C_6F_5)_4]^-$ employs two monoanionic cyclopentadienyl ligands,[27] a strategy for potentially improving upon these properties is to replace the monoanionic ligands with the dianionic cyclobutadienyl ligand (Cb), which should induce a stronger crystal field splitting, and hence, a stronger axial crystal field (Scheme 11).

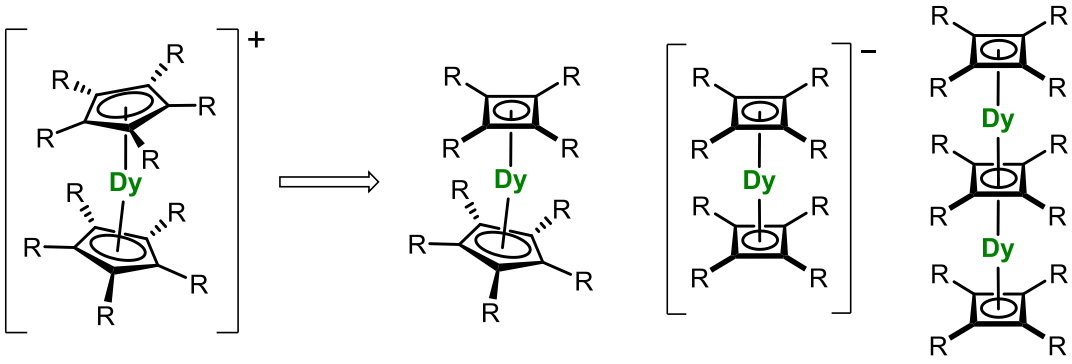

Scheme 11. A representation of current benchmark cationic metallocene SMMs (left) and potentially improved systems containing cyclobutadienyl ligands (right).

However, prior to our initial studies,[111,112] there were no lanthanide cyclobutadienyl complexes known to the literature and only one with an actinide.[119] This is because cyclobutadienyl pro-ligands are rare, which is not surprising as the highly strained anti-aromatic systems present a formidable synthetic challenge.

The pioneering research of Sekiguchi and co-workers into stable cyclobutadienes has laid the foundations for the research presented in the section, notably with the synthesis of a tetrakis(trimethylsilyl)cyclobutadiene (Scheme 12).[120–122] In this synthesis, the first step is

a [2+2]-cycloaddition reaction between bis(trimethylsilyl)acetylene and cyclopentadienyl cobalt(I) dicarbonyl, which forms the heteroleptic sandwich complex [Co{η^4-$C_4(SiMe_3)_4$}(η^5-Cp)] (**5**). Compound **5** can then be transmetalated in a reaction with excess lithium metal to form the aromatic dilithium salt [Li_2{μ-η^4:η^4-$C_4(SiMe_3)_4$}$(THF)_2$] (**6**). Compound **6** can then be oxidised using 1,2-dibromoethane to form the corresponding neutral cyclobutadiene [$C_4(SiMe_3)_4$] (Cb, **7**). This synthesis represents an important example of how the large coulombic repulsion that arises in the aromatic 6π-electron system of **6** and the highly strained anti-aromatic 4π-electron system of **7** can be stabilised via the careful choice of silyl substituents.

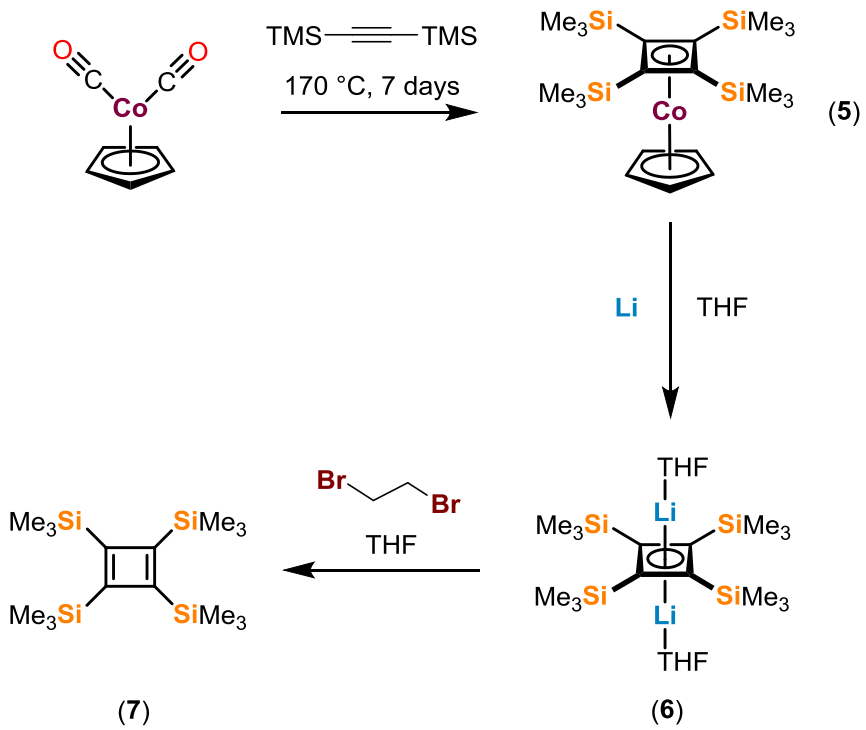

Scheme 12. Synthesis of tetrakis(trimethylsilyl) cyclobutadiene (Cb, **7**).[120–122]

Unfortunately, the synthetic route towards **7** has only been established on a small-scale (*ca*. 100 mg) and is complex and time consuming. This is perhaps another reason that explains the conspicuous absence of f-element cyclobutadienyl chemistry. The synthesis of synthetically useful amounts of Cb and Cb^{2-} is therefore required to study the coordination chemistry of cyclobutadienyl ligands with f-elements.

In this section, an improved and large-scale synthesis of $C_4(SiMe_3)_4$ and its alkali metal salts is described. The protocol is a modified version of the procedure reported by Sekiguchi and co-workers.

2.2.2. *Synthesis of [Co{η^4-$C_4(SiMe_3)_4$}(η^5-Cp)] (**5**), [Li_2{μ-η^4:η^4-$C_4(SiMe_3)_4$}$(THF)_2$] (**6**) and [$C_4(SiMe_3)_4$] (**7**)*

The reaction of $[Co(Cp)(CO)_2]$ with an excess of bis(trimethylsilyl)acetylene was carried out in the neat alkyne over 7 days at 170 °C, producing [Co{η^4-$C_4(SiMe_3)_4$}(η^5-Cp)] (**5**) in crude yields of 77 % (Scheme 13).

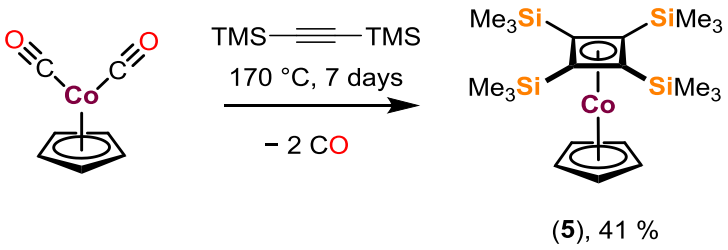

Scheme 13. Synthesis of **5**.

This reaction also produces several identifiable by-products, which is seemingly impossible to control.[134] However, **5** can be purified by column chromatography using pentane as the eluent to isolate the pure product as a yellow powder in a 41 % yield. Four different coloured bands can be observed during this purification process (Figure 48). These by-products have previously been isolated and characterised.[134] Spectroscopic analysis of **5** was consistent with the literature (Figure S10).[122,134] Attempts were made to decrease the 7-day reaction time by stopping the reaction after 3 days when the refluxing acetylene mixture changes colour from dark red to colourless. However, this resulted in reduced yields, therefore no further attempts were made to improve this initial step of the synthesis.

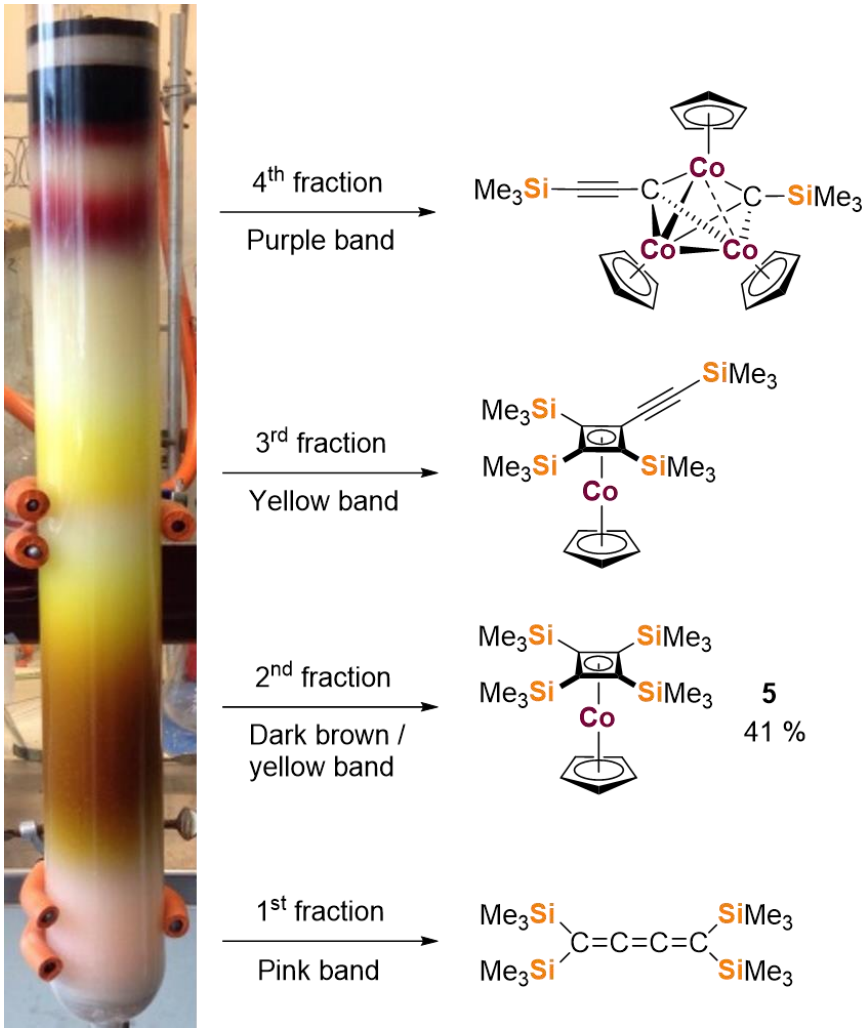

Figure 48. Column chromatography of crude **5**, with the known by-products identified.[134]

The second step involves the reaction of **5** with excess lithium metal in THF. Sekiguchi and co-workers have reported this reaction on a small scale using 100 mg of **5** and *ca.* 20 equivalents of lithium, with full consumption of the cobalt complex after 24 hours. After contacting Prof. Sekiguchi for advice, a modified synthesis using 4.5 g of **5** and *ca.* 40 equivalents of granular lithium metal in THF over 21 days (Scheme 14) was attempted, which produced the dilithium salt $[Li_2\{\mu\text{-}\eta^4\text{:}\eta^4\text{-}C_4(SiMe_3)_4\}(THF)_2]$ (**6**) in 40 % yields.

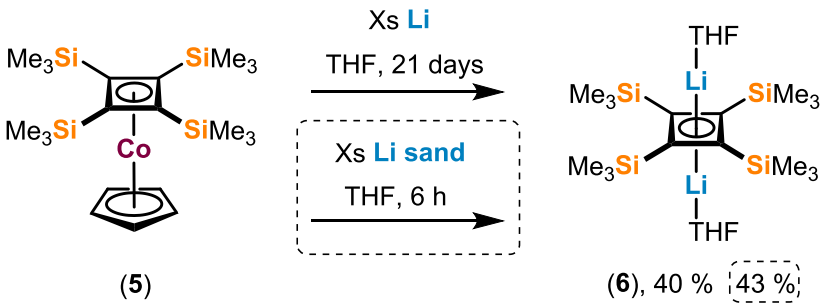

Scheme 14. Synthesis of **6**.

A reaction time of 21 days was far from ideal, and all attempts to reduce this by modifying reaction conditions have proved unsuccessful. Heating the reaction to 40 or 50 °C, and reducing reaction times to 10 days resulted in decomposition and no product isolation. However, by substituting granular lithium metal for lithium sand, the reaction time can be reduced to 6 hours (Scheme 14), which is presumably a consequence of the vastly increased surface area of the alkali metal. The reaction still requires excess lithium, however this can be reduced to 15 equivalents instead of 40 to achieve the same yields. Using more than 15 equivalents of lithium sand has no effect on increasing the yield of the reaction. However, by using extensively dried THF (additionally dried over Na/K alloy overnight prior to use), yields have consistently increased by 3 % to 43 %. All spectroscopic analysis of **6** was consistent with the literature (Figures S13-S15).[120] This reaction is now four times faster than the reported literature, at *ca.* 130 times the scale,[120] however isolated yields remain limited to 43 %.

The reaction of **5** with lithium sand can be followed by ^{1}H NMR spectroscopy, which shows full consumption of **5** after 6 hours and a signal at 4.97 ppm due to LiCp. This is further evidenced by ^{7}Li NMR spectroscopy, which displays two broad signals, one at −5.27 ppm and the other at −5.41 ppm, corresponding to the formation of **6** and LiCp, respectively (Figures S11, S12). This contrasts with literature, where no LiCp signals were reported.[122]

Consequently, this observation has implications for the mechanism of the reaction, which was proposed by Sekiguchi and co-workers (Scheme 15).

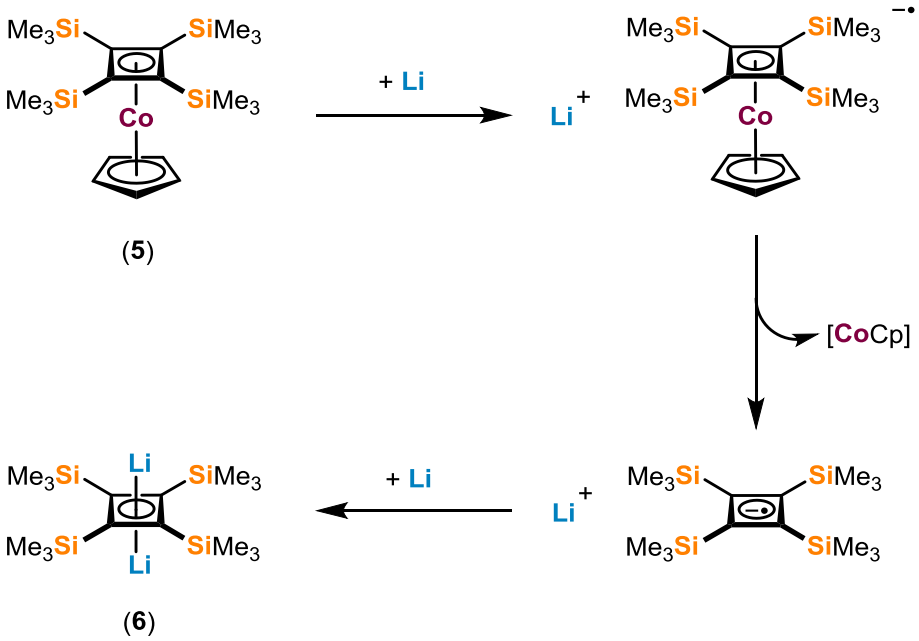

Scheme 15. Proposed mechanism in the formation of **6** by Sekiguchi and co-workers.[122]

The Sekiguchi mechanism is based on the non-formation of LiCp, inferring that the Cp ligand remains on cobalt. The reaction is proposed to proceed via a one-electron transfer from lithium to **5**, forming a radical anion $[Co\{\eta^4\text{-}C_4(SiMe_3)_4\}(\eta^5\text{-}Cp)]^{-\bullet}$. The Cb radical anion may then dissociate from cobalt, and further be reduced by lithium to form the dianionic species **6**.[122] Therefore, the observation of LiCp signals in our reactions indicates that a different reaction mechanism, or perhaps even multiple reaction mechanisms are occurring. This is evidenced by the relatively low maximum yields of 43 % obtained in this reaction, with no other by-products being identified. Regardless of the relatively low yields, this synthesis now represents a reproduceable and timely route to gram scale quantities of Li_2Cb.

The third step is also based on a modified literature procedure,[121] and involves a two-electron oxidation of **6** in hexane by the dropwise addition of meso-2,3-dibromobutane at 0 °C to form neutral 1,2,3,4-tetrakis(trimethylsilyl)cyclobuta-1,3-diene $[C_4(SiMe_3)_4]$ (**7**) (Scheme 16) in 80 % isolated yields.

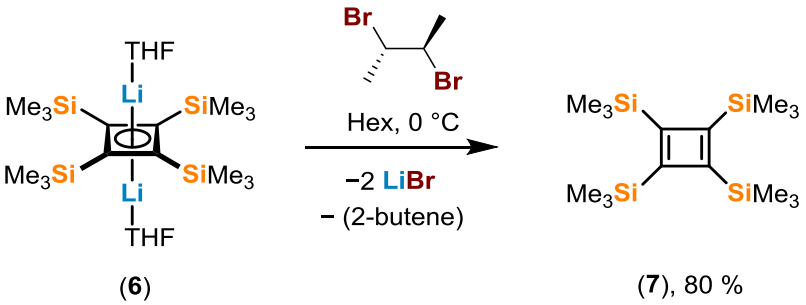

(**6**) (**7**), 80 %

Scheme 16. Synthesis of **7**.

The exothermic reaction instantaneously produces a white precipitate of LiBr. After *ca.* 1 min, the reaction was placed under vacuum to remove the volatile 2-butene by-product, which is essential to prevent the further Diels-Alder cycloaddition of butene with **7**.[122] Through Sekiguchi's work, compound **7** was the first cyclobutadiene to be isolated with four heteroatom substituents. Surprisingly, 20 years after the original synthesis, **7** is yet to be characterised by high-quality X-ray diffraction. Preliminary data has been obtained by Sekiguchi and co-workers (R_1 = 13.2 %, wR_2 = 32.8 %), which confirms the rectangular structure of the C_4 ring at 120 K, with C-C double bond distances of 1.37(1) and 1.39(1) Å, and C-C single bond distances of 1.58(1) Å.[121,122] This rectangular shape arises from a second-order Jahn-Teller distortion to remove the degeneracy of the HOMOs, consequently lowering the symmetry from D_{4h} to D_{2h} and converting the theoretical triplet ground state into a singlet (Figure 49).

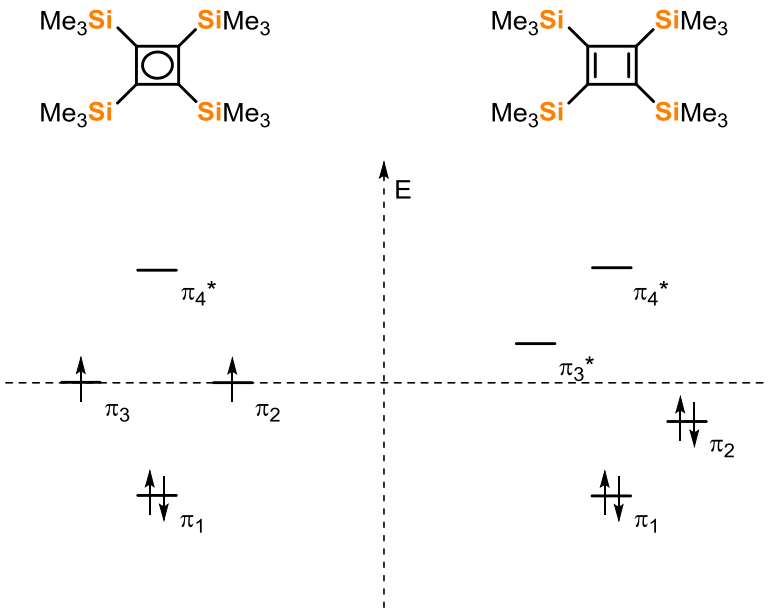

Figure 49. Molecular orbital diagram for the different conformations of **7**. Theoretical square-shaped (left) and the observed rectangular-shaped (right).

In contrast to the previous reports, this modified synthetic route uses meso-2,3-dibromobutane instead of 1,2-dibromoethane, which was recommended to us by Sekiguchi and co-workers for large scale synthesis. The temperature of the reaction has been modified to a dropwise addition at 0 °C instead of the reported and recommended room temperature, due to our observations of the exothermic nature of the reaction. This has resulted in increased yields of 80 %, compared to the reported yields of 64 %.[121,122] Spectroscopic analysis of **7** is consistent with the reported literature (Figure S16).

2.2.3. Synthesis of alkali metal cyclobutadienyl salts

Although we now have an efficient synthetic route to gram-scale quantities of Cb (**7**) and Li_2Cb (**6**), our initial reactivity studies of **6** with lanthanide trichlorides did not deliver the target compounds. Therefore, we decided to pursue the synthesis of different alkali metal salts of Cb^{2-}, specifically the larger sodium and potassium cations, which may be more effective in reactions with lanthanide salts. Both Na_2Cb and K_2Cb have been reported by Sekiguchi and co-workers; however, these compounds were only characterised by $^{13}C\{^1H\}$ and $^{29}Si\{^1H\}$ NMR spectroscopy.[122]

Alkali metal complexes of Cb can be synthesized by adding 2.5 equivalents of the metal to a solution of **7** in THF. The reactions were complete after 20 hours of stirring at room temperature and, after subsequent work up, inverse sandwich complexes of the type $[M_2\{\mu\text{-}\eta^4\text{:}\eta^4\text{-}C_4(SiMe_3)_4\}L]_n$ were crystallized with M = Na (L = THF, *n* = 2) (**8**),[112] M = K (L = nothing, *n* = 1) (**9**),[111] M = Rb (L = nothing, *n* = 1) (**10**) or Cs (L = η^6-toluene, *n* = 1) (**11**) (Scheme 17) .

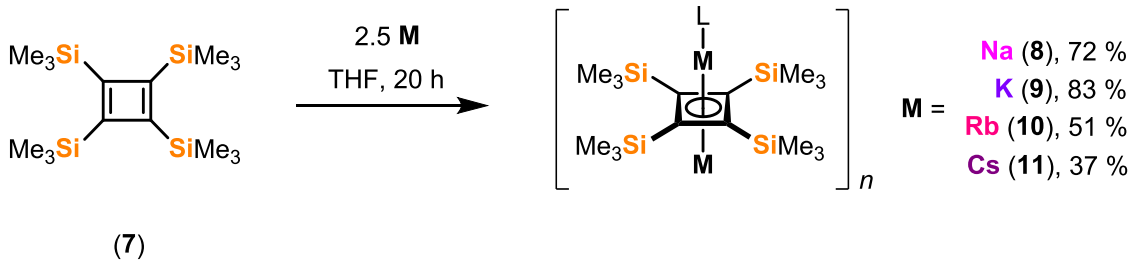

(**7**)

Scheme 17. Synthesis of alkali metal salts of Cb^{2-}.

*2.2.4. Characterization of $[Na_2\{\mu\text{-}\eta^4\text{:}\eta^4\text{-}C_4(SiMe_3)_4\}(THF)]_2$ (**8**)*

The synthesis and characterization of **8** has been adapted from the following publication: A. Chakraborty, B. M. Day, J. P. Durrant, M. He, J. Tang and R. A. Layfield, *Organometallics*, 2020, ***39***, 8-12.

Compound **8** was isolated as a yellow crystalline solid after layering hexane on a saturated THF solution. The solid-state molecular structure of **8** is a dimer in which two planar C_4 rings each interact with three sodium cations (Figure 50).

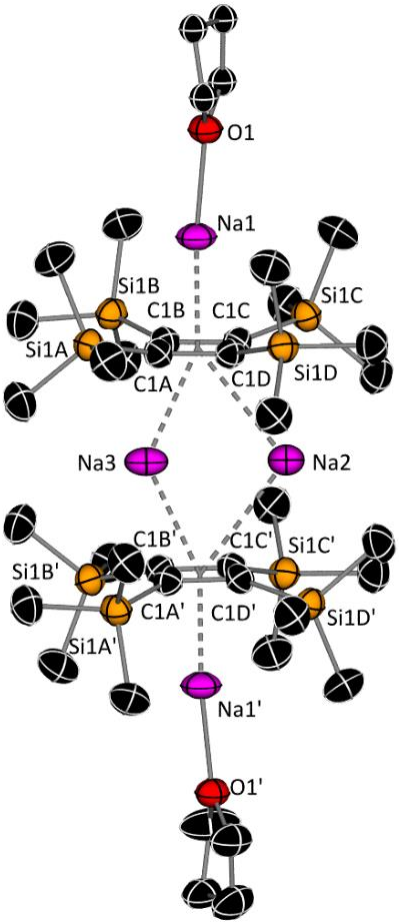

Figure 50. Molecular structure of $[Na_2\{\mu\text{-}\eta^4\text{:}\eta^4\text{-}C_4(SiMe_3)_4\}(THF)]_2$ (**8**). Thermal ellipsoids are set to 50 % probability and hydrogen atoms have been omitted for clarity. Selected bond distances (Å) for **8**: C1A-C1B 1.4878(18), C1-Si1 1.8315(13), Na1-O1 2.249(4), Na1-C1A-D 2.5394(16), Na1-Cb_{cent} 2.3113(13), Na2-C1A-D 2.634(2)-3.582(3), Na2-Cb_{cent} 2.963(2), Na3-C1A-D 2.4592(19)-3.095(3), Na3-Cb_{cent} 2.590(2).

Two disordered sodium atoms bridge between the two Cb rings via slipped η^4-interactions, and both Cb rings display an additional η^4-coordination mode to a sodium atom capped by a THF ligand. The square-planar C_4 rings have C–C distances of 1.4878(18) Å, indicating the

delocalized nature of the π-bonding in each ring. The Na1-Cb_{cent} distance of 2.3113(13) Å is *ca.* 0.41 Å further away from the C_4 ring compared to the analogous Li-Cb_{cent} distance in the DME adduct of Li_2Cb [$Li_2Cb(DME)_2$],[120] and the corresponding values for the bridging Na2-Cb_{cent} and Na3-Cb_{cent} distances are 2.963(2) and 2.590(2) Å, respectively. The $SiMe_3$ groups reside out of the plane of the C_4 ring by 0.3652(14) Å in the same direction, with an average C(ring)-Si distance of 1.8315 Å. This contrasts to the solid-state structures of $Li_2Cb(DME)_2$ and **7**, whereby the $SiMe_3$ groups deviate above and below the plane in an alternate fashion, probably due to steric repulsion.

The ^{1}H NMR spectrum of **8** in D_6-benzene with a few drops of D_8-THF shows a sharp singlet at 0.63 ppm (s, 36H), corresponding to the $SiMe_3$ groups. Two additional multiplets can be seen at 1.55 (m, 4H) and 3.63 ppm (m, 4H), indicating that the THF ligands remain coordinated in solution (Figure S17). The $^{13}C\{^1H\}$ NMR spectrum displays four signals which are assigned as such: 6.29 ppm ($SiMe_3$), 25.79 and 67.95 ppm (THF), and 104.63 ppm for the aromatic C_4 ring (Figure S18). The$^{29}Si\{^1H\}$ and $^{23}Na\{^1H\}$ spectra are also consistent with the solid-state molecular structure, each displaying a signal at −31.22 and −33.21 ppm, respectively, with the $^{23}Na\{^1H\}$ signal being extremely broad with FWHM = 1332 Hz (Figures S19, S20). The FTIR spectra of **8** is as expected, showing characteristic C-H absorptions corresponding to the C–H bonds in the range of 3000-2850 cm^{-1} (Figure 54, section 2.2.7.). Elemental analysis of **8** consistently delivered slightly lower carbon values with respect to the solid-state structure, % found (calculated) for $C_{40}H_{88}Na_4Si_8O_2$: C 50.93 (52.35), H 9.47 (9.66). However, by ^{1}H NMR analysis on several different samples, we have observed that the integration of THF signals can vary after exposing the sample to a dynamic vacuum, suggesting that these solvent molecules have a degree of lability. Applying this to the elemental analysis results, they are a good fit for 0.5 THF molecules per ring, with % found (calculated) for $C_{36}H_{80}Na_4Si_8O_1$: C 50.93 (51.13), H 9.47 (9.53).

*2.2.5. Characterization of [$K_2\{\mu$-η^4:η^4-$C_4(SiMe_3)_4\}$] (**9**)*

The synthesis and characterization of the dipotassium salt **9** has been described in a recent publication by Day *et al.*,[111] whereby the preformed Cb^{2-} unit [$K_2\{\mu$-η^4:η^4-$C_4(SiMe_3)_4\}$] was isolated in a 72 % yield. The solid-state molecular structure of **9** reveals an η^4-coordination

mode of the planar C_4 ring bound to two potassium atoms, one on each side of the ring (Figure 51). The C-C distances of 1.473(3)-1.487(3) Å are indicative of the dianionic aromatic 6π-electron system.

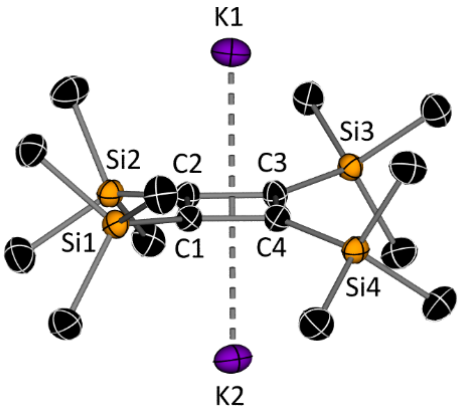

Figure 51. Molecular structure of $[K_2\{\mu\text{-}\eta^4\text{:}\eta^4\text{-}C_4(SiMe_3)_4\}]$ (**9**). Thermal ellipsoids are set to 50 % probability and hydrogen atoms have been omitted for clarity. Selected bond distances (Å) and angles (°) for **9**: C1-C2 1.480(3), C2-C3 1.473(3), C3-C4 1.487(3), C1-C4 1.480(3), C1-Si1 1.815(2), C2-Si2 1.822(2), C3-Si3 1.810(2), C4-Si4 1.811(2), K1-C1-4 2.857(3)-2.874(3), K1-Cb_{cent} 2.6640(15), K2-C1-4 2.828(3)-2.867(3), K2-Cb_{cent} 2.6465(15), K1-Cb_{cent}-K2 178.23(5).

As expected, the larger potassium cations in **9** are *ca.* 0.344 and 0.755 Å further away from the centre of the C_4 ring when compared to analogous sodium and lithium atoms in **8** and $Li_2Cb(DME)_2$, respectively. The $SiMe_3$ groups can be seen lying above and below the plane of the C_4 ring in an alternate fashion, as with $Li_2Cb(DME)_2$ and **7**, by 0.258(5), −0.293(5), 0.133(5) and −0.227(5) Å for Si1-4, respectively, with an average C(ring)-Si distance of 1.8145 Å. Repeated synthesis of compound **9** using 2.5 equivalents of potassium metal has resulted in yields of up to 83 %, an 11 % increase when compared to the reported literature (2.2 equivalents, 72 %). Spectroscopic analysis of **9** is consistent with the reported literature (Figures S21, S22).[111,122]

*2.2.6. Characterization of $[Rb_2\{\mu\text{-}\eta^4\text{:}\eta^4\text{-}C_4(SiMe_3)_4\}]$ (**10**)*

Compound **10** was isolated as a yellow crystalline solid from layering hexane on a saturated toluene solution. The solid-state molecular structure of **10** reveals an η^4-coordination mode of the planar C_4 ring bound to two rubidium cations, one on each side of the ring in

the same fashion as **9** (Figure 52). The C-C distances of 1.461(10)-1.489(10) Å and the square-planar ring are indicative of a delocalized 6π-electron system. The larger rubidium cations in **10** are 2.787(5) and 2.813(5) Å away from the centre of the Cb ring, which is *ca.* 0.155, 0.489 and 0.900 Å further away when compared to analogous potassium, sodium and lithium atoms in **9**, **8** and $Li_2Cb(DME)_2$, respectively. The $SiMe_3$ groups reside above and below the plane of the C_4 ring in an alternating fashion, in a similar manner to **9**, by −0.23(2), 0.18(2), −0.13(2) and 0.30(2) Å for Si1-4, respectively, with an average C(ring)-Si distance of 1.8145 Å.

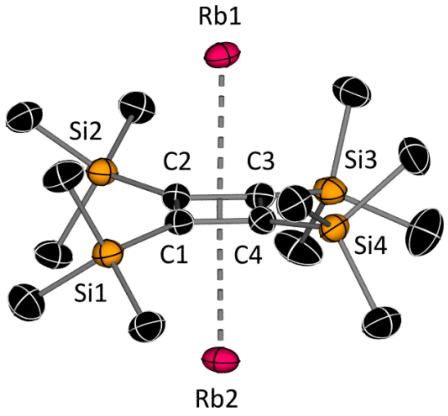

Figure 52. Molecular structure of $[Rb_2\{\mu\text{-}\eta^4\text{:}\eta^4\text{-}C_4(SiMe_3)_4\}]$ (**10**). Thermal ellipsoids are set to 30 % probability and hydrogen atoms have been omitted for clarity. Selected bond distances (Å) and angles (°) for **10**: C1-C2 1.489(10), C2-C3 1.476(11), C3-C4 1.469(11), C1-C4 1.461(10), C1-Si1 1.819(8), C2-Si2 1.815(7), C3-Si3 1.792(8), C4-Si4 1.832(8), Rb1-C1-4 2.960(9)-2.993(10), Rb1-Cb_{cent} 2.787(5), Rb2-C1-4 2.962(10)-3.032(9), Rb2-Cb_{cent} 2.813(5), Rb1-Cb_{cent}-Rb2 177.12(15).

The ^1H NMR spectrum of **10** in D_8-toluene shows only a singlet at 0.37 ppm (s, 36H), corresponding to the $SiMe_3$ groups (Figure S23). The $^{13}C\{^1H\}$ NMR spectrum displays two signals: one at 5.24 ppm corresponding to the $SiMe_3$ groups, and one at 110.37 ppm for the C_4 ring (Figure S24). The $^{29}Si\{^1H\}$ spectra displays the one expected signal at −31.66 ppm (Figure S25). The FTIR spectrum of **10** shows characteristic C-H absorptions corresponding to the C–H bonds in the range of 3000-2850 cm^{-1} (Figure 54, section 2.2.7.). Elemental analysis of **10** returned slightly lower carbon values with respect to the solid-state molecular structure, with % found (calculated) for $C_{16}H_{36}Rb_2Si_4$: C 36.43 (37.55), H 7.18 (7.09). This could be due to the highly air-sensitive nature of the complex, which may have decomposed prior to analysis, or incomplete combustion due to the formation of carbides.[135]

2.2.7. *Characterization of [$Cs_2\{\mu\text{-}\eta^4\text{:}\eta^4\text{-}C_4(SiMe_3)_4\}C_7H_8$] (**11**)*

Compound **11** was isolated as a yellow crystalline solid from layering hexane on a saturated toluene solution. The solid-state molecular structure of **11** reveals an η^4-coordination mode of the planar C_4 ring bound to two caesium atoms, with one of the caesium atoms being capped by an additional toluene molecule (Figure 53). The C-C distances are 1.474(7)-1.481(7) Å and, hence, are the same (within three standard deviations) as those in compounds **7**-**10**. The larger caesium cations in **11** are 2.958(2) and 2.959(2) Å away from the centre of the Cb ring, which are greater by *ca.* 0.158, 0.313, 0.647 and 1.058 Å when compared to analogous rubidium, potassium, sodium and lithium atoms in **10**, **9**, **8** and $Li_2Cb(DME)_2$, respectively.

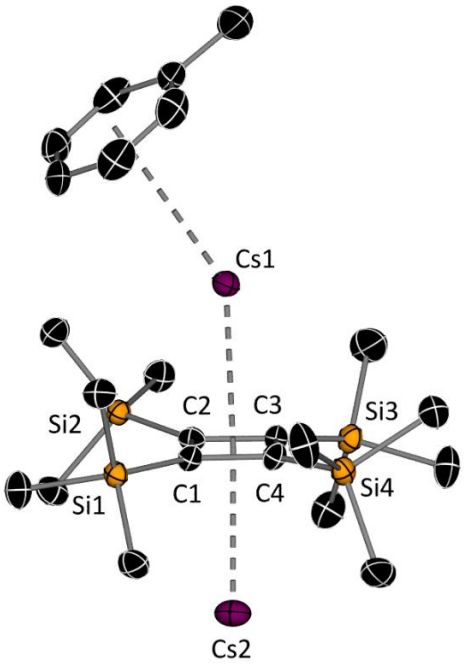

Figure 53. Molecular structure of [$Cs_2\{\mu\text{-}\eta^4\text{:}\eta^4\text{-}C_4(SiMe_3)_4\}C_7H_8$] (**11**). Thermal ellipsoids are set to 50 % probability and hydrogen atoms have been omitted for clarity. Selected bond distances (Å) and angles (°) for **11**: C1-C2 1.475(7), C2-C3 1.474(7), C3-C4 1.481(7), C1-C4 1.479(7), C1-Si1 1.820(5), C2-Si2 1.821(5), C3-Si3 1.819(5), C4-Si4 1.817(5), Cs1-C1-4 3.112(3)-3.170(4), Cs1-Cb_{cent} 2.958(2), Cs2-C1-4 3.114(4)-3.154(5), Cs2-Cb_{cent} 2.959(2), Cs1-Cb_{cent}-Cs2 177.11(9).

The average C(ring)-Si distance is 1.819 Å and the positions of the $SiMe_3$ groups in **11** contrast to those of the smaller alkali metals, whereby two of the $SiMe_3$ groups, Si1 and Si4, lie only slightly above the plane of the C_4 ring by 0.012(7) and 0.019(10) Å, respectively. The other two $SiMe_3$ groups, Si2 and Si3, lie above and below the plane of the C_4 ring by 0.219(10) Å and −0.319(2) Å, respectively. Si1 and Si4 have almost no deviation in their

positions with respect to the plane of the C_4 ring and each other, which is similar to the disodium salt **8**. The alternating deviation of Si2 and Si3 follows the same pattern observed in compounds **10**, **9**, **7**, and $Li_2Cb(DME)_2$, respectively.

The ^{1}H NMR spectrum of **11** in D_8-toluene shows a singlet at 0.37 ppm (s, 36H), corresponding to the $SiMe_3$ groups (Figure S26). The $^{13}C\{^{1}H\}$ NMR spectra displays the expected two signals at 112.46 and 4.54 ppm corresponding to the C_4 ring and $SiMe_3$ groups, respectively (Figure S27). The $^{29}Si\{^{1}H\}$ spectrum additionally shows one signal at −25.77 ppm (Figure S28), and a signal could be observed in the $^{133}Cs\{^{1}H\}$ NMR at −150.89 ppm (Figure S29). The FTIR spectrum of **11** is consistent with all previously characterised alkali metal Cb salts, showing characteristic C-H absorptions corresponding to the C–H bonds in the $SiMe_3$ groups in the range of 3000-2850 cm^{-1} (Figure 54). In a similar fashion to **10**, elemental analysis of **11** also returned slightly lower carbon values with respect to the solid-state molecular structure, with % found (calculated) for $C_{16}H_{36}Cs_2Si_4$: C 30.58 (31.68), H 6.13 (5.98).

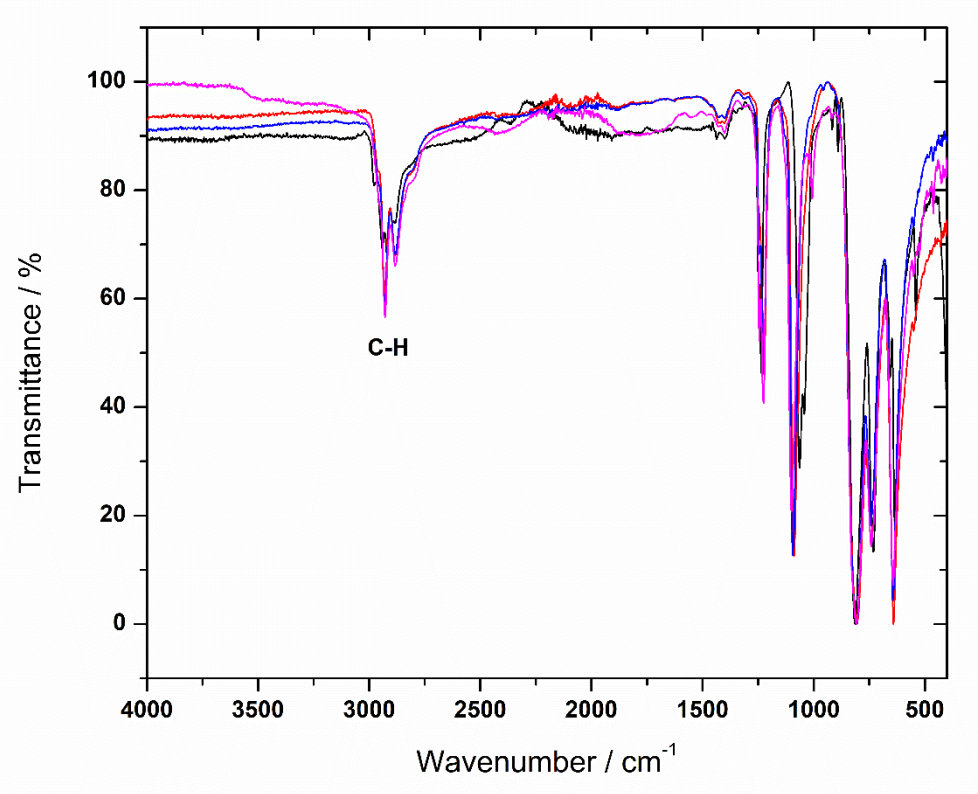

Figure 54. FTIR spectra of alkali metal cyclobutadienyl salts **8** (black line), **9** (red line), **10** (blue line) and **11** (magenta line). Selected absorptions (cm^{-1}): 3000-2850 (C-H).

2.2.8. Conclusions on improved synthesis of tetrakis(trimethylsilyl)cyclobutadiene

In this section, the improved and scaled-up synthesis of the dilithium cyclobutadienyl salt (**6**) and neutral [$C_4(SiMe_3)_4$] (**7**) was described. By using lithium sand and extensively dried THF, the dilithium salt **6** can be isolated in 43 % yields after only 6 hours, a marked improvement upon initial large-scale synthesis which took 21 days to yield 40 %. In contrast to the published work on the synthesis of Li_2Cb and Cb, we have observed the formation of LiCp in these reactions, as evidenced by ^1H and ^7Li NMR spectroscopy, which has implications for the mechanism proposed by Sekiguchi and co-workers to account for conversion of the cobalt complex **5** into the dilithium salt **6**. In the synthesis of **7**, yields can be increased by 16 % consistently when compared to the literature by cooling the reaction to 0 °C before the addition of meso-2,3-dibromobutane.

Moreover, the synthesis and characterization of the sodium, rubidium and caesium compounds **8**-**11** completes the full series of alkali metal salts of tetrakis(trimethylsilyl)cyclobutadiene. This has enabled a variety of cyclobutadienyl reagents to be used in f-element cyclobutadienyl chemistry, which will be explored in this thesis.

2.3. Cyclobutadienyl Rare-Earth Half-Sandwich Complexes

The work described in this section has been published in:

J. P. Durrant, J. Tang, A. Mansikkamäki and R. A. Layfield, *Chem. Commun.*, **2020**, *56*, 4708–4711.

2.3.1. Background

As covered in the introduction, initial attempts by our group to synthesise a bis-cyclobutadienyl sandwich complex have resulted in various activation modes of the trimethylsilyl substituents, either by deprotonation to form a 'tuck-in' equatorial ligand or a double ligand activation involving the 'tuck-in' form and simultaneous protonation of a Cb ring to form an η^3-allyl ligand.[111,112] Thus, we have yet to achieve the synthesis of a cyclobutadienyl lanthanide complex in which there is no ligand activation. In this section, we describe the synthesis, characterization, and theoretical calculations of the first 'pristine' cyclobutadienyl rare-earth half-sandwich complexes.

*2.3.2. Synthesis and characterization of [Ln{η^4-$C_4(SiMe_3)_4$}(κ^3-$BH_4)_2$(THF)Na]$_\infty$ (Ln = Y (**12**), Dy (**13**))*

The synthesis of the cyclobutadienyl half-sandwich complexes [Ln{η^4-$C_4(SiMe_3)_4$}(κ^3-$BH_4)_2$(THF)Na]$_\infty$ (Ln = Y (**12**), Dy (**13**)) was achieved by the dropwise addition of a solution of Na_2Cb (**8**) in benzene to a solution of $Ln(BH_4)_3(THF)_3$ (Ln = Y, Dy) in benzene (Scheme 18). Upon addition, a dark red solution was formed, which was swirled and left to stand for 20 hours, by which time yellow crystals of **12** or **13** were formed in yields of 64 and 48 %, respectively, which were washed with benzene and hexane and then isolated.

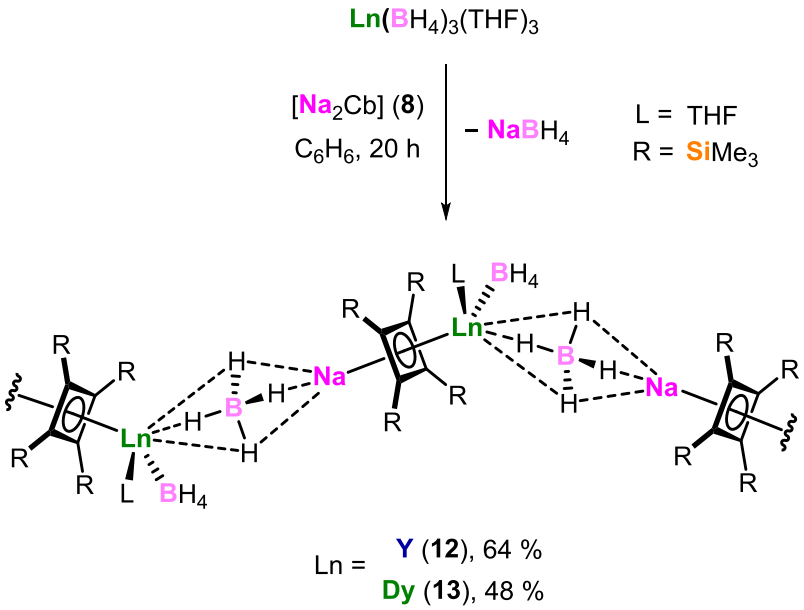

Scheme 18. Synthesis of **12** and **13**.

Attempts to stir the reaction mixtures resulted in an oily material that phase-separated from the reaction solvent, from which a product could not be isolated. Attempts were made to recrystallise the products isolated from the reaction mixtures. Crystals could be formed from a saturated THF solution layered with hexane and stored at −40 °C; however, these crystals were temperature sensitive and would begin to decompose / desolvate almost immediately upon removal from the freezer.

The solid-state structures of **12** and **13** consist of 1-D coordination polymers, whereby the asymmetric units feature two crystallographically unique half-sandwich complexes (Figure 55). Each unit consists of an η^4-coordinated Cb ligand bridging between sodium and the rare-earth metal. The rare-earth metal is also ligated by one THF ligand, a terminal κ^3-borohydride ligand, and a bridging μ-κ^3-κ^3-borohydride ligand to another sodium atom. A zig-zag coordination polymer is formed by virtue of a sodium atom interacting with another η^4-Cb unit (Figure 56).

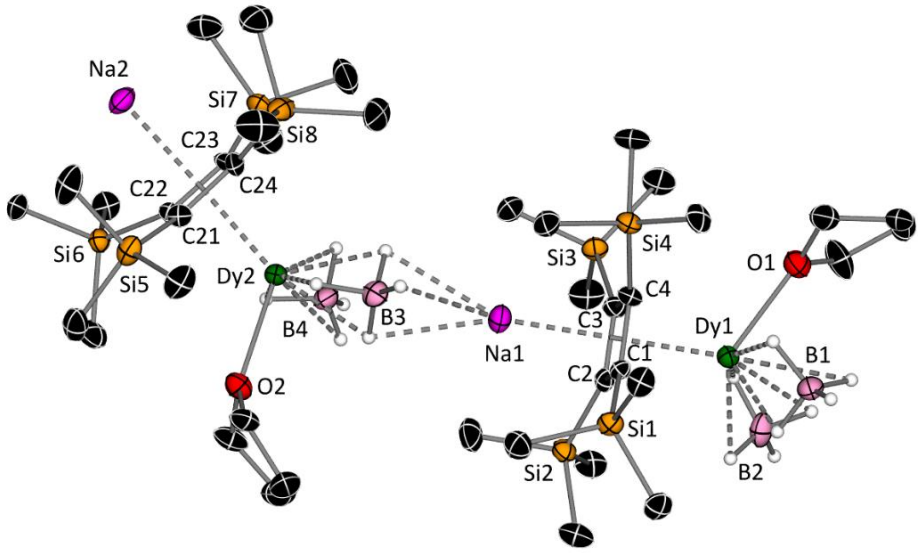

Figure 55. Molecular structure of the asymmetric unit of $[Dy\{\eta^4\text{-}C_4(SiMe_3)_4\}(\kappa^3\text{-}BH_4)_2(THF)Na]_\infty$ (**13**). Thermal ellipsoids are set to 50 % probability and for clarity, only the hydrogen atoms bound to boron are shown. Selected bond distances (Å) and angles (°) for **13**: C1-C2 1.479(12), C2-C3 1.481(12), C3-C4 1.490(12), C1-C4 1.495(12), C1-Si1 1.861(8), C2-Si2 1.861(9), C3-Si3 1.856(9), C4-Si4 1.856(9), Na1-Cb_{cent} 2.392(6), Dy1-Cb_{cent} 2.262(4), Dy1-B1 2.633(12), Dy1-B2 2.503(12), Dy1-O1 2.370(7), Na2-Cb_{cent} 2.373(6), Dy2-Cb_{cent} 2.267(4), Dy1-Cb_{cent}-Na1 178.4(2), Dy2-Cb_{cent}-Na2 177.7(2).

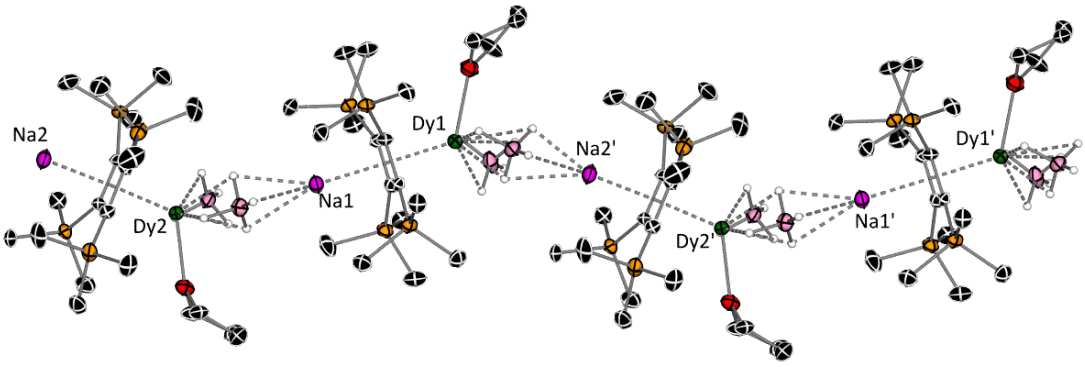

Figure 56. A segment of the polymeric structure of $[Dy\{\eta^4\text{-}C_4(SiMe_3)_4\}(BH_4)_2(THF)Na]_\infty$ (**13**). Thermal ellipsoids are set to 50 % probability and for clarity, only the hydrogen atoms bound to boron are shown. Selected bond distances (Å) for **13**: Dy1-Dy2 9.1194(8), Dy1-Dy2' 8.8845(8).

The C-C distances in the Cb ligand range from 1.479(12)-1.495(12) Å for **13** (C1-4), which is typical of previously reported dianionic aromatic Cb ligands coordinated to rare-earth elements.[111,112] For one Cb unit in **13** (C1-4), the Dy-C bond distances range from 2.489(9)-2.500(8) Å, with a Dy1-Cb_{cent} distance of 2.262(4) Å. It is noteworthy that **13** displays the shortest Dy-Cb_{cent} distance for any reported f-element cyclobutadienyl complex to date, as well as being 0.113 Å shorter than the Dy-Cp_{cent} distance in the analogous Cp^{iPr5} half-sandwich complex $[Dy(\eta^5\text{-}C_5{}^iPr_5)(\kappa^3\text{-}BH_4)_2(THF)]$.[27] The $SiMe_3$ groups of **13** lie out of the C_4

plane in the same direction by a range of 0.282(17)-0.470(17) and 0.224(17)-0.385(17) Å for C1-4 and C21-24, respectively, with an average C(ring)-Si distance of 1.859 Å.

The ^{1}H NMR spectrum of **12** in D_8-THF shows a singlet at 0.13 ppm (s, 36H), corresponding to the $SiMe_3$ groups. Four broad signals can be seen between −0.12-0.50 ppm, corresponding to the two BH_4 ligands. Three of these broad signals integrate to 2H, however the fourth signal cannot be accurately integrated as it occurs underneath the $SiMe_3$ signal. Two additional multiplets can be seen at 1.77 (4H) and 3.62 ppm (4H), indicative of the THF ligand remaining coordinated to yttrium (Figure S30). The $^{13}C\{^{1}H\}$ NMR spectrum of **12** displays four signals; one at 5.27 ppm corresponding to the $SiMe_3$ groups, two at 26.48 and 68.38 ppm relating to the THF ligand, and the final signal at 122.63 ppm for the C_4 ring (Figure S31). The $^{11}B\{^{1}H\}$ and ^{11}B spectra both display single broad signals centred at −23.00 ppm, with FWHM values of 276 and 377 Hz, respectively, which suggests that the two BH_4 ligands may be undergoing exchange between bridging and terminal positions in solution (Figures S32, S33). The $^{29}Si\{^{1}H\}$ and $^{23}Na\{^{1}H\}$ spectra each display singlets at −22.69 and −4.26 ppm (FWHM = 48 Hz), respectively (Figures S34, S35).

The FTIR spectra of compounds **12** and **13** are essentially identical, with absorptions at the same frequencies in the range of 4000-450 cm^{-1} (Figure 57). Characteristic absorptions corresponding to the $SiMe_3$ and THF C–H bonds can be seen in the range of 3000-2850 cm^{-1}, and two different types of B-H stretches can be seen at 2450 and 2300-2100 cm^{-1}, reflecting the terminal and bridging nature of the κ^3-borohydride ligands, respectively.[126] Despite repeated attempts, elemental analysis of **12** consistently returned lower carbon values with respect to the solid-state structure, a representative result being % found (calculated) for $C_{20}H_{52}YNaB_2Si_4O$: C 35.90 (43.32); H 8.76 (9.45). However, all spectroscopic analysis of **12** is consistent with the solid-state molecular structure determined by X-ray crystallography. Elemental analysis of **13** was consistent with the solid-state molecular structure, with % found (calculated) for $C_{20}H_{52}DyNaB_2Si_4O$: C 37.66 (38.25); H 8.50 (8.35).

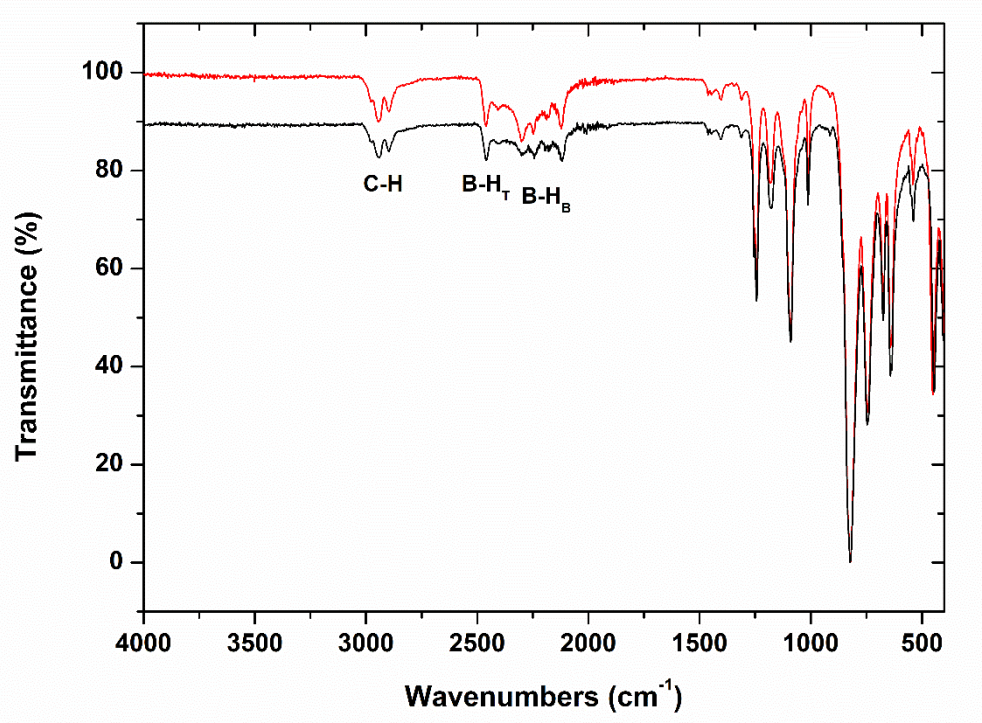

Figure 57. FTIR spectra of **12** (red line) and **13** (black line). Selected absorptions (cm^{-1}): 3000-2850 (C-H), 2450 ($B\text{-}H_T$), 2300-2100 ($B\text{-}H_B$).

*2.3.3. Synthesis and characterization of $[Ln\{\eta^4\text{-}C_4(SiMe_3)_4\}(\kappa^3\text{-}BH_4)_2(THF)K]_\infty$ (Ln = Y (**14**), Dy (**15**))*

The synthesis of the cyclobutadienyl half-sandwich complexes $[Ln\{\eta^4\text{-}C_4(SiMe_3)_4\}(\kappa^3\text{-}BH_4)_2(THF)K]_\infty$ (Ln = Y (**14**), Dy (**15**)) was achieved by the dropwise addition of a solution of K_2Cb (**9**) in benzene to a solution of $Ln(BH_4)_3(THF)_3$ in benzene (Scheme 19). Upon addition, a dark red solution formed, which was swirled and left to stand for 20 hours, by which time a yellow precipitate with some crystalline material had deposited. Subsequent work up produced pale yellow crystals of **14**, and yellow crystals of **15** by the slow evaporation of layered hexane on a saturated THF solution over 5 days in yields of 56 and 72 %, respectively.

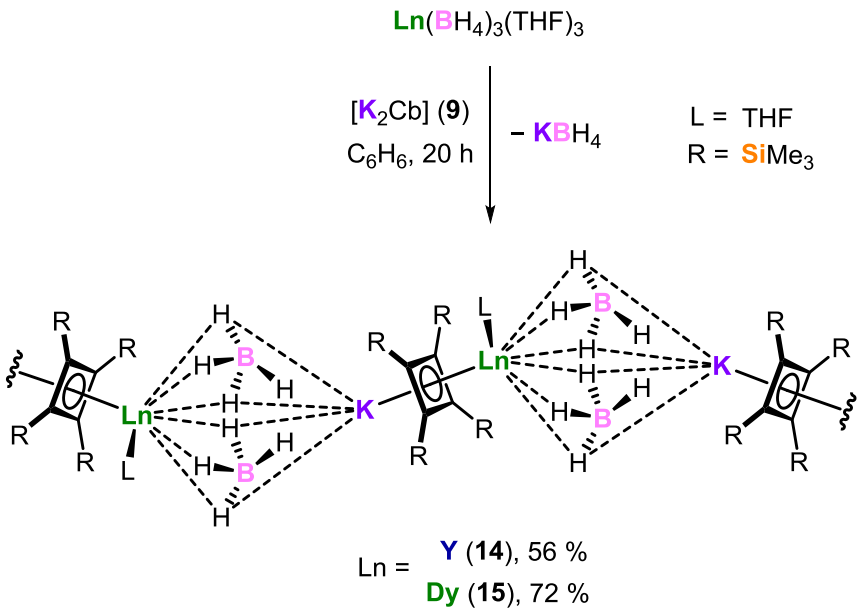

Scheme 19. Synthesis of **14** and **15**.

Compounds **14** and **15** are isostructural coordination polymers, whereby the asymmetric unit features an η^4-Cb coordination to potassium and the rare-earth metal, in addition to a THF ligand and two κ^3-borohydride ligands (Figure 58). The only noteable difference in these structures when compared to the sodium analogues is that the potassium cation interacts with both borohydride ligands owing to its larger radius (Figure 59).

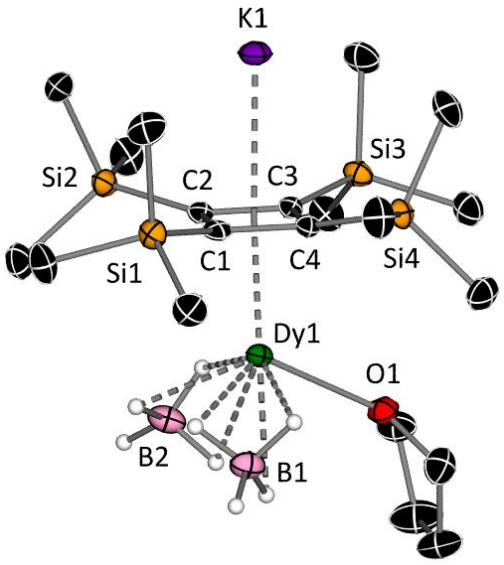

Figure 58. Molecular structure of the asymmetric unit of $[Dy\{\eta^4\text{-}C_4(SiMe_3)_4\}(\kappa^3\text{-}BH_4)_2(THF)K]_\infty$ (**15**). Thermal ellipsoids are set to 50 % probability and for clarity, only the hydrogen atoms bound to boron are shown. Selected bond distances (Å) and angles (°) for **15**: C1-C2 1.470(7), C2-C3 1.487(8), C3-C4 1.486(7), C1-C4 1.486(8), C1-Si1 1.857(6), C2-Si2 1.865(5), C3-Si3 1.859(6), C4-Si4 1.861(6), K1-Cb_{cent} 2.730(3), Dy1-Cb_{cent} 2.264(3), Dy1-B1 2.538(8), Dy1-B2 2.574(8), Dy1-O1 2.384(4), Dy1-Cb_{cent}-K1 176.46(13).

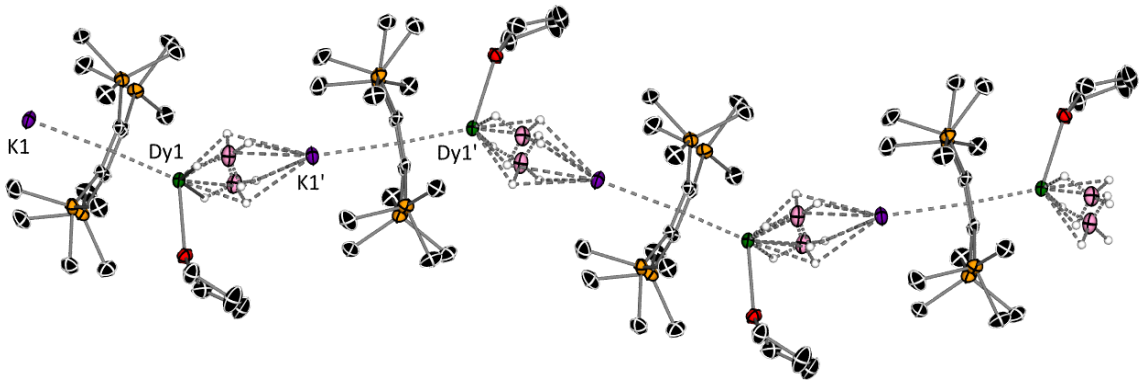

Figure 59. A segment of the polymeric structure of $[Dy\{\eta^4\text{-}C_4(SiMe_3)_4\}(\kappa^3\text{-}BH_4)_2(THF)K]_\infty$ (**15**). Thermal ellipsoids are set to 50 % probability and for clarity, only the hydrogen atoms bound to boron are shown. Selected bond distances (Å) for **15**: Dy1-Dy1' 9.1422(3).

The larger ionic radius of potassium is further reflected in the K1-Cb_{cent} distance of 2.730(3) Å for **15**, which is 0.338 Å further away than the analogous distance to sodium in **13**. The C-C distances in the Cb ring range from 1.470(7)-1.487(8) Å, and the Dy-C bond distances range from 2.473(5)-2.519(5) Å, with a Dy1-Cb_{cent} distance of 2.264(3) Å. These values are comparable to the sodium analogue **13**. The $SiMe_3$ groups of **15** reside out of the plane of the C_4 ring by a range of 0.236(11)-0.379(13) Å and are oriented away from the metal, with an average C(ring)-Si distance of 1.861 Å.

The ^1H NMR spectrum of **14** in D_8-THF is very similar to that of the sodium analogue **12**, and shows a singlet at 0.14 ppm (s, 36H), corresponding to the $SiMe_3$ groups. Four broad signals as a 1:1:1:1 quartet corresponding to the two BH_4 ligands occur between −0.02-0.60 ppm, each integrating to two ^1H. Two additional multiplets corresponding to the THF ligand occur at 1.77 (m, 4H) and 3.62 ppm (m, 4H) (Figure S36). The $^{13}C\{^1H\}$ NMR spectrum displays the expected four signals; one at 5.24 ppm corresponding to the $SiMe_3$ groups, two at 26.50 and 68.37 ppm relating to the THF molecule, and finally a doublet can be seen centered on 123.32 ppm corresponding to the C_4 ring, which arises through coupling to ^{89}Y ($^1J_{CY}$ = 4.45 Hz) (Figure S37). The $^{11}B\{^1H\}$ spectrum displays a sharp signal at −27.01 ppm (FWHM = 15 Hz), and the ^{11}B spectrum displays a 1:4:6:4:1 quintet centered on −27.00 ppm ($^1J_{BH}$ = 84 Hz) (Figures S38, S39). These sharp peaks in the boron NMR with well resolved coupling suggest that both borohydride ligands are in the same environment, which is supported by the solid-state structure of **14**. The $^{29}Si\{^1H\}$ spectrum displays a singlet at −22.58 ppm, which is near identical to the sodium analogue **12** (Figure S40).

The FTIR spectra of compounds **14** and **15** are comparable to those of the sodium analogues **12** and **13**, with key absorptions summarized in the caption to Figure 60. Despite repeated attempts, elemental analysis of **14** consistently returned slightly lower carbon values with respect to the solid-state structure, a representative result being % found (calculated) for $C_{20}H_{52}YKB_2Si_4O$: C 41.12 (42.10); H 8.73 (9.19). However, as with the sodium derivative **12**, all spectroscopic analysis of **14** is consistent with the solid-state molecular structure determined by X-ray crystallography. Elemental analysis of **15** was consistent with the solid-state molecular structure, with % found (calculated) for $C_{20}H_{52}DyKB_2Si_4O$: C 37.13 (37.29); H 8.04 (8.14).

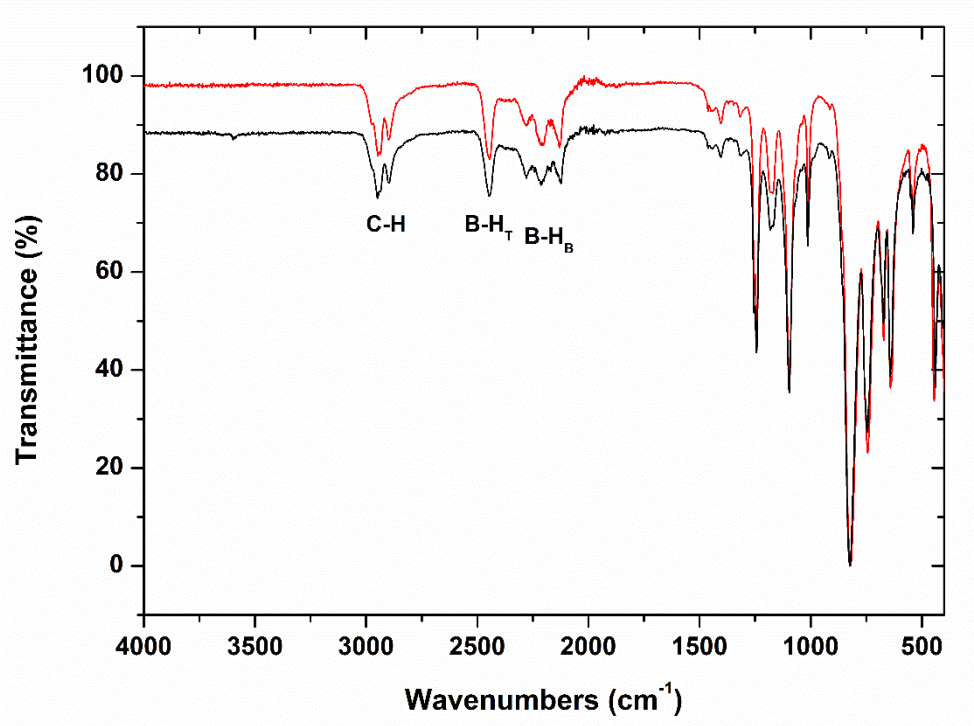

Figure 60. FTIR spectra of **14** (red line) and **15** (black line). Selected absorptions (cm^{-1}): 3000-2850 (C-H), 2450 ($B\text{-}H_T$), 2300-2100 ($B\text{-}H_B$).

2.3.4. Magnetic property measurements on $[Dy\{\eta^4\text{-}C_4(SiMe_3)_4\}(\kappa^3\text{-}BH_4)_2(THF)Na]_\infty$ (**13**) and $[Dy\{\eta^4\text{-}C_4(SiMe_3)_4\}(\kappa^3\text{-}BH_4)_2(THF)K]_\infty$ (**15**)

Compounds **13** and **15** provide the first opportunity to study the influence of a pristine Cb ligand on the dynamic magnetic properties of a dysprosium SMM. This is particularly important relative to analogous cyclopentadienyl half-sandwich complexes, as this allows meaningful comparisons between the two types of ligands.

In a static DC field of 1000 Oe, the $\chi_M T(T)$ plots for both **13** and **15** in the range of 2-300 K are almost identical, which show typical monometallic Dy^{3+} traits with a $^6H_{15/2}$ ground multiplets (Figure 61). At high temperatures, $\chi_M T$ approaches a free-ion value of 14.17 cm^3 K mol^{-1},[127] with values of 13.46 and 13.52 cm^3 K mol^{-1} for **13** and **15** at 300 K, respectively.

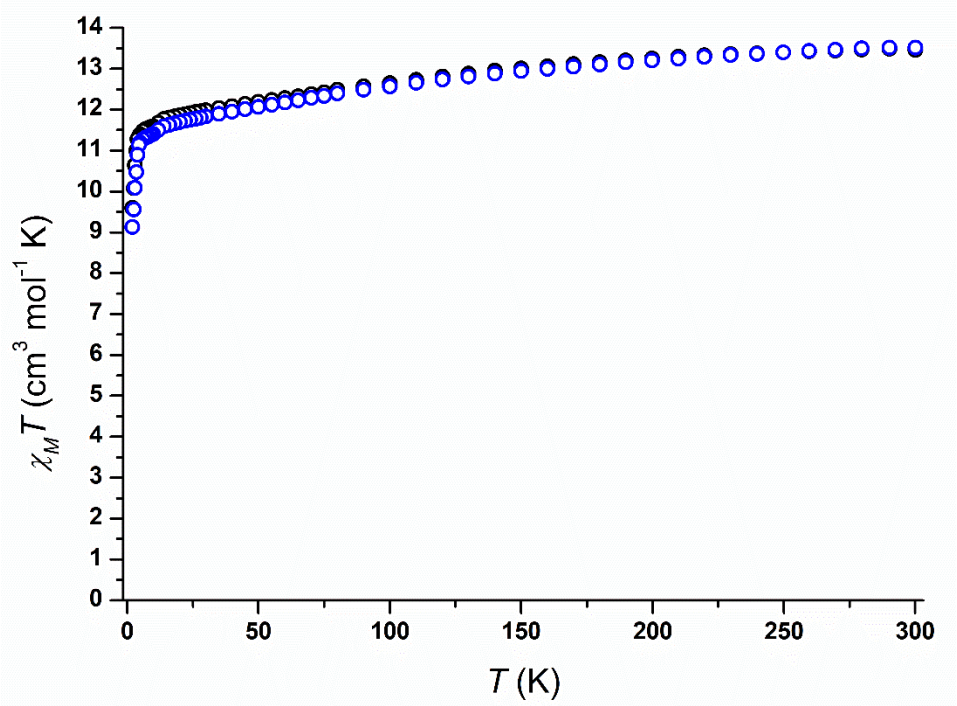

Figure 61. Plot of $\chi_M T(T)$ for **13** (left, black circles) and **15** (right, blue circles) in an applied field of 1000 Oe. For **13**, $\chi_M T$ (300 K) = 13.46 cm^3 K mol^{-1}, $\chi_M T$ (2 K) = 9.60 cm^3 K mol^{-1}. For **15**, $\chi_M T$(300 K) = 13.52 cm^3 K mol^{-1}, $\chi_M T$(2 K) = 9.13 cm^3 K mol^{-1}.

Upon lowering the temperature, a steady decrease in $\chi_M T$ occurs which drops sharply at very low temperature to values of 9.60 and 9.13 cm^3 K mol^{-1} for **13** and **15** at 2 K, respectively. The $\chi_M T$ values for **13** and **15** at 2 K are both lower than all previously characterised cyclopentadienyl half-sandwich complexes (**2** = 12.09, **4** = 10.39 and the Cp^{iPr5}

derivative = 10.39 cm^3 K mol^{-1}),[27] indicative of magnetic anisotropy and magnetic blocking in **13** and **15**.

Magnetization *vs.* field measurements for **13** and **15** are essentially identical and display typical curves for strongly anisotropic Dy^{3+} complexes (Figure 62). At a temperature of 1.9 K, as the field increases, *M* rises sharply at low fields before reaching values of 4.89 and 4.85 *N*β for **13** and **15** at 7 T, respectively, and approaching saturation.

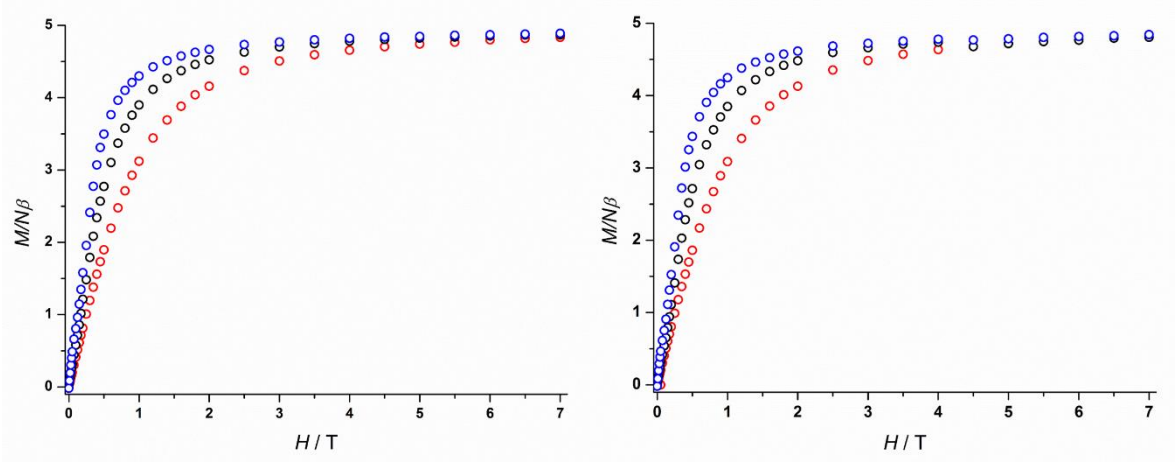

Figure 62. Field (*H*) dependence of the magnetisation (*M*) for **13** (left) and **15** (right) at 1.9 K (blue circles), 3.0 K (black circles) and 5.0 K (red circles). For **13**, *M* = 4.89 *N*β at 1.9 K and 7 T. For **15**, *M* = 4.85 *N*β at 1.9 K and 7 T.

The hysteresis behaviour of **13** and **15** was investigated at 1.9 K by applying a varying sweep rate across different fields (Figure 63). These measurements reveal waist-restricted hysteresis loops with rapid loss of magnetisation at zero-field and negligible coercivity. This is indicative that magnetic relaxation via QTM dominates the low-temperature regime in **13** and **15**, as seen in the analogous cyclopentadienyl half-sandwich complexes **2**, **4** and the Cp^{iPr5} derivative.[27]

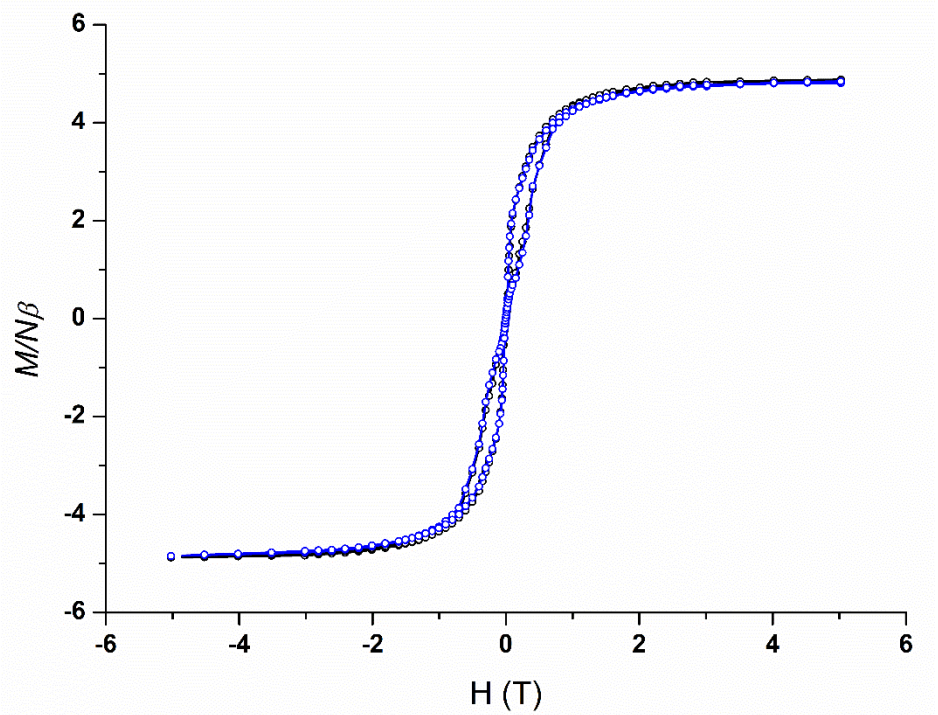

Figure 63. Magnetic hysteresis loops for **13** (black circles) and **15** (blue circles). The data were continuously collected at 1.9 K under a varying field sweep rate (1.1 mT s^{-1} |0-1| T, 3.0 mT s^{-1} |1-2| T, 4.5 mT s^{-1} |2-3| T and 8.5 mT s^{-1} |3-5| T). Solid lines are a guide to the eye.

A comparison of the waist-restricted hysteresis loops between |0-2| T for the Cp compound **4** and the Cb compound **15** can be seen in Figure 64. This image shows that the loops for the cyclobutadienyl half-sandwich complex are wider when compared to the cyclopentadienyl derivative when |H| > 0. This is indicative of slightly stronger magnetic blocking in the Cb compounds, which may be a consequence of a stronger axial crystal field, however, magnetic relaxation via QTM is still very prominent at zero-field.

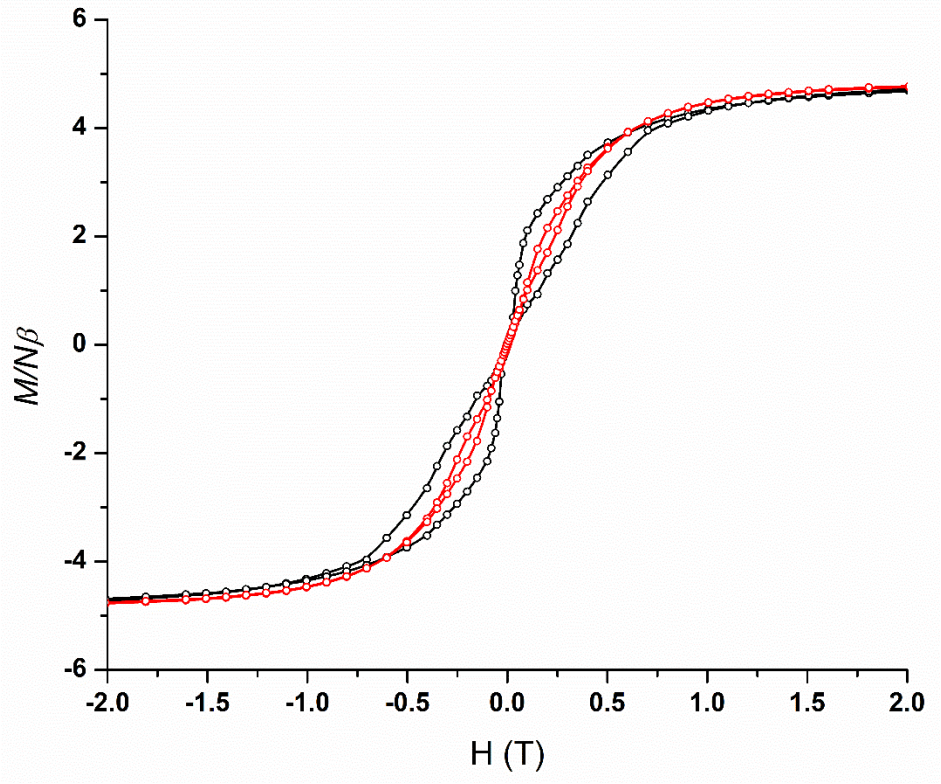

Figure 64. A comparison of magnetic hysteresis loops for **4** (red circles) and **15** (black circles) between |0-2| T. The data were continuously collected at 1.9 K under a varying field sweep rate (1.1 mT s^{-1} |0-1| T, 3.0 mT s^{-1} |1-2| T, 4.5 mT s^{-1}). Solid lines are a guide to the eye.

The SMM properties of compounds **13** and **15** were further probed by dynamic AC magnetic susceptibility measurements across a temperature range of 1.9-45 K. For compound **13**, the $\chi''(\nu)$ plots display maxima in the temperature range of 1.9-39 K (Figure 65). Between 1.9-9 K, the frequency at which the maxima occur are essentially temperature independent, indicating magnetic relaxation via QTM dominates across this low temperature regime. At higher temperatures, the frequency maxima become temperature dependent before reaching the upper frequency limit of 1488 Hz, indicating that thermally activated relaxation is dominant.

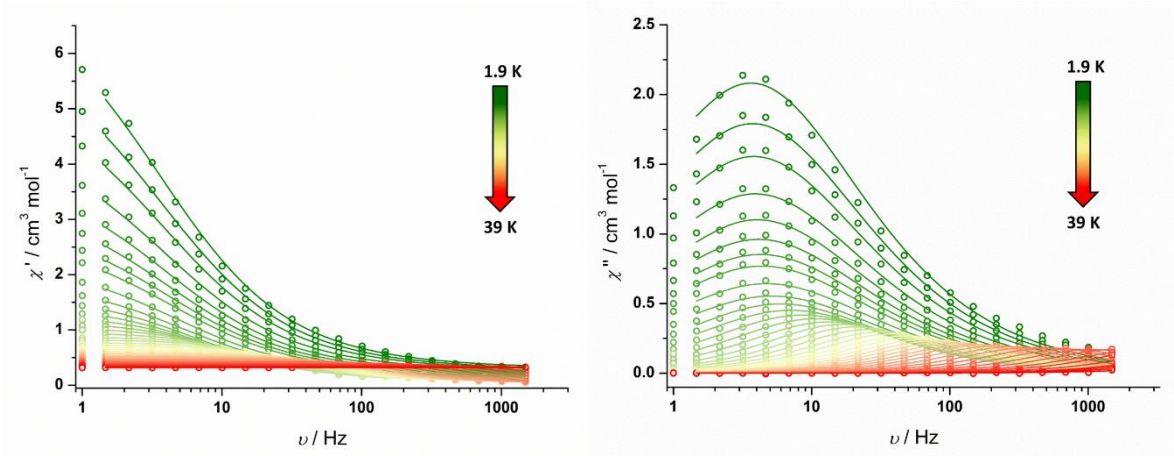

Figure 65. Frequency-dependence of the in-phase (χ') (left) and out-of-phase (χ'') (right) susceptibility for **13** in zero DC field at ν = 1-1488 Hz and temperatures of 1.9 to 39 K. Solid lines represent fits to the data using Equation 1. The lowest-frequency (1 Hz) data points were not included in the fit due an outlier at 13 K (see Figure 68).

For compound **15**, the $\chi''(\nu)$ data are very similar to that of **13**, consistent with the structural similarity between the two compounds. However, the maxima for **15** are slightly shifted to lower frequencies with respect to the same temperature (Figure 66).

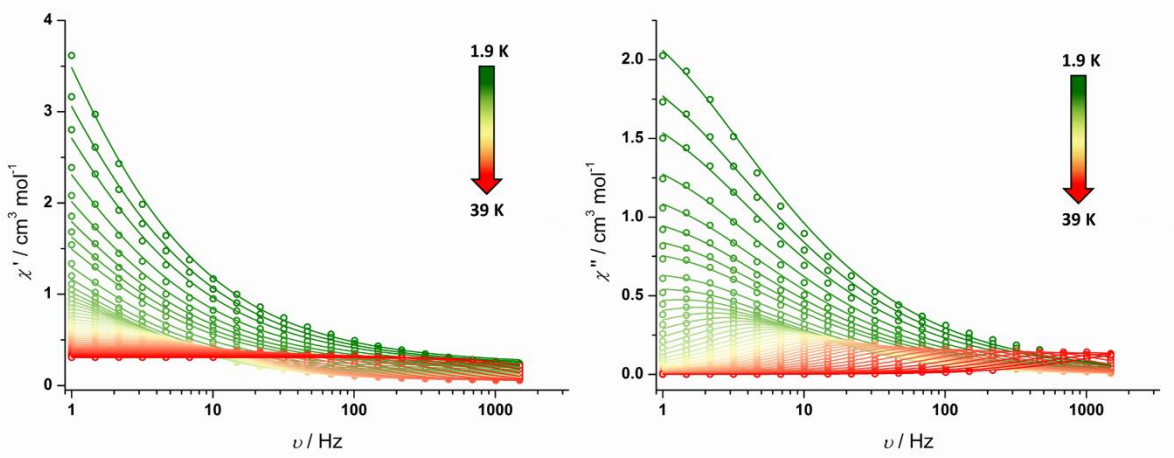

Figure 66. Frequency-dependence of the in-phase (χ') (left) and out-of-phase (χ'') (right) susceptibility for **15** in zero DC field at AC frequencies of ν = 1-1488 Hz and temperatures of 1.9-39 K. Solid lines represent fits to the data using Equation 1.

In order to probe the relaxation dynamics of **13**, the maxima from the $\chi'(\nu)$ and $\chi''(\nu)$ susceptibility measurements from 1.9-39 K were plotted against each other to give Cole-Cole plots, which were then fitted to the generalised Debye model shown in Equation 1 (Figures 67, 68, Supplementary Table S13). The lowest-frequency (1 Hz) data points were omitted from the fit due to an outlier at 13 K (Figure 68).

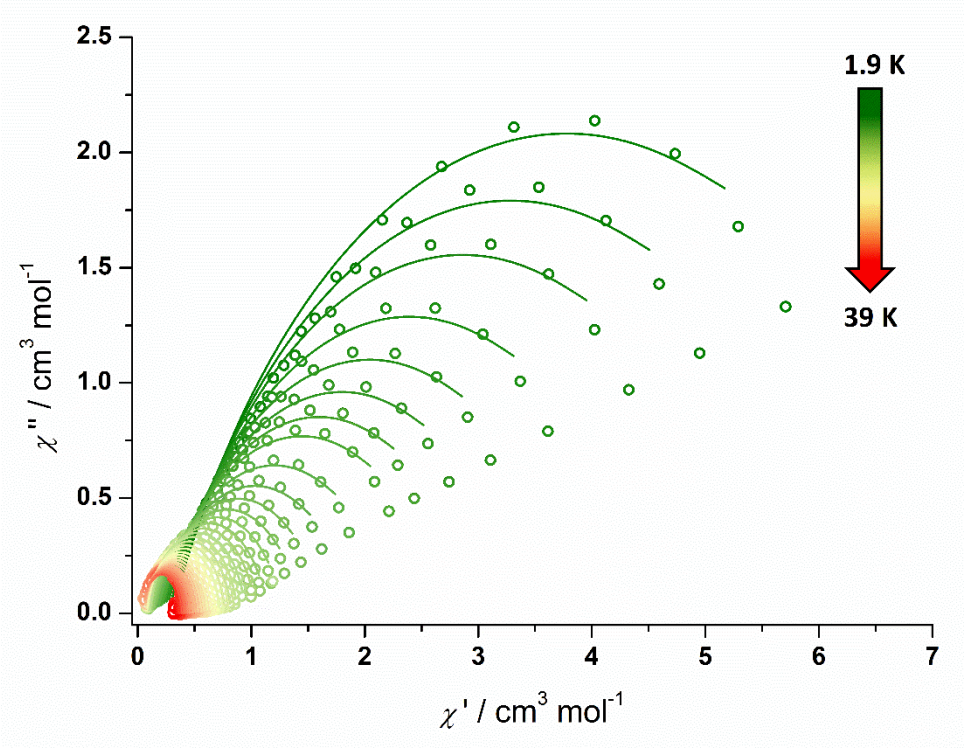

Figure 67. Cole-Cole plots for the AC susceptibilities in zero DC field for **13** from 1.9-39 K. Solid lines represent fits to the data using Equation 1. The lowest-frequency (1 Hz) data points were not included in the fit due an outlier at 13 K (see Figure 68).

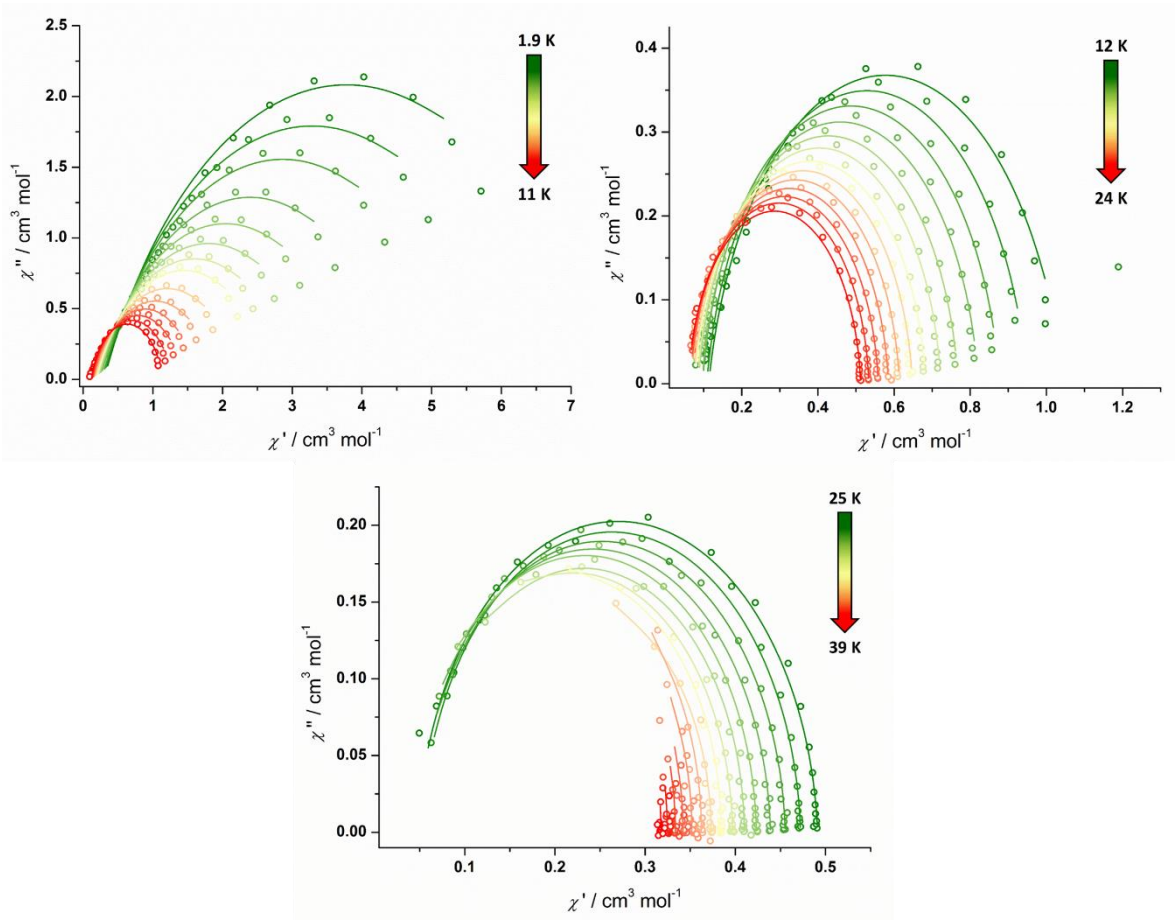

Figure 68. Cole-Cole plots for the AC susceptibilities in zero DC field for **13** from 1.9-11 K (top left), 12-24 K (top right) and 25-39 K (bottom). Solid lines represent fits to the data using Equation 1. The lowest-frequency (1 Hz) data points were not included in the fit due an outlier at 13 K.

Cole-Cole plots for compound **15** were formed by using the AC susceptibility data in the temperature range 1.9-39 K, which were then fitted to the generalised Debye model shown in Equation 1 (Figures 69, 70, Supplementary Table S13). The fits for both **13** and **15** show a good agreement with the experimental data, with α-parameters ranging from 0-0.31 and 0-0.43, and τvalues ranging from 0-0.044 and 0-0.35 s for **13** and **15**, respectively. The large range of values for the α-parameters in both cyclobutadienyl half-sandwich complexes indicate a broad distribution of relaxation times, suggesting multiple relaxation pathways across the measured temperature range.[11,130]

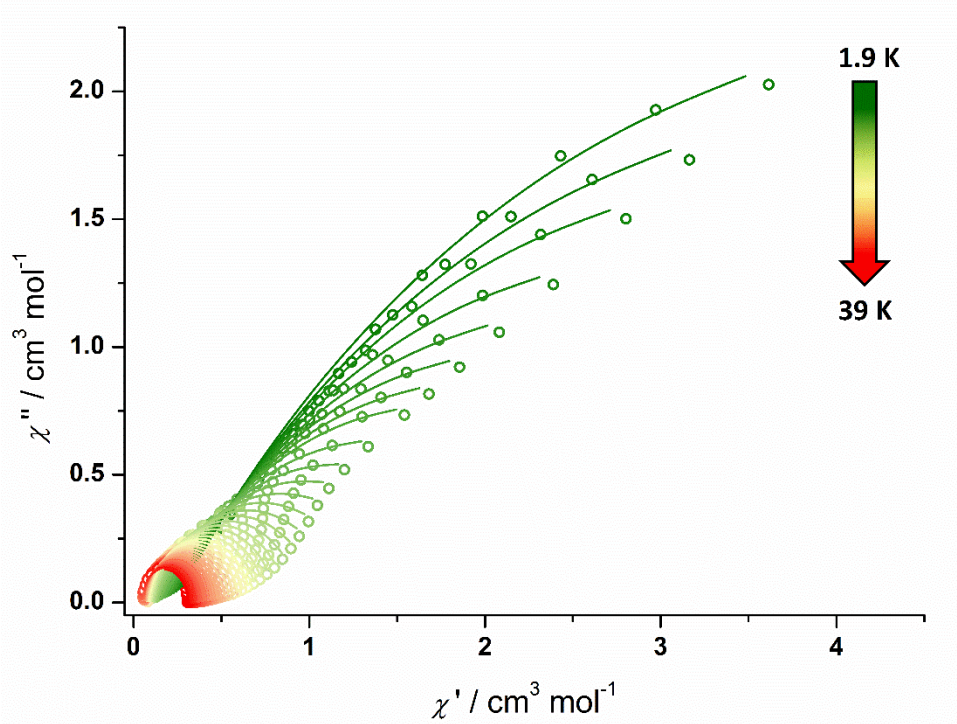

Figure 69. Cole-Cole plots for the AC susceptibilities in zero DC field for **15** from 1.9-39 K. Solid lines represent fits to the data using Equation 1.

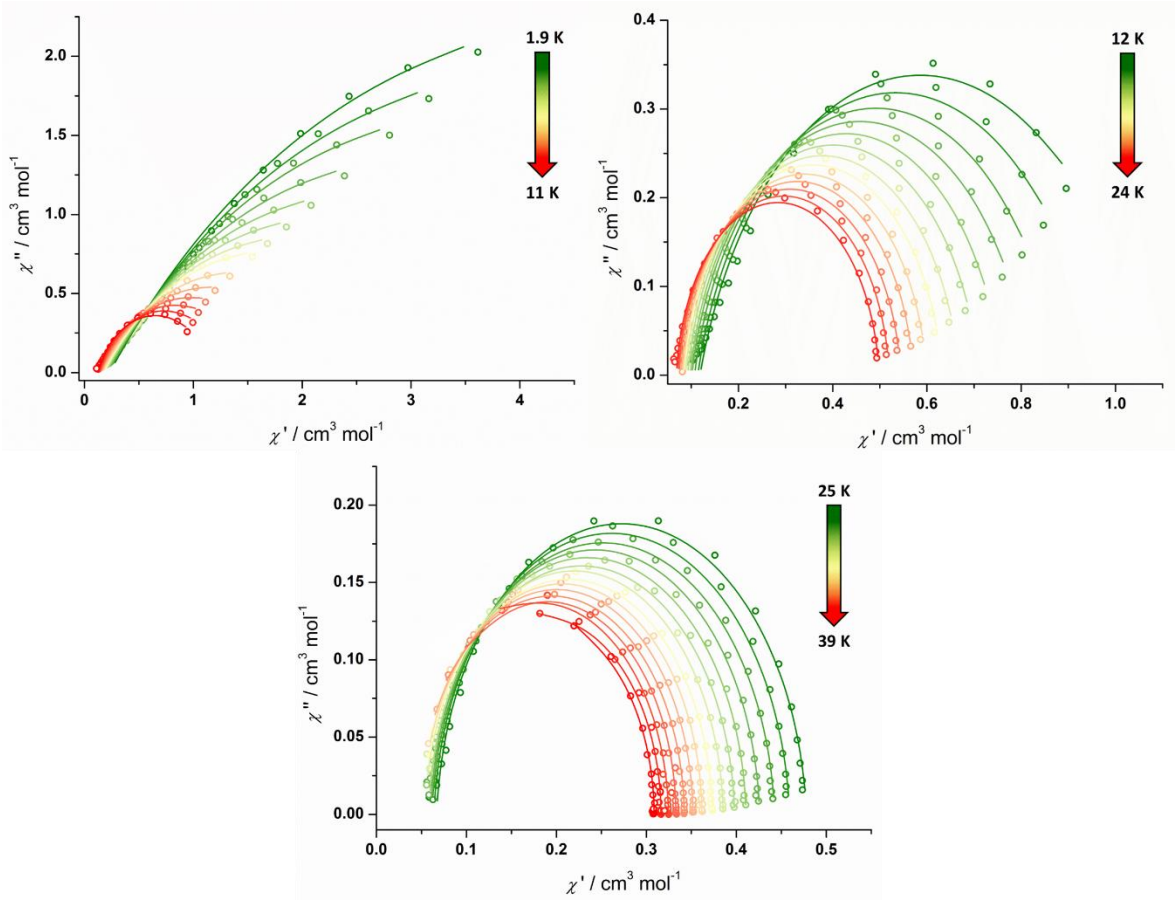

Figure 70. Cole-Cole plots for the AC susceptibilities in zero DC field for **15** from 1.9-11 K (top left), 12-24 K (top right) and 25-39 K (bottom). Solid lines represent fits to the data using Equation 1.

The temperature dependence of the relaxation times for **13** and **15** were analysed in the form of the natural log of the relaxation time *vs.* inverse temperature (Figure 71). Both sets of data show a similar temperature dependence of τ, and excellent fits to each data set (R^2 = 0.99962 and 0.99985 for **13** and **15**, respectively) were obtained by using Equation 2, which incorporates Orbach, Raman and QTM relaxation parameters.

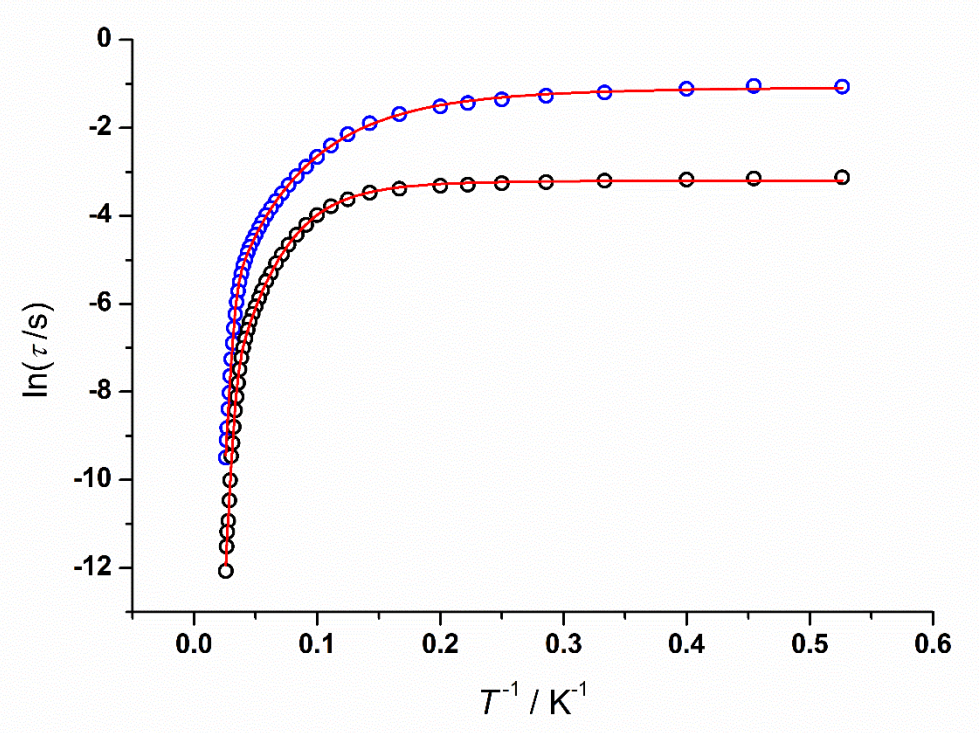

Figure 71. Plot of natural log of the relaxation time (τ) *vs.* inverse temperature for **13** (black circles) and **15** (blue circles). The data points are from the fit of respective AC susceptibility measurements. The solid red lines are the best fit to $\tau^{-1} = \tau_0^{-1} e^{-U_{\text{eff}}/k_B T} + CT^n + \tau_{QTM}^{-1}$, giving; (adjusted R^2 = 0.99962) U_{eff} = 371(7) cm^{-1}, τ_0 = 7.8(2) × 10^{-12} s, C = 4.1(7) × 10^{-3} s^{-1} K^{-n}, n = 3.85(6) and τ_{QTM} = 4.1(1) × 10^{-2} s for **13**, and (adjusted R^2 = 0.99985) U_{eff} = 357(4) cm^{-1}, τ_0 = 1.8(3) × 10^{-10} s, C = 1.4(2) × 10^{-2} s^{-1} K^{-n}, n = 2.90(4) and τ_{QTM} = 0.36(3) s for **15**.

At the highest temperatures in the $\ln\tau(T^{-1})$ plots, both compounds display an approximately linear relationship, indicative of relaxation via a thermally activated Orbach process, as described by the Arrhenius law. At lower temperatures, the data begins to deviate from this linearity, indicating that Raman relaxation is important. Below 5 K, the relaxation time is effectively temperature independent, indicating that relaxation via QTM is dominant. For compound **13**, fits to the data give U_{eff} = 371(7) cm^{-1}, τ_0 = 7.8(2) × 10^{-12} s, C = 4.1(7) × 10^{-3} s^{-1} K^{-n}, n = 3.85(6) and τ_{QTM} = 4.1(1) × 10^{-2} s. For compound **15**, fits to the data give U_{eff} = 357(4) cm^{-1}, τ_0 = 1.8(3) × 10^{-10} s, C = 1.4(2) × 10^{-2} s^{-1} K^{-n}, n = 2.90(4) and τ_{QTM} = 0.36(3) s. The values for the relaxation parameters of both cyclobutadienyl half-sandwich complexes are very similar, as expected based on the similar dysprosium coordination environments. The quantum tunnelling time for **13** is an order of magnitude faster than in **15**. In turn, the QTM times in **13** and **15** are one and two orders of magnitude slower when compared to the Cp half-sandwich complexes **4** (τ_{QTM} = 2.20(3) × 10^{-3} s) and [Dy(η^5-C$_5$^{i}Pr$_5$)(κ^3-BH$_4$)$_2$(THF)] (τ_{QTM} = 5.0(1) × 10^{-3} s), respectively. The Raman exponents

(n), and the attempt relaxation times (τ_0) are typical of monometallic Dy^{3+} metallocene SMMs, which generally range from 2-5 and 10^{-7}-10^{-12} s, respectively.[14,15,132]

Based on the solid-state structures of **13** and **15**, their SMM properties can be qualitatively described by each Dy^{3+} metal centre experiencing a strong axial crystal field from the dianionic cyclobutadienyl ligand, resulting in stronger crystal field splitting (relative to Cp) and, therefore, increased energy barriers to the reversal of magnetisation. However, as observed in all cyclopentadienyl half-sandwich complexes, a competing equatorial field that arises from the THF and borohydride ligands promote QTM at low temperatures. Relevant parameters are compared in Table 3.

Table 3. Dysprosium centroid distances and effective energy barriers of analogous lanthanide half-sandwich complexes.

Compound	Dy-C(ring)$_c$ / Å	U_{eff} / cm^{-1}	ref
2 [Dy{η^5-Cp^{ttt})(κ^3-BH$_4$)$_2$(THF)]	2.36131(6)†	165(5)	This work
4 [Dy(η^5-C$_5$Me$_4$^{t}Bu)(κ^3-BH$_4$)$_2$(THF)]	2.3166(2)	241(12)	This work
[Dy(η^5-C$_5$^{i}Pr$_5$)(κ^3-BH$_4$)$_2$(THF)]	2.377(1)	241(7)	[27]
13 [Dy{η^4-C$_4$(SiMe$_3$)$_4$}(κ^3-BH$_4$)$_2$(THF)Na]$_\infty$	2.262(4)	371(7)	This work
15 [Dy{η^4-C$_4$(SiMe$_3$)$_4$}(κ^3-BH$_4$)$_2$(THF)K]$_\infty$	2.264(3)	357(4)	This work

† Average distance between the disordered rings

The cyclobutadienyl half-sandwich complexes **13** and **15** represent an increase in the size of the effective energy barrier by 130 and 113 cm^{-1} (or possibly a 50 % increase), respectively, when compared to the best performing analogous cyclopentadienyl half-sandwich complexes **4** and [Dy(η^5-C$_5$^{i}Pr$_5$)(κ^3-BH$_4$)$_2$(THF)]. This is presumably a consequence of the stronger axial ligand field provided by the dianionic Cb ligands relative to that of the monoanionic Cp ligands, which is evidenced by the solid-state molecular structures, whereby the Dy-Cb$_{cent}$ distances are significantly shorter than the analogous Dy-Cp$_{cent}$ distances.

2.3.5. Theoretical calculations on $[Dy\{\eta^4\text{-}C_4(SiMe_3)_4\}(\kappa^3\text{-}BH_4)_2(THF)K]_\infty$ (**15**)

Due to the complicated nature of magnetic relaxation dynamics in organometallic lanthanide SMMs, multireference *ab initio* theoretical calculations have been established as an invaluable tool in which to aid the understanding of experimental data.[52–54] The calculations can be used to quantify the anisotropy of a system, as well as to help unravel relaxation processes and provide estimates for energy barriers. The anisotropy is quantified by the relative weight of the main values for gyromagnetic (g) tensors of each axis (g_x, g_y and g_z), where if one value is much larger than the others it is indicative of uniaxial magnetic anisotropy.[136] In the case of dysprosium, SMMs often possess ground-state g-tensors close to the Ising limit of $g_z = 20$, with g_x and $g_y = 0$,[13] and if this anisotropy is persevered in the excited crystal field states then it leads to higher effective energy barriers.

Therefore, the low-lying electronic states of **15** were investigated by multireference *ab initio* calculations on a model consisting of three $[Ln\{\eta^4\text{-}C_4(SiMe_3)_4\}(\kappa^3\text{-}BH_4)_2(THF)]^-$ units and two bridging K^+ ions (Figure 72).[54,137–143] All of the calculations presented in this thesis were conducted, and the results analysed, through collaboration with Dr Akseli Mansikkamäki at the University of Oulu (Finland). In order to study the central Dy^{3+} ion, the two terminal Dy^{3+} ions in the half-sandwich fragments were replaced by Y^{3+} ions. Density functional theory (DFT) calculations were carried out to ensure that no significant charge distribution of the central ion would be obtained by including a longer fragment of **15**.

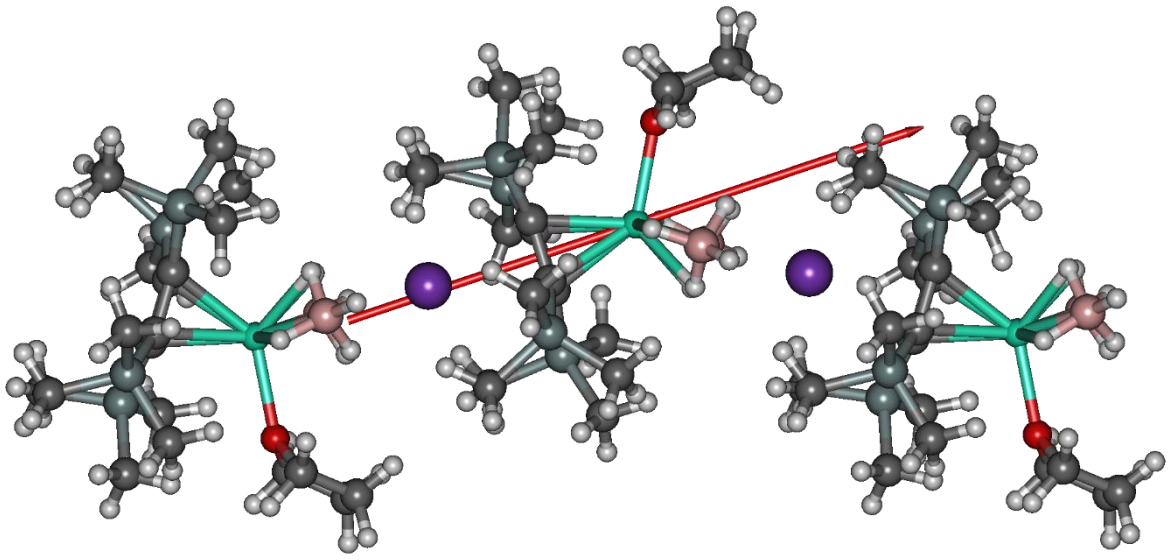

Figure 72. The principal magnetic axis of the ground Kramers' doublet (red arrow) calculated for the central Dy^{3+} ion in **15.** Dy = green (central), Y = green (terminal), Si = light grey, K = purple, B = pink, O = red, C = black, H = white.

The positions of hydrogen atoms were optimized using DFT calculations, whilst the positions of heavier atoms were kept fixed to their solid-state structure coordinates. The properties of the eight lowest Kramers' doublets (KD) arising from the crystal field split ground $^6H_{15/2}$ multiplet of the Dy^{3+} ion are listed in the Supplementary Table S18 and the principal magnetic axis of the ground KD is shown in Figure 72 (red arrow). The direction of the principal magnetic axis in the ground KD is clearly influenced by the strong axial interaction between the Dy^{3+} ion and the Cb^{2-} ligand.

The ground KD has a g_z = 19.835, with vanishingly small transverse components g_x and g_y = 0.001 and 0.001, respectively, suggesting that QTM should be slow at zero field. The transverse components become significant at the second excited KD (g_x = 0.534, g_y = 0.561), indicating that the barrier for magnetic relaxation is most probably crossed at this point. This results in a theoretically determined U_{eff} = 326 cm^{-1}, which is in good agreement with the experimentally determined value of 357(4) cm^{-1} for **15**. In theory, transitions up to the fourth excited KD could be possible as the transverse components remain small enough, however this is improbable.

Further insights into the effective energy barrier were modelled by calculating the transition magnetic moment matrix elements between the different states in the ground multiplet following a well-established method.[143] The results (Figure 73, Supplementary Table S19) indicate that the barrier is crossed at the second excited KD, which is consistent with previous calculations on the *g*-tensors and the experimental observations. The values of the transition magnetic moments remain relatively small up to the fifth excited KD, indicating that even minor modifications to the molecular structure, and hence the crystal field around Dy^{3+}, such as removing the THF solvent molecule, could significantly increase the barrier height.

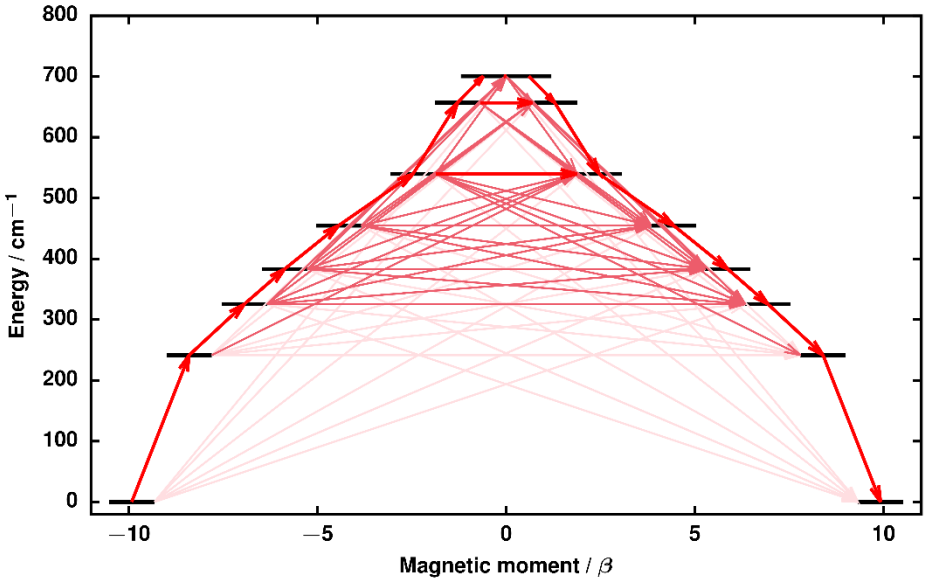

Figure 73. Calculated effective *ab initio* barriers for the relaxation of magnetisation in **15**. The arrows represent transition magnetic moments, with stronger arrows indicating larger values.

In order to gain further insight into the electronic structure of **15**, the *ab initio* crystal field parameters were calculated using a well-established methodology in the field (Supplementary Tables S20, S21).[54] The parameters can be understood qualitatively by considering the leading-order rank k = 2 parameters. If the diagonal B_2^0 parameter is large and negative, then it stabilizes the M_J = ±15/2 ground state. However, large values for the off-diagonal $B_2^{\pm 1}$ and $B_2^{\pm 2}$ parameters make appreciable contributions to reducing the overall axiality, and therefore anisotropy of the system. For **15**, the axial second-rank parameter B_2^0 = −377 cm^{-1}, which creates a relatively strong axial field. However, the off-diagonal second rank parameters of $|B_2^{\pm 1}|$ = 15 cm^{-1} and $|B_2^{\pm 2}|$ = 19 cm^{-1} lead to significant mixing of the different states characterised by a definite projection of the total angular momentum, which is present in all KDs.

The ratio of $|B_2^{\pm 2}|/|B_2^0|$ has previously been described to determine the rhombicity parameter of the crystal field, where the value lies between 0 (purely axial) and 1 (maximally rhombic).[144,145] However, in order to provide a measure of SMM performance against the current benchmark SMM [Dy(η^5-C$_5$^{i}Pr$_5$)(η^5-Cp*)]$^+$,[27] we have proposed that a *theoretical axiality factor*, Z, be defined as the ratio $|B_2^0|/|B_2^{\pm 2}|$, thus [Dy(η^5-C$_5$^{i}Pr$_5$)(η^5-Cp*)]$^+$ has Z = 39.5 (1195.305/30.226), and therefore the *relative theoretical axiality factor*, Z_{rel} = Z/39.5, may also be defined.[146] This analysis will allow for quantitative comparisons

between many different ligand systems and the current record SMM. Complex **15** therefore has a Z = 19.5 and Z_{rel} = 0.49. This is indicative that the axiality of the system, which originates from the strong interaction with the Cb^{2-} ligand, is not strong enough to overcome the significant non-axial components of the crystal field arising from the equatorial borohydride and THF ligands.

2.3.6. Conclusions on cyclobutadienyl half-sandwich SMMs

In this section, the synthesis of the first lanthanide cyclobutadienyl half-sandwich complexes $[Ln\{\eta^4\text{-}C_4(SiMe_3)_4\}(\kappa^3\text{-}BH_4)_2(THF)Na]_\infty$ (Ln = Y (**12**), Dy (**13**)) and $[Ln\{\eta^4\text{-}C_4(SiMe_3)_4\}(\kappa^3\text{-}BH_4)_2(THF)K]_\infty$ (Ln = Y (**14**), Dy (**15**)) was described. The cyclobutadienyl pro-ligands are transferred to the rare-earth elements in salt metathesis reactions without any activation of the $SiMe_3$ substituents, in contrast to all previous studies on related systems. Therefore, compounds **13** and **15** represent the first opportunity to study the influence of a pristine Cb ligand on the magnetic properties of Dy^{3+}, which has enabled us to test the hypothesis that the cyclobutadienyl ligand will produce stronger axial ligand fields compared to analogous cyclopentadienyl complexes, thus resulting in better SMM properties.

The static and dynamic magnetic properties of **13** and **15** were investigated by SQUID magnetometry, with the complexes showing typical Dy^{3+} traits in a static field with a $^6H_{15/2}$ ground multiplet. Dynamic measurements with a zero DC field revealed slow magnetic relaxation, with Orbach processes dominating the relaxation at higher temperatures (39-10 K), and a strong influence of QTM at lower temperatures (>10 K). Fitting the relaxation with Orbach, Raman and QTM parameters results in a U_{eff} = 371(7) cm^{-1} for **13**, and 357(4) cm^{-1} for **15**. Magnetic hysteresis measurements on both complexes reveal waist-restricted loops at 1.9 K, indicative of the strong QTM. Comparisons of **13** and **15** with the analogous Cp half-sandwich complexes **4** and $[Dy(\eta^5\text{-}C_5{}^iPr_5)(\kappa^3\text{-}BH_4)_2(THF)]$, reveal an increase in the effective energy barriers for the Cb half-sandwiches of 130 and 113 cm^{-1}, respectively. This is attributed to the stronger axial crystal field provided by the cyclobutadienyl ligands, which display reduced $Dy\text{-}Cb_{cent}$ distances when compared to the $Dy\text{-}Cp_{cent}$ distances in analogous cyclopentadienyl complexes. *Ab initio* calculations on **15** confirmed that the cyclobutadienyl ligand provides a strong axial crystal field interaction in relation to Dy^{3+}, with an excellent agreement between theoretical and experimental data.

Therefore, the main finding of this study strongly supports our hypothesis that cyclobutadienyl ligands can indeed provide a stronger axial crystal field for Dy^{3+} ions when compared to more conventionally used cyclopentadienyl ligands. Consequently, if a near-linear dysprosium sandwich complex of the type $[Dy(\eta^4\text{-Cb})_2]^-$ or $[Dy(\eta^4\text{-Cb})(\eta^5\text{-Cp})]$ could be synthesised, its SMM properties could well surpass those of the current benchmark $[Dy(\eta^5\text{-Cp}^R)_2]^+$ systems.

Chapter 3

Organometallic Rare-Earth Sandwich Complexes: Synthesis, Structure and Magnetic Studies

3.1. Cyclopentadienyl Rare-Earth Sandwich Complexes

3.1.1. Background

The magnetic properties of dysprosium sandwich complexes that feature two Cp^R ligands and an X ligand, *i.e.* $[Dy(\eta^5\text{-}Cp^R)_2X]$, can vary considerably and are typically much poorer SMMs than cationic $[Dy(\eta^5\text{-}Cp^R)_2]^+$ complexes. For example, the precursor complex $[Dy(\eta^5\text{-}Cp^{ttt})_2Cl]$ shows no U_{eff} or appreciable hysteresis, whereas the corresponding cation $[Dy(\eta^5\text{-}Cp^{ttt})_2]^+$ has a U_{eff} = 1277 cm^{-1} (or 1233 cm^{-1}) and T_H = 60 K.[22,23] A similar scenario arises in the precursor complex $[Dy(\eta^5\text{-}C_5{}^iPr_5)(\eta^5\text{-}Cp^*)(\kappa^2\text{-}BH_4)]$, which has a U_{eff} = 7(1) cm^{-1} and no appreciable hysteresis, with the cation $[Dy(\eta^5\text{-}C_5{}^iPr_5)(\eta^5\text{-}Cp^*)]^+$ displaying record properties of U_{eff} = 1541(11) cm^{-1} and T_H = 80 K.[27]

Thus, further investigations into the synthesis and characterization of precursor metallocenes and subsequent cationic metallocene complexes should provide further insight into how the steric and electronic properties of the various types of Cp ligand impact on SMM properties.

Building upon studies of the Cp^{ttt} half-sandwich complexes **1** and **2**, this section describes the synthesis, characterization, and magnetic properties of a heteroleptic dysprosium metallocene, which can in turn be used as a precursor to a cationic complex of the type $[Dy(\eta^5\text{-}Cp^R)_2]^+$.

3.1.2. Synthesis and characterisation of [Ln(η^5-Cp^{ttt})(η^5-Cp)(κ^2-BH$_4$)] (Ln = Y (**16**), Dy (**17**))*

The synthesis of the heteroleptic cyclopentadienyl sandwich complexes [Ln(η^5-Cp^{ttt})(η^5-Cp*)(κ^2-BH$_4$)] (Ln = Y (**16**), Dy (**17**)) was achieved by the salt metathesis reaction between NaCp* or KCp* and **1** or **2** in toluene at 108°C for three days (Scheme 20). After subsequent work up, storing a saturated hexane solution at –40 °C overnight resulted in the formation of white or pale yellow crystals of **16** and **17**, in yields of 74 and 70 %, respectively.

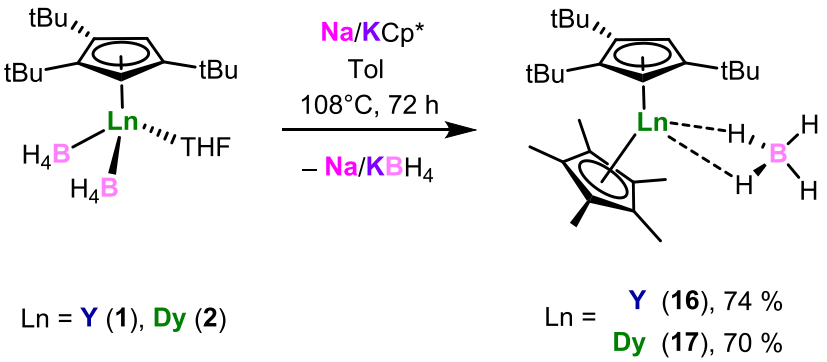

Scheme 20. Synthesis of **16** and **17**.

Compounds **16** and **17** are isostructural, both featuring η^5-coordination modes of the Cp^{ttt} and Cp* ligands, with one κ^2-borohydride ligand additionally coordinated to the metal centre (Figure 74). For **17**, the Dy-C bond distances range from 2.620(4)-2.737(4) Å and 2.614(4)-2.663(4) Å for the Cp^{ttt} and Cp* ligands, respectively, revealing a slightly more asymmetric coordination of the Cp^{ttt} ligand. The Dy-Cp^{ttt} centroid distance is 2.3779(18) Å, with the analogous Cp* distance lying slightly closer at 2.351(2) Å, resulting in a Cp$_c$-Dy-Cp$_c$ bending angle of 145.23(7)°. These distances are slightly shorter when compared to those of [Dy(η^5-C$_5$^{i}Pr$_5$)(η^5-Cp*)(κ^2-BH$_4$)], whereby the Dy-C bond distances range from 2.660(3)-2.685(3) and 2.626(3)-2.677(3) Å for the Cp^{iPr5} and Cp* ligands, with centroid distances of 2.3823(14) and 2.3636(16) Å, respectively. However, the Cp^{iPr5} derivative is more axial than **17** and displays a Cp$_c$-Dy-Cp$_c$ bending angle that is larger by *ca.* 5° (150.28(5)°). The Dy···B distance in **17** is *ca.* 0.05 Å longer than the analogous distance in the Cp^{iPr5} derivative, most likely a consequence of the decrease in steric bulk allowing for the slightly closer approach of both Cp^{ttt} and Cp* ligands to the Dy^{3+} metal centre.

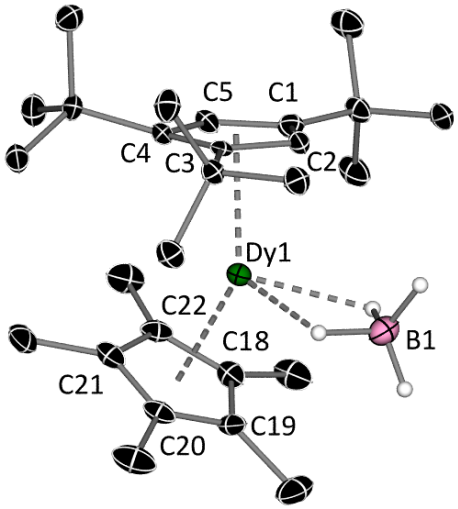

Figure 74. Molecular structure of [Dy(η^5-Cp^{ttt})(η^5-Cp*)(κ^2-BH$_4$)] (**17**). Thermal ellipsoids are set to 50 % probability and for clarity, only the hydrogen atoms bound to boron are shown. Selected bond distances (Å) and angles (°) for **17**: C1-C2 1.385(6), C2-C3 1.434(5), C3-C4 1.435(5), C4-C5 1.426(5), C1-C5 1.405(6), C18-C19 1.392(6), C19-C20 1.419(6), C20-C21 1.416(6), C21-C22 1.426(6), C18-C22 1.433(6), Dy1-Cp$_{cent}$ 2.3779(18) (C1-5), 2.351(2) (C18-22), Dy1-B1 2.731(6), Cp$_{cent}$-Dy1-Cp$_{cent}$ 145.23(7).

The ^{1}H NMR spectrum of the yttrium compound **16** in D$_6$-benzene shows signals that were assigned as follows: 6.48 ppm (s, 2H, Cp^{ttt} ring), 2.01 ppm (s, 15H, Cp*), 1.39 ppm (bs, 18H, ^{t}Bu) and 1.16 ppm (s, 9H, ^{t}Bu) (Figure S41). Signals corresponding to the BH$_4$ protons could not be observed, however the ^{1}H{^{11}B} spectrum in D$_6$-benzene displayed two additional overlapped signals at 1.28 and 1.26 ppm (s, 4H, BH$_4$) (Figure S43). The presence of two signals for the borohydride ligand instead of the expected one, as well as the significant broadening of the peak at 1.39 ppm in the ^{1}H NMR suggest that there may be some interaction between the two ^{t}Bu groups and the BH$_4$ ligand causing restricted rotation in solution.

The ^{13}C{^{1}H} NMR spectrum of **16** in D$_6$-benzene shows further evidence for restricted rotation, with significantly broadened peaks at 34.32 and 32.95 ppm, corresponding to the quaternary ^{t}Bu carbons and the methyl groups of two ^{t}Bu groups. Sharp signals corresponding to the third ^{t}Bu group were observed at 32.41 and 31.46 ppm, with the Cp* methyl carbons resonating at 12.45 ppm. A signal corresponding to the Cp* ring aromatic carbons was observed as a 1:1 doublet centred at 122.10 ppm ($^1J_{CY}$ = 2 Hz). Only one signal could be observed for the Cp^{ttt} ring, as a 1:1 doublet centred at 136.00 ppm ($^1J_{CY}$ = 2 Hz).

The other expected signals for the Cp^{ttt} ring carbons could not be observed, as they may coincide with the solvents carbon signals (Figure S45).

Variable temperature ^{1}H NMR on **16** revealed that upon heating the sample, the broad peak at 1.39 ppm for the two ^{t}Bu groups become much sharper, with no indication of any restricted rotation at 60 °C (Figure 75). The two overlapped signals for the borohydride ligand in the $^{1}H\{^{11}B\}$ spectrum at 1.28 and 1.26 ppm merge into a single broad signal at 60 °C that is slightly shifted and centred at 1.21 ppm (Figure S44).

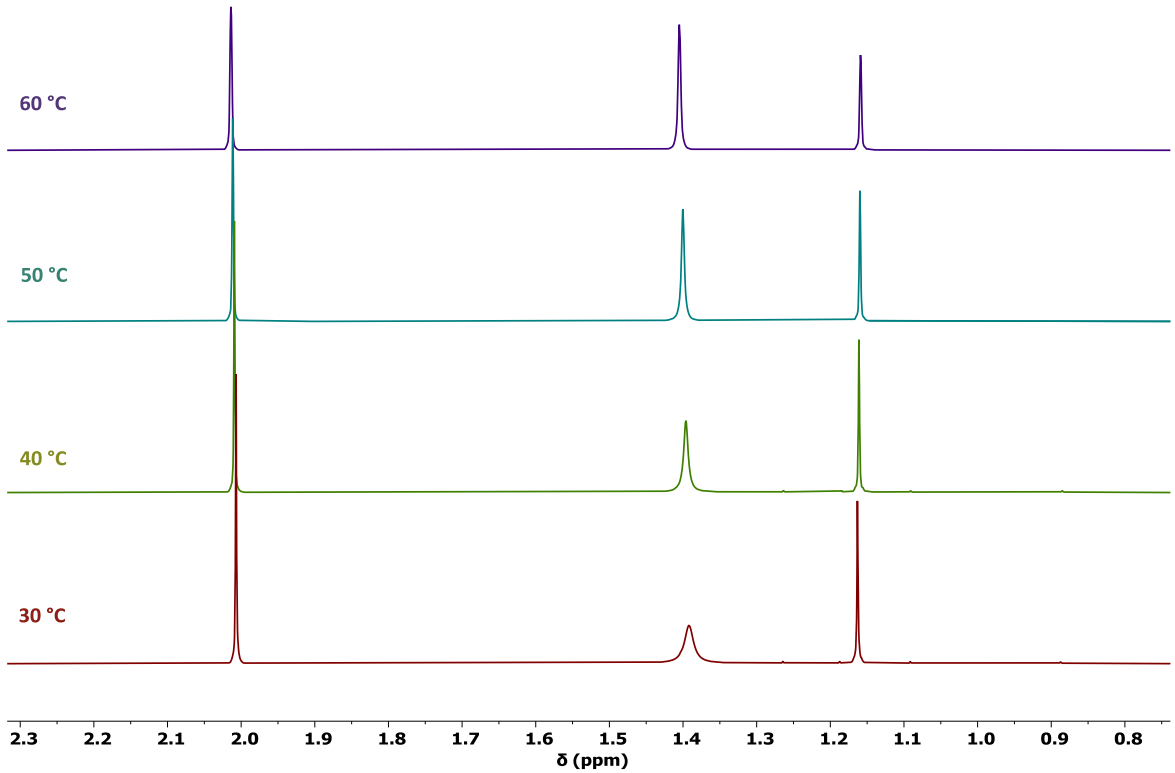

Figure 75. Variable temperature ^{1}H NMR of **16** in D_6-benzene from 30 to 60 °C.

In the $^{13}C\{^{1}H\}$ NMR of **16** at 60 °C, the broad signals that were evident at 30 °C have become much sharper, and the additional Cp^{ttt} ring carbons can be observed with assignments as follows: 136.07 ($\underline{C}p^{ttt}$ ring), 135.27 ($\underline{C}p^{ttt}$ ring), 122.19 ($\underline{C}p^{*}$ ring), 114.26 ($\underline{C}p^{ttt}$ ring), 34.35 (($\underline{C}(CH_3)_3)_2$), 33.12 ((C($\underline{C}H_3)_3)_2$), 32.47 ($\underline{C}(CH_3)_3$), 31.52 (C($\underline{C}H_3)_3$), 12.41 ($\underline{Me}_5$) (Figure 76).

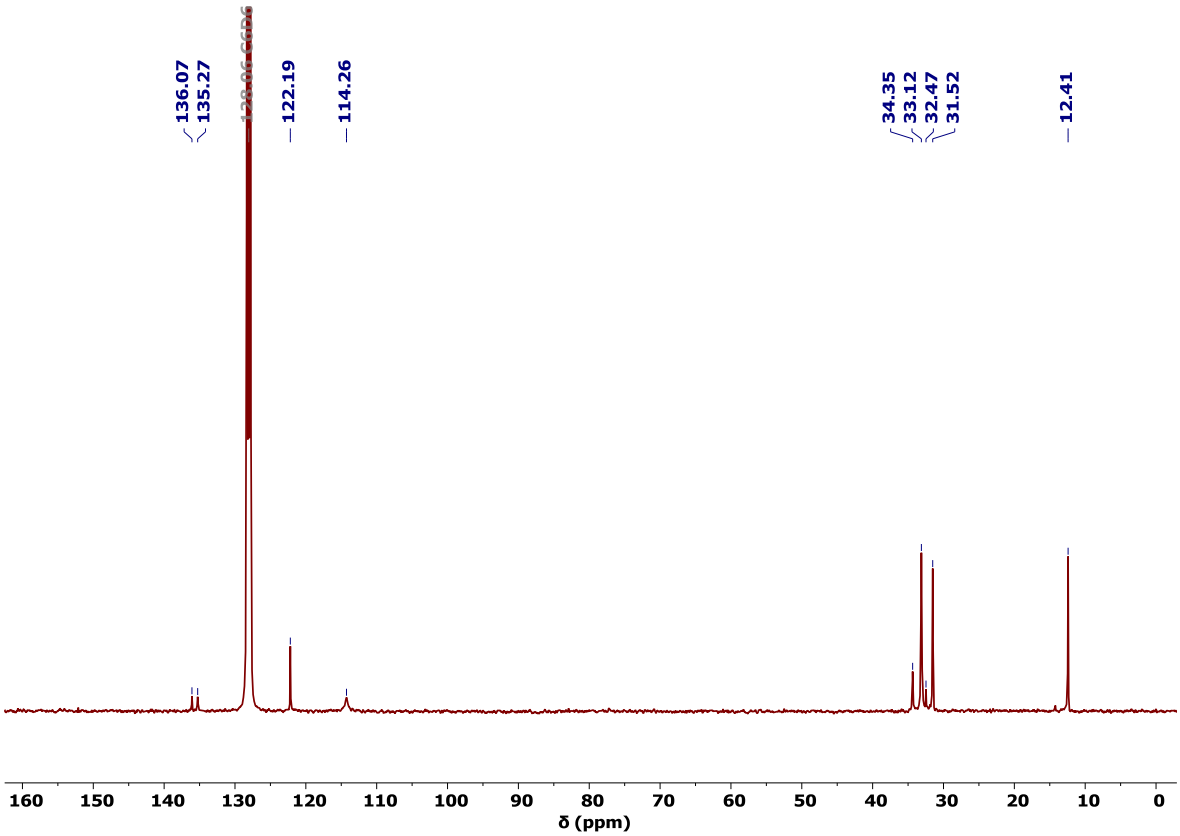

Figure 76. $^{13}C\{^{1}H\}$ NMR spectrum of **16** in D_8-benzene at 60 °C.

The $^{11}B\{^{1}H\}$ spectrum of **16** displays the expected singlet at −16.31 ppm (FWHM = 72 Hz), which splits into a 1:4:6:4:1 quintet in the ^{11}B spectrum centered at −16.32 ppm ($^{1}J_{BH}$ = 82 Hz) and are essentially unchanged at 60 °C (Figures S46-49). The FTIR spectra of compounds **16** and **17** show the expected absorptions at similar frequencies in the range of 4000-450 cm^{-1}, with the key stretches summarized in the caption to Figure 77. Elemental analyses of **16** and **17** were both consistent with their respective molecular formulae, with % found (calculated) for **16** $C_{27}H_{48}YB$: C 67.83 (68.65); H 11.07 (10.24), and **17** $C_{27}H_{48}DyB$: C 59.36 (59.40); H 8.95 (8.86).

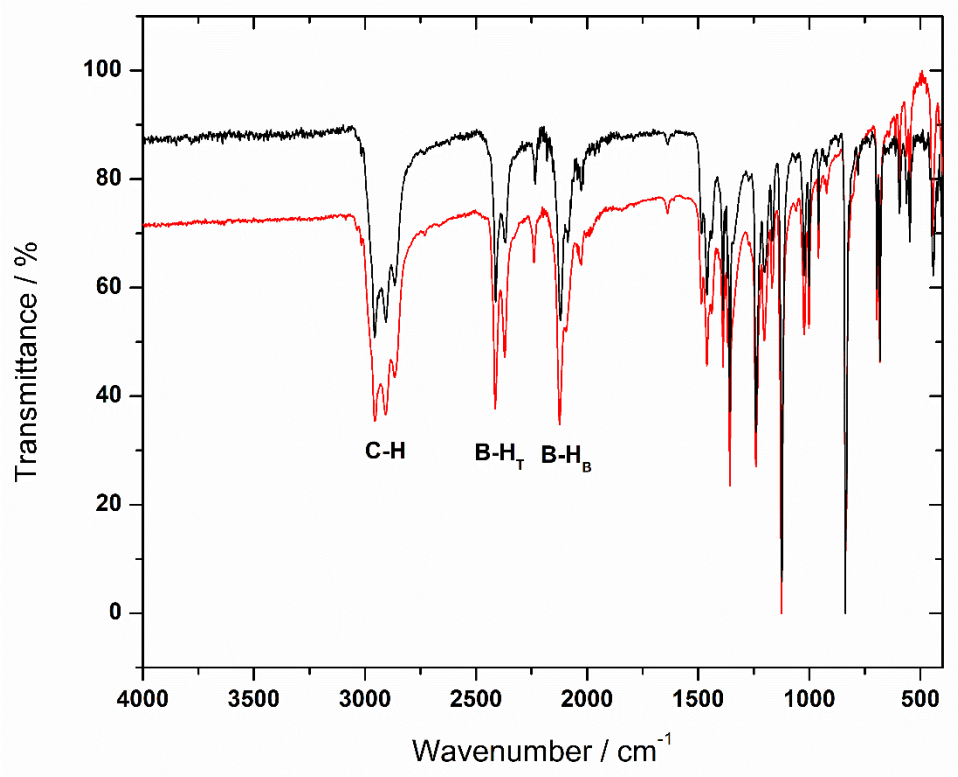

Figure 77. FTIR spectra of **16** (red line) and **17** (black line). Selected absorptions (cm^{-1}): 3000-2850 (C–H), 2400-2300 ($B–H_T$), 2150-2000 ($B–H_B$).

3.1.3. Magnetic property measurements on [Dy(η^5-Cp^{ttt})(η^5-Cp)(κ^2-BH$_4$)] (**17**)*

The magnetic susceptibility of compound **17** was investigated by SQUID magnetometry in both static and dynamic fields. In a static field of 1000 Oe, the magnetic susceptibility of **17** was found to be typical of a monometallic Dy^{3+} complex with a $^6H_{15/2}$ ground multiplet, with a $\chi_M T$ value of 13.61 cm^3 K mol^{-1} at 300 K, which lowers to 11.13 cm^3 K mol^{-1} at 2 K. A magnetization value of 4.94 Nβ was determined at 1.9 K and 7 T (Figure 78).

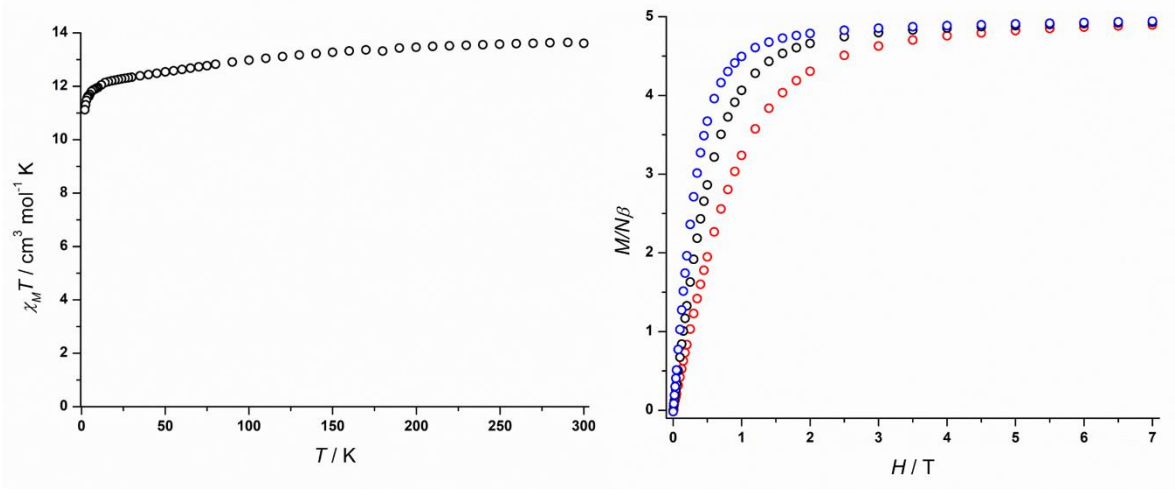

Figure 78. Plot of $\chi_M T(T)$ for **17** (left) in an applied field of 1000 Oe. $\chi_M T$ (300 K) = 13.61 cm^3 K mol^{-1}, $\chi_M T$ (2 K) = 11.13 cm^3 K mol^{-1}. Field (H) dependence of the magnetization (M) for **2** (right) at 1.9 K (blue circles), 3.0 K (black circles) and 5.0 K (red circles). M = 4.94 Nβ at 1.9 K and 7 T.

In a similar fashion to [Dy(η^5-C$_5$^{i}Pr$_5$)(η^5-Cp*)(κ^2-BH$_4$)],[27] the hysteresis of **17** is poor, with rapid loss of magnetization at zero-field and negligible coercivity at 1.9 K (Figure 79). This is a common feature of Dy^{3+} complexes containing strong equatorial ligand interactions, whereby QTM dominates the low-temperature magnetic relaxation.

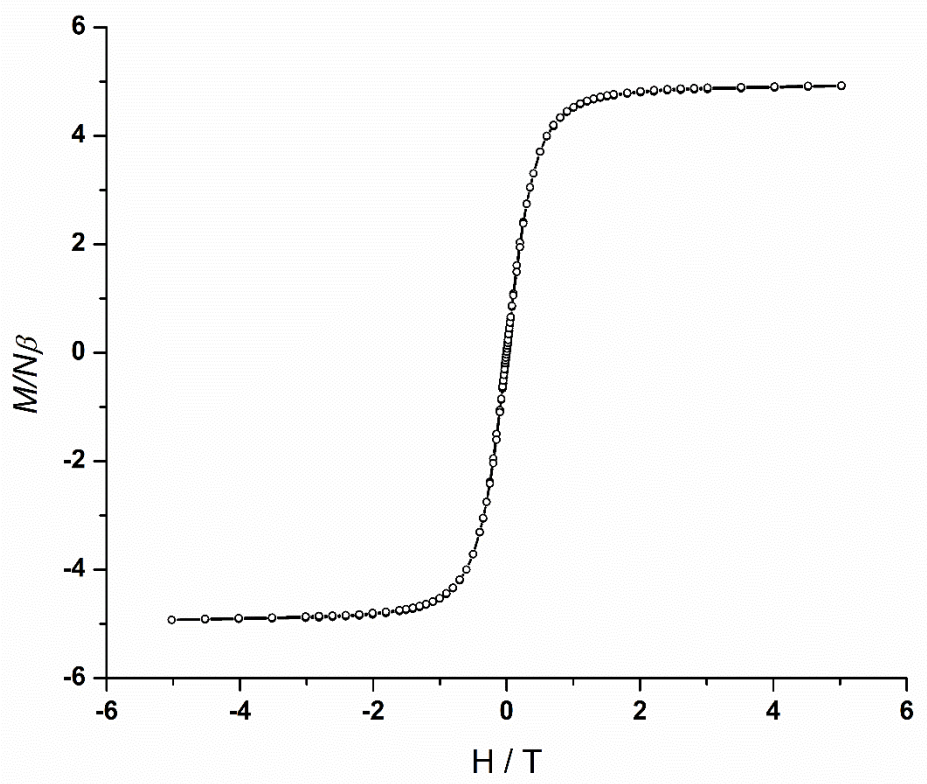

Figure 79. Magnetic hysteresis loops for **17**. The data were continuously collected at 1.9 K under a varying field sweep rate (11 Oe s^{-1} |0-1| T, 30 Oe s^{-1} |1-2| T, 45 Oe s^{-1} |2-3| T and 85 Oe s^{-1} |3-5| T). Solid lines are a guide to the eye.

Dynamic AC magnetic susceptibility measurements on **17** revealed slow magnetic relaxation properties in zero DC field, with the $\chi''(\nu)$ plots displaying maxima in the temperature range of 1.9-23 K (Figure 80). Below 5 K, the magnetic relaxation is dominated by a non-thermal process, whilst at higher temperatures, thermally activated relaxation dominates before the upper frequency limit of the SQUID magnetometer is reached.

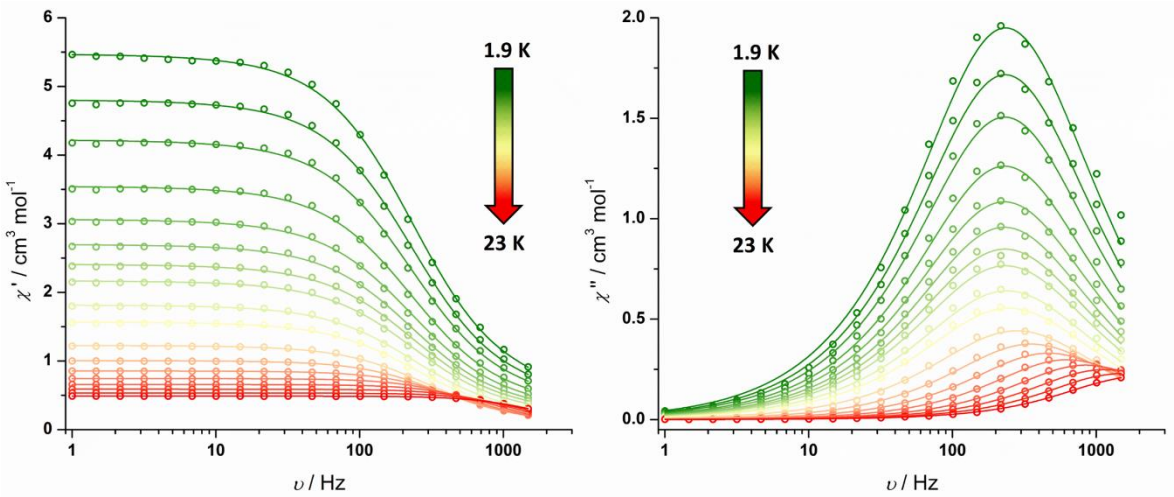

Figure 80. Frequency-dependence of the in-phase (χ') (left) and out-of-phase (χ'') (right) susceptibility for **17** in zero DC field at ν = 1-1488 Hz and temperatures of 1.9 to 23 K. Solid lines represent fits to the data using Equation 1.

The relaxation dynamics of **17** were probed further with Cole-Cole plots of $\chi''(\chi')$ across the temperature range 1.9-23 K, resulting in asymmetric semi-circular plots that were fitted to the generalised Debye model shown in Equation 1 (Figures 81, 82, Supplementary Table S14). The fit shows a good agreement with the experimental data, with α-parameters ranging from 0.02-0.14, and τ values ranging from 0-0.0007 s. The largest α- values occur at the lowest temperatures, suggesting that more than one time constant is present, with very fast magnetic relaxation times across the measured temperature range.[11,130]

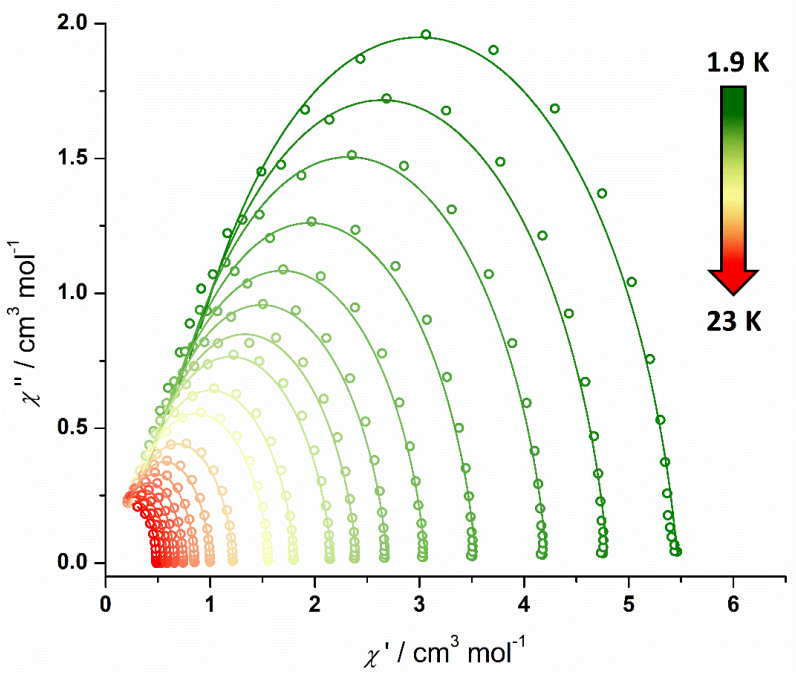

Figure 81. Cole-Cole plots for the AC susceptibilities in zero DC field for **17** from 1.9-23 K. Solid lines represent fits to the data using Equation 1.

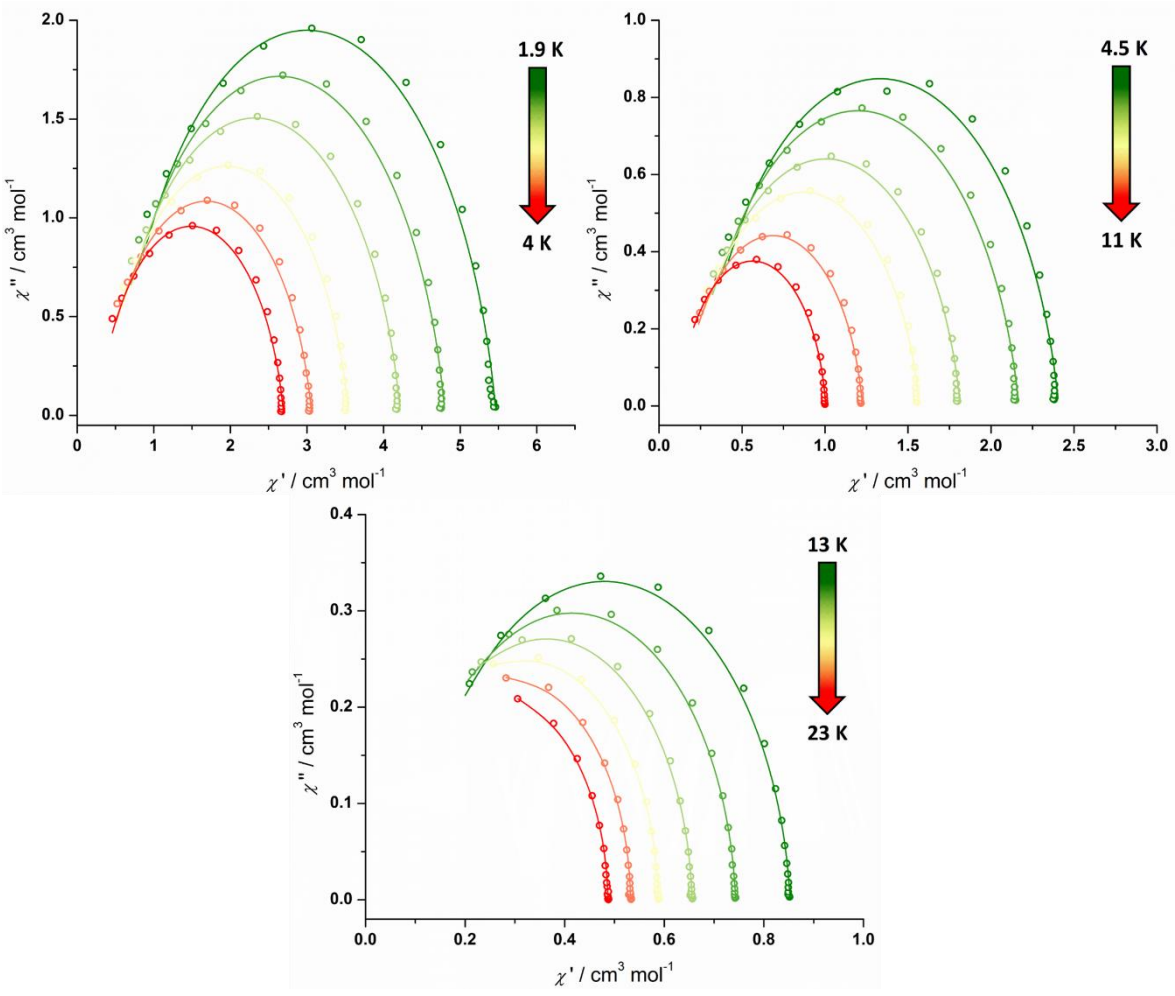

Figure 82. Cole-Cole plots for the AC susceptibilities in zero DC field for **17** from 1.9-4 K (top left), 4.5-11 K (top right) and 13-23 K (bottom). Solid lines represent fits to the data using Equation 1.

The temperature dependence of the relaxation times for **17** were analysed in the form of the natural log of the relaxation time *vs.* inverse temperature (Figure 83). The data shows features correlating to relaxation via Orbach, Raman and QTM processes, and an excellent fit to the data (R^2 = 0.99988) was obtained using Equation 2 and the following parameters: U_{eff} = 36(2) cm^{-1}, τ_0 = 2.1(4) × 10^{-5} s, C = 0.055(4) s^{-1} K^{-n}, n = 3.6(2) and τ_{QTM} = 6.89(3) × 10^{-4} s.

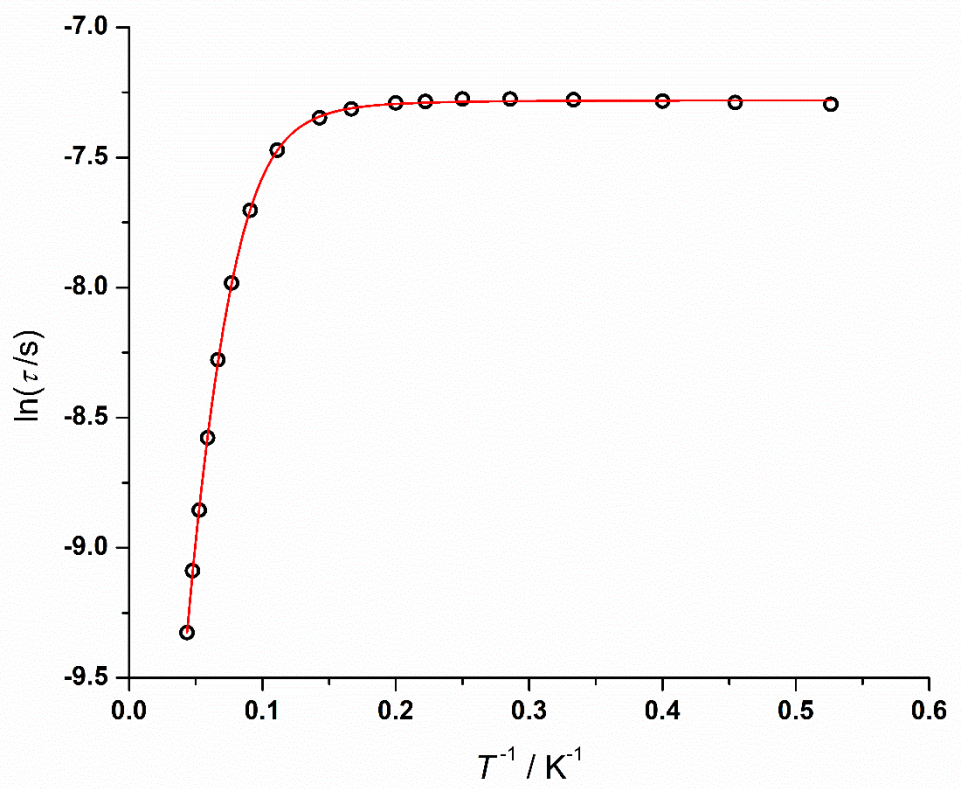

Figure 83. Plot of natural log of the relaxation time (τ) *vs.* inverse temperature for **17**. The black points are from the AC susceptibility measurements. The solid red line is the best fit (adjusted R^2 = 0.99988) to $\tau^{-1} = \tau_0^{-1} e^{-U_{eff}/k_B T} + CT^n + \tau_{QTM}^{-1}$, giving: U_{eff} = 36(2) cm^{-1}, τ_0 = 2.1(4) × 10^{-5} s, C = 0.055(4) s^{-1} K^{-n}, n = 3.6(2) and τ_{QTM} = 6.89(3) × 10^{-4} s.

In previous studies,[23] it has been shown that the C–H groups on Cp^{ttt} ligands can facilitate the magnetic relaxation dynamics due to spin-phonon coupling, which is consistent with results presented in this thesis on the half-sandwich complex **2**. However, despite the relatively small energy barrier of 36(2) cm^{-1}, complex **17** represents a slight improvement on the properties of the fully substituted Cp^{iPr5} derivative [Dy(η^5-C$_5$^{i}Pr$_5$)(η^5-Cp*)(κ^2-BH$_4$)], which has a U_{eff} = 7(1) cm^{-1} and τ_0 = 7.6(5) × 10^{-5} s. This comparison should be taken cautiously however, as the data for the Cp^{iPr5} complex was only fit to a linear Arrhenius

relationship in the high temperature region, with an R^2 = 0.9388, hence the barrier for this compound is only an estimate.[27]

Nevertheless, based on the available data, the slight improvement to the anisotropy barrier of **17** can perhaps be explained by the observed structural parameters. The Dy-Cp centroid distances for **17** are slightly shorter for the Cp^{ttt} *vs.* Cp^{iPr5} and the Cp* ligands by *ca.* 0.004 and 0.013 Å, respectively. However, the Cp_c-Dy-Cp_c bending angle of **17** is *ca.* 5° smaller, which results in reduced axiality. Thus, these results are consistent with the current magneto-structural corelations for Dy^{3+} SMMs, in which the strength of the axial crystal field has a greater impact on the magnetic properties when compared to axiality alone.[22,23,25,27]

3.1.4. Synthesis and characterization of [Dy{η⁵-Cp^ttt}(η⁵-Cp){B(C₆F₅)₄}] (**18**)*

In an attempt to synthesise the cationic separated ion pair derivative of **17** by abstraction of the borohydride ligand, *i.e.* $[Dy(\eta^5\text{-}Cp^{ttt})(\eta^5\text{-}Cp^*)]^+[B(C_6F_5)_4]^-$, the reaction of equimolar amounts of **17** and the electrophile $[Ph_3C]^+[B(C_6F_5)_4]^-$ was carried out in cold hexane (*ca.* −40°C) followed by warming to room temperature and stirring overnight (Scheme 21). Upon the addition of **17**, the fine powdered yellow suspension of $[Ph_3C]^+[B(C_6F_5)_4]^-$ in hexane becomes notably sticky, forming a bright yellow precipitate around the stirrer bar and the resulting supernatant becoming clear. After subsequent work up, pale-yellow crystals of **18** suitable for X-ray crystallography could be obtained in an isolated yield of 37 % by storing a saturated toluene solution layered with hexane at –40 °C over three days. The relatively low yields obtained for this complex could be a consequence of its very high solubility.

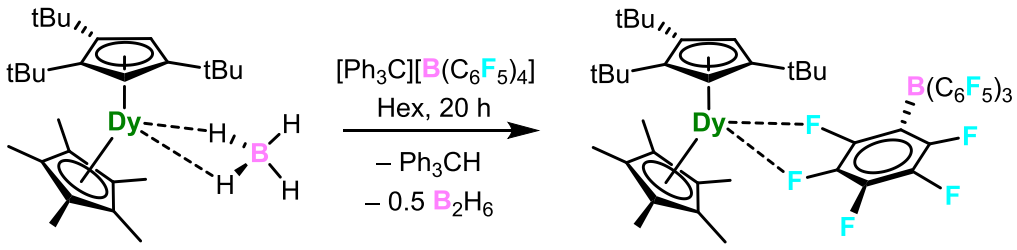

(**17**) (**18**), 37 %

Scheme 21. Synthesis of **18**.

X-ray crystallography revealed that the solid-state molecular structure of **18** is the contact ion-pair [Dy(η^5-Cp^{ttt})(η^5-Cp*){B(C$_6$F$_5$)$_4$}]. The dysprosium environment features η^5-coordination of the Cp^{ttt} and Cp* ligands and additional equatorial interactions of the [B(C$_6$F$_5$)$_4$]$^-$ counter anion through the *ortho*- and *meta*-fluorine atoms (Figure 84). The Dy–C bond distances range from 2.576(5)-2.721(5) and 2.590(5)-2.643(5) Å for the Cp^{ttt} and Cp*, respectively, revealing a more asymmetric coordination of the Cp^{ttt} ligand compared to the Cp* ligand, which is comparable with the precursor **17**. The Dy-Cp^{ttt} centroid distance is 2.347(2) Å, with the analogous Cp* distance lying slightly closer at 2.342(2) Å, which are only slightly shorter than the analogous distances in **17**. The Dy–F interactions with the counter-anion are also asymmetric, with distances of 2.491(3) and 2.599(3) Å. Due to these equatorial Dy–F interactions, the resulting Cp$_c$-Dy-Cp$_c$ bending angle is 144.67(7)°, which has slightly decreased when compared to the analogous bending angle in the precursor **17** of 145.23(7)°.

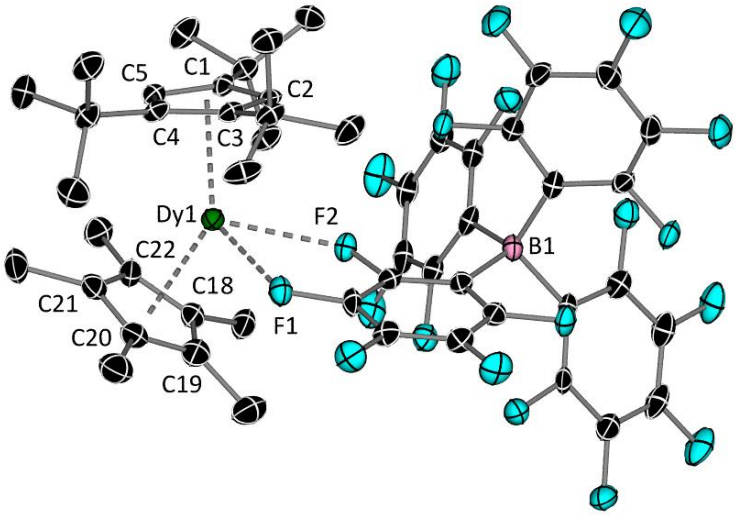

Figure 84. Molecular structure of [Dy(η^5-Cp^{ttt})(η^5-Cp*){B(C$_6$F$_5$)$_4$}] (**18**). Thermal ellipsoids are set to 50 % probability and hydrogen atoms have been omitted for clarity. Selected bond distances (Å) and angles (°) for **18**: C1-C2 1.412(6), C2-C3 1.419(6), C3-C4 1.442(6), C4-C5 1.439(6), C1-C5 1.414(6), C18-C19 1.396(8), C19-C20 1.437(7), C20-C21 1.400(8), C21-C22 1.419(7), C18-C22 1.421(7), Dy1-Cp$_{cent}$ 2.347(2) (C1-5), 2.342(2) (C18-22), Dy1-F1 2.491(3), Dy1-F2 2.599(3), Cp$_{cent}$-Dy1-Cp$_{cent}$ 144.67(7).

The ^{1}H NMR spectrum of **18** in D$_6$-benzene is consistent with the molecular structure, whereby broad signals could be observed at 2.11 (bs, 2H), 1.21 (bs, FWHM = 41 Hz, 18H), 0.84 (bs, FWHM = 33 Hz, CH$_3$, 15H) and −0.92 ppm (bs, FWHM = 50 Hz, ^{t}Bu, 9H) (Figure S50). These signals correspond to the two protons of the Cp^{ttt} ring, the two *tert*-butyl

groups in the same environment, the methyl protons of the Cp* and the final *tert*-butyl group, respectively. No signals could be observed in the $^{13}C\{^{1}H\}$, $^{11}B\{^{1}H\}$ or ^{11}B spectra due to the paramagnetic nature of **18**. In the case of the ^{19}F NMR spectrum, three broad signals could be observed at *ca.* −74, −142 and −215 ppm, however, these signals are only tentatively assigned due to difficulties associated with phasing the baseline in the region where they occur (Figure S51). The FTIR spectrum of **18** shows weak saturated C–H stretches in the range of 3000-2850 cm^{-1}, and a strong absorption at 1450 cm^{-1} corresponding to the C–F stretches of the $[B(C_6F_5)_4]^-$ anion (Figure 85).

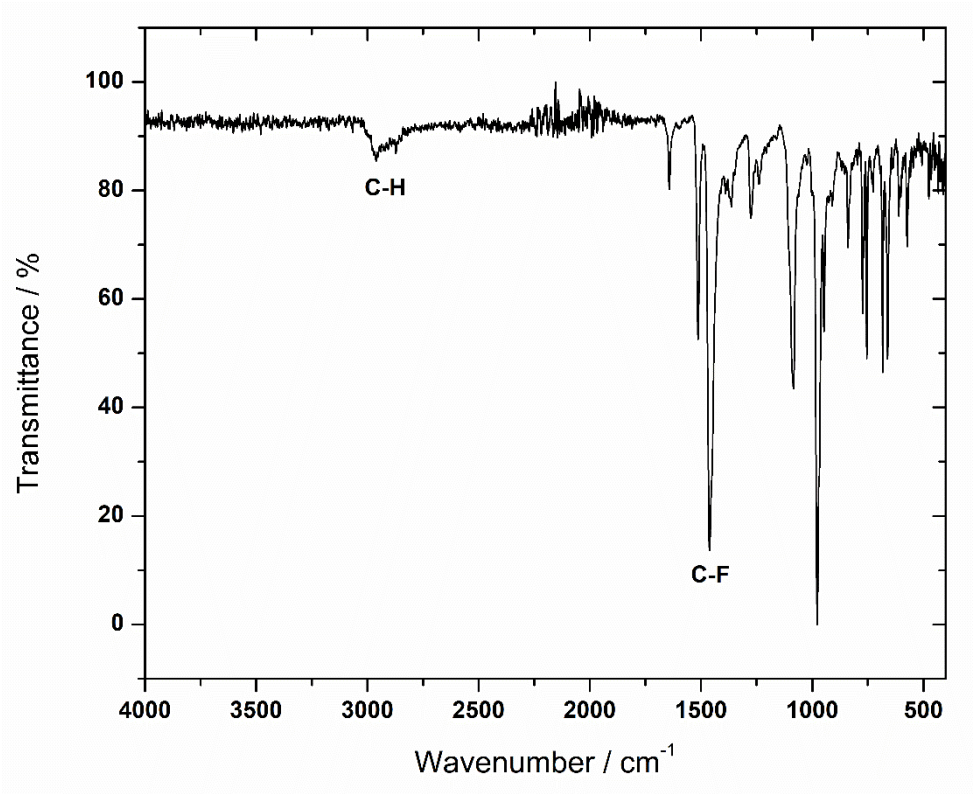

Figure 85. FTIR spectra of **18**. Selected absorptions (cm^{-1}): 3000-2850 (C-H), 1450 (C-F).

Unfortunately, both crude material and crystalline samples of **18** were temperature sensitive, with removal from the –40°C freezer resulting in decomposition into a purple material after *ca.* 24 hours. This is likely the cause of why satisfactory elemental analysis could not be obtained for this compound, a representative result being (%), found (calculated) for $C_{21}H_{45}DyB_2O$: C 51.98 (50.62); H 4.36 (3.66).

This temperature sensitivity has previously been observed in heavy lanthanide metallocene complexes of the type $[Ln(\eta^5\text{-}Cp^{ttt})_2]^+[B(C_6F_5)_4]^-$ (Ln = Sm, Gd, Tb, Ho, Er, Tm, Lu),[147,148]

however curiously not in the case of the dysprosium derivative.[22,23] Moreover, similar sensitivity has been observed across the lighter lanthanides of the type [Ln(η^5-Cp^{ttt})$_2${$B(C_6F_5)_4$}] (Ln = La, Ce, Pr, Nd) which form contact ion pairs through one *meta*-fluorine interaction.[149] In both cases, magnetic measurements were obtained by keeping the sample below −25 °C, however this was not feasible for magnetic measurements on **18** as our measurements are performed through collaboration with Prof. Jinkui Tang at the Changchun Institute of Applied Chemistry (China), and the sample would have decomposed prior to arrival.

3.1.5. Conclusions on cyclopentadienyl sandwich SMMs

In this section, the synthesis of the heteroleptic cyclopentadienyl sandwich complexes [Ln(η^5-Cp^{ttt})(η^5-Cp*)(κ^2-BH$_4$)] (Ln = Y (**16**), Dy (**17**)) and the contact ion pair metallocene [Dy(η^5-Cp^{ttt})(η^5-Cp*){B(C$_6$F$_5$)$_4$}] (**18**) was described. The combination of Cp^{ttt} and Cp* ligands were chosen in the hopes that the reduced steric bulk could result in a strengthening of the axial crystal ligand field around Dy^{3+} when compared to other bulkier metallocene [Dy(η^5-Cp^R)$_2$]$^+$ derivatives.

The static magnetic properties of **17** were investigated by SQUID magnetometry, with the complex showing typical Dy^{3+} traits in a static field with a $^6H_{15/2}$ ground multiplet. Dynamic measurements revealed SMM properties in zero DC field, and fitting the relaxation data with Orbach, Raman and QTM parameters results in a U_{eff} = 36(2) cm^{-1}. The strong influence of low temperature relaxation via QTM is evidenced by closed hysteresis loops at 1.9 K. Despite the relatively small anisotropy barrier, comparisons of **17** with the Cp^{iPr5} derivative [Dy(η^5-C$_5$^{i}Pr$_5$)(η^5-Cp*)(κ^2-BH$_4$)], *i.e.* the precursor complex to the current record SMM, reveal an improvement upon the reported U_{eff} = 7(1) cm^{-1}. Complex **17** features slightly shorter Dy-Cp centroid distances and hence a marginally stronger axial crystal field around the Dy^{3+} ion, however the axiality of **17** is not as large, with a decreased Cp$_c$-Dy-Cp$_c$ bending angle of *ca.* 5°. This is indicative that the strength of the axial crystal ligand field around Dy^{3+} ions plays a more important role when compared to the axiality of a system.

Attempts to abstract the borohydride ligand from **17** resulted in the formation of the contact ion pair complex **18**, which features two Dy–F interactions to the [B(C$_6$F$_5$)$_4$]$^-$ anion. Unfortunately, temperature sensitivity of **18** precluded magnetic characterization and comparisons of SMM properties with **17**.

3.2. Cyclobutadienyl Rare-Earth Sandwich Complexes

Some of the work described in this section is currently under peer review for publication:
J. P. Durrant, B. M. Day, J. Tang, A. Mansikkamäki and R. A. Layfield, *Manuscript submitted.*

3.2.1. Background

Building upon the findings described in the previous chapter, namely that pristine cyclobutadienyl ligands can provide a stronger axial crystal field for Dy^{3+} ions when compared to cyclopentadienyl ligands, this section describes progress towards the synthesis of a heteroleptic dysprosium sandwich complex of the type [Dy(Cb)(Cp^R)].

This complex has been chosen over the hypothetical compound of the type $[Dy(Cb)_2]^-$, which has proven difficult to synthetically access due to the various types of ligand activation we have previously observed (described in section 1.2.8.). A delicate balance exists between finding a cyclopentadienyl ligand with sufficient bulk to stabilise the electrophilic lanthanide centres and prevent additional coordination of equatorial ligands, without the steric bulk being too large to prevent the heteroleptic sandwich complexes from forming. Moreover, the overall neutral charge of a [Dy(Cb)(Cp^R)] complex would be more desirable for potential device applications, as it may be able to be purified and deposited onto surfaces by sublimation.

Therefore, this section describes the synthesis, characterization, as well as theoretical calculations of the first heteroleptic rare-earth cyclobutadienyl sandwich complexes utilising additional cyclopentadienyl and pentalene ligands. Investigations into their magnetic properties revealed that the crystal field around Dy^{3+} ions are dominated by the cyclobutadienyl ligands, further advancing our understanding of cyclobutadienyl lanthanide SMMs and providing a platform for a new generation of Cb-ligated SMMs that could potentially surpass the current state-of-the-art.

3.2.2. *Synthesis and characterization of [Ln{η^4-$C_4(SiMe_3)_4$}(η^5-Cp*)(κ^2-BH_4)Na(THF)$_5$] (Ln = Y (**19**), Dy (**20**)) and [Na(15-c-5)(THF)$_n$]$^+$[Ln{η^4-$C_4(SiMe_3)_4$}(η^5-Cp*)(κ^2-BH_4)]$^-$ (Ln = Y, n = 1 (**21**), Dy, n = 2 (**22**))*

Initial studies focused on the reactivity of the Cp^{ttt} half-sandwich complexes **1** and **2** with one equivalent of K_2Cb (**9**) (Scheme 22). In both cases, a sandwich complex was not formed; instead, ligand exchange and the formation of the Cb half-sandwich complexes **14** and **15** was observed. From this, we can infer two important observations: firstly, the dianionic Cb ligand displacing the Cp^{ttt} ligand at room temperature is indicative of the stronger electronic interaction between Cb^{2-} and Ln^{3+}. Secondly, the Cp^{ttt} ligand is too bulky for a complex of the type [Dy(η^4-Cb)(η^5-Cp^{ttt})] to form. We can, therefore, use this information to target Cp^R systems with reduced steric hinderance.

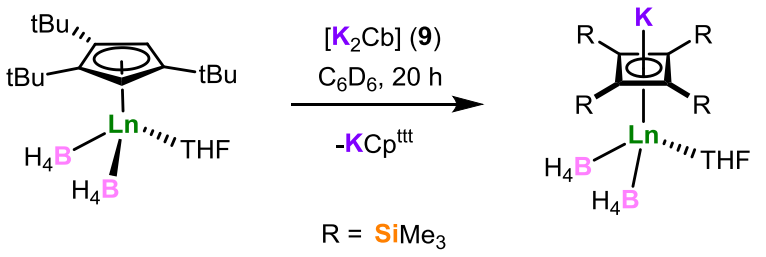

Scheme 22. Reaction between **1** and **2** and K_2Cb (**9**).

Thus, the moderately bulky Cp* ligand was used instead, and the synthesis of the heteroleptic sandwich complexes [Ln{η^4-$C_4(SiMe_3)_4$}(η^5-Cp*)(κ^2-BH_4)Na(THF)$_5$] (Ln = Y (**19**), Dy (**20**)) was achieved by the dropwise addition of one equivalent of NaCp* in THF to a yellow solution of **12**, or an orange solution of **13** in THF, respectively (Scheme 23). Upon addition, an instantaneous red (Ln = Y) or dark red (Ln = Dy) solution formed, which was left to stir for 20 hours to give a colourless precipitate. After subsequent work-up, orange crystals of **19** and **20** were obtained by layering hexane on a saturated THF solution and storing at −40 °C for 3 days in isolated yields of 50 and 53 %, respectively.

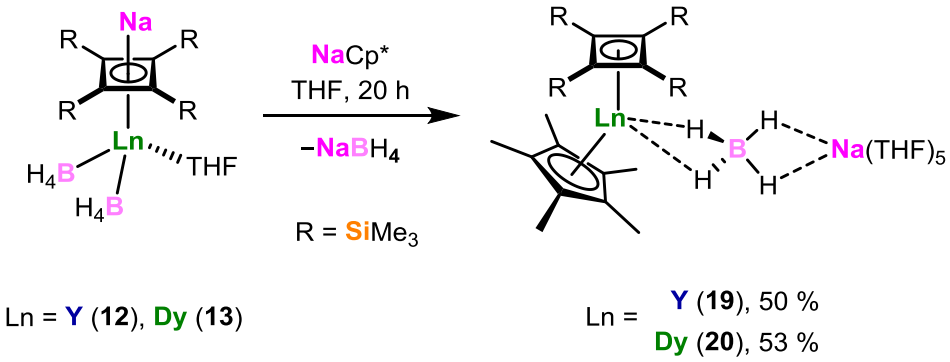

Scheme 23. Synthesis of **19** and **20**.

These crystals are temperature sensitive and re-dissolve quickly upon removal from the freezer. However, by pre-cooling a microscope slide and fomblin oil at *ca.* −40 °C, it was possible to mount crystals on the diffractometer and determine the structures of **19** and **20**. These complexes are isostructural, and feature a bent metallocene unit with an η^4-coordination of the Cb ligand and η^5-coordination of the Cp* ligand, with a bridging κ^2-borohydride ligand to a sodium atom that is capped by five THF ligands (Figure 86). In both **19** and **20**, the complexes display a disordered C_4 ring that is split across two positions (51:49 for **19**, 55:45 for **20**). In both complexes, the Ln–Cb distances are significantly shorter than the Ln–Cp distances. For the highest occupancy component of **20**, the Dy–C distances range from 2.481(11)-2.517(13) Å for the Cb ligand, and 2.656(6)-2.691(5) Å for the Cp* ligand. The Dy-Cb centroid distance therefore lies *ca.* 0.11 Å closer than the analogous Dy-Cp* distance, *i.e.* 2.2761(2) *vs.* 2.3859(3) Å, respectively, creating a Cb_c-Dy-Cp_c bending angle of 144.449(15)°. Two of the $SiMe_3$ groups (Si2 and Si4), reside just below and above the plane of the C4 ring by −0.16(6) and 0.15(8) Å, respectively, whilst the other two groups (Si1 and Si3), reside significantly above the plane by 1.02(3) and 0.69(3) Å, respectively. This demonstrates that the $SiMe_3$ groups possess a relatively high degree of flexibility.

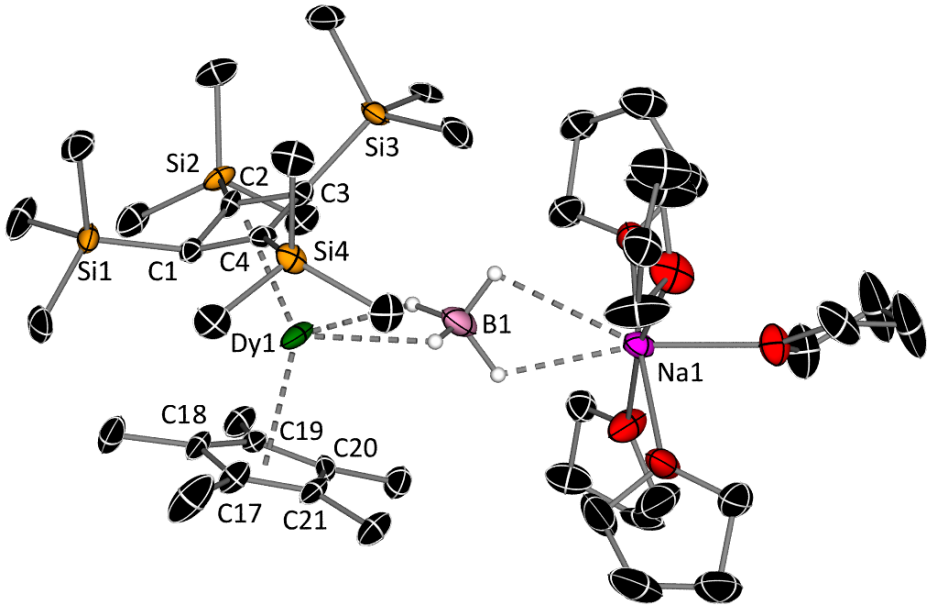

Figure 86. Molecular structure of [Dy{η^4-$C_4(SiMe_3)_4$}(η^5-Cp*)(κ^2-BH_4)Na$(THF)_5$] (**20**). Thermal ellipsoids are set to 50 % probability and for clarity, only the hydrogen atoms bound to boron are shown. Selected bond distances (Å) and angles (°) for the highest occupancy component of **20**: C1-C2 1.486(12), C2-C3 1.471(12), C3-C4 1.469(12), C1-C4 1.504(11), C17-C18 1.431(8), C18-C19 1.402(7), C19-C20 1.422(7), C20-C21 1.408(7), C17-C21 1.407(8), C1-Si1 1.819(13), C2-Si2 1.857(10), C3-Si3 1.857(14), C4-Si4 1.856(9), Dy1-Cb_{cent} 2.2761(2), Dy1-Cp_{cent} 2.3859(3), Dy1-B1 2.795(8), Cb_{cent}-Dy1-Cp_{cent} 144.449(15).

The ^{1}H NMR spectrum of the yttrium version **19** in D_8-THF revealed the presence of two isomers, with the major and minor components arising in a ratio of *ca.* 3:1 (Figure 87). The expected signals for the Cp* and $SiMe_3$ groups can be seen at 2.09 (s, CH_3, 15H) and 0.08 ppm (s, $SiMe_3$, 36H), with the minor component displaying signals for the same groups at 2.03 (s, CH_3, 5H) and 0.13 (s, $SiMe_3$, 13H), respectively. Signals for both isomers corresponding to THF at 3.61 and 1.77 ppm are overlapped and integrate to 11H each, which indicates that the five THF ligands observed in the solid-state do not remain coordinated in solution. Broad signals corresponding to the borohydride ligand could be seen as a 1:1:1:1 quartet in the range of 0.51 to −0.10 ppm, however these could not be accurately integrated due to overlap with the $SiMe_3$ signals at 0.13 and 0.08 ppm.

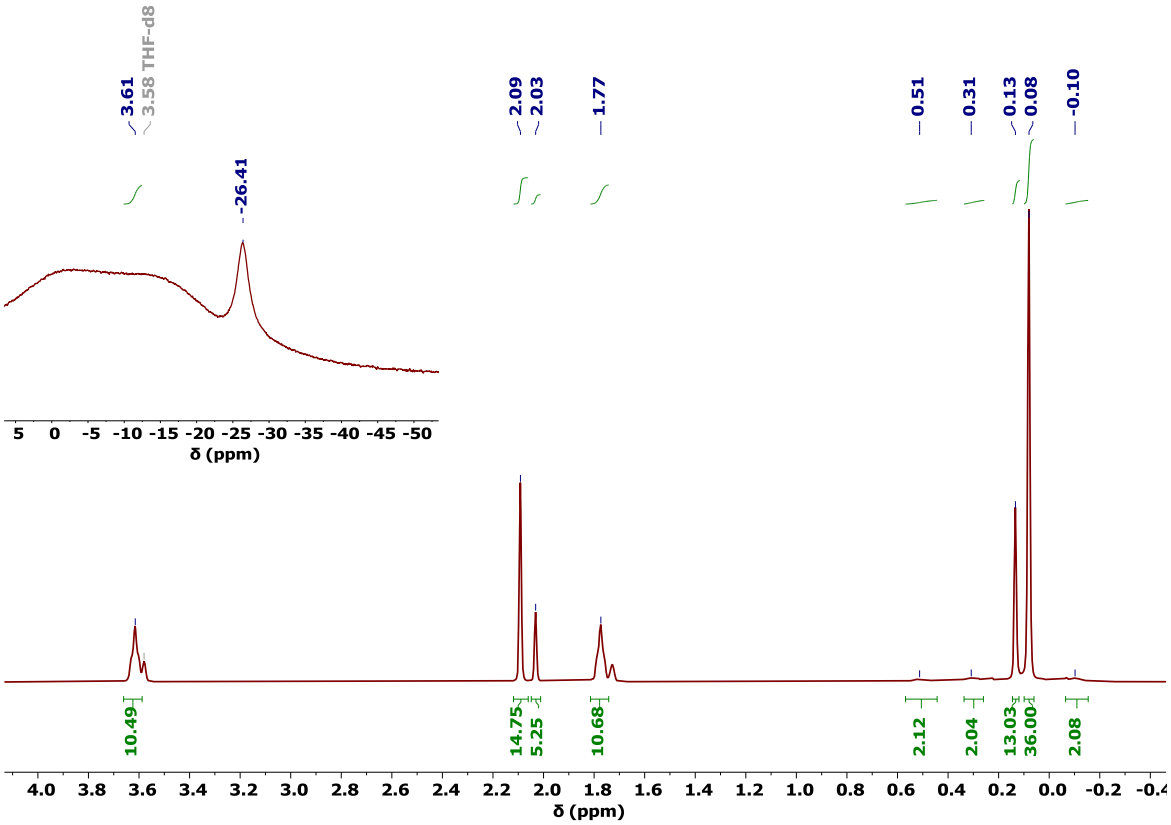

Figure 87. ^{1}H NMR spectrum of **19** in D_8-THF. Inset: $^{11}B\{^{1}H\}$ NMR spectrum of **19**.

The $^{13}C\{^{1}H\}$ NMR spectrum displays the expected signals corresponding to the two isomers observed in the ^{1}H NMR, which were interpreted as such: Major: 128.60 ($\underline{C}_4$ ring), 116.64 ($\underline{C}_5$ ring), 12.94 ($\underline{Me}_5$) and 4.86 ppm ($Si\underline{Me}_3$). Minor: 122.58 ($\underline{C}_4$ ring), 105.55 ($\underline{C}_5$ ring), 11.70 ($\underline{Me}_5$) and 5.31 ppm ($Si\underline{Me}_3$) (Figure S52). The $^{11}B\{^{1}H\}$ (Figure 87 inset) and ^{11}B NMR spectra display single broad peaks at −26.41 (s, FWHM = 205 Hz, BH_4) and −26.44 ppm (s, FWHM = 325 Hz, BH_4), respectively (Figures S53, S54), with the $^{29}Si\{^{1}H\}$ and $^{23}Na\{^{1}H\}$ NMR spectra also displaying single peaks at −19.45 and −5.76 ppm (FWHM = 90 Hz), respectively (Figures S55, S56).

The $SiMe_3$ signals for the minor component in the ^{1}H and $^{13}C\{^{1}H\}$ NMR spectra are very similar to that of the precursor half-sandwich **12**, however the $^{11}B\{^{1}H\}$, ^{11}B NMR, $^{29}Si\{^{1}H\}$ and ^{23}Na signals are all significantly shifted, indicating that these signals are most likely not caused by unreacted starting material. Due to the broadness of the $^{11}B\{^{1}H\}$, ^{11}B NMR and $^{23}Na\{^{1}H\}$ signals, this suggests that the two isomers may be undergoing exchange in solution on the NMR timescale, resulting in conformations with slightly different environments around the BH_4 and Na atoms.

The FTIR spectra of compounds **19** and **20** are similar and show the expected saturated C–H stretches in the range 3000-2850 cm^{-1}. Absorptions that correspond to a bridging bidentate B–H stretching mode can be observed in the range 2250-2100 cm^{-1}, however, very slight absorptions can also be observed at 2400 cm^{-1}, which could indicate the presence of a weak terminal B–H stretch (Figure 88).[126] Elemental analysis on both **19** and **20** returned lower carbon values than expected, even after taking into account the loss of all THF molecules coordinated to the sodium atom, with representative results being % found (calculated) for **19** $C_{26}H_{55}YBSi_4Na$: C 48.65 (51.81); H 9.64 (9.20), and **20** $C_{26}H_{55}DyBSi_4Na$: C 43.95 (46.17); H 8.69 (8.20). A possible explanation for these lower values could be due to the air-sensitive nature of the organometallic complexes, which may have decomposed prior to analysis, or incomplete combustion due to the formation carbides.[135]

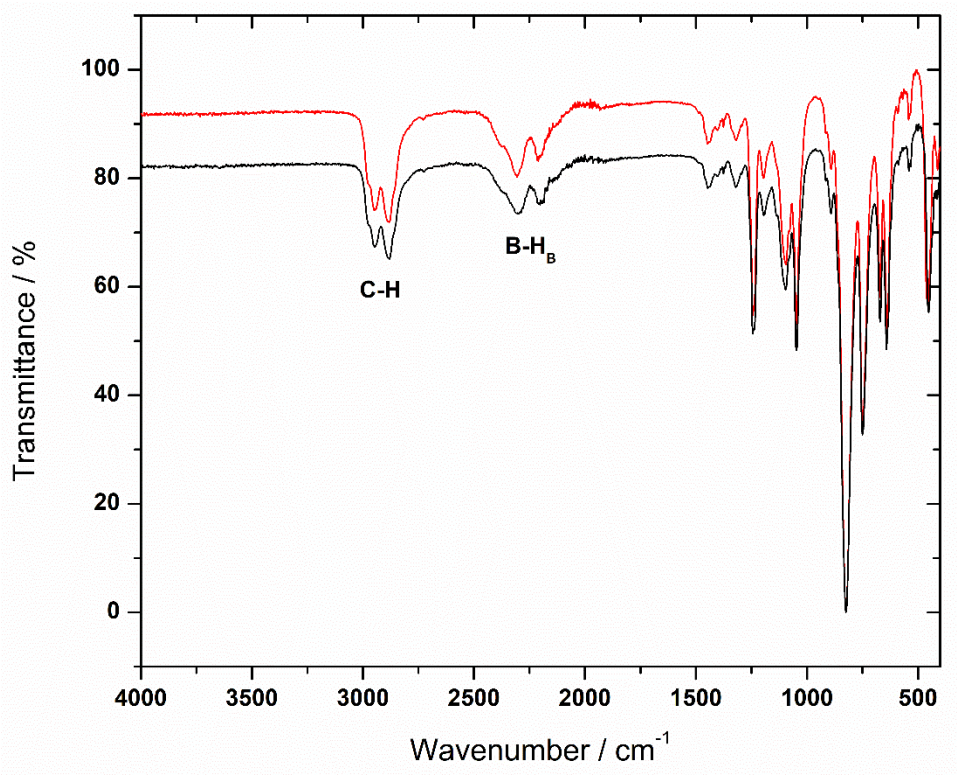

Figure 88. FTIR spectra of **19** (red line) and **20** (black line). Selected absorptions (cm^{-1}): 3000-2850 (C–H), 2250-2100 ($B–H_B$).

Due to the difficulty in isolating pure compounds of **19** and **20**, it was thought that the addition of a suitably sized crown ether could encapsulate the sodium atom and result in a single, more stable product. Thus, the synthesis of the separated ion pair sandwich complexes $[Na(15\text{-}c\text{-}5)(THF)_n]^+[Ln\{\eta^4\text{-}C_4(SiMe_3)_4\}(\eta^5\text{-}Cp^*)(\kappa^2\text{-}BH_4)]^-$ (Ln = Y, *n* = 1 (**21**), Dy, *n*

= 2 (**22**)) was achieved by the addition of a slight excess of 15-crown-5 to **19** or **20** in THF, respectively (Scheme 24). Red crystals of **21** and **22** were obtained by layering hexane on a saturated THF solution and storing at −40 °C for 3 days in isolated yields of 47 and 38 %, respectively.

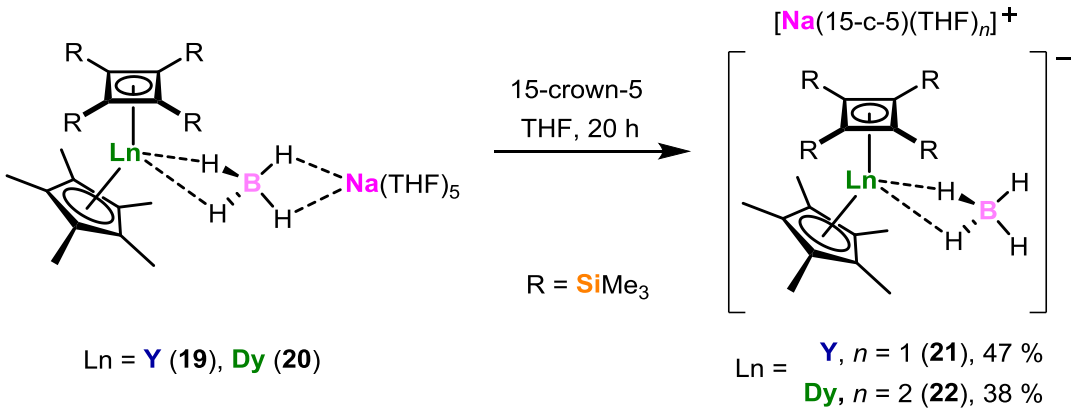

Scheme 24. Synthesis of **21** and **22**.

Compounds **21** and **22** contain isostructural complex anions, which feature η^4- and η^5-coordination modes of the C_4 and C_5 rings, respectively, with an equatorial κ^2-borohydride ligand coordinated to the metal centre, reminiscent to their precursors (Figure 89). In both compounds, the separated sodium cations are encapsulated by 15-crown-5, which are additionally ligated by one or two molecules of THF for **21** and **22**, respectively. The structural parameters of the anionic components are comparable to that of their precursors, however there is no longer any disorder of the C_4 ring. For **22**, the Dy–C bond distances range from 2.429(3)-2.586(3) and 2.662(3)-2.710(4) Å, with centroid distances of 2.2794(18) and 2.3983(15) Å for the Dy-Cb and Dy-Cp ligands, respectively. This results in a Cb_c-Dy-Cp_c bending angle of 147.57(6)°, which has slightly increased by *ca.* 3° compared to the precursor **20**. The $SiMe_3$ groups in **22** show a significant variation from the plane of the C_4 ring, with Si1 and Si4 residing above the plane by 0.481(7) and 0.349(7) Å, respectively, and Si2 and Si3 residing above and below the plane by 1.194(6) and −0.006(7) Å, respectively.

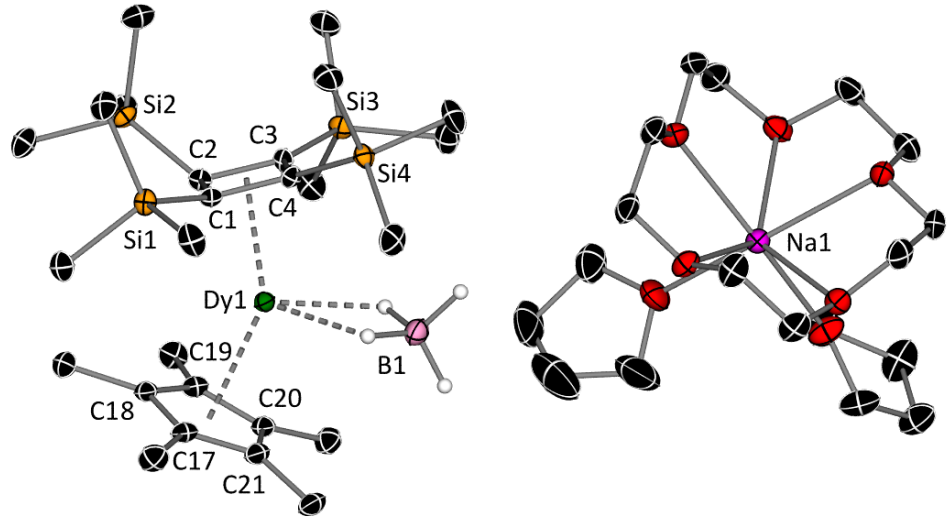

Figure 89. Molecular structure of $[Na(15\text{-}c\text{-}5)(THF)_2]^+[Dy\{\eta^4\text{-}C_4(SiMe_3)_4\}(\eta^5\text{-}Cp^*)(\kappa^2\text{-}BH_4)]^-$ (**22**). Thermal ellipsoids are set to 50 % probability and for clarity, only the hydrogen atoms bound to boron are shown. Selected bond distances (Å) and angles (°) for **22**: C1-C2 1.516(4), C2-C3 1.504(4), C3-C4 1.451(4), C1-C4 1.458(5), C17-C18 1.417(5), C18-C19 1.418(5), C19-C20 1.421(5), C20-C21 1.421(5), C17-C21 1.424(5), C1-Si1 1.829(3), C2-Si2 1.843(3), C3-Si3 1.848(3), C4-Si4 1.857(3), Dy1-Cb_{cent} 2.2794(18), Dy1-Cp_{cent} 2.3983(15), Dy1-B1 2.737(5), Cb_{cent}-Dy1-Cp_{cent} 147.57(6).

In a similar fashion to the precursor **19**, NMR spectroscopy of **21** in D_8-THF revealed the continued presence of two isomers, with the major and minor components arising in the ratio of *ca.* 1:0.7. The ^1H NMR can be seen in Figure 90, however due to the similarity with the precursor, the assignments for all NMR spectra of **21** can be found in the experimental section (Figures S57-S61). As there are still two sets of signals in very similar environments, a tentative explanation could be the borohydride ligand switching between κ^2- and κ^3-coordination modes in solution, or a change in environment around the BH_4 and Na atoms, *i.e.* a contact ion pair *vs.* separated ion pairs. To try and elucidate this behaviour, the ^1H, $^1H\{^{11}B\}$, $^{11}B\{^1H\}$ and ^{11}B NMR spectra of compound **21** were studied at variable temperatures from +60 to −60 °C. The results of these experiments revealed some complex solution-state behaviour, which require in depth variable temperature correlation studies in order to further explain. Therefore, these spectra can be seen in the future work section (5.2. Figures 139-141) and the experimental section (6.3. Figure S62).

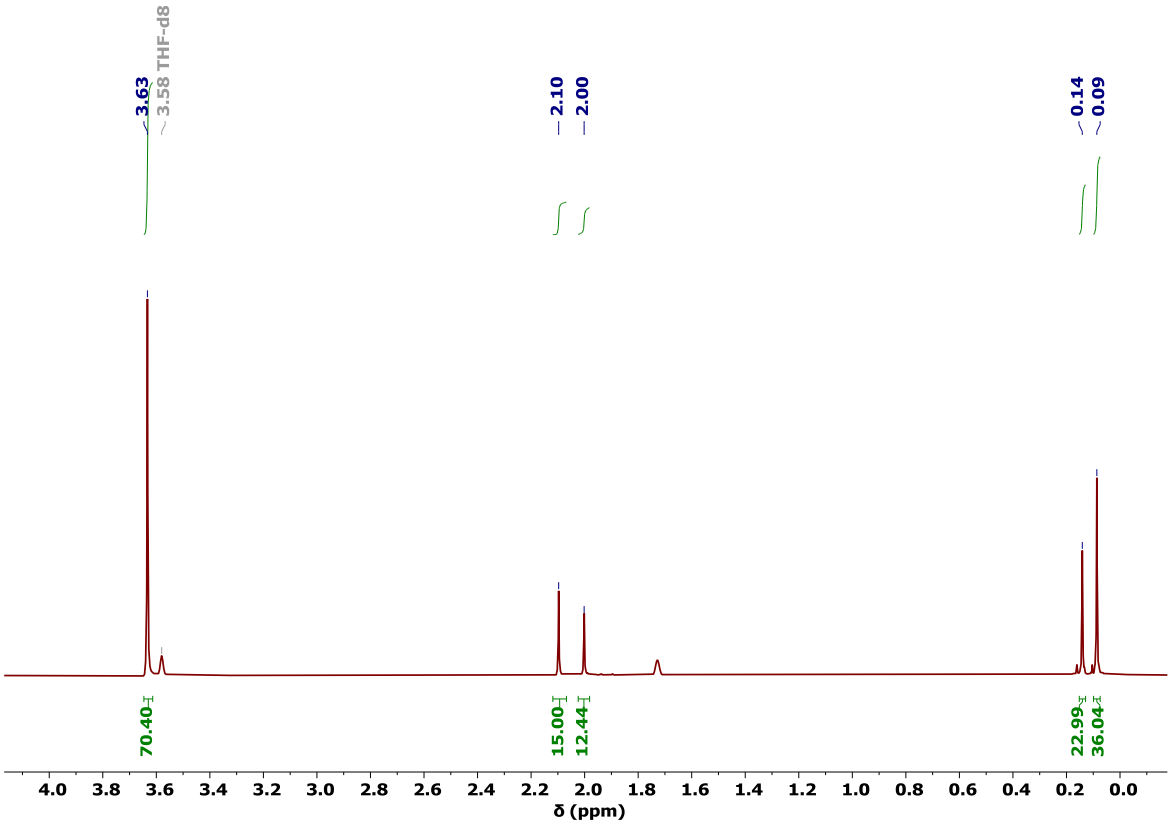

Figure 90. ^{1}H NMR spectrum of **21** in D_8-THF.

The FTIR spectra of compounds **21** and **22** show B–H absorptions corresponding to a bidentate borohydride coordination mode, with absorptions in the range 2450-2300 and 2150-2000 cm^{-1}, for the terminal and bridging modes, respectively.[126] The expected saturated C–H absorptions can additionally be seen in the range of 3000-2850 cm^{-1} (Figure 91). Elemental analyses on compounds **21** and **22** returned lower carbon and hydrogen values than expected, even after the potential loss of THF from the separated cations, perhaps for the same reasons described for the precursor complexes **19** and **20**. Representative results being % found (calculated) for **21** $C_{40}H_{83}YBNaSi_4O_6$: C 50.64 (53.67); H 9.17 (9.35), for **21**(−THF) $C_{36}H_{75}YBNaSi_4O_5$: C 50.64 (52.54); H 9.17 (9.19), for **22** $C_{44}H_{91}DyBNaSi_4O_7$: C 47.83 (50.77); H 8.60 (8.81) and for **22**(−2 THF) $C_{36}H_{75}DyBNaSi_4O_5$: C 47.83 (48.22); H 8.60 (8.43).

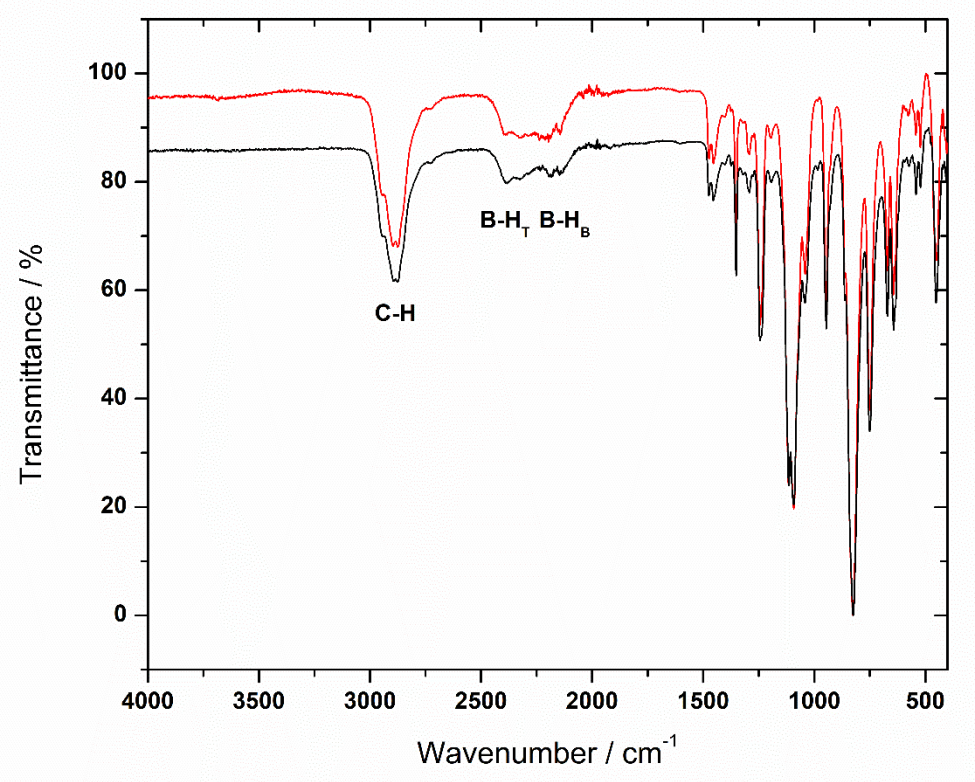

Figure 91. FTIR spectra of **21** (red line) and **22** (black line). Selected absorptions (cm^{-1}): 3000-2850 (C–H), 2400-2300 ($B–H_T$), 2150-2000 ($B–H_B$).

*3.2.3. Synthesis and characterization of [Ln{η⁴-C₄(SiMe₃)₄}(η⁵-C₅Me₄ᵗBu)(BH₄)Na(THF)₄]₄ (Ln = Y (**23**), Dy (**24**)) and [Na(15-c-5)(THF)₂]⁺[Ln{η⁴-C₄(SiMe₃)₄}(η⁵-C₅Me₄ᵗBu)(κ²-BH₄)]⁻ (Ln = Y (**25**), Dy (**26**))*

Investigations into increasing the steric bulk of the Cp* complexes **19-22** were carried out by using the Cp^{Me4tBu} ligand previously employed in the synthesis of the Cp half-sandwich complexes **3** and **4**. Thus, the synthesis of the heteroleptic sandwich complexes [Ln{η^4-$C_4(SiMe_3)_4$}(η^5-$C_5Me_4{}^tBu$)(BH_4)Na$(THF)_4]_4$ (Ln = Y (**23**), Dy (**24**)) was achieved by the dropwise addition of $NaCp^{Me4tBu}$ in THF to a yellow solution of **12**, or an orange solution of **13** in THF, respectively (Scheme 25). After subsequent work up, orange block-like crystals of **23** and **24** were obtained by layering hexane on a saturated THF solution and storing at −40 °C for 3 days. Unfortunately, in a similar situation to the Cp* analogues **19** and **20**, these crystals were extremely temperature sensitive and would immediately re-dissolve upon removal from the freezer. However, yields of 47 and 50 % were obtained for **19** and **20**, respectively, by drying the re-dissolved solutions under dynamic vacuum.

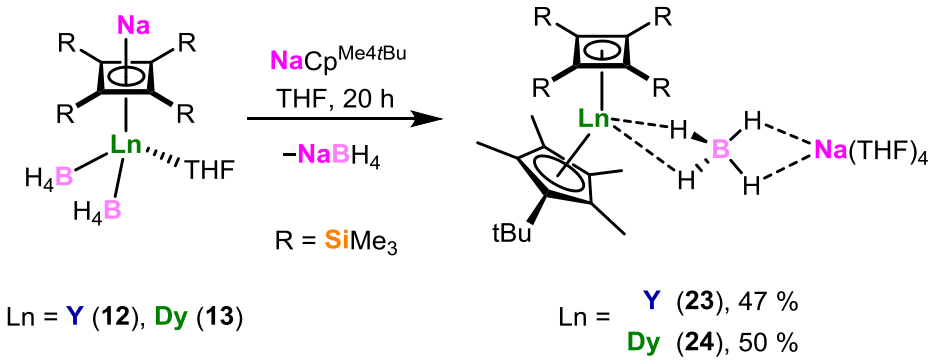

Scheme 25. Synthesis of **23** and **24**.

By pre-cooling a microscope slide and fomblin oil to *ca.* −40 °C, it was possible to mount single crystals of **23** and **24** on an X-ray diffractometer. However, these crystals subsequently produced extremely weak high-angle diffraction, preventing the collection of publishable-quality data. Despite the weak diffraction, the atom connectivity could be established, revealing that the asymmetic unit in the solid state structures of **23** and **24** feature four crystallographically unique $[Ln\{\eta^4\text{-}C_4(SiMe_3)_4\}(\eta^5\text{-}C_5Me_4{}^tBu)(BH_4)Na(THF)_4]$ molecules (Figures 92, 93).

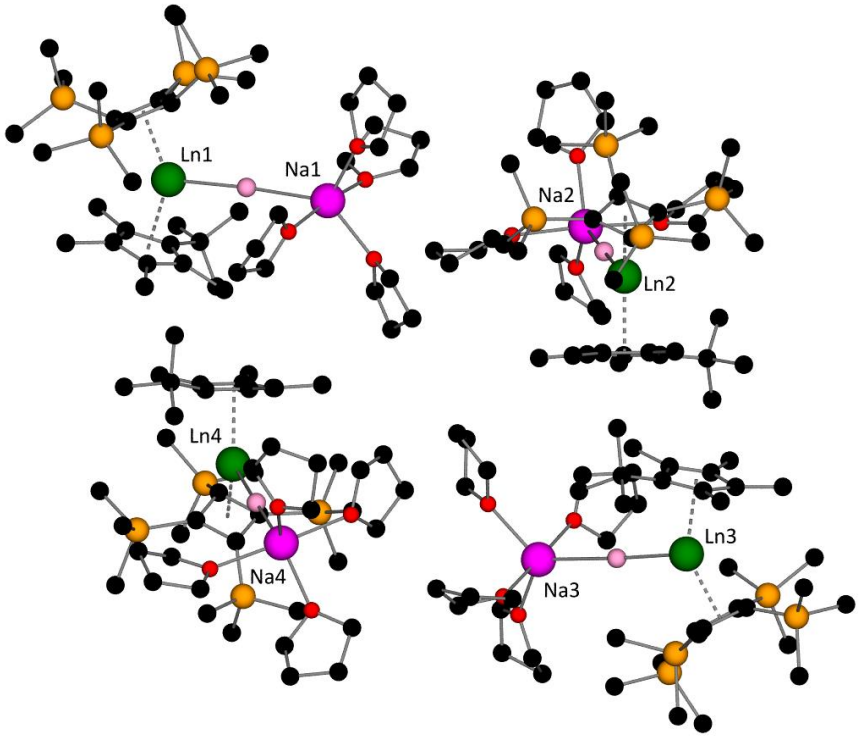

Figure 92. A ball and stick representation of the asymmetric unit of $[Ln\{\eta^4\text{-}C_4(SiMe_3)_4\}(\eta^5\text{-}C_5Me_4{}^tBu)(BH_4)Na(THF)_4]_4$ (Ln = Y (**23**), Dy (**24**)) for connectivity. Hydrogen atoms have been omitted for clarity.

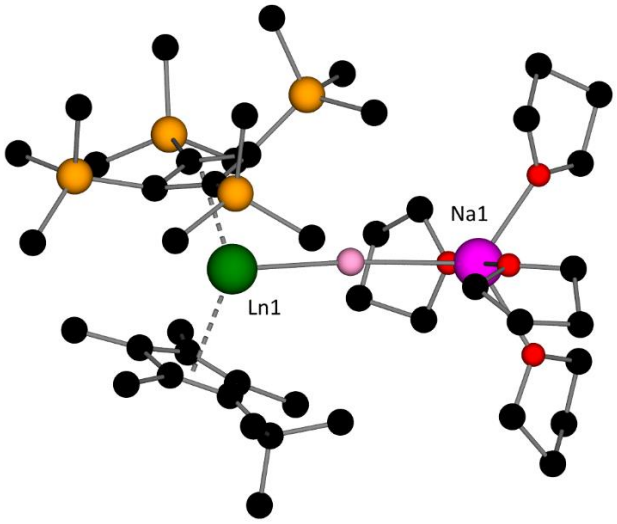

Figure 93. A ball and stick representation of a molecule within the asymmetric unit of [Ln{η^4-$C_4(SiMe_3)_4$}(η^5-$C_5Me_4{}^tBu$)(BH_4)$Na(THF)_4$]$_4$ (Ln = Y (**23**), Dy (**24**)) for connectivity. Hydrogen atoms have been omitted for clarity.

As with compound **19**, ^{1}H NMR spectroscopy of **23** in D_8-THF revealed the presence of two isomers, with the major / minor components arising in a ratio of *ca.* 7:1 (Figure 94). The ^{1}H NMR spectrum displays signals for the major component that were interpreted as follows: two singlets at 2.42 and 2.13 ppm both integrating to 6H corresponding to the two methyl groups on the C_5 ring, a singlet at 1.27 ppm corresponding to the ^{t}Bu group on the C_5 ring, and a singlet at 0.10 ppm corresponding to the $SiMe_3$ groups of the C_4 ring. Signals for the minor component corresponding to the same groups are observed at 2.20 (s, CH_3, 0.9H), 1.99 (s, CH_3, 0.9H), 1.36 (s, ^{t}Bu, 1.3H) and 0.14 ppm (s, $SiMe_3$, 2.5H). Signals for both isomers corresponding to THF ligands at 3.62 and 1.77 ppm are overlapped and integrate to 5H each, which indicates that the four THF ligands are not retained in solution. Signals corresponding to the borohydride ligand in the range of 0.8-0.0 ppm could be seen by significantly increasing the intensity, however these could not be accurately integrated.

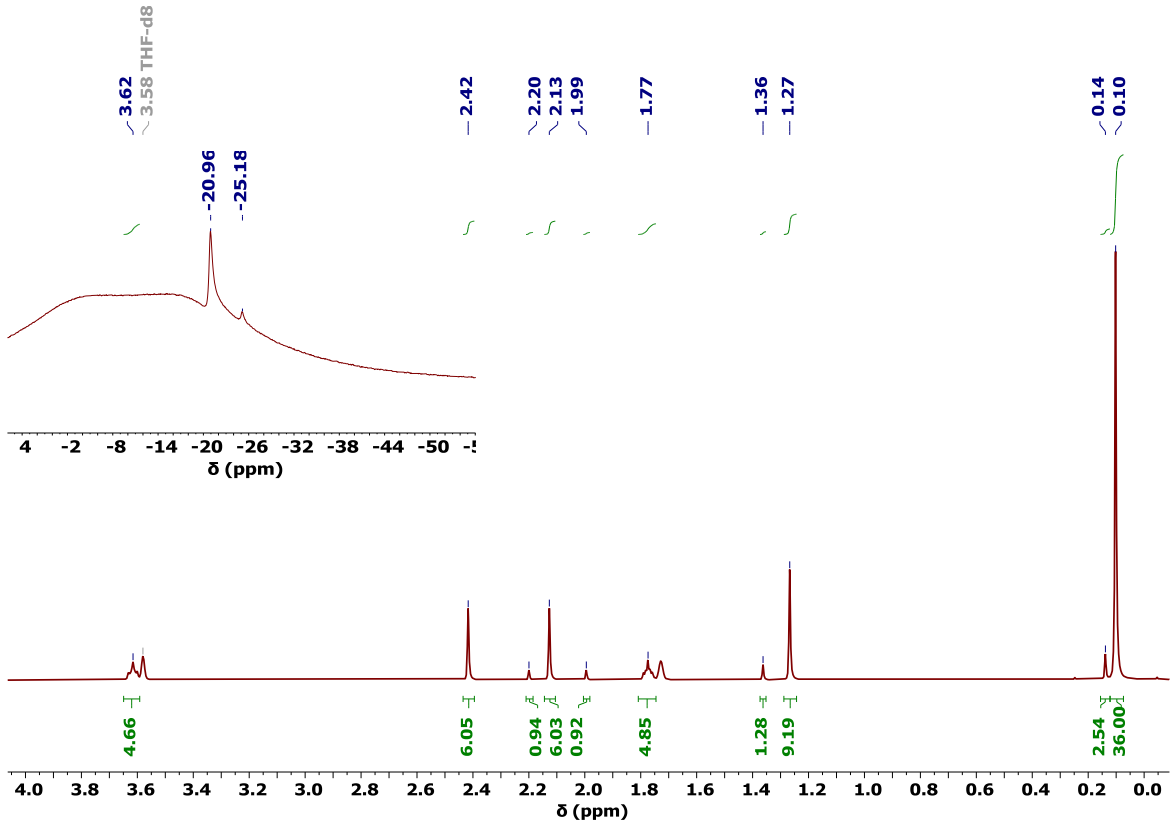

Figure 94. ^{1}H NMR spectrum of **23** in D_8-THF. Inset: $^{11}B\{^{1}H\}$ NMR spectrum of **23**.

In the $^{13}C\{^{1}H\}$ NMR spectrum of **23**, only signals corresponding to the major component could be observed, however, signals for the C_5 ring carbon attached to the ^{t}Bu group and the quaternary carbon of the ^{t}Bu group were too weak to distinguish from the baseline. The signals were interpreted as such: 129.46 ($\underline{C}_4$ ring), 117.79 ($\underline{C}_5$ ring), 116.56 ($\underline{C}_5$ ring), 68.38 ($\underline{C}H_2O$), 33.15 ($C(\underline{C}H_3)_3$), 26.54 ($\underline{C}H_2$), 17.20 ($\underline{C}H_3$), 13.41 ($\underline{C}H_3$), 5.38 ($Si\underline{Me}_3$) (Figure S63). The $^{11}B\{^{1}H\}$ NMR spectrum displays two peaks for the minor and major components at −20.96 (FWHM = 70 Hz) and −25.18 ppm (FWHM = 44 Hz), respectively (Figure 94 inset, Figure S64), which are shifted and much sharper signals in comparison to the precursor **12** (−23.00 ppm, FWHM = 276 Hz). The ^{11}B NMR spectrum displays a 1:4:6:4:1 quintet centered at −20.93 ppm ($^{1}J_{BH}$ = 81 Hz) for the major component, and a signal at −25.09 ppm for the minor component which was too weak to resolve any $^{1}J_{BH}$ coupling (Figure S65). The $^{29}Si\{^{1}H\}$ and $^{23}Na\{^{1}H\}$ NMR spectra both display singlets at −21.07 and −9.39 ppm (FWHM = 74 Hz), respectively (Figures S66, S67). In order to determine if the two observed species were undergoing exchange in solution, variable temperature ^{1}H NMR spectroscopy of **23** in D_8-THF was carried out in the temperature range of +50 to −70 °C (Figure 95). As the

temperature decreases, the signals for each species do not converge, indicative that they are not in exchange.

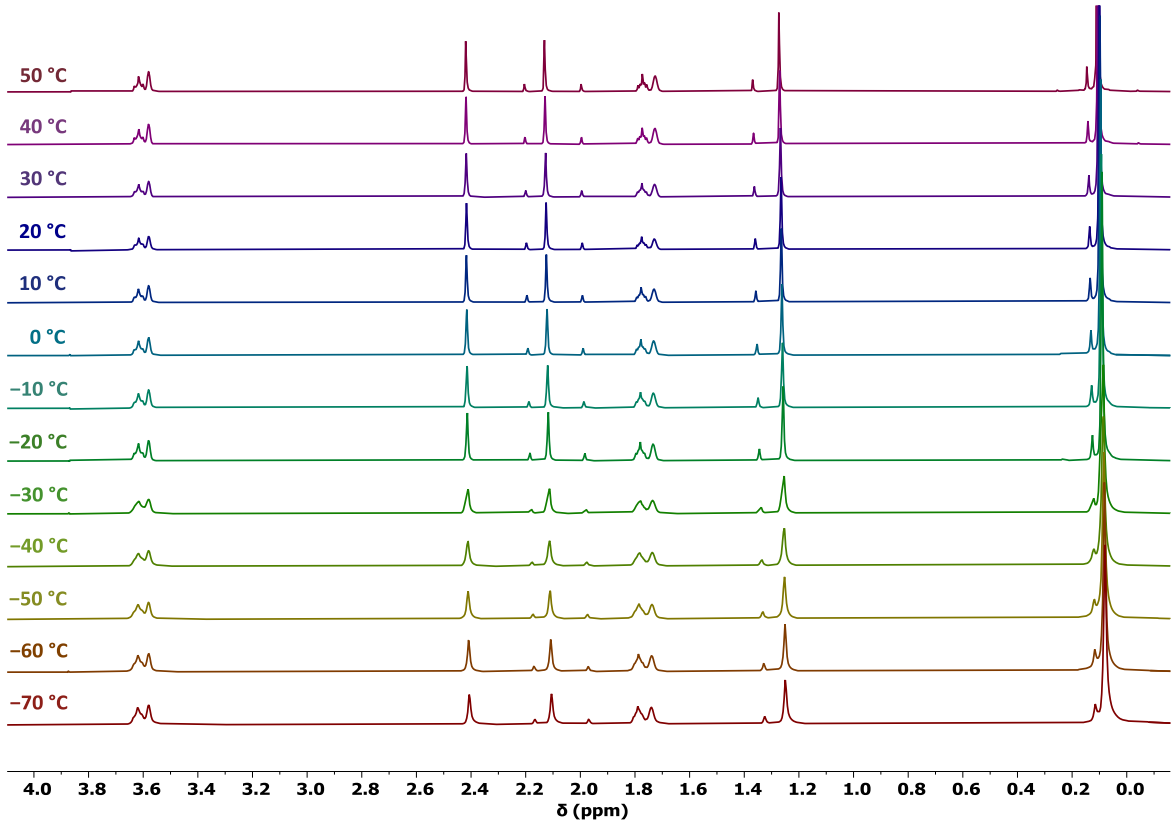

Figure 95. Variable temperature ^{1}H NMR of **23** in D_8-THF from +50 to −70 °C.

As expected, based on the structural similarity, the FTIR spectra of compounds **23** and **24** are comparable to the Cp* derivatives **19** and **20**, with the key absorptions summarized in the caption to Figure 96. In a similar situation to the Cp* derivatives, elemental analysis on **24** returned much lower carbon and hydrogen values than expected, even after taking into account the loss of all THF molecules coordinated to the sodium atom, with a representative result being % found (calculated) for **24**(−4 THF) $C_{29}H_{61}DyBSi_4Na$: C 37.42 (48.48); H 7.07 (8.56).

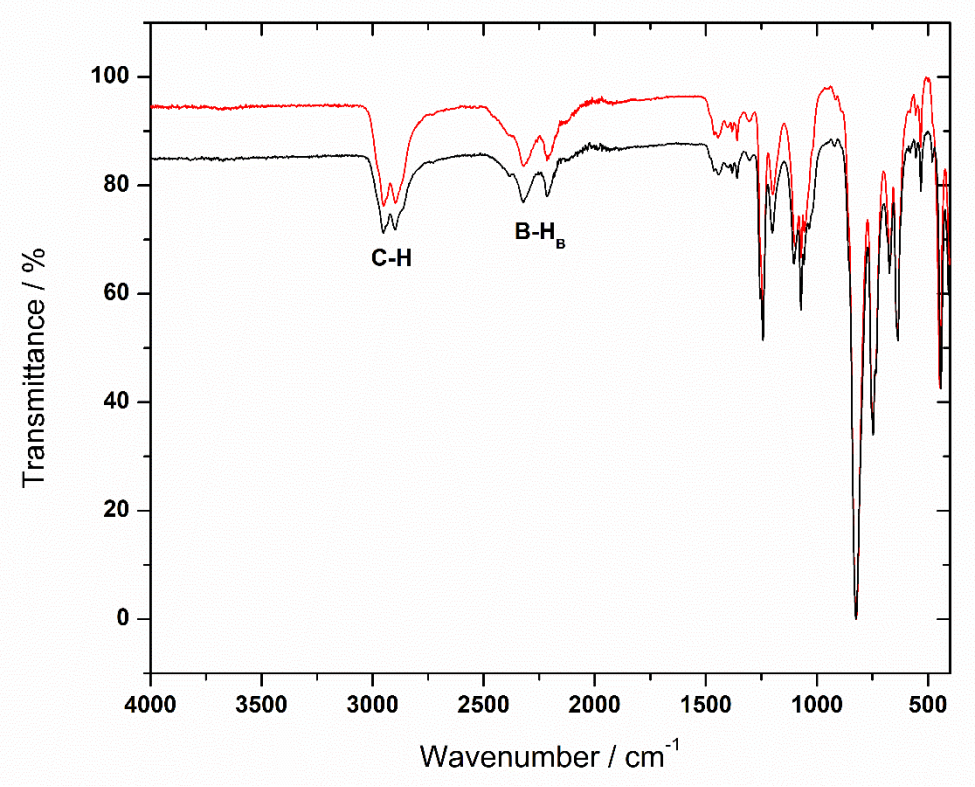

Figure 96. FTIR spectra of **23** (red line) and **24** (black line). Selected absorptions (cm^{-1}): 3000-2850 (C–H), 2300-2100 (B–H_B).

In a similar fashion to the Cp* derivatives described previously, the synthesis of the separated ion pair sandwich complexes $[Na(15\text{-}c\text{-}5)(THF)_2]^+[Ln\{\eta^4\text{-}C_4(SiMe_3)_4\}(\eta^5\text{-}C_5Me_4{}^tBu)(\kappa^2\text{-}BH_4)]^-$ (Ln = Y (**25**), Dy (**26**)) could be achieved by the addition of a slight excess of 15-crown-5 into a red solution of **23** or **24** in THF, respectively (Scheme 26). Red crystals of **25** and **26** were obtained by layering hexane on a saturated THF solution and storing at −40 °C for 3 days in isolated yields of 38 and 73 %, respectively.

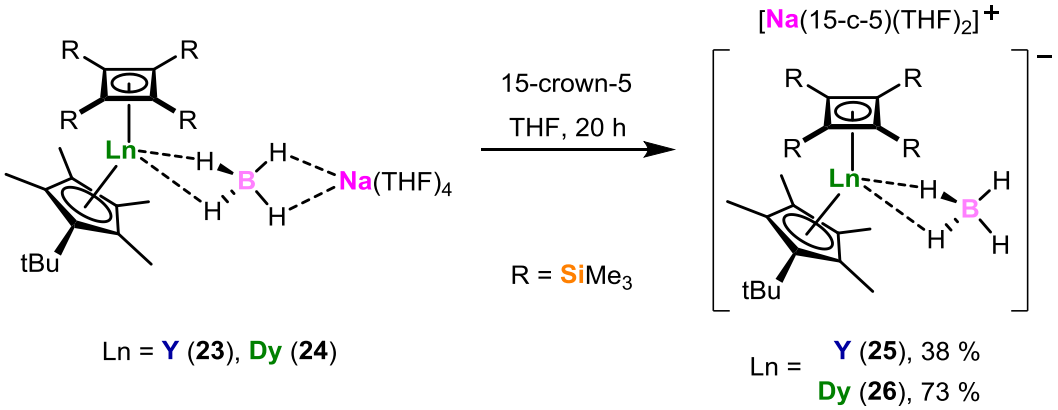

Scheme 26. Synthesis of **25** and **26**.

Compounds **25** and **26** are isostructural, with the separated anion being analogous to the Cp* derivatives **21** and **22**, and the separated sodium cation being encapsulated by 15-crown-5 and two THF ligands (Figure 97). As with the Cp* derivatives, the cyclobutadienyl ligands approach the Ln^{3+} ions more closely than the cyclopentadienyl ligands. For **26**, Dy–C bond distances range from 2.482(7)-2.523(6) and 2.667(6)-2.700(6) Å for the Cb and Cp ligands, resulting in a reduced Dy-Cb centroid distance when compared to the analogous Dy-Cp distance, *i.e.* 2.2728(4) *vs.* 2.3975(3) Å, respectively. This results in a Cb_c-Dy-Cp_c bending angle of 141.52(2)°, which is smaller than the analogous angle in the Cp* derivative **22** by *ca.* 6°, and is presumably a consequence of the increased steric bulk provided by the ^{t}Bu group in **26**. The bending of $SiMe_3$ groups for **26** out of the plane of the C_4 ring is comparable to those of the Cp* derivative **22**.

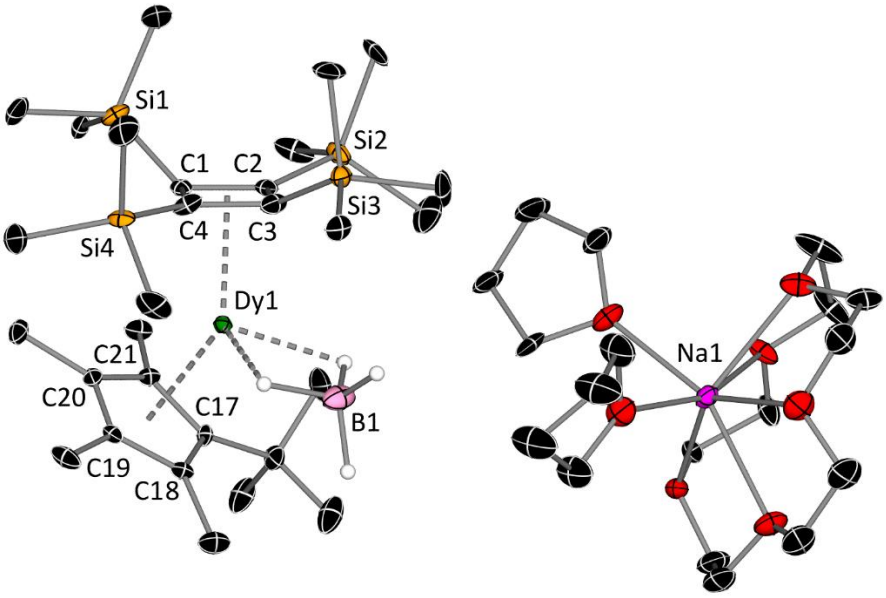

Figure 97. Molecular structure of $[Na(15\text{-}c\text{-}5)(THF)_2]^+[Dy\{\eta^4\text{-}C_4(SiMe_3)_4\}(\eta^5\text{-}C_5Me_4{}^tBu)(\kappa^2\text{-}BH_4)]^-$ (**26**). Thermal ellipsoids are set to 30 % probability and for clarity, only the hydrogen atoms bound to boron are shown. Selected bond distances (Å) and angles (°) for **26**: C1-C2 1.480(9), C2-C3 1.471(10), C3-C4 1.490(10), C1-C4 1.461(9), C17-C18 1.430(9), C18-C19 1.425(9), C19-C20 1.411(9), C20-C21 1.413(9), C17-C21 1.433(8), C1-Si1 1.854(7), C2-Si2 1.803(12), C3-Si3 1.820(7), C4-Si4 1.894(8), Dy1-Cb_{cent} 2.2728(4), Dy1-Cp_{cent} 2.3975(3), Dy1-B1 2.746(16), Cb_{cent}-Dy1-Cp_{cent} 141.52(2).

The ^{1}H NMR spectrum of the yttrium complex **25** in D_8-THF revealed the continued presence of two isomers, with the major and minor components in a ratio of *ca.* 3:1 for the Cp^{Me4tBu} groups, and a curiously higher ratio of *ca.* 1:0.8 for the $SiMe_3$ groups (Figure 98). The assignments for all NMR spectra of **25** can be found in the experimental section due to the similarity with the precursor **23** (Figures S70-S74). The $^{11}B\{^1H\}$ spectrum of **25** displays

a shift of the major peak to -24.87 ppm, with the minor peak being observed at -20.85 ppm (Figure 98 inset). Additionally, there is a shift in the $^{23}Na\{^{1}H\}$ NMR from −9.39 (FWHM = 75 Hz) in **23** to −5.82 ppm (FWHM = 362 Hz) in **25**.

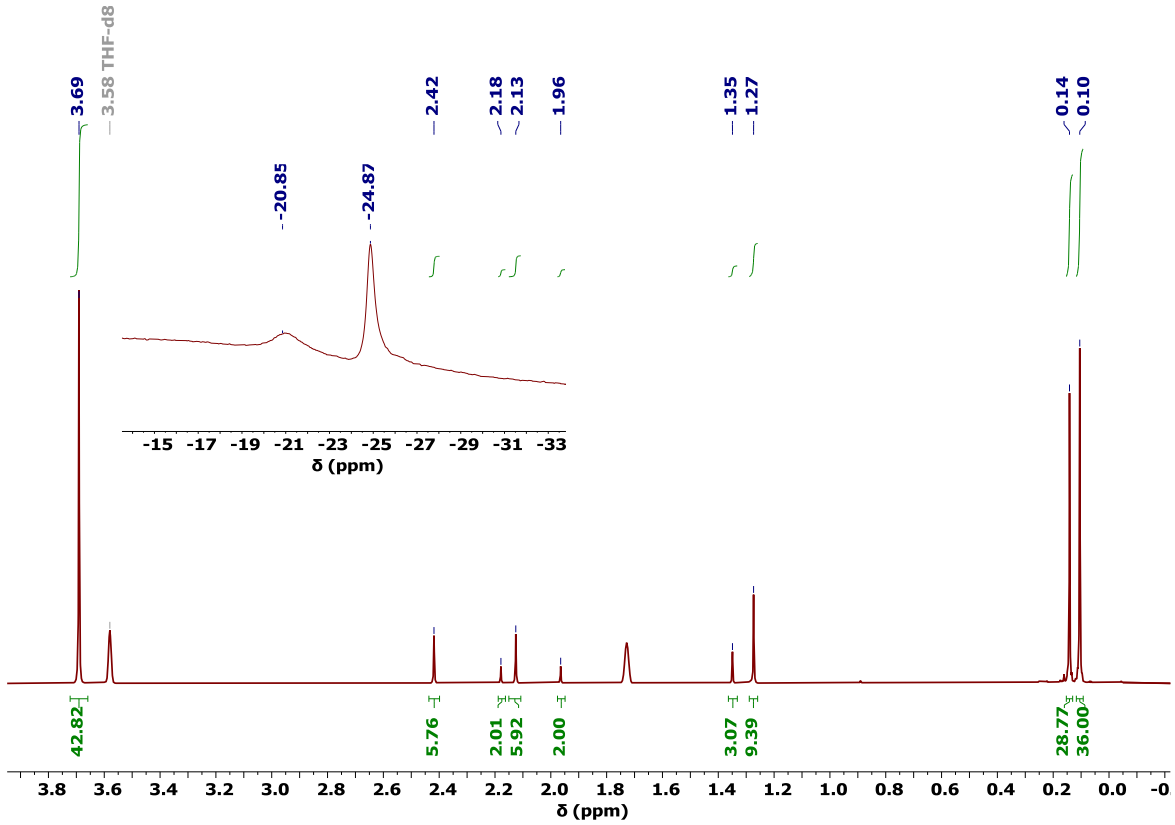

Figure 98. ^{1}H NMR spectrum of **25** in D_8-THF. Inset: $^{11}B\{^{1}H\}$ NMR spectrum of **25**.

Interestingly, if you compare the $^{11}B\{^{1}H\}$ spectrum of **25** with that of the precursor **23**, the major component in each compound seems to correlate with the opposite minor component (Figure 99). This suggests that the minor components observed in **23** and **25** could be due to a small amount of a separated cation or contact-ion pair in solution, respectively. Variable temperature ^{1}H, $^{1}H\{^{11}B\}$, $^{11}B\{^{1}H\}$ and ^{11}B NMR spectroscopy of **25** in D_8-THF in the temperature range of +30 to −60 °C revealed that in contrast to the Cp* derivative **21**, no significant shifts are observed at low temperature (Figures S75-S78).

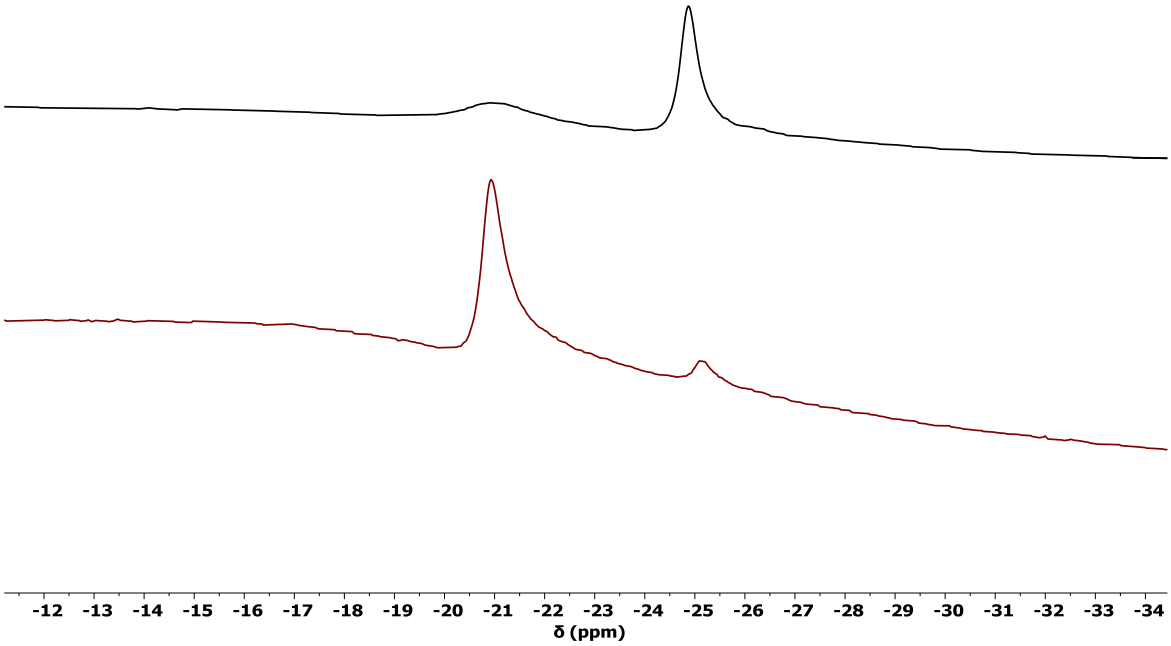

Figure 99. Comparison between the $^{11}B\{^{1}H\}$ NMR spectra of **23** (red line) and **25** (black line).

The FTIR spectra of compounds **25** and **26** are comparable to those of the Cp* derivatives **21** and **22**, with key absorptions summarized in the caption to Figure 100. Elemental analysis of **25** returned lower carbon and hydrogen values than expected, with a representative result being % found (calculated) for **25** $C_{47}H_{97}YBNaSi_4O_7$: C 50.23 (55.93); H 8.78 (9.69). However, analysis of **26** was consistent with its respective solid-state molecular structure, with % found (calculated) for **26** $C_{47}H_{97}DyBNaSi_4O_7$: C 51.53 (52.13); H 9.30 (9.03).

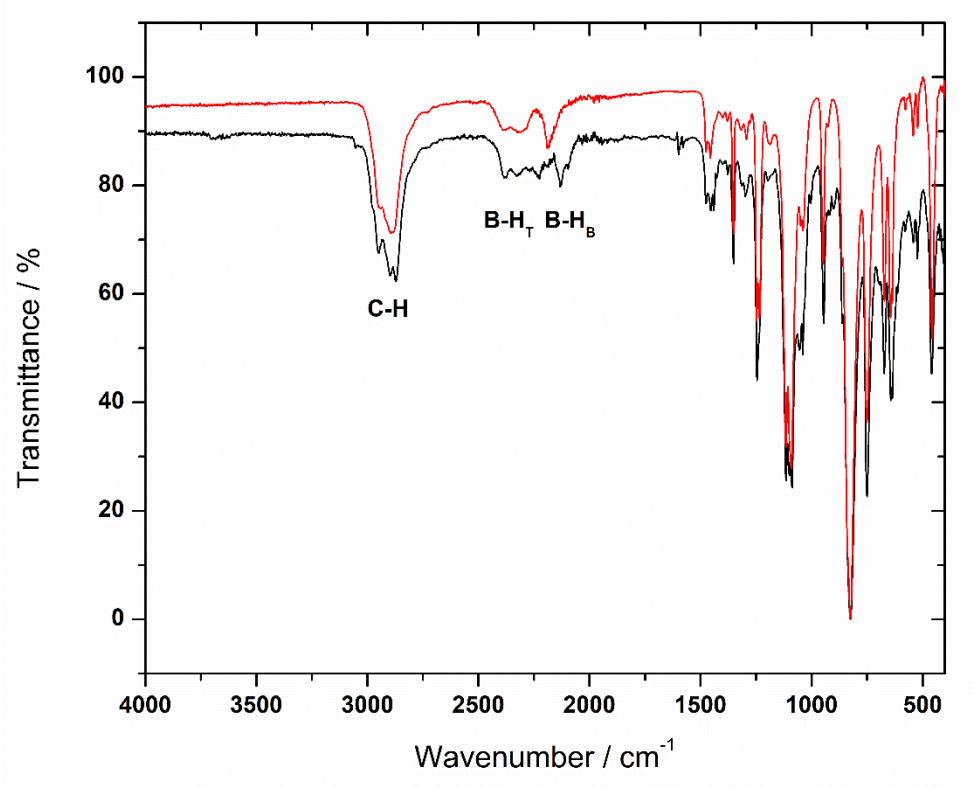

Figure 100. FTIR spectra of **25** (red line) and **26** (black line). Selected absorptions (cm^{-1}): 3000-2850 (C–H), 2400-2300 ($B–H_T$), 2150-2000 ($B–H_B$).

*3.2.4. Magnetic property measurements on $[Na(15\text{-}c\text{-}5)(THF)_2]^+[Dy\{\eta^4\text{-}C_4(SiMe_3)_4\}(\eta^5\text{-}C_5Me_4{}^tBu)(\kappa^2\text{-}BH_4)]^-$ (**26**)*

Compounds **19**-**26** are the first heteroleptic lanthanide sandwich complexes containing cyclobutadienyl ligands. Consequently, they provide the first opportunity to study the influence of the pristine Cb^{2-} ligand on the SMM properties of a Dy^{3+} sandwich complex, and to support our hypothesis that the properties should improve relative to structurally similar cyclopentadienyl ligated complexes. As analytically pure compound **26** was isolated in a good yield, this complex was investigated in detail.

In a static DC field of 1000 Oe, the magnetic susceptibility of **26** was found to be typical of a monometallic Dy^{3+} complex with a $^6H_{15/2}$ ground multiplet, with $\chi_M T$ values of 13.67 and 10.76 $cm^3\ K\ mol^{-1}$ at 300 and 2 K, respectively. In the field dependence of the magnetization plots, a magnetization value of 4.75 Nβ was observed at 1.9 K and 7 T (Figure 101).

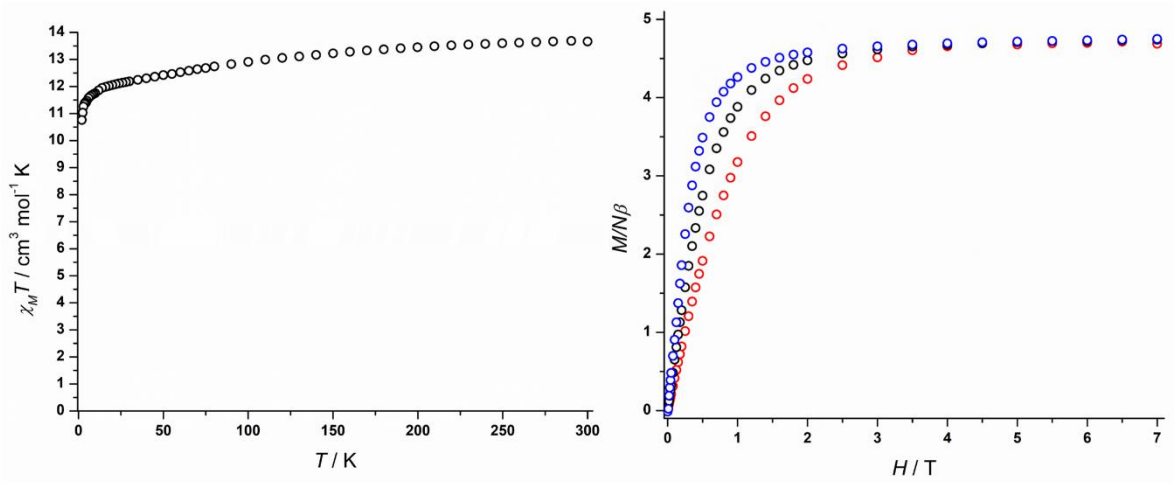

Figure 101. Plot of $\chi_M T(T)$ for **26** (left) in an applied field of 1000 Oe. $\chi_M T$ (300 K) = 13.67 cm^3 K mol^{-1}, $\chi_M T$ (2 K) = 10.76 cm^3 K mol^{-1}. Field (H) dependence of the magnetization (M) for **26** (right) at 1.9 K (blue circles), 3.0 K (black circles) and 5.0 K (red circles). M = 4.75 Nβ at 1.9 K and 7 T.

In a similar fashion to complex **17**, magnetic hysteresis measurements on **26** revealed the strong influence of QTM at zero-field, resulting in waist-restricted hysteresis loops at a temperature of 1.9 K (Figure 102). However, this is expected due to the influence of the equatorial borohydride ligand.

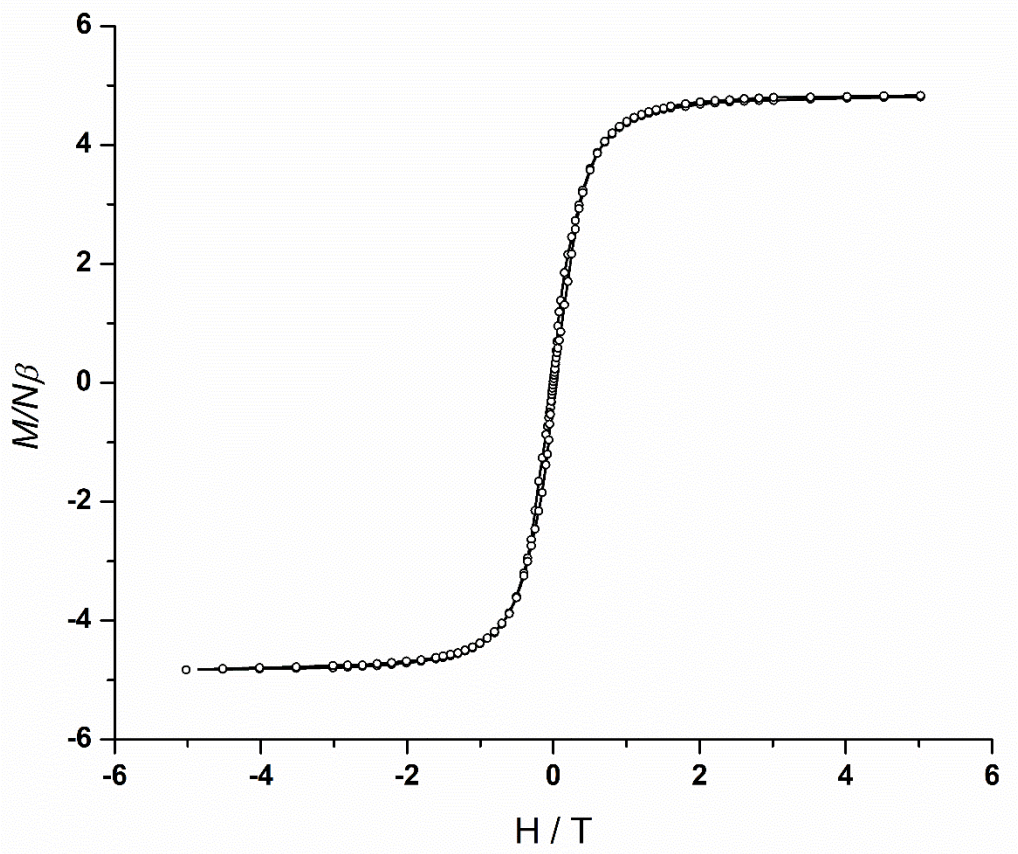

Figure 102. Magnetic hysteresis loops for **26**. The data were continuously collected at 1.9 K under a varying field sweep rate (11 Oe s^{-1} |0-1| T, 30 Oe s^{-1} |1-2| T, 45 Oe s^{-1} |2-3| T and 85 Oe s^{-1} |3-5| T). Solid lines are a guide to the eye.

The SMM properties of compound **26** were further probed by measuring the frequency-dependence of the in-phase and out-of-phase components of the AC susceptibility across a temperature range of 1.9-49 K and AC frequencies in the range ν = 1-1488 Hz. Maxima in the $\chi''(\nu)$ plots for **26** can be seen in the temperature range 1.9-31 K (Figure 103). As is typical for Dy^{3+} complexes with a non-negligible equatorial crystal field, below 5 K the frequency at which the maxima occur are temperature independent, indicating the dominance of QTM. Between 5-31 K, the frequency maxima become temperature dependent before reaching the upper frequency limit, indicating that thermally activated relaxation is now dominant.

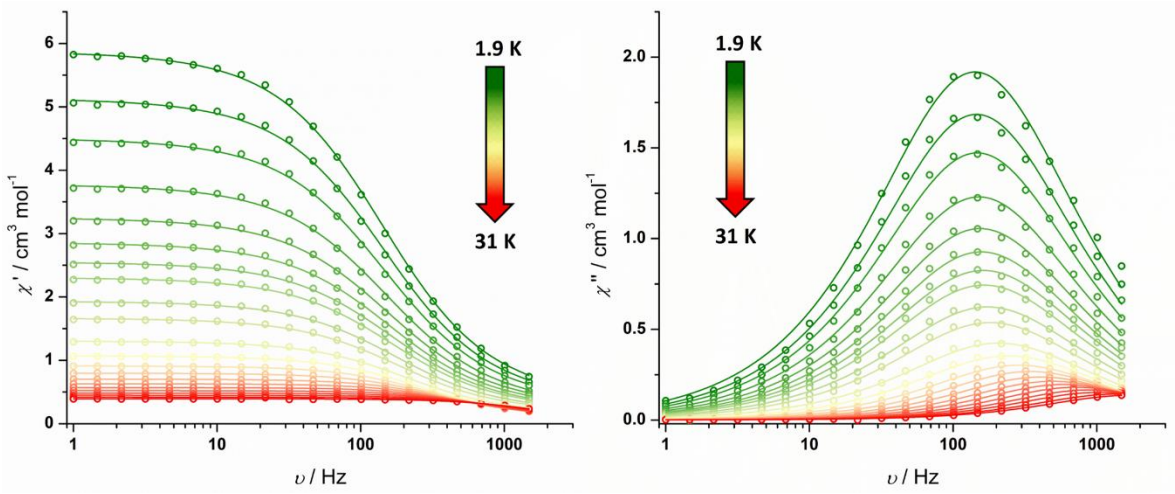

Figure 103. Frequency-dependence of the in-phase (χ') (left) and out-of-phase (χ'') (right) susceptibility for **26** in zero DC field at ν = 1-1488 Hz and temperatures of 1.9 to 31 K. Solid lines represent fits to the data using Equation 1.

Cole-Cole plots of $\chi''(\chi')$ across the temperature range of 1.9-31 K result in slightly asymmetric semi-circular plots that were fitted to the generalised Debye model shown in Equation 1 (Figures 104, 105, Supplementary Table S15). The fit shows a good agreement with the experimental data, with the extracted α-parameters ranging from 0.11-0.22, and τ values ranging from 0.10-1.12 ms.

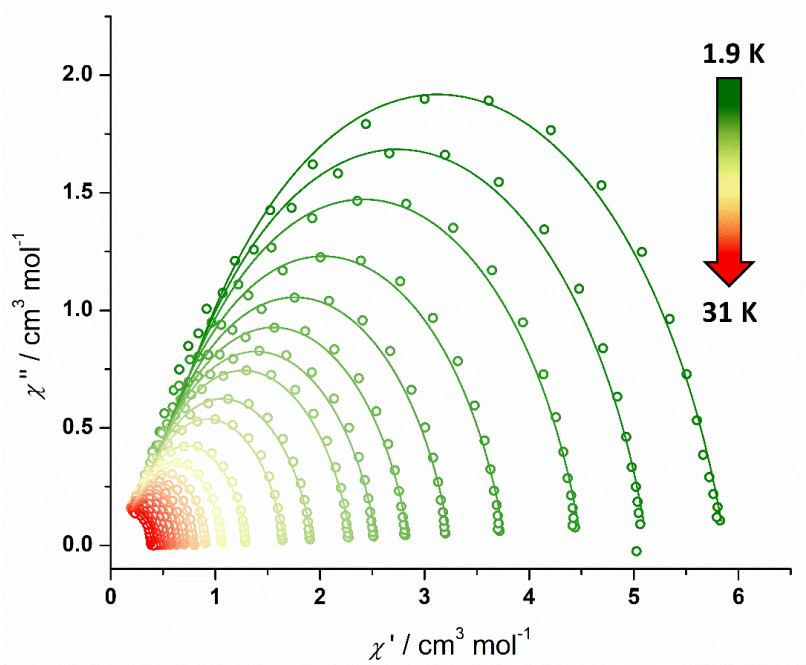

Figure 104. Cole-Cole plots for the AC susceptibilities in zero DC field for **26** from 1.9-31 K. Solid lines represent fits to the data using Equation 1.

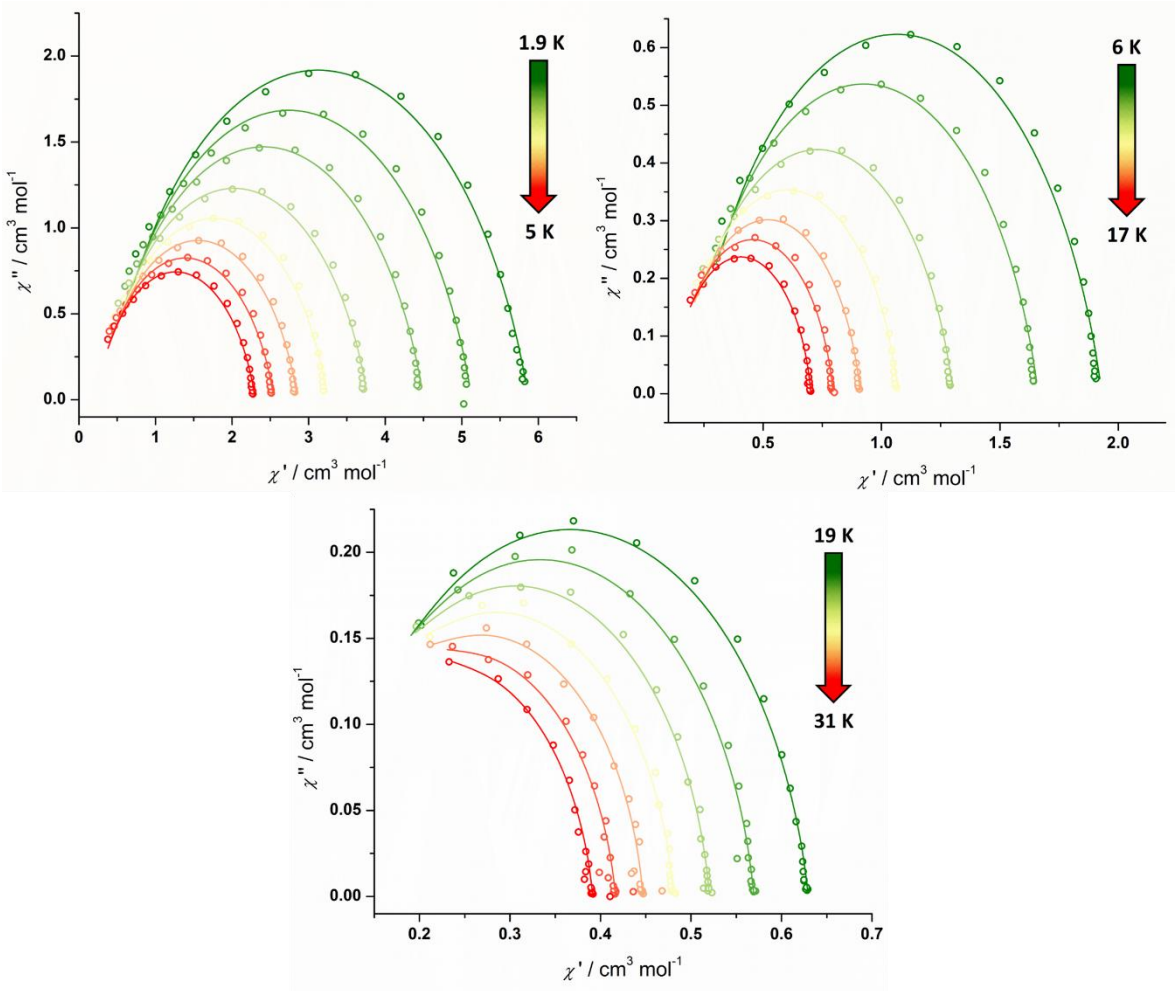

Figure 105. Cole-Cole plots for the AC susceptibilities in zero DC field for **26** from 1.9-5 K (top left), 6-17 K (top right) and 19-31 K (bottom). Solid lines represent fits to the data using Equation 1.

Plotting $\ln\tau$ against T^{-1} for compound **26** confirmed that τ has a weak temperature dependence at low temperatures indicative of QTM, with a strong temperature dependence at higher temperatures being the hallmark of thermally activated relaxation. A curved crossover region at intermediate temperatures can be taken as evidence for the involvement of Raman relaxation processes (Figure 106). By fitting the experimental data to Equation 2, incorporating Orbach, Raman and QTM relaxation processes, we found that there is no unique fit to the relaxation time data and that adjusted R^2 values of greater than 0.999 can be achieved with at least two sets of parameters. In one of these two fits, an R^2 = 0.99988 and values of U_{eff} = 127(17) cm^{-1}, $\tau_0 = 9.0(6) \times 10^{-7}$ s, C = 3.5(8) s^{-1} K^{-n}, n = 2.17(8) and τ_{QTM} = 1.10(1) ms can be obtained (Figure 106, blue line). However, as described in the next section (3.2.5.), theoretical calculations on **26** indicated that 127(17) cm^{-1} is roughly half the energy required for the system to relax via the first-excited Kramers' doublet, which is calculated to occur at 242 cm^{-1}. In light of what appears to be a spurious barrier,

a second fit with U_{eff} fixed at 242 cm^{-1} yielded an R^2 = 0.99918 and values of τ_0 = 6.0(9) × 10^{-9} s, C = 1.9(3) s^{-1} K^{-n}, n = 2.39(5) and τ_{QTM} = 1.08(1) ms (Figure 106, red line). The attempt relaxation time (τ_0) for this fit remains in the range typically observed for Dy^{3+} metallocene SMMs (10^{-7}-10^{-12} s),[14,15,132] and the Raman parameters are very similar for both fits, with the QTM times essentially staying the same.

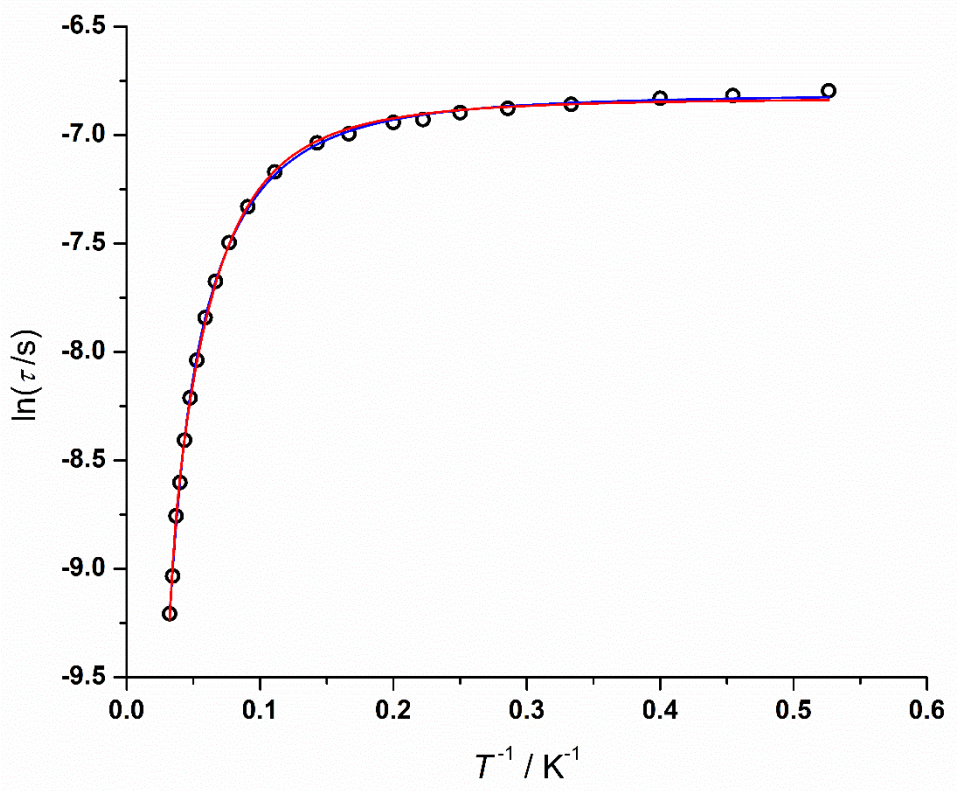

Figure 106. Plot of natural log of the relaxation time (τ) vs. inverse temperature for **26**. The black points are from the AC susceptibility measurements. The solid red line is the best fit (adjusted R^2 = 0.99918) to $\tau^{-1} = \tau_0^{-1}e^{-U_{eff}/k_BT} + CT^n + \tau_{QTM}^{-1}$, giving: U_{eff} (fixed) = 242 cm^{-1}, τ_0 = 6.0(9) × 10^{-9} s, C = 1.9(3) s^{-1} K^{-n}, n = 2.39(5) and τ_{QTM} = 1.08(1) × 10^{-3} s. The solid blue line is the best fit (adjusted R^2 = 0.99948) to $\tau^{-1} = \tau_0^{-1}e^{-U_{eff}/k_BT} + CT^n + \tau_{QTM}^{-1}$, giving: U_{eff} = 127(17) cm^{-1}, τ_0 = 9.0(6) × 10^{-7} s, C = 3.5(8) s^{-1} K^{-n}, n = 2.17(8) and τ_{QTM} = 1.10(1) × 10^{-3} s.

Comparing either of these fits to analogous cyclopentadienyl complexes, *i.e.* **17** and [Dy(η^5-C$_5$^{i}Pr$_5$)(η^5-Cp*)(κ^2-BH$_4$)], which have energy barriers of 36(2) and 7(1) cm^{-1}, respectively, the cyclobutadienyl complex **26** represents a marked improvement. Important structural parameters and SMM properties for these compounds can be seen in Table 4. This improvement can be qualitatively explained by the stronger crystal field interaction of the cyclobutadienyl ligand compared to cyclopentadienyl ligands with Dy^{3+}, an idea based on the significantly shorter Dy-Cb centroid distance in complex **26** of *ca.* 0.08 and 0.09 Å when compared to the shortest analogous Dy-Cp distances in **17** and [Dy(η^5-C$_5$^{i}Pr$_5$)(η^5-Cp*)(κ^2-

BH_4)], respectively. This relative strong Dy–Cb interaction occurs at the expense of the Cp^{Me4tBu} ligand, which is pushed further away from the Dy^{3+} ion. The improved SMM properties of the cyclobutadienyl complex **26** occur despite a slight decrease in axiality of *ca.* 3.7 and 8.8° when compared to analogous bend angles in **17** and [Dy(η^5-$C_5{}^iPr_5$)(η^5-Cp*)(κ^2-BH_4)], respectively. This once again highlights how the strength of the axial crystal ligand field around Dy^{3+} ions has a stronger influence on the SMM properties when compared to the axiality of a system, providing evidence that strict point symmetry is not a key consideration, and that pseudo axial symmetry is good enough in the design of Dy^{3+} SMMs.

Table 4. Structural parameters and SMM properties of analogous dysprosium cyclopentadienyl and cyclobutadienyl mixed sandwich complexes.

Compound	Dy-C(ring)$_c$ / Å	Bend Angle / °	U_{eff} / cm^{-1}	ref
17 [Dy(η^5-Cp^{ttt})(η^5-Cp*)(κ^2-BH_4)]	2.3779(18) (Cp^{ttt}), 2.351(2) (Cp*)	145.23(7)	36(2)	This work
[Dy(η^5-$C_5{}^iPr_5$)(η^5-Cp*)(κ^2-BH_4)]	2.3823(14) (Cp^{iPr5}), 2.3636(16) (Cp*)	150.28(5)	7(1)	[27]
26 [Na(15-c-5)$(THF)_2$]$^+$[Dy{η^4-$C_4(SiMe_3)_4$}(η^5-$C_5Me_4{}^tBu$)(κ^2-BH_4)]$^-$	2.2728(4) (Cb), 2.3975(3) (Cp)	141.52(2)	127(17) or 242	This work

3.2.5. Theoretical calculations on [Dy{η^4-$C_4(SiMe_3)_4$}(η^5-$C_5Me_4{}^tBu$)(κ^2-BH_4)]$^-$

The low-lying electronic states of the complex anion of **26** were investigated by multireference *ab initio* calculations on a model that was constructed using geometries extracted from the solid-state molecular structure, with positions of hydrogen atoms optimized using DFT calculations. The calculations and analysis of the results were conducted as part of a collaboration with Dr Akseli Mansikkamäki at the University of Oulu (Finland). The properties of the eight lowest Kramers' doublets (KD) arising from the crystal-field splitting of the ground $^6H_{15/2}$ multiplet of the Dy^{3+} ion are listed in the

Supplementary Table S22 and the principal magnetic axis of the ground KD is shown in Figure 107 (blue arrow).

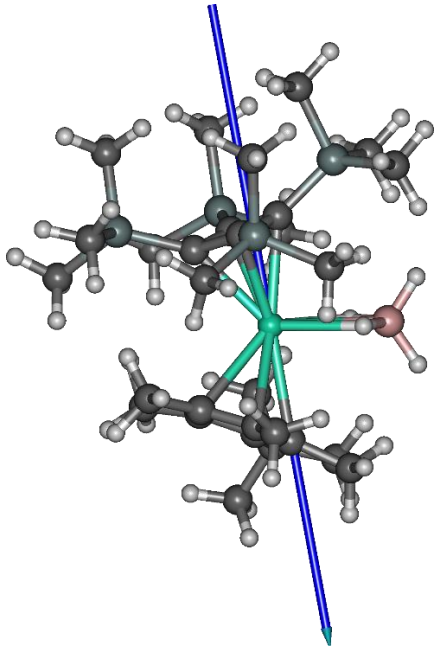

Figure 107. The principal magnetic axis of the ground Kramers' doublet (blue arrow) calculated for the Dy^{3+} ion in **26**. Dy = green, Si = light grey, B = pink, O = red, C = black, H = white.

Importantly, the direction of the principal magnetic axis in the ground KD is clearly orientated towards the Dy-Cb centroid axis rather than the Dy-Cp axis. This indicates that the crystal ligand field induced by the dianionic cyclobutadienyl ligand dominates over the monoanionic cyclopentadienyl ligand, further suggesting that Cb^{2-} ligands should be capable of creating a stronger crystal field splitting and hence increased anisotropy barriers, provided a sufficiently axial geometry can be retained.

The effective energy barrier of **26** was modelled using a well-established method in the field (as described in section 2.3.5.). The results indicate that there is a dominant axial crystal field around Dy^{3+}, with the anisotropy barrier being retained up to the sixth excited KD. (Figure 108, Supplementary Table S23). The ground KD has a g_z = 19.624, with small transverse components g_x and g_y = 0.009 and 0.016, respectively, which significantly increase by the first excited KD (g_x = 0.234, g_y = 0.380). This suggests that the theoretically determined energy barrier of U_{eff} = 242 cm^{-1} is most likely crossed at this point.

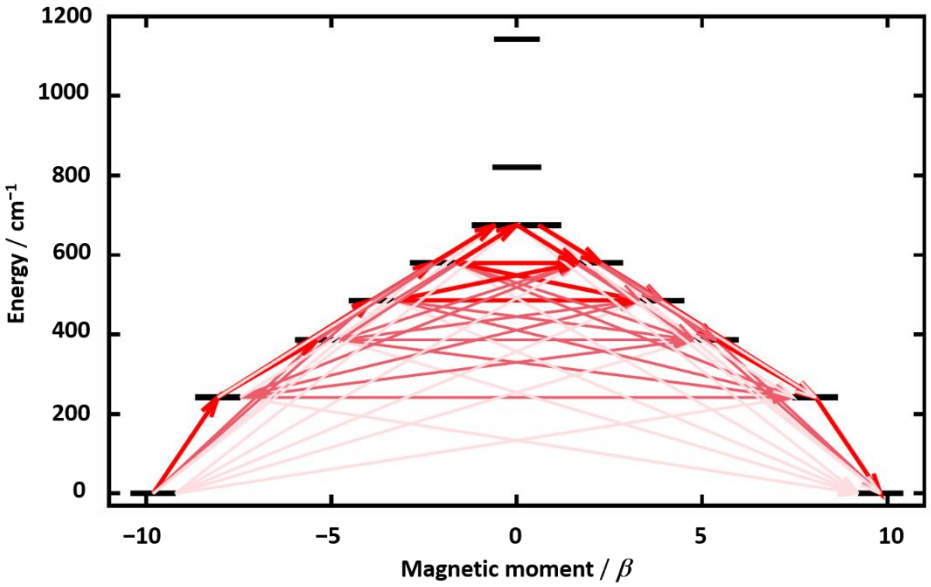

Figure 108. Calculated effective *ab initio* barriers for the relaxation of magnetization in **26**. The arrows represent transition magnetic moments, with stronger arrows indicating larger values.

As the calculated barrier is roughly double that of 127(17) cm^{-1} determined using the experimental data, it led us to consider different fits to the relaxation time data using different fit parameters. By fixing U_{eff} to that determined by the calculations, we were able to obtain a second excellent fit of the experimental data with reasonable values for the pre-exponential factor (τ_0) and Raman parameters (C and n), and with the QTM times essentially staying the same (Table 5). This suggests that an effective energy barrier of 242 cm^{-1} for **26** is appropriate given the experimental and theoretical agreements.

Table 5. Obtained parameters for fits to the magnetic relaxation time data of **26** to Equation 2.

R^2	U_{eff} (cm^{-1})	τ_0 (s)	C (s^{-1} K^{-n})	n	τ_{QTM} (ms)
0.99988	127(17)	$9.0(6) \times 10^{-7}$	3.5(8)	2.17(8)	1.10(1)
0.99918	242 (fixed)	$6.0(9) \times 10^{-9}$	1.9(3)	2.39(5)	1.08(1)

To further explore the nature of the crystal field environment around the Dy^{3+} ion in **26**, the *ab initio* crystal field parameters were also calculated (Supplementary Tables S24, S25). The axial second-rank parameter B_2^0 = −489 cm^{-1} creates a strong axial crystal field that stabilizes the M_J = ±15/2 ground state. However, the off-diagonal second rank parameters

are sufficiently large to promote significant mixing of the states and severely reduce the axiality of the system ($|B_2^{\pm 1}|$ = 26 cm^{-1} and $|B_2^{\pm 2}|$ = 249 cm^{-1}). Complex **26** therefore has an axiality parameter of Z = 1.96 and a relative axiality parameter of Z_{rel} = 0.050, which are significantly lower than the benchmark [Dy(η^5-C$_5$^{i}Pr$_5$)(η^5-Cp*)]$^+$ system (Z = 39.5, Z_{rel} = 1), but this is not unexpected based on the molecular structure of **26**, which features a strongly bent axial geometry and an equatorial borohydride ligand. A more meaningful comparison can be made with a cyclopentadienyl analogue of **26**, *i.e.* [Dy(η^5-C$_5$^{i}Pr$_5$)(η^5-Cp*)(κ^2-BH$_4$)], which has a Z = 1.81 and Z_{rel} = 0.046. Thus, the larger values for **26** indicate that cyclobutadienyl ligands can produce a stronger axial crystal field than cyclopentadienyl ligands in structurally similar complexes.

3.2.6. Attempts to synthesize [Ln({η^4-C$_4$(SiMe$_3$)$_4$}(η^5-Cp^R)] (Ln = Y, Dy) (R = Me$_5$, Me$_4$^{t}Bu)

With the promising SMM properties of compound **26** and, indeed, all other lanthanide-cyclobutadienyl complexes measured to date when compared to structurally similar cyclopentadienyl complexes, a complex of the type [Dy(η^4-Cb)(η^5-Cp^R)] is a key target. Therefore, the attempted removal of the equatorial borohydride ligand from **19**, **24** and **26** was investigated using various methods.

Initial attempts were carried out by reacting equimolar amounts of **24** with the electrophile [Ph$_3$C]$^+$[B(C$_6$F$_5$)$_4$]$^-$ (Scheme 27). Cold hexane (*ca.* −40 °C), in which both starting materials are insoluble, was added to a mixture of **24** and [Ph$_3$C]$^+$[B(C$_6$F$_5$)$_4$]$^-$ and was then allowed to warm to room temperature and stir overnight.

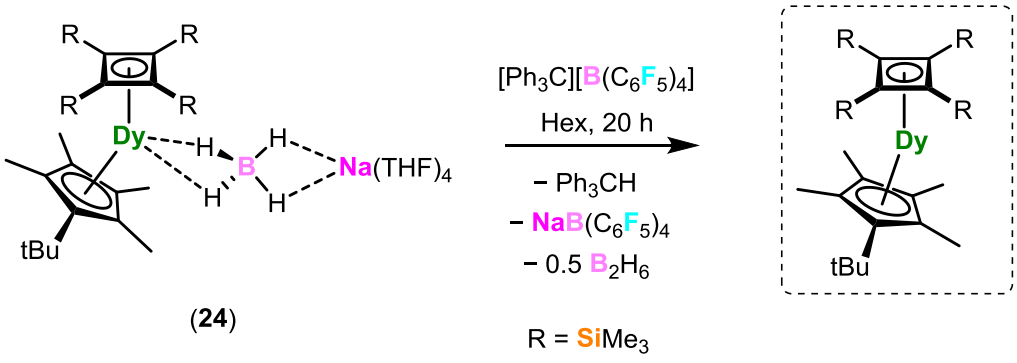

Scheme 27. Attempted synthesis of [Dy({η^4-C$_4$(SiMe$_3$)$_4$}(η^5-C$_5$Me$_4$^{t}Bu)] using **24** and [Ph$_3$C]$^+$[B(C$_6$F$_5$)$_4$]$^-$.

Upon completion, a colour change from colourless to orange and the formation of a white precipitate was observed. The orange solution was filtered and evaporated to dryness to give a residual oily product, before being redissolved in the minimum amount of hexane and placed into the freezer at −40 °C. No crystalline material could be obtained from the saturated hexane solution. Different solvents were investigated (pentane, tetramethylsilane, benzene and toluene) which all had a similar outcome and suggest a very high degree of solubility. Analysis on the residual oily orange material using Electron Ionization Mass Spectrometry (EI-MS) revealed molecular ion peaks at $[M]^+$ (*m*/*z*): 695, 681 and 621 (Figure 109). The target complex [Dy({η^4-$C_4(SiMe_3)_4$}(η^5-$C_5Me_4{}^tBu$)] has an *m*/*z* = 681, which is one of the observed peaks, however the peak at *m*/*z* = 695 could indicate the presence of [M + BH_3 or BH_4 or CH_3]. The peak at *m*/*z* = 621 could be due to fragmentation of the target product, *i.e.* [M – Me_4]. The precursor complex **24** (*m*/*z* = 718) was then investigated which revealed molecular ion peaks at $[M]^+$ (*m*/*z*): 681 and 608, suggesting only fragmentation could be observed, *i.e.* 681 = [M – $NaBH_4$] and 608 = [M − $NaBH_4$ – $SiMe_3$] (Figures S68, S69).

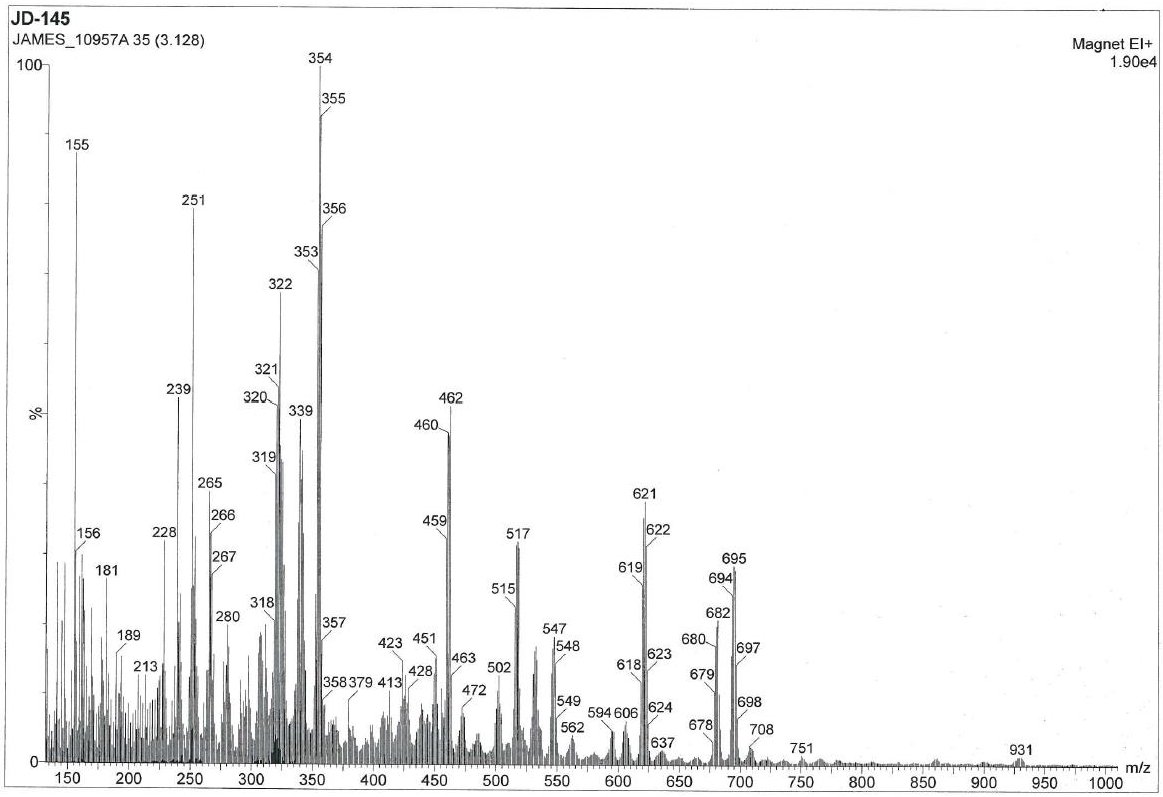

Figure 109. EI-MS of the product from reacting **24** with $[Ph_3C]^+[B(C_6F_5)_4]^-$.

Similar reactions between **24** or the separated ion-pair complex **26** with the super-electrophile $[(Et_3Si)_2(\mu\text{-}H)]^+[B(C_6F_5)_4]^-$ in cold hexane (*ca.* −40 °C) were investigated (Scheme 28), which resulted in the same observations, *i.e.* a colour change of the hexane solution from colourless to orange. After subsequent work up, unfortunately all crystallization attempts were again unsuccessful. After evaporating the solution to dryness, attempts to purify the residual sticky product via sublimation were also unsuccessful.

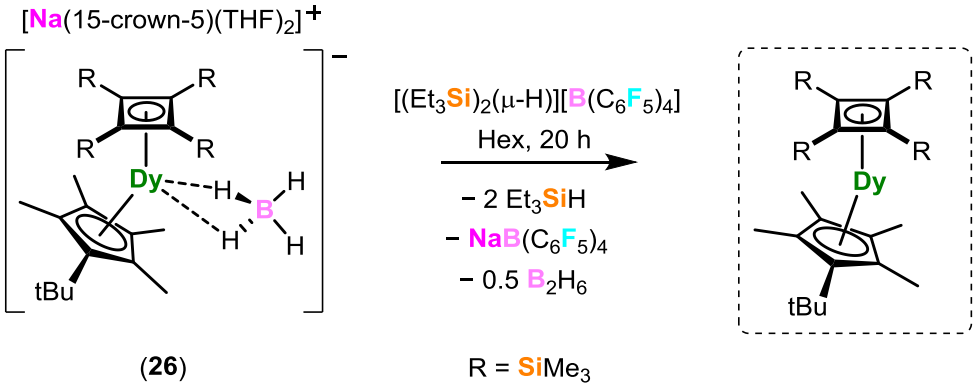

Scheme 28. Attempted synthesis of $[Dy(\{\eta^4\text{-}C_4(SiMe_3)_4\}(\eta^5\text{-}C_5Me_4{}^tBu)]$ using **26** and $[(Et_3Si)_2(\mu\text{-}H)]^+[B(C_6F_5)_4]^-$.

Further investigations were carried out between the reactivity of **24** with triethylammonium tetraphenylborate $[HNEt_3]^+[B(C_6H_5)_4]^-$ in hexane (Scheme 29). In this case, after stirring overnight, a yellow solution had formed with an observable white precipitate. The solution was filtered, and the volatiles removed before being transferred into the glovebox. The residual yellow solid was re-dissolved in the minimum amount of hexane and placed in the −40 °C freezer.

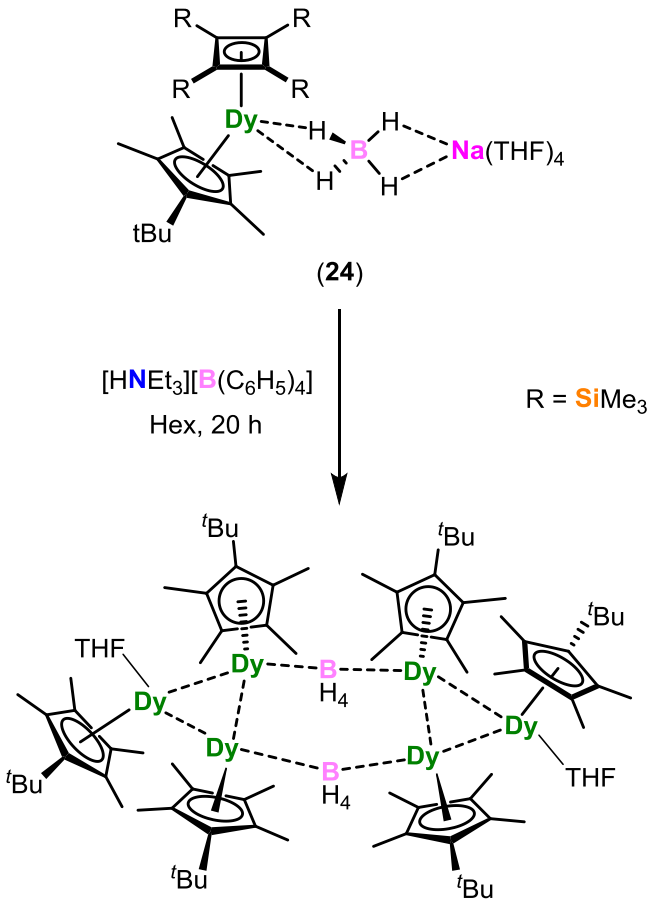

Scheme 29. Attempted synthesis of [Dy({η^4-C$_4$(SiMe$_3$)$_4$}(η^5-C$_5$Me$_4$^{t}Bu)] using **24** and [HNEt$_3$]$^+$[B(C$_6$H$_5$)$_4$]$^-$.

After a week, no crystalline material had formed, so the hexane solution was left to slowly evaporate, which resulted in the formation of a small amount of yellow crystals. These crystals were very weakly diffracting, however some atom connectivity could be established, which revealed a decomposition product containing six DyCp^{Me4tBu} half sandwich units (Figure 110). It should be noted that for this product to charge balance, it would require 10 hydride ligands. Unfortunately, as this is a by-product, problems with reproducibility precluded further characterization, and hence, the outcome of this reaction should be taken cautiously.

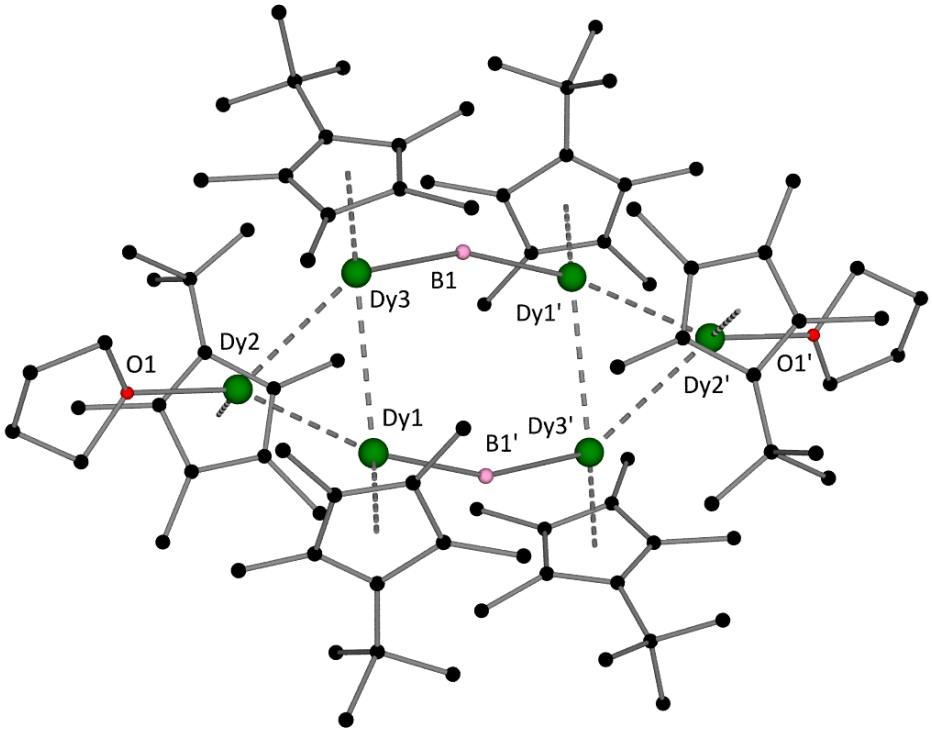

Figure 110. Decomposition product from the reaction of **24** with $[HNEt_3]^+[B(C_6H_5)_4]^-$.

As attempts to remove the borohydride ligands from the Cp^{Me4tBu} cyclobutadienyl sandwich complexes were proving unsuccessful, the reactivity of the yttrium Cp* derivative **19** with $[(Et_3Si)_2(\mu\text{-}H)]^+[B(C_6F_5)_4]^-$ was investigated to try and understand more about the reactivity using NMR spectroscopy (Scheme 30).

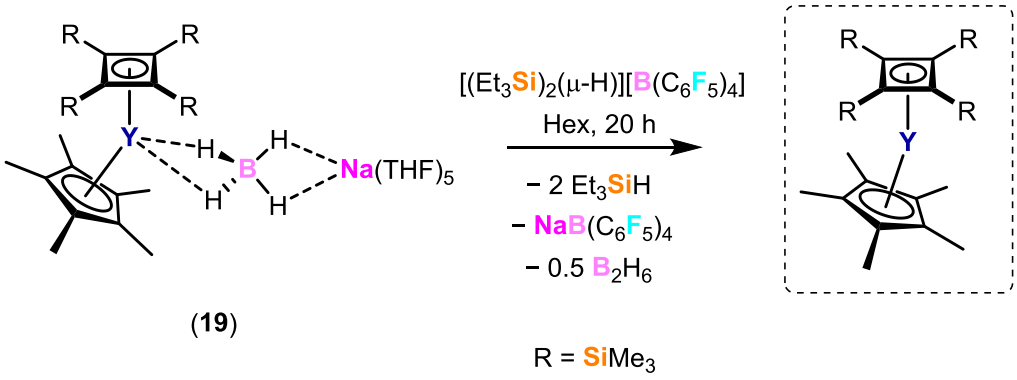

Scheme 30. Attempted synthesis of $[Y(\{\eta^4\text{-}C_4(SiMe_3)_4\}(\eta^5\text{-}Cp^*)]$ using $[(Et_3Si)_2(\mu\text{-}H)]^+[B(C_6F_5)_4]^-$.

The reaction proceeded in a similar fashion to previous attempts with **24** and **26**, and an orange solution with a white precipitate formed after stirring overnight. After subsequent

work up, attempts to crystallize once again proved unsuccessful. Unfortunately, NMR analysis on the product only revealed an intractable mixture of products.

Thus, despite several different approaches in the attempted removal of borohydride ligands from the cyclobutadienyl rare-earth sandwich complexes, all indications point towards decomposition being the most likely outcome in all of these reactions. It may be the case that the correct reaction conditions have not yet been found, or that the combination of Cb / Cp ligands investigated in this study are not sufficiently matched to stabilise the target [Dy(η^4-Cb)(η^5-Cp^R)] complex.

*3.2.7. Synthesis and characterization of [Dy{η^8-C$_8$(Si^{i}Pr$_3$)$_2$H$_4$}{η^4-C$_4$(SiMe$_3$)$_4$}K(THF)] (**27**) and [K(18-c-6)(THF)$_2$]$^+$[Dy{η^8-C$_8$(Si^{i}Pr$_3$)$_2$H$_4$}{η^4-C$_4$(SiMe$_3$)$_4$}]$^-$ (**28**)*

Only one pentalene-ligated SMM has been reported to date (described in section 1.2.6.). Therefore, we were interested in investigating the reactivity of Pn^{2-} ligands with Cb half-sandwich complexes. Due to the various possible coordination modes of Pn^{2-}, it could be possible to synthesize either an anionic monometallic complex of the type [Dy(η^8-Pn)(η^4-Cb)]$^-$, or an *anti*-bimetallic pentalene complex of the type [{Dy(η^4-Cb)}$_2$(μ:η^5:η^5-Pn)] (Figure 111). The former complex would be a cyclobutadienyl analogue of the monometallic pentalene SMM [Dy{η^8-C$_8$(Si^{i}Pr$_3$)$_2$H$_4$}(η^5-Cp*)],[100] and should allow a direct comparison of Cb^{2-} and Cp ligands and how they influence the crystal field splitting in a Dy^{3+} SMM.

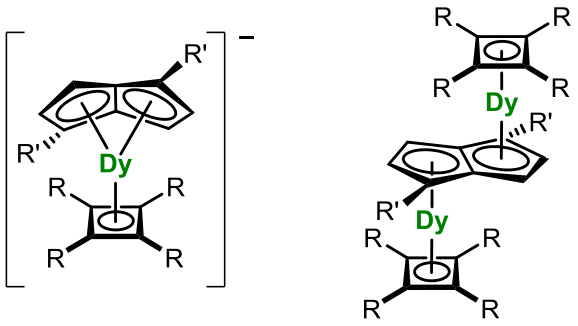

Figure 111. Hypothetical anionic monometallic (left) or *anti*-bimetallic (right) pentalene ligated dysprosium complexes with cyclobutadienyl ligands.

Thus, the synthesis of the heteroleptic sandwich complex [Dy{η^8-C$_8$(Si^{i}Pr$_3$)$_2$H$_4$}{η^4-C$_4$(SiMe$_3$)$_4$}K(THF)] (**27**) was achieved by the 1:1 salt metathesis reaction of K$_2$Pn^{TIPS} with the potassium Cb half-sandwich complex **15** (Scheme 31). Dropwise addition of a dark purple solution of K$_2$Pn^{TIPS} in THF to an orange solution of **15** in THF, cooled to −78 °C, produced a dark red solution. The reaction was warmed to room temperature and stirred overnight. After subsequent work up, orange crystals of **27** were isolated in a yield of 56 % by storing a saturated hexane solution at –40 °C for three days.

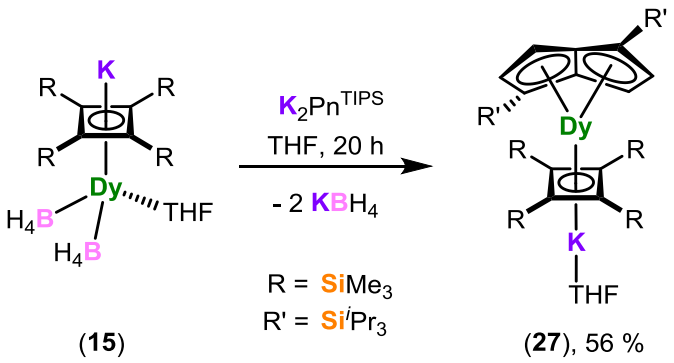

Scheme 31. Synthesis of **27**.

The solid-state molecular structure of **27** features η^8- and η^4-coordination modes of the Pn^{2-} and Cb^{2-} ligands to Dy^{3+}, respectively, with a potassium counter cation capped by a THF ligand interacting with the Cb^{2-} ligand (Figure 112). The pentalene ligand displays a fold-angle of 23.8(5)°, and hence, an asymmetric coordination to the Dy^{3+} ion, with the shortest Dy-C distances of 2.385(8) and 2.400(8) Å to the bridgehead carbons (C17 and C21) and much longer distances of 2.782(10)-2.831(8) Å to the wingtip carbons (C18 and C23), respectively. The Dy-C distances to the Cb ligand range from 2.47(3)-2.57(3) Å, with a Dy-Cb centroid distance of 2.306(11) Å, which is very similar to the analogous distances to the pentalene ligand of 2.282(5) and 2.300(4) Å. Two Cb$_c$-Dy-Pn$_c$ bending angles of 156.4(3) and 152.2(3)° are observed. Additionally, the SiMe$_3$ groups can be seen lying out of the plane of the C$_4$ ring in the same direction away from the Dy^{3+} ion in the range of 0.15-0.50 Å.

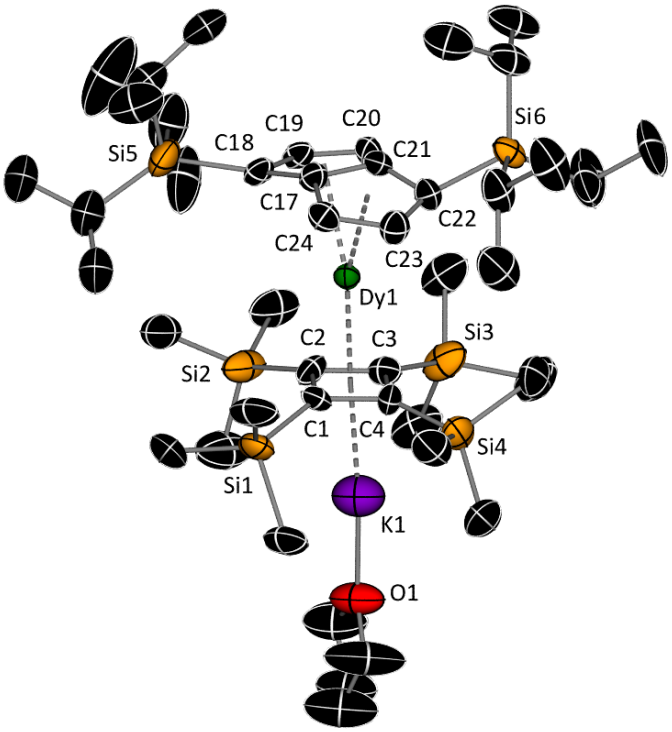

Figure 112. Solid-state structure of [Dy{η^8-$C_8(Si^iPr_3)_2H_4$}{η^4-$C_4(SiMe_3)_4$}K(THF)] (**27**). Thermal ellipsoids are set to 30 % probability and hydrogen atoms have been omitted for clarity. Selected bond distances (Å) and angles (°): C1-C2 1.453(9), C2-C3 1.454(9), C3-C4 1.453(9), C1-C4 1.454(9), C17-C18 1.495(13), C18-C19 1.445(15), C19-C20 1.41(2), C20-C21 1.423(13), C17-C21 1.420(11), C21-C22 1.420(11), C22-C23 1.421(12), C23-C24 1.419(12), C17-C24 1.420(11), C1-Si1 1.887(13), C2-Si2 1.877(18), C3-Si3 1.847(16), C4-Si4 1.852(16), Dy1-Cb_{cent} 2.306(11), Dy1-Pn_{cent} 2.282(5) (C17-21), 2.300(4) (C17-24), Cb_{cent}-Dy1-Pn_{cent} 156.4(3) (C17-21), 152.2(3) (C17-24).

In an attempt to synthesize an *anti*-bimetallic pentalene complex of the type [{Dy(η^4-Cb)}$_2$(μ:η^5:η^5-Pn)], the reaction between one equivalent of K_2Pn^{TIPS} and two of **15** was investigated, however this resulted in the formation of the same monometallic complex **27**. We were therefore interested to see if the contact potassium cation in **27** could be removed, and if it would have any effect on the structural parameters by potentially reducing the Dy-Cb centroid distance. Thus, the synthesis of the separated ion pair complex [K(18-c-6)(THF)$_2$]$^+$[Dy{η^8-$C_8(Si^iPr_3)_2H_4$}{η^4-$C_4(SiMe_3)_4$}]$^-$ (**28**) was achieved by adding one equivalent of 18-crown-6 to a red solution of **27** in THF (Scheme 32). After subsequent work up, red crystals of **28** in an isolated yield of 65 % were obtained by storing a saturated THF solution layered with hexane at –40 °C for three days.

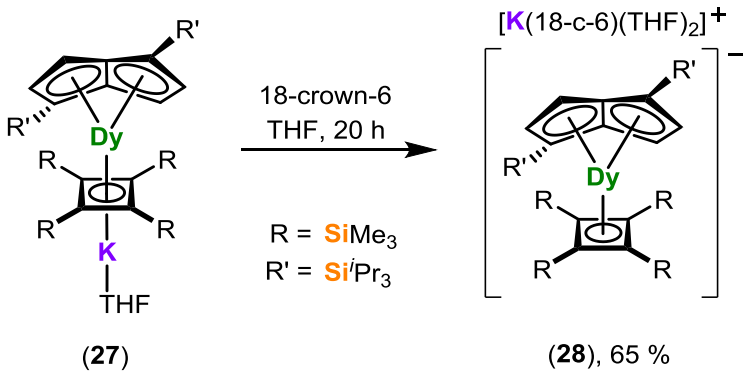

(**27**) (**28**), 65 %

Scheme 32. Synthesis of **28**.

The solid-state molecular structure of **28** features a separated $[Dy\{\eta^8\text{-}C_8(Si^iPr_3)_2H_4\}\{\eta^4\text{-}C_4(SiMe_3)_4\}]^-$ anion with the same coordination modes of the Pn and Cb ligands as the precursor, with the potassium counter ion now encapsulated within the 18-crown-6 and capped by two THF molecules (Figure 113). The anion is structurally very similar to the precursor **27**, with Dy-Cb and Dy-Pn centroid distances of 2.294(3), 2.301(6) and 2.296(4) Å, respectively, resulting in Cb_c-Dy-Pn_c bending angles of 152.89(12) and 157.46(17)° and a pentalene fold-angle of 24.3(6)°. The Dy–C distances for the Cb ligand are 2.469(5)-2.580(5) Å, with asymmetric interactions to the Pn^{2-} ligand of 2.405(8)-2.413(10) Å for the bridgehead carbons (C17 and C21) and 2.814(9)-2.825(14) Å to the wingtip carbons (C18 and C23). Two of the $SiMe_3$ groups (Si1 and Si3) only slightly bend out of the plane of the C4 ring by 0.11-0.17 Å, whereas the other two groups (Si2 and Si4) significantly bend out of the plane by 0.72-1.23 Å. This is likely due to the near perfect alignment of Si2 and Si4 with the Si^iPr_3 groups Si5 and Si6 on the pentalene ligand, respectively, resulting in steric repulsion.

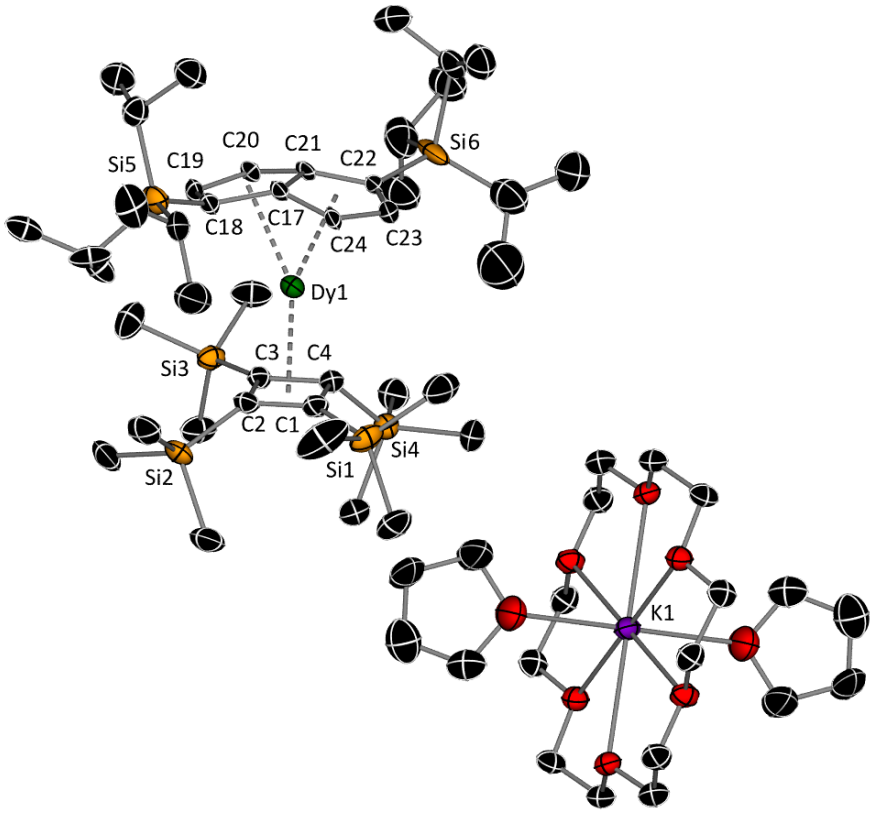

Figure 113. Solid-state structure of $[K(18\text{-}c\text{-}6)(THF)_2]^+[Dy\{\eta^8\text{-}C_8(Si^iPr_3)_2H_4\}\{\eta^4\text{-}C_4(SiMe_3)_4\}]^-$ (**28**). Thermal ellipsoids are set to 30 % probability and hydrogen atoms have been omitted for clarity. Selected bond distances (Å) and angles (°): C1-C2 1.458(7), C2-C3 1.472(7), C3-C4 1.510(7), C1-C4 1.501(7), C17-C18 1.469(9), C18-C19 1.406(9), C19-C20 1.399(10), C20-C21 1.438(10), C17-C21 1.451(9), C21-C22 1.443(9), C22-C23 1.419(10), C23-C24 1.415(10), C17-C24 1.439(10), C1-Si1 1.829(5), C2-Si2 1.851(5), C3-Si3 1.842(5), C4-Si4 1.830(5), Dy1-Cb_{cent} 2.294(3), Dy1-Pn_{cent} 2.301(6) (C17-21), 2.296(4) (C17-24), Cb_{cent}-Dy1-Pn_{cent} 152.89(12) (C17-21), 157.46(17) (C17-24).

In comparing the structures of **27** and **28** with that of the Cp* analogue $[Dy\{\eta^8\text{-}C_8(Si^iPr_3)_2H_4\}(\eta^5\text{-}Cp^*)]$,[100] the Dy-Cb centroid distances are *ca.* 0.04-0.05 Å shorter than the analogous Dy-Cp* distance, with the Dy-Pn centroid distances being longer by *ca.* 0.05-0.07 Å. The longer Dy-Pn centroid distances are most likely the cause of reduced pentalene fold-angles for **27** and **28** by *ca.* 3.1 and 2.6°, respectively, when compared to the analogous angle in the Cp* analogue, which is 26.9(4)°. The shorter distances to the dianionic cyclobutadienyl ligands suggest that the dominant interaction within the crystal field around the Dy^{3+} ions is with this ligand. These stronger interactions probably occur at the expense of the interactions with the Pn^{2-} ligands. The FTIR spectra of **27** and **28** are similar and show C–H stretches in the range of 3000-2850 cm^{-1} (Figure 114). Elemental analysis of **27** was consistent with the molecular structure, with % found (calculated) for $C_{46}H_{90}DyKSi_6O$: C 54.16 (53.68); H 9.09 (8.81). Analysis on **28** gave an excellent fit for the

loss of one THF ligand, which can be relatively labile in crown ether cations,[28] with % found (calculated) for $C_{58}H_{114}DyKSi_6O_7$, **28**(−THF): C 53.43 (53.85); H 8.87 (8.88).

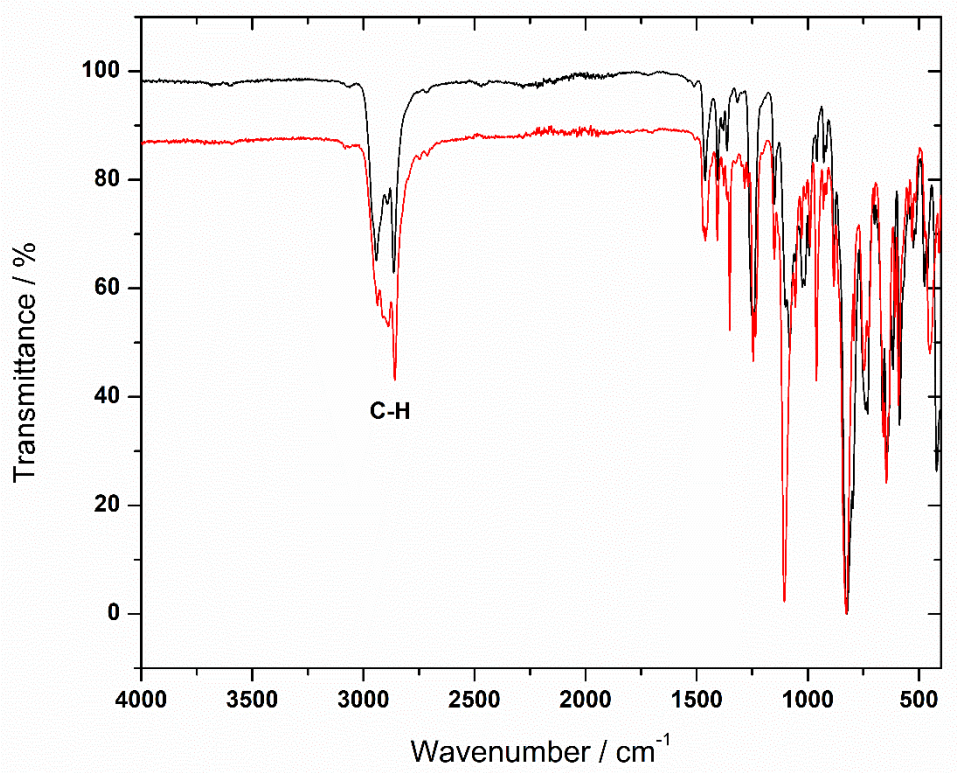

Figure 114. FTIR spectra of **27** (black line) and **28** (red line). Selected absorptions (cm^{-1}): 3000-2850 (C–H).

*3.2.8. Magnetic property measurements on [Dy{η⁸-C₈(Si^{i}Pr₃)₂H₄}{η⁴-C₄(SiMe₃)₄}K(THF)] (**27**) and [K(18-c-6)(THF)₂]⁺[Dy{η⁸-C₈(Si^{i}Pr₃)₂H₄}{η⁴-C₄(SiMe₃)₄}]⁻ (**28**)*

Compounds **27** and **28** are cyclobutadienyl analogues of the cyclopentadienyl complex [Dy{η^8-C_8(Si^{i}Pr$_3$)$_2$H$_4$}(η^5-Cp*)] and, therefore, allow direct comparison of the influence of dianionic Cb ligands on the SMM properties with that of monoanionic Cp ligands. Removal of the contact potassium ion in **27** to form the separated ion pair complex **28** should also provide insight into whether the presence of a contact ion changes the interaction between Cb^{2-} and Dy^{3+}.

In a static field of 1000 Oe, the magnetic susceptibility of **27** and **28** were both found to be typical of monometallic Dy^{3+} complexes with a $^6H_{15/2}$ ground multiplet. $\chi_M T$ values of 13.53

(**27**) and 13.49 (**28**) cm^3 K mol^{-1} are observed at 300 K, which steadily decrease before the onset of magnetic blocking and a sharp drop at low temperature, with values of 7.47 and 7.45 cm^3 K mol^{-1} at 2 K, respectively (Figure 115). In the field dependence of the magnetization plots, magnetization values of 4.95 and 4.98 Nβ are observed at 1.9 K and 7 T for **27** and **28**, respectively (Figure 116).

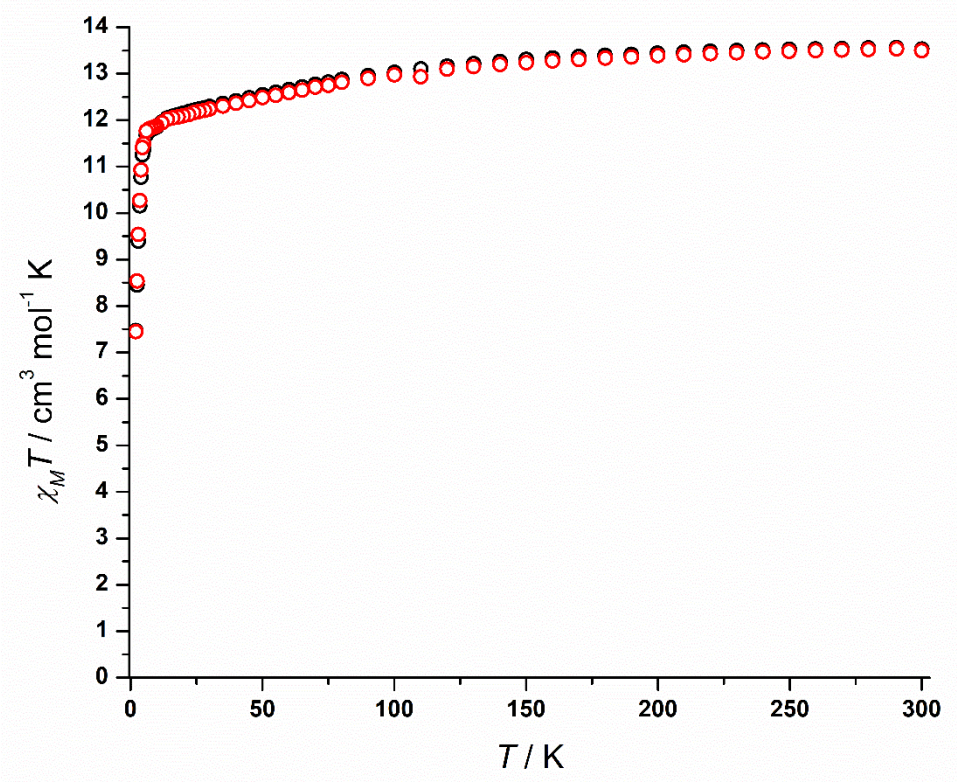

Figure 115. Plot of $\chi_M T(T)$ for **27** (black circles) and **28** (red circles) in an applied field of 1000 Oe. For **27** $\chi_M T$ (300 K) = 13.53 cm^3 K mol^{-1}, $\chi_M T$ (2 K) = 7.47 cm^3 K mol^{-1}. For **28** $\chi_M T$ (300 K) = 13.49 cm^3 K mol^{-1}, $\chi_M T$ (2 K) = 7.45 cm^3 K mol^{-1}.

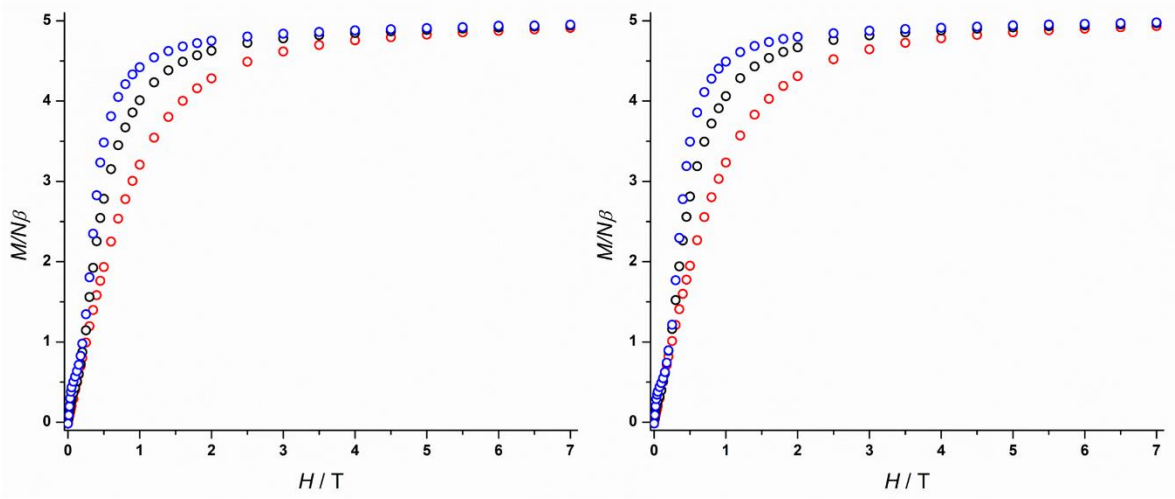

Figure 116. Field (*H*) dependence of the magnetization (*M*) at 1.9 K (blue circles), 3.0 K (black circles) and 5.0 K (red circles) for **27** (left) and **28** (right). For **27** *M* = 4.95 Nβ at 1.9 K and 7 T. For **28** *M* = 4.98 Nβ at 1.9 K and 7 T.

The hysteresis behaviour of compounds **27** and **28** are essentially identical, with waist-restricted hysteresis loops at 1.9 K and a precipitous loss of magnetization at zero-field, suggesting a strong influence of QTM at low temperatures for both complexes (Figure 117). These observations are comparable to those of [Dy{η^8-C_8(Si^iPr_3)$_2H_4$}(η^5-Cp*)], which also features waist-restricted hysteresis at low temperature.

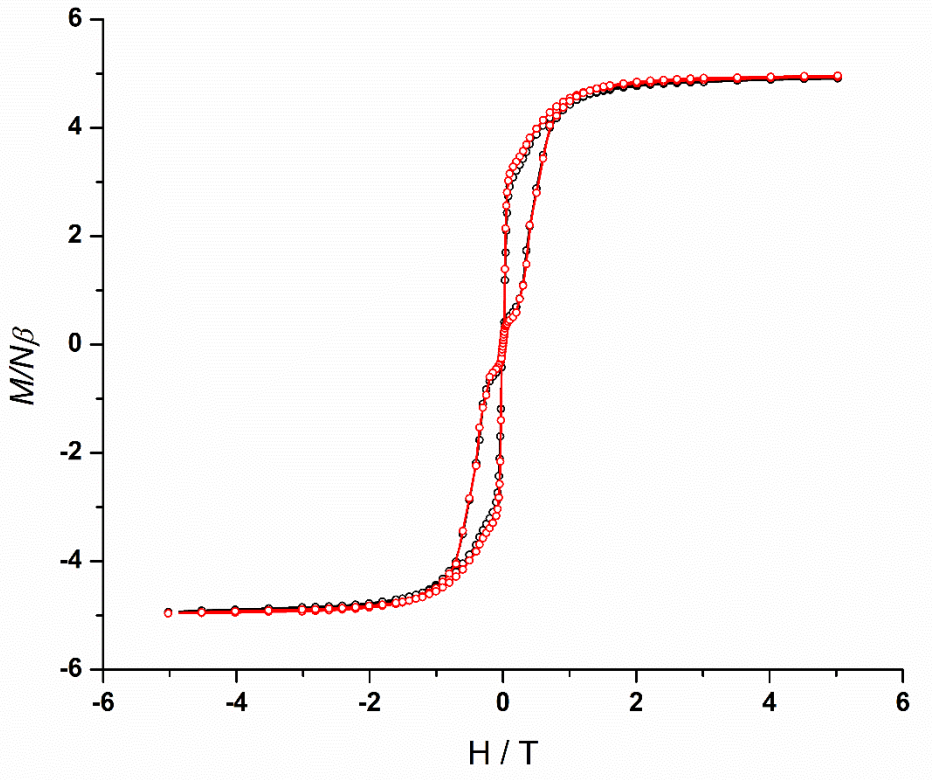

Figure 117. Magnetic hysteresis loops for **27** (black circles) and **28** (red circles). The data were continuously collected at 1.9 K under a varying field sweep rate (11 Oe s^{-1} |0-1| T, 30 Oe s^{-1} |1-2| T, 45 Oe s^{-1} |2-3| T and 85 Oe s^{-1} |3-5| T). Solid lines are a guide to the eye.

The SMM properties of compounds **27** and **28** were further probed by dynamic magnetic susceptibility measurements across temperature ranges of 1.9-75 and 2-62 K, respectively. The $\chi''(\nu)$ plots for both systems are similar, with maxima in the temperature range of 1.9-55 K (Figures 118, 119). The data suggest that below 4 K the magnetic relaxation is dominated by QTM, which is consistent with the hysteresis measurements. Above 5 K, thermally activated relaxation processes dominate.

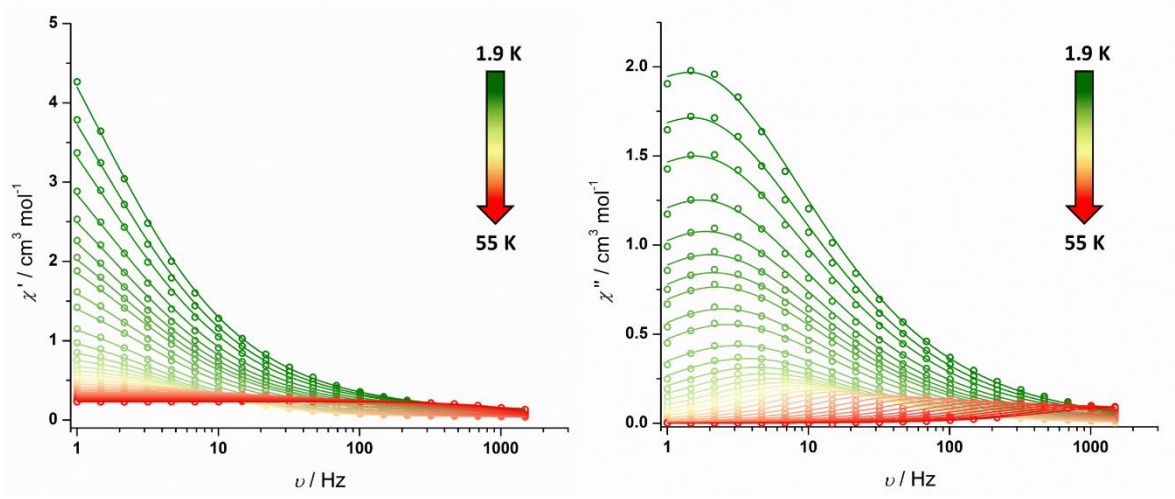

Figure 118. Frequency-dependence of the in-phase (χ') (left) and out-of-phase (χ'') (right) susceptibility for **27** in zero DC field at ν = 1-1488 Hz and temperatures of 1.9 to 55 K. Solid lines represent fits to the data using Equation 1.

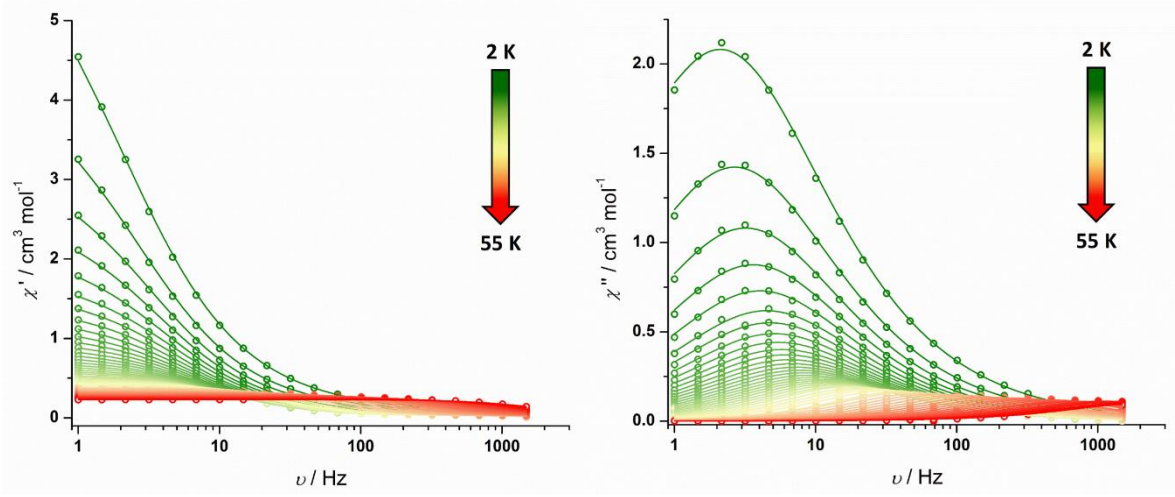

Figure 119. Frequency-dependence of the in-phase (χ') (left) and out-of-phase (χ'') (right) susceptibility for **28** in zero DC field at ν = 1-1488 Hz and temperatures of 2 to 55 K. Solid lines represent fits to the data using Equation 1.

Cole-Cole plots for **27** and **28** in the temperature ranges of 1.9-55 and 2-55 K, respectively, are also very similar. Fits of the data to the generalised Debye model shown in Equation 1 (Figures 120-123, Supplementary Tables S16, S17) show a good agreement with the experimental data, with α-parameters ranging from 0.06-0.35 and 0.09-0.27, and τ values ranging from 0-0.11 and 0-0.075 s, for **27** and **28**, respectively.

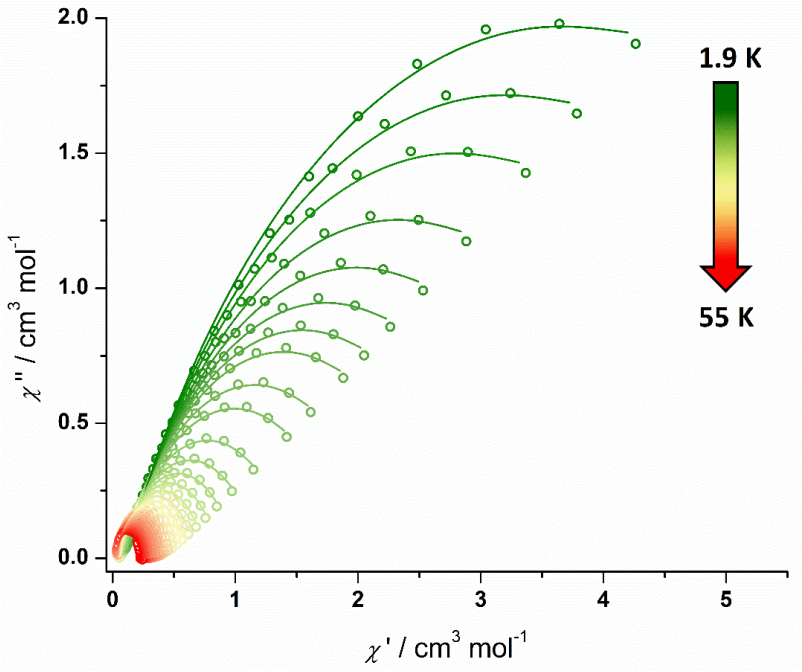

Figure 120. Cole-Cole plots for the AC susceptibilities in zero DC field for **27** from 1.9-55 K. Solid lines represent fits to the data using Equation 1.

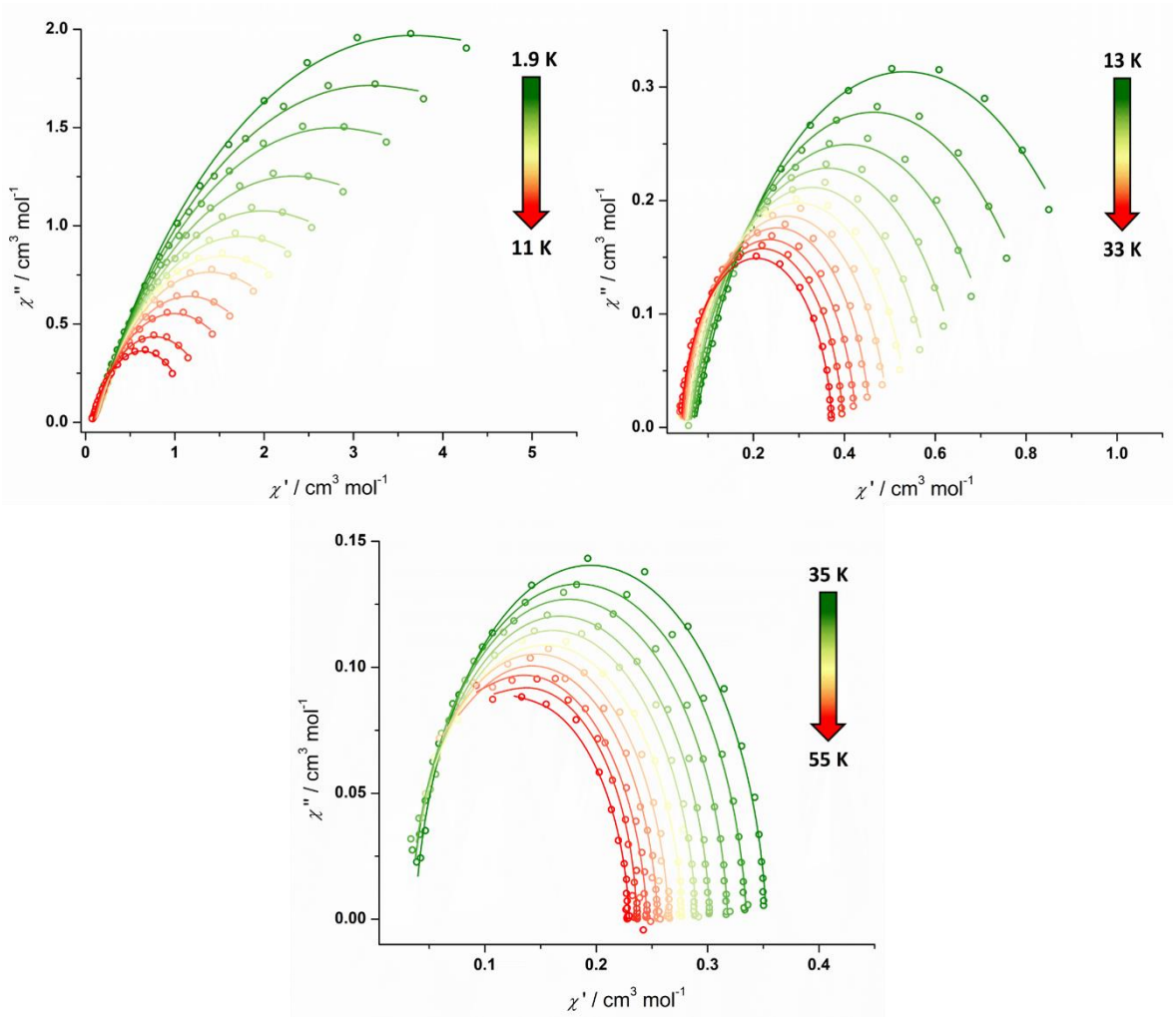

Figure 121. Cole-Cole plots for the AC susceptibilities in zero DC field for **27** from 1.9-11 K (top left), 13-33 K (top right) and 35-55 K (bottom). Solid lines represent fits to the data using Equation 1.

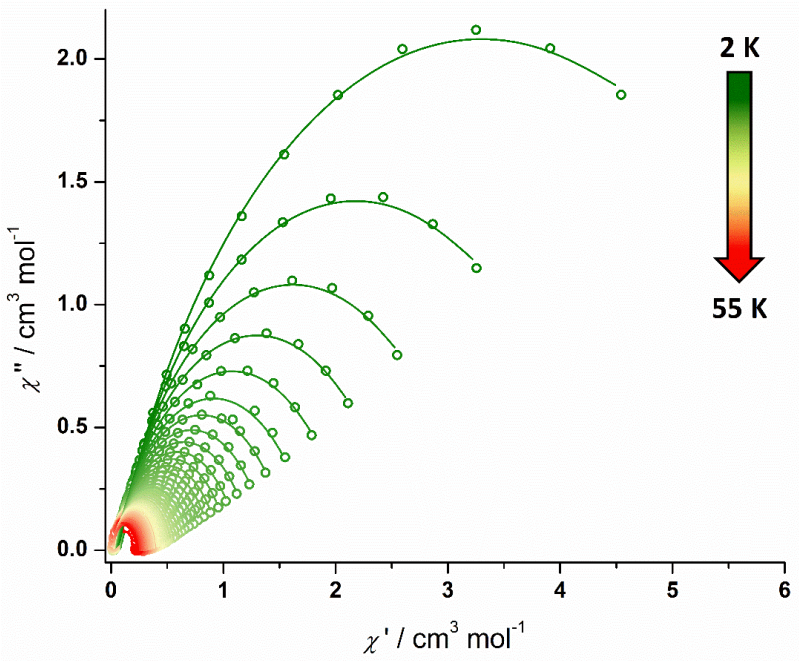

Figure 122. Cole-Cole plots for the AC susceptibilities in zero DC field for **28** from 2-55 K. Solid lines represent fits to the data using Equation 1.

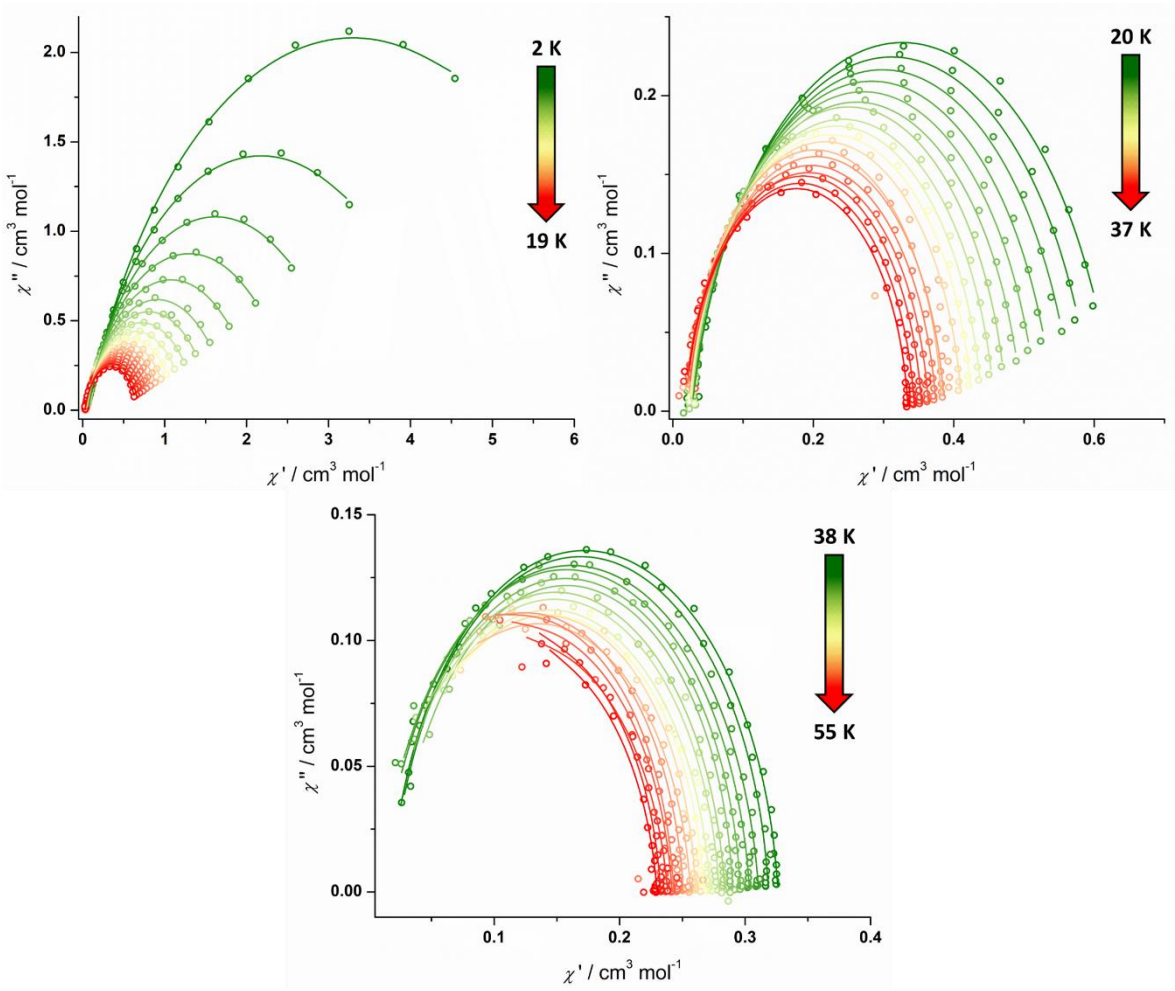

Figure 123. Cole-Cole plots for the AC susceptibilities in zero DC field for **28** from 2-19 K (top left), 20-37 K (top right) and 38-55 K (bottom). Solid lines represent fits to the data using Equation 1.

Plotting ln τ against T^{-1} for compound **27** reveals features corresponding to different relaxation mechanisms across the measured temperature range. Fitting the data to Equation 2 incorporating Orbach, Raman and QTM processes, gives an R^2 = 0.99945 and values of U_{eff} = 213(3) cm^{-1}, τ_0 = 4.76(5) × 10^{-7} s, C = 0.34(8) s^{-1} K^{-n}, n = 1.58(8) and τ_{QTM} = 0.114(5) s (Figure 124, red line). Similar to **26** (discussed in section 3.2.5.), theoretical calculations on **27** indicated that the experimental energy barrier is significantly lower than the calculated values, with the most likely transition occurring via the second or third excited KDs at 447 or 602 cm^{-1}, respectively (discussed in section 3.2.9.). Therefore, a second fit was investigated with the U_{eff} fixed at the value of the second excited KD of 447 cm^{-1}, which yielded an R^2 = 0.98858 and values of τ_0 = 9.8(2) × 10^{-10} s, C = 5(5) × 10^{-5} s^{-1} K^{-n}, n = 4.5(3) and τ_{QTM} = 0.075(5) s (Figure 124, blue line).

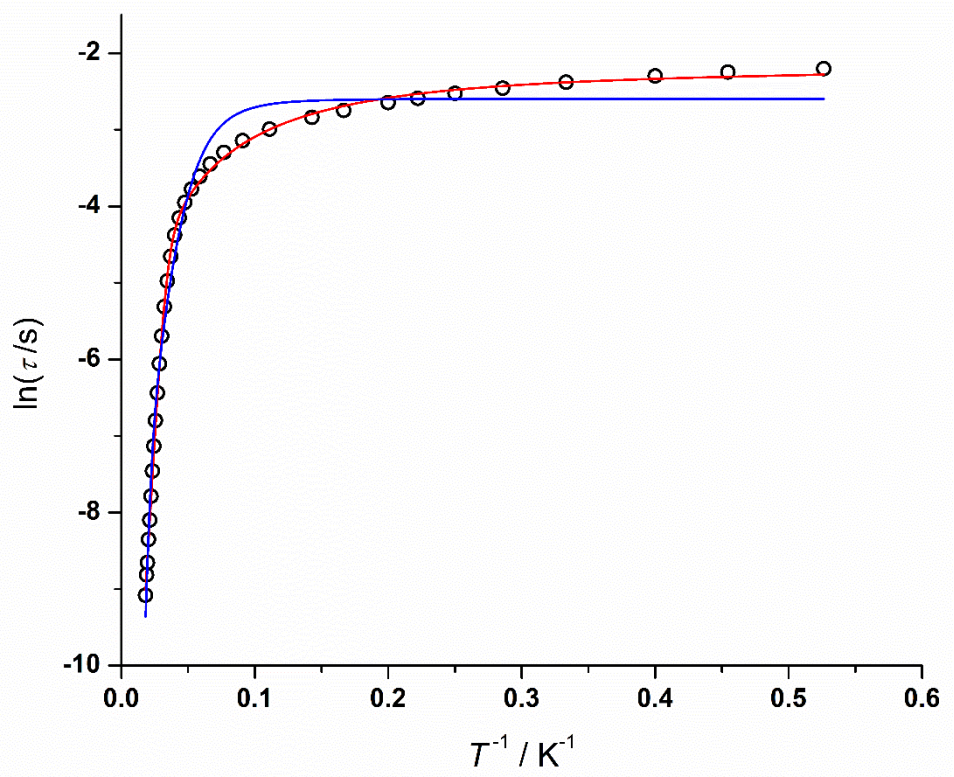

Figure 124. Plot of natural log of the relaxation time (τ) vs. inverse temperature for **27**. The black points are from the AC susceptibility measurements. The solid red line is the best fit (adjusted R^2 = 0.99945) to $\tau^{-1} = \tau_0^{-1}e^{-U_{eff}/k_BT} + CT^n + \tau_{QTM}^{-1}$, giving: U_{eff} = 213(3) cm^{-1}, τ_0 = 4.76(5) × 10^{-7} s, C = 0.34(8) s^{-1} K^{-n}, n = 1.58(8) and τ_{QTM} = 0.114(5) s. The solid blue line is the best fit (adjusted R^2 = 0.98858) to $\tau^{-1} = \tau_0^{-1}e^{-U_{eff}/k_BT} + CT^n + \tau_{QTM}^{-1}$, giving: U_{eff} (fixed) = 447 cm^{-1}, τ_0 = 9.8(2) × 10^{-10} s, C = 5(5) × 10^{-5} s^{-1} K^{-n}, n = 4.5(3) and τ_{QTM} = 0.075(5) s.

For the separated ion pair **28**, the lnτ(T^{-1}) plot and theoretical calculations were comparable to the contact ion **27**. A fit to the data using Equation 2 gives an R^2 = 0.99899

and values of U_{eff} = 222(3) cm^{-1}, τ_0 = 2.69(3) × 10^{-7} s, C = 0.8(2) s^{-1} K^{-n}, n = 1.38(9) and τ_{QTM} = 0.076(7) s (Figure 125, red line). A second fit was additionally investigated to match the energy barrier of the theoretically predicted second excited KD at 434 cm^{-1}, which yielded an R^2 = 0.99013 and values of τ_0 = 1.2(2) × 10^{-9} s, C = 5(4) × 10^{-6} s^{-1} K^{-n}, n = 5.2(3) and τ_{QTM} = 0.035(2) s (Figure 125, blue line).

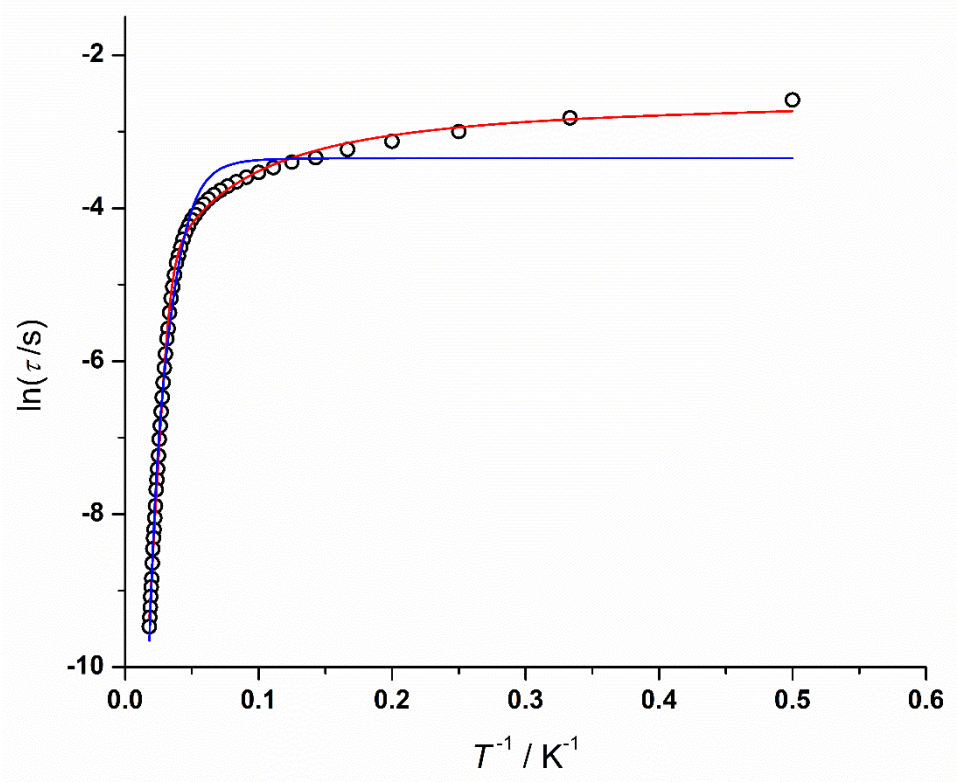

Figure 125. Plot of natural log of the relaxation time (τ) vs. inverse temperature for **28**. The black points are from the AC susceptibility measurements. The solid red line is the best fit (adjusted R^2 = 0.99899) to $\tau^{-1} = \tau_0^{-1}e^{-U_{\mathrm{eff}}/k_{\mathrm{B}}T} + CT^n + \tau_{QTM}^{-1}$, giving: U_{eff} = 222(3) cm^{-1}, τ_0 = 2.69(3) × 10^{-7} s, C = 0.8(2) s^{-1} K^{-n}, n = 1.38(9) and τ_{QTM} = 0.076(7) s. The solid blue line is the best fit (adjusted R^2 = 0.99013) to $\tau^{-1} = \tau_0^{-1}e^{-U_{\mathrm{eff}}/k_{\mathrm{B}}T} + CT^n + \tau_{QTM}^{-1}$, giving: U_{eff} (fixed) = 434 cm^{-1}, τ_0 = 1.2(2) × 10^{-9} s, C = 5(4) × 10^{-6} s^{-1} K^{-n}, n = 5.2(3) and τ_{QTM} = 0.035(2) s

For both **27** and **28**, fits to the experimental data using the theoretically determined energy barriers corresponding to the second excited KDs are significantly worse, which seem to underestimate the Raman components and overestimate the QTM. This is evidenced by the much lower values for the Raman coefficients (C) with a more pronounced curvature of the fit, with the τ_{QTM} values also being lower and displaying stronger temperature-dependence at low temperatures.

Based on the solid-state structures of **27** and **28**, in which the structural parameters are similar, their SMM properties can be qualitatively described by each Dy^{3+} metal centre experiencing a strong axial crystal field from the Cb^{2-} ligand. However, the Pn^{2-} ligand envelops the Dy^{3+} ion and introduces a competing equatorial ligand field via the wing-tip carbons, which is consistent with the reported properties of the cyclopentadienyl derivative [Dy{η^8-$C_8(Si^iPr_3)_2H_4$}(η^5-Cp*)].[100] By comparing the structural parameters of these mixed-sandwich complexes (Table 6), it is clear that the Cb^{2-} ligands once again dominate the crystal field when compared to an analogous Cp ligand, with shorter dysprosium centroid distances occurring at the expense of the Pn^{2-} ligands, resulting in larger energy barriers.

Table 6. Structural parameters and SMM properties of analogous dysprosium pentalene complexes with cyclopentadienyl and cyclobutadienyl ligands.

Compound	Dy-C(ring)$_c$ / Å	Bend Angle / °	U_{eff} / cm^{-1}	ref
[Dy{η^8-$C_8(Si^iPr_3)_2H_4$}(η^5-Cp*)]	2.235(3) (Pn), 2.344(5) (Cp*)	152.47(11), 153.05(11)	188(11)	100
27 [Dy{η^8-$C_8(Si^iPr_3)_2H_4$}{η^4-$C_4(SiMe_3)_4$}K(THF)]	2.282(5) (Pn), 2.300(4) (Pn), 2.306(11) (Cb)	156.4(3), 154.2(3)	213(3)	This work
28 [K(18-c-6)(THF)$_2$]$^+$[Dy{η^8-$C_8(Si^iPr_3)_2H_4$}{η^4-$C_4(SiMe_3)_4$}]$^-$	2.301(6) (Pn), 2.296(4) (Pn), 2.294(3) (Cb)	152.89(12), 157.46(17)	222(3)	This work

*3.2.9. Theoretical calculations on [Dy{η^8-$C_8(Si^iPr_3)_2H_4$}{η^4-$C_4(SiMe_3)_4$}K(THF)] (**27**) and [Dy{η^8-$C_8(Si^iPr_3)_2H_4$}{η^4-$C_4(SiMe_3)_4$}]$^-$*

The low-lying electronic states of **27** and the complex anion of **28** were investigated by multireference *ab initio* calculations on models constructed using coordinates of atoms from the solid-state molecular structures, with positions of hydrogen atoms optimized

using DFT calculations. The properties of the eight lowest Kramers' doublets (KD) arising from the crystal field splitting of the ground $^6H_{15/2}$ multiplet of the Dy^{3+} ions are listed in the Supplementary Tables S26 and S27, with the principal magnetic axes of the ground KDs shown in Figure 126 (blue arrow).

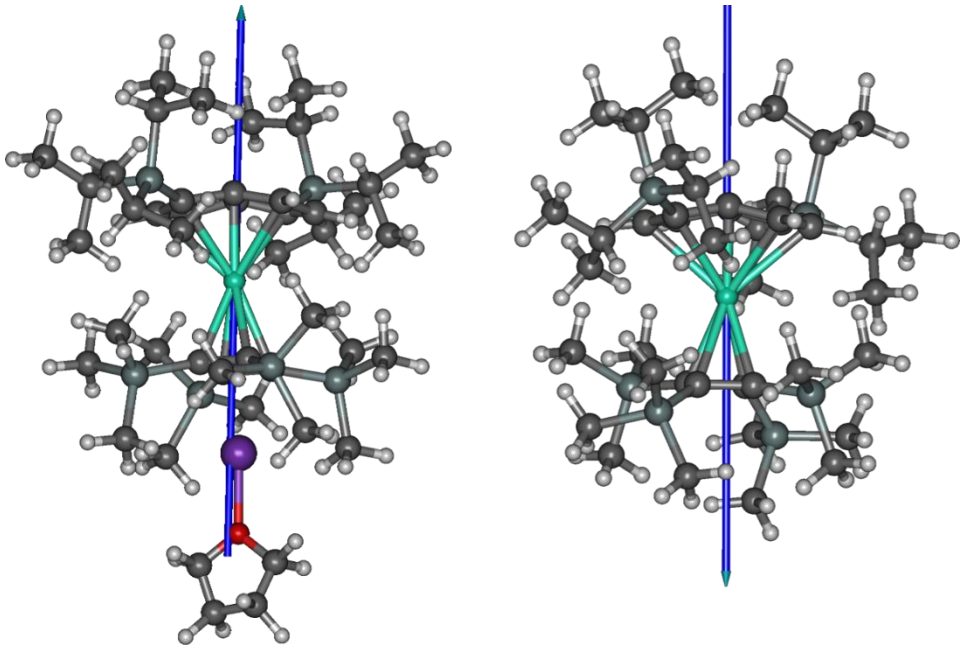

Figure 126. The principal magnetic axes of the ground Kramers' doublets (blue arrows) calculated for the Dy^{3+} ion in **27** (left) and **28** (right). Dy = green, Si = light grey, K = purple, O = red, C = black, H = white.

The principal magnetic axes in the ground KDs for **27** and **28** are both strongly axial, with the axiality also being retained in the lowest excited KDs. This is indicative that a strong crystal ligand field around Dy^{3+} is induced by the dianionic Cb^{2-} and Pn^{2-} ligands. This is further reflected from analysis of the *g*-tensors, in which the transverse components only become notable in the second excited KDs and are significant in the third excited doublets (for **27**, g_x = 0.424, g_y = 0.510, for **28**, g_x = 0.212, g_y = 0.27). These *g*-tensors would suggest that magnetic relaxation by Orbach mechanisms would most likely take place via the second or third excited KDs, which have a U_{eff} = 447 or 602, and 434 or 593 cm^{-1} for **27** and **28**, respectively (Figure 127, Supplementary Tables S28, S29). However, in both cases the experimental relaxation data is much closer to the energy of the first excited KDs of 236 and 228 cm^{-1} for **27** and **28**, respectively. These discrepancies led us to investigate different fits to the experimental relaxation time data as we had previously done with compound **26**. By fixing the U_{eff} to the energy barriers of the second excited KDs determined by the

calculations, in both cases poor fits are obtained that seem to underestimate the Raman components and overestimate QTM (see Figures 124, 125). Therefore, the experimental fits corresponding to a barrier crossing at the first excited KD are the most reasonable, which indicates that the axiality of the crystal field is somewhat overestimated in the calculations. The discrepancies between experiment and calculations could be due to the spin-phonon interactions not being properly considered in the relaxation model based on transition dipole magnetic moments.[146]

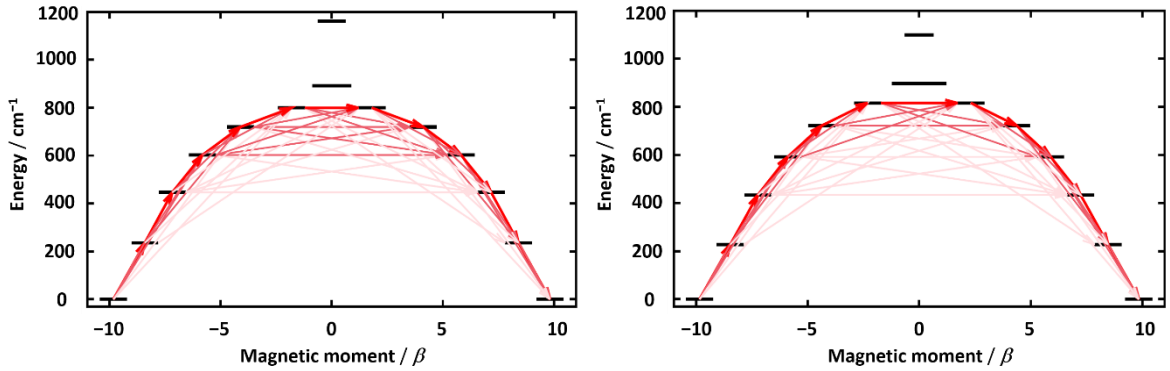

Figure 127. Calculated effective *ab initio* barriers for the relaxation of magnetization in **27** (left) and **28** (right). The arrows represent transition magnetic moments, with stronger arrows indicating larger values.

Further calculations into the *ab initio* crystal field parameters for **27** and **28** (Supplementary Tables S30-33) reveal negative and relatively large B_2^0 parameters, however the off-diagonal $B_2^{\pm 1}$ and $B_2^{\pm 2}$ parameters also make appreciable contributions reducing the overall axiality. These appreciable off-diagonal parameters can be explained by the wing-tip carbons of the Pn^{2-} ligands, which provide non-axial contributions to the crystal ligand field around the Dy^{3+} ions. Values of Z = 3.79, 5.22 and Z_{rel} = 0.096, 0.132 are calculated for **27** and **28**, respectively, which indicate that the potassium contact-ion in **27** only seems to slightly reduce the axiality in comparison to the separated ion pair **28**. The cyclopentadienyl analogue [Dy{η^8-C_8(Si^iPr_3)$_2H_4$}(η^5-Cp*)], has a Z = 1.18 and Z_{rel} = 0.030. Thus, the larger values for **27** and **28** further establish the dominance of cyclobutadienyl ligands over cyclopentadienyl in the crystal field splitting in Dy^{3+} SMMs.

3.2.10. Conclusions on cyclobutadienyl sandwich SMMs

In this section, the synthesis of the cyclobutadienyl rare-earth sandwich complexes **19**-**28** was described, which have all been isolated without activation of the trimethylsilyl substituents. The cyclobutadienyl ligands in **19**-**28** dominate the crystal field around Ln^{3+}, with shorter Ln-Cb centroid distances when compared to analogous Ln-Cp distances in structurally similar cyclopentadienyl complexes. The shorter interaction between Cb^{2-} and Ln^{3+} in the mixed sandwich complexes occur at the expense of the other Cp^{-} or Pn^{2-} ligands, which are pushed away from the metal.

The static and dynamic magnetic properties of $[Na(15\text{-}c\text{-}5)(THF)_2]^+[Dy\{\eta^4\text{-}C_4(SiMe_3)_4\}(\eta^5\text{-}C_5Me_4{}^tBu)(\kappa^2\text{-}BH_4)]^-$ (**26**), $[Dy\{\eta^8\text{-}C_8(Si^iPr_3)_2H_4\}\{\eta^4\text{-}C_4(SiMe_3)_4\}K(THF)]$ (**27**) and $[K(18\text{-}c\text{-}6)(THF)_2]^+[Dy\{\eta^8\text{-}C_8(Si^iPr_3)_2H_4\}\{\eta^4\text{-}C_4(SiMe_3)_4\}]^-$ (**28**) were investigated by SQUID magnetometry, with the complexes all showing typical Dy^{3+} traits. Dynamic measurements in zero DC field revealed slow magnetic relaxation properties, with Orbach processes dominating the relaxation at higher temperatures (31-5 K for **26**, 55-5 K for **27** and **28**), and a strong influence of QTM at lower temperatures (>5 K). Fitting the relaxation data with Orbach, Raman and QTM parameters results in a U_{eff} = 242 cm^{-1} for **26**, 213(3) cm^{-1} for **27**, and 222(3) cm^{-1} for **28**. Magnetic hysteresis measurements on all complexes reveal waist-restricted loops at 1.9 K, indicative of the strong QTM in the systems. Comparisons of **26** with analogous Cp sandwich complexes **17** and $[Dy(\eta^5\text{-}C_5{}^iPr_5)(\eta^5\text{-}Cp^*)(\kappa^2\text{-}BH_4)]$, which have a U_{eff} = 36(2) and 7(1) cm^{-1}, respectively, reveal a marked improvement upon the energy barriers. Comparisons of **27** and **28** with the Cp* analogue $[Dy\{\eta^8\text{-}C_8(Si^iPr_3)_2H_4\}(\eta^5\text{-}Cp^*)]$, also reveal an improvement upon the SMM properties, by *ca.* 25 and 34 cm^{-1}, respectively. The improved properties are ascribed to the stronger axial crystal field provided by the cyclobutadienyl ligands.

Ab initio calculations on **26**-**28** confirmed that the cyclobutadienyl ligands provide a strong axial crystal field interaction in relation to Dy^{3+}, with the principal magnetic axes of the ground KDs clearly orientated towards the Dy-Cb axis. However, significant transverse components arise due to the equatorial borohydride ligand in **26**, and the wing-tip carbons of the folded pentalene ligands in **27** and **28**.

The main finding is that the dianionic cyclobutadienyl ligand can replace cyclopentadienyl ligands in structurally similar dysprosium SMMs, resulting in improved effective energy barriers. Considering the dramatic improvement of the SMM properties when the equatorial borohydride ligand of [Dy(η^5-$C_5{}^iPr_5$)(η^5-Cp*)(κ^2-BH_4)] is removed and converted into the current benchmark SMM [Dy(η^5-$C_5{}^iPr_5$)(η^5-Cp*)]$^+$, the increase in the energy barrier of **26** relative to that of [Dy(η^5-$C_5{}^iPr_5$)(η^5-Cp*)(κ^2-BH_4)] is significant. Thus, if a pseudo-axial cyclobutadienyl complex of the type [Dy(η^4-Cb)$_2$]$^-$ or [Dy(η^4-Cb)(η^5-Cp^R)] could be synthesized, it is likely that they would display a stronger crystal field splitting, and hence, could surpass the current records set by a bis-cyclopentadienyl dysprosium metallocene complex.

All attempts to abstract the borohydride ligands have so far proved unsuccessful. This could be a consequence of incorrect reaction conditions, or that the combination of Cb / Cp ligands investigated in this study do not possess the ideal steric bulk in order to stabilise the target [Dy(η^4-Cb)(η^5-Cp^R)] complex. Nevertheless, the results presented in this chapter have further established the potential of the cyclobutadienyl ligand in supporting high-performance dysprosium SMMs.

Chapter 4

Cyclobutadienyl Rare-Earth Complexes from Direct Reduction of Cyclobutadiene with Rare-Earth Metals

4.1. Cyclobutadienyl Rare-Earth Complexes from Metallic Lanthanides and Iodine

4.1.1. Background

The majority of rare-earth organometallic compounds are synthesized using salt metathesis and transmetalation reactions. In contrast, the synthesis of compounds using metallic rare-earth sources is less common. Metal-vapor synthesis (MVS) is one possible route to novel complexes utilising metallic lanthanides, however this technique requires specialist equipment and is limited in scope.[65–68] Another route involves redox transmetalation and ligand exchange reactions between metallic lanthanides, organometallic reagents such as diorganomercurials, and pro-ligands such as phenols, amines or cyclopentadiene.[150–154]

The redox reactions between metallic lanthanides and a pro-ligand in the presence of an additional oxidant offers a convenient and atom-economical synthetic pathway. Nakamura and co-workers have used this approach to reduce COT with lanthanide metals in the presence of iodine to form the monomeric complexes [Ln(η^4-C_8H_8)I(THF)$_n$] (Ln = La, Ce, Pr, Nd and Sm) (Scheme 33).[155]

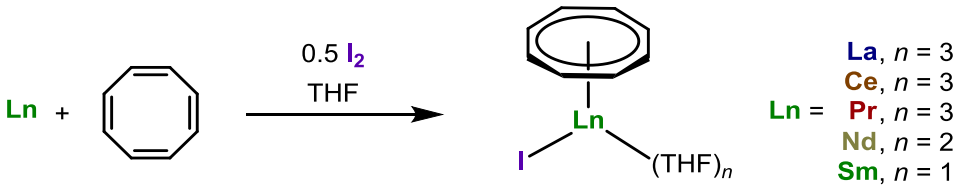

Scheme 33. Reported synthesis of [Ln(η^4-C_8H_8)I(THF)$_3$] (Ln = La, Ce, Pr, Nd and Sm).

This reactivity can be extended to many other pro-ligands and oxidants, which typically form dimeric complexes.[156] Anwander and co-workers have reported how a THF ligand in the monometallic complex [La(η^4-C_8H_8)I(THF)$_3$] can be displaced in a competing Lewis acid/base reaction with $AlMe_3$ to form a dimeric iodide-bridged complex [La(η^8-C_8H_8)(μ-I)(THF)$_2$]$_2$ (Scheme 34, Figure 128).[157]

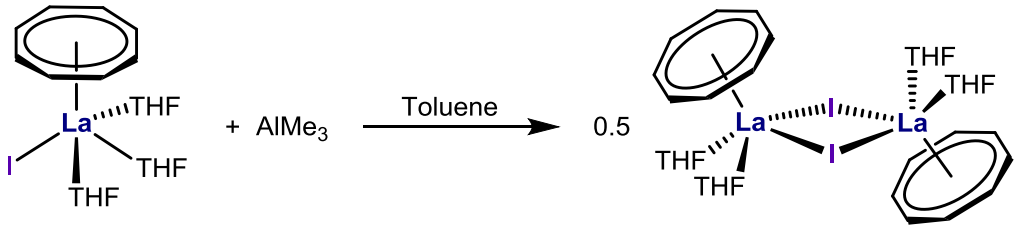

Scheme 34. Reported synthesis of $[La(\eta^8\text{-}C_8H_8)(\mu\text{-}I)(THF)_2]_2$.[157]

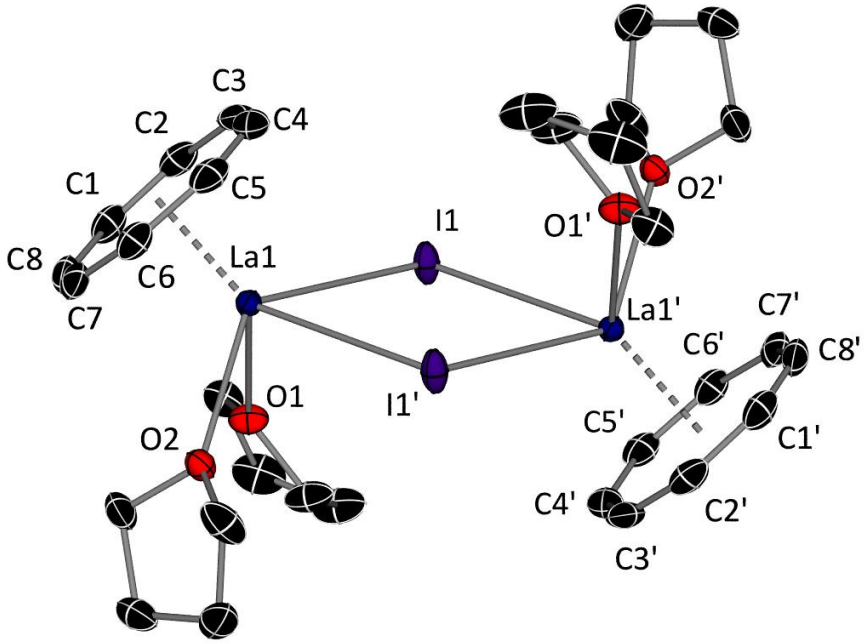

Figure 128. Molecular structure of $[La(\eta^8\text{-}C_8H_8)(\mu\text{-}I)(THF)_2]_2$. Thermal ellipsoids are set to 50 % probability and hydrogen atoms have been omitted for clarity.[157]

In this section, the reactivity of the neutral cyclobutadiene pro-ligand $[C_4(SiMe_3)_4]$ (**7**) and rare-earth metals in the presence of iodine is described. The main discovery is an alternative synthetic route to cyclobutadienyl rare-earth organometallic complexes.

*4.1.2. Synthesis and characterisation of $[Ln\{\eta^4\text{-}C_4(SiMe_3)_4\}(\mu\text{-}I)(THF)_2]_2$ (Ln = La (**29**), Ce (**30**), Pr (**31**), Sm (**32**)).*

The synthesis of the cyclobutadienyl iodide-bridged complexes $[Ln\{\eta^4\text{-}C_4(SiMe_3)_4\}(\mu\text{-}I)(THF)_2]_2$ (Ln = La (**29**), Ce (**30**), Pr (**31**), Sm (**32**)) was achieved by reduction of cyclobutadiene (**7**) in the presence of the corresponding lanthanide metal and half an equivalent of iodine (Scheme 35). After initial sonication of the reaction mixture, the

reactions were left to stir at room temperature for three days, by which time the initial red solutions had darkened. After subsequent work up, storing a saturated THF solution layered with hexane at –40 °C for three days resulted in the formation of orange, dark red or dark green crystals of **29**, **30** or **32**, in isolated yields of 68, 58 and 71 %, respectively. In the case of **31**, an isolated yield of 36 % was obtained after removal of $[PrI_3(THF)_4]$ by fractional crystallization.

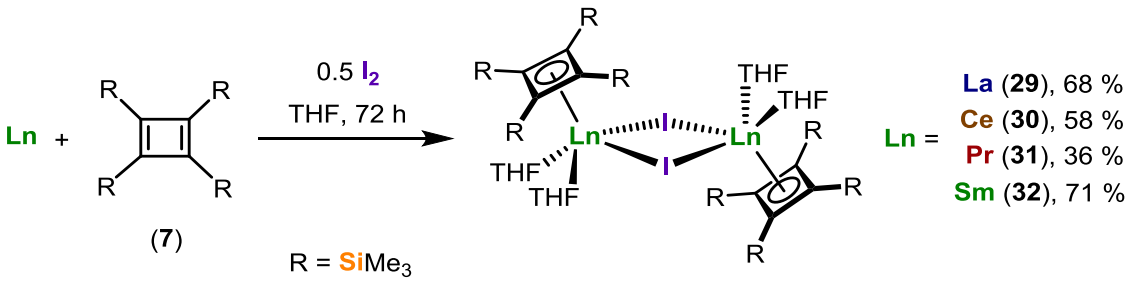

Scheme 35. Synthesis of **29**-**32**.

Compounds **29**-**32** are isostructural, all featuring an η^4-coordination mode of the cyclobutadienyl ligand, with two THF ligands and an iodide coordinated to the trivalent Ln^{3+} centre. A crystallographic inversion centre is located in the $\{Ln_2I_2\}$ ring, resulting in an iodide-bridged dimeric complex (Figure 129). This contrasts to prevously reported reactivity of COT, which form monomers under the same reaction conditions. In all complexes, the C_4 rings are square-shaped, confirming that Cb has been reduced to the dianion. For **29**, the C-C bond distances range from 1.480(6)-1.487(6) Å, and the La-C bond distances range from 2.591(4)-2.663(4) Å, resulting in an La-Cb centroid distance of 2.4073(3) Å. The $SiMe_3$ groups reside out of the plane of the C_4 ring by 0.447(8)-0.610(8) Å and are oriented away from the metal, with an average C(ring)-Si distance of 1.848 Å.

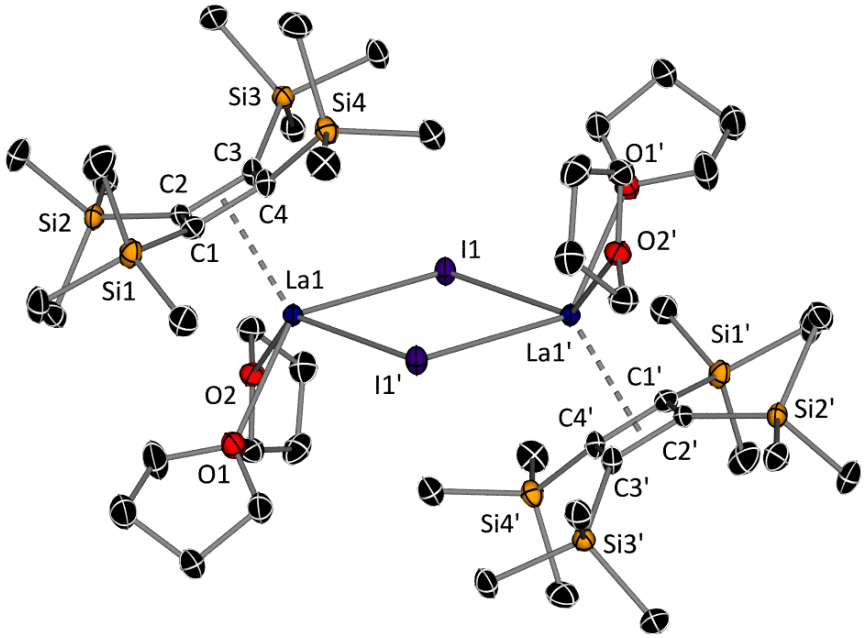

Figure 129. Molecular structure of $[La\{\eta^4\text{-}C_4(SiMe_3)_4\}(\mu\text{-}I)(THF)_2]_2$ (**29**). Thermal ellipsoids are set to 50 % probability and hydrogen atoms have been omitted for clarity. Selected bond distances (Å) and angles (°) for **29**: C1-C2 1.481(6), C2-C3 1.480(6), C3-C4 1.486(6), C1-C4 1.487(6), C1-Si1 1.843(5), C2-Si2 1.851(4), C3-Si3 1.859(4), C4-Si4 1.840(4), La1-Cb_{cent} 2.4073(3), La1-I1 3.2722(4), La1-O1 2.624(3), La1-O2 2.561(3), La1-I1' 3.2830(4), La1···La1' 4.9065(4), La1-I1-La1' 96.917(9), I1-La1-I1' 83.083(9).

A comparison of selected structural parameters for **29**-**32** is shown in Table 7. Moving across the lanthanide series from **29**-**32**, the Ln-C, Ln-Cb_c and Ln-I distances decrease slightly, which is consistent with the slight reduction in ionic radii of Ln^{3+}. In the structurally similar COT complex $[La(\eta^8\text{-}C_8H_8)(\mu\text{-}I)(THF)_2]_2$,[157] the La-C bond distances are significantly longer and range from 2.720(2)-2.753(7) Å. The La-I distance in the COT complex is longer by *ca.* 0.11 Å when compared to the analogous distance in **29**, which is presumably a consequence of the large COT ligand allowing for a closer approach to the metal centre. This is reflected in the reduced La-COT centroid distance of 2.0250(11) Å, and an increased La-I-La' bending angle of *ca.* 8.2°, *i.e.* 96.917(9) *vs.* 105.112(6)°.

Table 7. Structural parameters for the cyclobutadienyl lanthanide iodide-bridged complexes **29**-**32**.

Compound	Ln-C / Å	Ln-Cb_c / Å	Ln-I, Ln-I' / Å	Ln-I-Ln' / °
29 [La{η^4-$C_4(SiMe_3)_4$}(μ-I)$(THF)_2$]$_2$	2.591(4)-2.663(4)	2.4073(3)	3.2722(4), 3.2830(4)	96.917(9)
30 [Ce{η^4-$C_4(SiMe_3)_4$}(μ-I)$(THF)_2$]$_2$	2.575(4)-2.649(4)	2.3934(2)	3.2357(4), 3.2503(4)	97.828(10)
31 [Pr{η^4-$C_4(SiMe_3)_4$}(μ-I)$(THF)_2$]$_2$	2.545(7)-2.634(7)	2.3694(5)	3.2252(8), 3.2148(7)	98.241(17)
32 [Sm{η^4-$C_4(SiMe_3)_4$}(μ-I)$(THF)_2$]$_2$†	2.524(5)-2.555(7)	2.30861(19)	3.1978(3), 3.2021(3)	100.068(7)

† For the highest occupancy component in the crystal structure.

The ^{1}H NMR spectrum of **29** in D_8-THF shows the expected signals for the THF ligands at 3.61 (m, 8H) and 1.77 (m, 8H) ppm, and the $SiMe_3$ groups at 0.21 ppm (s, 36H) (Figure 130). In the $^{13}C\{^1H\}$ NMR spectrum of **29** in D_8-THF, signals can be observed at 138.57 and 5.10 ppm, corresponding to the C_4 ring and the $SiMe_3$ groups, respectively, and additional signals at 68.38 and 26.51 ppm can be seen for the THF ligands (Figure S79). The $^{29}Si\{^1H\}$ spectrum displays a signal at −20.84 ppm, which is in a similar range to all previously characterised diamagnetic lanthanide cyclobutadienyl complexes in this thesis (Figure 130 inset, Figure S80).

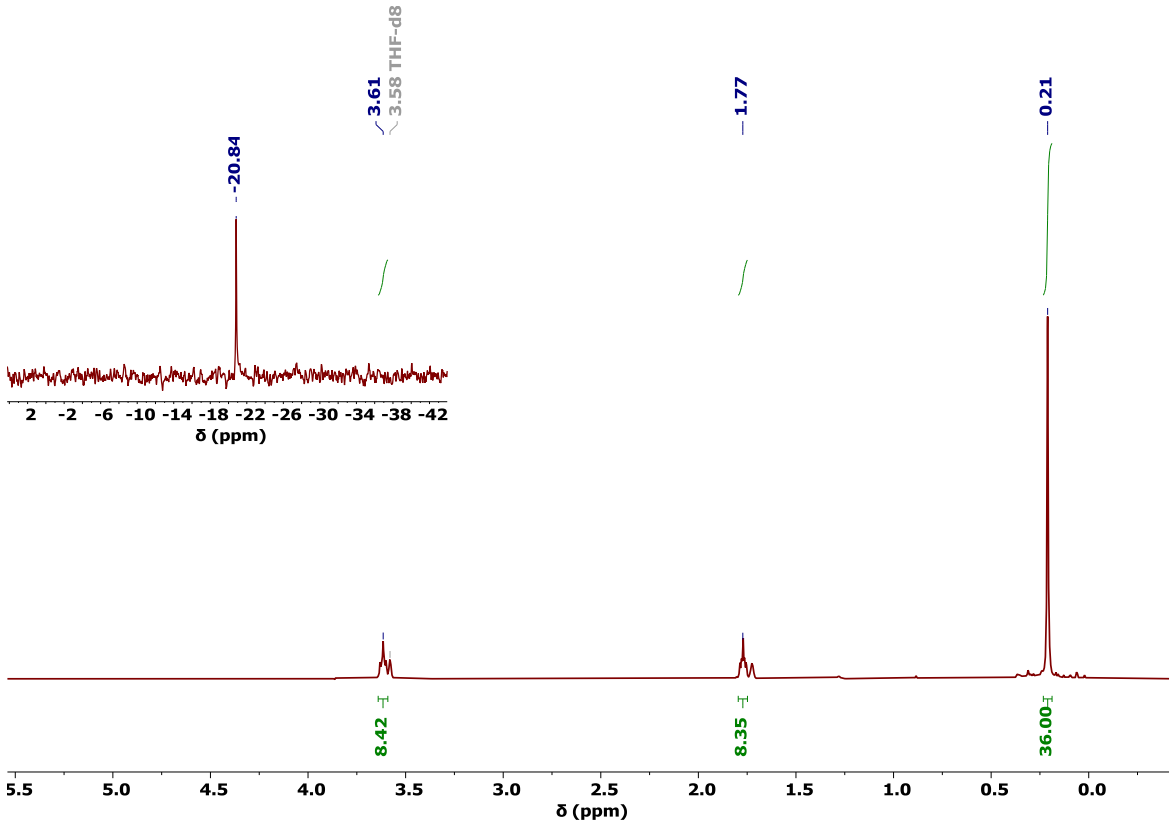

Figure 130. ^{1}H NMR spectrum of **29** in D_8-THF. Inset: ^{29}Si{^{1}H} NMR spectrum of **29**.

The paramagnetic compounds **30**-**32** were also characterised by NMR spectroscopy in D_8-THF, with the cerium and praseodymium compounds **30** and **31** both displaying broad signals in the ^{1}H NMR spectra corresponding to the $SiMe_3$ groups centred at 0.26 (FWHM = 220 Hz) and −1.26 ppm (FWHM = 800 Hz), respectively (Figures S82, S84). In the case of **30**, a broad signal in the ^{13}C{^{1}H} NMR spectrum corresponding to the $SiMe_3$ groups at 11.43 ppm could be observed, however a signal for the C_4 ring could not be observed (Figure S83). Additionally, no signals could be observed in the ^{13}C{^{1}H} NMR spectrum of **31**, or the ^{29}Si{^{1}H} and ^{29}Si-^{1}H heteronuclear multiple bond correlation (HMBC) NMR spectra of **30** and **31**. For the samarium compound **32**, a sharp signal corresponding to the $SiMe_3$ groups could be observed in the ^{1}H NMR spectrum at −0.05 ppm (FWHM = 7 Hz), as well as the expected signals in the ^{13}C{^{1}H} NMR at 103.38 and −0.77 ppm for the C_4 ring and $SiMe_3$ groups, respectively (Figures S85, S86). The ^{29}Si{^{1}H} NMR spectrum of **32** displayed a signal at 1.80 ppm, which is significantly shifted when compared to the typical value of *ca.* −20 ppm for diamagnetic cyclobutadienyl complexes (Figure S87). As expected due to their structural similarity, the FTIR spectra of compounds **29**-**32** are comparable, with absorptions at almost exactly the same frequencies in the range $\tilde{\nu}$ = 4000-450 cm^{-1} and C-H stretches at

3000-2850 cm^{-1} corresponding to the trimethylsilyl groups being the main features (Figure 131).

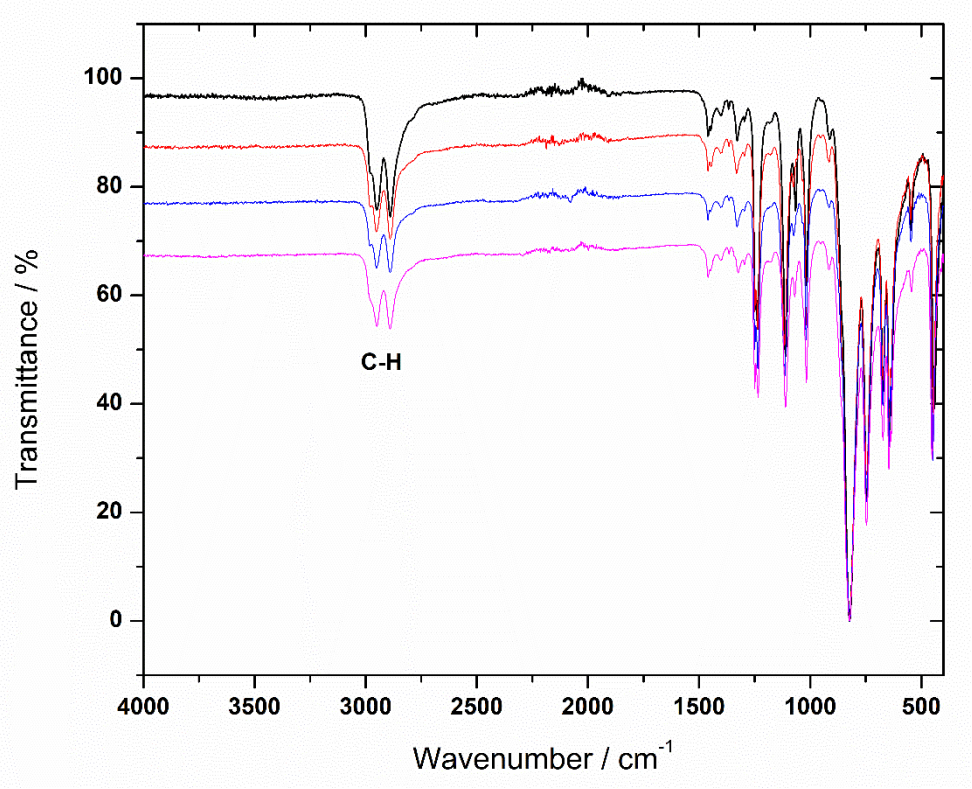

Figure 131. FTIR spectra of **29** (black line), **30** (red line), **31** (blue line) and **32** (magenta line). Selected absorptions (cm^{-1}): 3000-2850 (C-H).

Acquiring accurate elemental analyses compounds **29**-**32** proved to be extremely difficult, with consistently low carbon and hydrogen values obtained for each compound. Representative results being % found (calculated) for each compound as follows: **29** $C_{48}H_{104}La_2I_2Si_8O_4$: C 33.56 (38.39); H 6.07 (6.98), **30** $C_{48}H_{104}Ce_2I_2Si_8O_4$: C 32.08 (38.33); H 5.90 (6.97), **31** $C_{48}H_{104}Pr_2I_2Si_8O_4$: C 35.13 (38.29); H 6.53 (6.96), and **32** $C_{48}H_{104}Sm_2I_2Si_8O_4$: C 35.32 (37.82); H 6.67 (6.88). Due to these consistently low values, iodine analysis was carried out on **29**, which subsequently revealed an increase of the amount of expected iodine by *ca.* 7 %, *i.e.* 24.11 (16.90). As the praseodymium triiodide THF adduct $[PrI_3(THF)_4]$ was formed as a side-product in the reaction of **31**, a plausible explanation of the increased presence of iodine in analysis of **29** could be due to $[LaI_3(THF)_4]$ impurities. Taking this into account, a reasonable fit to the analytical data can be obtained with 0.3 equivalents of $[LaI_3(THF)_4]$ per molecule of $[La\{\eta^4\text{-}C_4(SiMe_3)_4\}(\mu\text{-}I)(THF)_2]_2$, with % found (calculated) for $C_{48}H_{104}La_2I_2Si_8O_4 \cdot 0.3\ C_{16}H_{32}LaI_3O_4$: C 33.56 (34.83); H 6.07 (6.25), I 24.11 (24.28). The slightly lower carbon values could be a consequence of the air-sensitive nature of the

organometallic complexes, which may have decomposed prior to analysis, or incomplete combustion due to the formation carbides.[135]

Izod and co-workers have previously reported the synthesis of $[LnI_3(THF)_4]$ (Ln = La, Pr) and $[LnI_3(THF)_{3.5}]$ (Ln = Nd, Sm, Gd, Dy, Er, Tm, Y) by reacting 1.5 equivalents of elemental iodine and the corresponding rare-earth metals in THF at room temperature.[158] In these reactions, the lanthanide triiodides precipitate out of the reactions after three days and are additionally purified by the removal of excess iodine by sublimation and Soxhlet extraction with THF over several hours. In the synthesis of **29**-**32**, the reactions were left for a similar reaction time (three days), and were filtered twice, once after the reaction was complete and again after re-dissolving the crude products in the minimum amount of THF before crystallization. However, it appears that the lanthanide triiodides retain a degree of solubility in the synthesis of **29**-**32**, even after fractional crystallization in the case of **31**. Compounds **29**-**32** are only sparingly soluble in non-polar solvents such as benzene and toluene, and attempts to recrystallize **29** via extraction with warm toluene (*ca.* 50 °C) resulted in vastly reduced yields (13 %), which were still potentially contaminated with triiodide impurities based on reactivity studies with the recrystallized material (described in section 4.1.4.).

EI-MS analysis on **29**, which has an *m*/*z* = 751 for the monomer $[La\{\eta^4\text{-}C_4(SiMe_3)_4\}I(THF)_2]$ or *m*/*z* = 1502 for the dimer $[La\{\eta^4\text{-}C_4(SiMe_3)_4\}(\mu\text{-}I)(THF)_2]_2$, revealed a molecular ion peak at $[M]^+$ (*m*/*z*): 342, which corresponds to the cyclobutadienyl ligand (*m*/*z* = 341). Subsequent fragmentation of the Cb ligand could also be observed, with molecular ion peaks at $[M]^+$ (*m*/*z*): 269, 239 and 181, *i.e.* 269 = $[M - SiMe_3]$, 239 = $[M - SiMe_3 - Me_2]$, 181 = $[M - (SiMe_3)_2 - Me]$ (Figure S81). This suggests that compound **29** is not thermally stable under the conditions of the EI-MS experiment and may decompose before vapour pressure is achieved. Further evidence for thermal instability was obtained by the attempted sublimation of crystalline **29**, which only resulted in decomposition.

Attempts to synthesise the neodymium and dysprosium analogues of **29**-**32** under the same reaction conditions resulted in the formation of $NdI_3(THF)_{3.5}$ and $DyI_3(THF)_{3.5}$, respectively (Scheme 36).

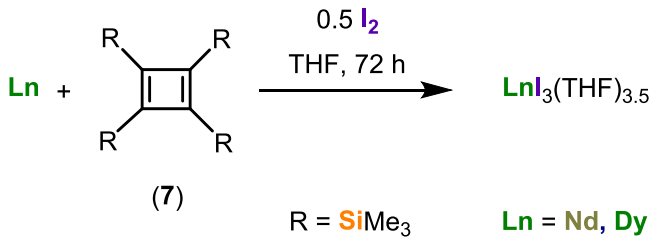

Scheme 36. Attempted synthesis of $[Ln\{\eta^4\text{-}C_4(SiMe_3)_4\}(\mu\text{-}I)(THF)_2]_2$ (Ln = Nd, Dy).

The unsuccessful dysprosium reaction is not surprising, as the smaller rare-earth metals have previously been established to be less reactive when trying to form analogous complexes to the lanthanum COT complex $[La(\eta^8\text{-}C_8H_8)(\mu\text{-}I)(THF)_2]_2$, even under harsher reaction conditions such as high temperature and pressure.[157] However, the unsuccessful neodymium reaction is more of an anomaly, as the synthesis of the Nd monomer $[Nd(\eta^8\text{-}C_8H_8)I(THF)_3]$ has previously been reported under similar reaction conditions using COT instead of Cb.[155,157] Moreover, a cyclobutadienyl iodide-bridged complex of Nd should be feasible based on the size of Nd atoms lying between that of lanthanum and samarium. Further attempts to heat the Nd reaction at 50 °C for three days resulted in decomposition and intractable product mixtures.

*4.1.3. Synthesis and characterisation of $[Ln\{\eta^3\text{-}C_4(SiMe_3)_4H\}(\mu\text{-}I)(THF)_2]_2$ (Ln = Eu (**33**), Yb (**34**)).*

Investigations into the reactivity of europium and ytterbium metals under the same reaction conditions as **29**-**32** did not produce the analogous Eu^{3+} and Yb^{3+} complexes, instead resulting in the synthesis of the protonated cyclobutenyl lanthanide iodide-bridged-bridged complexes $[Ln\{\eta^3\text{-}C_4(SiMe_3)_4H\}(\mu\text{-}I)(THF)_2]_2$ (Ln = Eu (**33**), Yb (**34**)) (Scheme 37). The reactions proceeded in a similar fashion to **29**-**32**, in which the reaction mixtures were intially sonicated and left to stir at room temperature for three days, by which time the solutions had turned much darker. After subsequent work up, storing a saturated THF solution layered with hexane at –40 °C for three days resulted in the formation of yellow crystals subsequently identified as the diiodides $[EuI_2(THF)_5]$ and $[YbI_2(THF)_5]$. After filtering the mother liquor and concentrating the solution, layering the saturated solution with

hexane and storing at –40 °C for a further three days resulted in the formation of yellow-green or dark red crystals of **33** or **34** in isolated in yields of 24 or 33 %, respectively.

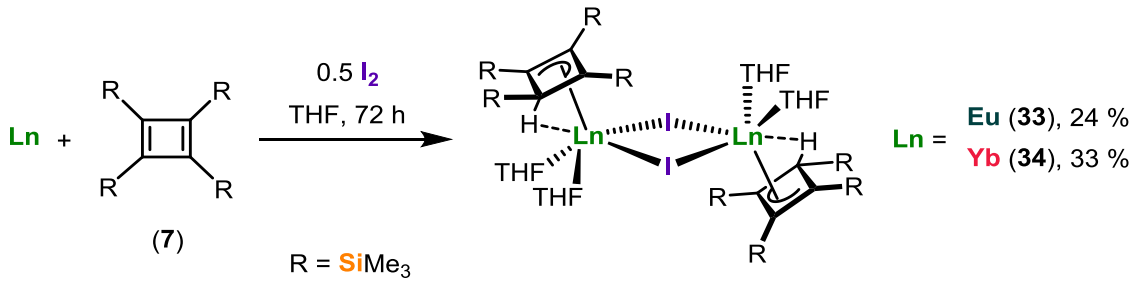

Scheme 37. Synthesis of **33** and **34**.

Compounds **33** and **34** are isostructural, and feature a protonated version of the cyclobutadienyl ligand, which adopts an η^3-cyclobutenyl coordination mode, with two THF ligands and an iodide coordinated to the divalent Ln^{2+} metal centre. As with complexes **29**-**32**, an inversion centre results in the iodide ligands bridging between two metal centres to form a dimeric complex (Figure 132).

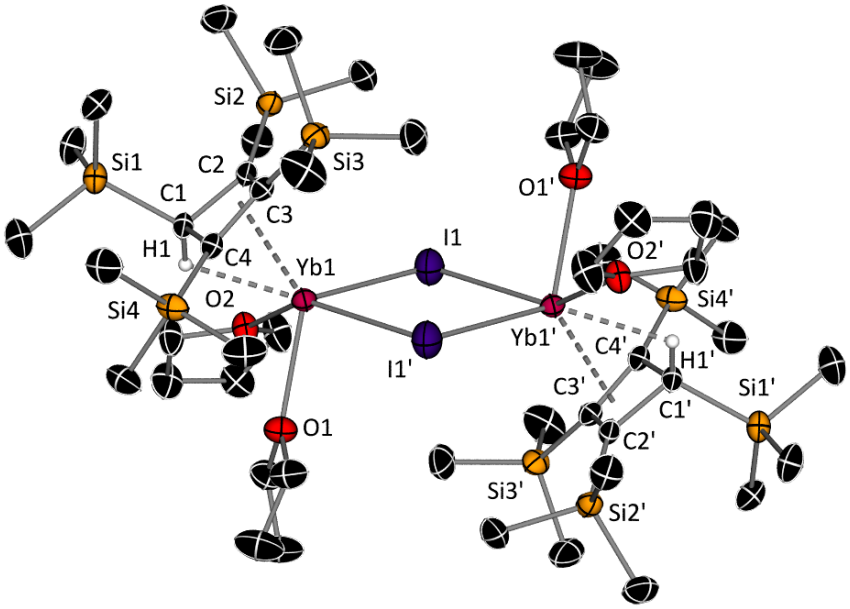

Figure 132. Molecular structure of [Yb{η^3-$C_4(SiMe_3)_4H$}(μ-I)$(THF)_2]_2$ (**34**). Thermal ellipsoids are set to 50 % probability and for clarity, only the hydrogen atoms of the protonated Cb rings are shown. Selected bond distances (Å) and angles (°) for **34**: C1-C2 1.558(9), C2-C3 1.434(10), C3-C4 1.424(10), C1-C4 1.558(9), C1-Si1 1.888(7), C2-Si2 1.843(7), C3-Si3 1.880(7), C4-Si4 1.838(7), Yb1-η^3-Cb_{cent} 2.5121(3), Yb1···H1 2.3700(3), Yb1-I1 3.0406(7), Yb1-O1 2.505(5), Yb1-O2 2.545(5), Yb1-I1' 3.0781(7), Yb1···Yb1' 4.7090(6), Yb1-I1-Yb1' 100.64(2), I1-Yb1-I1' 79.36(2).

In both complexes, the C_4 rings are distorted, with the protonated C1 of **34** residing above the plane of the 'allyl-type' C2-4 by 0.222(15) Å. In **34,** C1 features elongated C-C bond distances to C2 and C4 of 1.558(9) and 1.558(9) Å, with the C-C bond distances for C2-C4 of 1.434(10) and 1.424(10) Å, respectively. The Yb-C bond distances for Yb1-C2, Yb1-C3 and Yb1-C4 are 2.643(7), 2.773(7) and 2.669(7) Å, respectively, resulting in a Yb-η^3-Cb centroid distance of 2.5121(3) Å. These parameters are consistent with the monoanionic nature of the cyclobutenyl ring, which are comparable to the rare-earth cyclobutadienyl sandwich complexes [NaLn{η^4-$C_4(SiMe_3)_3$-κ-$CH_2(SiMe_2)$}{η^3-$C_4(SiMe_3)_4H$}] (Ln = Y, Dy, Lu) (discussed in section 1.2.8.), which also feature a similar type of protonated Cb ligand. In **34**, two of the $SiMe_3$ groups, Si2 and Si3, reside above the plane of the η^3-Cb ring by 0.211(14) and 0.29(2) Å, respectively, with Si4 lying in the plane. The $SiMe_3$ group attached to the protonated carbon of the C_4 ring (Si1) resides significantly out of the plane by 1.995(18) Å.

Compounds **33** and **34** were both analysed by NMR spectroscopy in D_8-THF solutions. The paramagnetic nature of **33** precluded the observation of any signals in the ^{1}H, ^{13}C{^{1}H}, ^{29}Si{^{1}H} or ^{29}Si-^{1}H HMBC NMR spectra. However, compound **34** was able to be fully characterised due to its diamagnetic $4f^{14}$ electronic configuration. The ^{1}H NMR spectrum of **34** shows signals for the three different trimethylsilyl environments at 0.23 (s, 9H), 0.18 (s, 18H) and 0.08 ppm (s, 9H), a signal at 2.69 ppm (s, 1H) corresponding to the protonated Cb ring, and two signals at 3.60 (m, 3H) and 1.76 ppm (m, 3H) for the THF ligands (Figure 133). The low integration for the THF signals may indicate exchange in solution with the reference solvent. In the ^{13}C{^{1}H} NMR spectrum of **34**, signals can be observed at 176.48 and 111.75 ppm for the C_4 ring carbons, a signal at 54.35 ppm corresponds to the protonated carbon of the C_4 ring, and three signals for the $SiMe_3$ groups can be observed at 3.60, 2.37 and 1.14 ppm. Additionally, very weak signals corresponding to the THF ligands can be seen at 68.39 and 26.55 ppm (Figure S88). No signals could be observed in a direct ^{29}Si{^{1}H} NMR experiment of **34**, however, a ^{29}Si-^{1}H HMBC correlation spectrum revealed three different silicon-proton correlations for the expected environments at –24.01/0.18, –17.00/0.23 and –4.51/0.08 ppm (Figure 133 inset, Figure S89).

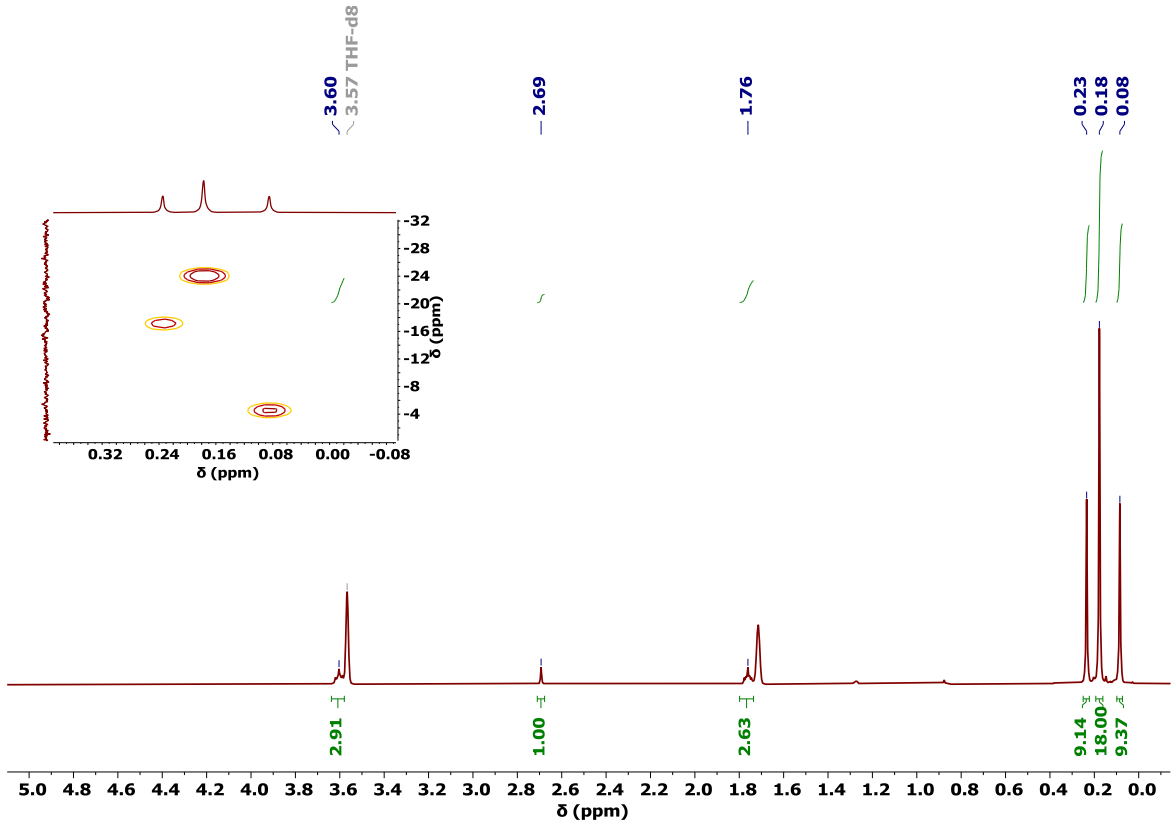

Figure 133. ^{1}H NMR spectrum of **34** in D_8-THF. Inset: ^{29}Si-^{1}H HMBC correlation NMR spectrum of **34**.

As with compounds **29**-**32**, elemental analyses on compounds **33** and **34** returned consistently low carbon and hydrogen values, with representative results being % found (calculated) for **33** $C_{48}H_{106}Eu_2I_2Si_8O_4$: C 26.02 (37.69); H 4.72 (6.98), and for **34** $C_{48}H_{106}Yb_2I_2Si_8O_4$: C 31.10 (36.68); H 5.89 (6.80). The results for the europium compound are significantly lower than expected and may contain a higher ratio of the corresponding diiodide impurity. The FTIR spectra of compounds **33** and **34** both display absorptions in the range 3000-2850 cm^{-1} corresponding to C-H stretches of the $SiMe_3$ groups, as well as weak absorptions at *ca.* 2750 cm^{-1} that correspond to the C-H stretch of the protonated C_4 rings. Compound **33** displays strong absorptions at *ca.* 1250 cm^{-1}, which are in the region expected for C-O stretches and may correlate to the presence of more THF ligands, *i.e.* **33** and $[EuI_2(THF)_5]$ impurities, which is consistent with the elemental analysis results. (Figure 134).

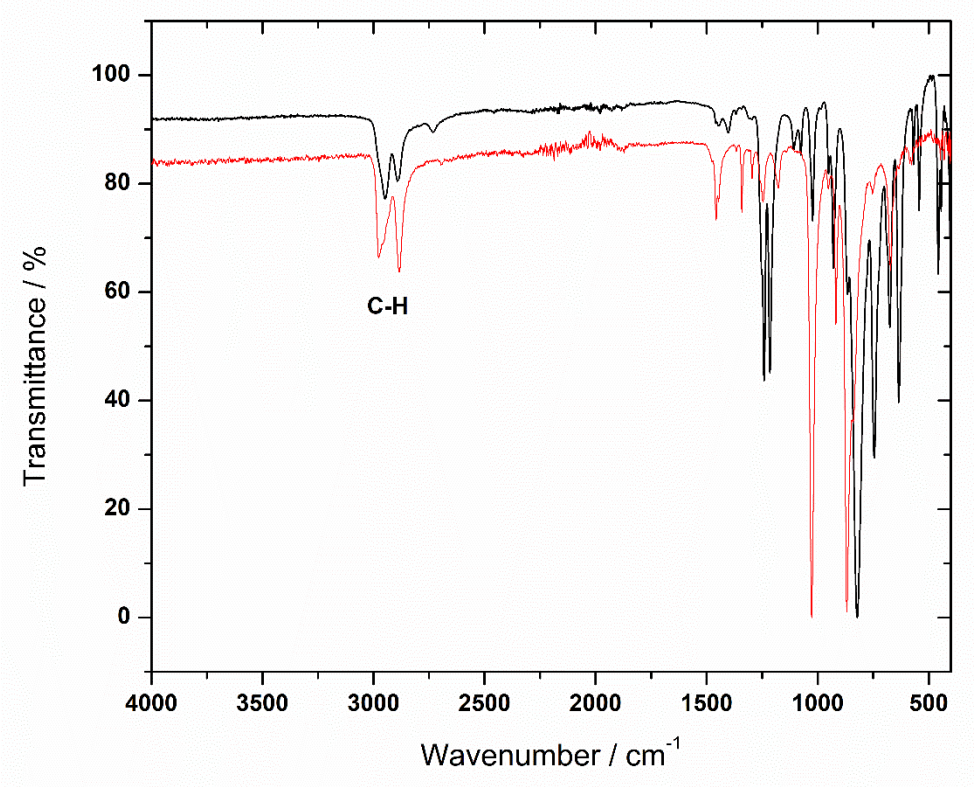

Figure 134. FTIR spectra of **33** (black line) and **34** (red line). Selected absorptions (cm^{-1}): 3000-2850 (C-H).

The source of the proton in compounds **33** and **34** could be adventitious air or moisture from the addition of iodine into the reaction. To test this, repeat reactions were carried out with the rigorous exclusion of air and moisture by using freshly sublimed iodine that was stored in a glovebox prior to use. However, this only resulted in the formation of the corresponding diiodides, *i.e.* $[LnI_2(THF)_5]$ (Ln = Eu, Yb). Therefore, this suggests that the activation of the cyclobutadienyl ligand requires an external proton source.

The unique nature of the monoanionic cyclobutenyl ring and the Ln^{2+} oxidation states of compounds **33** and **34** mean that there are no structurally similar COT complexes, however, there have been reports of structurally similar complexes containing monoanionic cyclopentadienyl ligands for the divalent lanthanides, such as $[Ln(\eta^5\text{-}Cp^*)(\mu\text{-}I)(THF)_2]_2$ (Ln = Sm, Eu, Yb).[159–161] These complexes are not synthesized under the same conditions employed in the synthesis of **33** and **34**, however they can be synthesized via two different procedures, either via the addition of an equimolar amount of NaCp* or KCp* to the corresponding lanthanide diiodide $[LnI_2(THF)_2]$ (Ln = Sm, Eu, Yb), or by the addition of $[Ln(\eta^5\text{-}Cp^*)_2(THF)_2]$ to $[LnI_2(THF)_2]$ (Ln = Sm, Yb) (Scheme 38).

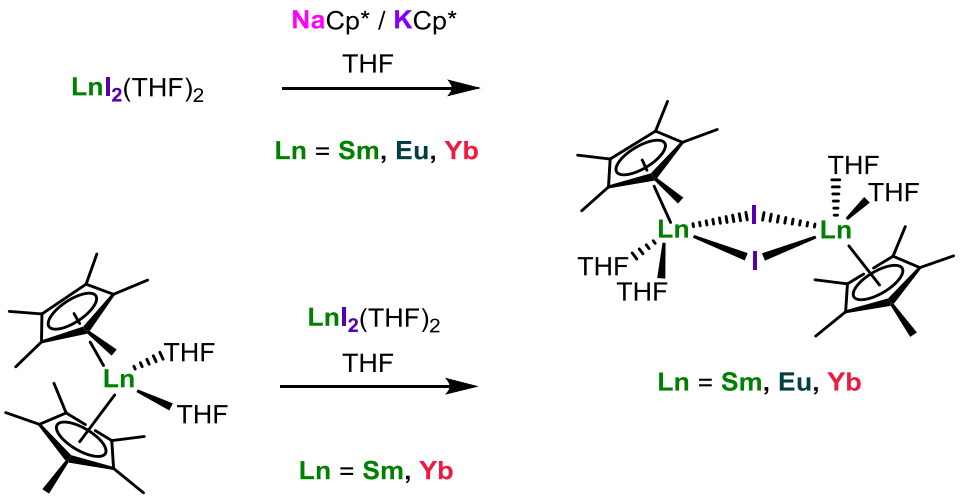

Scheme 38. Reported synthesis of $[Ln(\eta^5\text{-Cp*})(\mu\text{-I})(THF)_2]_2$ (Ln = Sm, Eu, Yb).[159–161]

The europium derivative $[Eu(\eta^5\text{-Cp*})(\mu\text{-I})(THF)_2]_2$ does not have any reported structural data, however, the ytterbium derivative $[Yb(\eta^5\text{-Cp*})(\mu\text{-I})(THF)_2]_2$ has been reported as its isotropically refined structure (Figure 135).[161] Comparisons should therefore be taken cautiously. However, based on the available data both **34** and $[Yb(\eta^5\text{-Cp*})(\mu\text{-I})(THF)_2]_2$ have the same average Yb-C bond distances of *ca.* 2.7 Å. The larger Cp ring allows for a closer approach to the ytterbium centre of *ca.* 0.1 Å, which is reflected in the centroid distances of 2.414(9) *vs.* 2.5121(3). The average Yb-O distances are slightly elongated for **34** by *ca.* 0.08 Å, however the average Yb-I distances are reduced by almost the same distance of *ca.* 0.9 Å. The Yb···Yb distance of **34** is longer by *ca.* 0.03 Å, which results in an increased Yb-I-Yb angle, and a reduced I-Yb-I angle of *ca.* 4.8°, respectively. These slight changes in structural parameters can feasibly be explained by the increased steric bulk of the tetra-trimethylsilyl substituents in **34** when compared to the Cp* ligand in $[Yb(\eta^5\text{-Cp*})(\mu\text{-I})(THF)_2]_2$.

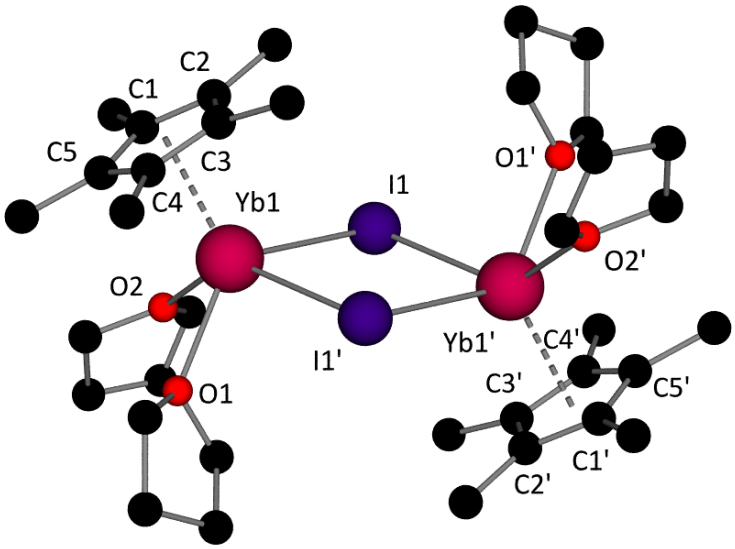

Figure 135. A ball and stick representation of the reported structure of $[Yb(\eta^5\text{-}Cp^*)(\mu\text{-}I)(THF)_2]_2$. Hydrogen atoms have been removed for clarity.[161]

4.1.4. Reactivity studies on iodide-bridged compounds

Prior to the knowledge that the iodide-bridged compounds **29**-**32** were likely contaminated with lanthanide triiodide impurities, some reactivity studies were investigated. Initially, a salt metathesis reaction between the lanthanum derivative **29** and two equivalents of KCp* was targeted. Upon the addition of KCp* to an orange solution of **29** in THF, no obvious colour change was observed, and the reaction was left to stir overnight at room temperature, by which time a white material had precipitated from the reaction. After subsequent work-up, a very small amount of orange needle-like crystals were obtained from a saturated hexane solution stored at –40 °C overnight, which were identified as the monomeric mixed sandwich complex $[La\{\eta^4\text{-}C_4(SiMe_3)_4\}(\eta^5\text{-}Cp^*)(THF)_2]$ (**35**). However, a second complex co-crystallized from the hexane solution as red block-like crystals, which were subsequently identified as the dimeric complex $[La\{\eta^4\text{-}C_4(SiMe_3)_4\}(\eta^5\text{-}Cp^*)(THF)(\mu\text{-}I)La(\eta^5\text{-}Cp^*)_2(THF)]$ (**36**) (Scheme 39). The two complexes could not be separated, therefore no meaningful yields could be obtained and the complexes could not be fully characterized.

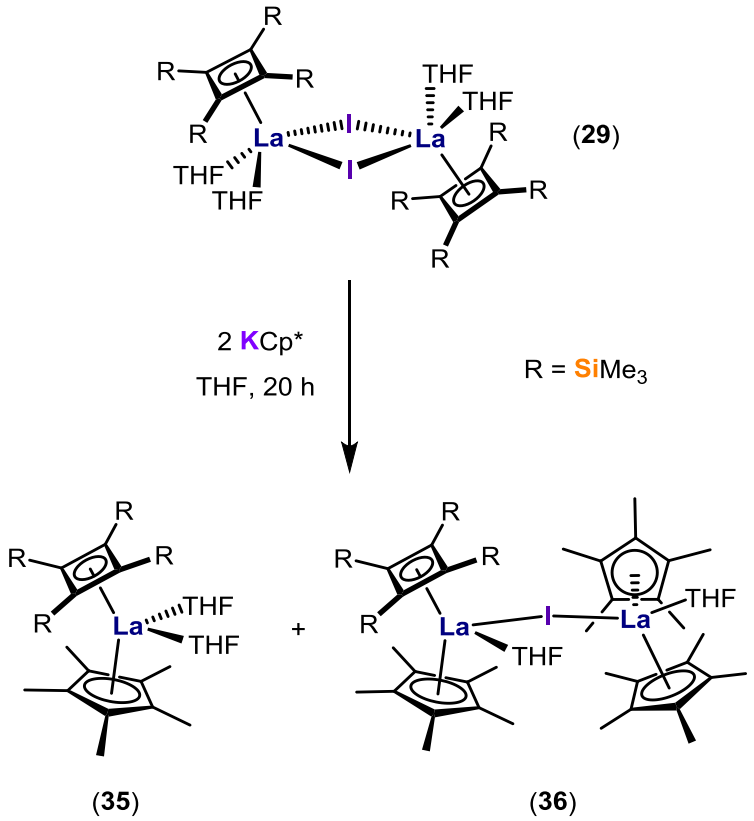

Scheme 39. Synthesis of **35** and **36**.

Compound **35** is the intended outcome of the reaction, however, unfortunately X-ray crystallography studies revealed extremely weak high angle diffraction, therefore preventing the collection of publishable-quality data (R_1 = 17.23 %, wR_2 = 48.54 %). Nevertheless, the atom connectivity could be established, revealing that **35** features a bent heteroleptic metallocene unit with an η^4-coordination of the Cb ligand and η^5-coordination of the Cp* ligand, with two THF ligands additionally coordinated to the lanthanum centre (Figure 136). The Cb ring is a square, indicating the dianionic aromatic character has been retained from the precursor.

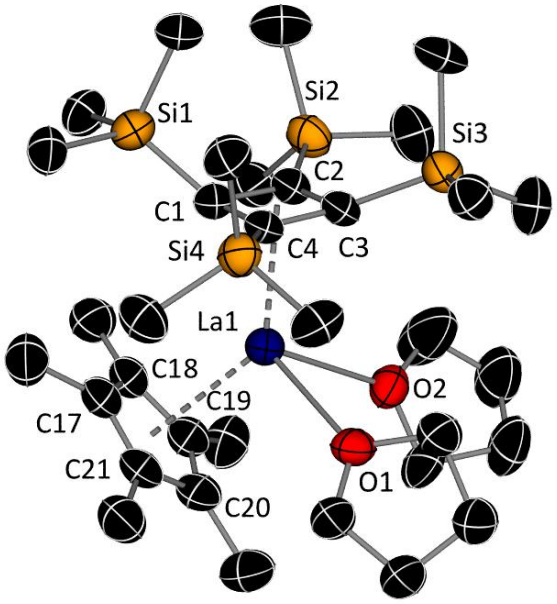

Figure 136. A representation of the molecular structure of [La{η^4-$C_4(SiMe_3)_4$}(η^5-Cp*)$(THF)_2$] (**35**) for connectivity (R_1 = 17.23 %, wR_2 = 48.54 %). Thermal ellipsoids are set to 30 % probability and hydrogen atoms have been omitted for clarity.

Compound **36** contains a similar unit to **35**, in which a bent metallocene unit features an η^4-Cb and η^5-Cp* ligand, however in this case only one THF ligand is coordinated to the lanthanum metal centre, with the complex forming a dimer via a bridging iodide ligand to a bis-η^5-Cp* metallocene with an additional THF ligand (Figure 137). The La(Cb)(Cp*) unit in **36** features a square Cb ligand, which coordinates to the lanthanum metal centre in an asymmetric fashion, with La-C bond distances ranging from 2.497(12)-2.758(9) Å and an La-Cb centroid distance of 2.4381(5) Å. These distances are shorter than those to the Cp* ligand (C17-21), in which the La-Cp* centroid distance is 2.6502(5) Å, and the La-C bond distances range from 2.887(6)-2.9353(5) Å. The bis-η^5-Cp* lanthanum unit features shorter La-C bond distances of 2.822(16)-2.858(17) Å.

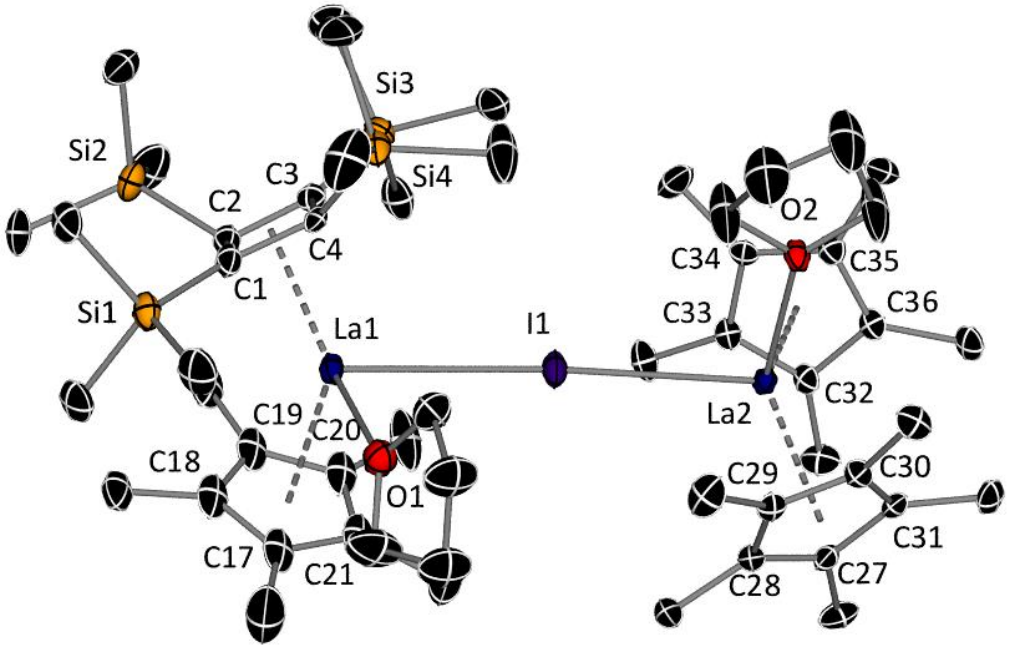

Figure 137. Molecular structure of [La{η^4-$C_4(SiMe_3)_4$}(η^5-Cp*)(THF)(μ-I)La(η^5-Cp*)$_2$(THF)] (**36**). Thermal ellipsoids are set to 30 % probability and hydrogen atoms have been omitted for clarity. Selected bond distances (Å) and angles (°) for **36**: C1-C2 1.430(7), C2-C3 1.431(7), C3-C4 1.431(7), C1-C4 1.432(7), C1-Si1 1.898(6), C2-Si2 1.851(11), C3-Si3 1.828(10), C4-Si4 1.865(8), La1-Cb_{cent} 2.4381(5), La1-Cp_{cent} 2.6502(5), La1-O1 2.659(11), La1-I1 3.3635(8), Cb_{cent}-La1-Cp_{cent} 140.56(2), La1-I1-La2 175.71(3), La2-O2 2.540(6), La2-Cp_{cent} 2.57366(18), Cp_{cent}-La2-Cp_{cent} 136.30(2), La1···La2 6.5640(7) Å.

A plausible explanation of the formation of **36** could be the simultaneous reaction of KCp* with the possible [$LaI_3(THF)_4$] impurity in the precursor **29** to form a complex of the type [La(η^5-Cp*)$_2$I(THF)], which could then react with **35** to form **36** (Scheme 40). Attempts to repeat the reaction using compound **29** that had been recrystallised from toluene resulted in the similar co-crystallization of **35** and **36**, with crystals of unreacted **29** additionally present.

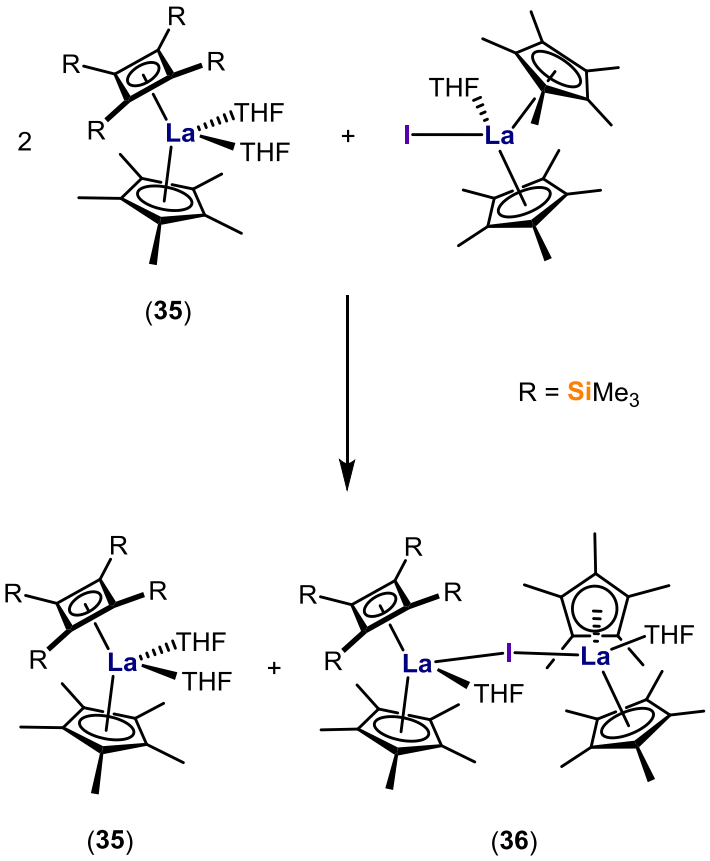

Scheme 40. Suggested reactivity in the formation of compounds **35** and **36**.

In order to see if this type of reactivity extended to another iodide-bridged compound, the reactivity of the samarium compound **32** with two equivalents of KCp* was investigated. Upon the addition of KCp* to a dark green solution of **32** in THF, an instant colour change to dark brown was observed, and the reaction was left to stir overnight at room temperature, by which time a white material had precipitated from the reaction. After subsequent work-up, a very small amount of red plate-like crystals were obtained from a saturated hexane solution stored at –40 °C over a week, which were subsequently identified as [Sm{η^3-$C_4(SiMe_3)_3$-κ-$CH_2(SiMe_2)H$}(η^5-Cp*)(THF)] (**37**) (Scheme 41).

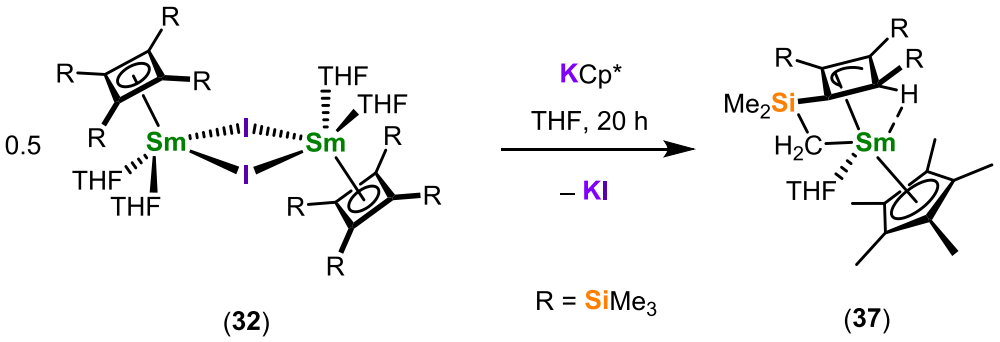

Scheme 41. Synthesis of **37**.

Unfortunately, only a few crystals were able to be isolated from this reaction, and X-ray diffraction studies revealed them to be heavily twinned with extremely weak high-angle diffraction. After a suitable crystal was found, when solving the structure it was found that the symmetry of the molecule had been overestimated (collected as monoclinic, solves as triclinic), thus preventing publishable-quality data (R_1 = 5.32 %, wR_2 = 15.64 %, 68 % complete as $P\bar{1}$). Nevertheless, the atom connectivity could be established, revealing a double activation of the cyclcobutadienyl ligand, whereby the C_4 ring has been protonated with the simultaneous deprotonation of a trimethylsilyl group to form a 'tuck-in' CH_2 ligand to the metal centre (Figure 138). Compound **37** shows that C1 resides out of the plane of the η^3-Cb ring, with significant bending of Si1, which is consistent with other protonated cyclobutenyl complexes **33** and **34**. The double ligand activation is comparable to that of [NaLn{η^4-$C_4(SiMe_3)_3$-κ-$CH_2(SiMe_2)$}{η^3-$C_4(SiMe_3)_4H$}] (Ln = Y, Dy, Lu) (discussed in section 1.2.8.), however in the case of **37** the double activation is on a single cyclobutadiene ligand. This demonstrates the versatility of the cyclobutadienyl ligand, and how it is capable of many different types of coordination modes to rare-earth metals.

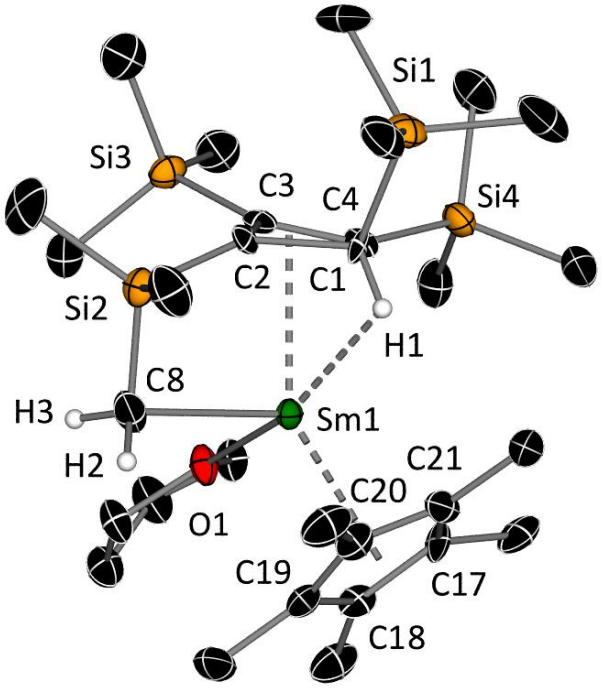

Figure 138. A representation of the molecular structure of [Sm{η^3-$C_4(SiMe_3)_3$-κ-$CH_2(SiMe_2)H$}(η^5-Cp*)(THF)] (**37**) for connectivity (R_1 = 5.32 %, wR_2 = 15.64 %, 68 % complete as $P\bar{1}$). Thermal ellipsoids are set to 50 % probability and for clarity, only the hydrogen atoms of the 'tuck-in' CH_2 (C8) and the protonated Cb ring and are shown.

Attempts to repeat reactions between **32** with KCp* or NaCp* were unsuccessful, and repeatedly produced crystals of $[SmI_2(THF)_5]$. The presence of divalent samarium indicates that a reduction has occurred from the trivalent precursor, thus further complicating the reactivity. This perhaps explains why compound **37** only formed as a few crystals, and as of yet, has not been able to be reproduced.

4.1.5. Conclusions on cyclobutadienyl rare-earth complexes from metallic lanthanides and iodine

In this section, the synthesis of the cyclobutadienyl lanthanide iodide-bridged complexes [Ln{η^4-$C_4(SiMe_3)_4$}(μ-I)$(THF)_2$]$_2$ (Ln = La (**29**), Ce (**30**), Pr (**31**), Sm (**32**)) was described, which have been formed by the one-pot reactions of the corresponding lanthanide metals with the neutral cyclobutadiene (**7**) in the presence of elemental iodine. The cyclobutadienyl ligands are directly reduced to their dianions in a similar fashion to previously reported reactivity with COT. However, in the case of cyclobutadiene, only dimeric complexes were

formed, which contrasts to the reactivity of COT, whereby monomeric complexes are formed.

In addition, the synthesis of the protonated cyclobutenyl lanthanide iodide-bridged complexes $[Ln\{\eta^3\text{-}C_4(SiMe_3)_4H\}(\mu\text{-}I)(THF)_2]_2$ (Ln = Eu (**33**), Yb (**34**)) was described. These complexes are formed in the presence of adventitous air or moisture, with rigourous air sensitive conditions resulting in non reactivity of the cyclobutadiene ligand. Their formation is presumed to be a consequence of the relative stability of the Ln^{2+} oxidation states for europium and ytterbium, which the versatile cyclobutadienyl ligand is able to accommodate via protonation to form a monoanionic ligand.

Unfortunately, the synthesis of compounds **29**-**34** is hindered by the suspected formation of the corresponding lanthanide triiodides $[LnI_3(THF)_4]$ (Ln = La, Ce, Pr, Sm) or diiodides $[LnI_2(THF)_5]$ (Ln = Eu, Yb), which were unable to be separated from the products. These impurities hinder further reactivity, with the salt metathesis reaction between **29** and KCp* resulting in the formation of $[La\{\eta^4\text{-}C_4(SiMe_3)_4\}(\eta^5\text{-}Cp^*)(THF)_2]$ (**35**) and $[La\{\eta^4\text{-}C_4(SiMe_3)_4\}(\eta^5\text{-}Cp^*)(THF)(\mu\text{-}I)La(\eta^5\text{-}Cp^*)_2(THF)]$ (**36**).

Therefore, the main finding of this study has added to the fundamental chemistry of cyclobutadiene with the rare-earth elements by exploring different routes to cyclobutadienyl complex formation other than salt metathesis reactions. The reactivity of cyclobutadiene is inherently more complicated than the larger COT ligand, however, this presents itself as an opportunity to explore further reactivity, of which this work has provided a platform to do so. Moreover, due to the complicated nature of these iodide compounds, it shifted our attention into exploring reactivity of pseudo-halide rare-earth borohydride compounds, which proved to be much more fruitful and formed the basis of Chapters 2 and 3.

Chapter 5

Conclusions and Future Work

5.1. Conclusions

In summary, the aims of this thesis have been successfully met in the majority of cases. The fundamental chemistry of the cyclobutadienyl ligand with rare-earth elements has been thoroughly explored. At the start of my studies, rare-earth cyclobutadienyl complexes were essentially unknown, and the work presented in this thesis has significantly developed our understanding of the basic synthetic chemistry needed to handle them successfully as ligands with these metals.

The improved, large-scale synthesis of the cyclobutadiene [$C_4(SiMe_3)_4$] (**7**) and its alkali metal salts (**8**-**11**) has enabled the synthesis of a range of rare-earth cyclobutadienyl half-sandwich (**12**-**15, 29**-**34**) and sandwich (**19**-**28**) complexes. The intact transfer of cyclobutadienyl ligands to rare-earth elements can be achieved via salt metathesis reactions with pseudo-halide rare-earth borohydride compounds at room temperature, which prevents undue ligand activation of trimethylsilyl substituents on the cyclobutadienyl ligand.

One of the main focuses of my research is single-molecule magnetism, which has developed significantly over the course of my studies. The work in this thesis has built upon the magneto-structural correlations that are currently employed to design and rationalize the properties of rare-earth organometallic SMMs. Steps have been taken towards improving upon these benchmark systems by introducing the dianionic cyclobutadienyl ligand to increase the strength of the crystal ligand field around the rare-earth metal. In all examples to date, the cyclobutadienyl ligands approach the rare-earth metals more closely when compared to structurally similar cyclopentadienyl complexes, as evidenced by crystallographic studies. Due to this stronger interaction, the effective energy barriers for all measured cyclobutadienyl complexes increased when compared to structurally similar cyclopentadienyl complexes. For the heteroleptic sandwich complex [Na(15-c-5)$(THF)_2$]$^+$[Dy{η^4-$C_4(SiMe_3)_4$}(η^5-$C_5Me_4{}^t$Bu)(κ^2-BH_4)]$^-$ (**26**), these improvements occur despite a significant decrease in axiality, highlighting how the strength of the axial crystal field around Dy^{3+} has more influence on the SMM properties than strictly axial symmetry.

Consequently, if a pseudo-axial cyclobutadienyl complex of the type $[Dy(Cb)_2]^-$ or [Dy(Cb)(Cp)] can be synthesized, they would have the potential to surpass the current benchmark SMM properties set by bis-cyclopentadienyl metallocene complexes.

5.2. Future Work

Cyclobutadienyl chemistry of the f-elements is still in its infancy, and there remains an opportunity to explore a plethora of organometallic chemistry with this fascinating ligand. For example, it may be possible to synthesize cyclobutadienyl derivatives of uranocene and cerocene, *i.e.* $[U\{\eta^4\text{-}C_4(SiMe_3)_4\}_2]$ and $[Ce\{\eta^4\text{-}C_4(SiMe_3)_4\}_2]$. In our studies we have observed how the tetrakis-trimethylsilyl cyclobutadienyl ligand is capable of various types of activation, such as protonation of the C_4 ring and deprotonation of a trimethylsilyl substituent to form a 'tuck-in' CH_2 ligand; however, the ligand can also be transferred onto f-elements without any activation.

Insight into what causes these types of ligand activation can only be gained through further complexation by variation of reactants and reaction conditions. For example, as we have observed different types of ligand activation when varying the alkali metal cyclobutadienyl pro-ligand, the alkali metals may play an important role in the stabilization and reactivity of cyclobutadienyl ligands. Moreover, variation in reaction conditions such as solvents and temperature would provide vital information.

NMR spectroscopy on the yttrium mixed sandwich complexes **19**, **21**, **23** and **25** revealed some interesting behaviour in solution, with the presence of what appears to be two isomers. Variable temperature ^1H NMR studies on $[Na(15\text{-}c\text{-}5)(THF)_2]^+[Y\{\eta^4\text{-}C_4(SiMe_3)_4\}(\eta^5\text{-}Cp^*)(\kappa^2\text{-}BH_4)]^-$ (**21**) has revealed the slight shift of signals with decreasing temperature, however the integration remains a similar ratio at all temperatures (Figure 139).

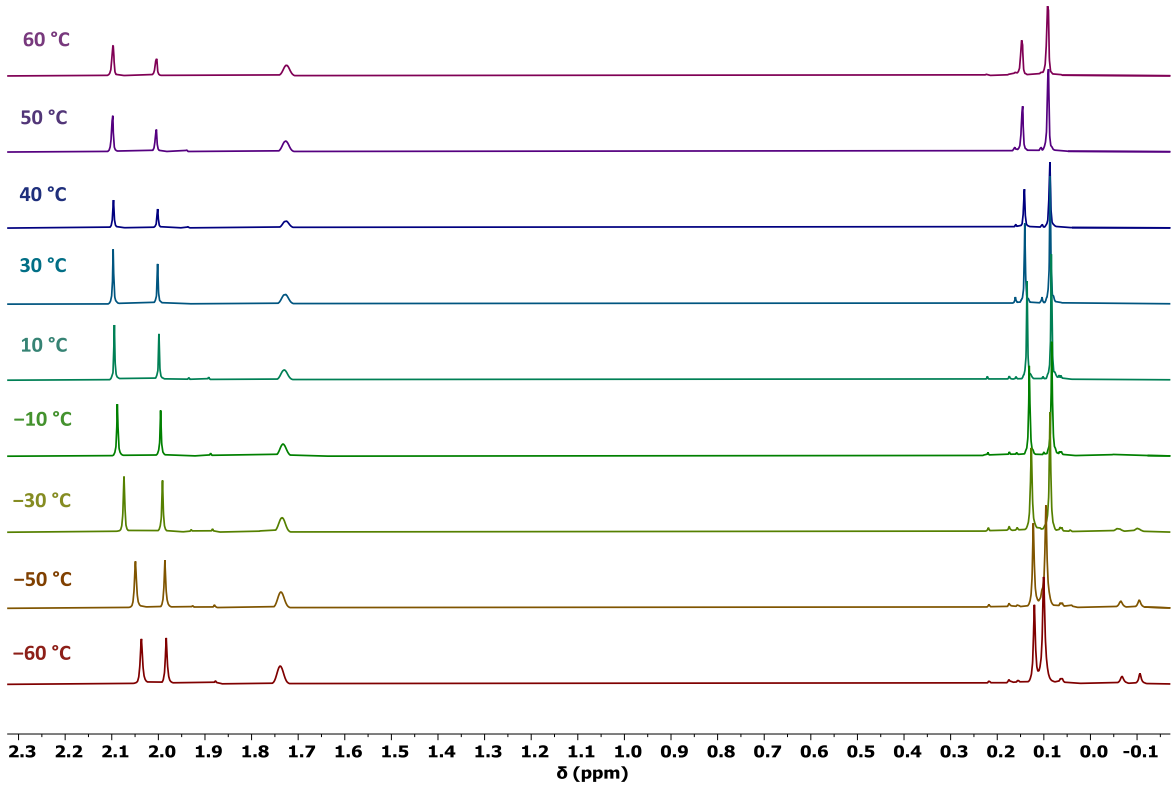

Figure 139. Variable temperature ^{1}H NMR of **21** in D_8-THF from +60 to −60 °C.

Interestingly, variable temperature $^{11}B\{^{1}H\}$ NMR spectroscopic studies on complex **21** revealed a slightly more complicated scenario, whereby multiple signals in the $^{11}B\{^{1}H\}$ NMR can be observed at a temperature of −60 °C at −22.55, −24.49, −26.24 and −40.01 ppm (Figure 140). In the ^{11}B proton coupled spectrum (Figure 141), the signals at −24.49 and −40.01 ppm have the expected splitting pattern of a BH_4, with the upfield signal centred at −40.01 ppm being close to that expected of $NaBH_4$ (−42.0 ppm in the solid-state).[162] Consequently, this indicates that several different species are present in solution at low temperatures, with a complex of the type [Y{η^4-$C_4(SiMe_3)_4$}(η^5-Cp*)] a possibility due to the observation of solvated $NaBH_4$. However, in depth variable temperature correlation studies are required to further elucidate the solution-state behaviour of these heteroleptic sandwich complexes.

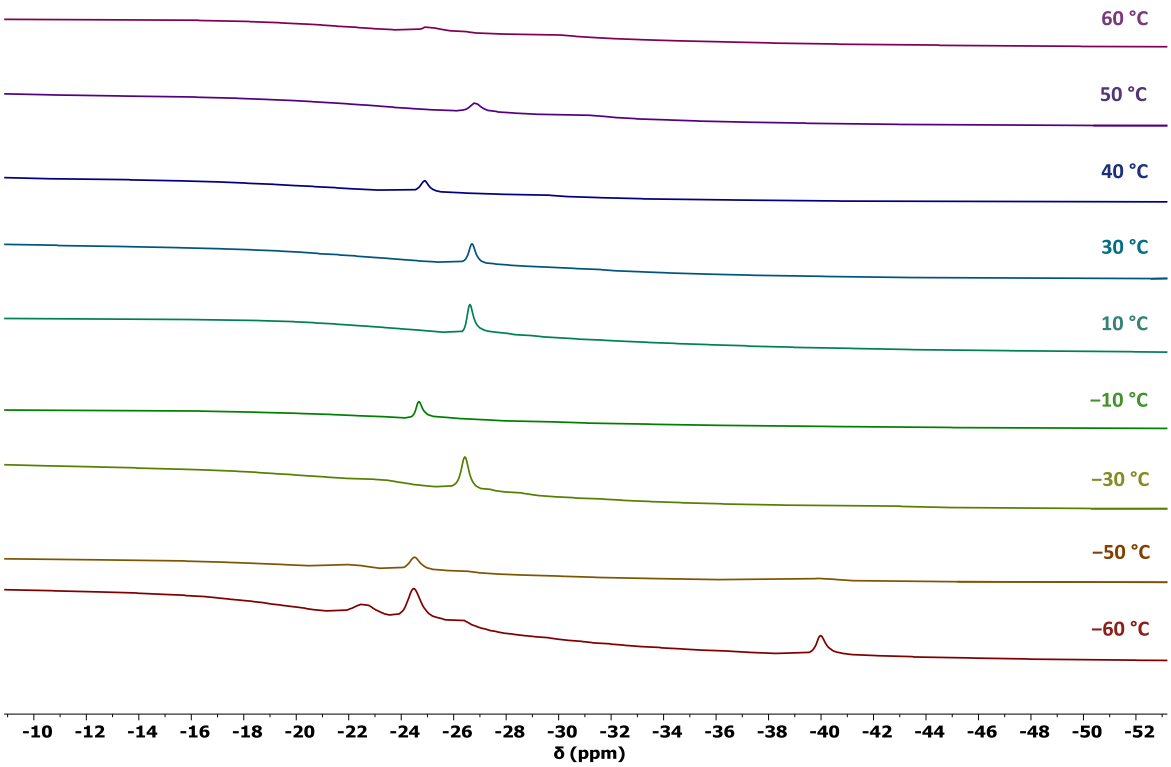

Figure 140. Variable temperature $^{11}B\{^{1}H\}$ NMR of **21** in D_8-THF from +60 to −60 °C.

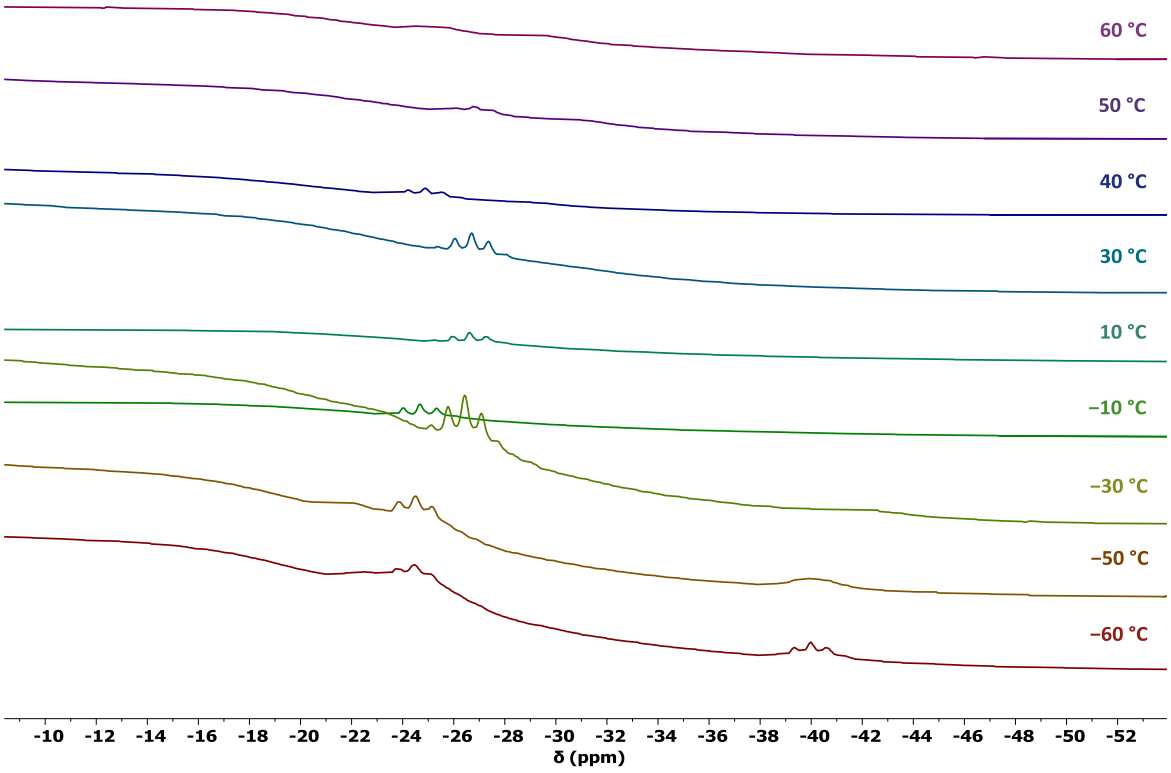

Figure 141. Variable temperature ^{11}B NMR of **21** in D_8-THF from +60 to −60 °C.

The promising results obtained in this thesis on the performance of dysprosium cyclobutadienyl-ligated SMMs has provided a platform to improve upon current benchmark systems. In particular, a complex of the type [Dy(Cb)(Cp)] is a key target, of which complexes **20**, **22**, **24**, and **26** are direct precursors. Therefore, future work will focus on the removal of the equatorial borohydride ligands by continuing to explore reactivity with electrophiles and oxidizing agents under varying reaction conditions (Scheme 42). If this line of research is unsuccessful, it is possible that the Cp* and Cp^{Me4tBu} ligands employed in this research do not possess sufficient steric bulk to stabilize the target complex. In which case, there remains a large scope to vary the steric bulk of the cyclopentadienyl ligand, which may prove fruitful. Dysprosium complexes have been the focus of research in this thesis, however the cyclobutadienyl ligand can additionally be extended to other lanthanides with oblate-spheroid shaped electron density, such as terbium and holmium, which may display some interesting SMM properties.

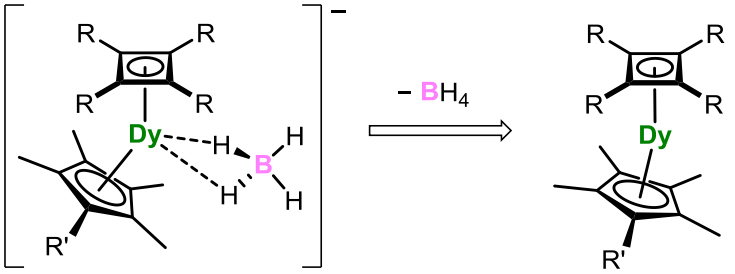

R = $SiMe_3$

R' = Me (**20**, **22**)
^{t}Bu (**24**, **26**)

Scheme 42. Removal of borohydride ligands from direct precursor complexes to form [Dy(Cb)(Cp)].

Chapter 6

Experimental and Supplementary Information

6.1. General considerations

All reactions were carried out under rigorous anaerobic, anhydrous conditions under an atmosphere of argon or nitrogen using standard Schlenk techniques or in an MBraun glovebox with an atmosphere with <5 ppm O_2 unless otherwise stated. All solvents were refluxed over an appropriate drying agent for a minimum of three days (molten potassium for benzene, D_6-benzene, toluene, D_8-toluene, THF, D_8-THF, and Na/K alloy for hexane), and then distilled, degassed via a minimum of three freeze-pump-thaw cycles, and stored in ampoules over potassium mirrors (benzene, toluene and hexane) or activated 4 Å molecular sieves (THF, D_6-benzene, D_8-toluene, D_8-THF).

Elemental analyses were carried out at MEDAC Ltd., Surrey, U.K, London Metropolitan University, U.K, and Microanalytisches Labor Pascher, Germany. NMR spectra were recorded on a Varian VNMR S400 spectrometer operating at 30°C unless otherwise stated at frequencies of 400 MHz (^{1}H), 128 MHz (^{11}B), 100 MHz (^{13}C), 106 MHz (^{23}Na), 80 MHz (^{29}Si), 155 MHz (^{7}Li) and 52 MHz (^{133}Cs). FTIR spectra were recorded on a Bruker Alpha spectrometer with a platinum-diamond ATR module.

Literature procedures were used to synthesize $[Ln(BH_4)_3(THF)_3]$ (Ln = Y, Dy), $[KCp^{ttt}]$, $[NaCp^{Me4tBu}]$, [NaCp*], [KCp*], $[HNEt_3]^+[B(C_6H_5)_4]^-$ and $[(Et_3Si)_2(\mu\text{-}H)]^+[B(C_6F_5)_4]^-$.[22,163–168] $[K_2Pn(Si^iPr_3)_2]$ was synthesized by Dr N. Tsoureas, with acknowledgement to Prof. F. G. N. Cloke for the use of materials and equipment.[169] The large-scale synthesis of $[C_4(SiMe_3)_4]$ (**7**) is described based on modified literature procedures by Sekiguchi and co-workers.[120–122] $[Co(\eta^5\text{-}Cp)(CO)_2]$ and bis(trimethylsilyl)acetylene were purchased from Merck Group. The purity of $[Co(\eta^5\text{-}Cp)(CO)_2]$ was checked prior to use, and the bis(trimethylsilyl)acetylene was degassed and stored over 4 Å molecular sieves prior to use.

Sodium and potassium metals were purchased from Sigma-Aldrich and the oxidised surfaces were removed before washing with pentane and storing in the glovebox prior to use. Rubidium and caesium metals were purchased from Merck Group and were stored in the glovebox prior to use. In the synthesis of $[Li_2\{\eta^4{:}\eta^4\text{-}C_4(SiMe_3)_4\}(THF)]_2$ (**8**), the THF was additionally dried over a Na/K alloy overnight to give a blue solution, which was then vacuum transferred into an ampoule containing activated 4 Å molecular sieves. For the synthesis of compound **8**, 15 equivalents of lithium powder were used when the sodium

content was high (~25 %), however 10 equivalents of lithium powder are sufficient for a lower sodium content (~3 %).

Lanthanide metals were purchased from Alfa Aesar (La (powder) & Eu (chunks)) and Sigma-Aldrich (Ce, Pr, Nd, Sm, Dy (powders) & Yb (chips)), stored under Ar and used as purchased. $[Ph_3C]^+[B(C_6F_5)_4]^-$ was purchased from Alfa Aesar and stored in the glovebox prior to use. Iodine was purchased from Sigma Aldrich and used as purchased unless otherwise stated. 15-crown-5 was purchased from Sigma-Aldrich, degassed and stored over activated 4 Å molecular sieves in an argon glovebox prior to use. 18-crown-6 was purchased from Sigma-Aldrich, sublimed and stored in an argon glovebox prior to use.

6.2. Experimental for Chapter 2

Synthesis of $[Y(\eta^5\text{-}Cp^{ttt})(\kappa^3\text{-}BH_4)_2(THF)]$ (1). Toluene (15 mL) was added to a mixture of $[KCp^{ttt}]$ (273 mg, 1.00 mmol) and $[Y(BH_4)_3(THF)_3]$ (350 mg, 1.00 mmol). The resulting off-white suspension was heated and left to stir overnight at 60°C, by which time a white precipitate had deposited from the reaction. The reaction mixture was filtered, the solvent removed *in vacuo* and the product was extracted in hexane (3 × 10 mL) and filtered. The filtrate was concentrated *in vacuo* until incipient crystallisation occurred. The suspension was then gently warmed to re-dissolve the microcrystalline solid and the solution was stored at –40°C overnight to yield white crystals of **1** suitable for X-ray crystallography (312 mg, 74 %).

^{1}H NMR (δ/ppm, D_6-benzene): 6.40 (s, C_5 ring, 2H), 3.53 (m, CH_2O, 4H), 1.55 (s, ^{t}Bu, 18H), 1.26 (s, ^{t}Bu, 9H), 1.00 (m, CH_2, 4H).

^{1}H{^{11}B} NMR (δ/ppm, D_6-benzene): 6.40 (s, C_5 ring, 2H), 3.53 (m, CH_2O, 4H), 1.55 (s, ^{t}Bu, 18H), 1.26 (s, ^{t}Bu, 9H), 1.06 (s, BH_4, FWHM = 22 Hz, 8H), 1.00 (m, CH_2, 4H).

^{13}C{^{1}H} NMR (δ/ppm, D_6-benzene): 137.84 (d, $^1J_{CY}$ = 1 Hz, $\underline{C}_5$ ring), 137.81 (d, $^1J_{CY}$ = 2 Hz, $\underline{C}_5$ ring), 111.37 (d, $^1J_{CY}$ = 1 Hz, $\underline{C}_5$ ring), 73.70 ($\underline{C}H_2O$), 34.33 (($\underline{C}(CH_3)_3)_2$), 34.09 ((C($\underline{C}H_3)_3)_2$), 32.77 ($\underline{C}(CH_3)_3$), 31.94 (C($\underline{C}H_3)_3$), 24.83 ($\underline{C}H_2$).

$^{11}B\{^{1}H\}$ NMR (δ/ppm, D_6-benzene): −22.69 (s, FWHM = 48 Hz, BH_4).

^{11}B NMR (δ/ppm, D_6-benzene): −22.69 (quint., $^{1}J_{BH}$ = 86 Hz, BH_4).

FTIR ($\bar{\nu}$/cm^{-1}): 3000-2850 (m, b, C-H), 2450 (m, s, B-H_T), 2300-2100 (m, b, B-H_B).

Elemental analysis (%), found (calculated) for **1** $C_{21}H_{45}YB_2O$: C 59.29 (59.47); H 10.60 (10.70).

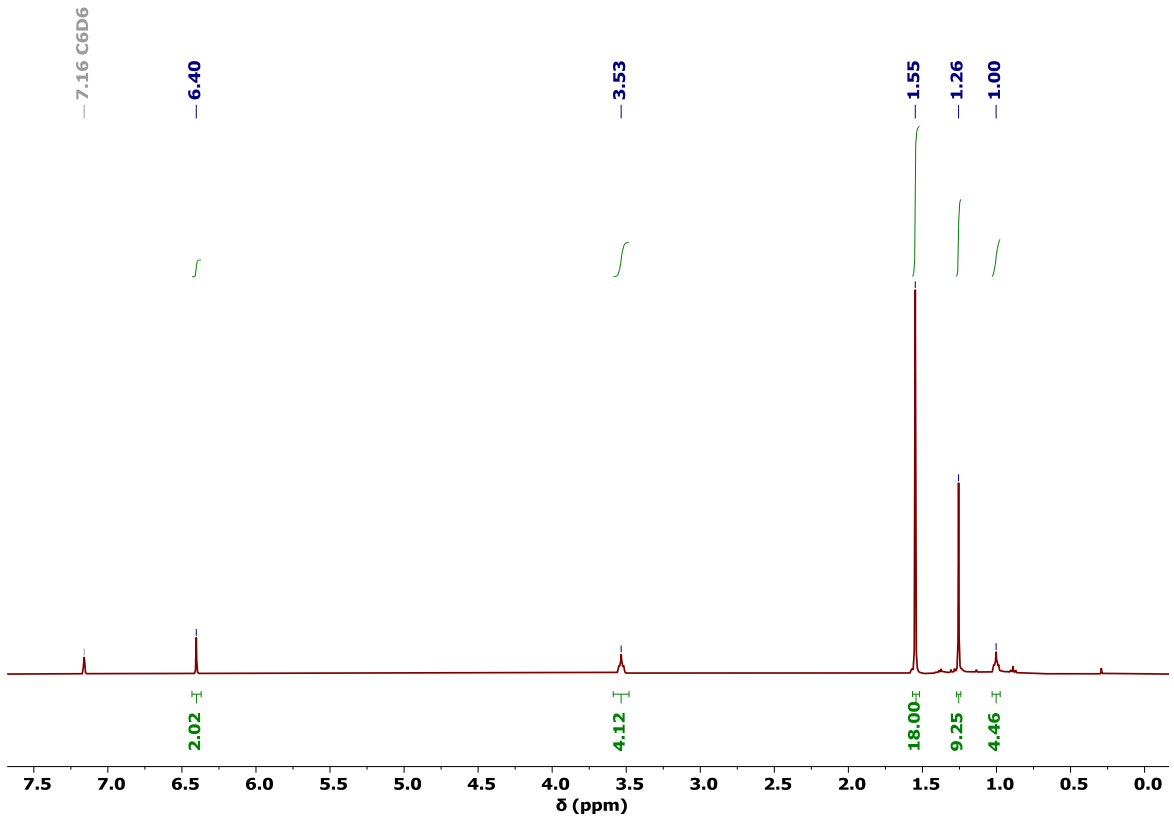

Figure S1. ^{1}H NMR spectrum of **1** in D_6-benzene.

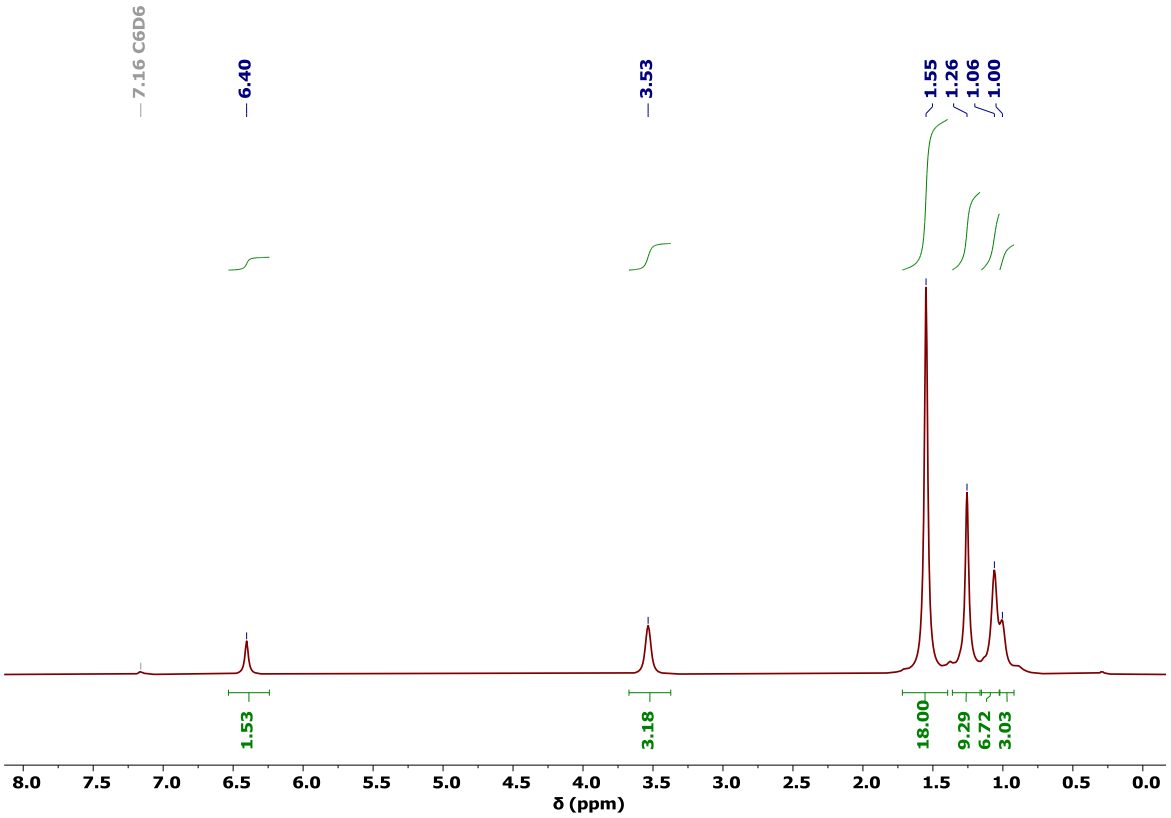

Figure S2. $^{1}H\{^{11}B\}$ NMR spectrum of **1** in D_6-benzene.

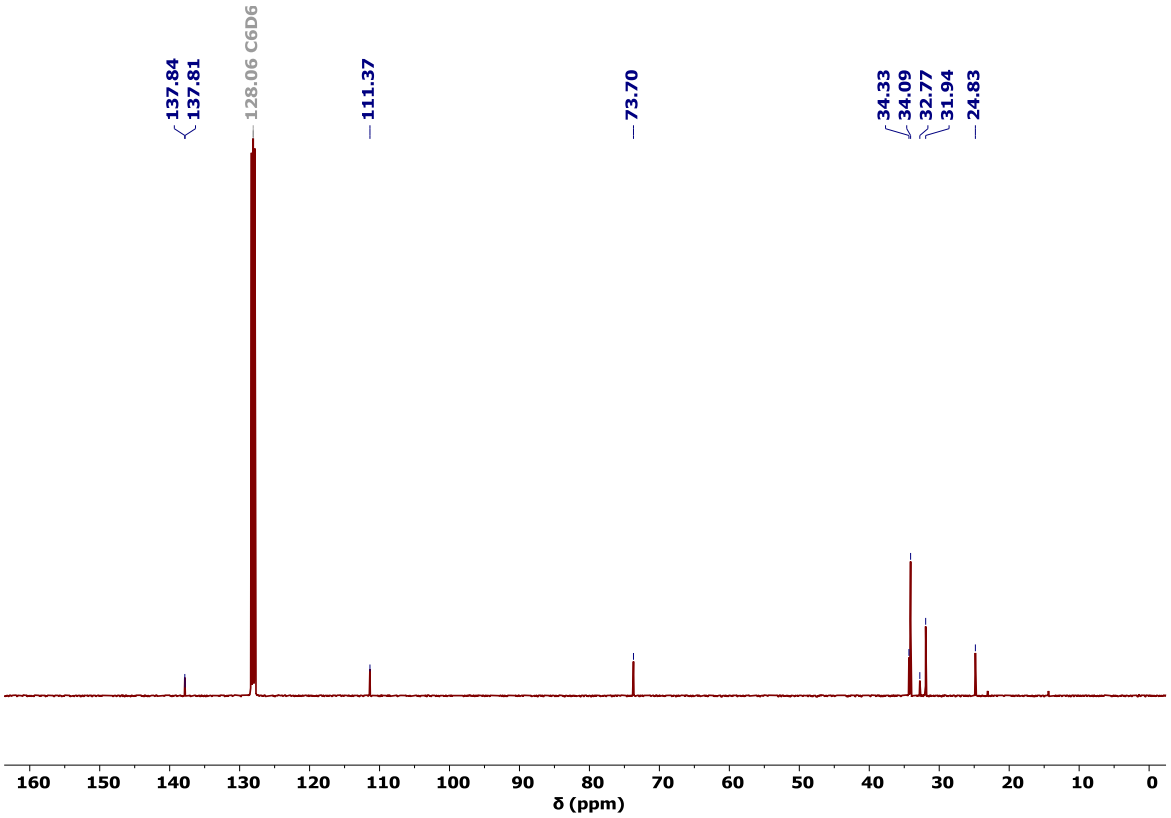

Figure S3. $^{13}C\{^{1}H\}$ NMR spectrum of **1** in D_6-benzene.

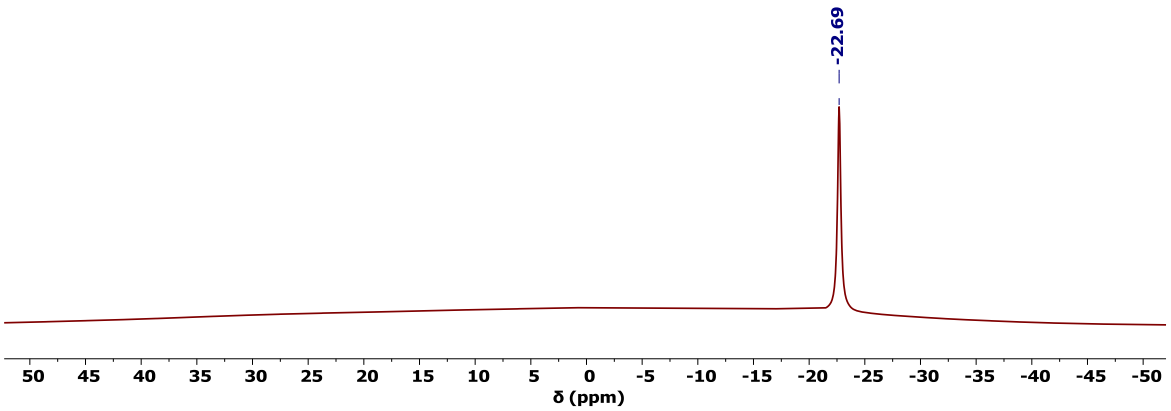

Figure S4. $^{11}B\{^{1}H\}$ NMR spectrum of **1** in D_6-benzene.

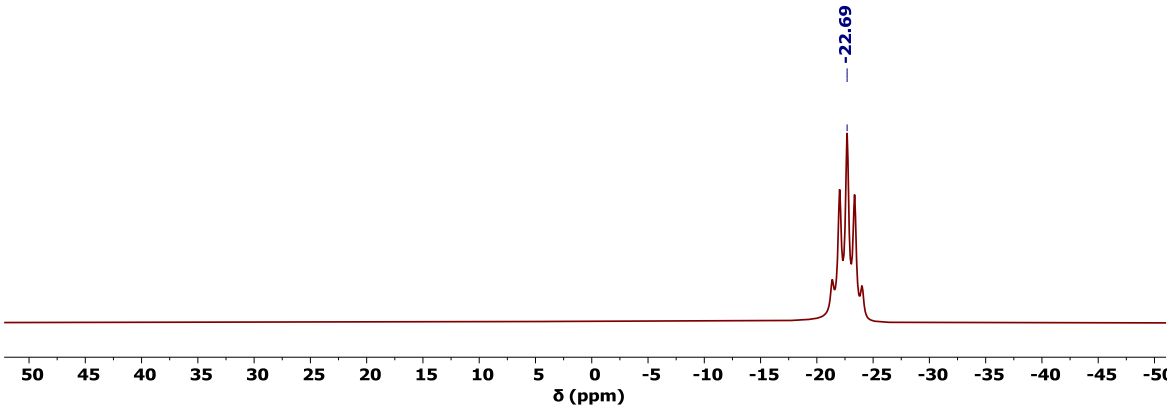

Figure S5. ^{11}B NMR spectrum of **1** in D_6-benzene.

Synthesis of [Dy(η^5-Cp^{ttt})(κ^3-BH$_4$)$_2$(THF)] (2). Compound **2** was synthesised by following the same procedure as for **1**, using [KCp^{ttt}] (1.50 g, 5.50 mmol) and [Dy(BH$_4$)$_3$(THF)$_3$] (2.33 g, 5.50 mmol). Pale-yellow crystals of **2** suitable for X-ray crystallography were obtained by storing a saturated hexane solution at –40°C overnight (1.96 g, 72 %).

FTIR ($\bar{\nu}$/cm^{-1}): 3000-2850 (m, b, C-H), 2450 (m, s, B-H$_T$), 2300-2100 (m, b, B-H$_B$).

Elemental analysis (%), found (calculated) for **2** $C_{21}H_{45}DyB_2O$: C 50.54 (50.68); H 9.06 (9.11).

Synthesis of [Y(η^5-C$_5$Me$_4$^{t}Bu)(κ^3-BH$_4$)$_2$(THF)] (3). Toluene (10 mL) was added to a mixture of [NaCp^{Me4tBu}] (65 mg, 0.33 mmol) and [Y(BH$_4$)$_3$(THF)$_3$] (114 mg, 0.33 mmol). The resulting off-white suspension was heated and left to stir overnight at 60°C, by which time a white precipitate had deposited from the reaction. The reaction mixture was filtered, the solvent removed *in vacuo* and the product was extracted in hexane (3 × 10 mL) and filtered. The filtrate was concentrated *in vacuo* until incipient crystallisation occurred. The suspension

was then gently warmed to re-dissolve the microcrystalline solid and the solution was stored at –40°C overnight to yield white crystals of **3** suitable for X-ray crystallography (72 mg, 60 %).

^{1}H NMR (δ/ppm, D_6-benzene): 3.43 (m, CH_2O, 4H), 2.39 (s, Me_2, 6H), 1.92 (s, Me_2, 6H), 1.52 (s, ^{t}Bu, 9H), 0.99 (m, CH_2, 4H), 0.93 (1:1:1:1 q, $^{1}J_{HB}$ = 84 Hz, BH_4, 8H).

^{13}C{^{1}H} NMR (δ/ppm, D_6-benzene): 151.94 ($\underline{C}_5$ ring), 133.27 ($\underline{C}_5$ ring), 121.71 (d, $^{1}J_{CY}$ = 12.4 Hz, $\underline{C}_5$ ring), 73.50 ($\underline{C}H_2O$), 35.51 ($\underline{C}(CH_3)_3$), 32.84 ($C(\underline{C}H_3)_3$), 24.90 ($\underline{C}H_2$), 15.80 (($\underline{C}H_3)_2$), 11.71 (($\underline{C}H_3)_2$).

^{11}B{^{1}H} NMR (δ/ppm(D_6-benzene)): −23.23 (s, FWHM = 26 Hz, BH_4).

^{11}B NMR (δ/ppm, D_6-benzene): −23.24 (quint., $^{1}J_{BH}$ = 86 Hz, BH_4).

FTIR ($\bar{\nu}$/cm^{-1}): 3000-2850 (m, b, C-H), 2450 (m, s, B-H_T), 2300-2100 (m, b, B-H_B).

Elemental analysis (%), found (calculated) for **3** $C_{17}H_{37}YB_2O$: C 54.76 (55.48); H 10.38 (10.13).

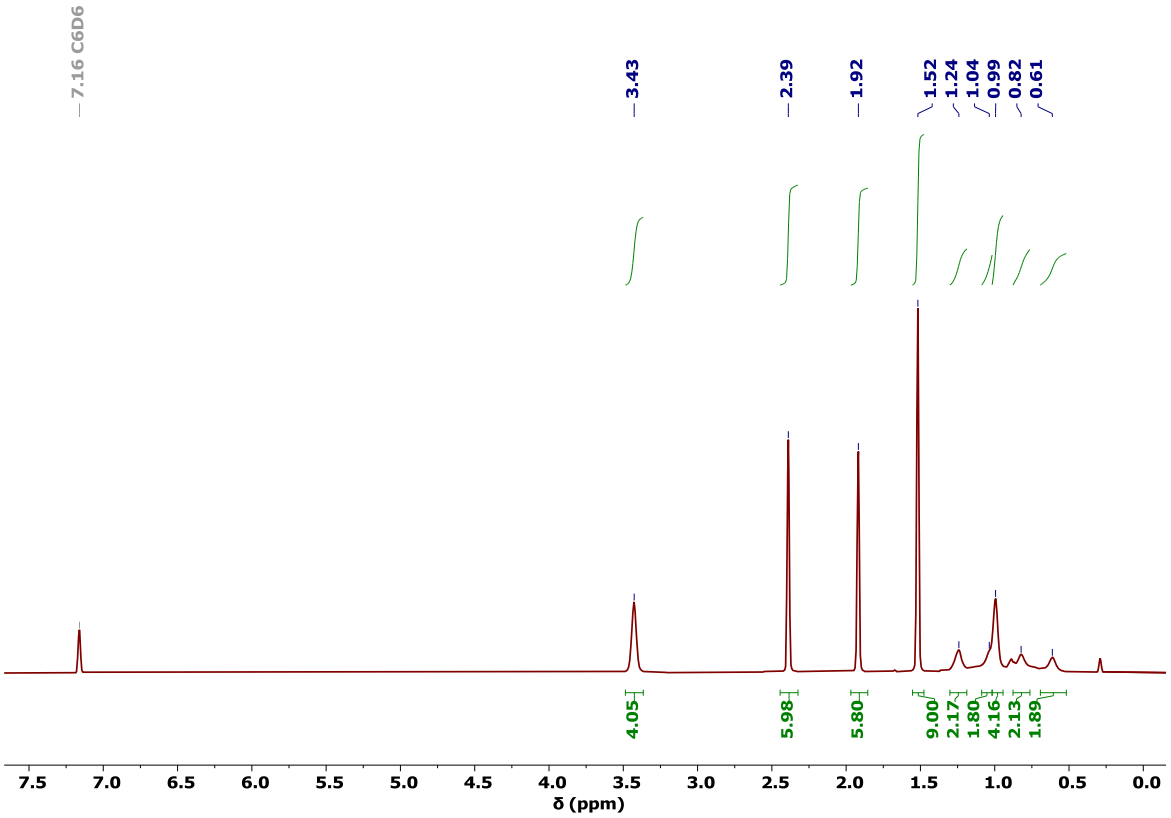

Figure S6. ^{1}H NMR spectrum of **3** in D_6-benzene.

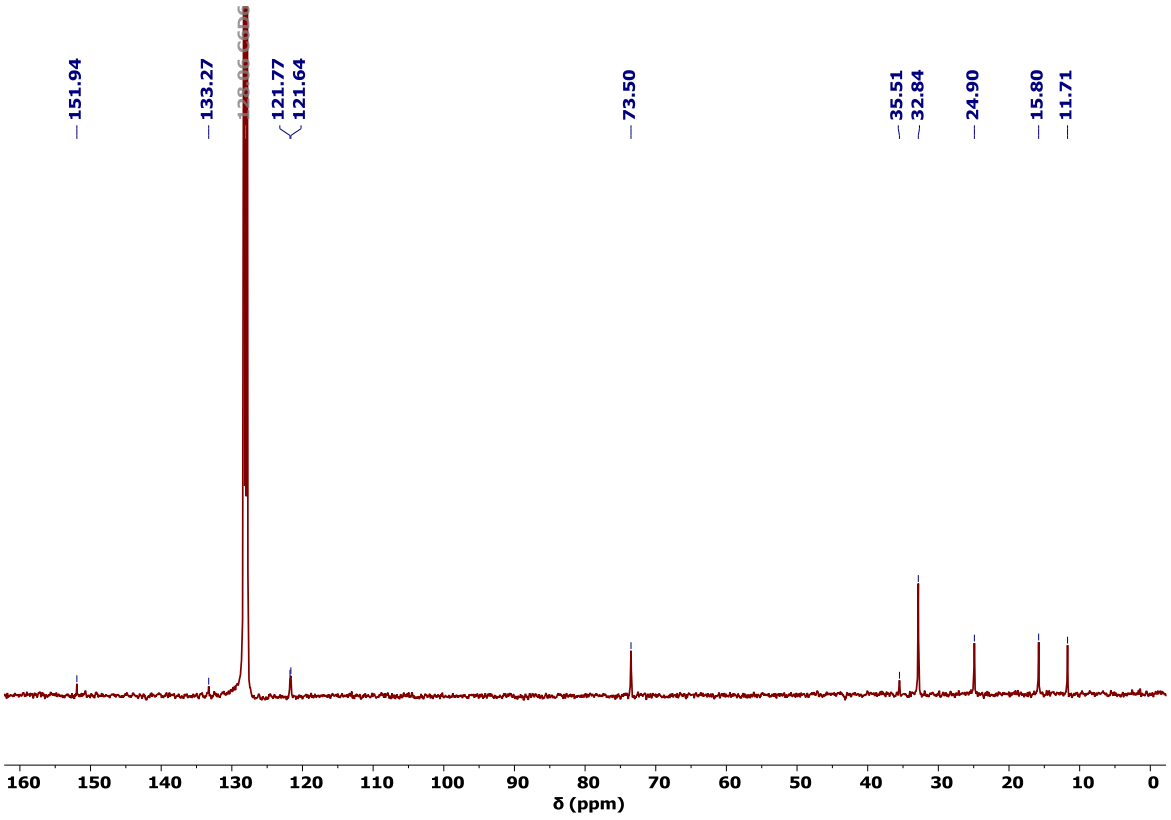

Figure S7. $^{13}C\{^{1}H\}$ NMR spectrum of **3** in D_6-benzene.

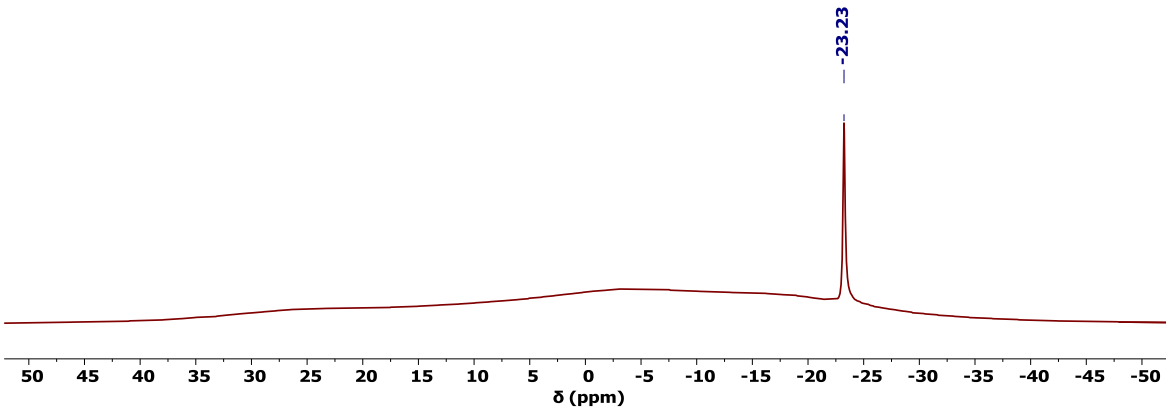

Figure S8. $^{11}B\{^{1}H\}$ NMR spectrum of **3** in D_6-benzene.

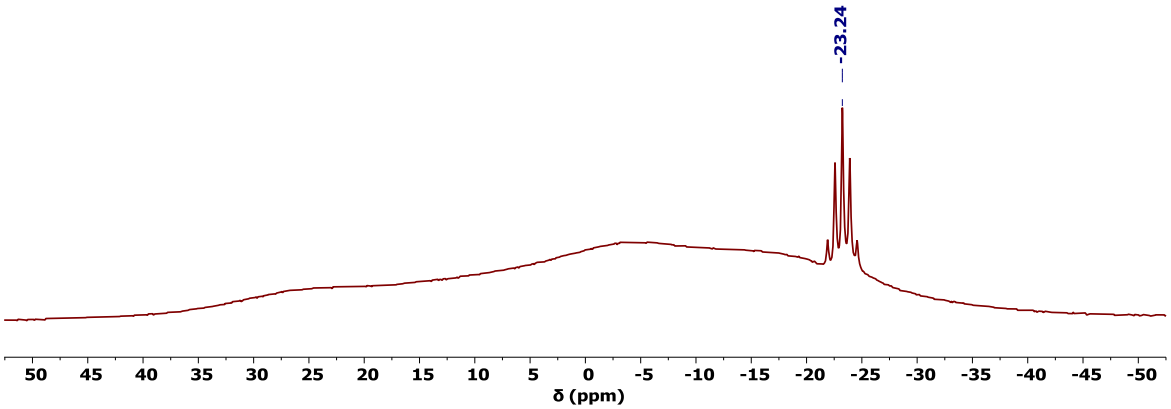

Figure S9. ^{11}B NMR spectrum of **3** in D_6-benzene.

Synthesis of [Dy(η^5-$C_5Me_4{}^tBu$)(κ^3-BH_4)$_2$(THF)] (4). Compound **4** was synthesised by following the same procedure as for **3**, using [$NaCp^{Me4tBu}$] (120 mg, 0.60 mmol) and [$Dy(BH_4)_3(THF)_3$] (254 mg, 0.60 mmol). Storing a saturated hexane solution at –40°C overnight resulted in pale-yellow crystals of **4** suitable for X-ray crystallography (164 mg, 62 %).

FTIR ($\bar{\nu}$/cm^{-1}): 3000-2850 (m, b, C-H), 2450 (m, s, B-H_T), 2300-2100 (m, b, B-H_B).

Elemental analysis (%), found (calculated) for **4** $C_{17}H_{37}DyB_2O$: C 46.15 (46.24); H 8.54 (8.45).

Synthesis of [Co{η^4-$C_4(SiMe_3)_4$}(η^5-Cp)] (5). [Co(η^5-Cp)$(CO)_2$] (12.50 g, 16.9 mL, 69.4 mmol), and bis(trimethylsilyl)acetylene (25.00 g, 33.2 mL, 147 mmol) were placed into a 250 mL round-bottomed flask equipped with a glass coated stirrer bar and a condenser. The reaction mixture was heated at 170 °C for 7 days using a silicone oil bath with stirring. The mixture initially refluxes as a deep red colour, before turning colourless after a few

days. It is extremely important to have an open system, otherwise the CO by-product will hinder the reaction. After 7 days, the reaction mixture was cooled to 60 °C, and the volatiles removed *in vacuo* before being dried overnight to give the crude product as a black powder (25.20 g, 78 %). Purification via column chromatography using pentane as the eluent gives the pure product **5** (second band) as a yellow powder (13.10 g, 41 %). ^{1}H NMR analysis of **5** is consistent with the reported literature and can be isolated in air.[122,134]

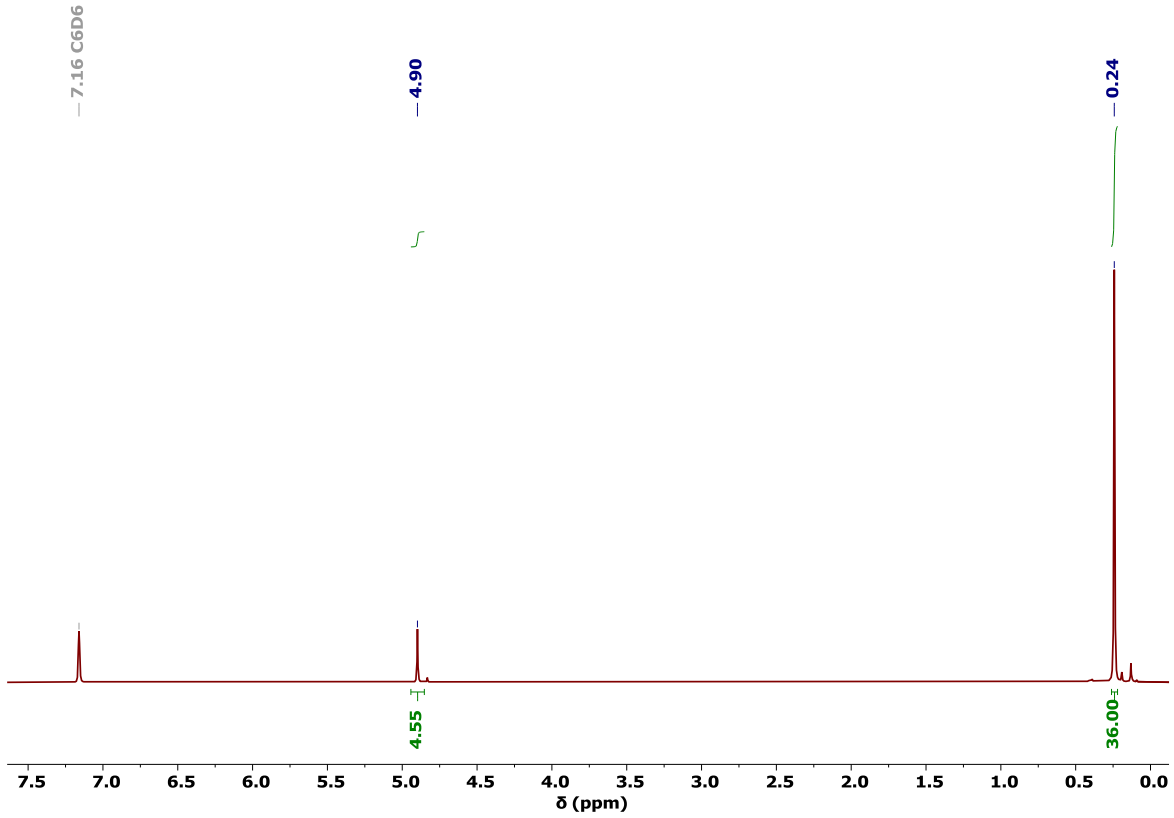

Figure S10. ^{1}H NMR spectra of **5** in D_6-benzene. 4.90 ppm (s, Cp, 5H), 0.24 ppm (s, $SiMe_3$, 36H).

Synthesis of $[Li_2\{\mu\text{-}\eta^4\text{:}\eta^4\text{-}C_4(SiMe_3)_4\}(THF)]_2$ (6). In a glovebox, **5** (13.10 g, 30.90 mmol) was added to an ampoule equipped with a glass coated stirrer bar and dissolved in THF (50 mL) to give an orange solution. Lithium powder (3.22 g, 463 mmol, 15 eq.) was added into the ampoule in small portions to control the exothermic nature of the reaction, and the resulting mixture was left to stir for 6 hours. An aliquot of the reaction was analysed by ^{1}H NMR indicating the complete consumption of **5** and the formation of LiCp. The THF was then removed *in vacuo* (1×10^{-2} mbar) to give a black powder, which was then extracted with warm hexane (*ca.* 40-50°C) (3 × 75 mL) and filtered through flame-dried Celite. The hexane was removed *in vacuo* to give **6** as colourless to off-yellow crystals (6.10 g, 43 %) Analysis of crystalline **6** is consistent with the reported literature.[120,122]

Aliquot ^{1}H NMR (δ/ppm, D_6-benzene with a few drops of D_8-THF): 5.65 (s, LiCp), 0.50 (s, $SiMe_3$, 36H).

Aliquot ^{7}Li NMR (δ/ppm, D_6-benzene with a few drops of D_8-THF): −5.41 (Li_2Cb, FWHM = 11 Hz), −5.27 (LiCp, FWHM cannot be determined due to overlap).

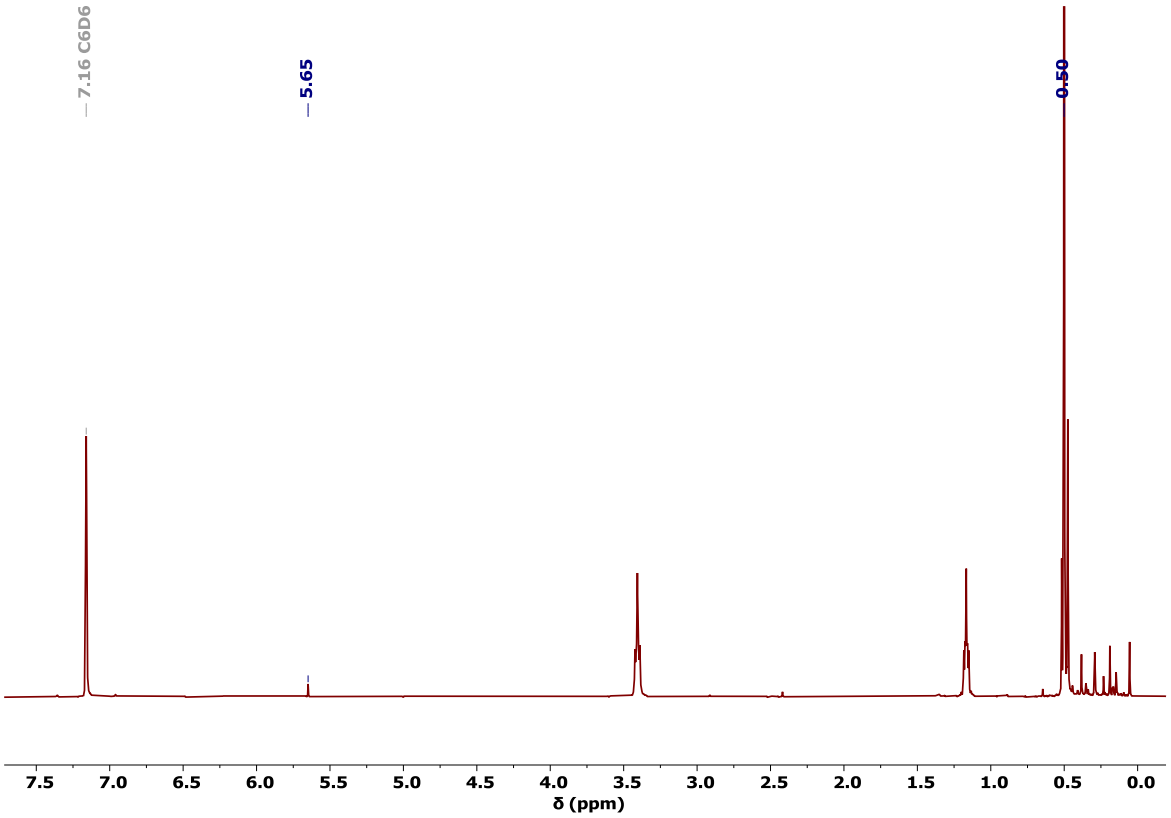

Figure S11. Aliquot ^{1}H NMR during the synthesis of **6** in D_6-benzene with a few drops of D_8-THF.

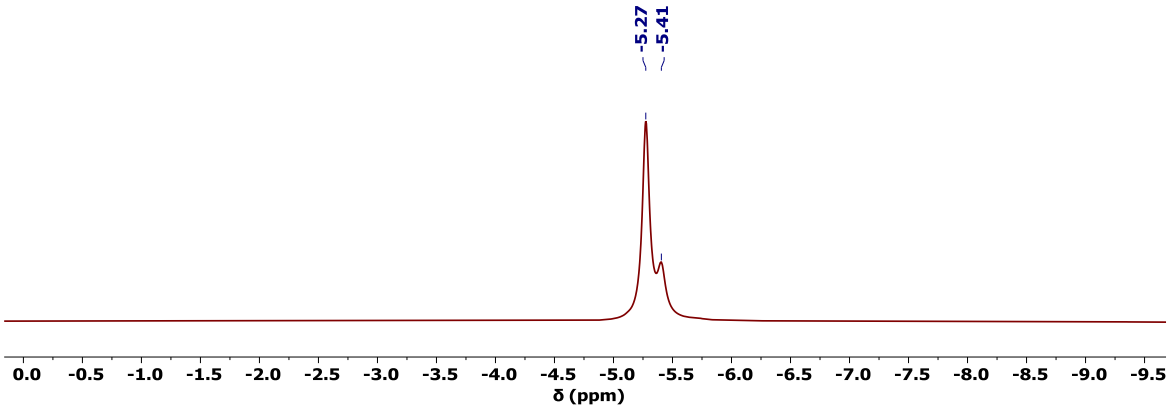

Figure S12. Aliquot ^{7}Li NMR during the synthesis of **6** in D_6-benzene with a few drops of D_8-THF.

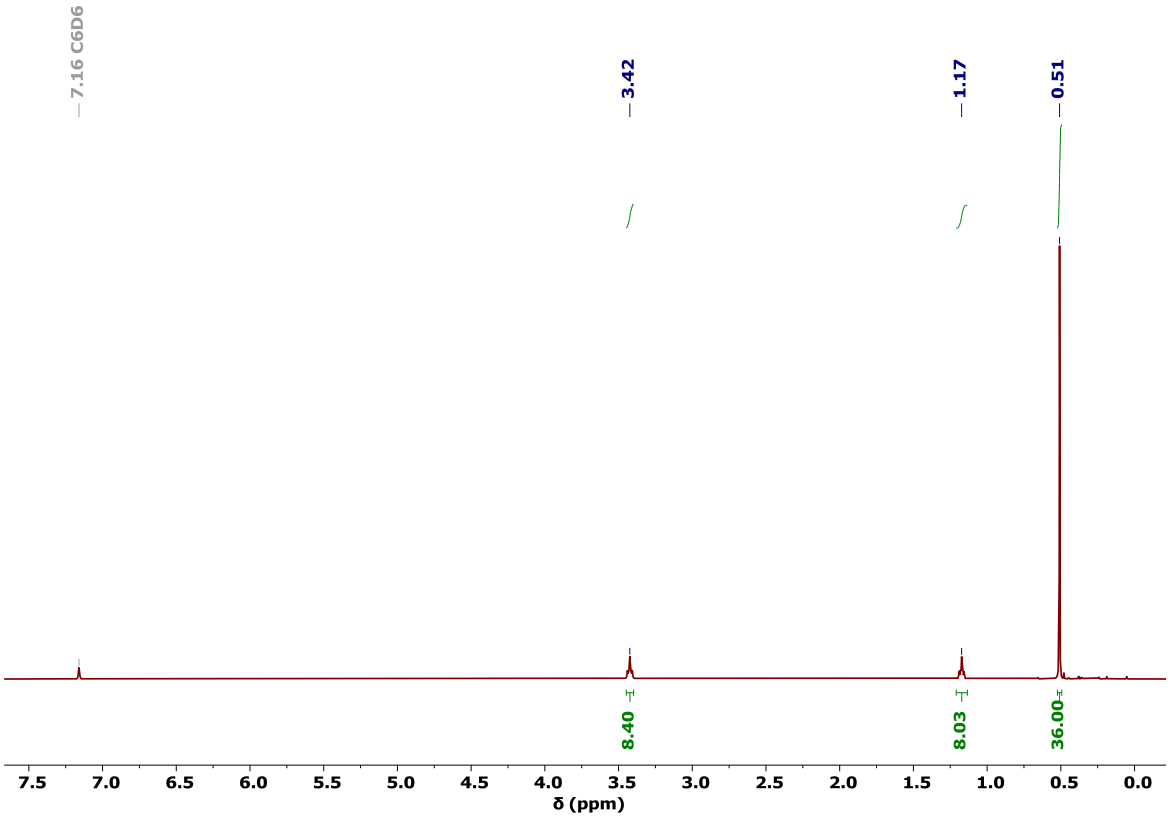

Figure S13. ^{1}H NMR spectra of **6** in D_6-benzene. 3.42 ppm (m, THF, 8H), 1.17 ppm (m, THF, 8H), 0.51 ppm (s, $SiMe_3$, 36H).

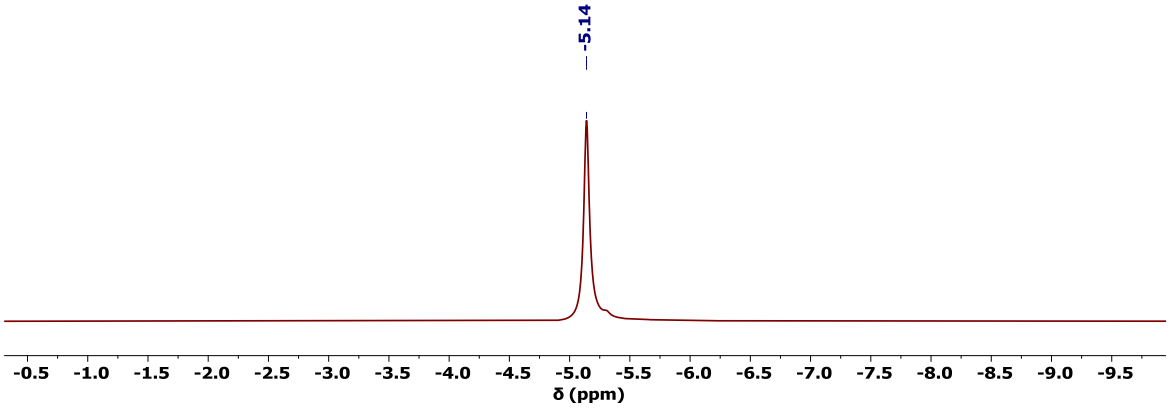

Figure S14. ^{7}Li NMR spectra of **6** in D_6-benzene.

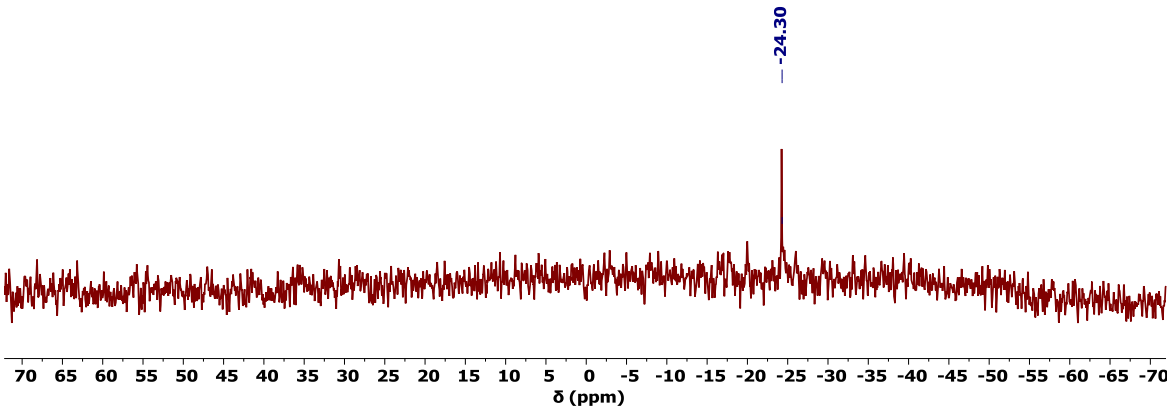

Figure S15. ^{29}Si{^{1}H} NMR spectra of **6** in D_6-benzene.

Synthesis of [$C_4(SiMe_3)_4$] (7). An off-yellow solution of **6** (6.10 g, 12.2 mmol) in hexane (50 mL) was cooled to 0 °C. Meso-2,3-dibromobutane (5.27 g, 3.0 mL, 24.4 mmol) was added quickly into the reaction mixture via cannula transfer, resulting in the instant formation of a white precipitate. The reaction mixture was stirred for a short time (*ca.* 1 min) before being placed under vacuum and all volatiles were removed. The product was then extracted by hexane (3 × 50 mL) and filtered through flame-dried Celite. The hexane was removed *in vacuo*, and the resulting crude red solid was sublimed at 60 °C under reduced pressure (1 × 10^{-2} mbar) to give **7** as deep red crystals (3.32 g, 80 %). Analysis of **7** is consistent with the reported literature.[121,122]

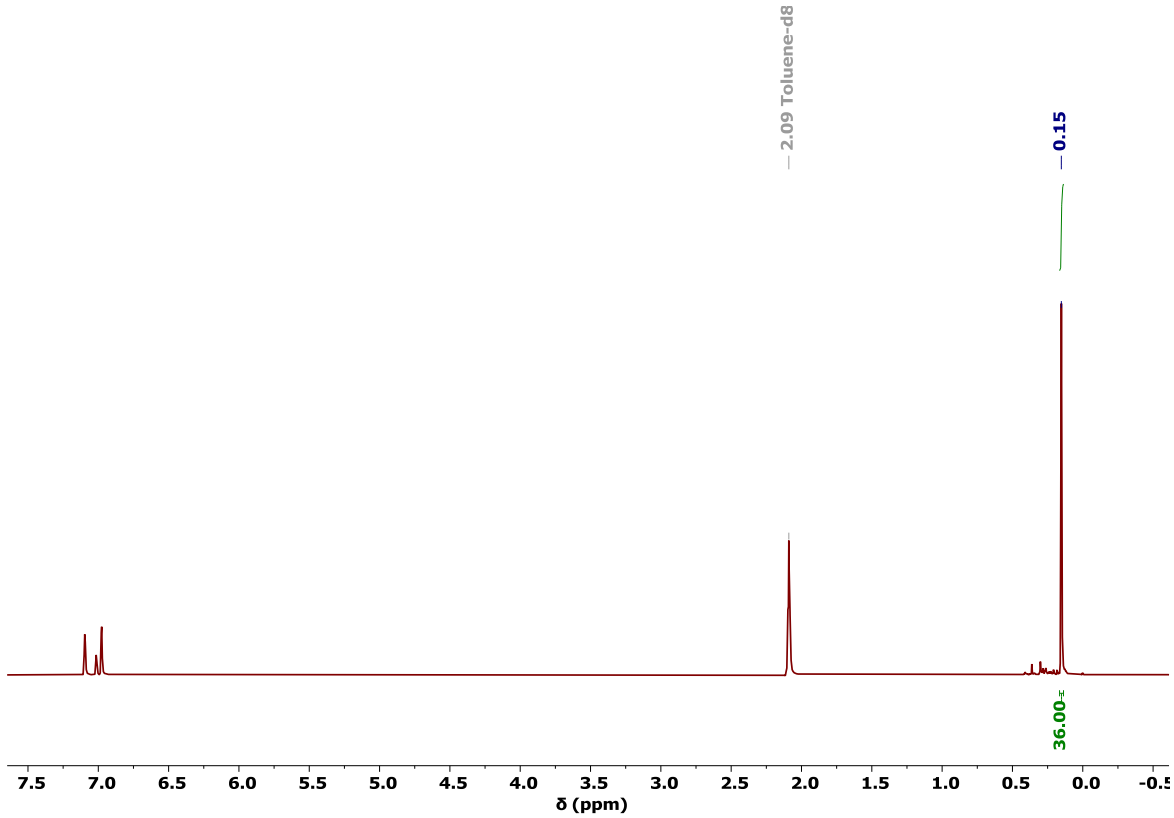

Figure S16. ^{1}H NMR spectra of **7** in D_8-toluene. 0.15 ppm (s, $SiMe_3$, 36H)

Synthesis of [$Na_2\{\mu\text{-}\eta^4\text{:}\eta^4\text{-}C_4(SiMe_3)_4\}THF]_2$ (8). Sodium metal (41 mg, 1.80 mmol) was added into a red solution of **7** (245 mg, 0.72 mmol) in THF (10 mL). The resulting red solution was left to stir for 20 h, by which time the solution became dark orange. The solution was filtered, and the solvent removed *in vacuo* to give a yellow solid which was washed with hexane (3 × 20 mL) to give **8** as a pastel yellow powder (237 mg, 72 %.). Yellow crystals of **8** were obtained by layering hexane on a saturated THF solution and storing at –40°C for three days (36 mg, 72 % based on 50 mg of crude **8**).

^{1}H NMR (δ/ppm, D_6-benzene with a few drops of D_8-THF): 3.53 (m, CH_2O, 4H), 1.45 (m, CH_2, 4H) 0.53 (s, $SiMe_3$, 36H).

$^{13}C\{^{1}H\}$ NMR (δ/ppm, D_6-benzene with a few drops of D_8-THF): 104.13 ($\underline{C}_4$ ring), 67.46 ($\underline{C}H_2O$), 25.29 ($\underline{C}H_2$), 5.79 ($Si\underline{Me}_3$).

$^{29}Si\{^{1}H\}$ NMR (δ/ppm, D_6-benzene with a few drops of D_8-THF): –31.22.

^{23}Na NMR (δ/ppm, D_6-benzene with a few drops of D_8-THF): –33.21 (FWHM = 1332 Hz).

FTIR ($\bar{\nu}$/cm^{-1}): 3000-2850 (m, b, C-H).

Elemental analysis (%), found (calculated) for **8** $C_{40}H_{88}Na_4Si_8O_2$: C 50.93 (52.35), H 9.47 (9.66), for **8**(–THF) $C_{36}H_{80}Na_4Si_8O_1$: C 50.93 (51.13), H 9.47 (9.53).

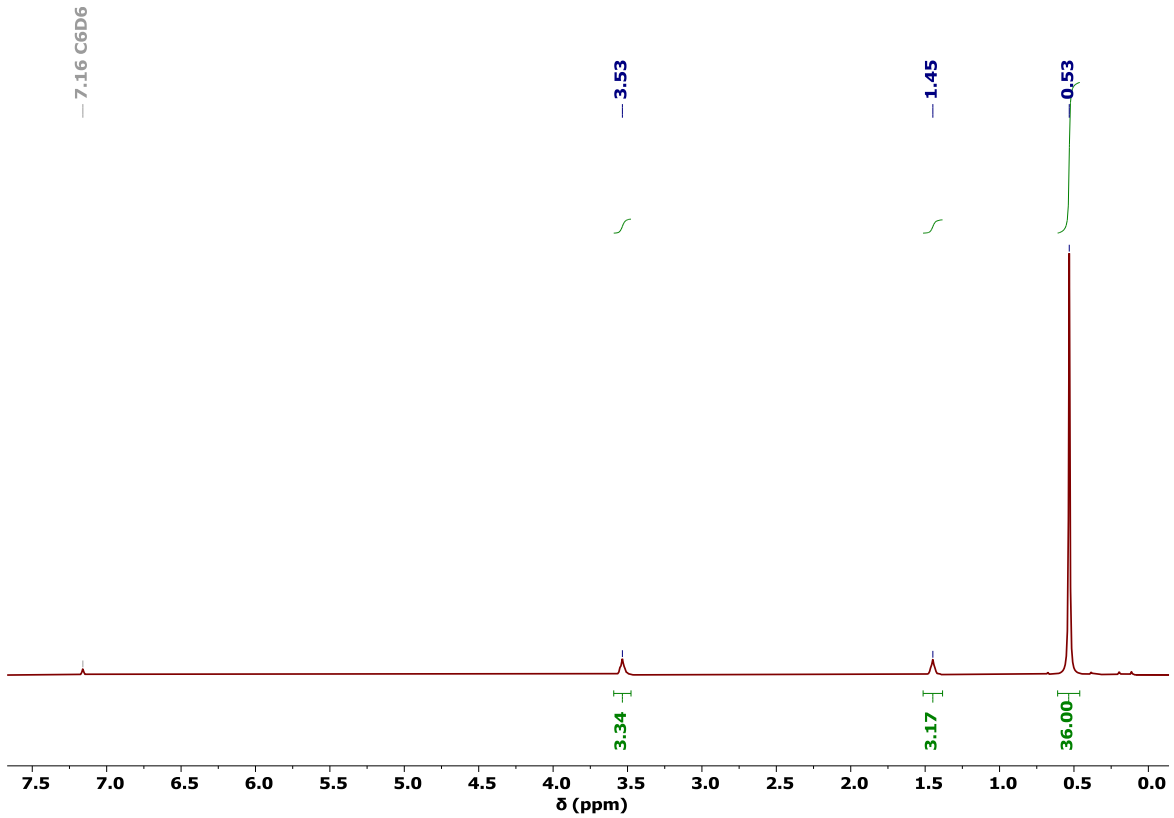

Figure S17. ^{1}H NMR spectrum of **8** in D_6-benzene with a few drops of D_8-THF.

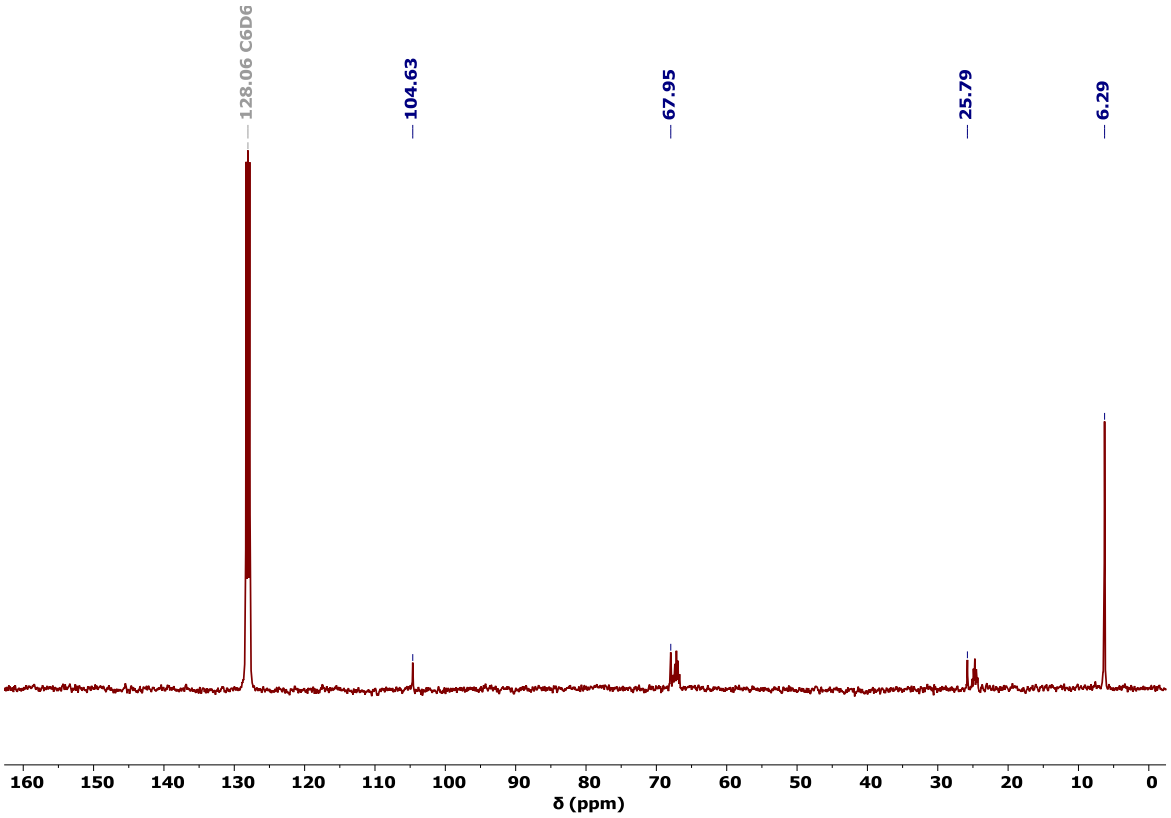

Figure S18. $^{13}C\{^{1}H\}$ NMR spectrum of **8** in D_6-benzene with a few drops of D_8-THF.

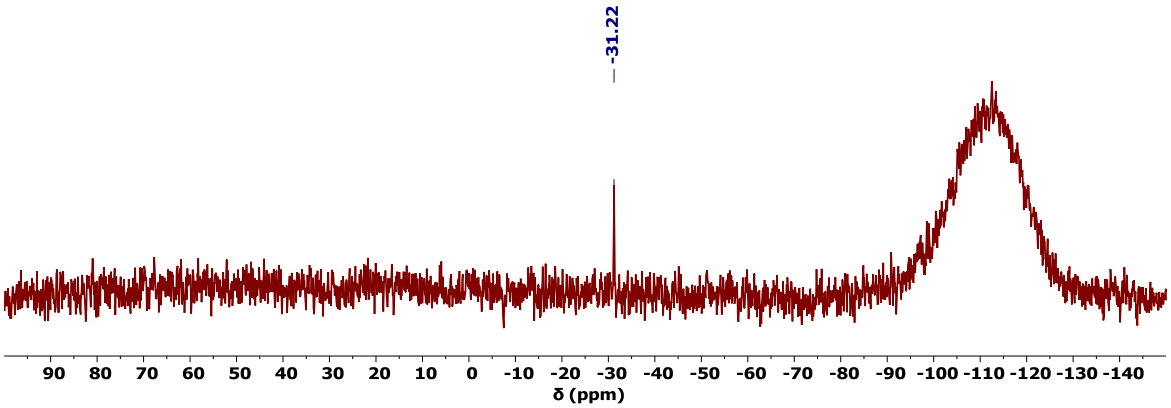

Figure S19. $^{29}Si\{^{1}H\}$ NMR spectrum of **8** in D_6-benzene with a few drops of D_8-THF. The broad peak corresponds to the NMR tube.

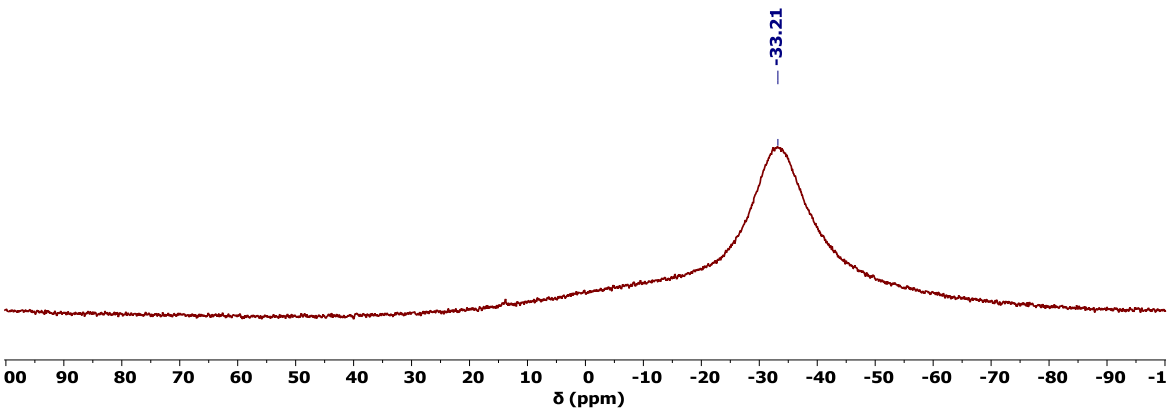

Figure S20. $^{23}Na\{^{1}H\}$ NMR spectrum of **8** in D_6-benzene with a few drops of D_8-THF.

Synthesis of [$K_2\{\mu\text{-}\eta^4\text{:}\eta^4\text{-}C_4(SiMe_3)_4\}$] (9). Compound **9** was synthesised by following the same procedure as for **8**, using **7** (400 mg, 1.17 mmol) and potassium metal (115 mg, 2.93 mmol). **9** was isolated as a yellow powder (406 mg, 83 %). Analysis of **9** is consistent with the reported literature.[111,122]

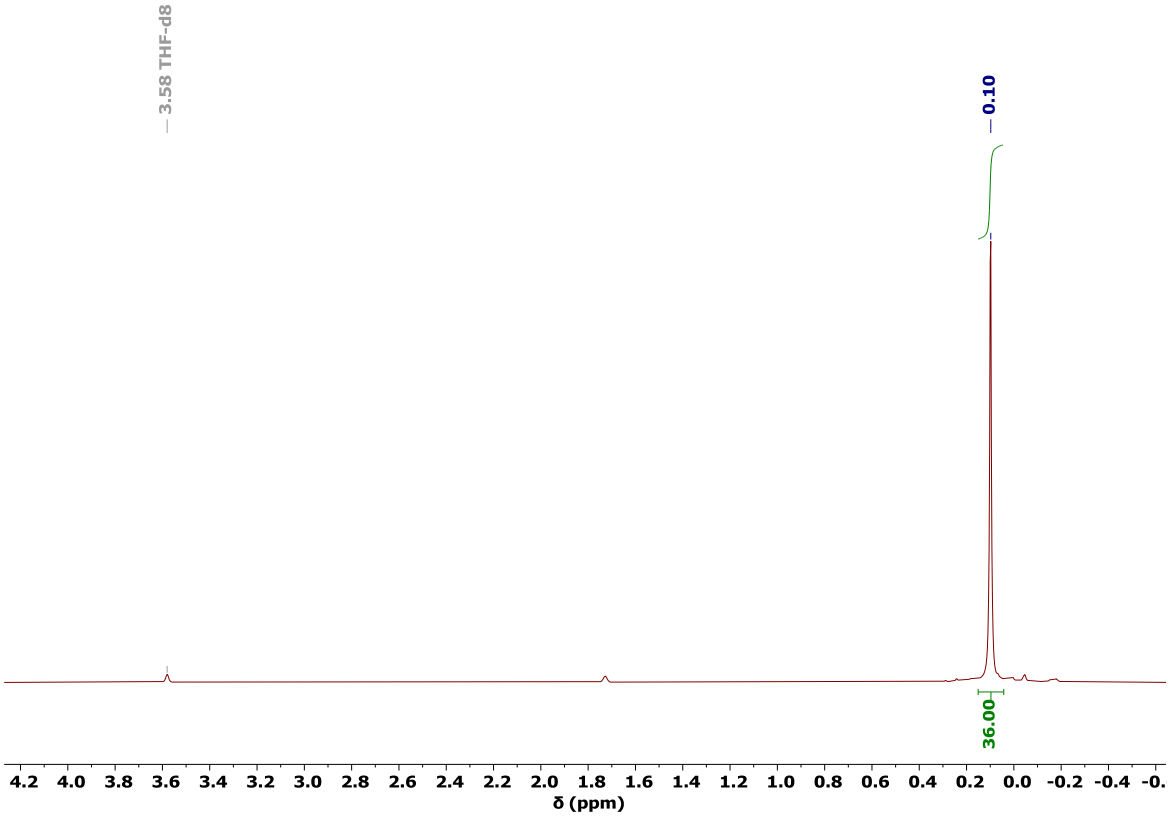

Figure S21. ^{1}H NMR spectrum of **9** in D_8-THF. 0.10 ppm (s, $SiMe_3$, 36H).

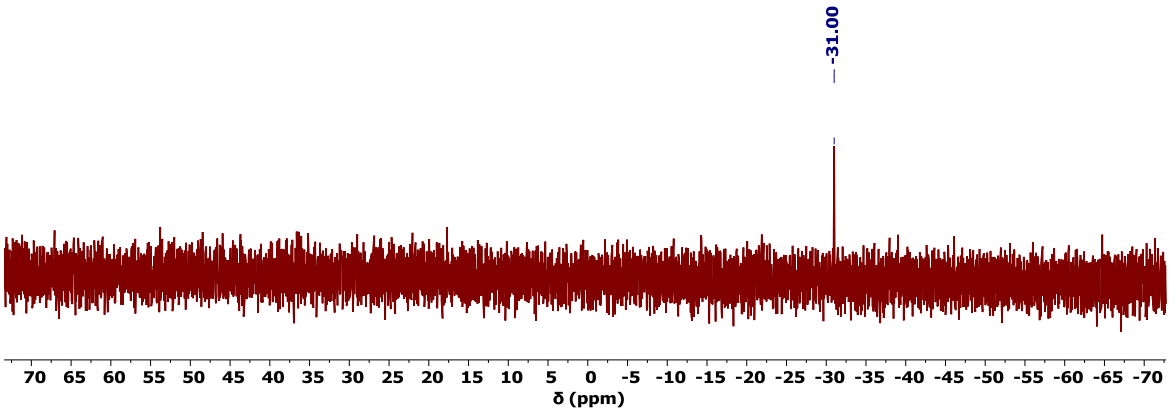

Figure S22. $^{29}Si\{^1H\}$ NMR spectrum of **9** in D_8-THF.

Synthesis of [$Rb_2\{\mu\text{-}\eta^4\text{:}\eta^4\text{-}C_4(SiMe_3)_4\}$] (10). Compound **10** was synthesised by following the same procedure as for **8**, using **7** (100 mg, 0.29 mmol) and rubidium metal (63 mg, 0.73 mmol). Crude **10** was isolated as a yellow powder (91 mg, 61 %). Yellow crystals of **10** were obtained by layering hexane on a saturated toluene solution and storing at –40°C for three days (76 mg, 51 %)

^{1}H NMR (δ/ppm, D_8-toluene): 0.37 (s, $SiMe_3$, 36H).

$^{13}C\{^1H\}$ NMR (δ/ppm, D_8-toluene): 110.37 ($\underline{C}_4$ ring), 5.24 ($Si\underline{Me}_3$).

$^{29}Si\{^1H\}$ NMR (δ/ppm, D_8-toluene): −31.66.

FTIR ($\bar{\nu}$/cm^{-1}): 3000-2850 (m, b, C-H).

Elemental analysis (%), found (calculated) for **10** $C_{16}H_{36}Rb_2Si_4$: C 36.43 (37.55), H 7.18 (7.09).

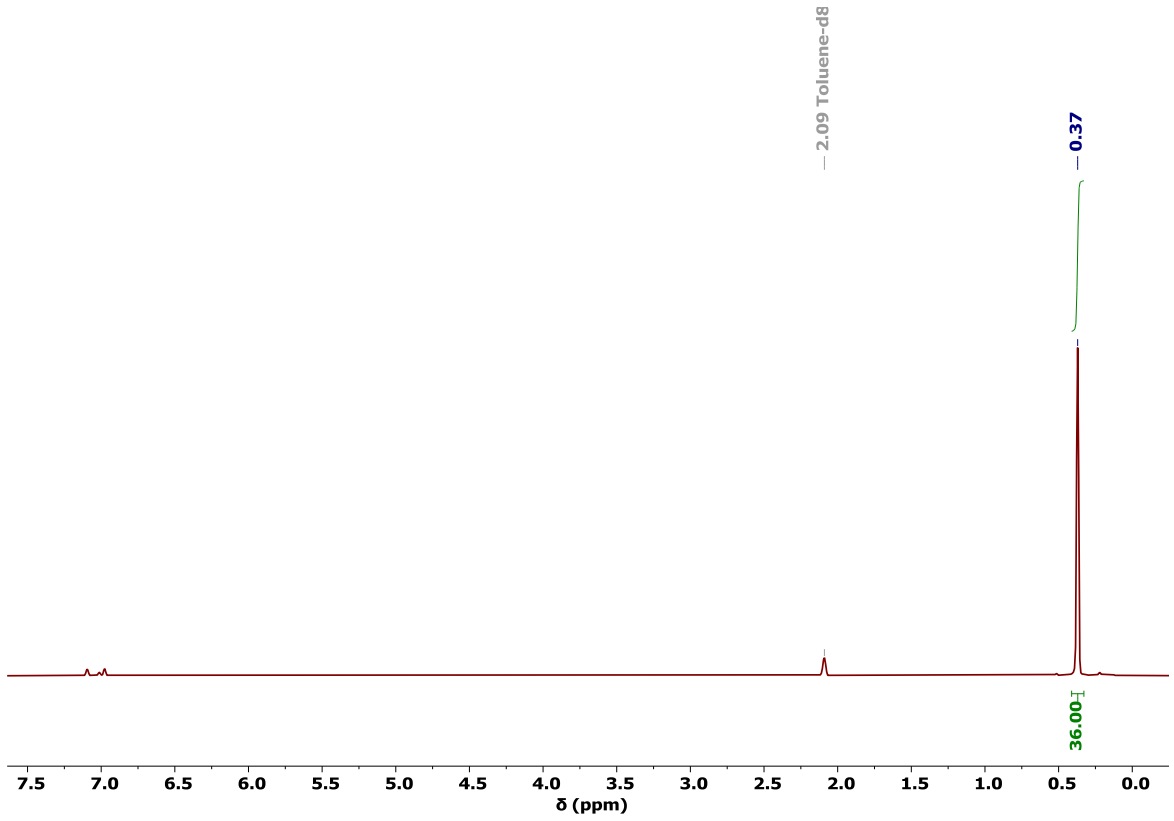

Figure S23. ^{1}H NMR spectrum of **10** in D_8-toluene.

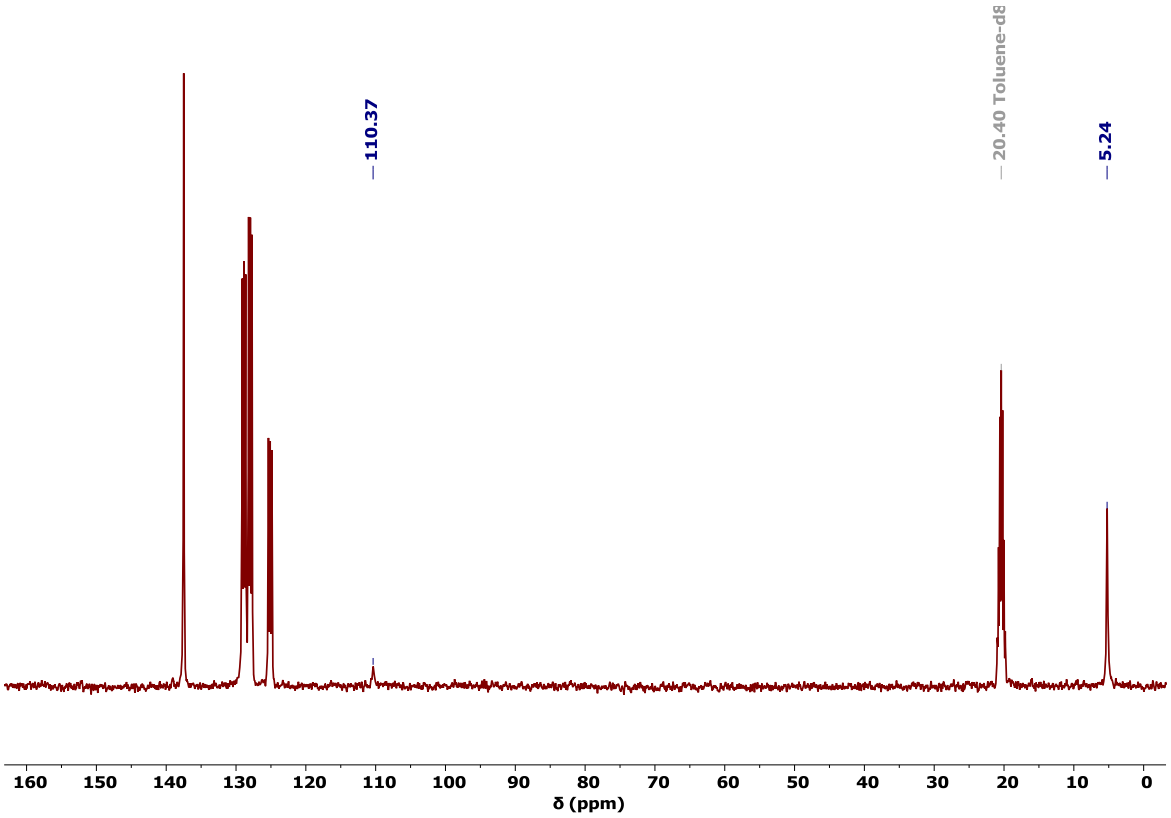

Figure S24. $^{13}C\{^{1}H\}$ NMR spectrum of **10** in D_8-toluene.

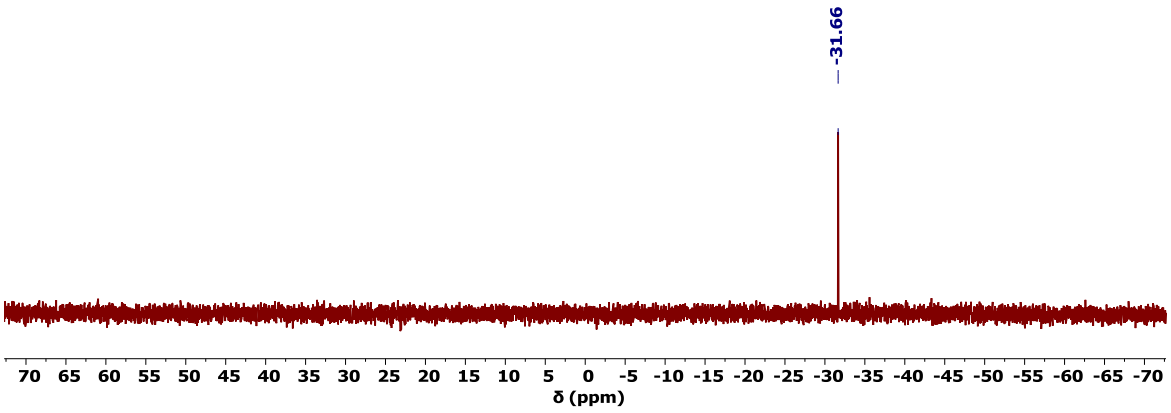

Figure S25. $^{29}Si\{^{1}H\}$ NMR spectrum of **10** in D_8-toluene.

Synthesis of $[Cs_2\{\mu\text{-}\eta^4\text{:}\eta^4\text{-}C_4(SiMe_3)_4\}C_7H_8]$ (11). Compound **11** was synthesised by following the same procedure as for **8**, using **7** (100 mg, 0.29 mmol) and caesium metal (97 mg, 0.73 mmol). Crude **11** was isolated as a yellow powder (119 mg, 67 %). Red crystals of **11** were obtained by layering hexane on a saturated toluene solution and storing at –40°C for three days. Upon washing the red crystals with hexane, the crystals turn yellow indicating the loss of toluene (66 mg, 37 %).

^{1}H NMR (δ/ppm, D_8-toluene): 0.37 (s, $SiMe_3$, 36H).

$^{13}C\{^{1}H\}$ NMR (δ/ppm, D_8-toluene): 112.46 ($\underline{C}_4$ ring), 4.54 ($Si\underline{Me}_3$).

$^{29}Si\{^{1}H\}$ NMR (δ/ppm, D_8-toluene): −25.77.

$^{133}Cs\{^{1}H\}$ NMR (δ/ppm, D_8-toluene): –150.89.

FTIR ($\bar{\nu}$/cm^{-1}): 3000-2850 (m, b, C-H).

Elemental analysis (%), found (calculated) for **11** $C_{16}H_{36}Cs_2Si_4$: C 30.58 (31.68), H 6.13 (5.98).

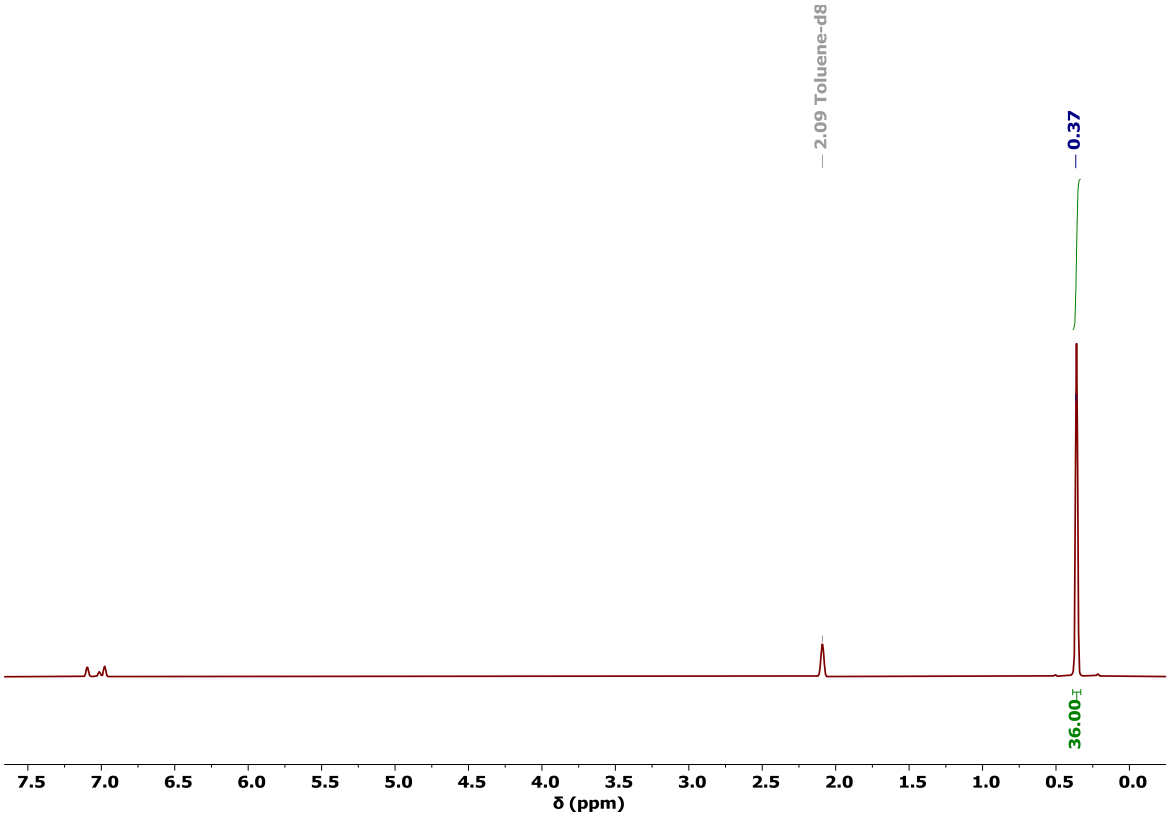

Figure S26. ^{1}H NMR spectrum of **11** in D_8-toluene.

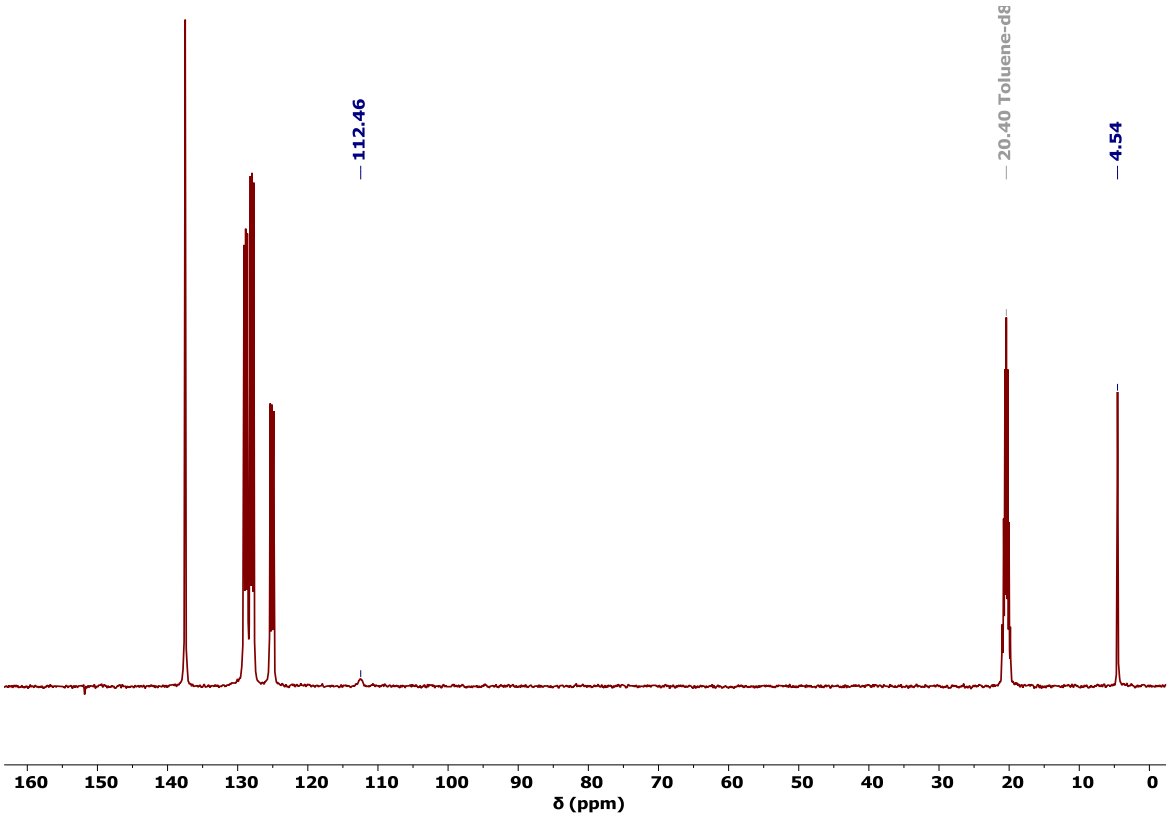

Figure S27. $^{13}C\{^{1}H\}$ NMR spectrum of **11** in D_8-toluene.

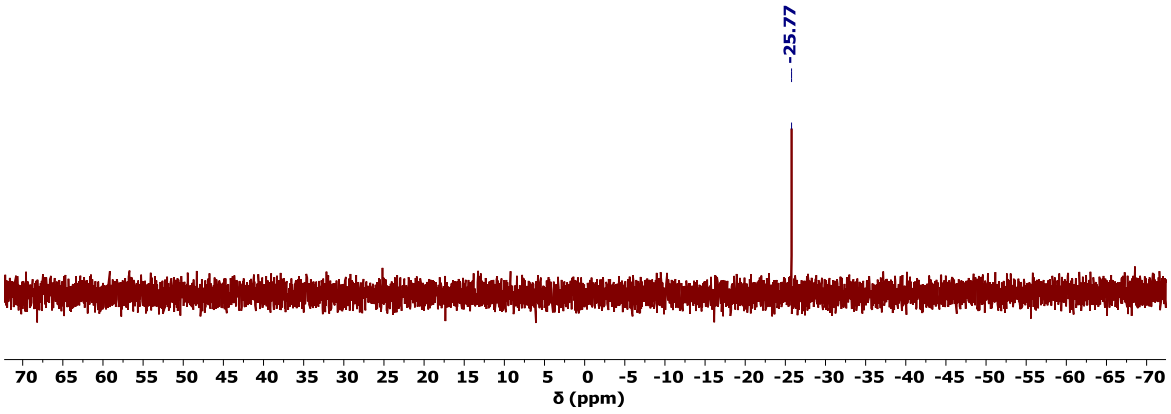

Figure S28. $^{29}Si\{^{1}H\}$ NMR spectrum of **11** in D_8-toluene.

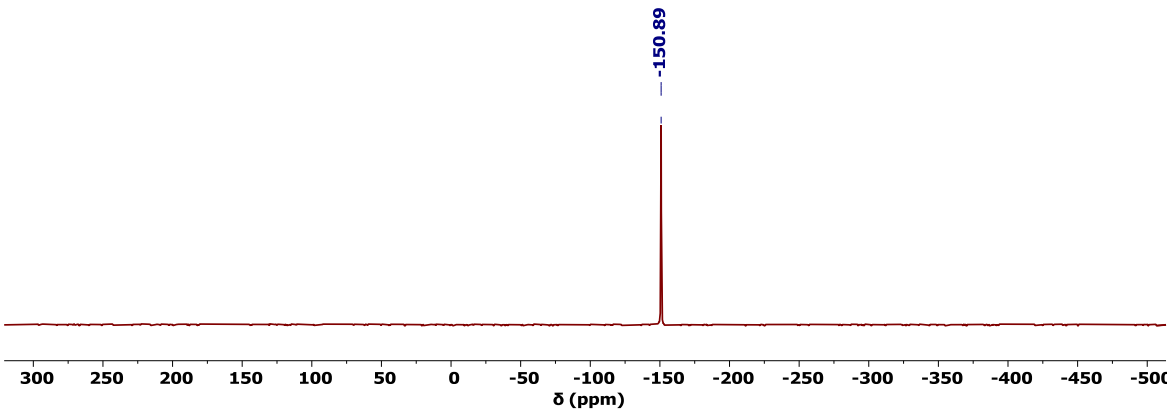

Figure S29. $^{133}Cs\{^{1}H\}$ NMR spectrum of **11** in D_8-toluene.

Synthesis of [Y{η^4-$C_4(SiMe_3)_4$}(κ^3-BH_4)$_2$(THF)Na]$_\infty$ (12). A solution of **8** (200 mg, 0.44 mmol) in benzene (20 mL) was added dropwise into a solution of [Y(BH_4)$_3$(THF)$_3$] (152 mg, 0.44 mmol) in benzene (20 mL). The resulting dark red solution was swirled and left to stand for 20 hours, by which time yellow crystals of **12** suitable for X-ray crystallography had formed, which were washed with benzene and hexane and then isolated (155 mg, 64 %).

^{1}H NMR (δ/ppm, D_8-THF): 3.62 (m, CH_2O, 4H), 1.77 (m, CH_2, 4H), 0.20 (bs, 1:1:1:1 q, $^1J_{HB}$ = 82 Hz, BH_4, could not be accurately integrated due to overlap with $SiMe_3$ signal at 0.13 ppm), 0.13 (s, $SiMe_3$, 36H).

^{13}C{^{1}H} NMR (δ/ppm, D_8-THF): 122.63 ($\underline{C}_4$ ring), 68.38 ($\underline{C}H_2O$), 26.48 ($\underline{C}H_2$), 5.27 (Si$\underline{Me}_3$).

^{11}B{^{1}H} NMR (δ/ppm, D_8-THF): −23.00 (bs, FWHM = 276 Hz, BH_4).

^{11}B NMR (δ/ppm, D_8-THF): −23.00 (bs, FWHM = 377 Hz,BH_4).

^{29}Si{^{1}H} NMR (δ/ppm, D_8-THF): −22.69.

^{23}Na NMR (δ/ppm, D_8-THF): −4.26 (FWHM = 48 Hz).

FTIR ($\bar{\nu}$/cm^{-1}): 3000-2850 (m, b, C-H), 2450 (m, s, B-H_T), 2300-2100 (m, b, B-H_B).

Despite repeated attempts, satisfactory elemental analysis could not be obtained for this compound, a representative result being (%), found (calculated) for **12** $C_{20}H_{52}YNaB_2Si_4O$: C 35.90 (43.32); H 8.76 (9.45). However, the spectroscopic analysis of this compound is consistent with the molecular structure determined by X-ray crystallography.

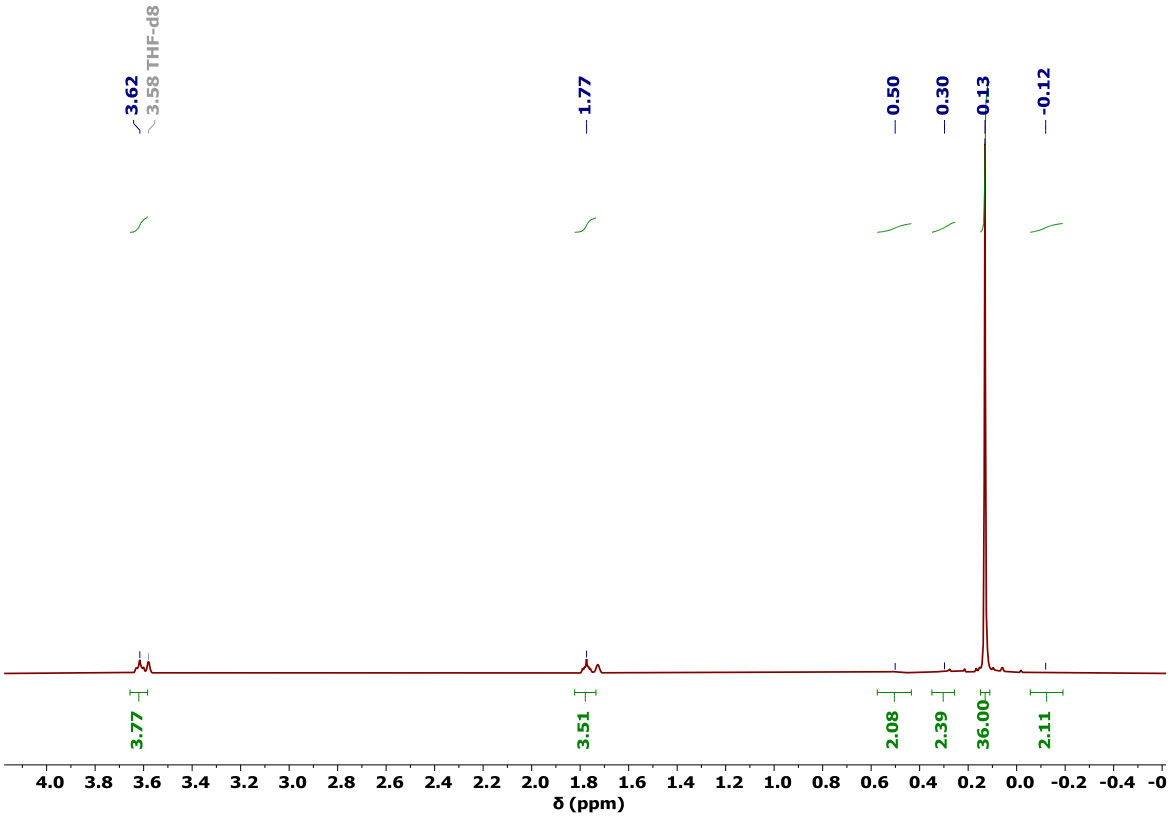

Figure S30. ^{1}H NMR spectrum of **12** in D_8-THF.

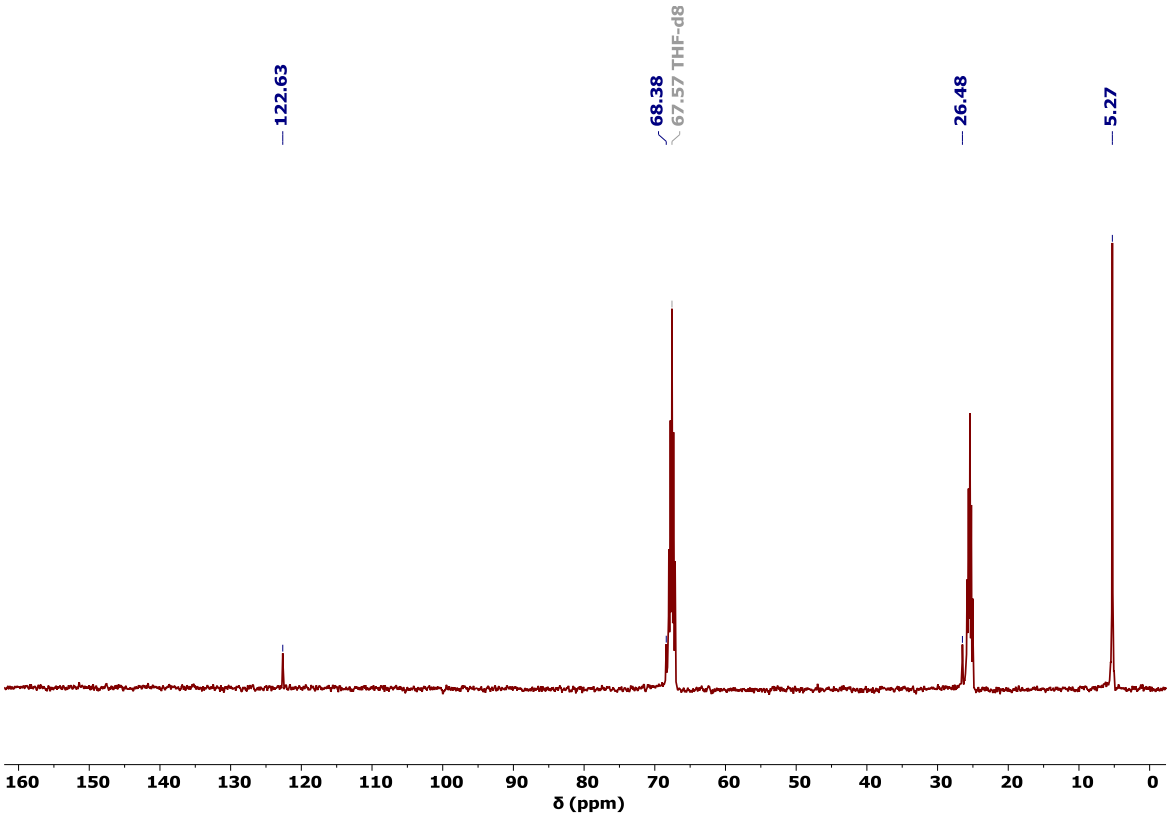

Figure S31. $^{13}C\{^{1}H\}$ NMR spectrum of **12** in D_8-THF.

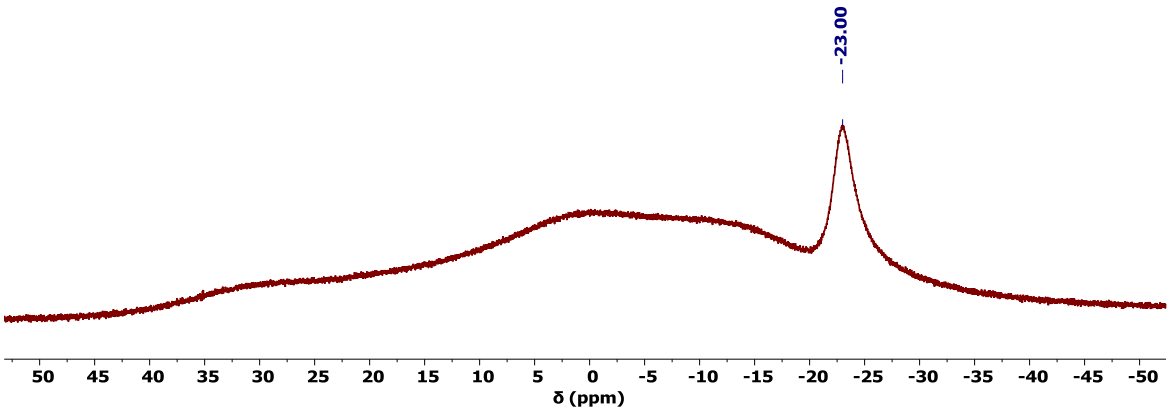

Figure S32. $^{11}B\{^{1}H\}$ NMR spectrum of **12** in D_8-THF.

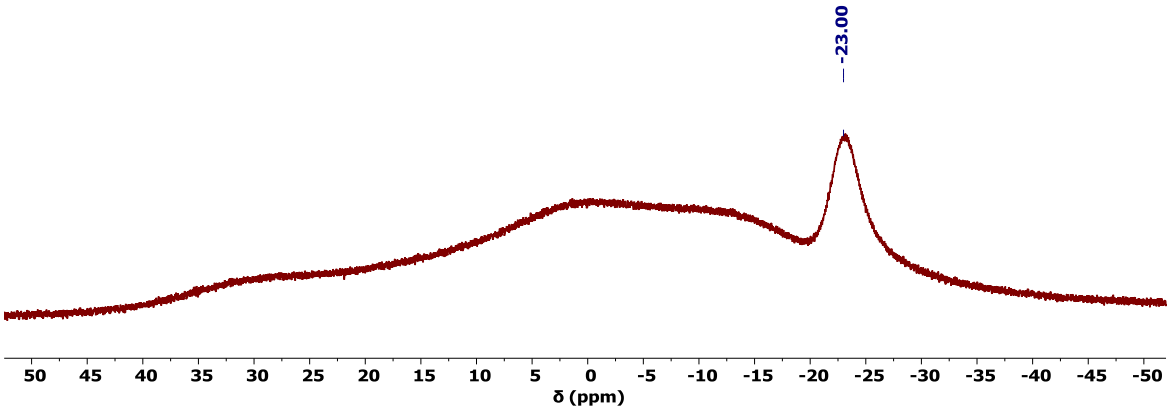

Figure S33. ^{11}B NMR spectrum of **12** in D_8-THF.

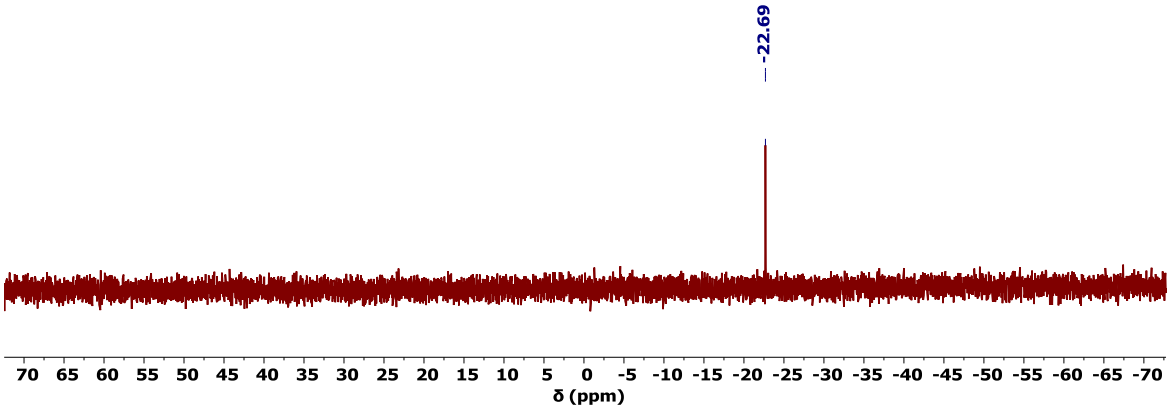

Figure S34. $^{29}Si\{^{1}H\}$ NMR spectrum of **12** in D_8-THF.

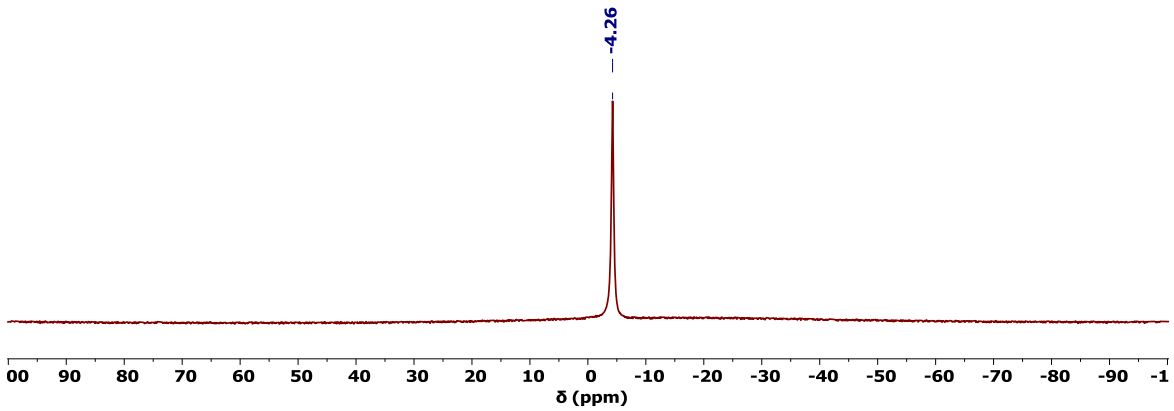

Figure S35. $^{23}Na\{^{1}H\}$ NMR spectrum of **12** in D_8-THF.

Synthesis of $[Dy\{\eta^4\text{-}C_4(SiMe_3)_4\}(\kappa^3\text{-}BH_4)_2(THF)Na]_\infty$ (13). Compound **13** was synthesised by following the same procedure as for **12**, using **8** (237 mg, 0.52 mmol) and $[Dy(BH_4)_3(THF)_3]$ (219 mg, 0.52 mmol). Yellow crystals of **13** suitable for X-ray crystallography formed from the crude reaction mixture, which were washed with benzene and hexane and then isolated (156 mg, 48 %).

FTIR ($\bar{\nu}$/cm^{-1}): 3000-2850 (m, b, C-H), 2450 (m, s, B-H_T), 2300-2100 (m, b, B-H_B).

Elemental analysis (%), found (calculated) for **13** $C_{20}H_{52}DyNaB_2Si_4O$: C 37.66 (38.25); H 8.50 (8.35).

Synthesis of $[Y\{\eta^4\text{-}C_4(SiMe_3)_4\}(\kappa^3\text{-}BH_4)_2(THF)K]_\infty$ (14). A solution of **9** (200 mg, 0.48 mmol) in benzene (20 mL) was added dropwise into a solution of $[Y(BH_4)_3(THF)_3]$ (167 mg, 0.48 mmol) in benzene (20 mL). The resulting dark red solution was swirled and left to stand for 20 hours, by which time a yellow precipitate (with some crystalline material) had deposited. The benzene was decanted, and the resulting solid was washed with hexane (3 × 20 mL), extracted with THF (2 × 20 mL) and filtered. The solvent was removed *in vacuo* to give a yellow powder subsequently identified as **14** (194 mg, 71 %). Pale yellow crystals of **14** suitable for single-crystal X-ray diffraction were obtained by the slow evaporation of layered hexane on a saturated THF solution over five days (151 mg, 56 %).

^{1}H NMR (δ/ppm, D_8-THF): 3.62 (m, CH_2O, 4H), 1.77 (m, CH_2, 4H), 0.29 (1:1:1:1 q, $^{1}J_{HB}$ = 83 Hz, BH_4, 8H), 0.14 (s, $SiMe_3$, 36H).

$^{13}C\{^{1}H\}$ NMR (δ/ppm, D_8-THF): 123.32 (d, $^{1}J_{CY}$ = 4.45 Hz, $\underline{C}_4$ ring), 68.37 ($\underline{C}H_2O$), 26.50 ($\underline{C}H_2$), 5.24 ($SiMe_3$).

$^{11}B\{^{1}H\}$ NMR (δ/ppm, D_8-THF): −27.01 (s, FWHM = 15 Hz, BH_4).

^{11}B NMR (δ/ppm, D_8-THF): −27.00 (quint, $^{1}J_{BH}$ = 84 Hz, BH_4).

$^{29}Si\{^{1}H\}$ NMR (δ/ppm, D_8-THF): −22.58.

FTIR ($\bar{\nu}$/cm^{-1}): 3000-2850 (m, b, C-H), 2450 (m, s, B-H_T), 2300-2100 (m, b, B-H_B).

Elemental analysis (%), found (calculated) for **14** $C_{20}H_{52}YKB_2Si_4O$: C 41.12 (42.10); H 8.73 (9.19).

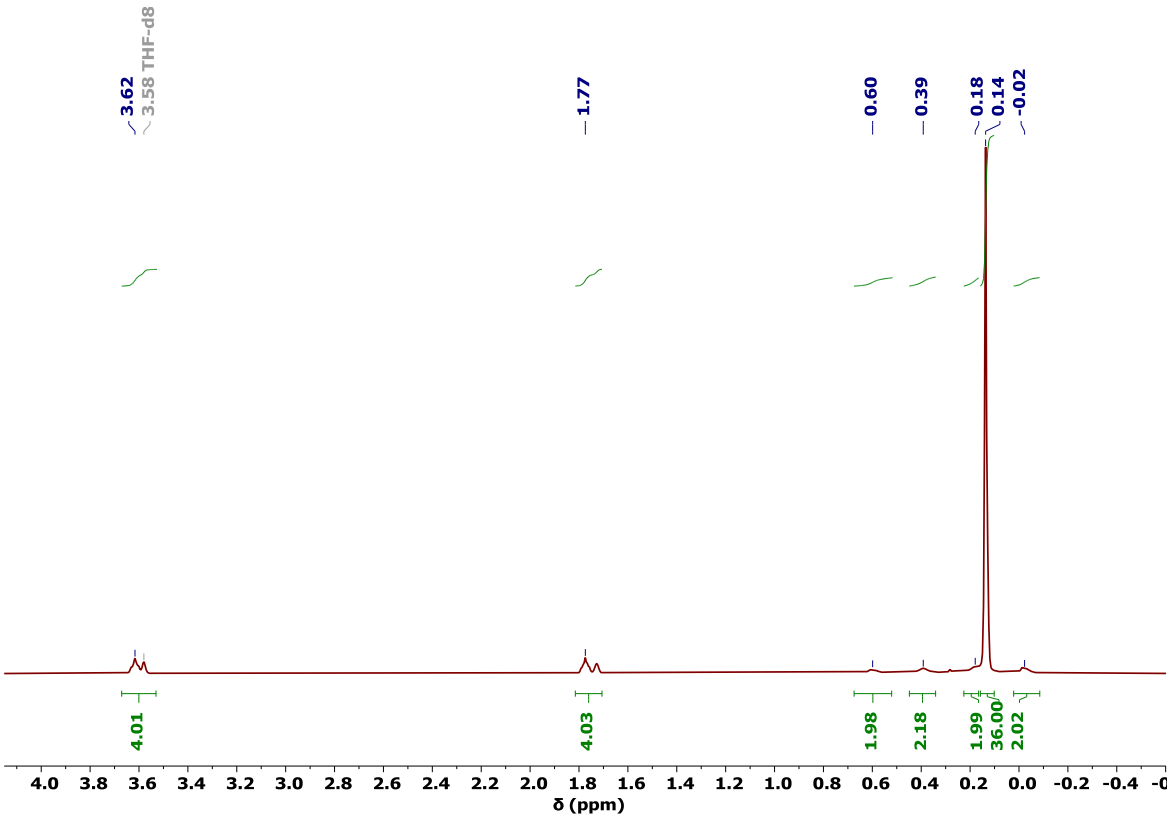

Figure S36. ^{1}H NMR spectrum of **14** in D_8-THF.

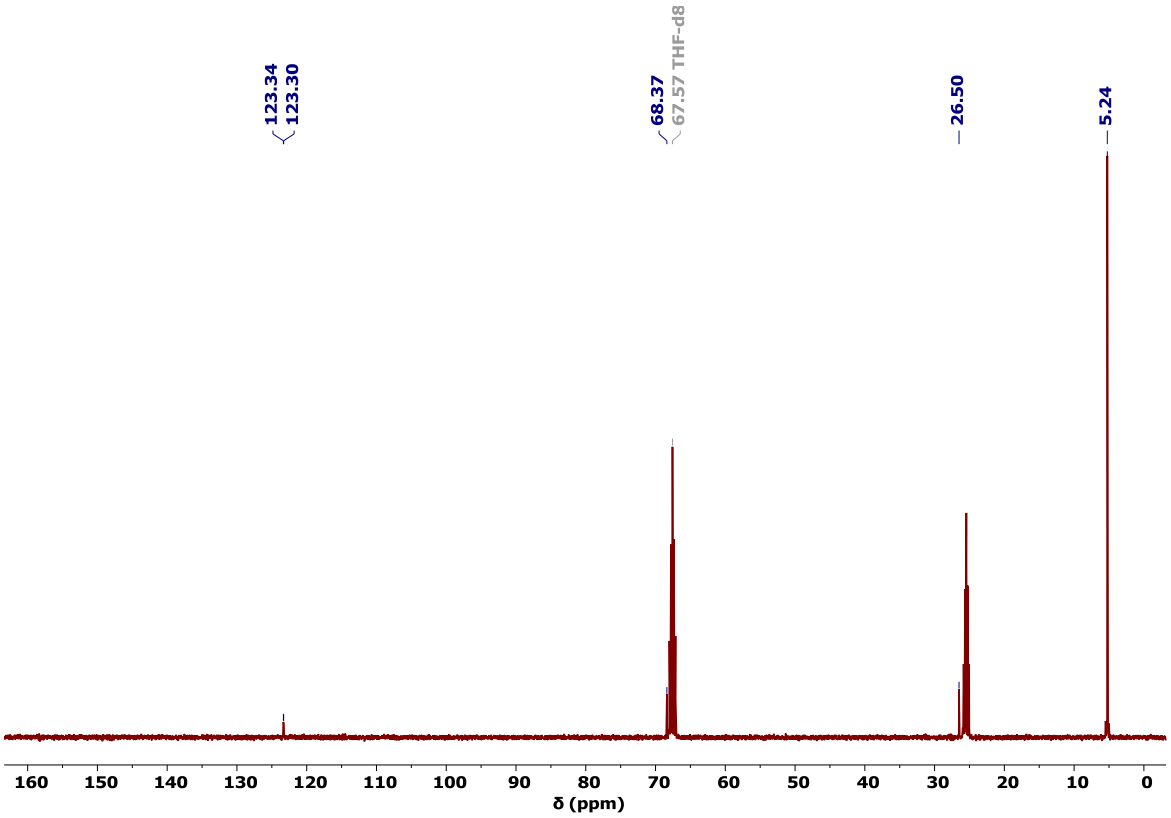

Figure S37. $^{13}C\{^{1}H\}$ NMR spectrum of **14** in D_8-THF.

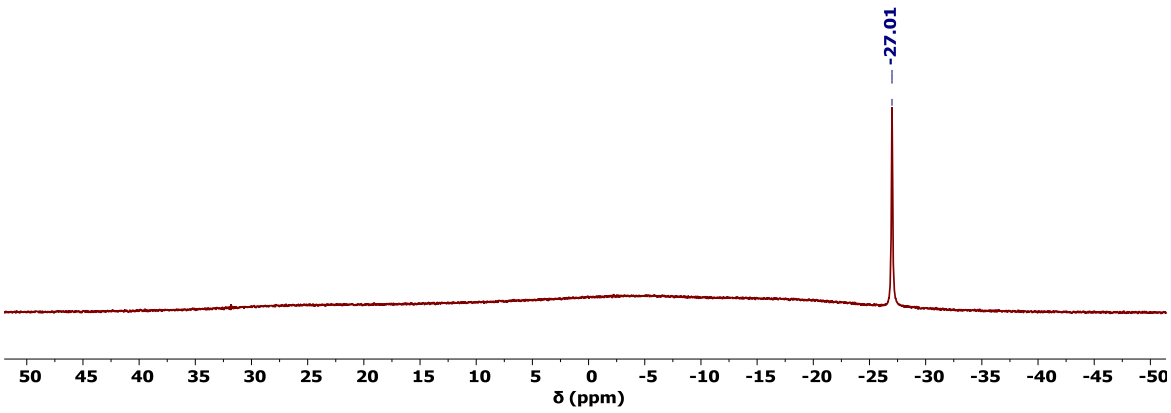

Figure S38. $^{11}B\{^{1}H\}$ NMR spectrum of **14** in D_8-THF.

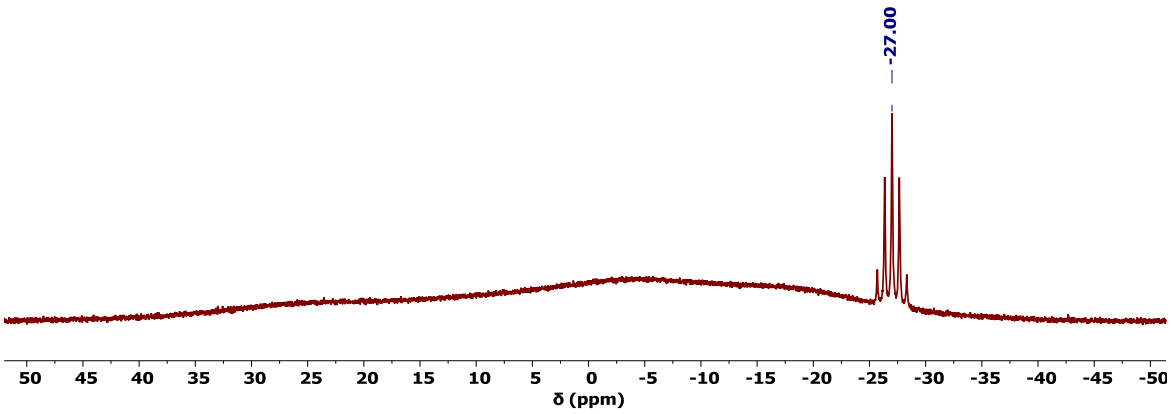

Figure S39. ^{11}B NMR spectrum of **14** in D_8-THF.

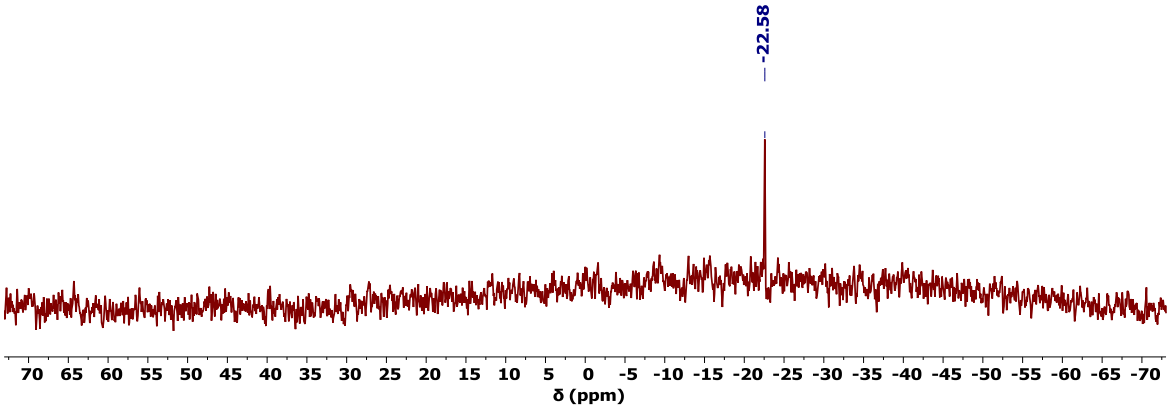

Figure S40. ^{29}Si{^{1}H} NMR spectrum of **14** in D_8-THF.

Synthesis of [Dy{η^4-C$_4$(SiMe$_3$)$_4$}(κ^3-BH$_4$)$_2$(THF)K]$_\infty$ (15). Compound **15** was synthesised by following the same procedure as for **14**, using **9** (500 mg, 1.19 mmol) and [Dy(BH$_4$)$_3$(THF)$_3$] (505 mg, 1.19 mmol). The solvent was removed *in vacuo* to give a yellow powder subsequently identified as **15** (655 mg, 85 %). Yellow crystals of **15** suitable for X-ray crystallography were obtained by the slow evaporation of layered hexane on a saturated THF solution over five days (108 mg, 72 % based on 150 mg of crude **15**).

FTIR ($\bar{\nu}$/cm^{-1}): 3000-2850 (m, b, C-H), 2450 (m, s, B-H$_T$), 2300-2100 (m, b, B-H$_B$).

Elemental analysis (%), found (calculated) for **15** $C_{20}H_{52}DyKB_2Si_4O$: C 37.13 (37.29); H 8.04 (8.14).

Synthesis of [Y(η^5-Cp^{ttt})(η^5-Cp*)(κ^2-BH$_4$)] (16). Toluene (15 mL) was added to a mixture of **1** (192 mg, 0.45 mmol) and [NaCp*] (72 mg, 0.45 mmol). The resulting off-white suspension was heated and left to stir at 108°C for three days, by which time a white precipitate had deposited from the reaction. The reaction mixture was filtered, the solvent removed *in vacuo* and the product was extracted in hexane (3 × 10 mL) and filtered. The filtrate was concentrated *in vacuo* until incipient crystallisation occurred. The suspension was then gently warmed to re-dissolve the microcrystalline solid and the solution was stored at –40°C overnight to yield white crystals of **16** suitable for X-ray crystallography (158 mg, 74 %).

^{1}H NMR (δ/ppm, D$_6$-benzene): 6.48 (bs, C$_5$ ring, 2H), 2.01 (s, CH$_3$, 15H), 1.39 (bs, ^{t}Bu, 18H), 1.16 (s, ^{t}Bu, 9H)

^{1}H{^{11}B} NMR (δ/ppm, D$_6$-benzene): 6.48 (bs, C$_5$ ring, 2H), 2.01 (s, CH$_3$, 15H), 1.39 (bs, ^{t}Bu, 18H), 1.28 & 1.26 (s, BH$_4$, 4H), 1.16 (s, ^{t}Bu, 9H)

^{13}C{^{1}H} NMR (δ/ppm, D$_6$-benzene): 136.00 (d, $^1J_{CY}$ = 2 Hz, C$_5$ ring), 122.10 (d, $^1J_{CY}$ = 2 Hz, C$_5$(Me$_5$) ring), 34.32 (bs, (C(CH$_3$)$_3$)$_2$), 32.95 (bs, (C(CH$_3$)$_3$)$_2$), 32.41 (C(CH$_3$)$_3$), 31.46 (C(CH$_3$)$_3$), 12.45 (Me$_5$).

^{11}B{^{1}H} NMR (δ/ppm, D$_6$-benzene): −16.31 (s, FWHM = 72 Hz, BH$_4$). At 60 °C: −16.61 (s, FWHM = 52 Hz, BH$_4$).

^{11}B NMR (δ/ppm, D$_6$-benzene): −16.32 (quint, $^1J_{BH}$ = 82 Hz, BH$_4$). At 60 °C: −16.61 (quint, $^1J_{BH}$ = 84 Hz, BH$_4$).

FTIR ($\bar{\nu}$/cm^{-1}): 3000-2850 (m, b, C-H), 2400-2300 (m, d, B-H$_T$), 2150-2000 (m, bs, B-H$_B$).

Elemental analysis (%), found (calculated) for **16** C$_{27}$H$_{48}$YB: C 67.83 (68.65); H 11.07 (10.24).

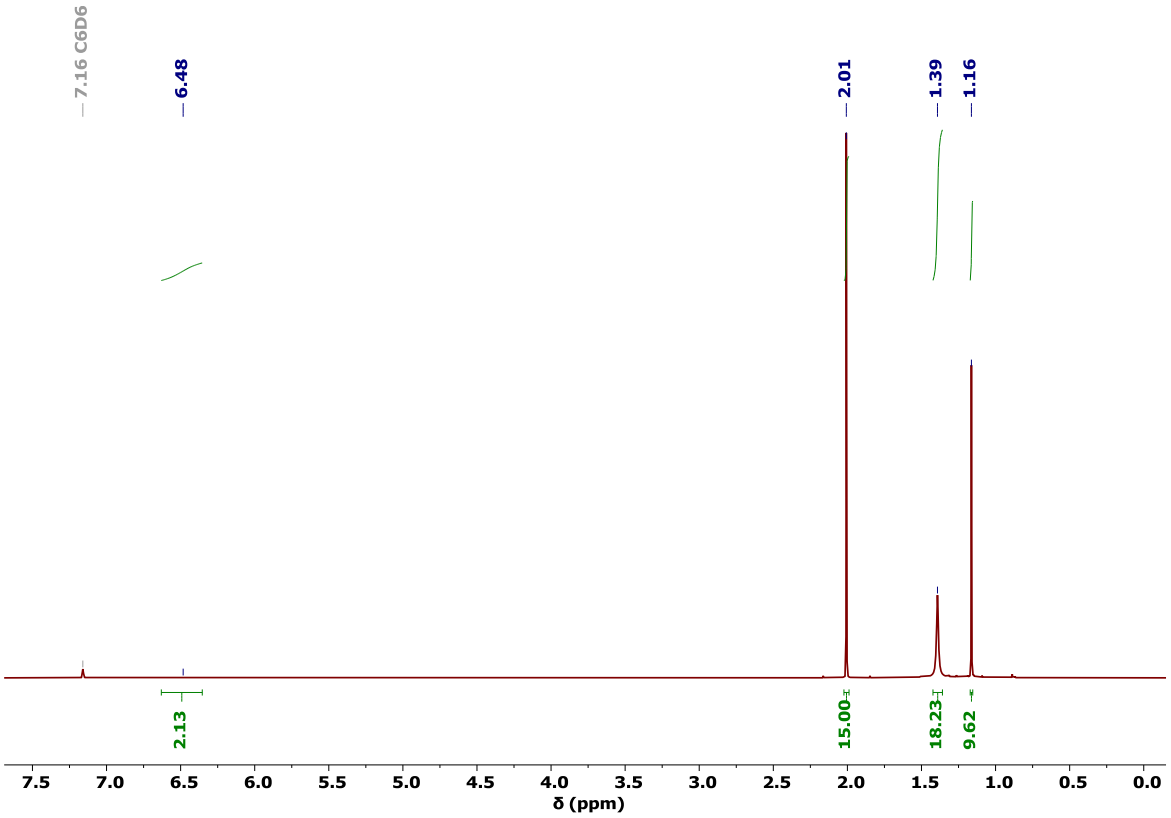

Figure S41. ^{1}H NMR spectrum of **16** in D_6-benzene.

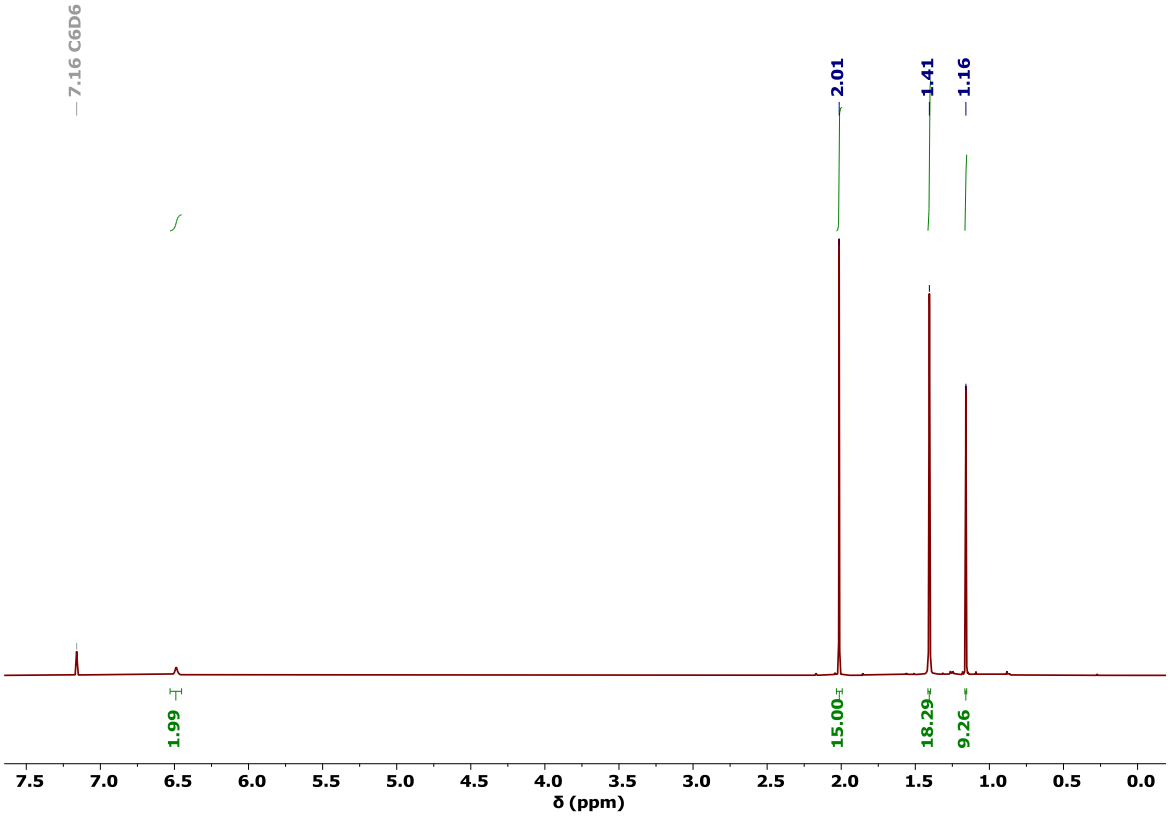

Figure S42. ^{1}H NMR spectrum of **16** in D_6-benzene at 60 °C.

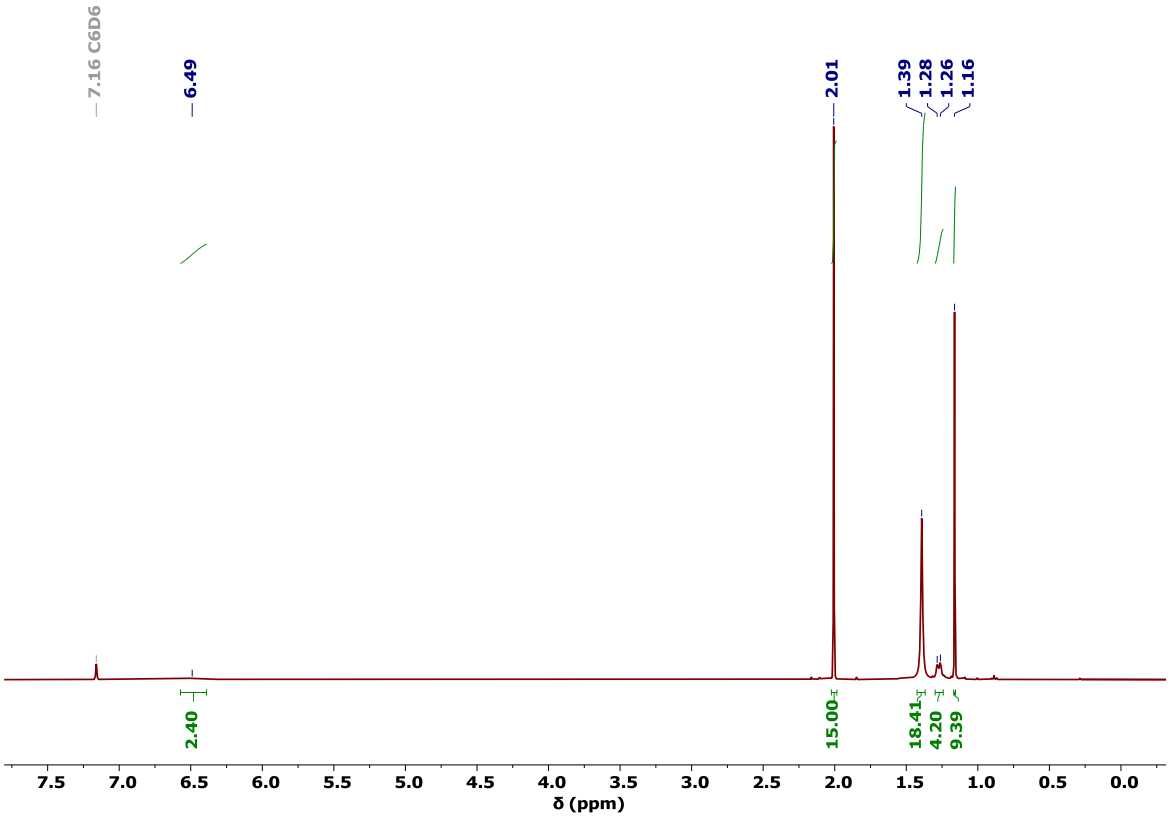

Figure S43. $^{1}H\{^{11}B\}$ NMR spectrum of **16** in D_6-benzene.

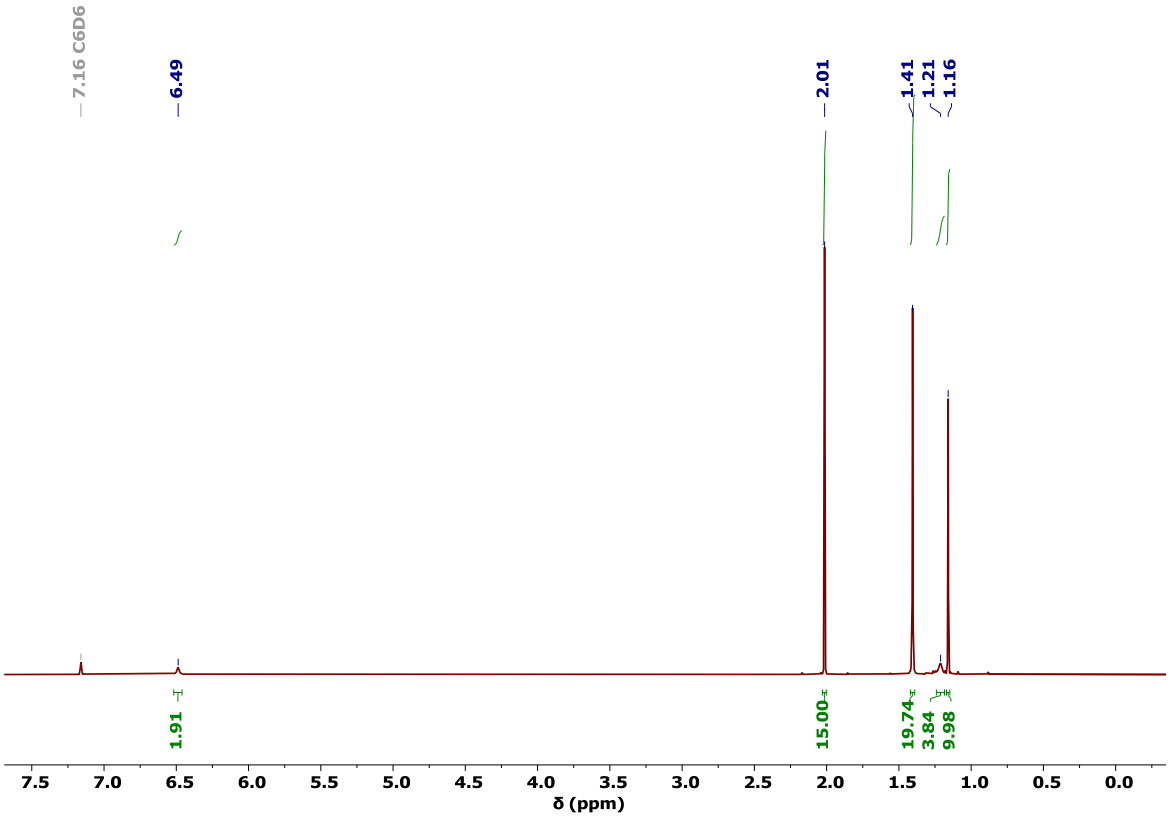

Figure S44. $^{1}H\{^{11}B\}$ NMR spectrum of **16** in D_6-benzene at 60 °C.

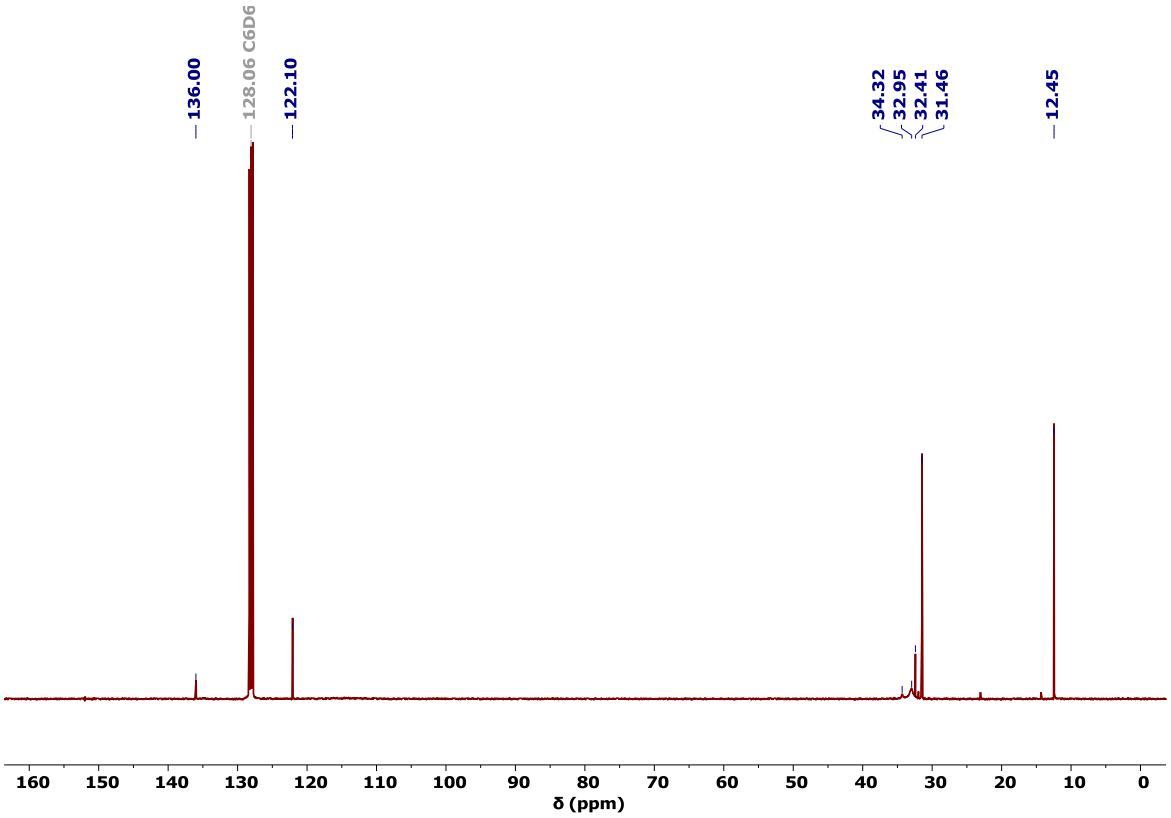

Figure S45. $^{13}C\{^{1}H\}$ NMR spectrum of **16** in D_6-benzene.

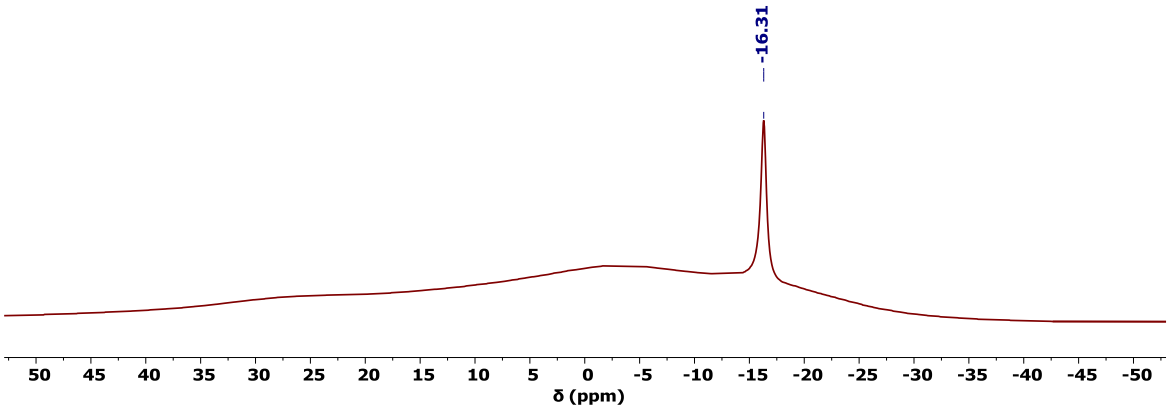

Figure S46. $^{11}B\{^{1}H\}$ NMR spectrum of **16** in D_6-benzene.

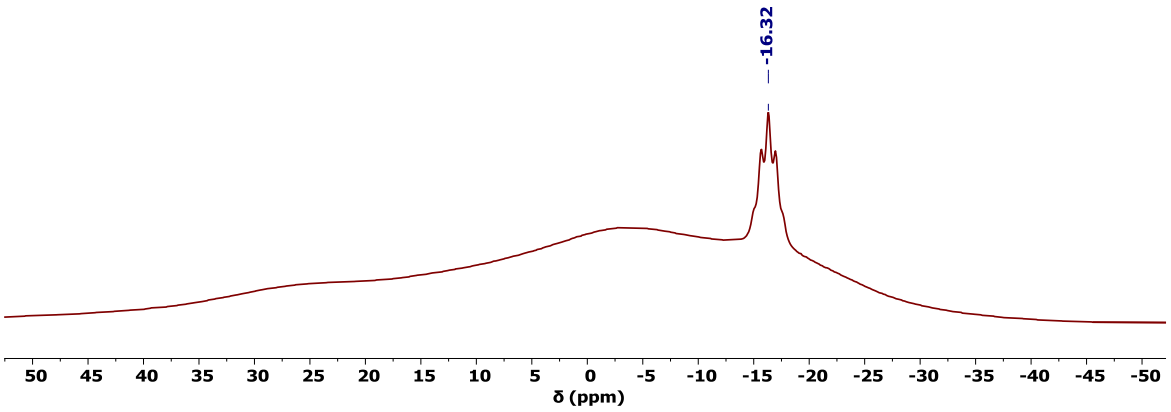

Figure S47. ^{11}B NMR spectrum of **16** in D_6-benzene.

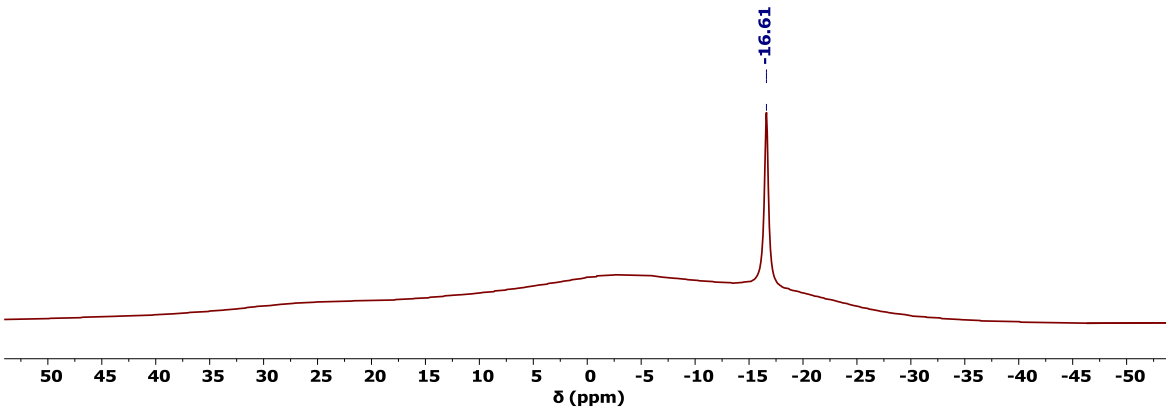

Figure S48. $^{11}B\{^{1}H\}$ NMR spectrum of **16** in D_6-benzene at 60 °C.

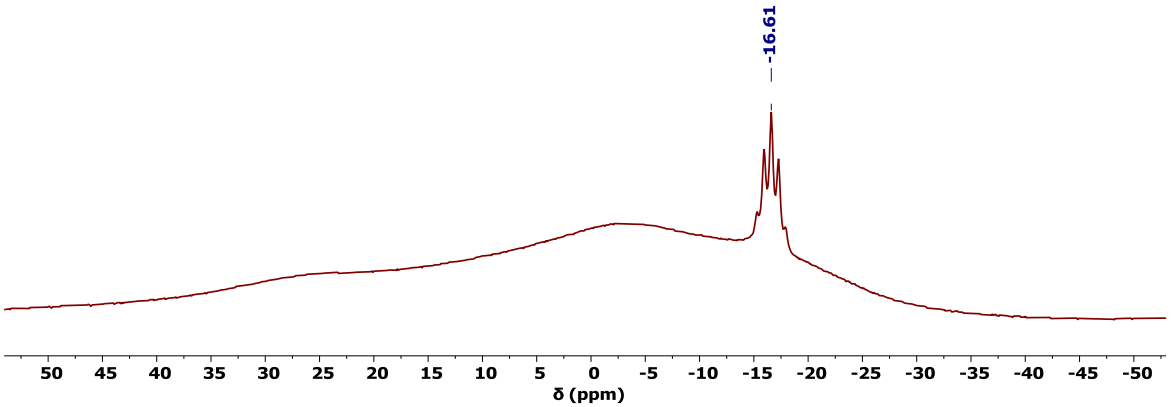

Figure S49. ^{11}B NMR spectrum of **16** in D_6-benzene at 60 °C.

Synthesis of [Dy(η^5-Cp^{ttt})(η^5-Cp*)(κ^2-BH$_4$)] (17). Compound **17** was synthesised by following the same procedure as for **16**, using **2** (474 mg, 0.95 mmol) and [KCp*] (166 mg, 0.95 mmol). Pale-yellow crystals of **17** suitable for X-ray crystallography were obtained by storing a saturated hexane solution at –40°C overnight (365 mg, 70 %).

FTIR ($\bar{\nu}$/cm^{-1}): 3000-2850 (m, b, C-H), 2400-2300 (m, d, B-H$_T$), 2150-2000 (m, bs, B-H$_B$).

Elemental analysis (%), found (calculated) for **17** $C_{27}H_{48}DyB$: C 59.36 (59.40); H 8.95 (8.86).

Synthesis of [Dy(η^5-Cp^{ttt})(η^5-Cp*){B(C$_6$F$_5$)$_4$}] (18). A pale-yellow solution of **17** (165 mg, 0.30 mmol) in cold hexane (*ca.* −40°C) (5 mL) was added dropwise into a suspension of $[Ph_3C]^+[B(C_6F_5)_4]^-$ (278 mg, 0.30 mmol) in cold hexane (*ca.* −40°C) (2 mL). After complete addition of **17**, a sticky bright yellow precipitate had formed, with the resulting supernatant becoming clear. The resulting mixture was left to stir overnight, by which time a yellow suspension had formed. After letting the suspension settle, the clear solution was decanted

and the suspension was washed with hexane (5 × 10 mL). The suspension was dried *in vacuo* to give a yellow solid (360 mg, 98 %). Pale-yellow crystals of **18** suitable for X-ray crystallography were obtained by storing a saturated toluene solution layered with hexane at –40°C over three days (134 mg, 37 %). These crystals were temperature sensitive, with removal from the –40°C freezer resulting in decomposition into a purple material after *ca.* 24 hours.

^{1}H NMR (δ/ppm, D_6-benzene): 2.11 (bs, Cp^{ttt} ring, 2H), 1.21 (bs, FWHM = 41 Hz, ^{t}Bu, 18H), 0.84 (bs, FWHM = 33 Hz, CH_3, 15H), −0.92 (bs, FWHM = 50 Hz, ^{t}Bu, 9H).

FTIR ($\bar{\nu}$/cm^{-1}): 3000-2850 (w, b, C-H), 1450 (s, s, C-F).

Despite repeated attempts, satisfactory elemental analysis could not be obtained for this compound, a representative result being (%), found (calculated) for **18** $C_{51}H_{44}DyBF_{20}O$: C 51.98 (50.62); H 4.36 (3.66).

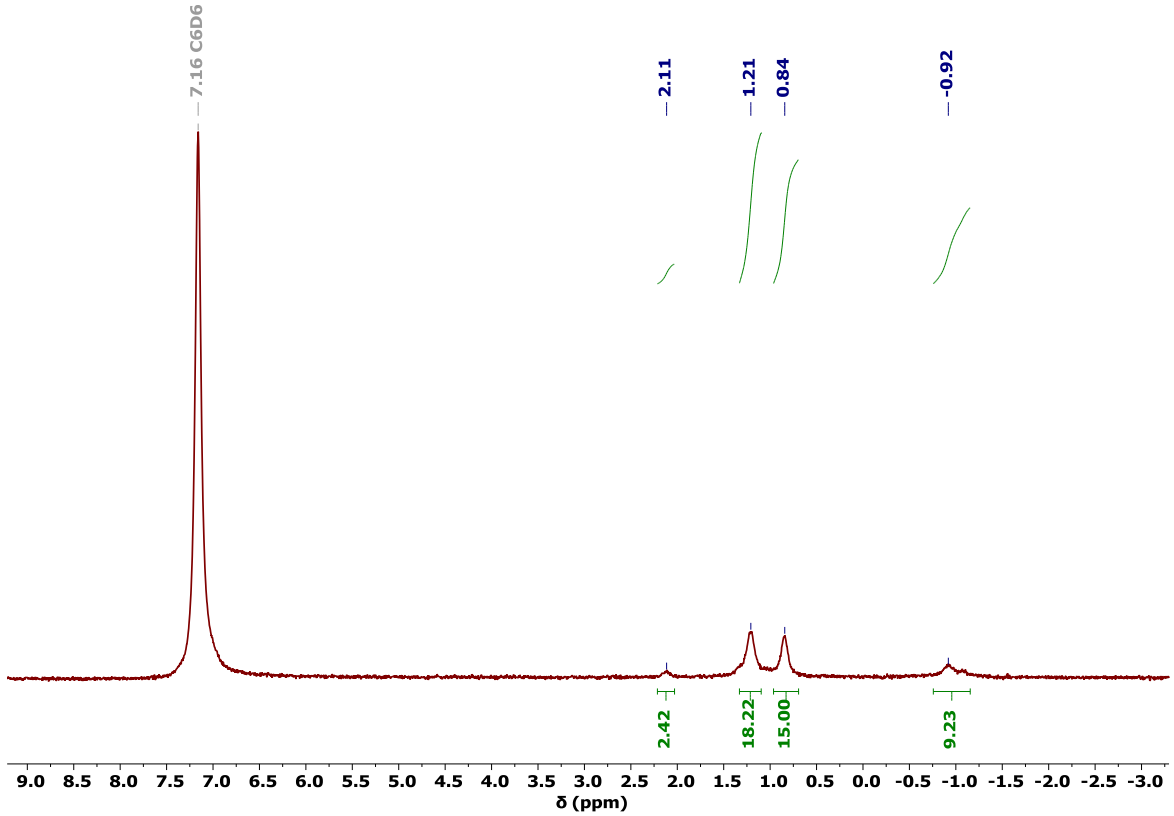

Figure S50. ^{1}H NMR spectra of **17** in D_6-benzene.

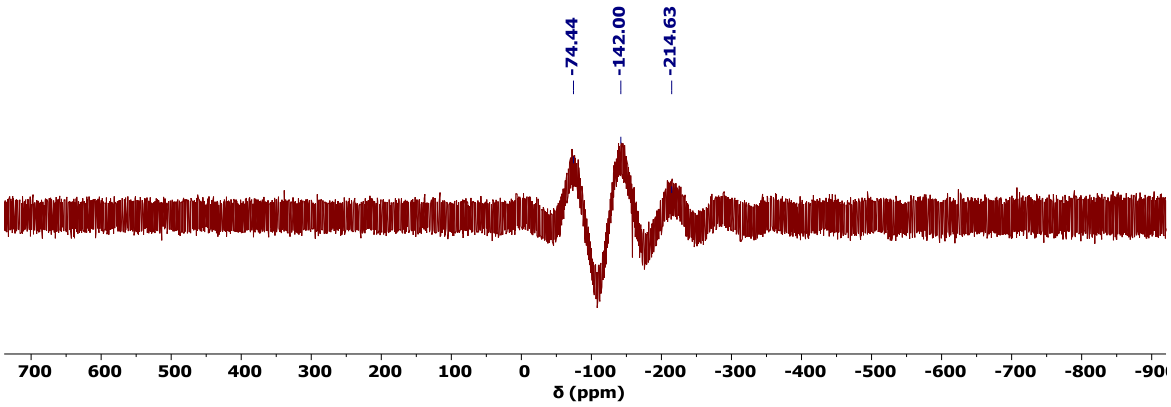

Figure S51. ^{19}F NMR spectra of **17** in D_6-benzene.

Synthesis of [Y{η^4-C$_4$(SiMe$_3$)$_4$}(η^5-Cp*)(κ^2-BH$_4$)Na(THF)$_5$] (19). A colourless solution of [NaCp*] (65 mg, 0.41 mmol) in THF (2 mL) was added dropwise into a yellow solution of **12** (233 mg, 0.41 mmol) in THF (5 mL). The resulting red solution was left to stir for 20 hours, by which time a white precipitate had deposited from the reaction. The reaction mixture was filtered, and the solvent removed *in vacuo* to yield a crude orange powder subsequently identified as **19** (231 mg, 59 %). Orange crystals of **19** suitable for X-ray crystallography were obtained by layering hexane on a saturated THF solution and storing at –40°C for three days (196 mg, 50 %). These crystals were temperature sensitive and would re-dissolve within *ca.* 30 seconds of being removed from the freezer.

NMR spectroscopy of **19** revealed the presence of two isomers, with the major / minor components arising in a ratio of *ca.* 3:1.

^{1}H NMR (δ/ppm, D_8-THF): Major: 2.09 (s, CH_3, 15H), 0.08 (s, $SiMe_3$, 36H). Minor: 2.03 (s, CH_3, 5H), 0.13 (s, $SiMe_3$, 13H). Major / minor overlapped: 3.61 (m, CH_2O, 11H, THF), 1.77 (s, CH_2, 11H, THF), 0.21 (bs, 1:1:1:1 q, $^1J_{HB}$ = 81 Hz, could not be accurately integrated due to overlap with $SiMe_3$ signals at 0.13 & 0.08 ppm).

^{13}C{^{1}H} NMR (δ/ppm, D_8-THF): Major: 149.20 ($\underline{C}_4$ ring), 116.64 ($\underline{C}_5$ ring), 12.94 ($C_5\underline{Me}_5$), 4.86 ($Si\underline{Me}_3$). Minor: 128.60 ($\underline{C}_4$ ring), 105.55 ($\underline{C}_5$ ring), 11.70 ($C_5\underline{Me}_5$), 5.31 ($Si\underline{Me}_3$). Major / minor overlapped: 68.38 ($\underline{C}H_2O$), 26.52 ($\underline{C}H_2$).

^{11}B{^{1}H} NMR (δ/ppm, D_8-THF): Major / minor overlapped: −26.41 (s, FWHM = 205 Hz, BH_4).

^{11}B NMR (δ/ppm, D_8-THF): Major / minor overlapped: −26.44 (s, FWHM = 325 Hz, BH_4).

^{29}Si{^{1}H} NMR (δ/ppm, D_8-THF): Major / minor overlapped: −19.45.

^{23}Na NMR (δ/ppm, D_8-THF): Major / minor overlapped: −5.76 (FWHM = 90 Hz).

FTIR ($\bar{\nu}$/cm^{-1}): 3000-2850 (m, b, C-H), 2250-2100 (m, b, B-H_B).

Satisfactory elemental analysis could not be obtained for this compound, a representative result being (%), found (calculated) for **19** $C_{46}H_{95}YBNaSi_4O_5$: C 48.64 (57.36); H 9.64 (9.94), for **19**(−5 THF) $C_{26}H_{55}YBNaSi_4$: C 48.64 (51.81); H 9.64 (9.20).

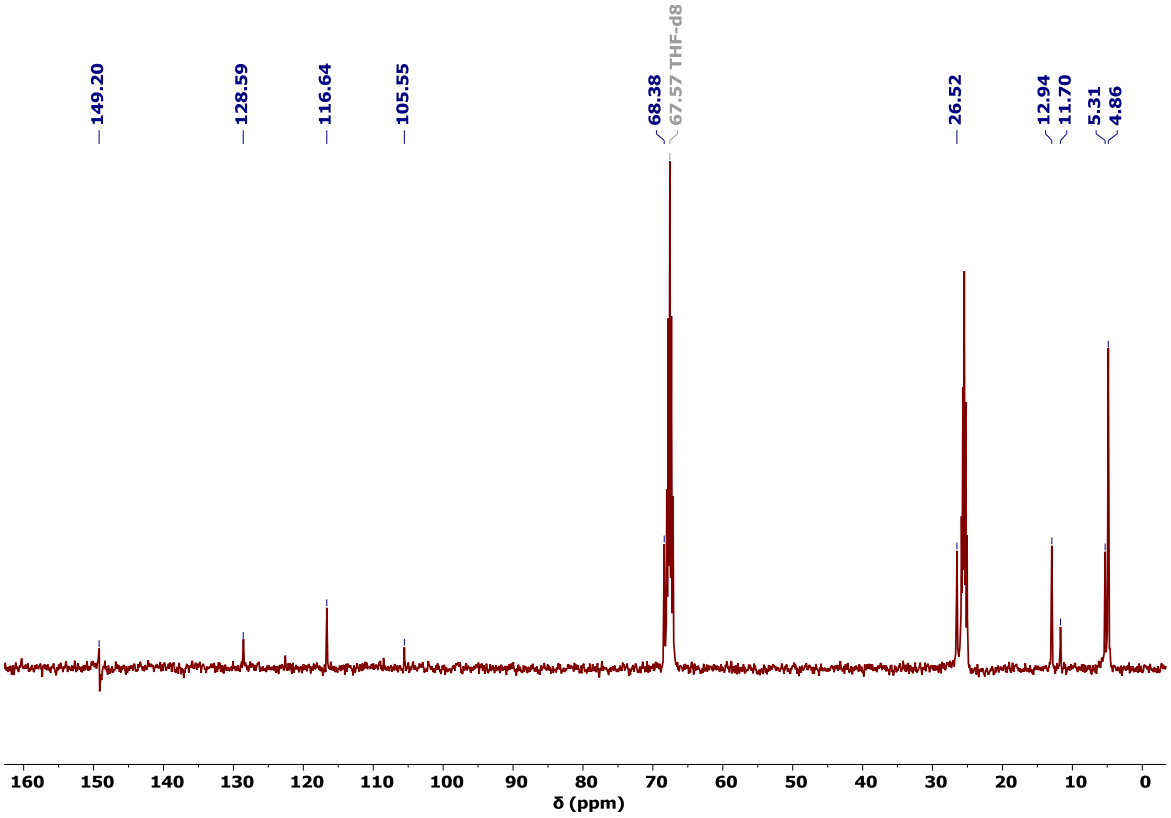

Figure S52. ^{13}C{^{1}H} NMR spectrum of **19** in D_8-THF.

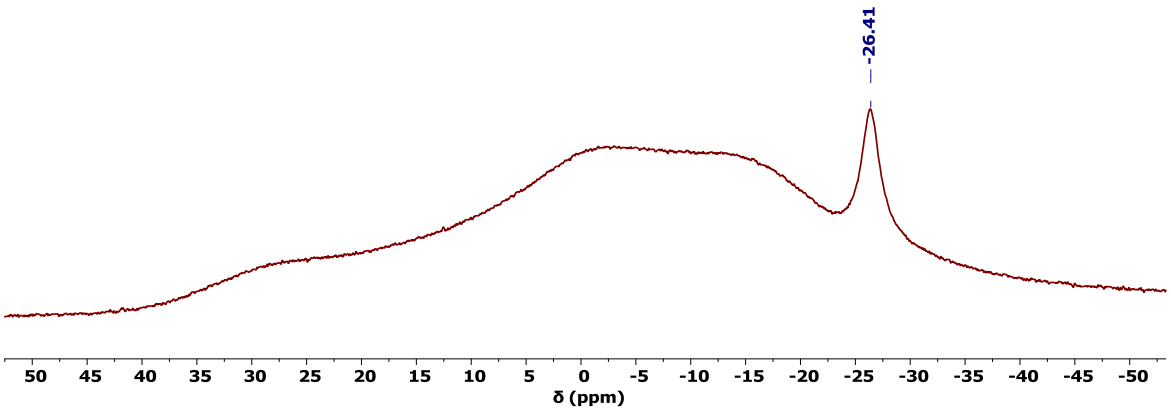

Figure S53. $^{11}B\{^{1}H\}$ NMR spectrum of **19** in D_8-THF.

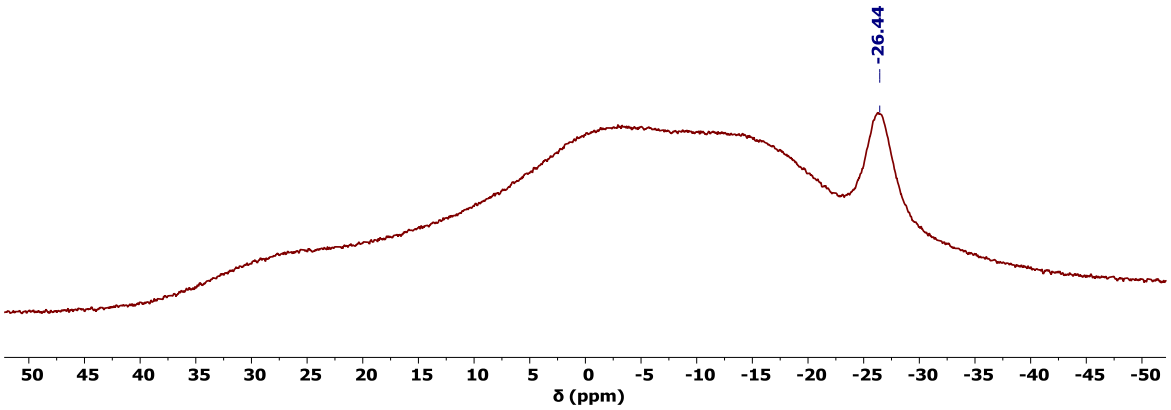

Figure S54. ^{11}B NMR spectrum of **19** in D_8-THF.

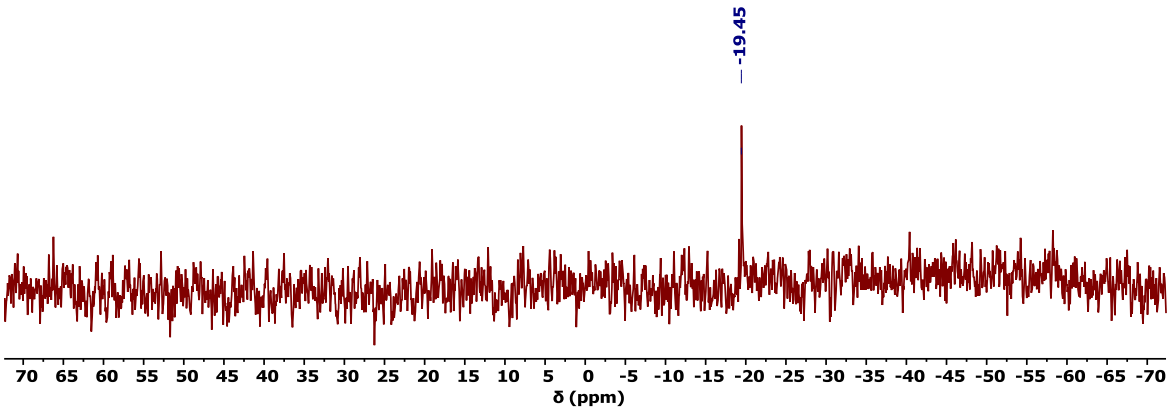

Figure S55. $^{29}Si\{^{1}H\}$ NMR spectrum of **19** in D_8-THF.

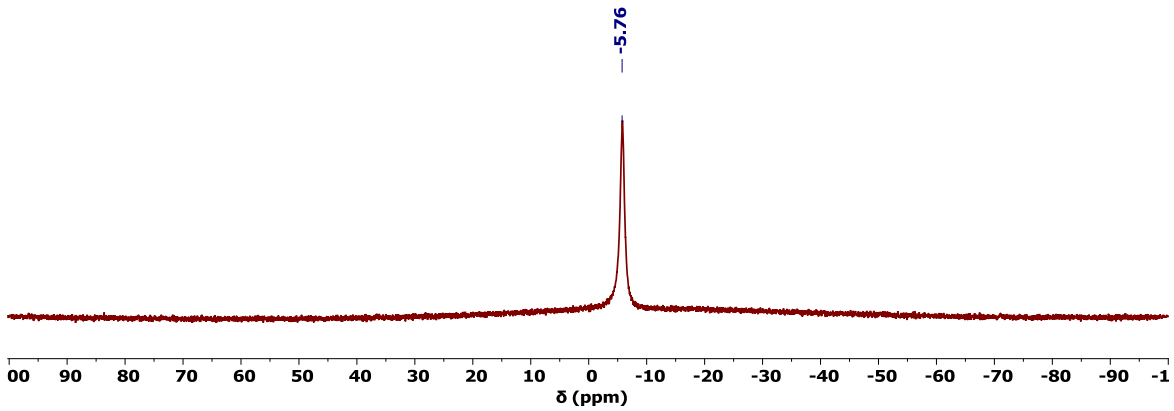

Figure S56. $^{23}Na\{^{1}H\}$ NMR spectrum of **19** in D_8-THF.

Synthesis of [Dy{η⁴-C₄(SiMe₃)₄}(η⁵-Cp*)(κ²-BH₄)Na(THF)₅] (20). Compound **20** was synthesised by following the same procedure as for **19**, using **13** (255 mg, 0.41 mmol) and [NaCp*] (64 mg, 0.41 mmol). A crude orange powder was subsequently identified as **20** (241 mg, 57 %). Orange crystals of **20** suitable for X-ray crystallography were obtained by layering hexane on a saturated THF solution and storing at –40°C for three days (222 mg, 53 %). These crystals were temperature sensitive and would re-dissolve within *ca.* 30 seconds of being removed from the freezer.

FTIR ($\bar{\nu}$/cm^{-1}): 3000-2850 (m, b, C-H), 2250-2100 (m, b, B-H_B).

Despite repeated attempts, satisfactory elemental analysis could not be obtained for this compound, a representative result being (%), found (calculated) for **20** $C_{46}H_{95}DyBNaSi_4O_5$: C 42.39 (53.28); H 8.13 (9.24), for **20**(−5 THF) $C_{26}H_{55}DyBNaSi_4$: C 42.39 (46.17); H 8.13 (8.20).

Synthesis of [Na(15-c-5)(THF)]⁺[Y{η⁴-C₄(SiMe₃)₄}(η⁵-Cp*)(κ²-BH₄)]⁻ (21). 15-crown-5 (22 mg, 20 μL, 0.10 mmol) was added dropwise into a red solution of **19** (50 mg, 0.083 mmol) in THF (2 mL) and the resulting solution was left to stand for 20 h. The resulting red solution was filtered, layered with hexane and stored at –40°C for three days, resulting in the formation of red crystals of **21** suitable for X-ray crystallography (35 mg, 47 %).

NMR spectroscopy of **21** revealed the presence of two isomers, with the major / minor components arising in a ratio of *ca.* 1:0.7.

^{1}H NMR (δ/ppm, D_8-THF): Major: 2.10 (s, CH_3, 15H), 0.09 (s, $SiMe_3$, 36H). Minor: 2.00 (s, CH_3, 12H), 0.14 (s, $SiMe_3$, 23H). Major / minor overlapped: 3.66 (s, CH_2, 70H, crown).

^{13}C{^{1}H} NMR (δ/ppm, D_8-THF): Major: 147.31 ($\underline{C}_4$ ring), 116.58 ($\underline{C}_5$ ring), 12.99 ($C_5\underline{Me}_5$), 4.95 ($Si\underline{Me}_3$). Minor: 128.34 ($\underline{C}_4$ ring), 105.02 ($\underline{C}_5$ ring), 12.47 ($C_5\underline{Me}_5$), 5.38 ($Si\underline{Me}_3$). Major / minor overlapped: 69.85 ($\underline{C}H_2$).

^{11}B{^{1}H} NMR (δ/ppm, D_8-THF): Major / minor overlapped: −24.81 (s, FWHM = 44 Hz, BH_4).

^{11}B NMR (δ/ppm, D_8-THF): Major / minor overlapped: −24.81 (quint., $^{1}J_{BH}$ = 84 Hz, BH_4).

^{29}Si{^{1}H} NMR (δ/ppm, D_8-THF): Major: −23.05. Minor: −22.71.

^{23}Na NMR (δ/ppm, D_8-THF): Major / minor overlapped: −9.24 (FWHM = 66 Hz).

FTIR ($\bar{\nu}$/cm^{-1}): 3000-2850 (m, b, C-H), 2400-2300 (w, d, B-H_T), 2150-2000 (w, b, B-H_B).

Satisfactory elemental analysis could not be obtained for this compound, a representative result being (%), found (calculated) for **21** $C_{40}H_{83}YBNaSi_4O_6$: C 50.64 (53.67); H 9.17 (9.35), for **21**(−THF) $C_{36}H_{75}YBNaSi_4O_5$: C 50.64 (52.54); H 9.17 (9.19).

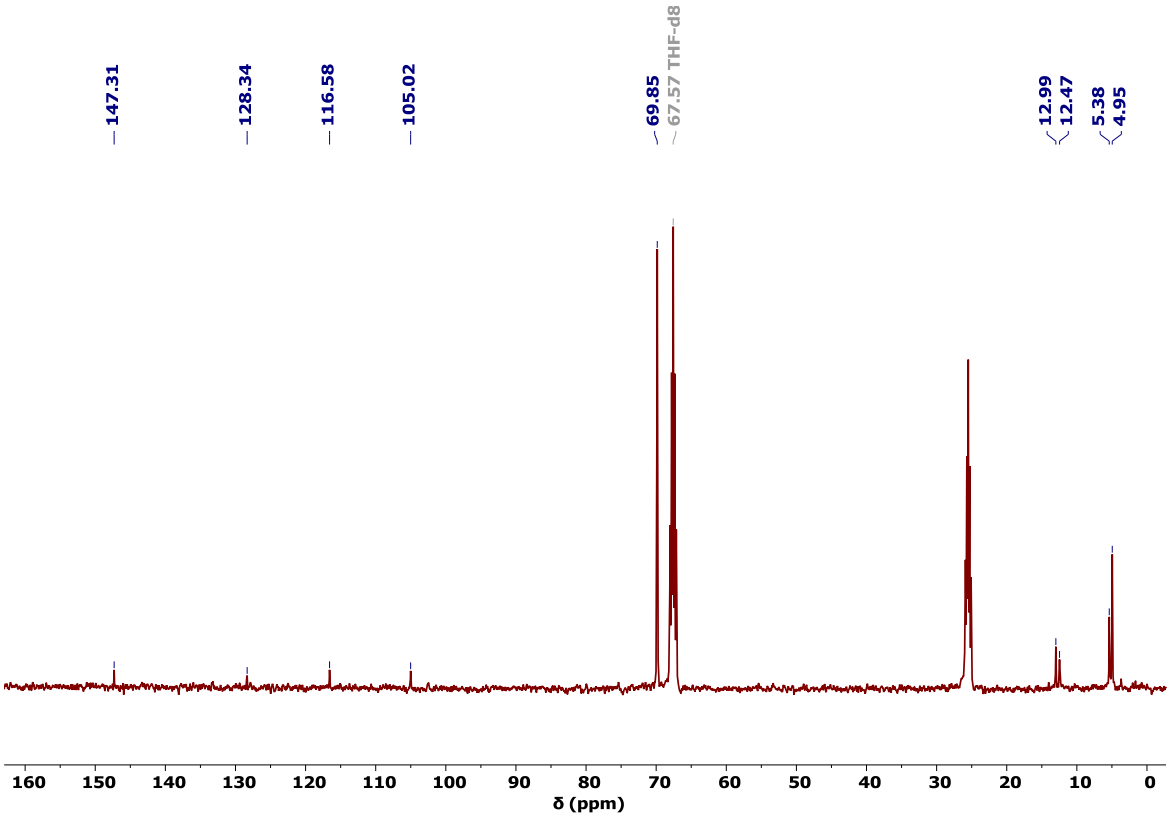

Figure S57. $^{13}C\{^{1}H\}$ NMR spectrum of **21** in D_8-THF.

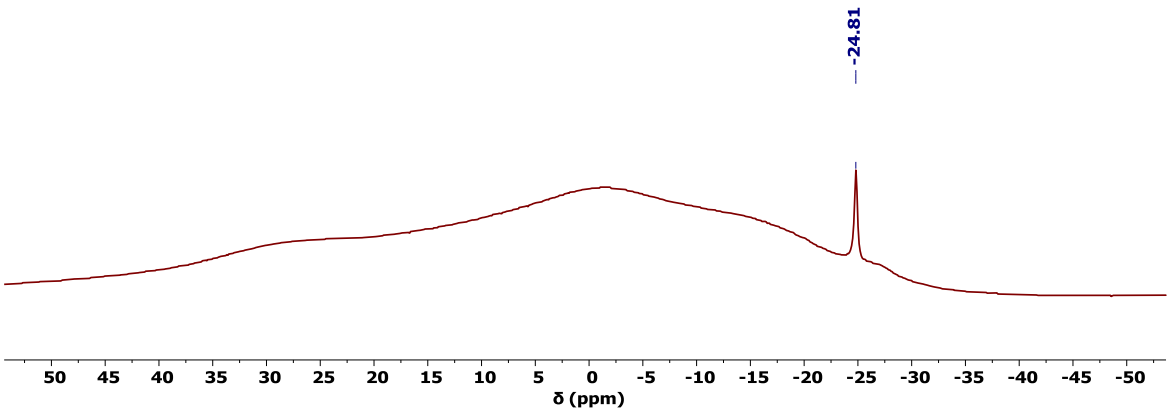

Figure S58. $^{11}B\{^{1}H\}$ NMR spectrum of **21** in D_8-THF.

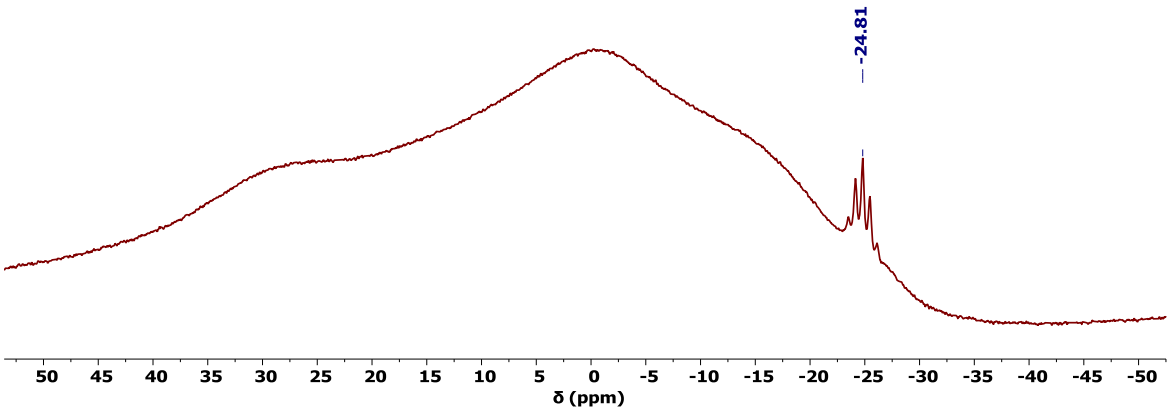

Figure S59. ^{11}B NMR spectrum of **21** in D_8-THF.

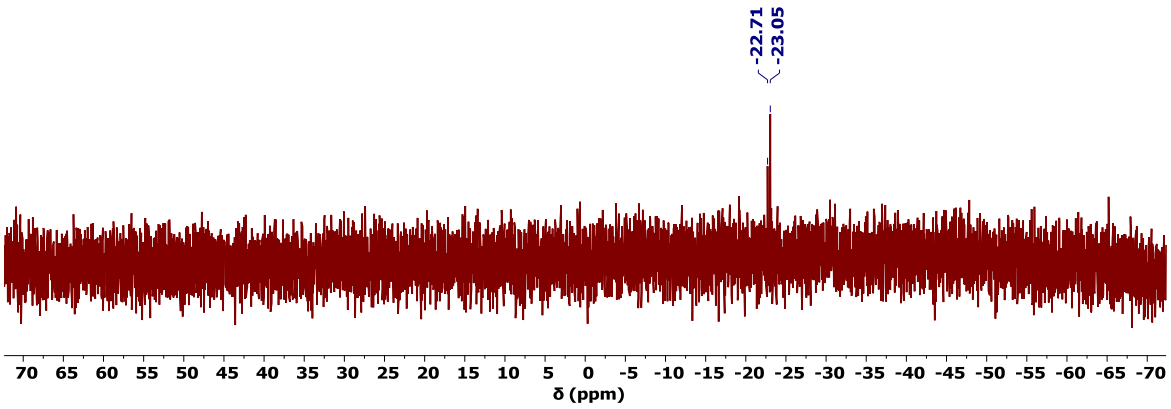

Figure S60. $^{29}Si\{^{1}H\}$ NMR spectrum of **21** in D_8-THF.

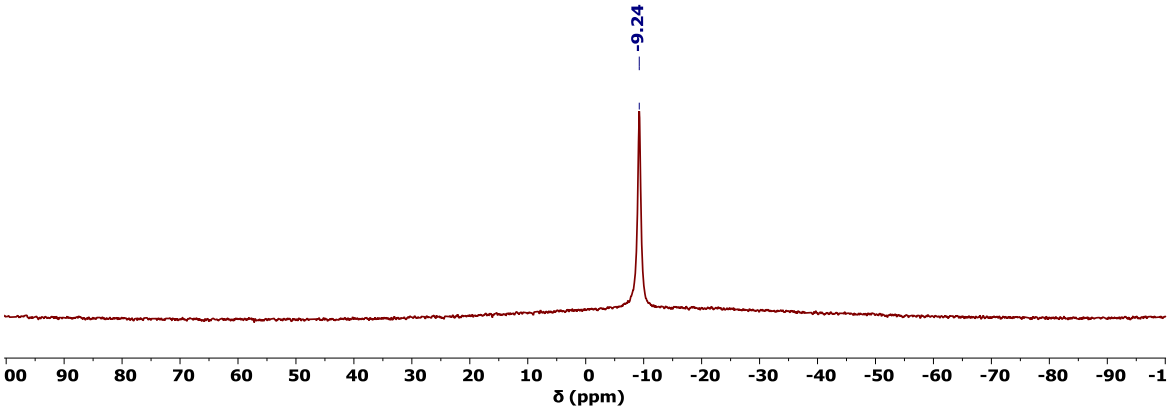

Figure S61. $^{23}Na\{^{1}H\}$ NMR spectrum of **21** in D_8-THF.

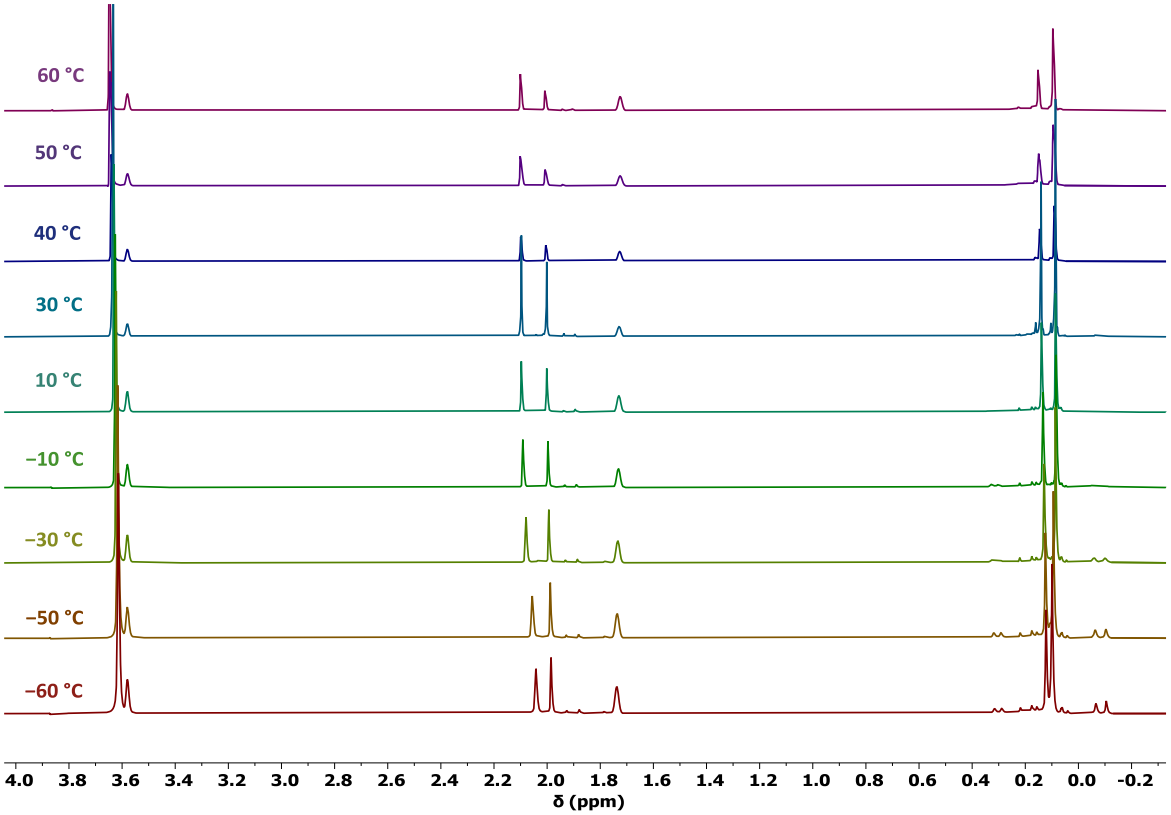

Figure S62. Variable temperature $^{1}H\{^{11}B\}$ NMR spectra of **21** in D_8-THF from +60 to −60 °C.

Synthesis of $[Na(15\text{-}c\text{-}5)(THF)_2]^+[Dy\{\eta^4\text{-}C_4(SiMe_3)_4\}(\eta^5\text{-}Cp^*)_5\}(\kappa^2\text{-}BH_4)]^-$ (22). 15-crown-5 (20 mg, 18 μL, 0.090 mmol) was added dropwise into a red solution of **20** (50 mg, 0.074 mmol) in THF (2 mL) and the resulting solution was left to stand for 20 h. The resulting red solution was filtered, layered with hexane and stored at –40°C for three days, resulting in the formation of red crystals of **22** suitable for X-ray crystallography (29 mg, 38 %).

FTIR ($\bar{\nu}$/cm^{-1}): 3000-2850 (m, b, C-H), 2400-2300 (w, d, B-H$_T$), 2150-2000 (w, b, B-H$_B$).

Satisfactory elemental analysis could not be obtained for this compound, a representative result being (%), found (calculated) for **22** $C_{44}H_{91}DyBNaSi_4O_7$: C 47.83 (50.77); H 8.60 (8.81), for **22**(−THF) $C_{40}H_{83}DyBNaSi_4O_6$: C 47.83 (49.59); H 8.60 (8.64), for **22**(−2 THF) $C_{36}H_{75}DyBNaSi_4O_5$: C 47.83 (48.22); H 8.60 (8.43).

Synthesis of $[Y\{\eta^4\text{-}C_4(SiMe_3)_4\}(\eta^5\text{-}C_5Me_4{}^tBu)(BH_4)Na(THF)_4]_4$ (23). An off-white solution of [NaCp^{Me4tBu}] (16 mg, 0.081 mmol) in THF (2 mL) was added dropwise into a yellow solution of **12** (46 mg, 0.081 mmol) in THF (5 mL). The resulting red solution was left to stir for 20 hours, by which time a white precipitate had deposited from the reaction. The reaction mixture was filtered, and the solvent removed *in vacuo* to yield a crude orange powder subsequently identified as **23** (44 mg, 59 %). Orange crystals of **23** could be obtained by layering hexane on a saturated THF solution and storing at –40°C for three days (35 mg, 47 %), however these crystals were extremely temperature sensitive and would immediately re-dissolve within seconds of being removed from the freezer. The yield is based on drying the re-dissolved crystalline material under dynamic vacuum.

NMR spectroscopy of **23** revealed the presence of two isomers, with the major / minor components arising in a ratio of *ca.* 7:1.

^{1}H NMR (δ/ppm, D_8-THF): Major: 3.62 (s, CH_2O, 5H, overlapped with minor component), 2.42 (s, Me_2, 6H), 2.13 (s, Me_2, 6H), 1.27 (s, ^{t}Bu, 9H), 0.10 (s, $SiMe_3$, 36H). Minor: 2.20 (s, Me_2, 0.9H), 1.99 (s, Me_2, 0.9H), 1.36 (s, ^{t}Bu, 1.3H), 0.14 (s, $SiMe_3$, 2.5H).

^{13}C{^{1}H} NMR (δ/ppm, D_8-THF): Major: 129.46 ($\underline{C}_4$ ring), 117.79 ($\underline{C}_5$ ring), 116.56 ($\underline{C}_5$ ring), 68.38 ($\underline{C}H_2O$), 33.15 (C($\underline{C}H_3)_3$), 26.54 ($\underline{C}H_2$), 17.20 ($\underline{Me}_2$), 13.41 ($\underline{Me}_2$), 5.38 (Si$\underline{Me}_3$). Signals

corresponding to the C_5 ring carbon attached to the ^{t}Bu group, the quaternary carbon of the ^{t}Bu group, and all of the minor components could not be observed.

$^{11}B\{^1H\}$ NMR (δ/ppm, D_8-THF): Major: −20.96 (s, FWHM = 70 Hz, BH_4). Minor: −25.18 (s, FWHM = 44 Hz, BH_4).

^{11}B NMR (δ/ppm, D_8-THF): Major: −20.93 (quint., $^1J_{BH}$ = 81 Hz, BH_4). Minor: −25.09 (s, BH_4).

$^{29}Si\{^1H\}$ NMR (δ/ppm, D_8-THF): −21.07.

^{23}Na NMR (δ/ppm, D_8-THF): −9.39 (FWHM = 74 Hz).

FTIR ($\bar{\nu}$/cm^{-1}): 3000-2850 (m, b, C-H), 2250-2100 (m, b, B-H_B).

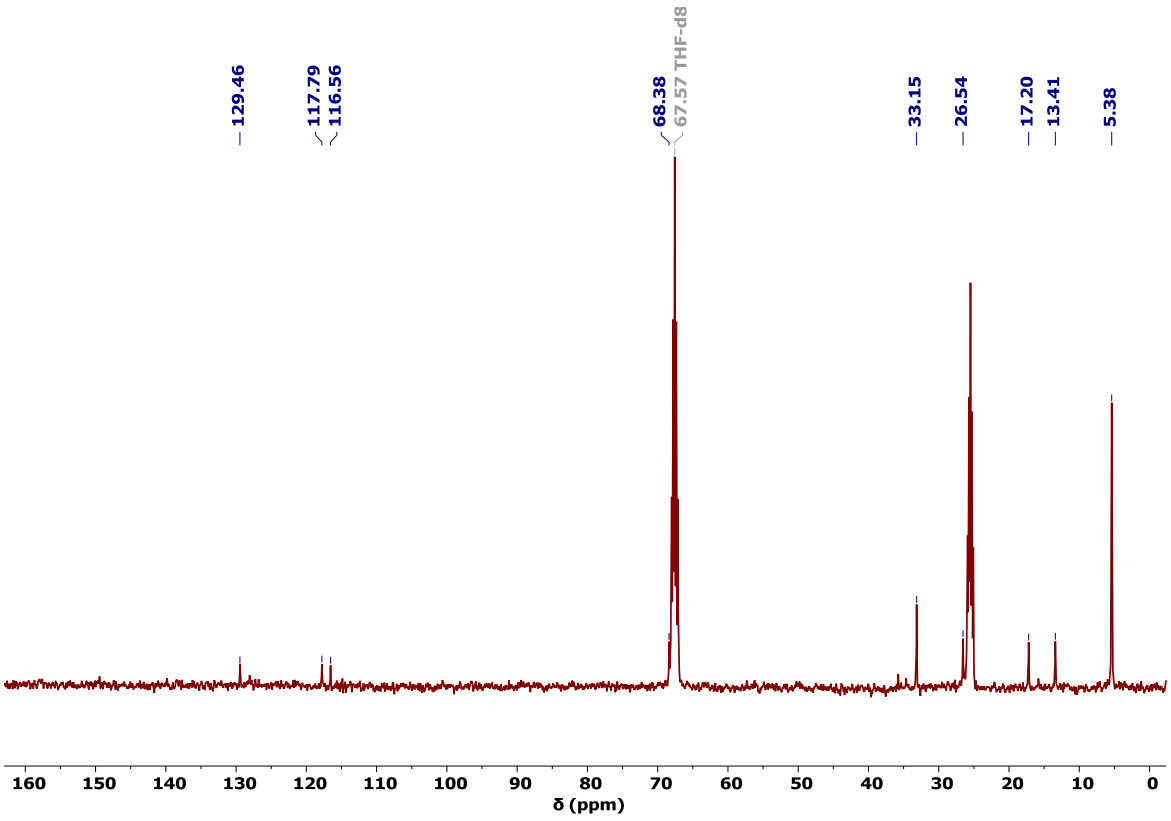

Figure S63. $^{13}C\{^1H\}$ NMR spectrum of **23** in D_8-THF.

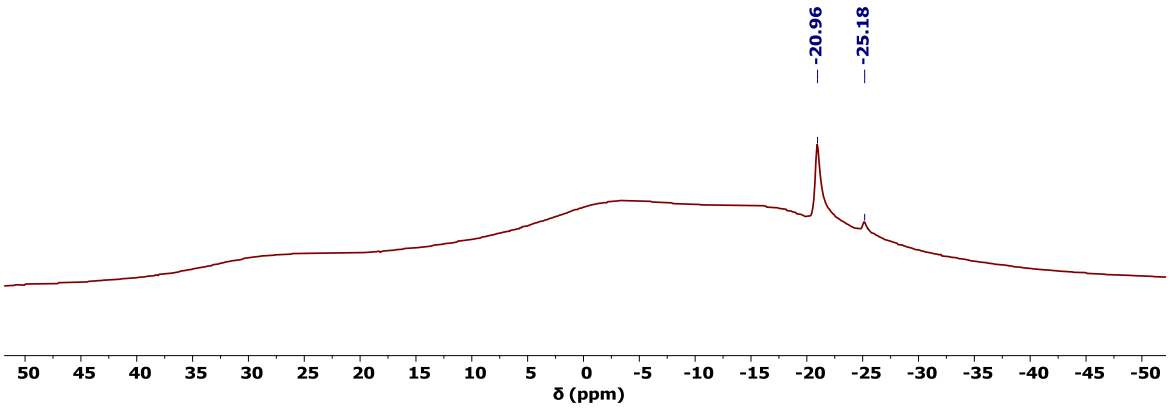

Figure S64. $^{11}B\{^{1}H\}$ NMR spectrum of **23** in D_8-THF.

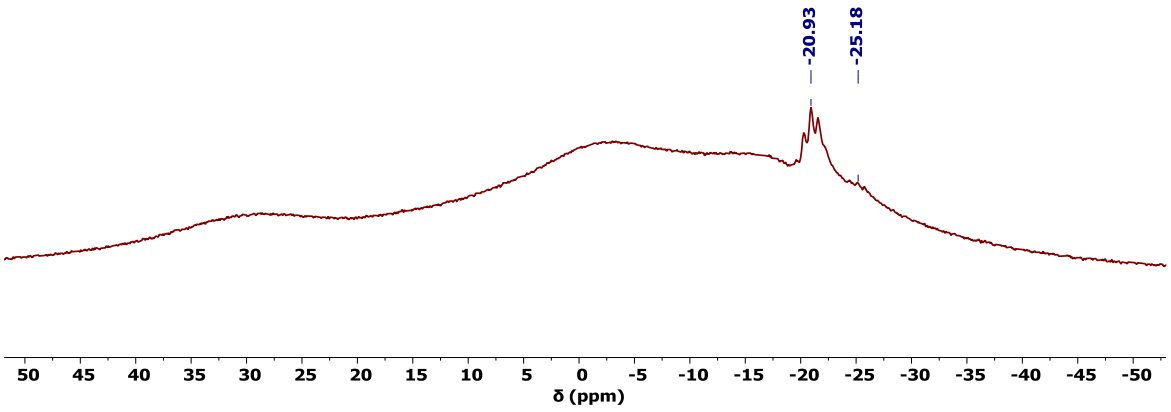

Figure S65. ^{11}B NMR spectrum of **23** in D_8-THF.

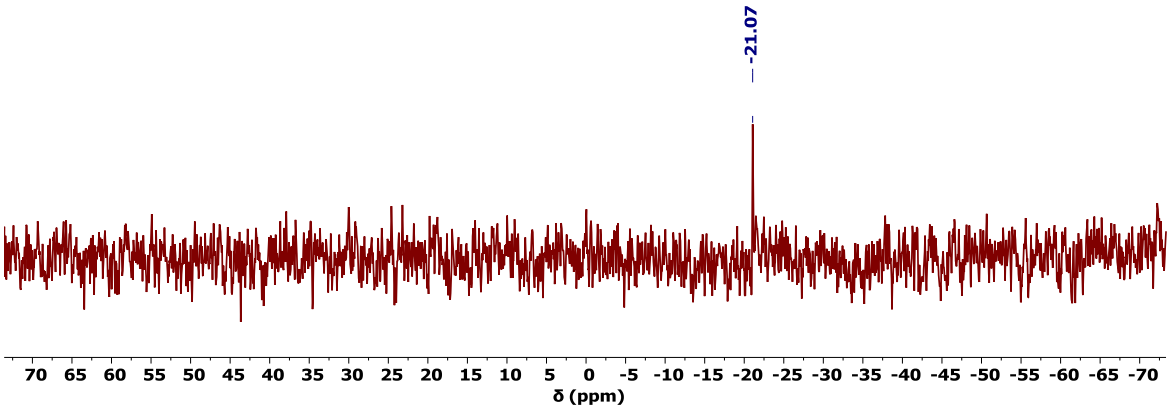

Figure S66. $^{29}Si\{^{1}H\}$ NMR spectrum of **23** in D_8-THF.

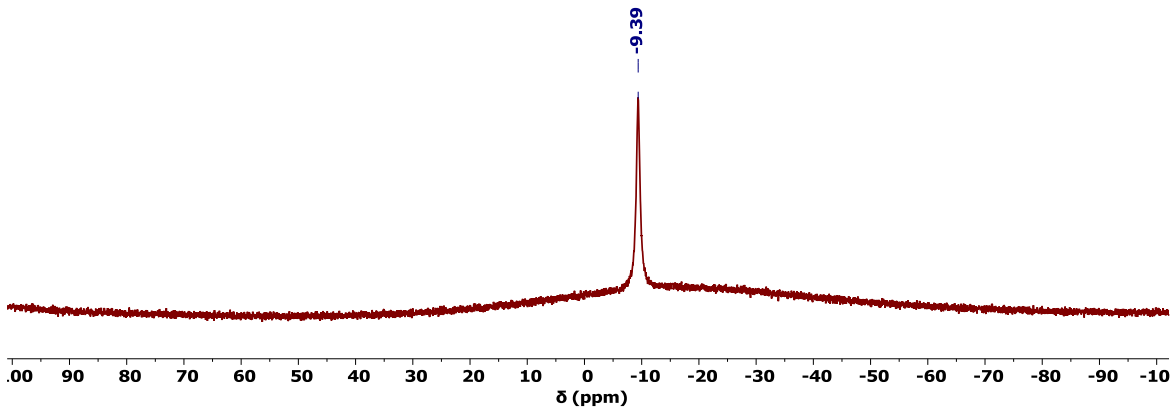

Figure S67. $^{23}Na\{^{1}H\}$ NMR spectrum of **23** in D_8-THF.

Synthesis of [Dy{η^4-C$_4$(SiMe$_3$)$_4$}(η^5-C$_5$Me$_4$^{t}Bu)(BH$_4$)Na(THF)$_4$]$_4$ (24). Compound **24** was synthesised by following the same procedure as for **23**, using **13** (242 mg, 0.39 mmol) and [NaCp^{Me4tBu}] (77 mg, 0.39 mmol). The solvent was removed *in vacuo* to yield an orange powder subsequently identified as **24** (235 mg, 61 %). Orange crystals of **24** could be obtained by layering hexane on a saturated THF solution and storing at –40°C for three days (195 mg, 50 %), however these crystals were extremely temperature sensitive and would immediately re-dissolve within seconds of being removed from the freezer. The yield is based on drying the re-dissolved crystalline material under dynamic vacuum.

FTIR ($\bar{\nu}$/cm^{-1}): 3000-2850 (m, b, C-H), 2250-2100 (m, b, B-H$_B$).

EI-MS (*m*/*z*): [M]$^+$ **24** = 718; 681 (10 %) [M – NaBH$_4$], 608 (20 %) [M − NaBH$_4$ – SiMe$_3$].

Satisfactory elemental analysis could not be obtained for this compound, even after taking into account the potential loss of THF, with a representative result being (%), found (calculated) for **24** C$_{45}$H$_{93}$DyBSi$_4$NaO$_4$: C 37.42 (53.68); H 7.07 (9.31), for **24**(−4 THF) C$_{29}$H$_{61}$DyBSi$_4$Na: C 37.42 (48.48); H 7.07 (8.56).

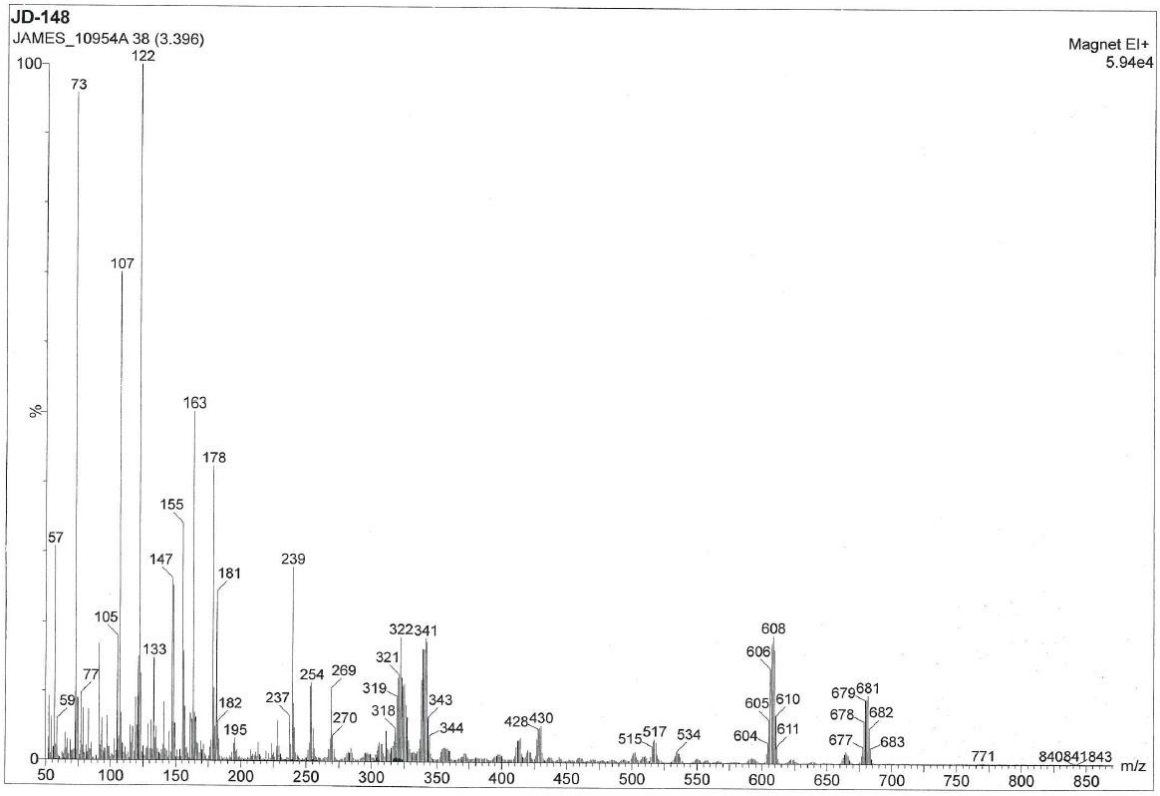

Figure S68. EI-MS spectrum of **24.**

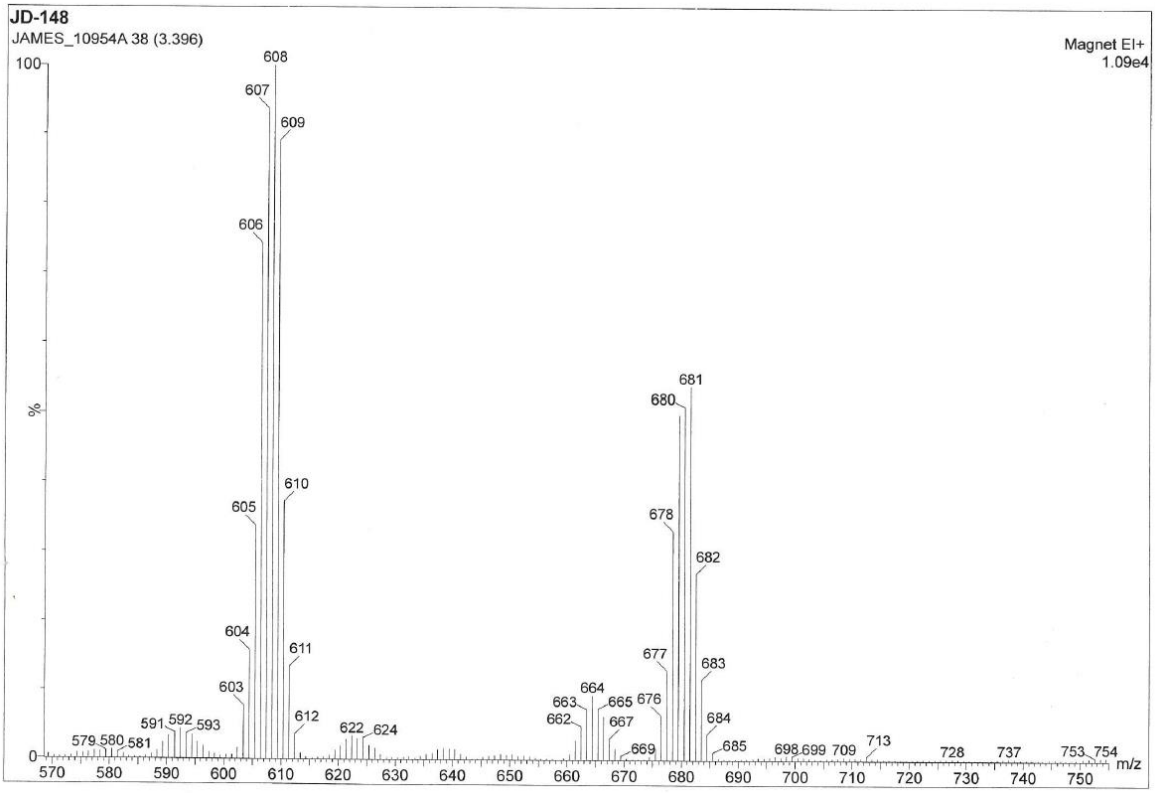

Figure S69. EI-MS spectrum of **24.**

Synthesis of $[Na(15\text{-}c\text{-}5)(THF)_2]^+[Y\{\eta^4\text{-}C_4(SiMe_3)_4\}(\eta^5\text{-}C_5Me_4{}^tBu)(\kappa^2\text{-}BH_4)]^-$ (25). 15-crown-5 (34 mg, 30 μL, 0.15 mmol) was added dropwise into a red solution of **23** (82 mg, 0.13 mmol) in THF (4 mL) and the resulting solution was left to stand for 20 h. The resulting red solution was filtered, layered with hexane and stored at –40°C for three days, resulting in the formation of red crystals of **25** suitable for X-ray crystallography (49 mg, 38 %).

NMR spectroscopy of **25** revealed the presence of two isomers, with the major / minor components arising in a ratio of *ca.* 10:1.

^{1}H NMR (δ/ppm, D_8-THF): Major: 3.69 (s, CH_2 crown, 24H, overlapped with minor component), 2.41 (s, Me_2, 6H), 2.12 (s, Me_2, 6H), 1.27 (s, ^{t}Bu, 9H), 0.10 (s, $SiMe_3$, 36H). Minor: 3.69 (s, CH_2 crown, 24H, overlapped with major component)), 2.18 (s, Me_2, 0.6H), 1.96 (s, Me_2, 0.6H), 1.35 (s, ^{t}Bu, 0.9H), 0.10 (s, $SiMe_3$, 3.6H).

^{13}C{^{1}H} NMR (δ/ppm, D_8-THF): Major: 129.04 ($\underline{C}_4$ ring), 117.63 ($\underline{C}_5$ ring), 116.49 ($\underline{C}_5$ ring), 69.71 ($\underline{C}H_2$), 68.38 ($\underline{C}H_2O$), 34.76 ($\underline{C}(CH_3)_3$), 33.16 ($C(\underline{C}H_3)_3$), 26.53 ($\underline{C}H_2$), 17.22 ($\underline{Me}_2$), 13.40 ($\underline{Me}_2$), 5.43 ($Si\underline{Me}_3$). Signals corresponding to the C_5 ring carbon attached to the ^{t}Bu group and for the minor component could not be observed, except for a signal at 5.35 ($Si\underline{Me}_3$).

^{11}B{^{1}H} NMR (δ/ppm, D_8-THF): Major: −24.87 (s, FWHM = 55 Hz, BH_4). Minor: −20.85 (s, FWHM = 154 Hz, BH_4).

^{11}B NMR (δ/ppm, D_8-THF): Major: −24.86 (quint., $^1J_{BH}$ = 85 Hz, BH_4). Minor: −26.67 (s, BH_4).

^{29}Si{^{1}H} NMR (δ/ppm, D_8-THF): −21.07.

^{23}Na NMR (δ/ppm, D_8-THF): −5.82 (FWHM = 362 Hz).

FTIR ($\bar{\nu}$/cm^{-1}): 3000-2850 (m, b, C-H), 2400-2300 (w, d, B-H_T), 2150-2000 (w, bs, B-H_B).

Satisfactory elemental analysis could not be obtained for this compound, a representative result being (%), found (calculated) for $C_{47}H_{97}YBNaSi_4O_7$: C 50.23 (55.93); H 8.78 (9.69), for $C_{43}H_{89}YBNaSi_4O_6$, **25**(−THF): C 50.23 (55.11); H 8.78 (9.57).

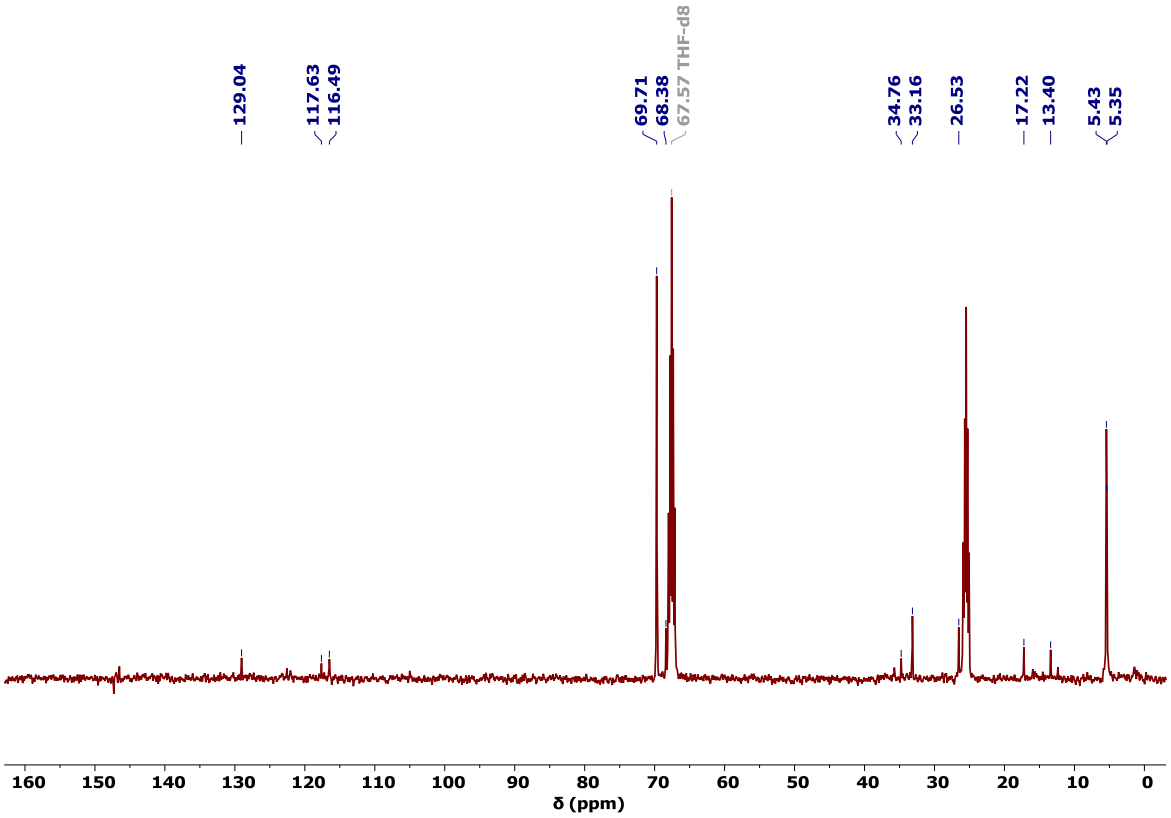

Figure S70. $^{13}C\{^{1}H\}$ NMR spectrum of **25** in D_8-THF.

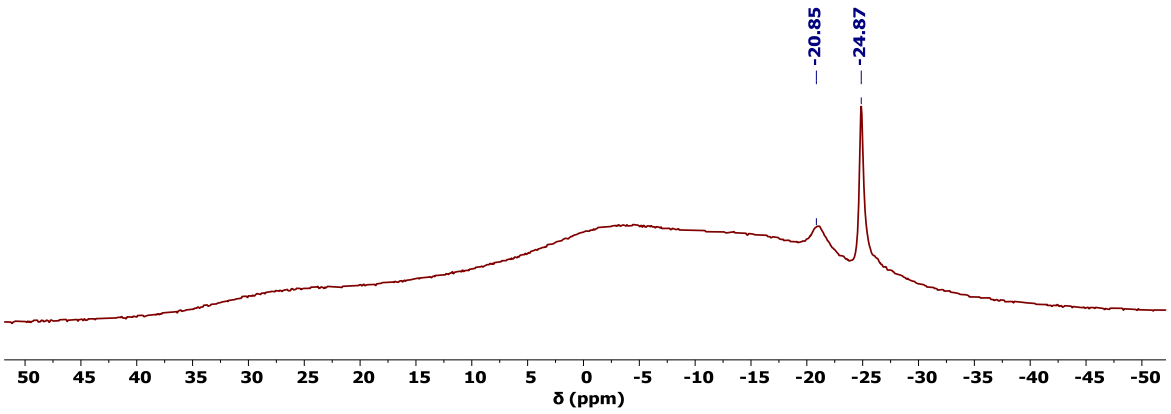

Figure S71. $^{11}B\{^{1}H\}$ NMR spectrum of **25** in D_8-THF.

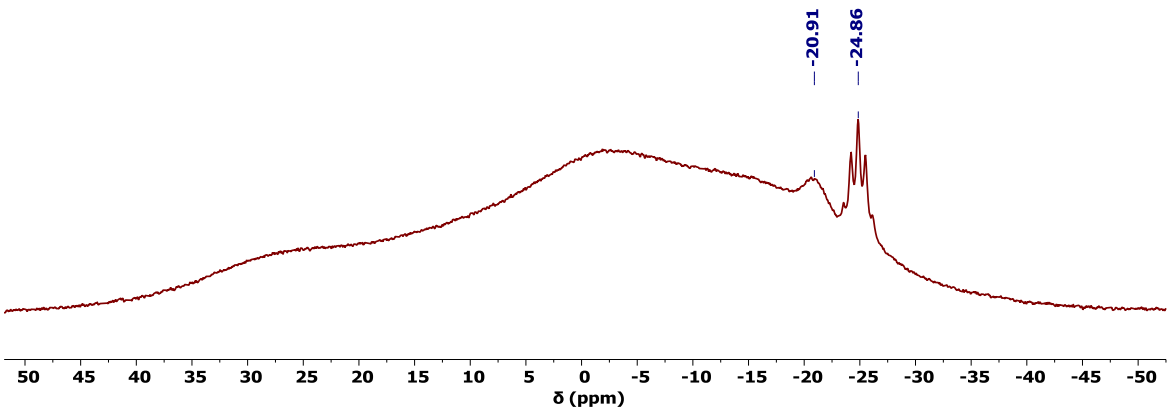

Figure S72. ^{11}B NMR spectrum of **25** in D_8-THF.

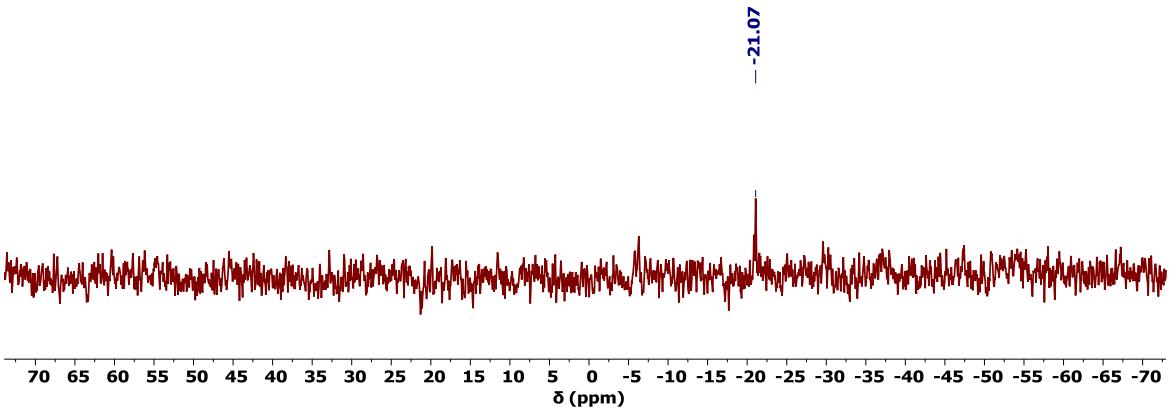

Figure S73. $^{29}Si\{^{1}H\}$ NMR spectrum of **25** in D_8-THF.

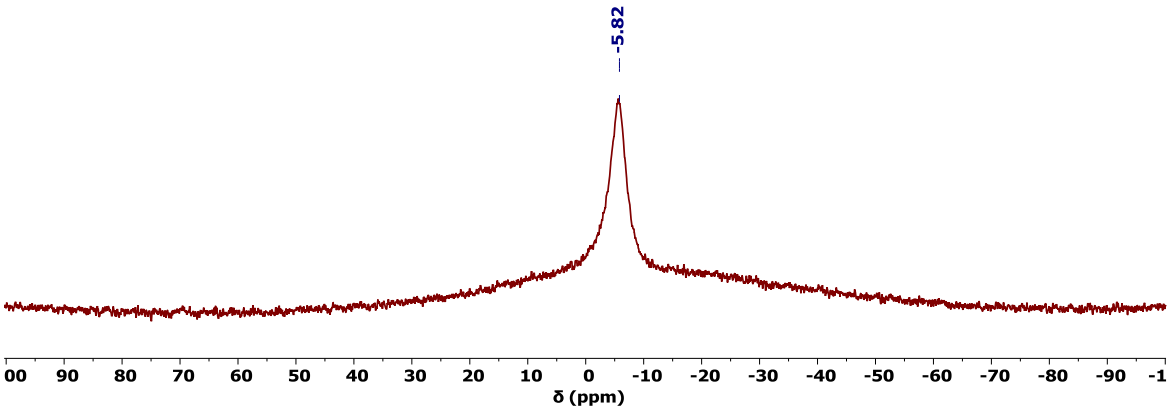

Figure S74. $^{23}Na\{^{1}H\}$ NMR spectrum of **25** in D_8-THF.

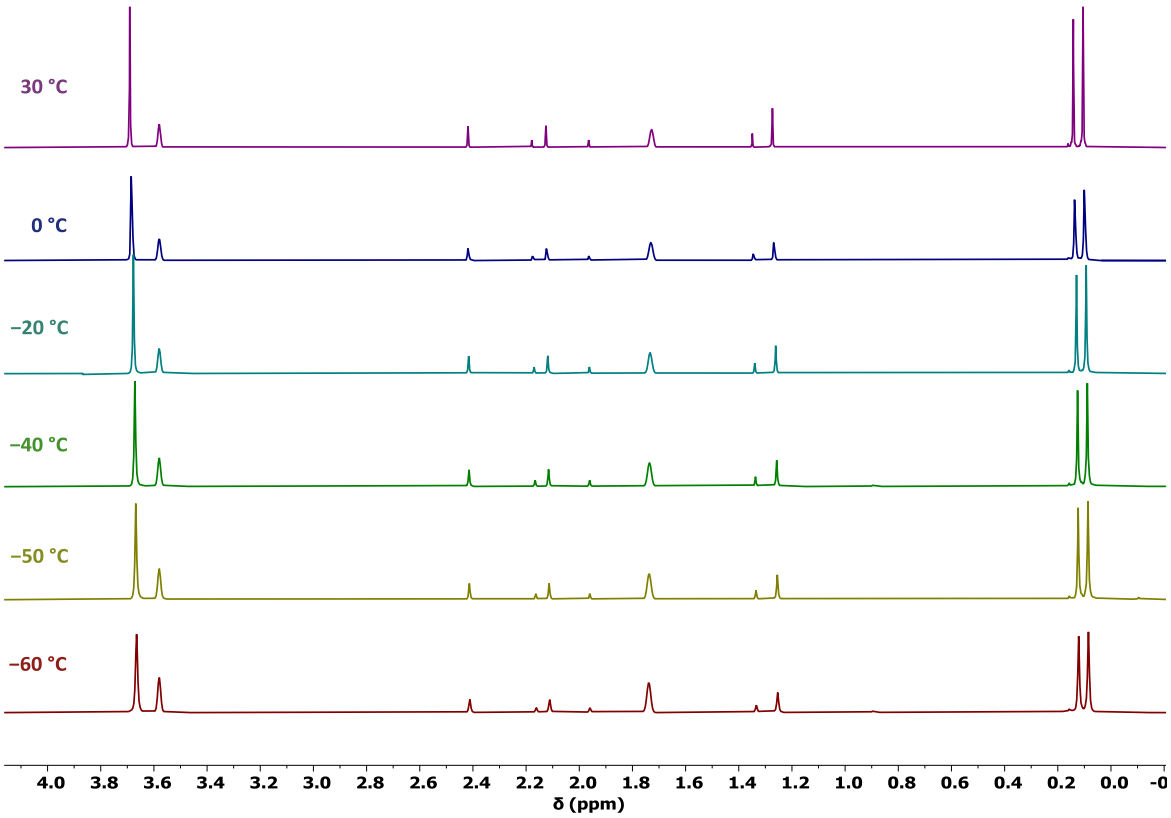

Figure S75. Variable temperature ^{1}H NMR spectra of **25** in D_8-THF from +30 to −60 °C.

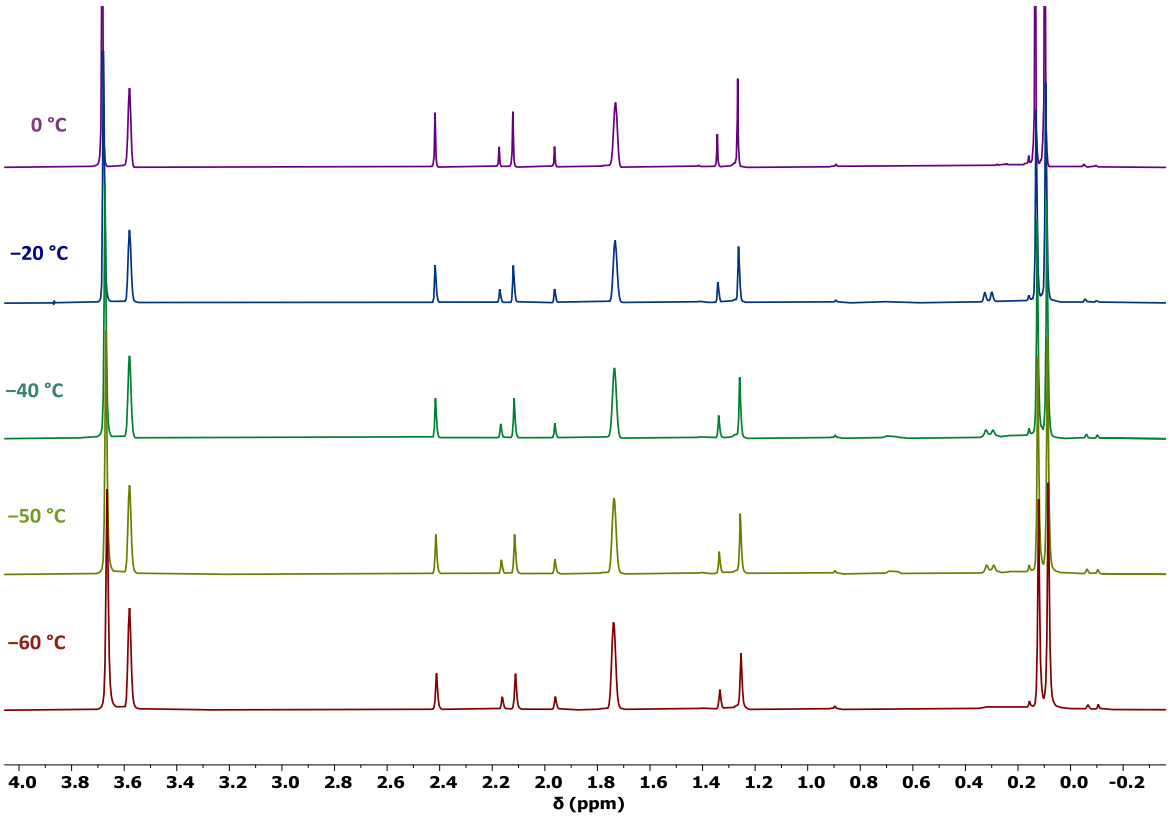

Figure S76. Variable temperature $^{1}H\{^{11}B\}$ NMR spectra of **25** in D_8-THF from 0 to −60 °C.

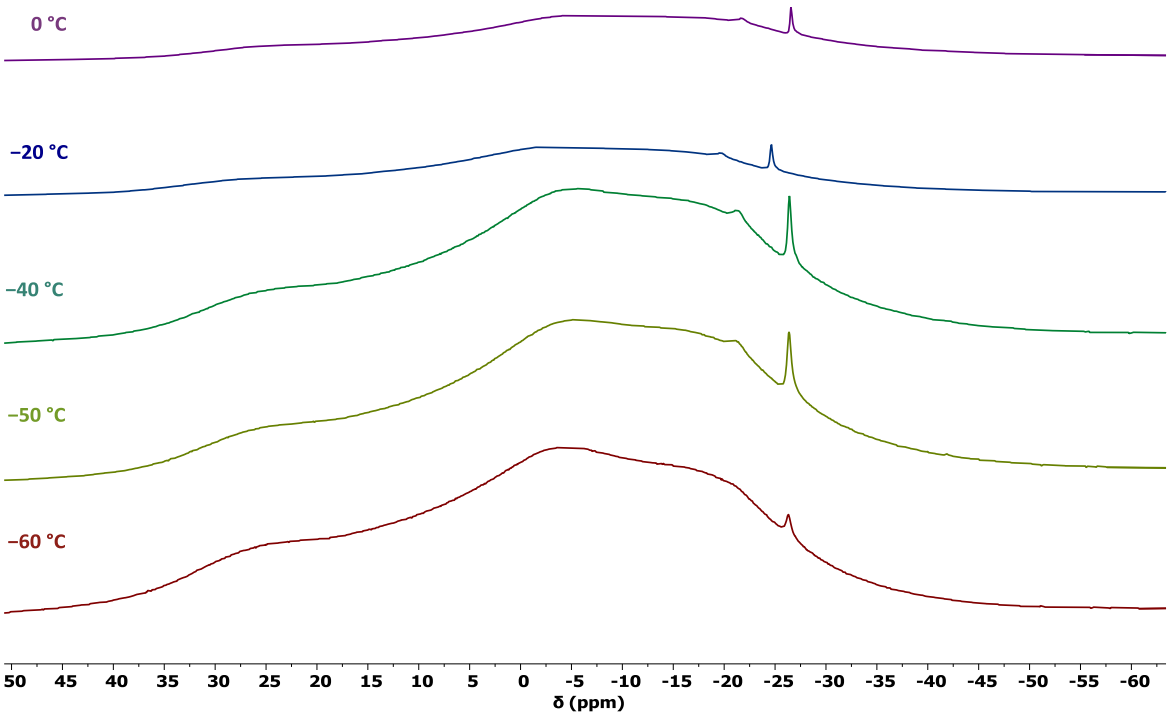

Figure S77. Variable temperature $^{11}B\{^{1}H\}$ NMR spectra of **25** in D_8-THF from 0 to −60 °C.

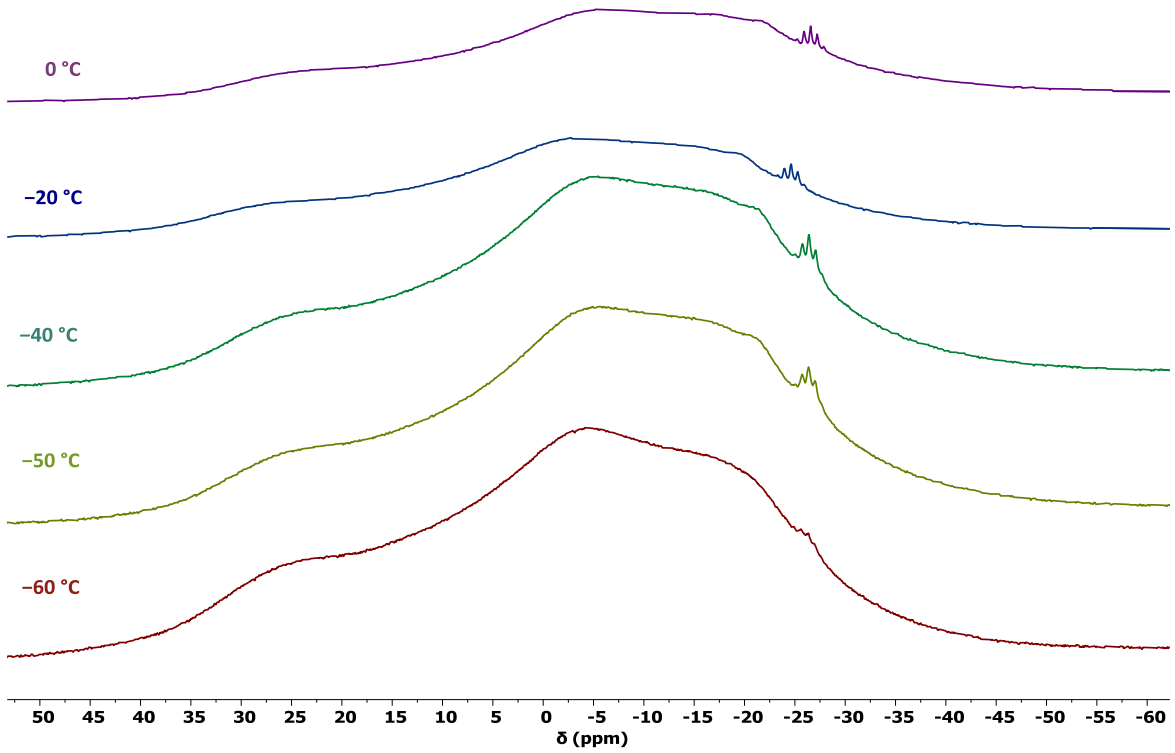

Figure S78. Variable temperature ^{11}B NMR spectra of **25** in D_8-THF from 0 to −60 °C.

Synthesis of [Na(15-c-5)(THF)$_2$]$^+$[Dy{η^4-C$_4$(SiMe$_3$)$_4$}(η^5-C$_5$Me$_4$^{t}Bu)(κ^2-BH$_4$)]$^-$ (26). 15-crown-5 (9 mg, 8 μL, 0.41 mmol) was added dropwise into a red solution of **24** (195 mg, 0.27 mmol) in THF (2 mL) and the resulting solution was left to stand for 20 h. The resulting red solution was filtered, layered with hexane and stored at –40°C for three days, resulting in the formation of red crystals of **26** suitable for X-ray crystallography (32 mg, 73 %).

FTIR ($\bar{\nu}$/cm^{-1}): 3000-2850 (m, b, C-H), 2400-2300 (w, d, B-H$_T$), 2150-2000 (w, bs, B-H$_B$).

Elemental analysis (%), found (calculated) for $C_{47}H_{97}DyBNaSi_4O_7$: C 51.53 (52.13); H 9.30 (9.03).

Synthesis of [Dy{η^8-C$_8$(Si^{i}Pr$_3$)$_2$H$_4$}{η^4-C$_4$(SiMe$_3$)$_4$}K(THF)] (27). A dark purple solution of [K$_2$Pn(Si(^{i}Pr$_3$)$_2$)] (230 mg, 0.47 mmol) in THF (10 mL) was added dropwise to an orange solution of **15** (300 mg, 0.47 mmol) in THF (15 mL) cooled to –78 °C. The resulting dark red solution was warmed to room temperature and stirred overnight, by which time a white precipitate had deposited. The reaction mixture was filtered, and the solvent removed *in vacuo* to yield a crude orange powder, subsequently identified as **27** (406 mg, 85 %). Orange

crystals of **27** suitable for X-ray crystallography were obtained by storing a saturated hexane solution at –40 °C for three days (268 mg, 56 %).

FTIR ($\bar{\nu}$/cm^{-1}): 3000-2850 (m, b, C-H).

Elemental analysis (%), found (calculated) for $C_{46}H_{90}DyKSi_6O$: C 54.16 (53.68); H 9.09 (8.81).

Synthesis of [K(18-c-6)(THF)$_2$]$^+$[Dy{η^8-C$_8$(Si^{i}Pr$_3$)$_2$H$_4$}{η^4-C$_4$(SiMe$_3$)$_4$}]$^-$ (28). A solution of 18-crown-6 (33 mg, 0.13 mmol) in THF (3 mL) was added dropwise into a dark red solution of **27** (130 mg, 0.13 mmol) in THF (10 mL) and stirred overnight. The resulting dark red reaction mixture was filtered, and the solvent removed *in vacuo* to yield a crude orange-red powder subsequently identified as **28** (143 mg, 83 %). Red crystals of **28** suitable for X-ray crystallography were obtained by washing the crude material with hexane, and storing a saturated THF solution layered with hexane at –40 °C for three days (112 mg, 65 %).

FTIR ($\bar{\nu}$/cm^{-1}): 3000-2850 (m, b, C-H).

Elemental analysis (%), found (calculated) for $C_{62}H_{122}DyKSi_6O_8$: C 53.43 (54.53); H 8.87 (9.00), for $C_{58}H_{114}DyKSi_6O_7$, **28**(–THF): C 53.43 (53.85); H 8.87 (8.88).

6.4. Experimental for Chapter 4

Synthesis of [La{η^4-C$_4$(SiMe$_3$)$_4$}(μ-I)(THF)$_2$]$_2$ (29). Lanthanum metal (41 mg, 0.29 mmol) was added to a red solution of **7** (100 mg, 0.29 mmol) in THF (10 mL). Iodine (37 mg, 0.15 mmol) was added into the reaction and the mixture was sonicated for 5 minutes, with the colour of the solution changing from red to dark red / brown. The reaction mixture was left to stir at room temperature for three days. After this time, the mixture was left to settle before being filtered, and the solvent removed *in vacuo.* The crude product was dissolved in the minimum amount of THF and re-filtered before layering with hexane and storing at –40°C over three days to yield orange crystals of **29** suitable for X-ray crystallography (149 mg, 68 %).

^{1}H NMR (δ/ppm, D$_8$-THF): 3.61 (m, CH$_2$O, 8H), 1.77 (m, CH$_2$, 8H), 0.21 (s, SiMe$_3$, 36H).

^{13}C{^{1}H} NMR (δ/ppm, D$_8$-THF): 138.57 (C$_4$ ring), 68.38 (<u>C</u>H$_2$O), 26.51 (<u>C</u>H$_2$), 5.10 (Si<u>Me</u>$_3$).

$^{29}Si\{^{1}H\}$ NMR (δ/ppm, D_8-THF): –20.84.

FTIR ($\bar{\nu}$/cm^{-1}): 3000-2850 (m, b, C-H).

Elemental analysis (%), found (calculated) for **29** $C_{48}H_{104}La_2I_2Si_8O_4$: C 33.56 (38.39); H 6.07 (6.98), I 24.11 (16.90), for **29**(+0.3 $LaI_3(THF)_4$) $C_{48}H_{104}La_2I_2Si_8O_4 \cdot 0.3\ C_{16}H_{32}LaI_3O_4$: C 33.56 (34.83); H 6.07 (6.25), I 24.11 (24.28).

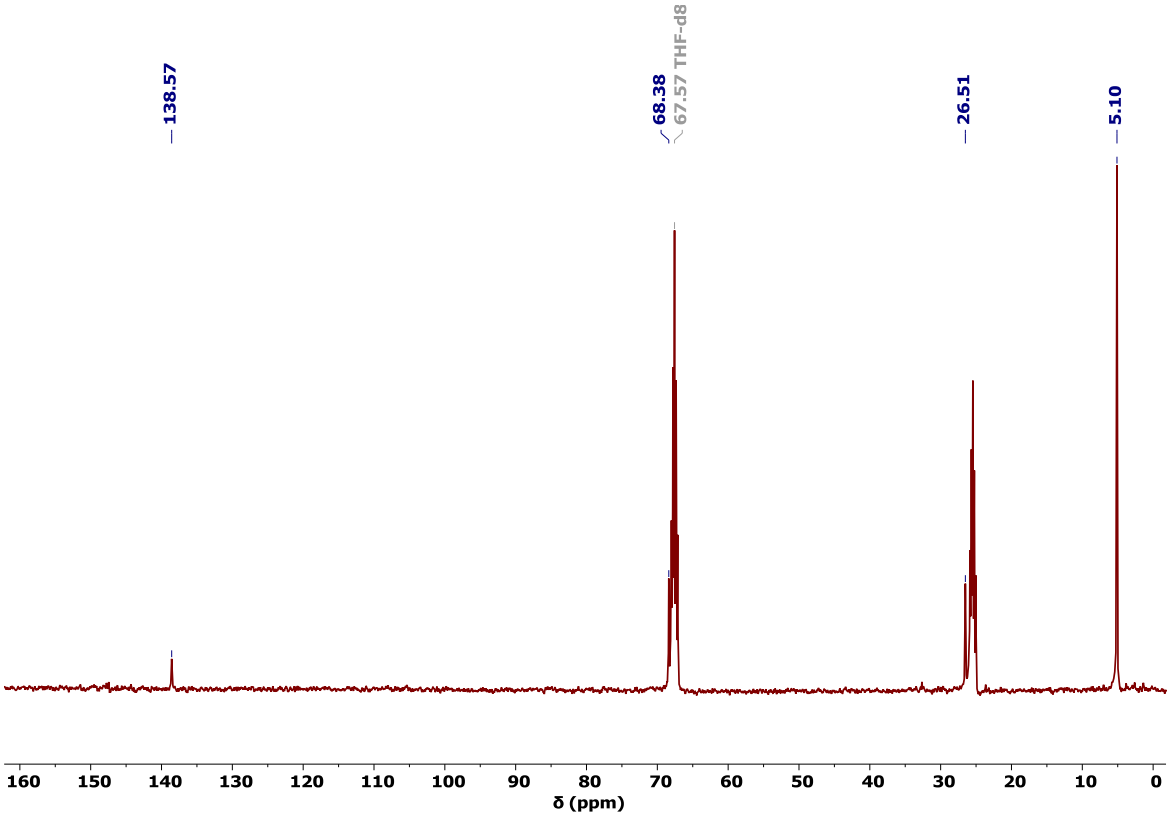

Figure S79. $^{13}C\{^{1}H\}$ NMR spectrum of **29** in D_8-THF.

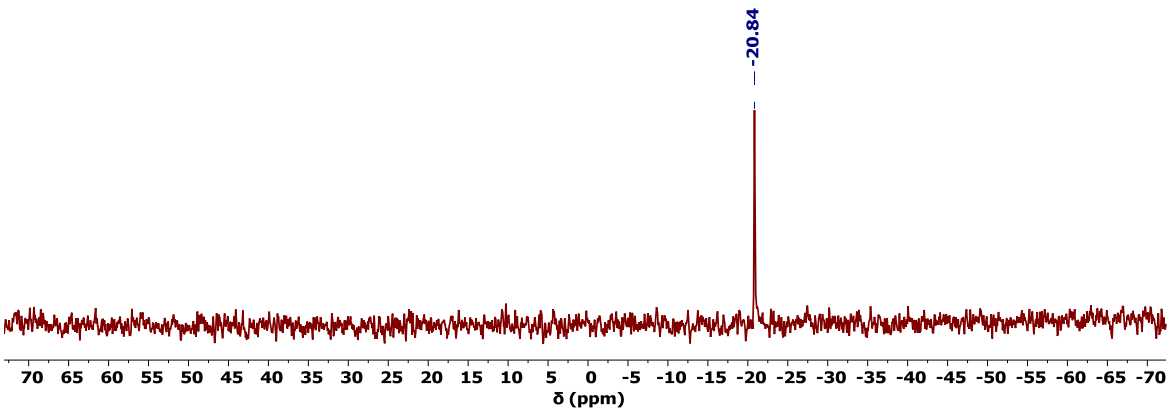

Figure S80. $^{29}Si\{^{1}H\}$ NMR spectrum of **29** in D_8-THF.

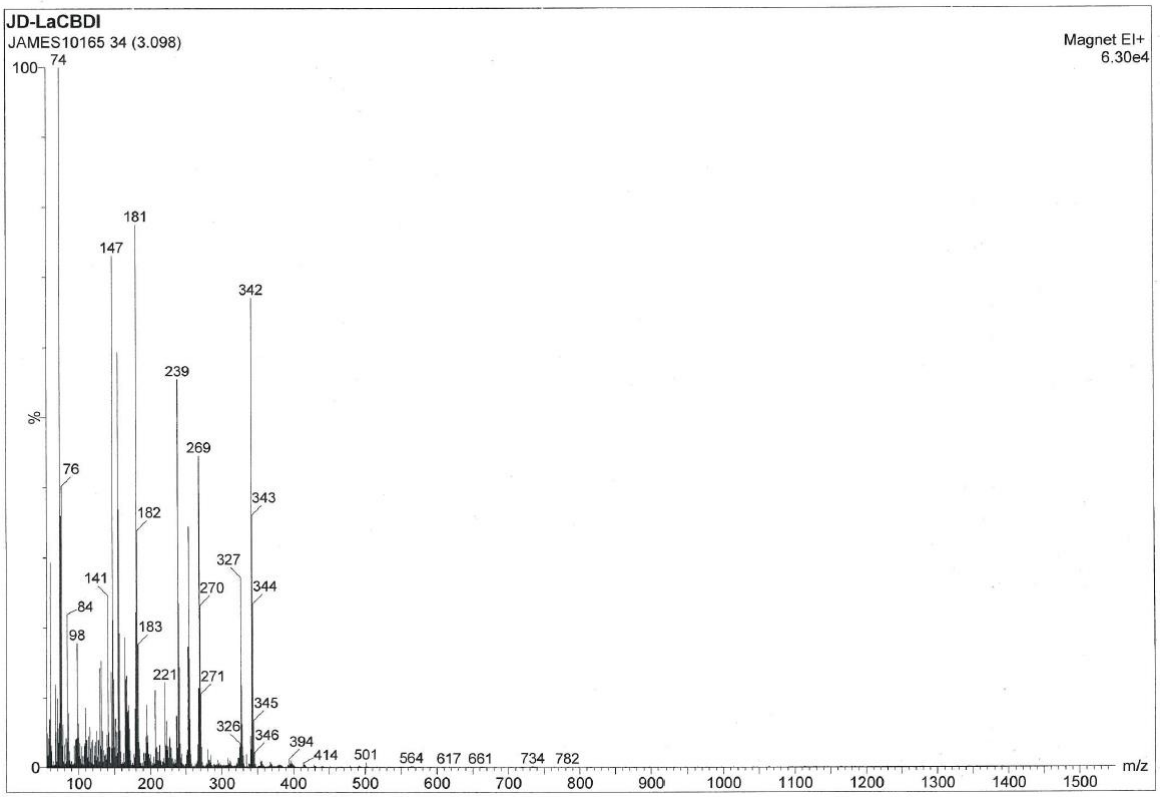

Figure S81. EI-MS spectrum of **29.**

Synthesis of [Ce{η^4-C$_4$(SiMe$_3$)$_4$}(μ-I)(THF)$_2$]$_2$ (30). Compound **30** was synthesised by following the same procedure as for **29**, using cerium metal (74 mg, 0.53 mmol), **7** (180 mg, 0.53 mmol) and iodine (67 mg, 0.26 mmol). Dark red crystals of **30** suitable for X-ray crystallography were obtained by storing a saturated THF solution layered with hexane at –40°C for seven days (128 mg, 58 %).

^{1}H NMR (δ/ppm, D$_8$-THF): 3.62 (m, CH$_2$O, 12H), 1.79 (m, CH$_2$, 12H), –0.26 (bs, SiMe$_3$, 36H).

^{13}C{^{1}H} NMR (δ/ppm, D$_8$-THF): 68.39 (CH$_2$O), 26.60 (CH$_2$), 11.43 (SiMe$_3$). A signal corresponding to the C$_4$ ring could not be observed.

^{29}Si{^{1}H} or ^{29}Si-^{1}H HMBC NMR (δ/ppm, D$_8$-THF): A signal could not be observed.

FTIR ($\bar{\nu}$/cm^{-1}): 3000-2850 (m, b, C-H).

Elemental analysis (%), found (calculated) for C$_{48}$H$_{104}$Ce$_2$I$_2$Si$_8$O$_4$: C 32.08 (38.33); H 5.90 (6.97).

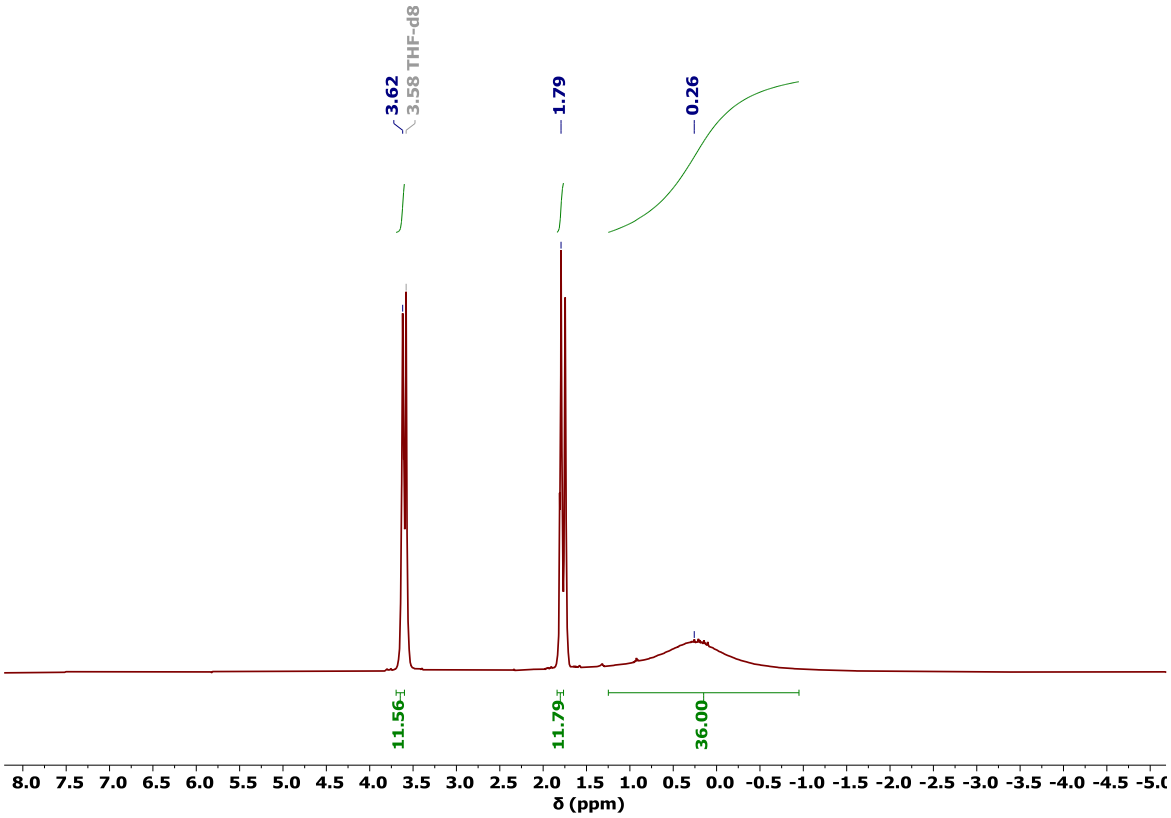

Figure S82. ^{1}H NMR spectrum of **30** in D_8-THF.

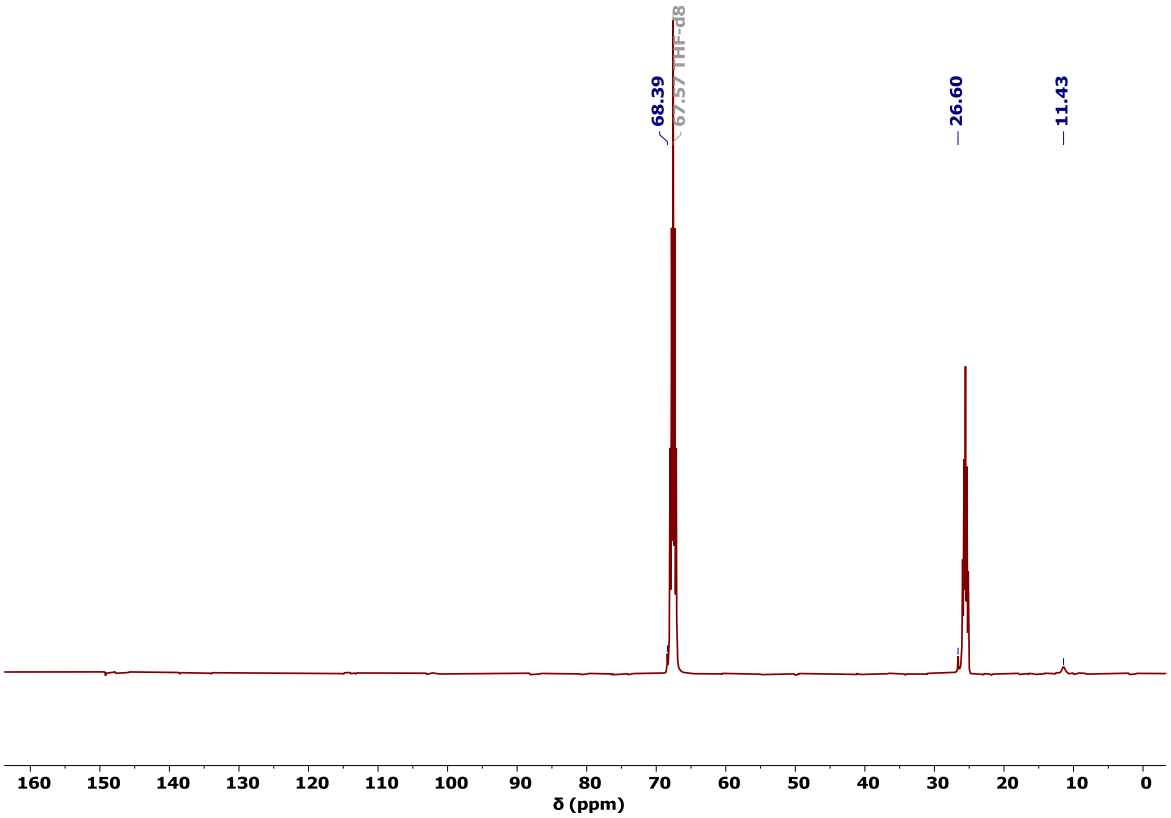

Figure S83. ^{13}C{^{1}H} NMR spectrum of **30** in D_8-THF.

Synthesis of $[Pr\{\eta^4\text{-}C_4(SiMe_3)_4\}(\mu\text{-}I)(THF)_2]_2$ (31). Compound **31** was synthesised by following the same procedure as for **29**, using praseodymium metal (41 mg, 0.29 mmol), **7** (100 mg, 0.29 mmol) and iodine (37 mg, 0.15 mmol). Storing a saturated THF solution layered with hexane at –40°C for three days resulted in the formation of yellow crystals of $[PrI_3(THF)_4]$. The mother liquor was filtered, and the solution left to slowly evaporate for approximately 6 hours, before being layered with hexane and stored at –40°C for three days to give dark red crystals of **31** suitable for X-ray crystallography (80 mg, 36 %).

^{1}H NMR (δ/ppm, D_8-THF): 3.62 (m, CH_2O, 12H), 1.80 (m, CH_2, 12H), –1.26 (bs, $SiMe_3$, 36H).

$^{13}C\{^1H\}$ NMR (δ/ppm, D_8-THF): Signals corresponding to the C_4 ring or $SiMe_3$ groups could not be observed.

$^{29}Si\{^1H\}$ or ^{29}Si-^{1}H HMBC NMR (δ/ppm, D_8-THF): No signals could not be observed.

FTIR ($\bar{\nu}$/cm^{-1}): 3000-2850 (m, b, C-H).

Elemental analysis (%), found (calculated) for $C_{48}H_{104}Pr_2I_2Si_8O_4$: C 35.13 (38.29); H 6.53 (6.96).

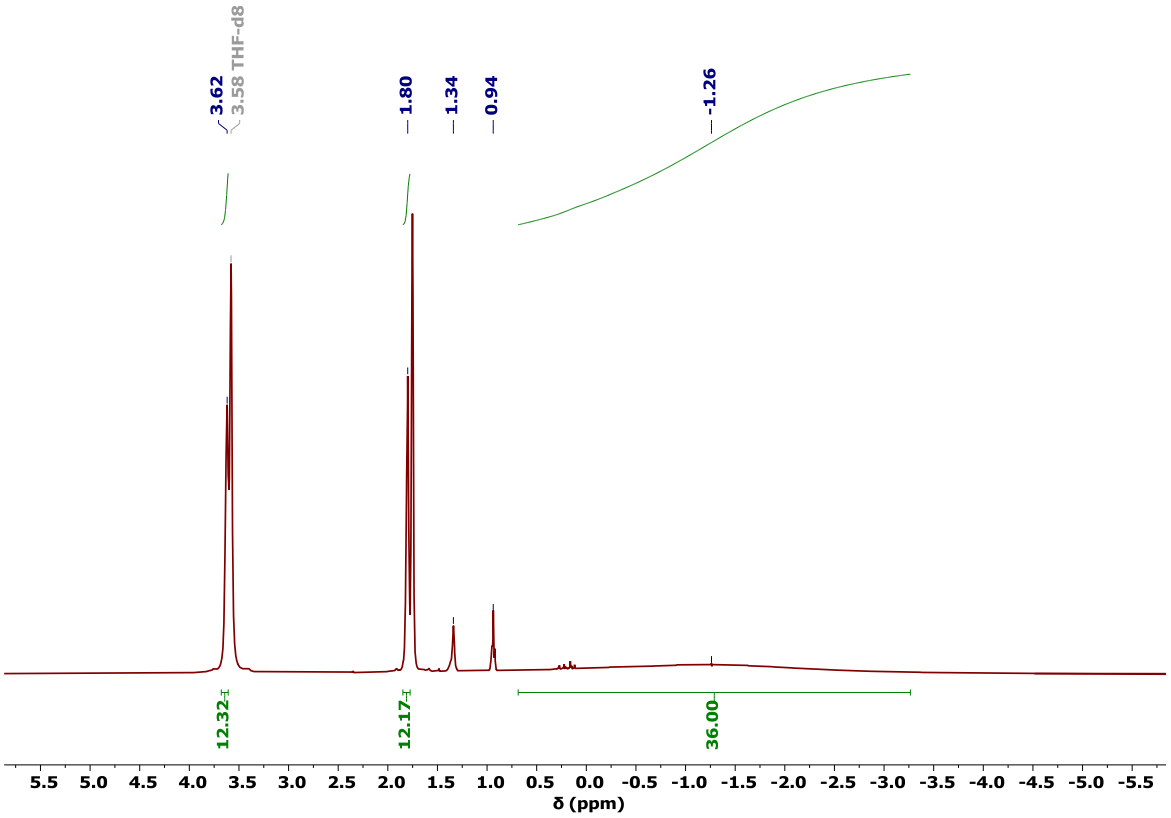

Figure S84. ^{1}H NMR spectrum of **31** in D_8-THF. The peaks at 1.34 and 0.94 ppm correspond to residual hexane from washing the crystals.

Synthesis of [Sm{η^4-C$_4$(SiMe$_3$)$_4$}(μ-I)(THF)$_2$]$_2$ (32). Compound **32** was synthesised by following the same procedure as for **29**, using samarium metal (44 mg, 0.29 mmol), **7** (100 mg, 0.29 mmol) and iodine (37 mg, 0.26 mmol). Dark green crystals of **32** suitable for X-ray crystallography were obtained by storing a saturated THF solution layered with hexane at –40°C for seven days (159 mg, 71 %).

^{1}H NMR (δ/ppm, D_8-THF): 3.62 (m, CH_2O, 7H), 1.79 (m, CH_2, 5H), –0.05 (s, $SiMe_3$, 36H).

^{13}C{^{1}H} NMR (δ/ppm, D_8-THF): 103.38 ($\underline{C}_4$ ring), 68.38 ($\underline{C}H_2O$), 26.43 ($\underline{C}H_2$), –0.77 (Si$\underline{Me}_3$).

^{29}Si{^{1}H} NMR (δ/ppm, D_8-THF): –1.80.

FTIR ($\bar{\nu}$/cm^{-1}): 3000-2850 (m, b, C-H).

Elemental analysis (%), found (calculated) for $C_{48}H_{104}Sm_2I_2Si_8O_4$: C 35.32 (37.82); H 6.67 (6.88).

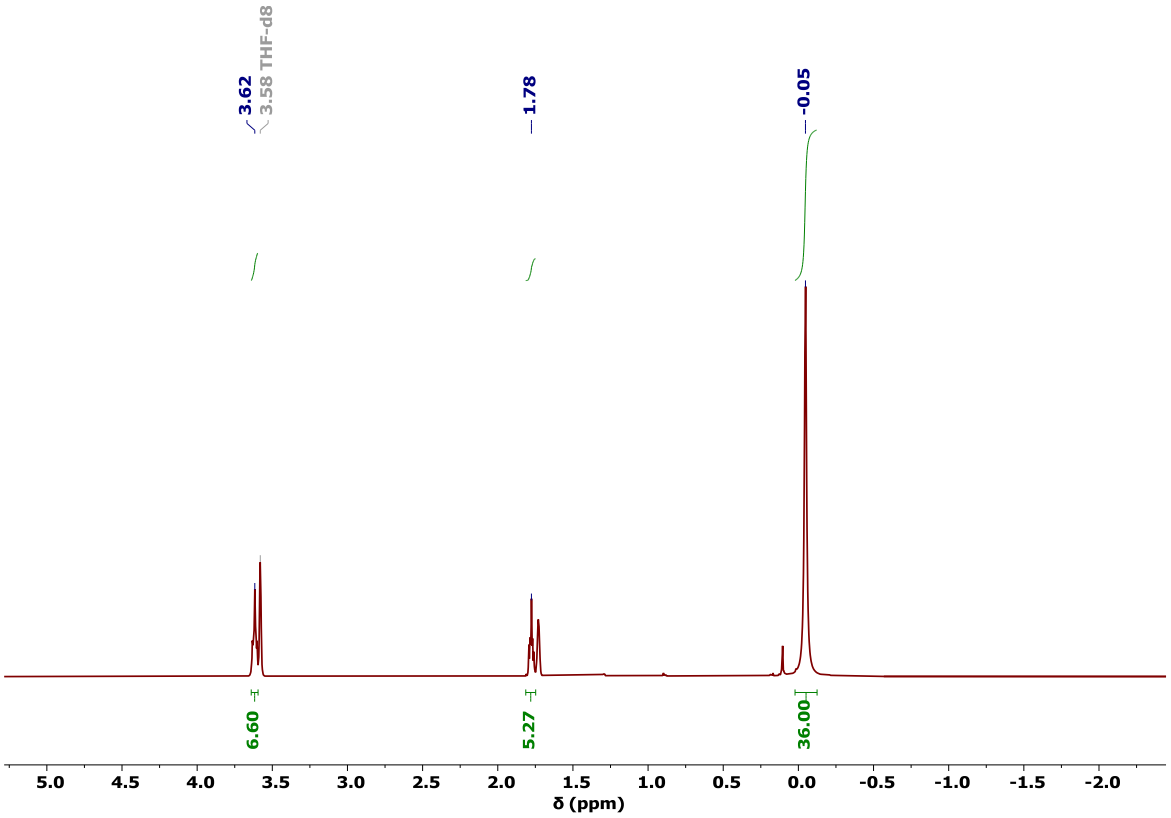

Figure S85. ^{1}H NMR spectrum of **32** in D_8-THF.

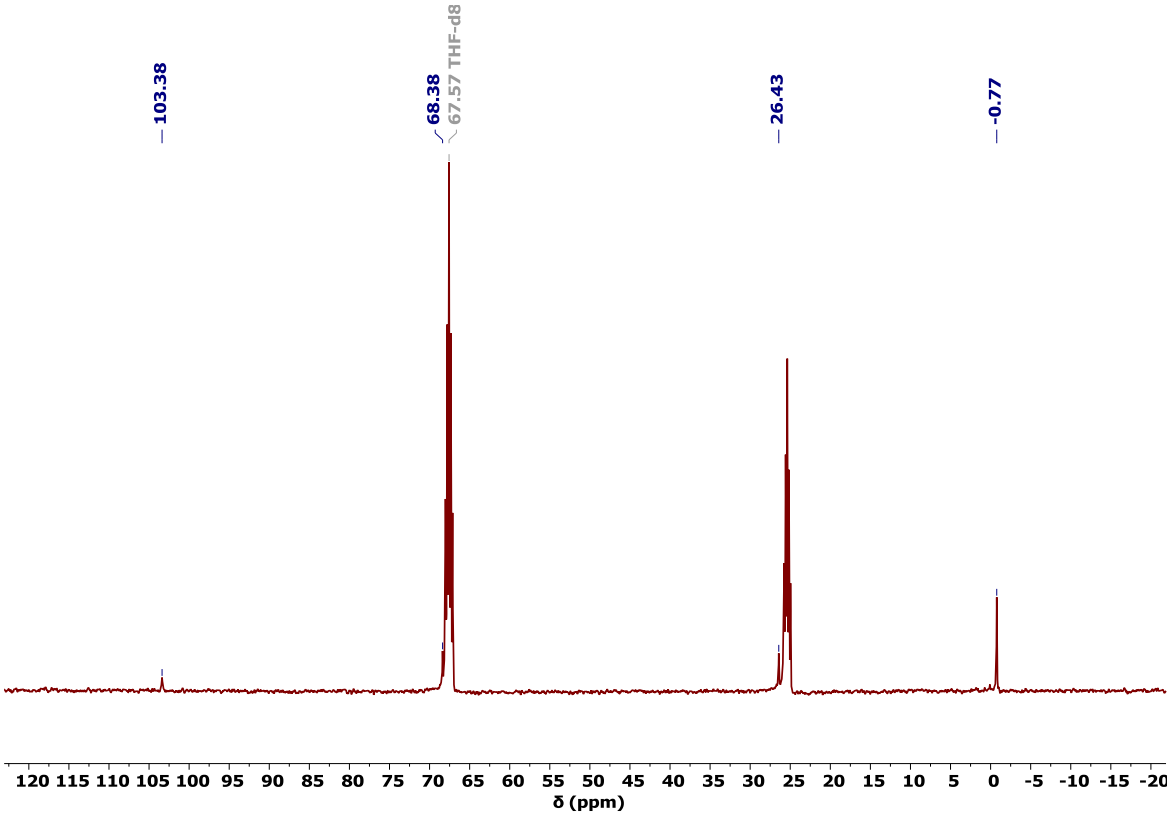

Figure S86. $^{13}C\{^{1}H\}$ NMR spectrum of **32** in D_8-THF.

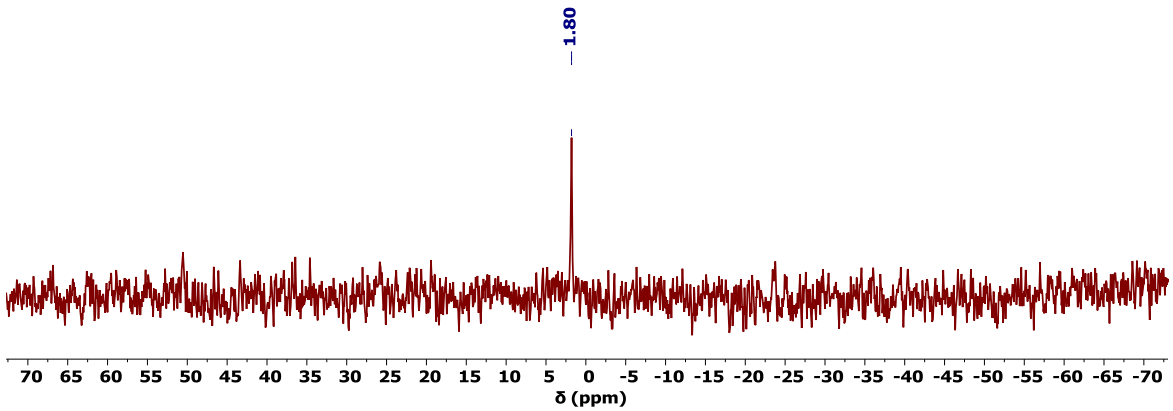

Figure S87. $^{29}Si\{^{1}H\}$ NMR spectrum of **32** in D_8-THF.

Synthesis of [Eu{η³-C₄(SiMe₃)₄H}(μ-I)(THF)₂]₂ (33). Europium metal (60 mg, 0.40 mmol) was added to a red solution of **7** (100 mg, 0.29 mmol) in THF (10 mL). Iodine (37 mg, 0.15 mmol) was added into the reaction and the mixture was sonicated for 20 minutes, with no obvious colour change of the solution. The reaction mixture was left to stir at room temperature for three days. After this time, the solution had changed from red to dark brown with a yellow microcrystalline precipitate, which was left to settle before being filtered, and the solvent removed *in vacuo.* The crude product was dissolved in the minimum amount of THF, layered with hexane and stored at –40°C over three days to yield yellow crystals of $[EuI_2(THF)_5]$. The mother liquor was filtered, and the solution left to slowly evaporate for approximately 6 hours, before being layered with hexane and stored at –40°C for three days to give yellow-green crystals of **33** suitable for X-ray crystallography (53 mg, 24 %).

No signals could be observed in a D_8-THF solution of **33** for ^{1}H, $^{13}C\{^{1}H\}$, $^{29}Si\{^{1}H\}$ or ^{29}Si-^{1}H HMBC NMR.

FTIR ($\bar{\nu}$/cm^{-1}): 3000-2850 (m, b, C-H).

Elemental analysis (%), found (calculated) for $C_{48}H_{106}Eu_2I_2Si_8O_4$: C 26.02 (37.69); H 4.72 (6.98).

Synthesis of [Yb{η³-C₄(SiMe₃)₄H}(μ-I)(THF)₂]₂ (34). Compound **34** was synthesised by following the same procedure as for **33**, using ytterbium metal (41 mg, 0.24 mmol), **7** (833mg, 0.24 mmol) and iodine (30 mg, 0.12 mmol). The crude product was dissolved in

the minimum amount of THF, layered with hexane and stored at –40°C over three days to yield yellow crystals of $[YbI_2(THF)_4]$. The mother liquor was filtered, and the solution left to slowly evaporate for approximately 6 hours, before being layered with hexane and stored at –40°C for three days to give dark red crystals of **34** suitable for X-ray crystallography (59 mg, 33 %).

^{1}H NMR (δ/ppm, D_8-THF): 3.60 (m, CH_2O, 3H), 2.69 (s, C_4H, 1H), 1.76 (m, CH_2, 3H), 0.23 (s, $SiMe_3$, 9H), 0.18 (s, $SiMe_3$, 18H), 0.08 (s, $SiMe_3$, 9H).

^{13}C{^{1}H} NMR (δ/ppm, D_8-THF): 176.48 ($\underline{C}_4$ ring), 111.75 ($\underline{C}_4$ ring), 68.39 ($\underline{C}H_2O$), 54.35 ($H\underline{C}_4$ ring), 26.55 ($\underline{C}H_2$), 3.60 (($Si\underline{Me}_3)_2$), 2.37 ($Si\underline{Me}_3$), 1.14 ($Si\underline{Me}_3$).

^{29}Si{^{1}H} NMR (δ/ppm, D_8-THF): No signals could be observed.

^{29}Si-^{1}H HMBC NMR (δ/ppm, D_8-THF) ^{29}Si/^{1}H: –24.01/0.18, –17.00/0.23, –4.51/0.08.

FTIR ($\bar{\nu}$/cm^{-1}): 3000-2850 (m, b, C-H).

Elemental analysis (%), found (calculated) for $C_{48}H_{106}Yb_2I_2Si_8O_4$: C 31.10 (36.68); H 5.89 (6.80).

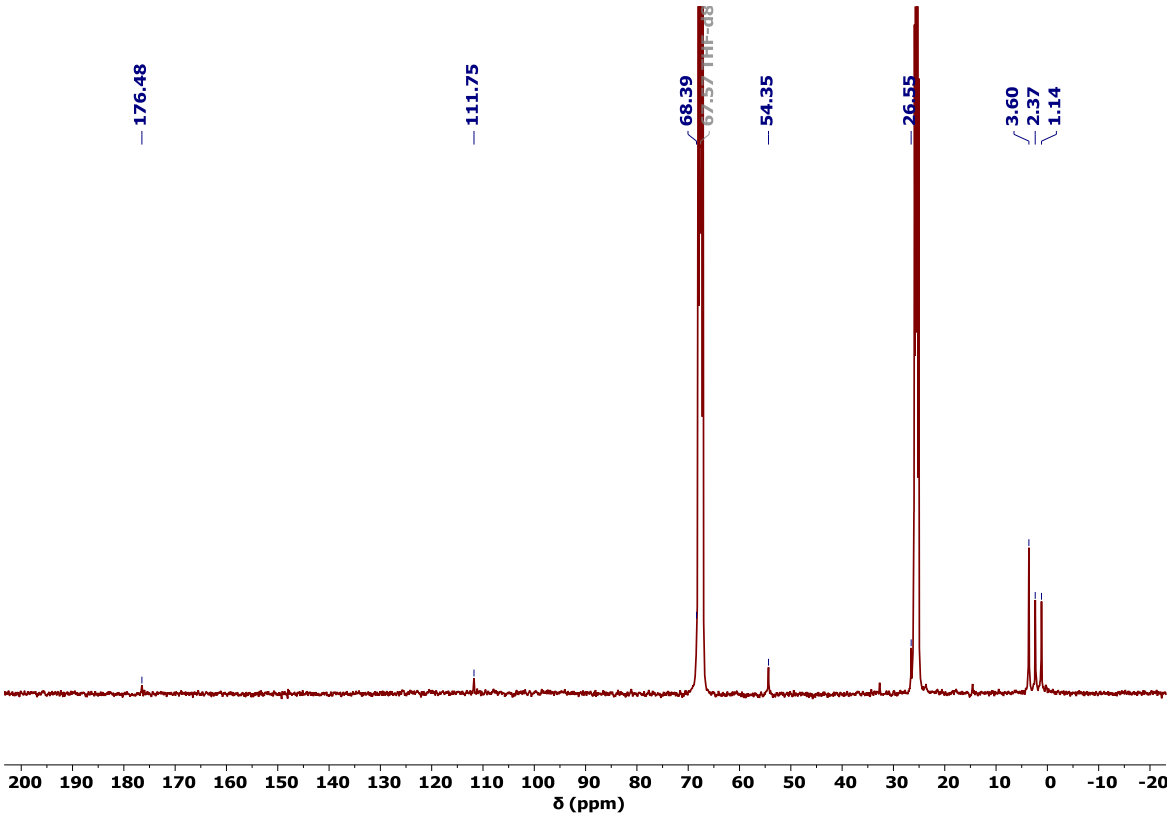

Figure S88. $^{13}C\{^{1}H\}$ NMR spectrum of **34** in D_8-THF.

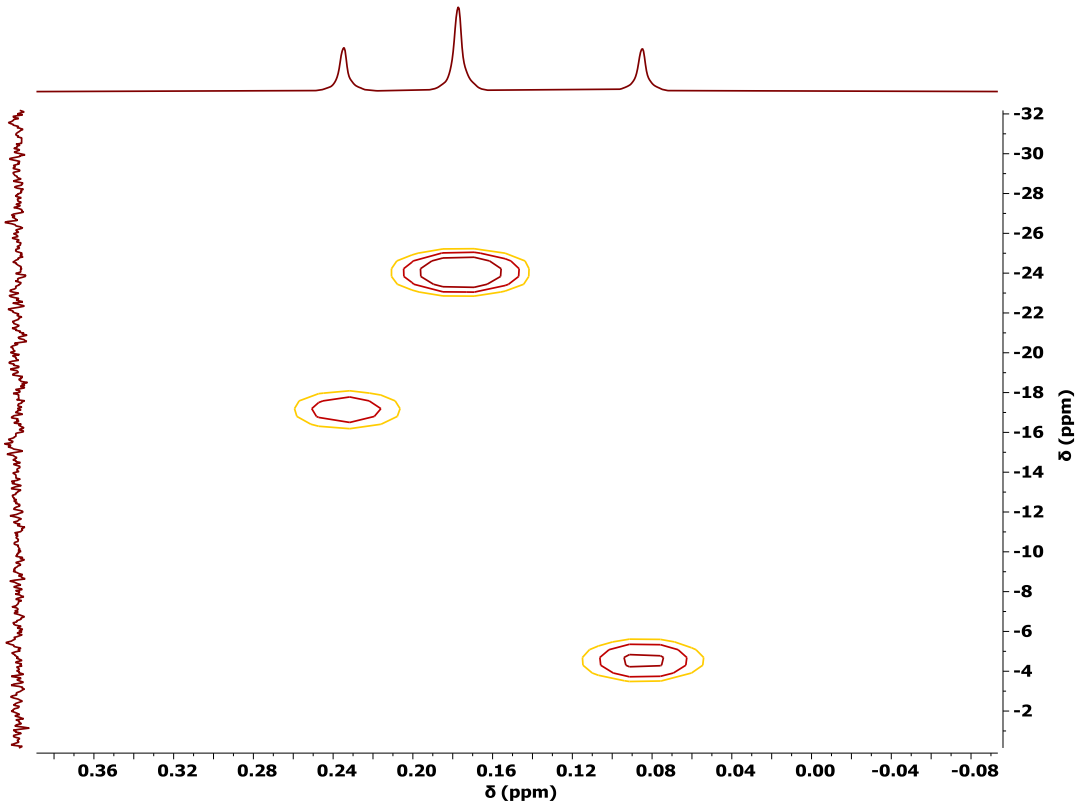

Figure S89. ^{29}Si-^{1}H HMBC correlation NMR spectrum of **34** in D_8-THF.

Synthesis of [La{η^4-C$_4$(SiMe$_3$)$_4$}(η^5-Cp*)(THF)$_2$] (35) and [La{η^4-C$_4$(SiMe$_3$)$_4$}(η^5-Cp*)(THF)(μ-I)La(η^5-Cp*)$_2$(THF)] (36). [KCp*] (18 mg, 0.11 mmol) was added to an orange solution of **29** (80 mg, 0.05 mmol) in THF (5 mL). The resulting orange solution was left to stir overnight at room temperature, by which time a white precipitate had deposited from the reaction. The reaction mixture was filtered, and the solvent removed *in vacuo* to yield a crude orange material. The material was redissolved in the minimum amount of hexane and stored at –40°C overnight to yield a very small amount of orange needle-like crystals subsequently identified as **35**. A second complex co-crystallized from the hexane solution as red block-like crystals, which were subsequently identified as **36**. The two complexes could not be separated, therefore no meaningful yields could be obtained and the complexes were only characterized by X-ray crystallography. Repeat reactions using **29** recrystallised from toluene resulted in the similar co-crystallization of **35** and **36**, with unreacted **29** additionally detected via X-ray crystallography.

Synthesis of [Sm{η^3-C$_4$(SiMe$_3$)$_3$-κ-CH$_2$(SiMe$_2$)H}(η^5-Cp*)(THF)] (37). [KCp*] (22 mg, 0.13 mmol) was added to a dark green solution of **32** (95 mg, 0.06 mmol) in THF (5 mL). The resulting dark brown solution was left to stir overnight at room temperature, by which time a white precipitate had deposited from the reaction. The reaction mixture was filtered, and the solvent removed *in vacuo* to yield a crude brown material. The material was redissolved in the minimum amount of hexane and stored at –40°C for seven days to yield a very small amount of red block-like crystals subsequently identified as **37**. Repeat reactions using [KCp*] or [NaCp*] resulted in the formation of dark yellow-brown crystals subsequently identified as [SmI$_2$(THF)$_5$] by X-ray crystallography.

6.5. X-ray crystallography supplementary information

Single-crystal X-ray diffraction measurements were carried out on an Agilent Gemini Ultra diffractometer using CuKα radiation (λ = 1.54184 Å), an Agilent Technologies SuperNova diffractometer using MoKα radiation (λ = 0.71073 Å) or a Rigaku FR-X diffractometer using either CuKα or MoKα radiation. Structures were solved in Olex2 with SHELXT using intrinsic phasing and were refined with SHELXL using least squares minimisation.[170–172] Anisotropic thermal parameters were used for the non-hydrogen atoms and isotropic parameters for the hydrogen atoms. Hydrogen atoms on carbons were added geometrically and refined using a riding model. Compounds **5**, **6**, **7**, and **9** have previously been reported.[111,120–122,134] Structures **8**, **11**, **30**, **33** and **34** were collected by Dr B. M. Day, who additionally solved **8**, **11** and **27**, with input on **36**. Structure **10** was collected and solved by Dr N. Tsoureas. All other structures were collected and solved by the author, with Dr N. Tsoureas gratefully acknowledged for advice and assistance with crystallography.

Crystals of **12**, **13**, **14**, **15** and **31** were all twinned, so were processed using the twinning software within CrysAlisPro. Three components were found for **12** (50/25/20 %), and two components were found for **13** (60/35 %), **14** (68/32 %), **15** (70/30 %) and **31** (80/15 %). The data was solved using hklf 4 and refined against hklf 5. In the case of **27**, the structure was found to be disordered over a mirror plane and so was modelled free from special position constraints with 50 % occupancy.

Table S1. Crystal data and structure refinement parameters for compounds **1**-**4**.

Compound	**1**	**2**	**3**	**4**
empirical formula	$C_{21}H_{45}YB_2O$	$C_{21}H_{45}DyB_2O$	$C_{17}H_{37}YB_2O$	$C_{17}H_{37}DyB_2O$
formula weight	424.10	497.69	367.99	441.58
crystal system	monoclinic	monoclinic	monoclinic	monoclinic
space group	$P2_1/c$	$P2_1/c$	$P2_1/n$	$P2_1/n$
a (Å)	18.1896(9)	18.1666(5)	8.2884(2)	8.2931(3)
b (Å)	8.9828(4)	8.9870(2)	19.9641(4)	19.9703(7)
c (Å)	16.4067(6)	16.4031(3)	12.5630(2)	12.5536(5)
α (°)	90	90	90	90
β (°)	113.891(5)	113.855(3)	100.988(2)	101.148(4)
γ (°)	90	90	90	90
V (Å^3)	2451.1(2)	2449.24(11)	2040.69(7)	2039.84(13)
Z	4	4	4	4
T (K)	100.00(10)	100(1)	100(1)	100(1)
ρ_{calc} (g/cm^3)	1.149	1.350	1.198	1.438
F (000)	912.0	1020.0	784.0	892.0
Reflections collected	7091	17872	11472	13416
Independent reflections	4341	4727	3878	3826
R_{int}	0.0407	0.0555	0.0416	0.0570
GOF on F^2	1.058	1.038	1.047	1.049
R_1[a]	0.0453	0.0379	0.0365	0.0419
R_w[b]	0.1101	0.0999	0.0951	0.1135

[a] $R_1[I>2\sigma(I)] = \sum||F_o|-|F_c||/\sum|F_o|$; [b] R_w[all data] $= [\sum\{w(F_o^2-F_c^2)^2\}/\sum\{w(F_o^2)^2\}]^{1/2}$

Table S2. Crystal data and structure refinement parameters for compounds **8**, **10** and **11**.

Compound	**8**	**10**	**11**
empirical formula	$C_{40}H_{88}Na_4O_2Si_8$	$C_{16}H_{36}Rb_2Si_4$	$C_{23}H_{44}Cs_2Si_4$
formula weight	917.78	511.75	698.76
crystal system	tetragonal	monoclinic	monoclinic
space group	*P*4/*nnc*	$P2_1/c$	$P2_1$
a (Å)	11.35330(10)	17.7431(18)	11.3204(4)
b (Å)	11.35330(10)	11.0123(11)	11.7847(4)
c (Å)	21.9076(2)	13.6005(16)	12.6517(4)
α (°)	90	90	90
β (°)	90	111.699(13)	113.758(4)
γ (°)	90	90	90
V (Å^3)	2823.83(6)	2469.1(5)	1544.80(11)
Z	2	4	2
T (K)	200.00(10)	100(2)	150.00(10)
ρ_{calc} (g/cm^3)	1.079	1.377	1.502
F (000)	1000.0	1048.0	696.0
Reflections collected	12872	15905	18543
Independent reflections	1284	4384	6313
R_{int}	0.0178	0.1056	0.0290
GOF on F^2	1.127	1.170	1.002
R_1[a]	0.0321	0.0828	0.0250
R_w[b]	0.0970	0.2730	0.0461

[a] $R_1[I>2\sigma(I)] = \sum||F_o|-|F_c||/\sum|F_o|$; [b] R_w[all data] $= [\sum\{w(F_o^2-F_c^2)^2\}/\sum\{w(F_o^2)^2\}]^{1/2}$

Table S3. Crystal data and structure refinement parameters for compounds **12**-**15**.

Compound	**12**	**13**	**14**	**15**
empirical formula	$C_{40}H_{104}Y_2Na_2B_4Si_8O_2$	$C_{40}H_{104}Dy_2Na_2B_4Si_8O_2$	$C_{20}H_{52}YKB_2Si_4O$	$C_{20}H_{52}DyKB_2Si_4O$
formula weight	1108.99	1256.17	570.60	644.19
crystal system	triclinic	triclinic	monoclinic	monoclinic
space group	*P–1*	*P–1*	$P2_1/n$	$P2_1/n$
a (Å)	10.929(2)	10.9592(4)	10.7817(4)	10.8460(3)
b (Å)	16.497(4)	16.5329(8)	17.5986(5)	17.5547(4)
c (Å)	17.2819(10)	17.2892(7)	16.9013(6)	16.9092(3)
α (°)	90.747(10)	90.676(4)	90	90
β (°)	90.198(11)	90.257(3)	91.955(3)	91.916(2)
γ (°)	92.00(2)	92.791(4)	90	90
V (Å^3)	3113.7(11)	3128.6(2)	3205.03(19)	3217.68(13)
Z	2	2	4	4
T (K)	100	100	100	100
ρ_{calc} (g/cm^3)	1.183	1.333	1.183	1.330
F (000)	1184.0	1292.0	1216.0	1324.0
Reflections collected	24473	17751	11390	10395
Independent reflections	24473	17751	11390	10395
R_{int} [†]	17.63	15.52	6.27	6.85
GOF on F^2	1.047	0.933	0.855	0.902
R_1[a]	0.0736	0.0604	0.0341	0.0458
R_w[b]	0.2307	0.1524	0.0765	0.1140

[a] $R_1[I>2\sigma(I)] = \sum||F_o|-|F_c||/\sum|F_o|$; [b] R_w[all data] $= [\sum\{w(F_o^2-F_c^2)^2\}/\sum\{w(F_o^2)^2\}]^{1/2}$

[†] Based on hklf 4.

Table S4. Crystal data and structure refinement parameters for compounds **16**-**18**.

Compound	**16**	**17**	**18**
empirical formula	$C_{27}H_{48}YB$	$C_{27}H_{48}DyB$	$C_{51}H_{44}DyBF_{20}$
formula weight	472.37	545.96	1210.17
crystal system	monoclinic	monoclinic	triclinic
space group	$P2_1/c$	$P2_1/c$	*P–1*
a (Å)	8.7976(2)	8.794(3)	11.2819(5)
b (Å)	11.5878(2)	11.579(4)	12.7328(6)
c (Å)	26.0848(4)	13.6005(16)	18.4263(10)
α (°)	90	90	81.110(4)
β (°)	91.912(2)	90	85.702(4)
γ (°)	90	90	67.637
V (Å^3)	2657.73(9)	2642.2(15)	2418.1(2)
Z	4	4	2
T (K)	149.99(10)	100(2)	100
ρ_{calc} (g/cm^3)	1.181	1.372	1.662
F (000)	1016.0	1124.0	1202.0
Reflections collected	8173	7754	13516
Independent reflections	4722	4640	9054
R_{int}	0.0335	0.0305	0.0437
GOF on F^2	1.023	1.028	1.017
R_1[a]	0.0341	0.0329	0.0479
R_w[b]	0.0861	0.0727	0.1165

[a] $R_1[I>2\sigma(I)] = \sum||F_o|-|F_c||/\sum|F_o|$; [b] R_w[all data] $= [\sum\{w(F_o^2-F_c^2)^2\}/\sum\{w(F_o^2)^2\}]^{1/2}$

Table S5. Crystal data and structure refinement parameters for compounds **19**-**22**.

Compound	**19**	**20**	**21**	**22**
empirical formula	$C_{46}H_{95}YBSi_4NaO_5$	$C_{46}H_{95}DyBSi_4NaO_5$	$C_{40}H_{83}YBSi_4NaO_6$	$C_{44}H_{91}DyBSi_4NaO_7$
formula weight	963.28	1036.87	895.13	1040.82
crystal system	monoclinic	monoclinic	orthorhombic	orthorhombic
space group	$P2_1/c$	$P2_1/c$	*Pbca*	$P2_12_12$
a (Å)	15.9288(3)	15.9421(7)	22.4327(3)	31.1059(2)
b (Å)	14.6042(2)	14.6022(5)	20.2593(3)	14.86900(10)
c (Å)	23.9979(3)	23.9850(8)	23.1518(4)	11.98800(10)
α (°)	90	90	90	90
β (°)	95.900(2)	95.856(4)	90	90
γ (°)	90	90	90	90
V (Å^3)	5553.00(15)	5554.3(4)	10521.8(3)	5544.61(7)
Z	4	4	8	4
T (K)	100(1)	99.9(5)	109(1)	100.00(10)
ρ_{calc} (g/cm^3)	1.152	1.240	1.130	1.330
F (000)	2088.0	2196.0	3856.0	2196.0
Reflections collected	34843	17021	25355	61080
Independent reflections	9874	9833	10062	10722
R_{int}	0.0618	0.0625	0.0492	0.0580
GOF on F^2	0.981	1.010	1.018	1.021
R_1[a]	0.0426	0.0528	0.0401	0.0237
R_w[b]	0.1119	0.1164	0.0949	0.0530

[a] $R_1[I>2\sigma(I)] = \sum||F_o|-|F_c||/\sum|F_o|$; [b] R_w[all data] $= [\sum\{w(F_o^2-F_c^2)^2\}/\sum\{w(F_o^2)^2\}]^{1/2}$

Table S6. Crystal data and structure refinement parameters for compounds **25**-**28**.

Compound	**25**	**26**	**27**	**28**
empirical formula	$C_{47}H_{97}YBSi_4NaO_7$	$C_{47}H_{97}DyBSi_4NaO_7$	$C_{46}H_{90}DySi_6KO$	$C_{70}H_{138}Dy_{10}Si_6KO$
formula weight	1009.31	1082.90	1029.31	1509.94
crystal system	monoclinic	monoclinic	monoclinic	triclinic
space group	$P2_1/c$	$P2_1/c$	$P2_1/m$	$P\bar{1}$
a (Å)	16.4042(2)	16.5631(2)	10.3825(2)	13.5715(7)
b (Å)	14.6279(2)	14.5735(2)	21.3004(4)	14.7132(6)
c (Å)	23.8840(2)	23.7561(3)	12.4091(3)	24.4618(12)
α (°)	90	90	90	74.369(4)
β (°)	98.4630(10)	98.7160(10)	91.536(2)	81.883(4)
γ (°)	90	90	90	62.547(5)
V (Å^3)	5668.77(12)	5668.08(13)	2743.30(10)	4173.4(4)
Z	4	4	2	2
T (K)	100(1)	100(1)	99.8(8)	100(1)
ρ_{calc} (g/cm^3)	1.183	1.269	1.246	1.202
F (000)	2184.0	2292.0	1086.0	1614.0
Reflections collected	79006	30974	17150	37150
Independent reflections	10976	10384	5157	14665
R_{int}	0.0489	0.0487	3.58	5.13
GOF on F^2	1.138	1.178	1.054	0.953
R_1[a]	0.0551	0.0691	0.0561	0.0539
R_w[b]	0.1167	0.1502	0.1575	0.1386

[a] $R_1[I>2\sigma(I)] = \sum||F_o|-|F_c||/\sum|F_o|$; [b] R_w[all data] $= [\sum\{w(F_o^2-F_c^2)^2\}/\sum\{w(F_o^2)^2\}]^{1/2}$

Table S7. Crystal data and structure refinement parameters for compounds **29**-**32**.

Compound	**29**	**30**	**31**	**32**
empirical formula	$C_{54}H_{118}La_2I_2Si_8O_4$	$C_{56}H_{120}Ce_2I_2Si_8O_6$	$C_{56}H_{120}Pr_2I_2Si_8O_6$	$C_{52}H_{112}Sm_2I_2Si_8O_5$
formula weight	1587.82	1648.27	1649.85	1596.63
crystal system	triclinic	triclinic	triclinic	monoclinic
space group	*P*–1	*P*–1	*P*–1	$P2_1/n$
a (Å)	11.3961(5)	11.4098(4)	11.4255(10)	11.1542(2)
b (Å)	11.6168(6)	11.8395(5)	11.8069(8)	16.1959(3)
c (Å)	15.0889(8)	15.2335(5)	15.2268(13)	19.8151(4)
α (°)	76.898(4)	77.007(3)	76.814(7)	90
β (°)	86.933(4)	86.101(3)	85.958(7)	95.395(2)
γ (°)	68.602(4)	67.960(4)	67.898(7)	90
V (Å^3)	1810.51(17)	1858.31(13)	1852.7(3)	3563.79(12)
Z	1	1	1	2
T (K)	100	124.99(10)	150.0(3)	149.9(3)
ρ_{calc} (g/cm^3)	1.456	1.473	1.479	1.488
F (000)	806.0	838.0	840.0	1612.0
Reflections collected	34843	19237	10838	28467
Independent reflections	11899	6524	10838	7274
R_{int}	0.0421	0.0362	†	0.0438
GOF on F^2	0.977	1.091	0.899	1.040
$R_1{}^a$	0.0344	0.0365	0.0494	0.0293
$R_w{}^b$	0.0841	0.1012	0.1159	0.0593

$^a R_1[I>2\sigma(I)] = \sum||F_o|-|F_c||/\sum|F_o|$; $^b R_w[\text{all data}] = [\sum\{w(F_o^2-F_c^2)^2\}/\sum\{w(F_o^2)^2\}]^{1/2}$

†Twinned data set does not display an R_{int}

Table S8. Crystal data and structure refinement parameters for compounds **33** and **34**.

Compound	**33**	**34**
empirical formula	$C_{54}H_{120}Eu_2I_2Si_8O_4$	$C_{54}H_{120}Yb_2I_2Si_8O_6$
formula weight	1615.93	1658.09
crystal system	triclinic	Triclinic
space group	*P*–1	*P*–1
a (Å)	10.2918(7)	10.3119(3)
b (Å)	13.6100(9)	13.3768(5)
c (Å)	14.7291(10)	14.6695(4)
α (°)	68.792(6)	68.213(3)
β (°)	72.407(6)	71.406(3)
γ (°)	81.056(6)	81.630(3)
V (Å^3)	1831.0(2)	1780.04(11)
Z	1	1
T (K)	125.00(10)	150.01(10)
ρ_{calc} (g/cm^3)	1.466	1.547
F (000)	820.0	834.0
Reflections collected	22560	37387
Independent reflections	6507	7282
R_{int}	0.1148	0.0501
GOF on F^2	1.082	1.049
R_1[a]	0.0701	0.0480
R_w[b]	0.2098	0.1401

[a] $R_1[I>2\sigma(I)] = \sum||F_o|-|F_c||/\sum|F_o|$; [b] R_w[all data] $= [\sum\{w(F_o^2-F_c^2)^2\}/\sum\{w(F_o^2)^2\}]^{1/2}$

Table S9. Crystal data and structure refinement parameters for compounds **35**-**37**.

Compound	**35**	**36**	**37**
empirical formula	$C_{34}H_{66}LaSi_4O_2$	$C_{60}H_{111}La_2ISi_4O_2$	$C_{30}H_{59}SmSi_4O$
formula weight	758.13	1381.56	698.48
crystal system	triclinic	orthorhombic	triclinic
space group	*P–1*	*Pnma*	*P–1*
a (Å)	11.7166(5)	26.4661(2)	10.2749(12)
b (Å)	17.7129(7)	15.6346(2)	10.3669(12)
c (Å)	19.9488(7)	16.13460(10)	18.496(2)
α (°)	86.039(3)	90	92.778(10)
β (°)	83.379(3)	90	92.274(10)
γ (°)	86.429(3)	90	112.579(11)
V (Å^3)	4096.5(3)	6676.29(11)	1813.4(4)
Z	4	4	2
T (K)	150	100	150.0(3)
ρ_{calc} (g/cm^3)	1.229	1.374	1.279
F (000)	1596.0	2840.0	730.0
Reflections collected	42174	98844	7663
Independent reflections	14251	6707	7663
R_{int}	0.1141	0.0718	†
GOF on F^2	1.563	1.230	1.084
R_1[a]	0.1723	0.0549	0.0532
R_w[b]	0.4854	0.1195	0.1564

[a] $R_1[I>2\sigma(I)] = \sum||F_o|-|F_c||/\sum|F_o|$; [b] R_w[all data] $= [\sum\{w(F_o^2-F_c^2)^2\}/\sum\{w(F_o^2)^2\}]^{1/2}$

†Twinned data set does not display an R_{int}

6.6. Magnetic property measurements supplementary information

All of the magnetic property measurements presented in this thesis were conducted through collaboration with Prof. Jinkui Tang at the Changchun Institute of Applied Chemistry, Chinese Academy of Sciences (China).

Magnetic measurements were recorded on a Quantum Design MPMS-XL7 SQUID magnetometer equipped with a 7 T magnet. The samples were restrained in eicosane and sealed in 7 mm NMR tubes. Direct current (DC) magnetic susceptibility measurements were performed on polycrystalline samples of **2** (26.2 mg), **4** (31.3 mg), **13** (10.7 mg), **15** (25.0 mg), **17** (32.3 mg), **26** (16.0 mg), **27** (30.5 mg) and **28** (31.3 mg) in the temperature range 1.9-300 K and using an applied field of 1000 Oe. AC susceptibility measurements were performed using an AC field of 3 Oe in zero DC field. Diamagnetic corrections were made using Pascal's constants for all the constituent atoms.[173]

Table S10. Relaxation fitting parameters for **2** corresponding to Figures 36-38.

T / K	χ_T / cm^3 mol^{-1}	χ_S / cm^3 mol^{-1}	α	τ / s
1.9	7.36689	0.34538	0.32326	0.01877
2.2	6.45672	0.31276	0.31886	0.01794
2.5	5.65353	0.28187	0.31768	0.01750
3	4.73890	0.24499	0.31515	0.01676
3.5	4.09566	0.21952	0.31237	0.01612
4	3.56705	0.20203	0.30537	0.01506
4.5	3.17736	0.19202	0.29468	0.01399
5	2.84501	0.18341	0.28213	0.01275
6	2.34305	0.17437	0.24369	0.00992
7	1.99197	0.16595	0.20298	0.00733
8	1.72829	0.15325	0.17087	0.00525
9	1.52925	0.14136	0.14760	0.00377
10	1.37234	0.12867	0.13248	0.00272
11	1.24542	0.12021	0.12040	0.00198
12	1.14565	0.11034	0.11673	0.00146
13	1.05712	0.10581	0.11078	0.00108
14	0.98129	0.10580	0.10617	0.00079
15	0.91979	0.10542	0.10153	0.00058
16	0.86183	0.10869	0.09490	0.00041
17	0.81112	0.11197	0.08478	0.00028
18	0.76559	0.12597	0.06629	0.00018
19	0.72494	0.11510	0.06077	0.00011
20	0.68835	0.14835	0.03836	0.00007

Table S11. Relaxation fitting parameters for **4** corresponding to Figures 44-46.

T / K	χ_T / cm^3 mol^{-1}	χ_S / cm^3 mol^{-1}	α	τ / s
1.9	5.73836	0.37113	0.15813	0.00226
2.2	5.04956	0.34590	0.15607	0.00225
2.5	4.44454	0.31657	0.15898	0.00225
3	3.74037	0.28107	0.16223	0.00222
3.5	3.22921	0.25321	0.16596	0.00219
4	2.84105	0.23266	0.16716	0.00215
4.5	2.53934	0.21541	0.16964	0.00210
5	2.30754	0.20270	0.16948	0.00205
6	1.93229	0.18169	0.16951	0.00195
7	1.66963	0.16371	0.17125	0.00186
8	1.45832	0.15268	0.16410	0.00175
9	1.29886	0.14547	0.15551	0.00164
10	1.16984	0.13935	0.14247	0.00151
11	1.06361	0.13290	0.13081	0.00136
12	0.97774	0.12726	0.11543	0.00122
13	0.90272	0.12021	0.10139	0.00107
14	0.83770	0.11567	0.08558	0.00093
15	0.78419	0.10940	0.07458	0.00080
16	0.73522	0.10237	0.06286	0.00067
17	0.69220	0.09738	0.05191	0.00055
18	0.65339	0.09048	0.04297	0.00042
19	0.61968	0.08337	0.03881	0.00031
20	0.58797	0.07135	0.03470	0.00020
21	0.56066	0.06780	0.03494	0.00013
22	0.53530	0.00832	0.06051	0.00006

Table S12. Relaxation fitting parameters for **13** corresponding to Figures 65, 67 and 68.

T / K	χ_T / cm^3 mol^{-1}	χ_S / cm^3 mol^{-1}	α	τ / s
1.9	7.26107	0.30207	0.30902	0.04387
2.2	6.28936	0.28112	0.31106	0.04273
2.5	5.46138	0.26881	0.30823	0.04176
3	4.54540	0.24193	0.30922	0.04079
3.5	3.86001	0.22912	0.30120	0.03935
4	3.38374	0.21128	0.30242	0.03858
4.5	2.99540	0.19885	0.29871	0.03730
5	2.70321	0.18636	0.29758	0.03642
6	2.24430	0.16756	0.29045	0.03389
7	1.91107	0.15156	0.28065	0.03093
8	1.63086	0.14472	0.24378	0.02664
9	1.44204	0.13431	0.22530	0.02272
10	1.27504	0.12817	0.19294	0.01860
11	1.14273	0.12060	0.16115	0.01490
12	1.04326	0.11270	0.13948	0.01195
13	0.94965	0.10814	0.10768	0.00953
14	0.87670	0.09710	0.09263	0.00763
15	0.82133	0.09625	0.08406	0.00622
16	0.76860	0.08614	0.08007	0.00498
17	0.72313	0.08439	0.06938	0.00413
18	0.68347	0.07701	0.07311	0.00338
19	0.64816	0.07357	0.06645	0.00281
20	0.61420	0.06792	0.06227	0.00233
21	0.58512	0.06562	0.05725	0.00197
22	0.55834	0.06514	0.05112	0.00166

23	0.53367	0.06161	0.04547	0.00138
24	0.51195	0.06046	0.04628	0.00112
25	0.49122	0.04848	0.04364	0.00091
26	0.47217	0.05363	0.02951	0.00073
27	0.45525	0.04989	0.02915	0.00056
28	0.43907	0.04520	0.02798	0.00041
29	0.42342	0.04283	0.02039	0.00030
30	0.40998	0.05437	0.00664	0.00022
31	0.39692	0.04448	0.01247	0.00015
32	0.38435	0.04132	0.00000	0.00011
33	0.37303	0.06053	0.00000	0.00008
34	0.36239	0.00000	0.00000	0.00005
35	0.35179	0.00000	0.00000	0.00003
36	0.34198	0.00000	0.00000	0.00002
37	0.33352	0.00000	0.00000	0.00001
38	0.32470	0.00000	0.00000	0.00001
39	0.31767	0.00000	0.00000	0.00001

Table S13. Relaxation fitting parameters for **15** corresponding to Figures 66, 69 and 70.

T / K	χ_T / cm^3 mol^{-1}	χ_S / cm^3 mol^{-1}	α	τ / s
1.9	9.16763	0.23175	0.41935	0.34616
2.2	8.02566	0.21819	0.42749	0.35221
2.5	6.88190	0.21616	0.42426	0.32825
3	5.63352	0.20883	0.42033	0.30172
3.5	4.74741	0.19856	0.41710	0.28003
4	4.08750	0.19029	0.41219	0.25859
4.5	3.57429	0.18282	0.40629	0.23816
5	3.17964	0.17446	0.40118	0.22052
6	2.57348	0.16168	0.38569	0.18544
7	2.13048	0.15128	0.36297	0.15016
8	1.79036	0.14424	0.33126	0.11732
9	1.52737	0.13706	0.29587	0.09038
10	1.32470	0.13219	0.25739	0.07017
11	1.17338	0.12454	0.22739	0.05588
12	1.05268	0.11851	0.19519	0.04495
13	0.95419	0.11373	0.16640	0.03678
14	0.87678	0.10679	0.14661	0.03050
15	0.81485	0.10115	0.13058	0.02581
16	0.75810	0.09794	0.11204	0.02187
17	0.71025	0.09249	0.10013	0.01860
18	0.66882	0.08790	0.09101	0.01596
19	0.63263	0.08423	0.08190	0.01380
20	0.59962	0.08189	0.07281	0.01196
21	0.57124	0.07836	0.06501	0.01044
22	0.54425	0.07444	0.06003	0.00905

23	0.52016	0.07212	0.05368	0.00790
24	0.49829	0.06855	0.05036	0.00675
25	0.47781	0.06690	0.04365	0.00586
26	0.45908	0.06390	0.04007	0.00491
27	0.44246	0.06168	0.03818	0.00408
28	0.42587	0.06020	0.02893	0.00330
29	0.41080	0.05851	0.02385	0.00258
30	0.39801	0.05795	0.02209	0.00196
31	0.38537	0.05425	0.01791	0.00143
32	0.37351	0.05301	0.01946	0.00101
33	0.36186	0.05148	0.01138	0.00070
34	0.35180	0.04949	0.01040	0.00048
35	0.34218	0.04722	0.01327	0.00033
36	0.33288	0.04845	0.00706	0.00023
37	0.32462	0.03663	0.01892	0.00015
38	0.31620	0.05470	0.00286	0.00011
39	0.30864	0.04725	0.00554	0.00008

Table S14. Relaxation fitting parameters for **17** corresponding to Figures 80-82.

T / K	χ_T / cm^3 mol^{-1}	χ_S / cm^3 mol^{-1}	α	τ / s
1.9	5.47211	0.52802	0.14080	0.00068
2.2	4.80445	0.48006	0.13653	0.00068
2.5	4.22096	0.42279	0.13733	0.00069
3	3.54433	0.35903	0.13805	0.00069
3.5	3.06311	0.30669	0.14256	0.00069
4	2.69660	0.28208	0.13734	0.00069
4.5	2.40809	0.25481	0.14114	0.00069
5	2.16783	0.22857	0.14000	0.00068
6	1.81518	0.19649	0.13851	0.00067
7	1.56842	0.17133	0.13707	0.00064
9	1.22491	0.14995	0.11434	0.00057
11	1.00360	0.12475	0.08860	0.00045
13	0.85289	0.10589	0.06582	0.00034
15	0.74324	0.08762	0.04871	0.00025
17	0.65584	0.07131	0.03542	0.00019
19	0.58786	0.05972	0.02689	0.00014
21	0.53228	0.05706	0.01755	0.00011
23	0.48693	0.04984	0.01889	0.00009

Table S15. Relaxation fitting parameters for **26** corresponding to Figures 103-105.

T / K	χ_T / cm^3 mol^{-1}	χ_S / cm^3 mol^{-1}	α	τ / s
1.9	5.87479	0.37708	0.21770	0.00112
2.2	5.13241	0.35678	0.21102	0.00109
2.5	4.50309	0.32720	0.21135	0.00108
3	3.77442	0.28369	0.21171	0.00105
3.5	3.24832	0.26947	0.20846	0.00103
4	2.85615	0.25430	0.20495	0.00101
4.5	2.55000	0.22802	0.20672	0.00098
5	2.30379	0.22646	0.20170	0.00097
6	1.93099	0.19881	0.19878	0.00092
7	1.66217	0.18871	0.19081	0.00088
9	1.30290	0.15816	0.18161	0.00077
11	1.06990	0.13662	0.16689	0.00066
13	0.91093	0.13079	0.15348	0.00056
15	0.79619	0.11639	0.14302	0.00046
17	0.70214	0.11228	0.12881	0.00039
19	0.62967	0.10196	0.12501	0.00032
21	0.56957	0.09720	0.10859	0.00027
23	0.52052	0.09143	0.09930	0.00022
25	0.48092	0.08862	0.09847	0.00018
27	0.44692	0.08875	0.09372	0.00016
29	0.41671	0.07336	0.11116	0.00012
31	0.39144	0.06707	0.10905	0.00010

Table S16. Relaxation fitting parameters for **27** corresponding to Figures 118, 120 and 121.

T / K	χ_T / cm^3 mol^{-1}	χ_S / cm^3 mol^{-1}	α	τ / s
1.9	7.21172	0.10109	0.35247	0.11077
2.2	6.28422	0.10505	0.35128	0.10593
2.5	5.47238	0.11096	0.34708	0.10054
3	4.53654	0.11571	0.33962	0.09267
3.5	3.86217	0.11508	0.33206	0.08564
4	3.36595	0.11359	0.32510	0.08006
4.5	2.97852	0.11146	0.31796	0.07507
5	2.67465	0.10873	0.31182	0.07094
6	2.21822	0.10190	0.30177	0.06410
7	1.89151	0.09485	0.29212	0.05861
9	1.46392	0.08412	0.27744	0.05028
11	1.18624	0.07648	0.25698	0.04320
13	0.99793	0.07115	0.23653	0.03706
15	0.86174	0.06697	0.21653	0.03185
17	0.75416	0.06077	0.19875	0.02708
19	0.66872	0.05886	0.17333	0.02295
21	0.60055	0.05563	0.15062	0.01923
23	0.54490	0.05193	0.12930	0.01577
25	0.49850	0.04865	0.10946	0.01259
27	0.45821	0.04643	0.08886	0.00953
29	0.42660	0.04300	0.08204	0.00691
31	0.39789	0.04127	0.06665	0.00494
33	0.37348	0.03993	0.05887	0.00337
35	0.35275	0.03723	0.06163	0.00234
37	0.33505	0.03293	0.06886	0.00160

39	0.31818	0.03225	0.06322	0.00112
41	0.30222	0.03314	0.05881	0.00080
43	0.28984	0.03260	0.06114	0.00058
45	0.27777	0.03094	0.06818	0.00042
47	0.26516	0.02710	0.06614	0.00030
49	0.25523	0.02994	0.06019	0.00024
51	0.24575	0.02446	0.07296	0.00017
53	0.23636	0.03865	0.03343	0.00015
55	0.22971	0.03373	0.06338	0.00011

Table S17. Relaxation fitting parameters for **28** corresponding to Figures 119, 122 and 123.

T / K	χ_T / cm^3 mol^{-1}	χ_S / cm^3 mol^{-1}	α	τ / s
2	6.53947	0.05827	0.26765	0.07548
3	4.29565	0.06177	0.24091	0.05967
4	3.18636	0.05897	0.22348	0.04989
5	2.54420	0.05341	0.21362	0.04393
6	2.10828	0.04978	0.20870	0.03949
7	1.78101	0.04648	0.20479	0.03543
8	1.56988	0.04271	0.19788	0.03345
9	1.39377	0.04069	0.19528	0.03116
10	1.25477	0.03680	0.19542	0.02923
11	1.14068	0.03549	0.19443	0.02745
12	1.04791	0.03284	0.18873	0.02588
13	0.96607	0.03420	0.18356	0.02446
14	0.89700	0.03142	0.17978	0.02312
15	0.83941	0.03096	0.17646	0.02187
16	0.78752	0.03147	0.17146	0.02064
17	0.73830	0.02926	0.16309	0.01933
18	0.69689	0.02885	0.15973	0.01808
19	0.66125	0.02729	0.15765	0.01685
20	0.62763	0.02669	0.14985	0.01576
21	0.59715	0.02622	0.14262	0.01457
22	0.57017	0.02665	0.13455	0.01345
23	0.54218	0.02471	0.12494	0.01218
24	0.51865	0.02416	0.11668	0.01099
25	0.49744	0.02568	0.10737	0.00983
26	0.47559	0.02486	0.08789	0.00897

27	0.45835	0.02562	0.08825	0.00765
28	0.44086	0.02497	0.07794	0.00655
29	0.42657	0.02306	0.07816	0.00563
30	0.41177	0.02134	0.07343	0.00469
31	0.38278	0.02250	0.04052	0.00380
32	0.38683	0.02191	0.06632	0.00332
33	0.37514	0.01846	0.07440	0.00272
34	0.36432	0.02179	0.06728	0.00227
35	0.35456	0.01734	0.06664	0.00187
36	0.34410	0.01856	0.06391	0.00155
37	0.33495	0.01823	0.06148	0.00128
38	0.32615	0.01769	0.06936	0.00107
39	0.31849	0.01954	0.06042	0.00089
40	0.31074	0.01217	0.07704	0.00072
41	0.30351	0.01122	0.07154	0.00061
42	0.29628	0.01813	0.05742	0.00053
43	0.28999	0.02495	0.04029	0.00046
44	0.28374	0.01421	0.06627	0.00037
45	0.27931	0.01645	0.06539	0.00032
46	0.27213	0.01650	0.07120	0.00027
47	0.26692	0.02029	0.05918	0.00025
48	0.26041	0.02214	0.03862	0.00021
49	0.25647	0.01292	0.07252	0.00018
50	0.25068	0.00000	0.06540	0.00014
51	0.24295	0.00000	0.05159	0.00013
52	0.24167	0.00000	0.07388	0.00011
53	0.23828	0.00000	0.10205	0.00010

54	0.23259	0.00000	0.06764	0.00009
55	0.22973	0.00000	0.08804	0.00008

6.7. Theoretical calculations supplementary information

All of the calculations presented in this thesis were conducted, and the results analysed, through collaboration with Dr Akseli Mansikkamäki at the University of Oulu (Finland).

The geometries used in the calculations were extracted from the respective crystal structures. Non-coordinated counterions were removed from the structures. The positions of hydrogen atoms were optimized using density functional theory (DFT), while the positions of heavier atoms were frozen to their crystal-structure coordinates. The DFT calculations were carried out using the *ADF* 2019 code.[174,175] The pure PBE exchange-correlation functional[176] was used along with the empirical DFT-D3 dispersion correction[176] utilizing the Becke–Johnson damping function.[176] Scalar relativistic effects were treated using the zeroth-order regular approximation (ZORA) as implemented in *ADF*.[177–179] Valence-triple-ζ-quality Slater-type basis sets with two sets of polarization functions (TZ2P), specifically designed for ZORA calculations, were used for all atoms in the geometry optimizations.[180] Static electron correlation effects at the Dy ion were simulated by averaging the orbital occupations of the nine 4*f* electrons over the seven 4*f* orbitals. In practice this means that the occupations of the seven highest β orbitals were set to 0.285714, while the occupations of other orbitals were kept as integers. The "NumericalQuality" keyword in *ADF* was set to "Good" and the geometry convergence thresholds were increased to 10^{-4}, 10^{-4}, 10^{-3} and 10^{-1} atomic units for energy, energy gradient, bond length and bond angle, respectively.

The multireference calculations were carried out using the *OpenMolcas* 19.11 quantum chemistry code.[180] State-averaged complete active space self-consistent field (SA-CASSCF) calculations were first carried out.[181,182] The active space consisted of the nine 4*f* electrons in the seven 4*f* orbitals. All 21 sextet, 224 quartet and 490 doublet states were solved in three separate SA calculations. Spin-orbit coupling (SOC) was then taken into account using the spin-orbit restricted active space state interaction (SO-RASSI) methodology.[183] 21 sextet, 128 quartet and 130 doublet states, corresponding to an energy cut-off of 50,000

cm^{-1}, were included in the SO-RASSI treatment. The SOC operator was constructed using the atomic mean-field integral (AMFI) formalism[184,185] in the basis of the SA-CASSCF eigenstates and diagonalized to yield the final spin-orbit coupled eigenstates. The static magnetic properties (**g**-tensors, *ab initio* crystal-field parameters and transition magnetic moments) were calculated using the SINGLE_ANISO_OPEN module in OpenMolcas.[54,186,187] Scalar relativistic effects were treated using the scalar exact two-component (X2C) transformation.[188] Roos' relativistically contracted atomic natural orbital (ANO-RCC) basis sets were used throughout.[189–191] The Dy ions were treated using a VQZP basis. The H, B and C atoms in the conjugated skeletons of the Cb, Cp and Pn ligands and the coordinated $[BH_4]^-$ anions were treated using VTZP basis sets. The Si atoms were treated using a VTZP basis sets, whereas the C and H atoms in the substituent groups were treated using VDZP and VDZ basis sets, respectively. The K atom was treated using a VDZP basis set, whereas the remaining atoms were treated using a minimal basis. Cholesky decomposition with a threshold of 10^{-8} atomic units was used in storage of the two-electron integrals.

Table S18. Energies and principal components of the **g**-tensors of the eight lowest Kramers' doublets (KD) of the ground $^6H_{15/2}$ multiplet of **15**.

	E / cm^{-1}	g_x	g_y	g_z	θ [a]
KD1	0	0.000926	0.001305	19.834476	0.0°
KD2	242	0.093017	0.117100	17.079967	169.5°
KD3	326	0.534145	0.561381	14.226165	167.1°
KD4	383	0.008395	0.950690	11.947312	10.7°
KD5	455	2.296561	3.068187	9.469676	21.2°
KD6	540	3.441120	5.710016	9.389138	92.0°
KD7	657	8.141186	5.698843	2.441712	7.3°
KD8	701	11.595478	9.230990	1.146477	1.9°

[a] The angle between the principal magnetic axis of the given doublet and the that of the ground doublet.

Table S19. Magnitudes of transition magnetic moment matrix elements (in Bohr magneton) calculated for **15**.

Initial KD	Final KD	Climbing transition	Crossing transition
1	1	3.3057	0.0004
2	2	3.5341	0.0353
3	3	3.0179	0.1849
4	4	2.3354	0.2106
5	5	2.2264	0.9224
6	6	1.3073	2.4009
7	7	0.8998	2.2470
8	8	1.0008	3.3929
1	2	1.7216	0.0029
2	3	2.4080	0.0543
3	4	2.9182	0.1920
4	5	3.0462	0.2086
5	6	3.0339	0.7972
6	7	2.5446	0.6687
7	8	3.3316	0.5610
1	3	0.4082	0.0209
2	4	0.3287	0.0691
3	5	0.6150	0.1352
4	6	0.6450	0.3560
5	7	0.3770	0.8656
6	8	0.1642	0.9943
1	4	0.3391	0.0108
2	5	0.5794	0.0316
3	6	0.3279	0.1476
4	7	0.2120	0.3394

5	8	0.4243	0.2449
1	5	0.0976	0.0205
2	6	0.1422	0.1586
3	7	0.1696	0.1361
4	8	0.1204	0.2931
1	6	0.0770	0.0178
2	7	0.1703	0.0336
3	8	0.2768	0.1614
1	7	0.0288	0.0218
2	8	0.1531	0.0589
1	8	0.0268	0.0155

Table S20. *Ab initio* crystal-field parameters B_k^q (in cm^{-1}) calculated for **15** listed in the Iwahara–Chibotaru notation.[192,193]

k	*q*	Re(B_k^q)	Im(B_k^q)	$\lvert B_k^q \rvert$
2	0	–376.668572	0.000000	376.668572
2	1	10.148887	–10.972468	14.946403
2	2	13.212098	–14.032149	19.273316
4	0	3.365113	0.000000	3.365113
4	1	–0.019546	–0.269856	0.270563
4	2	–6.425327	11.427467	13.109989
4	3	–2.604809	29.215574	29.331464
4	4	4.118578	28.888473	29.180585
6	0	–36.637984	0.000000	36.637984
6	1	–4.670457	4.211427	6.288822
6	2	–8.180194	8.934668	12.113788
6	3	0.819490	–4.643460	4.715218

6	4	0.473932	–6.374391	6.391985
6	5	–11.019572	–9.660280	14.654419
6	6	10.504192	1.653741	10.633575
8	0	0.373640	0.000000	0.373640
8	1	0.068580	–0.038346	0.078572
8	2	0.151947	–0.131781	0.201132
8	3	0.002206	0.113874	0.113895
8	4	0.012709	0.195364	0.195777
8	5	0.111084	0.107703	0.154724
8	6	–0.048048	–0.004215	0.048232
8	7	0.011732	–0.004243	0.012476
8	8	0.023321	–0.026911	0.035610
10	0	0.008366	0.000000	0.008366
10	1	0.001941	0.000249	0.001957
10	2	–0.004284	–0.002800	0.005118
10	3	–0.005126	–0.015152	0.015995
10	4	–0.004848	–0.009302	0.010489
10	5	0.007978	0.007734	0.011112
10	6	0.001320	0.000509	0.001415
10	7	0.011056	0.000711	0.011079
10	8	0.007886	–0.004500	0.009080
10	9	0.006036	–0.005363	0.008075
10	10	–0.000211	0.006376	0.006379
12	0	0.004428	0.000000	0.004428
12	1	–0.000190	–0.000996	0.001014
12	2	0.002124	–0.002837	0.003544
12	3	0.000258	0.001064	0.001095

12	4	–0.000019	–0.000104	0.000106
12	5	0.001232	0.000743	0.001439
12	6	–0.000836	0.000099	0.000842
12	7	–0.000100	–0.000135	0.000168
12	8	–0.000231	0.000083	0.000245
12	9	–0.000283	0.000262	0.000386
12	10	0.000107	0.000396	0.000410
12	11	–0.000424	–0.000492	0.000650
12	12	0.000354	0.000118	0.000374
14	0	–0.000004	0.000000	0.000004
14	1	–0.000007	0.000008	0.000011
14	2	–0.000011	0.000015	0.000019
14	3	0.000003	–0.000002	0.000004
14	4	0.000001	0.000001	0.000001
14	5	0.000001	0.000001	0.000002
14	6	–0.000001	0.000000	0.000001
14	7	0.000003	–0.000001	0.000003
14	8	0.000000	0.000000	0.000001
14	9	0.000000	0.000001	0.000001
14	10	–0.000001	–0.000002	0.000002
14	11	0.000001	0.000002	0.000003
14	12	0.000000	0.000000	0.000000
14	13	0.000001	0.000000	0.000001
14	14	0.000001	0.000000	0.000001

[a] The CF parameters are only listed for positive values of q. The values with negative q are given by $B_{k-q} = (-1)^q B_{kq}^*$.

Table S21. Squared magnitudes of the projections of the *ab initio* CF eigenstates calculated for **15** onto angular momentum eigenstates characterized by a total angular momentum J = 15/2 and an angular momentum projection M.

M	KD1		KD2		KD3		KD4		KD5		KD6		KD7		KD8	
–15/2	**0.847**	**0.144**	0.000	0.000	0.001	0.004	0.003	0.000	0.000	0.000	0.000	0.000	0.000	0.000	0.000	0.000
–13/2	0.000	0.000	**0.004**	**0.922**	0.011	0.049	0.002	0.000	0.004	0.004	0.001	0.001	0.000	0.002	0.000	0.000
–11/2	0.007	0.001	0.000	0.050	**0.141**	**0.600**	0.145	0.006	0.018	0.010	0.005	0.011	0.002	0.000	0.002	0.002
–9/2	0.000	0.000	0.000	0.007	0.025	0.124	**0.678**	**0.059**	0.031	0.030	0.013	0.006	0.005	0.017	0.003	0.001
–7/2	0.000	0.000	0.000	0.011	0.000	0.004	0.064	0.009	**0.445**	**0.402**	0.016	0.004	0.003	0.011	0.015	0.017
–5/2	0.000	0.000	0.000	0.001	0.005	0.022	0.002	0.000	0.021	0.010	**0.307**	**0.491**	0.092	0.020	0.017	0.011
–3/2	0.000	0.000	0.000	0.004	0.001	0.001	0.023	0.002	0.003	0.003	0.075	0.055	**0.114**	**0.702**	0.014	0.005
–1/2	0.000	0.000	0.000	0.002	0.008	0.005	0.001	0.005	0.008	0.011	0.004	0.010	0.000	0.032	**0.336**	**0.578**
1/2	0.000	0.000	0.002	0.000	0.005	0.008	0.005	0.001	0.011	0.008	0.010	0.004	0.032	0.000	**0.578**	**0.336**
3/2	0.000	0.000	0.004	0.000	0.001	0.001	0.002	0.023	0.003	0.003	0.055	0.075	**0.702**	**0.114**	0.005	0.014
5/2	0.000	0.000	0.001	0.000	0.022	0.005	0.000	0.002	0.010	0.021	**0.491**	**0.307**	0.020	0.092	0.011	0.017
7/2	0.000	0.000	0.011	0.000	0.004	0.000	0.009	0.064	**0.402**	**0.445**	0.004	0.016	0.011	0.003	0.017	0.015
9/2	0.000	0.000	0.007	0.000	0.124	0.025	**0.059**	**0.678**	0.030	0.031	0.006	0.013	0.017	0.005	0.001	0.003
11/2	0.001	0.007	0.050	0.000	**0.600**	**0.141**	0.006	0.145	0.010	0.018	0.011	0.005	0.000	0.002	0.002	0.002
13/2	0.000	0.000	**0.922**	**0.004**	0.049	0.011	0.000	0.002	0.004	0.004	0.001	0.001	0.002	0.000	0.000	0.000
15/2	**0.144**	**0.847**	0.000	0.000	0.004	0.001	0.000	0.003	0.000	0.000	0.000	0.000	0.000	0.000	0.000	0.000

Table S22. Energies and principal components of the **g**-tensors of the eight lowest Kramers' doublets (KD) of the ground $^6H_{15/2}$ multiplet of **26**.

	E / cm^{-1}	g_x	g_y	g_z	θ [a]
KD1	0	0.00892	0.01548	19.62434	0.0°
KD2	242	0.23432	0.37985	16.30245	8.4°
KD3	386	1.69921	1.91848	13.37681	36.9°
KD4	486	2.64726	4.99014	8.97824	30.8°
KD5	580	3.73311	4.59844	9.54713	88.4°
KD6	675	1.14778	1.51743	13.79530	89.8°
KD7	821	0.07935	0.11918	17.03248	90.1°
KD8	1142	0.00149	0.00240	19.78590	90.0°

[a] The angle between the principal magnetic axis of the given doublet and the that of the ground doublet.

Table S23. Magnitudes of transition magnetic moment matrix elements (in Bohr magneton) calculated for **26**.

Initial KD	Final KD	Climbing transition	Crossing transition
1	1	3.270723	0.004067
1	2	1.816594	0.015690
1	3	0.439783	0.044220
1	4	0.112066	0.028040
1	5	0.069273	0.031111
1	6	0.031182	0.052896
1	7	0.024782	0.019968
1	8	0.006085	0.006893
2	2	3.112271	0.103044
2	3	2.513508	0.235163
2	4	1.142419	0.203697
2	5	0.146728	0.155801
2	6	0.061691	0.047503
2	7	0.054300	0.050329
2	8	0.017630	0.022692
3	3	3.117397	0.680722
3	4	3.108069	0.779783
3	5	0.820663	0.326853
3	6	0.117437	0.190814
3	7	0.063101	0.020960
3	8	0.027766	0.028347
4	4	2.001637	1.338568
4	5	3.034389	1.247653
4	6	0.364887	0.544258
4	7	0.129622	0.110907

4	8	0.018501	0.026233
5	5	0.907703	2.224675
5	6	2.384944	1.347259
5	7	0.178099	0.339365
5	8	0.083089	0.083618
6	6	0.336503	2.542494
6	7	1.696840	1.262215
6	8	0.090388	0.098003
7	7	0.598727	2.865092
7	8	1.082637	1.308627
8	8	3.328911	0.433699

Table S24. *Ab initio* crystal-field parameters B_k^q (in cm^{-1}) calculated for **26** listed in the Iwahara–Chibotaru notation.[192,193]

k	*q*	Re(B_k^q)	Im(B_k^q)	$\lvert B_k^q \rvert$
2	0	−488.628052	0.000000	488.628052
2	1	−1.770343	−26.114585	26.174523
2	2	248.968094	−8.533045	249.114281
4	0	−18.877515	−0.000000	18.877515
4	1	0.974853	17.193406	17.221020
4	2	−9.848078	−0.884634	9.887730
4	3	2.788306	9.903302	10.288345
4	4	10.711146	−4.144374	11.484968
6	0	−15.420268	−0.000000	15.420268
6	1	0.873194	−1.712827	1.922562
6	2	20.605365	0.991802	20.629220
6	3	1.668957	−9.564200	9.708725

6	4	−7.108821	−0.216820	7.112127
6	5	0.400810	−3.513403	3.536191
6	6	9.189532	−0.112310	9.190219
8	0	0.771366	0.000000	0.771366
8	1	−0.038032	−0.183194	0.187100
8	2	−0.773408	−0.012016	0.773501
8	3	−0.052150	0.318554	0.322794
8	4	−0.003933	−0.009346	0.010140
8	5	−0.007086	0.021004	0.022167
8	6	−0.067805	0.004848	0.067979
8	7	0.003012	−0.019040	0.019277
8	8	0.037793	−0.004706	0.038085
10	0	0.001493	−0.000000	0.001493
10	1	−0.000290	0.023759	0.023761
10	2	−0.000019	−0.000693	0.000693
10	3	−0.002309	0.004601	0.005148
10	4	0.002866	0.001061	0.003057
10	5	−0.001251	0.008620	0.008710
10	6	−0.002040	−0.000177	0.002048
10	7	−0.000152	−0.006268	0.006270
10	8	0.005415	0.000487	0.005437
10	9	0.000632	−0.001791	0.001900
10	10	0.001658	−0.001210	0.002053
12	0	0.004163	0.000000	0.004163
12	1	−0.000266	−0.001727	0.001748
12	2	−0.002904	0.000020	0.002904
12	3	−0.000035	0.000795	0.000795

12	4	0.001609	0.000088	0.001611
12	5	0.000199	−0.000832	0.000855
12	6	−0.000495	−0.000045	0.000497
12	7	−0.000050	0.000243	0.000248
12	8	−0.000151	−0.000031	0.000154
12	9	−0.000016	0.000098	0.000100
12	10	−0.000263	−0.000008	0.000263
12	11	0.000006	−0.000109	0.000109
12	12	0.000275	−0.000008	0.000275
14	0	−0.000022	−0.000000	0.000022
14	1	0.000001	0.000000	0.000001
14	2	0.000016	−0.000001	0.000016
14	3	0.000002	0.000002	0.000002
14	4	−0.000008	−0.000001	0.000008
14	5	−0.000001	−0.000001	0.000001
14	6	0.000005	0.000000	0.000005
14	7	0.000000	0.000001	0.000001
14	8	−0.000000	−0.000000	0.000000
14	9	−0.000000	0.000000	0.000000
14	10	0.000001	0.000000	0.000001
14	11	−0.000000	0.000000	0.000000
14	12	−0.000000	−0.000000	0.000000
14	13	0.000000	−0.000000	0.000000
14	14	0.000000	0.000000	0.000000

[a] The CF parameters are only listed for positive values of q. The values with negative q are given by $B_{k-q} = (-1)^q B_{kq}^*$.

Table S25. Squared magnitudes of the projections of the *ab initio* CF eigenstates calculated for **26** onto angular momentum eigenstates characterized by a total angular momentum J = 15/2 and an angular momentum projection M.

M	KD1		KD2		KD3		KD4		KD5		KD6		KD7		KD8	
–15/2	0.109	0.846	0.000	0.001	0.006	0.022	0.001	0.013	0.000	0.001	0.000	0.001	0.000	0.000	0.000	0.000
–13/2	0.000	0.000	0.002	0.843	0.003	0.063	0.011	0.025	0.043	0.001	0.007	0.000	0.001	0.001	0.000	0.000
–11/2	0.005	0.038	0.000	0.009	0.086	0.344	0.033	0.343	0.008	0.061	0.002	0.057	0.006	0.007	0.001	0.001
–9/2	0.000	0.000	0.000	0.116	0.002	0.043	0.041	0.106	0.432	0.011	0.166	0.005	0.038	0.030	0.008	0.003
–7/2	0.000	0.002	0.000	0.005	0.046	0.167	0.002	0.000	0.039	0.085	0.020	0.369	0.097	0.118	0.012	0.038
–5/2	0.000	0.000	0.000	0.016	0.000	0.064	0.055	0.140	0.025	0.005	0.137	0.027	0.216	0.161	0.114	0.040
–3/2	0.000	0.000	0.001	0.003	0.038	0.053	0.037	0.047	0.074	0.130	0.002	0.011	0.110	0.172	0.087	0.235
–1/2	0.000	0.000	0.001	0.004	0.012	0.051	0.057	0.086	0.042	0.045	0.166	0.029	0.028	0.016	0.336	0.127
1/2	0.000	0.000	0.004	0.001	0.051	0.012	0.086	0.057	0.045	0.042	0.029	0.166	0.016	0.028	0.127	0.336
3/2	0.000	0.000	0.003	0.001	0.053	0.038	0.047	0.037	0.130	0.074	0.011	0.002	0.172	0.110	0.235	0.087
5/2	0.000	0.000	0.016	0.000	0.064	0.000	0.140	0.055	0.005	0.025	0.027	0.137	0.161	0.216	0.040	0.114
7/2	0.002	0.000	0.005	0.000	0.167	0.046	0.000	0.002	0.085	0.039	0.369	0.020	0.118	0.097	0.038	0.012
9/2	0.000	0.000	0.116	0.000	0.043	0.002	0.106	0.041	0.011	0.432	0.005	0.166	0.030	0.038	0.003	0.008
11/2	0.038	0.005	0.009	0.000	0.344	0.086	0.343	0.033	0.061	0.008	0.057	0.002	0.007	0.006	0.001	0.001
13/2	0.000	0.000	0.843	0.002	0.063	0.003	0.025	0.011	0.001	0.043	0.000	0.007	0.001	0.001	0.000	0.000
15/2	0.846	0.109	0.001	0.000	0.022	0.006	0.013	0.001	0.001	0.000	0.001	0.000	0.000	0.000	0.000	0.000

Table S26. Energies and principal components of the **g**-tensors of the eight lowest Kramers' doublets (KD) of the ground $^6H_{15/2}$ multiplet of **27**.

	E / cm^{-1}	g_x	g_y	g_z	θ [a]
KD1	0	0.00065	0.00095	19.65219	0.0°
KD2	236	0.00877	0.00958	16.82059	1.0°
KD3	447	0.06025	0.06905	14.36307	2.0°
KD4	602	0.42376	0.50981	11.66440	3.4°
KD5	719	2.41778	2.65534	8.29950	8.1°
KD6	800	3.60593	5.76957	10.08113	88.7°
KD7	892	0.48072	1.11393	15.79259	90.8°
KD8	1162	0.00285	0.00492	19.62304	89.9°

[a] The angle between the principal magnetic axis of the given doublet and the that of the ground doublet.

Table S27. Energies and principal components of the **g**-tensors of the eight lowest Kramers' doublets (KD) of the ground $^6H_{15/2}$ multiplet of **28**.

	E / cm^{-1}	g_x	g_y	g_z	θ [a]
KD1	0	0.00049	0.00072	19.69399	0.0°
KD2	228	0.00591	0.00597	16.95159	2.2°
KD3	434	0.03664	0.04400	14.50732	4.2°
KD4	593	0.21194	0.27	11.78959	2.8°
KD5	722	1.17392	1.42428	8.78852	6.6°
KD6	816	6.98066	6.02358	4.49167	16.0°
KD7	897	1.06355	2.90099	14.22865	92.4°
KD8	1100	0.01334	0.02608	19.35561	89.8°

[a] The angle between the principal magnetic axis of the given doublet and the that of the ground doublet.

Table S28. Magnitudes of transition magnetic moment matrix elements (in Bohr magneton) calculated for **27**.

Initial KD	Final KD	Climbing transition	Crossing transition
1	1	3.275365	0.000267
1	2	1.797116	0.000483
1	3	0.241095	0.000276
1	4	0.194111	0.000889
1	5	0.049208	0.007495
1	6	0.019410	0.008521
1	7	0.009726	0.008292
1	8	0.003668	0.002831
2	2	2.873634	0.003059
2	3	2.354716	0.003847
2	4	0.294039	0.001616

2	5	0.188009	0.005528
2	6	0.055897	0.040384
2	7	0.029922	0.032788
2	8	0.013183	0.011148
3	3	2.508224	0.021568
3	4	2.763925	0.023921
3	5	0.313509	0.057102
3	6	0.075179	0.015980
3	7	0.042545	0.049037
3	8	0.036371	0.028431
4	4	2.086771	0.155993
4	5	3.058253	0.135879
4	6	0.350908	0.357397
4	7	0.289936	0.222460
4	8	0.123805	0.092096
5	5	1.554916	0.849227
5	6	3.091049	0.414051
5	7	0.525459	1.048066
5	8	0.250642	0.221877
6	6	0.735296	2.729987
6	7	2.198322	1.044597
6	8	0.343576	0.305524
7	7	1.244040	2.703586
7	8	0.925055	1.429811
8	8	3.408605	0.280834

Table S29. Magnitudes of transition magnetic moment matrix elements (in Bohr magneton) calculated for **29**.

Initial KD	Final KD	Climbing transition	Crossing transition
1	1	3.282332	0.000202
1	2	1.784177	0.000376
1	3	0.278847	0.000301
1	4	0.246321	0.000789
1	5	0.073616	0.003553
1	6	0.011179	0.004669
1	7	0.004807	0.003969
1	8	0.001894	0.001925
2	2	2.976238	0.001981
2	3	2.345128	0.002679
2	4	0.315360	0.001868
2	5	0.234010	0.004523
2	6	0.096692	0.022154
2	7	0.025883	0.028724
2	8	0.012181	0.007446
3	3	2.609040	0.013461
3	4	2.781676	0.013885
3	5	0.236505	0.021645
3	6	0.069991	0.039196
3	7	0.081107	0.041371
3	8	0.046125	0.008263
4	4	2.092984	0.080474
4	5	3.097611	0.077712
4	6	0.329325	0.212422
4	7	0.235932	0.163263

4	8	0.141990	0.070857
5	5	1.654753	0.434816
5	6	3.193685	0.418440
5	7	0.414633	0.954147
5	8	0.335904	0.255383
6	6	0.980518	2.144649
6	7	2.707761	1.082968
6	8	0.446506	0.411842
7	7	1.460122	2.558953
7	8	0.946497	1.488574
8	8	3.279057	0.654074

Table S30. *Ab initio* crystal-field parameters B_k^q (in cm^{-1}) calculated for **27** listed in the Iwahara–Chibotaru notation.[192,193]

k	*q*	Re(B_k^q)	Im(B_k^q)	$\lvert B_k^q \rvert$
2	0	−598.848671	−0.000000	598.848671
2	1	6.099383	−2.065023	6.439471
2	2	157.784173	−4.200693	157.840080
4	0	20.038778	0.000000	20.038778
4	1	−0.027160	3.717197	3.717296
4	2	15.663675	0.018395	15.663686
4	3	−1.438030	0.066054	1.439546
4	4	17.226368	−11.056282	20.469224
6	0	−10.133563	0.000000	10.133563
6	1	−1.685848	−2.056558	2.659232
6	2	19.148669	0.389814	19.152637
6	3	1.237093	−0.171646	1.248944

6	4	−15.146470	4.364466	15.762745
6	5	−0.367230	−0.971369	1.038468
6	6	2.487988	0.286683	2.504451
8	0	0.491596	−0.000000	0.491596
8	1	0.074040	0.039969	0.084139
8	2	−0.702026	0.016362	0.702217
8	3	−0.008526	0.061605	0.062192
8	4	0.297566	−0.120664	0.321100
8	5	0.004751	0.013286	0.014109
8	6	−0.093150	0.016564	0.094611
8	7	−0.000960	−0.004616	0.004715
8	8	0.005773	−0.004927	0.007590
10	0	0.025381	0.000000	0.025381
10	1	−0.000739	0.000785	0.001078
10	2	0.002926	−0.000518	0.002972
10	3	0.000618	−0.002780	0.002848
10	4	0.001464	0.002493	0.002892
10	5	0.002070	0.001131	0.002359
10	6	−0.008608	0.002444	0.008949
10	7	0.000558	−0.001492	0.001593
10	8	−0.003962	0.006133	0.007301
10	9	−0.000558	−0.000504	0.000751
10	10	0.000771	−0.000574	0.000961
12	0	0.004190	−0.000000	0.004190
12	1	0.000812	−0.000517	0.000962
12	2	−0.002293	0.000365	0.002322
12	3	−0.000290	0.000285	0.000407

12	4	0.001333	−0.000161	0.001342
12	5	−0.000022	−0.000147	0.000148
12	6	−0.000393	0.000113	0.000409
12	7	−0.000061	0.000062	0.000087
12	8	0.000435	−0.000348	0.000557
12	9	0.000044	0.000059	0.000073
12	10	−0.000108	0.000029	0.000112
12	11	−0.000004	−0.000012	0.000012
12	12	0.000024	0.000005	0.000025
14	0	−0.000020	−0.000000	0.000020
14	1	−0.000005	0.000000	0.000005
14	2	0.000016	−0.000002	0.000016
14	3	0.000000	0.000001	0.000001
14	4	−0.000008	0.000001	0.000008
14	5	−0.000001	0.000000	0.000001
14	6	0.000005	−0.000002	0.000006
14	7	−0.000000	−0.000000	0.000000
14	8	−0.000000	0.000000	0.000001
14	9	0.000000	−0.000000	0.000000
14	10	−0.000000	0.000001	0.000001
14	11	0.000000	−0.000000	0.000000
14	12	−0.000000	0.000000	0.000001
14	13	−0.000000	−0.000000	0.000000
14	14	−0.000000	0.000000	0.000000

[a] The CF parameters are only listed for positive values of q. The values with negative q are given by $B_{k-q} = (-1)^q B_{kq}^*$.

Table S31. *Ab initio* crystal-field parameters B_k^q (in cm^{-1}) calculated for **28** listed in the Iwahara–Chibotaru notation.[192,193]

k	q	Re(B_k^q)	Im(B_k^q)	$\lvert B_k^q \rvert$
2	0	−602.759450	−0.000000	602.759450
2	1	−14.624570	1.786592	14.733295
2	2	115.142108	−6.743509	115.339412
4	0	28.003772	0.000000	28.003772
4	1	0.941639	2.197372	2.390634
4	2	15.883818	−1.183679	15.927862
4	3	2.194066	6.045896	6.431701
4	4	3.428588	−5.773983	6.715214
6	0	−8.845629	−0.000000	8.845629
6	1	2.966482	−2.714969	4.021327
6	2	19.575301	1.564558	19.637726
6	3	−5.022562	−1.624568	5.278764
6	4	−11.132759	1.112996	11.188257
6	5	−0.301582	−0.106896	0.319967
6	6	2.298968	0.083095	2.300469
8	0	0.380161	0.000000	0.380161
8	1	−0.114972	0.069175	0.134178
8	2	−0.668717	−0.030083	0.669393
8	3	0.123283	0.096387	0.156490
8	4	0.208807	−0.038502	0.212327
8	5	0.006196	−0.003587	0.007159
8	6	−0.068204	0.006675	0.068530
8	7	−0.002586	−0.004553	0.005236
8	8	−0.001971	−0.002936	0.003536

10	0	0.023100	−0.000000	0.023100
10	1	−0.001548	0.000033	0.001548
10	2	0.009260	−0.001715	0.009418
10	3	−0.005910	−0.001898	0.006207
10	4	0.000849	0.001104	0.001392
10	5	−0.002281	0.002566	0.003434
10	6	−0.006417	−0.000171	0.006419
10	7	−0.001652	−0.001906	0.002522
10	8	0.000176	0.001687	0.001696
10	9	−0.000312	0.000163	0.000352
10	10	−0.000235	−0.000399	0.000463
12	0	0.004158	0.000000	0.004158
12	1	−0.001702	−0.000906	0.001928
12	2	−0.001929	0.000382	0.001966
12	3	0.000785	0.000249	0.000823
12	4	0.001198	0.000030	0.001199
12	5	−0.000259	−0.000374	0.000454
12	6	−0.000226	0.000065	0.000235
12	7	0.000205	0.000076	0.000219
12	8	0.000230	−0.000067	0.000240
12	9	0.000012	−0.000001	0.000012
12	10	−0.000066	0.000007	0.000066
12	11	−0.000001	−0.000000	0.000001
12	12	0.000018	0.000001	0.000018
14	0	−0.000018	−0.000000	0.000018
14	1	0.000008	0.000001	0.000008
14	2	0.000013	−0.000000	0.000013

14	3	−0.000006	0.000001	0.000006
14	4	−0.000008	−0.000000	0.000008
14	5	0.000004	0.000001	0.000004
14	6	0.000003	−0.000001	0.000003
14	7	0.000000	−0.000000	0.000000
14	8	−0.000000	0.000000	0.000000
14	9	−0.000000	−0.000000	0.000000
14	10	0.000000	0.000000	0.000000
14	11	−0.000000	−0.000000	0.000000
14	12	−0.000000	0.000000	0.000000
14	13	−0.000000	−0.000000	0.000000
14	14	0.000000	0.000000	0.000000

[a] The CF parameters are only listed for positive values of q. The values with negative q are given by $B_{k-q} = (-1)^q B_{kq}^*$.

Table S32. Squared magnitudes of the projections of the *ab initio* CF eigenstates calculated for **27** onto angular momentum eigenstates characterized by a total angular momentum J = 15/2 and an angular momentum projection M.

M	KD1		KD2		KD3		KD4		KD5		KD6		KD7		KD8	
–15/2	0.708	0.250	0.000	0.000	0.000	0.042	0.000	0.000	0.000	0.000	0.000	0.000	0.000	0.000	0.000	0.000
–13/2	0.000	0.000	0.879	0.063	0.000	0.000	0.051	0.007	0.000	0.000	0.000	0.000	0.000	0.000	0.000	0.000
–11/2	0.030	0.010	0.000	0.000	0.004	0.896	0.001	0.000	0.001	0.056	0.001	0.001	0.000	0.001	0.000	0.000
–9/2	0.000	0.000	0.050	0.004	0.000	0.002	0.763	0.098	0.003	0.005	0.043	0.010	0.013	0.005	0.004	0.000
–7/2	0.001	0.000	0.000	0.000	0.000	0.053	0.003	0.001	0.008	0.742	0.020	0.035	0.027	0.078	0.001	0.030
–5/2	0.000	0.000	0.003	0.000	0.000	0.000	0.063	0.008	0.008	0.005	0.375	0.106	0.213	0.090	0.127	0.001
–3/2	0.000	0.000	0.000	0.000	0.000	0.003	0.000	0.001	0.002	0.153	0.008	0.051	0.104	0.351	0.003	0.321
–1/2	0.000	0.000	0.000	0.000	0.000	0.000	0.003	0.001	0.016	0.003	0.278	0.072	0.094	0.023	0.508	0.004
1/2	0.000	0.000	0.000	0.000	0.000	0.000	0.001	0.003	0.003	0.016	0.072	0.278	0.023	0.094	0.004	0.508
3/2	0.000	0.000	0.000	0.000	0.003	0.000	0.001	0.000	0.153	0.002	0.051	0.008	0.351	0.104	0.321	0.003
5/2	0.000	0.000	0.000	0.003	0.000	0.000	0.008	0.063	0.005	0.008	0.106	0.375	0.090	0.213	0.001	0.127
7/2	0.000	0.001	0.000	0.000	0.053	0.000	0.001	0.003	0.742	0.008	0.035	0.020	0.078	0.027	0.030	0.001
9/2	0.000	0.000	0.004	0.050	0.002	0.000	0.098	0.763	0.005	0.003	0.010	0.043	0.005	0.013	0.000	0.004
11/2	0.010	0.030	0.000	0.000	0.896	0.004	0.000	0.001	0.056	0.001	0.001	0.001	0.001	0.000	0.000	0.000
13/2	0.000	0.000	0.063	0.879	0.000	0.000	0.007	0.051	0.000	0.000	0.000	0.000	0.000	0.000	0.000	0.000
15/2	0.250	0.708	0.000	0.000	0.042	0.000	0.000	0.000	0.000	0.000	0.000	0.000	0.000	0.000	0.000	0.000

Table S33. Squared magnitudes of the projections of the *ab initio* CF eigenstates calculated for **28** onto angular momentum eigenstates characterized by a total angular momentum $J = 15/2$ and an angular momentum projection M.

M	KD1		KD2		KD3		KD4		KD5		KD6		KD7		KD8	
–15/2	0.941	0.023	0.000	0.000	0.034	0.000	0.001	0.000	0.000	0.000	0.000	0.000	0.000	0.000	0.000	0.000
–13/2	0.000	0.000	0.751	0.210	0.001	0.000	0.037	0.000	0.001	0.000	0.000	0.000	0.000	0.000	0.000	0.000
–11/2	0.033	0.001	0.002	0.001	0.927	0.001	0.006	0.000	0.028	0.001	0.000	0.000	0.000	0.000	0.000	0.000
–9/2	0.000	0.000	0.027	0.008	0.012	0.000	0.910	0.000	0.009	0.000	0.005	0.024	0.000	0.003	0.000	0.001
–7/2	0.001	0.000	0.000	0.000	0.023	0.000	0.015	0.000	0.831	0.031	0.006	0.024	0.038	0.016	0.014	0.001
–5/2	0.000	0.000	0.001	0.000	0.001	0.000	0.026	0.000	0.011	0.003	0.108	0.532	0.057	0.166	0.011	0.083
–3/2	0.000	0.000	0.000	0.000	0.002	0.000	0.003	0.000	0.072	0.001	0.049	0.001	0.384	0.173	0.287	0.028
–1/2	0.000	0.000	0.000	0.000	0.000	0.000	0.001	0.000	0.006	0.006	0.023	0.227	0.051	0.111	0.052	0.523
1/2	0.000	0.000	0.000	0.000	0.000	0.000	0.000	0.001	0.006	0.006	0.227	0.023	0.111	0.051	0.523	0.052
3/2	0.000	0.000	0.000	0.000	0.000	0.002	0.000	0.003	0.001	0.072	0.001	0.049	0.173	0.384	0.028	0.287
5/2	0.000	0.000	0.000	0.001	0.000	0.001	0.000	0.026	0.003	0.011	0.532	0.108	0.166	0.057	0.083	0.011
7/2	0.000	0.001	0.000	0.000	0.000	0.023	0.000	0.015	0.031	0.831	0.024	0.006	0.016	0.038	0.001	0.014
9/2	0.000	0.000	0.008	0.027	0.000	0.012	0.000	0.910	0.000	0.009	0.024	0.005	0.003	0.000	0.001	0.000
11/2	0.001	0.033	0.001	0.002	0.001	0.927	0.000	0.006	0.001	0.028	0.000	0.000	0.000	0.000	0.000	0.000
13/2	0.000	0.000	0.210	0.751	0.000	0.001	0.000	0.037	0.000	0.001	0.000	0.000	0.000	0.000	0.000	0.000
15/2	0.023	0.941	0.000	0.000	0.000	0.034	0.000	0.001	0.000	0.000	0.000	0.000	0.000	0.000	0.000	0.000

Chapter 7

References

1 R. Sessoli, D. Gatteschi, A. Caneschi and M. A. Novak, *Nature*, 1993, **365**, 141–143.

2 A. Caneschi, D. Gatteschi, R. Sessoli, A. L. Barra, L. C. Brunel and M. Guillot, *J. Am. Chem. Soc.*, 1991, **113**, 5873–5874.

3 R. Sessoli, H. L. Tsai, A. R. Schake, S. Wang, J. B. Vincent, K. Folting, D. Gatteschi, G. Christou and D. N. Hendrickson, *J. Am. Chem. Soc.*, 1993, **115**, 1804–1816.

4 M. N. Leuenberger and D. Loss, *Nature*, 2001, **410**, 789–793.

5 J. M. Clemente-Juan, E. Coronado and A. Gaita-Ariñoa, *Chem. Soc. Rev.*, 2012, **41**, 7464–7478.

6 K. Bader, D. Dengler, S. Lenz, B. Endeward, S. Da Jiang, P. Neugebauer and J. Van Slageren, *Nat. Commun.*, 2014, **5**, 1–5.

7 M. Shiddiq, D. Komijani, Y. Duan, A. Gaita-Ariño, E. Coronado and S. Hill, *Nature*, 2016, **531**, 348–351.

8 R. Sessoli, *Nature*, 2017, **548**, 400–401.

9 T. Komeda, K. Katoh and M. Yamashita, in *Molecular Technology*, Wiley-VCH Verlag GmbH & Co. KGaA, Weinheim, Germany, 2019, pp. 263–304.

10 J. L. Liu, Y. C. Chen and M. L. Tong, *Chem. Soc. Rev.*, 2018, **47**, 2431–2453.

11 C. V. Topping and S. J. Blundell, *J. Phys. Condens. Matter*, 2019, **31**, 013001.

12 D. N. Woodruff, R. E. P. Winpenny and R. A. Layfield, *Chem. Rev.*, 2013, **113**, 5110–5148.

13 R. A. Layfield, *Organometallics*, 2014, **33**, 1084–1099.

14 J. P. Durrant, R. Collins, M. He and R. A. Layfield, in *Handbook on the Physics and Chemistry of Rare Earths*, 2019, vol. 55, pp. 89–121.

15 M. J. Heras Ojea, L. C. H. Maddock and R. A. Layfield, in *Topics in Organometallic Chemistry*, 2019, vol. 64, pp. 253–280.

16 J. D. Rinehart and J. R. Long, *Chem. Sci.*, 2011, **2**, 2078–2085.

17 N. Ishikawa, M. Sugita, T. Ishikawa, S. Y. Koshihara and Y. Kaizu, *J. Am. Chem. Soc.*, 2003, **125**, 8694–8695.

18 J. Sievers, *Zeitschrift für Phys. B Condens. Matter*, 1982, **45**, 289–296.

19 H. Eschrig and M. Richter, *Solid State Commun.*, 1986, **59**, 861–864.

20 Y. C. Chen, J. L. Liu, L. Ungur, J. Liu, Q. W. Li, L. F. Wang, Z. P. Ni, L. F. Chibotaru, X. M. Chen and M. L. Tong, *J. Am. Chem. Soc.*, 2016, **138**, 2829–2837.

21 Y.-S. Ding, N. F. Chilton, R. E. P. Winpenny and Y.-Z. Zheng, *Angew. Chem. Int. Ed.*, 2016, 1–5.

22 F.-S. Guo, B. M. Day, Y.-C. Chen, M.-L. Tong, A. Mansikkamäki and R. A. Layfield, *Angew. Chem. Int. Ed.*, 2017, **56**, 11445–11449.

23 C. A. P. Goodwin, F. Ortu, D. Reta, N. F. Chilton and D. P. Mills, *Nature*, 2017, **548**, 439–442.

24 S. K. Gupta and R. Murugavel, *Chem. Commun.*, 2018, **54**, 3685–3696.

25 K. R. McClain, C. A. Gould, K. Chakarawet, S. J. Teat, T. J. Groshens, J. R. Long and B. G. Harvey, *Chem. Sci.*, 2018, **9**, 8492–8503.

26 A. B. Canaj, S. Dey, E. R. Martí, C. Wilson, G. Rajaraman and M. Murrie, *Angew. Chem. Int. Ed.*, 2019, **58**, 14146–14151.

27 F.-S. Guo, B. M. Day, Y.-C. Chen, M.-L. Tong, A. Mansikkamäki and R. A. Layfield, *Science*, 2018, **362**, 1400–1403.

28 J. D. Rinehart, M. Fang, W. J. Evans and J. R. Long, *J. Am. Chem. Soc.*, 2011, **133**, 14236–14239.

29 J. D. Rinehart, M. Fang, W. J. Evans and J. R. Long, *Nat. Chem.*, 2011, **3**, 538–542.

30 S. Demir, M. I. Gonzalez, L. E. Darago, W. J. Evans and J. R. Long, *Nat. Commun.*, 2017, **8**, 2144.

31 P. L. Arnold, M. W. McMullon, J. Rieb and F. E. Kühn, *Angew. Chem. Int. Ed.*, 2015, **54**, 82–100.

32 M. Nishiura, F. Guo and Z. Hou, *Acc. Chem. Res.*, 2015, **48**, 2209–2220.

33 T. Pugh, N. F. Chilton and R. A. Layfield, *Chem. Sci.*, 2017, **8**, 2073–2080.

34 J. Andrez, J. Pécaut, P.-A. Bayle and M. Mazzanti, *Angew. Chem. Int. Ed.*, 2014, **53**, 10448–10452.

35 F. T. Edelmann, J. H. Farnaby, F. Jaroschik and B. Wilson, *Coord. Chem. Rev.*, 2019, **398**, 113005.

36 J. Luzon and R. Sessoli, *Dalton Trans.*, 2012, **41**, 13556–13567.

37 F. S. Guo, A. K. Bar and R. A. Layfield, *Chem. Rev.*, 2019, **119**, 8479–8505.

38 L. Sorace, C. Benelli and D. Gatteschi, *Chem. Soc. Rev.*, 2011, **40**, 3092–3104.

39 L. Escalera-Moreno, J. J. Baldoví, A. Gaita-Ariño and E. Coronado, *Inorg. Chem.*, 2019, **58**, 11883–11892.

40 G. Wilkinson and J. M. Birmingham, *J. Am. Chem. Soc.*, 1954, **76**, 6210–6210.

41 J. M. Birmingham and G. Wilkinson, *J. Am. Chem. Soc.*, 1956, **78**, 42–44.

42 B. M. Day, F.-S. Guo and R. A. Layfield, *Acc. Chem. Res.*, 2018, **51**, 1880–1889.

43 P. Zhang, Y.-N. Guo and J. Tang, *Coord. Chem. Rev.*, 2013, **257**, 1728–1763.

44 C. R. Ganivet, B. Ballesteros, G. De La Torre, J. M. Clemente-Juan, E. Coronado and T. Torres, *Chem. Eur. J.*, 2013, **19**, 1457–1465.

45 R. A. Layfield, J. J. W. McDouall, S. A. Sulway, F. Tuna, D. Collison and R. E. P. Winpenny, *Chem. Eur. J.*, 2010, **16**, 4442–4446.

46 S. A. Sulway, R. A. Layfield, F. Tuna, W. Wernsdorfer and R. E. P. Winpenny, *Chem. Commun.*, 2012, **48**, 1508–1510.

47 F. Tuna, C. A. Smith, M. Bodensteiner, L. Ungur, L. F. Chibotaru, E. J. L. McInnes, R. E. P. Winpenny, D. Collison and R. A. Layfield, *Angew. Chem. Int. Ed.*, 2012, **51**, 6976–6980.

48 T. Pugh, F. Tuna, L. Ungur, D. Collison, E. J. L. McInnes, L. F. Chibotaru and R. A. Layfield, *Nat. Commun.*, 2015, **6**, 7492.

49 T. Pugh, V. Vieru, L. F. Chibotaru and R. A. Layfield, *Chem. Sci.*, 2016, **7**, 2128–2137.

50 T. Pugh, N. F. Chilton and R. A. Layfield, *Angew. Chem. Int. Ed.*, 2016, **55**, 11082–11085.

51 N. F. Chilton, D. Collison, E. J. L. McInnes, R. E. P. Winpenny and A. Soncini, *Nat. Commun.*, 2013, **4**, 1–7.

52 N. F. Chilton, *Inorg. Chem.*, 2015, **54**, 2097–2099.

53 Y. S. Meng, S. Da Jiang, B. W. Wang and S. Gao, *Acc. Chem. Res.*, 2016, **49**, 2381–2389.

54 L. Ungur and L. F. Chibotaru, *Chem. Eur. J.*, 2017, **23**, 3708–3718.

55 J. Liu, Y.-C. Chen, J.-L. Liu, V. Vieru, L. Ungur, J.-H. Jia, L. F. Chibotaru, Y. Lan, W. Wernsdorfer, S. Gao, X.-M. Chen and M.-L. Tong, *J. Am. Chem. Soc.*, 2016, **138**, 5441–5450.

56 S. K. Gupta, T. Rajeshkumar, G. Rajaraman and R. Murugavel, *Chem. Sci.*, 2016, **7**, 5181–5191.

57 S. Demir, J. M. Zadrozny and J. R. Long, *Chem. Eur. J.*, 2014, **20**, 9524–9529.

58 S. Demir, J. M. Zadrozny, M. Nippe and J. R. Long, *J. Am. Chem. Soc.*, 2012, **134**, 18546–18549.

59 C. A. Gould, K. R. McClain, J. M. Yu, T. J. Groshens, F. Furche, B. G. Harvey and J. R. Long, *J. Am. Chem. Soc.*, 2019, **141**, 12967–12973.

60 M. E. Fieser, M. R. Macdonald, B. T. Krull, J. E. Bates, J. W. Ziller, F. Furche and W. J. Evans, *J. Am. Chem. Soc.*, 2015, **137**, 369–382.

61 E. O. Fischer and W. Hafner, *Zeitschrift für Naturforsch. B*, 1955, **10**, 665–668.

62 M. Cesari, U. Pedretti, Z. Zazzetta, G. Lugli and W. Marconi, *Inorg. Chim. Acta*, 1971, **5**, 439–444.

63 F. A. Cotton and W. Schwotzer, *J. Am. Chem. Soc.*, 1986, **108**, 4657–4658.

64 P. D. Schumacher, J. L. Doyle, J. O. Schenk and S. B. Clark, *Rev. Anal. Chem.*, 2013, **32**, 159–171.

65 J. G. Brennan, F. G. N. Cloke, A. A. Sameh and A. Zalkin, *J. Chem. Soc., Chem. Commun.*, 1987, 1668–1669.

66 D. M. Anderson, F. G. N. Cloke, P. A. Cox, N. Edelstein, J. C. Green, T. Pang, A. A. Sameh and G. Shalimoff, *J. Chem. Soc., Chem. Commun.*, 1989, 53–55.

67 W. A. King, T. J. Marks, D. M. Anderson, D. J. Duncalf and F. G. N. Cloke, *J. Am. Chem. Soc.*, 1992, **114**, 9221–9223.

68 F. G. N. Cloke, *Chem. Soc. Rev.*, 1993, **22**, 17–24.

69 S.-S. Liu, J. W. Ziller, Y.-Q. Zhang, B.-W. Wang, W. J. Evans and S. Gao, *Chem. Commun.*, 2014, **50**, 11418–11420.

70 S.-S. Liu, B. Yan, Z.-S. Meng, C. Gao, B.-W. Wang and S. Gao, *Inorg. Chem. Commun.*, 2017, **86**, 312–314.

71 Y.-S. Meng, L. Xu, J. Xiong, Q. Yuan, T. Liu, B.-W. Wang and S. Gao, *Angew. Chem. Int. Ed.*, 2018, **57**, 4673–4676.

72 M. C. Cassani, Y. K. Gun'ko, P. B. Hitchcock and M. F. Lappert, *Chem. Commun.*, 1996, **3**, 1987–1988.

73 M. C. Cassani, D. J. Duncalf and M. F. Lappert, *J. Am. Chem. Soc.*, 1998, **120**, 12958–12959.

74 M. C. Cassani, Y. K. Gun'ko, P. B. Hitchcock, M. F. Lappert and F. Laschi, *Organometallics*, 1999, **18**, 5539–5547.

75 W. Huang, J. J. Le Roy, S. I. Khan, L. Ungur, M. Murugesu and P. L. Diaconescu, *Inorg. Chem.*, 2015, **54**, 2374–2382.

76 W. Huang, F. Dulong, T. Wu, S. I. Khan, J. T. Miller, T. Cantat and P. L. Diaconescu, *Nat. Commun.*, 2013, **4**, 1–7.

77 W. Huang and P. L. Diaconescu, *Dalton Trans.*, 2015, **44**, 15360–15371.

78 T. Arliguie, M. Lance, M. Nierlich, J. Vigner and M. Ephritikhine, *J. Chem. Soc., Chem. Commun.*, 1994, **179**, 847–848.

79 T. Arliguie, M. Lance, M. Nierlich, J. Vigner and M. Ephritikhine, *J. Chem. Soc., Chem. Commun.*, 1995, **44**, 183–184.

80 J. T. Miller and C. W. Dekock, *J. Organomet. Chem.*, 1981, **216**, 39–48.

81 T. Arliguie, M. Lance, M. Nierlich and M. Ephritikhine, *J. Chem. Soc., Dalton Trans.*, 1997, 2501–2504.

82 K. L. M. Harriman, J. J. Le Roy, L. Ungur, R. J. Holmberg, I. Korobkov and M. Murugesu, *Chem. Sci.*, 2017, **8**, 231–240.

83 W. Wernsdorfer, N. Aliaga-Alcalde, D. N. Hendrickson and G. Christou, *Nature*, 2002, **416**, 406–409.

84 J. J. Le Roy, L. Ungur, I. Korobkov, L. F. Chibotaru and M. Murugesu, *J. Am. Chem. Soc.*, 2014, **136**, 8003–8010.

85 A. Streitwieser and U. Mueller-Westerhoff, *J. Am. Chem. Soc.*, 1968, **90**, 7364–7364.

86 A. Greco, S. Cesca and W. Bertolini, *J. Organomet. Chem.*, 1976, **113**, 321–330.

87 N. M. Edelstein, P. G. Allen, J. J. Bucher, D. K. Shuh, C. D. Sofield, N. Kaltsoyannis, G. H. Maunder, M. R. Russo and A. Sella, *J. Am. Chem. Soc.*, 1996, **118**, 13115–13116.

88 M. D. Walter, C. H. Booth, W. W. Lukens and R. A. Andersen, *Organometallics*, 2009, **28**, 698–707.

89 A. Kerridge, R. Coates and N. Kaltsoyannis, *J. Phys. Chem. A*, 2009, **113**, 2896–2905.

90 O. Mooßen and M. Dolg, *Chem. Phys. Lett.*, 2014, **594**, 47–50.

91 S. Da Jiang, B. W. Wang, H. L. Sun, Z. M. Wang and S. Gao, *J. Am. Chem. Soc.*, 2011, **133**, 4730–4733.

92 H. Schumann, R. D. Köhn, F. W. Reier, A. Dietrich and J. Pickardt, *Organometallics*, 1989, **8**, 1388–1392.

93 S.-D. Jiang, S.-S. Liu, L.-N. Zhou, B.-W. Wang, Z.-M. Wang and S. Gao, *Inorg. Chem.*, 2012, **51**, 3079–3087.

94 K. R. Meihaus and J. R. Long, *J. Am. Chem. Soc.*, 2013, **135**, 17952–17957.

95 L. Ungur, J. J. Leroy, I. Korobkov, M. Murugesu and L. F. Chibotaru, *Angew. Chem. Int. Ed.*, 2014, **53**, 4413–4417.

96 M. Jeletic, P. H. Lin, J. J. Le Roy, I. Korobkov, S. I. Gorelsky and M. Murugesu, *J. Am. Chem. Soc.*, 2011, **133**, 19286–19289.

97 J. J. Le Roy, M. Jeletic, S. I. Gorelsky, I. Korobkov, L. Ungur, L. F. Chibotaru and M. Murugesu, *J. Am. Chem. Soc.*, 2013, **135**, 3502–3510.

98 J. J. Le Roy, I. Korobkov and M. Murugesu, *Chem. Commun.*, 2014, **50**, 1602–1604.

99 Y. S. Meng, C. H. Wang, Y. Q. Zhang, X. B. Leng, B. W. Wang, Y. F. Chen and S. Gao, *Inorg. Chem. Front.*, 2016, **3**, 828–835.

100 A. F. R. Kilpatrick, F.-S. Guo, B. M. Day, A. Mansikkamäki, R. A. Layfield and F. G. N. Cloke, *Chem. Commun.*, 2018, **54**, 7085–7088.

101 K. Kawasaki, R. Sugiyama, T. Tsuji, T. Iwasa, H. Tsunoyama, Y. Mizuhata, N. Tokitoh and A. Nakajima, *Chem. Commun.*, 2017, **53**, 6557–6560.

102 M. Xémard, S. Zimmer, M. Cordier, V. Goudy, L. Ricard, C. Clavaguéra and G. Nocton, *J. Am. Chem. Soc.*, 2018, **140**, 14433–14439.

103 L. Münzfeld, C. Schoo, S. Bestgen, E. Moreno-Pineda, R. Köppe, M. Ruben and P. W. Roesky, *Nat. Commun.*, 2019, **10**, 1–7.

104 F. Mares, K. O. Hodgson and A. Streitwieser, *J. Organomet. Chem.*, 1971, **28**, C24–C26.

105 H. C. Longuet-Higgins and L. E. Orgel, *J. Chem. Soc.*, 1956, 1969.

106 R. Criegee and G. Schröder, *Angew. Chem.*, 1959, **71**, 70–71.

107 W. Hübel, E. H. Braye, A. Clauss, E. Weiss, U. Krüerke, D. A. Brown, G. S. D. King and C. Hoogzand, *J. Inorg. Nucl. Chem.*, 1959, **9**, 204–210.

108 J. D. Dunitz, H. C. Mez, O. S. Mills and H. M. M. Shearer, *Helv. Chim. Acta*, 1962, **45**, 647–665.

109 R. P. Dodge and V. Schomaker, *Nature*, 1960, **186**, 798–799.

110 G. F. Emerson, L. Watts and R. Pettit, *J. Am. Chem. Soc.*, 1965, **87**, 131–133.

111 B. M. Day, F. S. Guo, S. R. Giblin, A. Sekiguchi, A. Mansikkamäki and R. A. Layfield, *Chem. Eur. J.*, 2018, **24**, 16779–16782.

112 A. Chakraborty, B. M. Day, J. P. Durrant, M. He, J. Tang and R. A. Layfield, *Organometallics*, 2020, **39**, 8–12.

113 A. Efraty, *Chem. Rev.*, 1977, **77**, 691–744.

114 R. Gleiter and D. B. Werz, *Organometallics*, 2005, **24**, 4316–4329.

115 D. Kumar, M. Deb, J. Singh, N. Singh, K. Keshav and A. J. Elias, *Coord. Chem. Rev.*, 2016, **306**, 115–170.

116 N. V. Shvydkiy and D. S. Perekalin, *Coord. Chem. Rev.*, 2017, **349**, 156–168.

117 C. Yu, W.-X. Zhang and Z. Xi, *Organometallics*, 2018, **37**, 4100–4104.

118 P. M. N. ĐỖ, N. G. Akhmedov, J. L. Petersen, B. S. Dolinar and C. Milsmann, *Chem. Commun.*, 2020, **56**, 5397–5400.

119 D. Patel, J. McMaster, W. Lewis, A. J. Blake and S. T. Liddle, *Nat. Commun.*, 2013, **4**, 2323.

120 A. Sekiguchi, T. Matsuo and H. Watanabe, *J. Am. Chem. Soc.*, 2000, **122**, 5652–5653.

121 A. Sekiguchi, M. Tanaka, T. Matsuo and H. Watanabe, *Angew. Chem. Int. Ed.*, 2001, **40**, 1675–1677.

122 T. Matsuo and A. Sekiguchi, *Bull. Chem. Soc. Jpn.*, 2004, **77**, 211–226.

123 J. Long, A. O. Tolpygin, A. V. Cherkasov, K. A. Lyssenko, Y. Guari, J. Larionova and A. A. Trifonov, *Organometallics*, 2019, **38**, 748–752.

124 J. Wu, S. Demeshko, S. Dechert and F. Meyer, *Chem. Commun.*, 2020, **56**, 3887–3890.

125 L. Ungur and L. F. Chibotaru, *Inorg. Chem.*, 2016, **55**, 10043–10056.

126 T. J. Marks and J. R. Kolb, *Chem. Rev.*, 1977, **77**, 263–293.

127 L. Sorace and D. Gatteschi, in *Lanthanides and Actinides in Molecular Magnetism*, Wiley-VCH Verlag GmbH & Co. KGaA, Weinheim, Germany, 2015, vol. 2, pp. 1–26.

128 R. Sessoli and A. K. Powell, *Coord. Chem. Rev.*, 2009, **253**, 2328–2341.

129 K. Liu, X. Zhang, X. Meng, W. Shi, P. Cheng and A. K. Powell, *Chem. Soc. Rev.*, 2016, **45**, 2423–2439.

130 Y. N. Guo, G. F. Xu, Y. Guo and J. Tang, *Dalton Trans.*, 2011, **40**, 9953–9963.

131 D. Reta and N. F. Chilton, *Phys. Chem. Chem. Phys.*, 2019, **21**, 23567–23575.

132 A. Castro-Alvarez, Y. Gil, L. Llanos and D. Aravena, *Inorg. Chem. Front.*, 2020, **7**, 2478–2486.

133 K. L. M. Harriman, J. L. Brosmer, L. Ungur, P. L. Diaconescu and M. Murugesu, *J. Am. Chem. Soc.*, 2017, **139**, 1420–1423.

134 J. R. Fritch, K. P. C. Vollhardt, M. R. Thompson and V. W. Day, *J. Am. Chem. Soc.*, 1979, **101**, 2768–2770.

135 F. P. Gabbaï, P. J. Chirik, D. E. Fogg, K. Meyer, D. J. Mindiola, L. L. Schafer and S. L. You, *Organometallics*, 2016, **35**, 3255–3256.

136 J. Luzon and R. Sessoli, *Dalton Trans.*, 2012, **41**, 13556–13567.

137 B. O. Roos, *Adv. Chem. Phys.*, 1987, **69**, 399–455.

138 P. Siegbahn, A. Heiberg, B. Roos and B. Levy, *Phys. Scr.*, 1980, **21**, 323–327.

139 B. O. Roos, P. R. Taylor and P. E. M. Siegbahn, *Chem. Phys.*, 1980, **48**, 157–173.

140 P. E. M. Siegbahn, J. Almlöf, A. Heiberg and B. O. Roos, *J. Chem. Phys.*, 1981, **74**, 2384–2396.

141 P. Å. Malmqvist, B. O. Roos and B. Schimmelpfennig, *Chem. Phys. Lett.*, 2002, **357**, 230–240.

142 L. F. Chibotaru and L. Ungur, *J. Chem. Phys.*, 2012, **137**, 064112.

143 L. Ungur, M. Thewissen, J.-P. Costes, W. Wernsdorfer and L. F. Chibotaru, *Inorg. Chem.*, 2013, **52**, 6328–6337.

144 C. Rudowicz and R. Bramley, *J. Chem. Phys.*, 1985, **83**, 5192–5197.

145 C. Rudowicz, *J. Chem. Phys.*, 1986, **84**, 5045–5058.

146 J. P. Durrant, B. M. Day, J. Tang, A. Mansikkamäki and R. A. Layfield, *Manuscript Submitted.*

147 C. A. P. Goodwin, D. Reta, F. Ortu, N. F. Chilton and D. P. Mills, *J. Am. Chem. Soc.*, 2017, **139**, 18714–18724.

148 C. A. P. Goodwin, D. Reta, F. Ortu, J. Liu, N. F. Chilton and D. P. Mills, *Chem. Commun.*, 2018, **54**, 9182–9185.

149 J. Liu, D. Reta, J. A. Cleghorn, Y. X. Yeoh, F. Ortu, C. A. P. Goodwin, N. F. Chilton and D. P. Mills, *Chem. Eur. J.*, 2019, **25**, 7749–7758.

150 G. B. Deacon, G. D. Fallon, C. M. Forsyth, S. C. Harris, P. C. Junk, B. W. Skelton and A. H. White, *Dalton Trans.*, 2006, 802–812.

151 S. Beaini, G. B. Deacon, M. Hilder, P. C. Junk and D. R. Turner, *Eur. J. Inorg. Chem.*, 2006, **2006**, 3434–3441.

152 J. M. Bakker, G. B. Deacon, C. M. Forsyth, P. C. Junk and M. Wiecko, *Eur. J. Inorg. Chem.*, 2010, **2010**, 2813–2825.

153 C. J. Weiss and T. J. Marks, *Dalton Trans.*, 2010, **39**, 6576–6588.

154 Z. Guo, R. Huo, Y. Q. Tan, V. Blair, G. B. Deacon and P. C. Junk, *Coord. Chem. Rev.*, 2020, **415**, 213232.

155 K. Mashima, Y. Nakayama, A. Nakamura, N. Kanehisa, Y. Kai and H. Takaya, *J. Organomet. Chem.*, 1994, **473**, 85–91.

156 K. Mashima and A. Nakamura, *J. Chem. Soc., Dalton Trans.*, 1999, 3899–3907.

157 C. Meermann, K. Ohno, K. W. Törnroos, K. Mashima and R. Anwander, *Eur. J. Inorg. Chem.*, 2009, 76–85.

158 K. Izod, S. T. Liddle and W. Clegg, *Inorg. Chem.*, 2004, **43**, 214–218.

159 W. J. Evans, J. W. Grate, H. W. Choi, I. Bloom, W. E. Hunter and J. L. Atwood, *J. Am. Chem. Soc.*, 1985, **107**, 941–946.

160 A. F. Williams, F. Grandjean, G. J. Long, T. A. Ulibarri and W. J. Evans, *Inorg. Chem.*, 1989, **28**, 4584–4588.

161 S. P. Constantine, G. M. De Lima, P. B. Hitchcock, J. M. Keates and G. A. Lawless, *Chem. Commun.*, 1996, **4**, 2421–2422.

162 Z. Łodziana, P. Błoński, Y. Yan, D. Rentsch and A. Remhof, *J. Phys. Chem. C*, 2014, **118**, 6594–6603.

163 S. M. Cendrowski-Guillaume, G. Le Gland, M. Nierlich and M. Ephritikhine,

Organometallics, 2000, **19**, 5654–5660.

164 H. Sitzmann, *Zeitschrift für Naturforsch. B*, 1989, **44**, 1293–1297.

165 K. E. du Plooy, J. du Toit, D. C. Levendis and N. J. Coville, *J. Organomet. Chem.*, 1996, **508**, 231–242.

166 T. K. Panda, M. T. Gamer and P. W. Roesky, *Organometallics*, 2003, **22**, 877–878.

167 N. M. Kuuloja, T. M. Kylmälä, J. E. Tois, R. E. Sjöholm and R. G. Franzén, *Synth. Commun.*, 2011, **41**, 1052–1063.

168 S. J. Connelly, W. Kaminsky and D. M. Heinekey, *Organometallics*, 2013, **32**, 7478–7481.

169 F. G. N. Cloke, M. C. Kuchta, R. M. Harker, P. B. Hitchcock and J. S. Parry, *Organometallics*, 2000, **19**, 5795–5798.

170 O. V. Dolomanov, L. J. Bourhis, R. J. Gildea, J. A. K. Howard and H. Puschmann, *J. Appl. Crystallogr.*, 2009, **42**, 339–341.

171 G. M. Sheldrick, *Acta Cryst.*, 2015, **A71**, 3–8.

172 G. M. Sheldrick, *Acta Cryst.*, 2015, **C71**, 3–8.

173 D. Gatteschi, R. Sessoli and J. Villain, *Molecular Nanomagnets*, Oxford University Press, Oxford, 2006.

174 C. Fonseca Guerra, J. G. Snijders, G. te Velde and E. J. Baerends, *Theor. Chem. Accounts Theory, Comput. Model. (Theoretica Chim. Acta)*, 1998, **99**, 391–403.

175 G. te Velde, F. M. Bickelhaupt, E. J. Baerends, C. Fonseca Guerra, S. J. A. van Gisbergen, J. G. Snijders and T. Ziegler, *J. Comput. Chem.*, 2001, **22**, 931–967.

176 J. P. Perdew, K. Burke and M. Ernzerhof, *Phys. Rev. Lett.*, 1996, **77**, 3865–3868.

177 E. van Lenthe, E. J. Baerends and J. G. Snijders, *J. Chem. Phys.*, 1993, **99**, 4597–4610.

178 E. van Lenthe, E. J. Baerends and J. G. Snijders, *J. Chem. Phys.*, 1994, **101**, 9783–9792.

179 E. van Lenthe, R. van Leeuwen, E. J. Baerends and J. G. Snijders, *Int. J. Quantum Chem.*, 1996, **57**, 281–293.

180 E. Van Lenthe and E. J. Baerends, *J. Comput. Chem.*, 2003, **24**, 1142–1156.

181 B. O. Roos, P. R. Taylor and P. E. M. Sigbahn, *Chem. Phys.*, 1980, **48**, 157–173.

182 P. E. M. Siegbahn, J. Almlöf, A. Heiberg and B. O. Roos, *J. Chem. Phys.*, 1981, **74**, 2384–2396.

183 P. Å. Malmqvist, B. O. Roos and B. Schimmelpfennig, *Chem. Phys. Lett.*, 2002, **357**, 230–240.

184 B. A. Heß, C. M. Marian, U. Wahlgren and O. Gropen, *Chem. Phys. Lett.*, 1996, **251**, 365–371.

185 O. Christiansen, J. Gauss and B. Schimmelpfennig, *Phys. Chem. Chem. Phys.*, 2000, **2**, 965–971.

186 L. F. Chibotaru and L. Ungur, *J. Chem. Phys.*, 2012, **137**, 064112.

187 L. Ungur and L. F. Chibotaru, in *Lanthanides and Actinides in Molecular Magnetism*, Wiley-VCH Verlag GmbH & Co. KGaA, Weinheim, Germany, 2015, pp. 153–184.

188 W. Kutzelnigg and W. Liu, *J. Chem. Phys.*, 2005, **123**, 241102.

189 P.-O. Widmark, P.-Å. Malmqvist and B. O. Roos, *Theor. Chim. Acta*, 1990, **77**, 291–306.

190 B. O. Roos, V. Veryazov and P.-O. Widmark, *Theor. Chem. Acc.*, 2004, **111**, 345–351.

191 B. O. Roos, R. Lindh, P.-Å. Malmqvist, V. Veryazov, P.-O. Widmark and A. C. Borin, *J. Phys. Chem. A*, 2008, **112**, 11431–11435.

192 N. Iwahara and L. F. Chibotaru, *Phys. Rev. B*, 2015, **91**, 174438.

193 N. Iwahara, L. Ungur and L. F. Chibotaru, *Phys. Rev. B*, 2018, **98**, 054436.